Study on the Variability of Planetary Boundary Layer (PBL), associated Aerosol Dynamics and Resultant Radiative Forcing - Analysis from In-Situ and Satellite Data

A THESIS SUBMITTED IN PARTIAL FULFILLMENT FOR THE DEGREE OF

DOCTOR OF PHILOSOPHY

IN THE SCHOOL OF EARTH, OCEAN, AND ATMOSPHERIC SCIENCES
GOA UNIVERSITY

By

SHAIKH NEHA SALIM
School of Earth, Ocean, and Atmospheric Sciences
Goa University
Taleigao Plateau, Goa, India - 403206

APRIL 2023

DECLARATION

I, Shaikh Neha Salim, hereby declare that this thesis represents work which has been carried out by me and that it has not been submitted, either in part or full, to any other University or Institution for the award of any research degree.

Place: Goa University, Goa, India

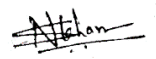

Date: Shaikh Neha Salim

CERTIFICATE

I hereby certify that the above Declaration of the candidate, Shaikh Neha Salim is true, and the work was carried out under my supervision.

Prof. Harilal B. Menon
Research Supervisor
Goa University
Goa, India - 403206

Dedicated

To

My Beloved Grandmother

As an expression of gratitude and remembrance for being the biggest source of inspiration to pursue higher studies,

I dedicate this to Late Mrs. Noorjahan Hassan Shaikh !!!

An Investment in Knowledge Pays the Best Interest!

- Benjamin Franklin

ACKNOWLEDGMENTS

Doctoral dissertation cannot be completed from the individual work alone. I feel humble in acknowledging my gratitude to all the individuals who inspired, encouraged, supported, and helped me throughout in the progress and completion of my thesis. I am thankful and indebted to all of them, especially all the teachers in my life.

First and foremost, I express my deep sense of gratitude and sincere thanks to my research supervisor Prof. Harilal B. Menon, one of the brilliant professors of our country. I have been immensely lucky and extremely privileged to get an opportunity to work under his supervision. I am highly indebted to his unparalleled mentorship, generosity, and immense patience towards me during these many years. His infectious enthusiasm and incredible knowledge with a wealth of wisdom has always inspired and taught me to continually strive for excellence in every aspect of life. Aside from having a huge positive impact of his consistent guidance on my academic development, his support, encouragement, reassurance, and patience in times of breakdown is personally very much appreciable. I thank him for all the valuable advice and useful discussions. Wholeheartedly, I am thankful to him for giving me the freedom and guidance to work independently and for always being there to hear and resolve difficulties for completing this doctoral work. Coming from pure physics background gave me some confidence over equations and analysis, but I had poor knowledge on subjects such as, geography, oceanography, weather, and global climate scenarios, and he was the first person to introduce me to these field areas. He has perfectly blended me into the subject of meteorology by developing an insight in me on the scientific approach of understanding the atmospheric datasets and their interpretations. I feel immensely blessed for the person I have evolved personally, professionally, and academically under his supervision. It has been an immense pleasure in working with him, for which I shall be grateful to him forever.

I am utterly grateful for all the support, patience, and encouragement received from Dr. N. V. P. Kiran Kumar from Space Physics Lab (SPL) of Vikram Sarabhai Space Centre (VSSC) of Indian Space Research Organization (ISRO) for his support and guidance for analyzing atmospheric datasets. I am thankful to him for the valuable advice and useful discussions. Thanks for always supporting me and influencing my scientific thinking and working abilities. Also, I am very thankful to Dr. K. Rajeev from SPL, ISRO for all the support received during my Ph.D. research work. I am sincerely grateful to my research committee, Dr. Ramesh Kumar MR (Former Scientist of National Institute of Oceanography, Goa) and Prof. V. M. Matta (Goa University, Goa). They generously helped me during all the review sessions with their valuable comments and suggestions which have significantly improved my work. I am immensely thankful to SPL-VSSC, ISRO for the fellowship and instrumentation support received throughout the tenure of PhD under the projects entitled "Aerosol Radiative Forcing Over India (ARFI)" and "Network of Observatories for Boundary Layer Experiments (NOBLE)" executed under the International Geosphere-Biosphere Programme (IGBP).

Ministry of Earth Sciences (MoES), Government of India funded institute "National Centre for Polar and Antarctica Research (NCPOR)", Goa is highly acknowledged for providing logistic support for successfully conducting atmospheric measurements in the Indian Ocean sector of Southern Ocean (ISSO) reaching up to Antarctica during three field campaigns (i.e., IXth, Xth, and XIth Indian Expeditions to Southern Ocean). My sincere thanks to all the scientists, fellow colleagues, and the crew members on-board ORV *S. A. Agulhas* for their ingenious support and cooperation in data retrieval. The sincere assistance of Dr. Shrivardan Hulswar and Mrs. Atiba Shaikh for onboard data collection are highly appreciated. My sincere thanks to Dr. Arjun Adhikari, all colleagues and administrative staff at School of Earth, Ocean, and Atmospheric Sciences, Goa University, for their assistance in the academic works and administrative support for the completion of my doctoral thesis from Goa University.

I duly acknowledge the NOAA Air Resources Laboratory (ARL) for the development of the HYSPLIT transport and dispersion model, the NASA Langley Atmospheric Science Data Center and Centre National d'Etudes Spatiales (CNES) for the provision of the Cloud-Aerosol Lidar and Infrared Pathfinder Satellite Observations (CALIPSO), and Climate Data Store (CDS) for providing meteorological dataset from fifth generation ECMWF atmospheric reanalysis product (ECMWF-ERA-5). My sincere thanks to Mr. Satya and Mr. Thamizharasan from Indian Institute of Science (IISc), Bangalore for their generous help onboard ship for radiosondes launches. In respect to adapt python programming skills, significant support received from Dr. Aditya Narayan from Gothenburg University, Sweden, either offline or online irrespective of the time has extremely helped me in analyzing the datasets used in this thesis. I am in debted to the assistance offered by each one who remain unmentioned here but made an invaluable contribution towards my PhD.

Good friends are another key to a successful PhD, and I couldn't have done this better without their distraction, motivation, scientific advice, delicious foods, and great friendship over the last many years and forevermore. I thank Fariha, Dilnawaz, Pingal, Shahin, Priyesh, Alok, Tariq. Finally, in closing, last but above all, I owe everything to my most beloved late grandmother and grandfather – for their immense love and efforts. Also, thanks go to my family members – especially to my father (Salim Shaikh), mother (Nazneen Shaikh), sisters (Firdous, Fatima, Ayesha), brother (Mohd. Amin), and the youngest motivation, my nephew (Mohd. Hasan) who are pillars of strength in my life. Lastly, my beloved husband Dr. Mohd. Tarique, I heartily thank him for his unwavering support, otherworldly patience, motivation, and immense love and affection during every phase of this process. Really these accomplishments would not have been possible without your support! Of the many other people who deserve to be named here, I can, but list a few: Mrs. Pushpa and Dr. Sundeep. I thank them all for making this possible for me.

ABSTRACT

This thesis has been formulated with a view to understanding and quantifying the structure and physical processes that drives climatically sensitive lower layers of the atmosphere i.e., atmospheric boundary layer (ABL) and its sub-layer i.e., atmospheric surface layer (ASL) over geographically and topographically distinct regions of the globe. Climatic significance of these layers lies in the fact that, since the evolution of life on earth, all type of weather patterns, residence of all forms of lives, occurrence of different extreme weather events, and release, suspension, trapping, and mobility of all forms of natural and anthropogenic emissions continuously occurs and are regulated within these layers. However, since the industrial revolution, an increasing anthropogenic input i.e., aerosols and trace gases have been continually fed in these layers. Because of this, significant perturbations have been forced in the inherent structure and functioning of these atmospheric layers. The nature of perturbations induced in these layers are dependent on the physiochemical properties of anthropogenic inputs and the meteorological settings specific to a geographic location. The perturbations driven by the coupled interaction between meteorology and anthropogenic inputs have portrayed both positive (warming) as well as negative (cooling) feedback on rapidly changing global climate. Realizing the importance of these atmospheric layers and their interaction with aerosols, and their role in regulating present and future earth's climate, Indian Space Research Organization has initiated an ISRO's Geosphere-Biosphere Programme. Under this Programme, two projects entitled "Network of Observatories for Boundary Layer Experiments (NOBLE)" and "Aerosol Radiative Forcing Over India (ARFI)" have been executed and the study conducted in this thesis constitutes a part of these projects.

In this thesis, a combination of in-situ, satellite-derived, and model simulated datasets have been used for studying the dynamic nature of ASL, ABL, and aerosols over two geographically diverse regions of the globe. The first region is a tropical coastal region (Goa, 15.46°N,

73.83°E) of the Indian sub-continent, while the other region is the Indian Ocean Sector of Southern Ocean (ISSO) extending up to the Prydz Bay region of Antarctica encompassing the area from 24°S to 68°S.

The thesis begins by presenting an investigation of the micrometeorological turbulence characteristics of ASL over a region in Indian sub-continent using yearlong in-situ measurements collected from 32 m tall meteorological tower installed in the campus of Goa University. Being a costal site, the region experiences meso-scale land-sea breeze circulation concurrent with diurnal transitions, however, on a seasonal scale, this regional land-sea breeze circulation is experienced during all seasons i.e., pre-monsoon, post-monsoon, and winter except during summer-monsoon. During monsoon, the prominent flow of sea breeze was due to the onset of strong south-west monsoonal winds, i.e., from sea to land. Observations revealed that the structure and turbulence characteristics of coastal ASL were modulated by land and sea breeze phenomenon. Analysis of surface layer fluxes of heat, energy, and momentum revealed strong diurnal and seasonal fluctuations that contributed to stabilized or destabilized atmospheric surface layer during daytime and nighttime in different seasons. Examination of surface layer turbulence showed that the flux-variance in the atmospheric surface layer were defined by Monin-Obukhov Similarity Theory (MOST), and the turbulence within the surface layer over the study site was highly dependent on varying stages of stability.

Considering significant variability of ABL characteristics above land and oceans, this thesis further dealt with studying the thermodynamic structure of marine ABL (MABL) over oceanic region extending from subtropics to poles. This study was performed by analyzing a total of 75 high resolution atmospheric soundings launched in the area covering from 24°S to 68°S and 57°E to 79°E during three cruises onboard ORV *S. A. Agulhas* during the austral summers of 2017, 2018, and 2020. The track of all three cruises, passed through crucial planetary scale oceanic fronts i.e., Sub-tropical front (STF), Sub-Antarctic Front (SAF), Polar Front (PF),

Southern Antarctic Circumpolar Current Front (SACCF), and Southern boundary of ACC (SB) formed in the Indian Ocean sector of Southern Ocean (ISSO) as well as in Prydz Bay region of coastal Antarctica. Special attention was taken while taking couple of soundings at/near each front. These soundings were analyzed to develop an understanding of the role of oceanic fronts in dictating the vertical structure and the thermodynamic stability of MABL. Associated to prevailing stability/instability of MABL over each frontal regions, the spatial and vertical distribution of clouds and inversions, along with the physical processes responsible for driving such a weather system over this oceanic domain were studied. Analysis revealed strong dependence of vertical stability of MABL on the air-sea temperature gradient, that varied sharply across distinct oceanic fronts of ISSO. In the subtropical frontal regions, surface based convective mixing and decoupling of thermodynamically coupled surface-based mixed layer were common. Unique distribution of clouds and inversions were recorded within the MABL of ISSO with presence of low level multi-layered thick clouds prominently in mixed phase (super-cooled water or ice). ISSO recorded frequent high level multiple inversions with the strongest multiple inversions observed in the polar front region. This unique cloud and inversion characteristics recorded in ISSO regions were the result of highly stabilized MABL governed by dominant physical process of condensation and precipitation regulated via strong advective motions of colder air masses. Higher MABL stability, intense winds, and its associated wind shear in the ISSO supported occurrences of numerous mesoscale low-pressure stormy cyclonic systems. Snow and fog were common phenomenon of the ISSO regions. Towards the end of south pole, in high-latitude ISSO and in coastal Antarctic region, soundings revealed occurrence of weak low-level surface-based convection while at upper altitudes above the surface, sublimation supported virga conditions accounted for the presence of ice or super-cooled water clouds.

Together with the detailed characterization of MABL from 24°S to 68°S, study in this thesis also describes the coupled effect of aerosol-boundary layer dynamics, and its associated effect on atmospheric radiative forcing and heating rate due to aerosols in the least explored oceanic region of ISSO. In-situ measurements of total columnar aerosol depth of composite aerosols and mass concentrations of black carbon aerosols along with surface and vertical meteorological measurements were used. Satellite-derived measurements describing vertical distribution of aerosols and cloud sub-types, model estimated radiative forcing and heating rate estimates provided a complete insight on aerosol-boundary layer dynamics occurring over the oceanic study region. These observations highlighted the crucial role played by thermodynamic state and the dynamics of MABL in governing the distribution, accumulation, and the dispersion of aerosols via several physical processes unique to each front. Analysis revealed surprisingly higher loading of dust, dusty marine, and black carbon aerosols over the oceanic polar front region. This higher loading was weakly attributed to long-range advection of anthropogenic origin aerosols while strongly attributed to the unique boundary layer dynamics specific to polar front region i.e., significant stabilization of MABL, occurrence of baroclinic instabilities, and intense mid-latitude cyclonic systems. These dynamics significantly contributed to higher accumulation and enhanced confinement of such anthropogenic as well as natural origin aerosols in this remote oceanic region. Such higher aerosol loading is alarming, as these aerosols can act as cloud condensation nuclei's, by which they may either enhance or reduce cloud formation depending upon their characteristic nature. If these aerosols are of solar irradiance absorbing type, atmospheric warming is likely to be enhanced, while scattering type of aerosols are likely to induce a cooling effect, and an overall consequence will lead to alterations in the radiative balance of this climatically sensitive oceanic region on a planetary scale.

List of Publications

Published Articles:

1. **Shaikh Neha Salim**, Arjun Adhikari, Atiba A. Shaikh, Harilal B. Menon, N. V. P. Kiran Kumar, K. Rajeev, 2023a. Aerosol-boundary layer dynamics and its effect on aerosol radiative forcing and atmospheric heating rate in the Indian Ocean sector of Southern Ocean. ***Science of The Total Environment***, 858: 159770, *http://dx.doi.org/10.1016/j.scitotenv.2022.159770*

2. **Shaikh Neha Salim**, Harilal B. Menon, N. V. P. Kiran Kumar, K. Rajeev, 2023b. Study of micrometeorological characteristics of the atmospheric surface layer over a tropical coastal station in Goa. ***Meteorology and Atmospheric Physics***, 135, 3, *https://doi.org/10.1007/s00703-022-00940-3*

3. **Shaikh Neha Salim**, Arjun Adhikari, Harilal B. Menon, N. V. P. Kiran Kumar, K. Rajeev, 2023c, Thermodynamic characteristics of Marine Atmospheric Boundary Layer across Frontal Regions of the Indian Ocean Sector of Southern Ocean based on Three Field Campaigns, ***Atmospheric Research***, 106678, *https://doi.org/10.1016/j.atmosres.2023.106678*

4. Atiba A. Shaikh, **Shaikh Neha Salim**, Harilal B. Menon, Aerosol and atmospheric dynamics over the tropical Indian ocean: A study from the IInd International Indian Ocean Expedition, ***Atmospheric Pollution Research***, 101797, *https://doi.org/10.1016/j.apr.2023.101797*

Manuscript under Preparation:

5. **Shaikh Neha Salim**, Arjun Adhikari, Harilal B. Menon, N. V. P. Kiran Kumar, K. Rajeev, Effect of synoptic forcing factors on the characteristics of Atmospheric Boundary Layer in Prydz Bay, East Antarctica, *In prep*. *for* ***Science of The Total Environment***

List of Conferences

1. Shaikh Neha Salim, Arjun Adhikari, Harilal. B. Menon, N. V. P. Kiran Kumar, K. Rajeev (2022) "Thermodynamic characteristics of marine atmospheric boundary layer over the Indian Ocean sector of the Southern Ocean (ISSO) based on three field campaigns", ***10th SCAR Open Science Conference***, organized virtually from 1st–10th August 2022. **(Oral Presentation)**

2. Shaikh Neha Salim, Harilal. B. Menon, N. V. P. Kiran Kumar (2021) "Spatiotemporal variability of the thermodynamic characteristics of the marine atmospheric boundary layer (MABL) over the Indian Ocean and Southern Ocean (15°N to 70°S)", ***EGU General Assembly*** organized virtually from 19th–30th April 2021. **(Oral Presentation)**

3. Shaikh Neha Salim, Harilal. B. Menon (2019) "Spatial Variability in the Thermodynamic Structure of the Atmosphere over the Indian Ocean sector of Southern Ocean up to Antarctica", ***Young Polar Scientist Meet*** during ***National Conference of Polar Sciences*** held at NCPOR, Goa on 21st August 2019. **(Oral Presentation)**

4. Shaikh Neha Salim, Harilal. B. Menon (2019) "Spatial Variability in the Thermodynamic Structure of the Atmosphere over the Indian Ocean sector of Southern Ocean until Antarctica", ***National Conference of Polar Sciences*** at NCPOR, Goa from 20th–22nd August 2019. **(Poster Presentation)**

5. Shaikh Neha Salim, Harilal. B. Menon, N. V. P. Kiran Kumar, K. Rajeev (2019) "Application of Monin-Obukhov Similarity Theory over a tropical coastal region of Goa, India" at ***20th National Space Science Symposium*** held at Savitribai Phule Pune University, Pune from 29th– 31st January 2019. **(Oral Presentation)**

6. Shaikh Neha Salim, Harilal. B. Menon, N. V. P. Kiran Kumar, A.A.A. Shaikh (2018) "Impact of surface layer energy and flux exchanges on the near surface black carbon (BC)

aerosols over a tropical coastal region Goa, India" at ***National Conference on "Aerosol Impact: Human Health to Climate Change: Indian Aerosol Science and Technology Association*** held at Indian Institute of Technology, IIT, Delhi from 26th–28th November 2018. **(Oral Presentation)**

Contents

List of Symbols

Acronyms

ARC	Agulhas Retroflection Current
ARF	Agulhas Return Front
ACC	Antarctic Circumpolar Current
AZ	Antarctic Zone
ABLE	Arctic Boundary layer Experiment
ABL	Atmospheric Boundary Layer
ASL	Atmospheric Surface Layer
ASSO	Australian sector of Southern Ocean
AT	Air temperature measured using slow response sensors fixed at three different heights i.e., 4 m, 18m, and 20 m on 32 m meteorological tower in Goa region
AWS	Automatic Weather Station
CCN	Cloud Condensation Nuclei
CL	Cloud Layer
CALIPSO	Cloud-Aerosol Lidar and Infrared Pathfinder Satellite Observation
CA	Coastal Antarctica
CVA	Conserved Variable Analysis
CBL	Convective Boundary Layer
ECMWF-ERA5	Fifth Generation Atmospheric Reanalysis Product developed by European Centre for Medium-Range Weather Forecasts
FIFE	First International Satellite Land Surface Climatology Project Field Experiments
GDAS	Global Data Assimilation System
GPS	Global Positioning System

HYSPLIT	Hybrid Single-Particle Lagrangian Integrated Trajectory
HAPEX	Hydrological and Atmospheric Boundary Layer Experiment
INP	Ice Nucleating Particle
IWC	Ice-Water Cloud
ISSO	Indian Ocean sector of Southern Ocean
SOE	Indian Southern Ocean Expedition
ISRO	Indian Space Research Organization
INV	Inversion
LUT	Look-Up Table
LNB	Low Noise Block down-converter
MABL	Marine Atmospheric Boundary Layer
MERRA	Modern-Era Retrospective analysis for Research and Applications
MOST	Monin-Obukhov Similarity Theory
NOAA-ARL	National Oceanic and Atmospheric Administration - Air Resources Laboratory
PF1	Northern Polar Front
SAF1	Northern Sub-Antarctic Front
NSTF	Northern Sub-Tropical Front
ORV	Oceanic Research Vessel
OT	Onward Track
OPAC	Optical Properties of Aerosols and Clouds
RL	Radiosonde Launch
RT	Return Track
SBDART	Santa Barbara DISORT Atmospheric Radiative Transfer
SACCF	Southern Antarctic Circumpolar Current Front
SB	Southern Boundary of Antarctic Circumpolar Current

SO	Southern Ocean
PF2	Southern Polar Front
SAF2	Southern Sub- Antarctic Front
SSTF	Southern Sub-Tropical Front
SBL	Stable Boundary Layer
STF	Sub-Tropical Front
STIO	Sub-Tropical Indian Ocean
SLW	Super-cooled Liquid Water
TIBL	Thermal Internal Boundary Layer
TS	Time Series Station
VSSC	Vikram Sarabhai Space Centre
UTC	Coordinated Universal Time

Variables

AOD	Aerosol Optical Depth
dT (T_{SST}-T_{air})	Air-Sea Temperature Gradient
ASY	Asymmetric Parameter
HR	Atmospheric Heating Rate
P	Atmospheric Pressure
ATM	Atmospheric Radiative Flux
BC	Black Carbon
DARF	Clear sky Direct Shortwave Aerosol Radiative Forcing
CF	Cloud Fraction
R^2_{Random}	Coefficient of Determination from Self-Correlation
r_{wT}	Correlation Coefficient for Heat Flux
r_{uw}	Correlation Coefficient for Momentum Flux

R^2_{data}	Correlation Coefficient for the Original Dataset
T_d	Dew Point Temperature
θ_e	Equivalent Potential Temperature
EIS	Estimated Inversion Strength
u^*	Frictional Velocity
z	Height Above the Surface
LCL	Lifting Condensation Level
LTS	Lower Tropospheric Stability
MSLP	Mean Sea Level Pressure
v	Meridional Wind Component
r	Mixing Ratio
Γ_m^{850}	Moist Adiabatic Potential Temperature Gradient at 850 hPa
τ	Momentum Flux
L	Obukhov Length
θ	Potential Temperature
SFC	Radiative Flux at Surface
TOA	Radiative Flux at the Top of Atmosphere
RH	Relative Humidity
r_s	Saturated Mixing Ratio
SP	Saturation Pressure
SST	Sea Surface Temperature
H	Sensible Heat Flux
SSA	Single Scattering Albedo
q	Specific Humidity
σ_u	Standard Deviation of Horizonal Wind Component

σ_v	Standard Deviation of Meridional Wind Component
σ_w	Standard Deviation of Vertical Wind Component
σ_T	Standard deviation of Sonic derived Air Temperature
z_o	Surface Roughness Length
T_{LCL}	Temperature at Lifting Condensation Level
T_{air}	Near surface air temperature measured using automated weather station fixed onboard ORV S. A. Agulhas in Southern Ocean
T	Vertical profiles of air temperature measured using radiosondes in Southern Ocean
T_*	Temperature Scaling Parameter
T_t	Travel Time
R^2_{diff}	True Physical Variance indicating Turbulent Process
USA-1	Ultrasonic Anemometer
e	Vapour Pressure of Air
w	Vertical Wind Component
θ_v	Virtual Potential Temperature
T_v	Virtual Temperature
WD	Wind Direction
WS	Wind Speed
u	Zonal Wind Component

Constants

g	Acceleration due to Gravity
ρ	Density of Air
R_a	Gas Constant for Dry Air
R_v	Gas Constant for Water Vapor

L_v	Latent Heat of Vaporization
C_p	Specific Heat of Air at Constant Pressure
v	Speed of Light
c	Speed of Sound
κ	Von Karman Constant

List of Figures

for wind direction). In these frontal regions lying in STIO domains, conditions when $SST > T_{air,}$ formation of well-evolved mixed layer structures are clearly seen from nearly uniform variation of θv and r, whereas during conditions of $SST < T_{air,}$ significantly stable boundary layers were observed. Owing to increased boundary layer stabilization, formation of well developed mixed layers are significatly reduced and higher stabilization is clearly depicted with gradual increasing (decreasing) tendency of θv and r. Highest MABL destabilization was observed in SSTF region, leading to formation of well-mixed layer extending up to the height of nearly 1,270 m altitude. 116

Figure 4.3 Mean vertical thermodynamic profiles of air temperature (T in ℃, blue line), dew point temperature (T_d in ℃, yellow line), relative humidity (RH in %, green line), virtual potential temperature (θv in K, red line bottom x-axis), mixing ratio (r in g kg^{-1}, magenta line, and upper magenta x-axis), wind speed (WS in m s^{-1}, black line bottom x-axis), and wind direction (WD in degrees, brown line, and upper brown x-axis) up to 4,000 m altitude for upper air soundings released in frontal regions of the Indian Ocean sector of Southern Ocean (ISSO). The left panel represents sounding profiles where $SST > T_{air}$ in (a) SAF1, (c) SAF2, (d) PF1, (f) PF2, and the right panel represents sounding profiles where $SST < T_{air}$ in (b) SAF1, (e) PF1, (g) PF2. The shaded area represents 1 standard deviation (except for wind direction). In these frontal regions of ISSO, significant stabilization of MABL could be observed, and in consequence, formation of well-developed mixed layers structures was observed to be significantly suppressed. A combined effect of highly stable boundary layer conditions, coupled with high-speed winds (>32 m s^{-1} within 4,000 m) advecting multiple types of air masses (cold/warm), aided by the formation of multiple cold/occluded fronts significantly enhances the frequent occurrences of low-pressure stormy cyclonic systems in these mid-latitude regions of ISSO. Polar jet streams inducing strong westerly winds exceeding 32 m s^{-1} within ~4,000 m altitudes could be observed in this figure. 120

Figure 4.4 Mean vertical thermodynamic profiles of air temperature (T in ℃, blue line), dew point temperature (T_d in ℃, yellow line), relative humidity (RH in %, green line), virtual potential temperature (θv in K, red line bottom x-axis), mixing ratio (r in g kg^{-1}, magenta line, and upper magenta x-axis), wind speed (WS in m s^{-1}, black line bottom x-axis), and wind direction (WD in degrees, brown line, and upper brown x-axis) up to 4,000 m altitude for upper air soundings released in frontal regions of High-latitude Southern Ocean (HLSO). The left panel represents sounding profiles where $SST > T_{air}$ in (b) SB and (d) CA while the right panel represents sounding profiles where $SST < T_{air}$ in (a) SACCF, (c) SB, and (e) CA. The shaded area represents 1 standard deviation (except for wind direction). In these frontal regions of HLSO, significant decrease in the heat and water vapor content within MABL could be seen with large decrease in the values of T and RH from close to surface to 5000 m altitude. Significant boundary layer stratification could be observed in SB region mainly due to different air masses advected by wind flow from differing directions near 60°S. In coastal Antarctic region of Prydz Bay, during conditions of $SST > T_{air}$ formation of shallow mixed layer structures could be observed with nearly uniform variation of θv and r up to few meters above the sea surface. 124

Figure 4.5 (a) Schematic diagram of conserved variables ($\theta e - q$) depicting the effect of physical processes such as convective mixing, precipitation/evaporation, and radiative heating/cooling in modifying the mixing line structure. (b) The $\theta e - q$ diagram obtained over ten frontal regions of ISSO. Obtained structure of air parcel motion in all frontal regions are colored as: surface – 1,000 m (in red), 1,000 – 2,000 m (in magenta), 2,000 – 3,000 m (in blue), and 3,000 – 4,000 m (in green). (c) The $\theta e - q$ diagram obtained over ten frontal regions of ISSO but for clear variability of structure of air parcel motion, scales for x and y axis are varied accordingly for each frontal regions with altitudes marked in km. In STIO region, instability induced by convective activities were prominent, and is depicted with fluctuations in both

List of Tables

Chapter 1

Introduction

1.1. Introduction

In the last few decades, rapid urbanization and industrialization have deteriorated the quality of air by increasing emissions of anthropogenic aerosols within the earth's atmosphere IPCC (2013); (Pörtner et al., 2022). As a result, the earth's atmosphere is presently loaded with abundant natural as well as anthropogenic aerosols (IPCC, 2014). An atmosphere in such a state poses serious threat to the environment, human health, and the regional as well as global climate (Licker, 2022). These aerosol species exhibits varying physiochemical and optical properties and are suspended in the air, predominantly in the lowest layer of the atmosphere lying close to the earth's surface (Lui et al., 2015). This layer is commonly referred as the planetary boundary layer (PBL) or atmospheric boundary layer (ABL) (Figure 1.1; Stull, 1988; Garratt, 1994). (Figure 1.1; Stull, 1988; Garratt, 1994). The ABL acts as a lid, shielding the free troposphere above from the direct impact of the processes taking place on the surface of Earth. Lives on earth, and all forms of weather and climate systems, occur in this layer through continuous exchanges of heat, momentum, moisture, aerosols, trace gases, and other pollutants (Carslaw et al., 2010; Li et al., 2017). All these exchanges are dynamically regulated as a function of atmospheric motions, stability, and convective potential of ABL (e.g., mechanical and thermal turbulence), depending upon the diurnal, spatial, temporal, and topographic characteristics of the region (Stull, 1988; Arya, 2001; Quan et al., 2020). The thermal stratification within ABL affects the intensity of thermal turbulence (i.e., buoyancy) as well as the depth of ABL (Miao et al., 2009). The resultant ABL structures and processes affect the quality of air by horizontal as well as vertical dispersion and transport of aerosols (Arya, 1999). Moreover, the shallowness of ABL is partly responsible for cases of severe atmospheric

pollution (Miao and Liu, 2019). Thus, the exchange of aerosols of varying physiochemical and optical properties driven by the ABL dynamics holds stronger potential to modulate incoming shortwave radiative fluxes, cloud microphysics, precipitation pattern, and the formation of cloud condensation nuclei's (CCN's) (Albrecht, 1989; Fan et al., 2016; Michibata, 2020). The coupled interaction of aerosols and meteorology plays a significant role in governing the regional as well as global pollution levels, the earth's total radiation budget, water cycle balance, and global climate on a larger scale (IPCC, 2013, 2014). Hence, a proper understanding of the dynamic characteristics of ABL (i.e., local ABL processes/structures) and aerosols (distribution, quantification, and regional transport) over regions of the varying geographical and meteorological conditions across the globe becomes extremely crucial.

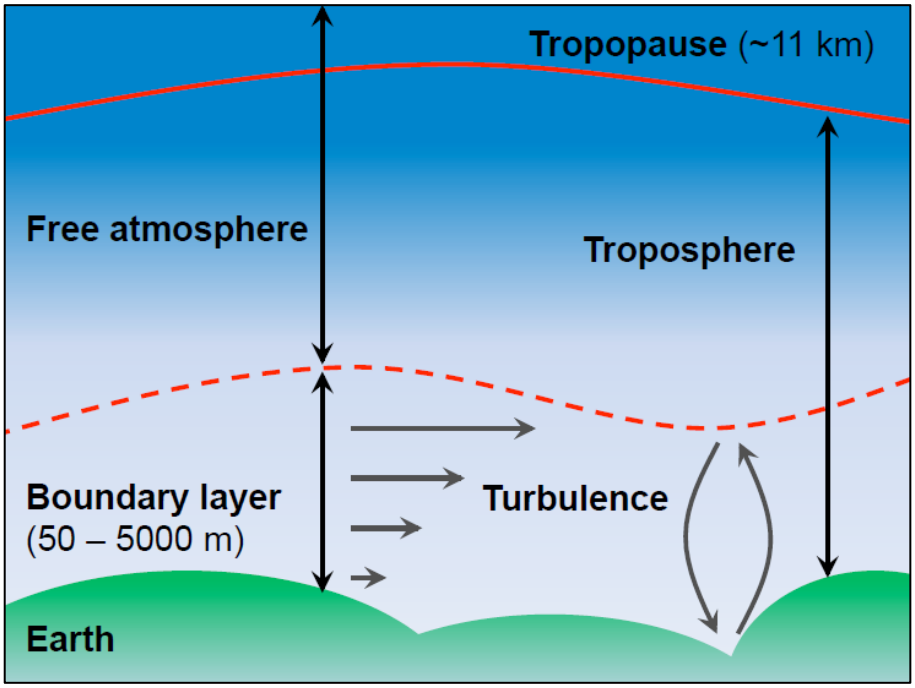

Figure 1.1 A schematic representation of the atmosphere, indicating the atmospheric boundary layer (ABL) lying in the lowest part of the troposphere (not drawn to scale). The bottom boundary conditions provided by the earth's surface induces exchanges of momentum, heat, and moisture fluxes. These exchanges drive mechanical (wind-induced shear) as well as

thermal (solar heating) turbulence distinguishing this layer from the rest of the atmosphere (Modified after Stull (1988)).

From this perspective, over the past several decades, numerous experiments using ground-based, tethersonde, balloon borne, and airborne measurements (Lenschow, 1973; Kaimal et al., 1976; Brost et al., 1982a; Nicholls, 1984; Garratt and Physick, 1985; Kunhikrishnan et al., 1993; Carter et al., 1995; Wilczak, J. et al., 1996; Luhar et al., 1998b; Rao and Fuelberg, 2000; Angevine et al., 2001; Stevens et al., 2002; Miller and Keim, 2003; Franchito et al., 2007; Plant and Keith, 2007; Hogan et al., 2009; Lothon et al., 2009; Tucker et al., 2010; Barlow et al., 2011; De Tomasi et al., 2011; Svensson et al., 2011; Busse and Knupp, 2012; Harvey et al., 2013; Jensen et al., 2016; Solanki et al., 2016a; Wang and Wang, 2016; Mahrt et al., 2018a; Manninen et al., 2018; Segal Rozenhaimer et al., 2018a; Barman et al., 2019; Chandra et al., 2019b; Pal and Lee, 2019; Solanki et al., 2019a; Truong et al., 2020a; Barman et al., 2021; LeMone et al., 2021) and theoretical and modelling based studies (Monin and Obukhov, 1954; Deardorff, 1974; Willis and Deardorff, 1974; Deardorff et al., 1980; Driedonks, 1982; Moeng, 1984; Moeng and Wyngaard, 1984; Pielke and Segal, 1986; Avissar and Pielke, 1989; Moeng and Wyngaard, 1989; Kaimal and Wyngaard, 1990; Hadfield et al., 1991a; Kaimal and Finnigan, 1994; Ramis and Romero, 1995; Angevine et al., 2001; Atkinson et al., 2001; Savijärvi and Matthews, 2004; Beare et al., 2006; Savijärvi, 2006; Basu et al., 2008a; Kumar et al., 2010; Holtslag et al., 2013; Hariprasad et al., 2014; Fedorovich et al., 2017; Efstathiou et al., 2018; Listowski et al., 2019; Edwards et al., 2020) have emerged from across the globe, including from different parts of India (Winston Prakash et al., 1993a; Ramachandran et al., 1994b; Gera et al., 1996; Manghnani et al., 2000; Satyanarayana et al., 2000; Prabha et al., 2002; Subrahamanyam, D.B. et al., 2003; Moorthy et al., 2005b; Kumar and Jain, 2006; Sandeep et al., 2014a; Solanki et al., 2016b; Sathyanadh et al., 2017; Anurose et al., 2018; Deb Burman et al., 2018; Nair et al., 2018; Kannemadugu, 2019; Prasad et al.,

2019; Rai and Pattnaik, 2019; Sudeepkumar et al., 2020; Reddy et al., 2021; Seetha et al., 2023). These studies were focused on addressing different aspects of ABL properties and its influence on weather and climate as well as probed into its role in pollutant dispersion over distinct land-based regions such as coastal, inland, arid, and mountainous terrains as well as over oceanic regions (Mohanty and Mohan Kumar, 1990; Parasnis and Morwal, 1991; Murty et al., 1996; Satyanarayana et al., 2003; Ramana, et al., 2004; Aravind et al., 2022). From these studies, ample of knowledge has emanated on the properties of boundary layer which varied significantly across spatiotemporal scales in regions of distint geographical and meteorological conditions (Augstein et al., 1974; Fitzjarrald and Garstang, 1981; Stull, 1988; Garratt, 1992; Kaimal and Finnigan, 1994; Miller and Keim, 2003; Talbot et al., 2007; Liu and Liang, 2010; Sandeep et al., 2014b; Solanki et al., 2016a; LeMone et al., 2019; Pal and Lee, 2019; Finnigan et al., 2020; Truong et al., 2020a). Bhumralkar (1975) highlighted that the diurnal variation of net radiative energy budget at the surface accounts for prominent diurnal variation of soil temperature over continental regions, which tend to produce strong diurnal variation of atmospheric temperature close to land surface (Arya, 1988). This, along with frictional effects leads to formation of atmospheric turbulent eddies over a wide range of temporal and spatial scales (Garratt, 1992). This aerodynamic drag between surface and overlying atmosphere is one of the main mechanisms by which energy is eventually dissipated in large-scale atmospheric motions. Studies further highlighted that turbulent kinetic energy varies diurnally and plays an important role in the vertical transfer of heat, momentum, water vapor, aerosols, pollutant gases and all other trace constituents prevailing within the boundary layer (Krishnamurti et al., 1998). In the entire atmospheric column, friction and turbulence intensity are strongest at the base of ABL, and it strongly determines the extend of vertical mixing of air inside the ABL as well as the transfer of moisture and pollutants between ABL and above free troposphere. These studies also highlighted that over continental regions, ABL height varies

from less than a few hundred meters during nocturnal cloud-free conditions to a few kilometers during clear sky conditions (Arya, 1988; Stull, 1988; Garratt, 1994; Foken and Napo, 2008). Land surface heterogeneities such as topographic settings, vegetation, soil type, surface reflectively, proximity of water bodies accounts for significant diurnal and spatial variations of ABL evolution (Stull, 1988; Bhat et al., 2003; Alappattu and Kunhikrishnan, 2010; Winning et al., 2017; Lang et al., 2018; Truong et al., 2020a). The entire exchange of energy (through both mechanical and radiation), mass, energy, aerosols, water vapor, and gases between earth's surface and free troposphere takes place through the ABL dynamics (Arya, 1988). The ABL regulates the dispersion of aerosols and pollutants from their source regions and the spatial extend of their transport (both horizontal and vertical) determines the air quality of any region (Moorthy et al., 1993; Parameswaran, 2001; Babu and Moorthy, 2002; Pradeep Kumar et al., 2003; Takashi et al., 2003; Moorthy et al., 2005a; Singh et al., 2005; Pant et al., 2006; Satheesh et al., 2006a; Satheesh et al., 2006b; Nair et al., 2007; Moorthy et al., 2008; Satheesh et al., 2008; Menon et al., 2011; Srivastava et al., 2011; Menon et al., 2014; Bharali et al., 2019; Govardhan et al., 2019). Also, enhanced trapping of aerosols and atmospheric pollutants within shallow ABL tend to dilute aerosol and pollutant concentrations in biosphere and enable their long-range transport to regional and planetary scales (Nair et al., 2007). Stable ABL enhances fog formations which likely increases trapping of moisture, thereby preventing its vertical ascent or vertical cloud development.

The ABL is observed to drastically vary over continental, coastal, marine, and regions of mountains terrains. Past studies over continental regions indicated that during fair-weather conditions, ABL exhibits a well-defined structure and pronounced diurnal evolution (Stull, 1988; Angevine et al., 2020). During the noontime, formation of well-developed convective boundary layer occurs due initiation of strong turbulent eddy motions (Lyons and Cole, 1973; Venkatram, 1977; Stull, 1988; Luhar et al., 1998a; Angevine et al., 2020). However, during

the late evening and nighttime, stable boundary layers are likely wherein wind shears strongly generate sporadic turbulence causing atmospheric mixing (Parameswaran et al., 1997; Babu and Moorthy, 2002; Cai et al., 2014; Kaser et al., 2017; Mahrt et al., 2018b) (Parameswaran et al., 1997; Babu and Moorthy, 2002; Cai et al., 2004; Kaser et al., 2017; Mahrt, 2017; (Beare et al., 2006). Boundary layer over continent shows drastic variations in ABL over the coast, inland, arid, or complex mountains terrains. As the coast acts a boundary separating drastically different land and oceanic surfaces, it exhibits inhomogeneous ABL (Kunhikrishnan et al., 1993; Ramachandran et al., 1994b). Contrasting to inland regions, coastal ABL is significantly regulated by several complex factors, among them few dominant factors are (a) differential heating between land and ocean surfaces which causes daytime sea-breeze and nighttime land-breeze to flow (b) difference in the surface friction between land and ocean influences the sea breeze front and its propagation (c) coastal circulation results in formation of thermal internal boundary layer, and (d) steep orographic features are common characteristics of coastal regions (Simpson et al., 1977; Garratt, 1990; Jeeva Prakash et al., 1992; Winston Prakash et al., 1993b; Miller et al., 2003; Steyn, 2003; Porson et al., 2007a, 2007c; Talbot et al., 2007; Kala et al., 2010a; Kala et al., 2011; Muppa et al., 2016; Anurose et al., 2018; Pal and Lee, 2019; Reddy et al., 2021; Yang et al., 2022). The combination of these factors regulates the coastal meteorology and coastal boundary layer properties. Another feature of boundary layer in coastal regions is the onset of land-sea breeze circulation. During daytime sea breeze, advection of cooler and moist marine origin air mass propagates over land which induces a net cooling effect in the atmosphere (Kuwagata et al., 1994), and tend to supply more moisture for enhanced cloud formations in the daytime evolving coastal convective boundary layer (Clarke et al., 2013). Further, in addition to coastal regions, most part of the earth's surface is covered by topographically complex regions, where boundary layer properties in these regions are dependent on the air flow modified by the horizontal pressure gradients imposed due to the

complexities laid by small hills to mountains range (Zeman and Jensen, 1987; Raupach and Finnigan, 1997; Monti et al., 2002; Abedi et al., 2021). Past studies highlighted that over similar complex terrains exhibiting steep terrains, pollutant transport can be modified by downslope gravity currents (Banta et al., 1990; Finnigan et al., 2020). As the wind flows over the hill, the vertical advection of air parcels is affected by the against restoring gravity induced force. However, if the hills are large enough to disturb the entire ABL and the overlying stable atmosphere above, then buoyancy effects play a crucial role for the vertical movement of air parcels (Kaimal and Finnigan, 1994).

On the other hand, open ocean regions experience high temporal and spatial homogeneity of temperature near the surface (Smith and Reynolds, 2004a). Unlike land surfaces where direct interaction of atmospheric flow and consequent heat exchange is largely limited within the canopy, the interaction between the atmosphere and ocean surface extends deeper down to several tens of meters (de Boyer Montégut et al., 2004a). Owing to remarkably higher heat capacity of ocean and the deeper mixing, diurnal variation of sea surface temperature (*SST*) in open ocean is mostly limited to less than 1-2 ℃; and the *SST* variations are quite prominent in larger spatial scales particularly in regions of upwelling, and over period of several days to seasonal and interannual scales at a given region. As a result, in open ocean regions, weak diurnal variations of ABL have been observed (Lui and Liang, 2010; Johnson and Ciesielski, 2017), while in longer period and large spatial domains, variations are noticed to be quite significant. Numerous studies have reported significant temporal variations of marine ABL (MABL) height due to variations in weather systems and large-scale circulations (Augstein et al., 1974; Bhat et al., 2000; Bhat et al., 2003; Ramana et al., 2004a; Alappattu and Kunhikrishnan, 2010; de Szoeke et al., 2017; Johnson and Ciesielski, 2017; Lang et al., 2018; Truong et al., 2020a). Typical variation of MABL height varies from less than 500 m to about 1000 m, depending on the state of atmospheric stability, occurrences of clouds, and weather

systems (Albrecht et al., 1995; Bhat et al., 2003; Bony and Dufresne, 2005; Truong et al., 2020a). The top of MABL is often characterized by the occurrence of boundary layer clouds (Albrecht et al., 1995; Bony and Dufresne, 2005). Presence of optically think marine stratocumulus clouds have been reported throughout the year over the southeast and northeast of Pacific, the southeast of Atlantic and southern Indian Ocean (Subrahamanyam and Radhika 2003b; Wood and Bretherton, 2004). Substantial diurnal variations in the frequency of occurrence and its geometric thickness have been observed, which critically influences the thermal structure and mixing within MABL (Bony and Dufresne, 2005). Also, decoupling of MABL has been observed using ship-borne radiosonde measurements in these oceanic regions (Bretherton, 1997; Bhat et al., 2000; Morwal and Seetaramayya, 2003; Subrahamanyam and Radhika 2003b; Alappattu and Kunhikrishnan, 2010; Jones et al., 2011; Johnson and Ciesielski, 2017; Zheng and Li, 2019a; Truong et al., 2020b). Remote sensing measurements have been used to describe the seasonal climatology of MABL height over global oceans (Ratnam and Basha, 2010; Guo et al., 2011; Ao et al., 2012; McGrath-Spangler and Denning, 2013; Winning et al., 2017; Vignon et al., 2019a). Few satellites based lidar measurements e.g., Cloud-aerosol Lidar and infrared pathfinder satellite observation (CALIPSO) have utilized aerosol and their mixing within ABL as a proxy to determine the MABL structure over different regions across the globe (Boers and Eloranta, 1986; Luo et al., 2014).

Considering the significance of ABL from weather and climate perspective, in the present thesis, the characteristics of ABL over continent as well as over the oceanic domain, together with the dynamics of aerosols and their radiative impacts have been examined. A tropical coastal region from the Indian continent has been chosen to study the micrometeorological turbulence characteristics of the lowest layer of ABL (i.e., the atmospheric surface layer (ASL). Followed by this study, the vertical thermodynamic characteristics of MABL and its coupled interaction with aerosols, and their effect on clear sky

direct shortwave radiative forcing and atmospheric heating rate have been studied over one of the least explored oceanic domains (i.e., Indian Ocean sector of Southern Ocean and Antarctica) encompassing between 24°S and 68°S.

1.2. The Atmospheric Boundary Layer (ABL)

The atmospheric boundary layer is defined as "lowest part of the troposphere which is strongly influenced by the presence of the earth's surface and responds to surface forcing with a time scale of about an hour or less" (Arya, 1988; Stull, 1988; Garratt, 1994; Kaimal and Finnigan, 1994). The nature of the surface (i.e., land or ocean), determines the characteristic properties of ABL. In addition, several other factors such as latitude (Garratt, 1982, 1994), time of day and year (Brümmer et al., 2012), and synoptic conditions, such as uneven heating/cooling of the surface of land or ocean and topography control the properties of ABL (Sinclair et al., 2010). Among all the aforementioned factors, the domain factors that decide the characteristic nature of ABL is the 24 hour cycle of incoming solar insolation (Arya, 2001). In response to which strong diurnal pattern of net radiative balance i.e., sum of upwelling and downwelling solar and terrestrial fluxes tends to induce a net surplus radiative energy at the surface and a net deficit radiative energy within the atmosphere. This imbalance in the net radiative energy is balanced by exchange of surface layer fluxes i.e., sensible, and latent heat flux via continuous motions of turbulent eddies occurring between the surface and the atmosphere (Trenberth et al., 2009; Mauder et al., 2020). Qualitatively, turbulent motion of eddies is defined as the chaotic motion of air consisting of three-dimensional eddies of different sizes interacting with one another. Large scale eddies having maximum energies generally reach a size of several thousand meters, then tend to progressively cascade down into small-scale eddies dissipating energy through frictional effects (Nieuwstadt, 1984; Garratt, 1994; Nieuwstadt and Duynkerke, 1996; Honnert et al., 2020). In addition to frictional effects, the aerodynamic drag between the surface and the atmosphere eventually causes energy dissipation of large-scale atmospheric

motions occurring within ABL. These microscale turbulence and large-scale motions determines the vertical mixing of air within ABL which directly or indirectly controls the exchange of moisture, aerosols, pollutant gases, and all trace constituents between the ABL and free troposphere (Caughey, 1984; Barthelmie et al., 2014; Honnert et al., 2020). Associated to these interactions, the energetics, and the thermodynamics of the atmosphere (ABL in particular) shows strong diurnal patterns which regulates the water content (in all forms i.e., vapor, solid, and liquid) within ABL, which indirectly plays a vital role in energy transfer, radiative balance, and formation of different weather systems and climate patterns (Chepfer et al., 2019). Collectively these factors, determine the depth of the ABL which typically varies from 50 m to 5,000 m altitude over regions varying geographically and topographically (Stull, 1988; Garratt, 1994; Foken and Napo, 2008). For instance, over land, its surface heterogeneities i.e., surface topography, surface reflectance, vegetation, type of soil, its proximity to water bodies accounts for prominent spatial and diurnal variations in the properties and height of ABL (Foken and Napo, 2008; Bou-Zeid et al., 2020). Thus, on the diurnal cycle, ABL height over land varies from few kilometers during clear sky daytime conditions to few hundred meters during nighttime conditions (Arya, 1988; Garratt, 1994; Foken and Napo, 2008). However, over ocean surface, the diurnal variation of ABL is significantly reduced due to less change in the sea surface temperature (*SST*), because of the higher specific heat capacity of water as well as due to vertical mixing of heat content over a larger depth of ocean water i.e., within oceanic mixed layer. As a result, significantly suppressed diurnal and short-scale spatial variations occurs within the MABL, thereby resulting in slow changes in the properties and height of MABL (Stull, 1988; Bhat et al., 2003; Alappattu and Kunhikrishnan, 2010; Winning et al., 2017; Lang et al., 2018; Truong et al., 2020a). In the past, numerous studies have been conducted to improve understanding on the characteristics of ABL, its interaction with aerosols, and its influence on weather and climate using in-situ and remote observations

(Lenschow, 1973; Kaimal et al., 1976; Brost et al., 1982a; Brost et al., 1982b; Garratt and Physick, 1985; Wilczak, J. et al., 1996; Luhar et al., 1998b; Rao and Fuelberg, 2000; Angevine et al., 2001; Stevens et al., 2002; Miller et al., 2004; Plant and Keith, 2007; Hogan et al., 2009; Tucker et al., 2010; Barlow et al., 2011; Harvey et al., 2013; Jensen et al., 2016; Wang and Wang, 2016; Tang et al., 2017; Mahrt et al., 2018a; Manninen et al., 2018; Barman et al., 2019; Chandra et al., 2019b; Solanki et al., 2019b; Pal et al., 2020; Truong et al., 2020b; Barman et al., 2021; LeMone et al., 2021; Solanki et al., 2021; Liu et al., 2022) and using theoretical formulations and model simulations (Monin and Obukhov, 1954; Deardorff, 1974; Willis and Deardorff, 1974; Deardorff, 1980; Deardorff et al., 1980; Driedonks, 1982; Moeng, 1984; Moeng and Wyngaard, 1984; Pielke and Segal, 1986; Wyngaard, 1990; Hadfield et al., 1991b; Ramis and Romero, 1995; Avissar and Schmidt, 1998; Atkinson et al., 2001; Savijärvi and Matthews, 2004; Cuxart et al., 2006; Savijärvi, 2006; Basu et al., 2008a; Basu et al., 2008b; Kumar et al., 2010; Holtslag et al., 2013; Hariprasad et al., 2014; Efstathiou et al., 2018; Angevine et al., 2020; Honnert et al., 2020; Liu et al., 2020; Liu et al., 2022).

1.2.1. Diurnal evolution of ABL

During clear sky conditions, ABL exhibits a clear diurnal cycle over land (Stull, 1988). Figure 1.2 indicates the variation occurring in an idealized boundary layer for 24 hours diurnal cycle. During clear sky conditions, the boundary layer tends to be unstably stratified. Incident solar forcing heats air closer to the earth's surface which makes near-surface air mass warmer and less dense than the surrounding air. This led to a positive buoyancy force, which raises the unstable and less dense air parcels vertically upwards forming convective thermals. These thermal drives convection in ABL forming daytime convective boundary layer (CBL). In CBL, these thermals efficiently mix heat, moisture, momentum, and mass. Owing to this, temperature

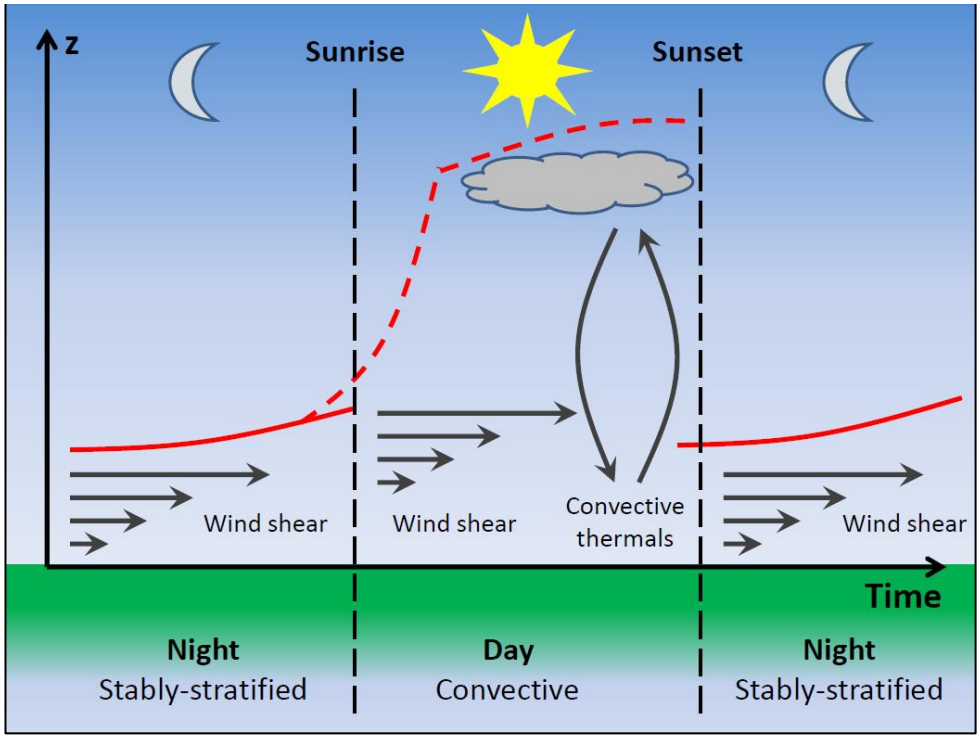

Figure 1.2 Diurnal evolution experienced by an idealized clear sky atmospheric boundary layer (ABL). The depth of diurnally evolved ABL is shown in a red solid and dashed line (Modified after (Stull, 1988)).

and wind profiles vary mostly uniformly with height in this layer. The convection is further inhibited in CBL by a strong inversion, where a sharp increase in temperature occurs, thus forming the top of CBL. The depth of this layer is determined by the strength of convection. In the tropics, it is typically 3,000 to 4,000 m while in mid-latitudes it is around 1,000 to 2,000 m altitudes (Stull, 1988). Figure 1.3 depicts a typical potential temperature (θ) profile for a convectively driven boundary layer. In addition to convective turbulence, turbulence driven by shear production by wind occurs in the boundary layer. This kind of turbulence is prominent in mid-latitudes and polar regions, where purely convective-driven turbulence is a rare phenomenon. The preceding description of the diurnal evolution of ABL is observed under clear sky conditions whereas the presence of stratocumulus clouds weakens the nature of the diurnal cycle (Lock, 2004). Weakening of ABL evolution is caused due to lesser

heating/cooling of the earth's surface causing a reduction in the buoyancy intensity under such cloudy/overcast conditions. As a result, the production of wind-driven shear dominates over

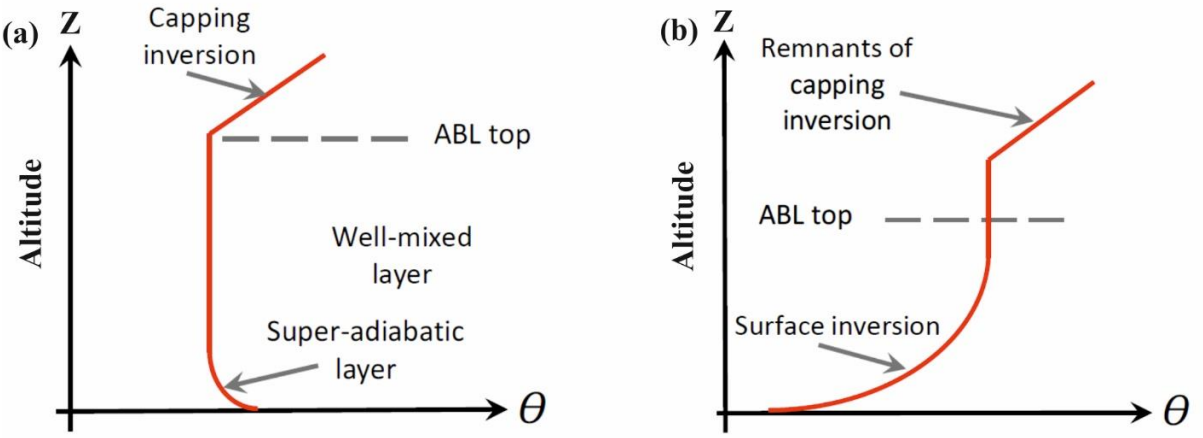

Figure 1.3 The typical profile of potential temperature in (a) a buoyancy-driven convectively formed ABL with a well-evolved mixed layer and (b) an idealized stably stratified ABL (Modified after (Stull, 1988)).

buoyancy effects. In contrast, the properties of nighttime ABL are very different from that of daytime ABL discussed above (Garratt, 1982; Högström et al., 1982). With sunset, the intensity of incoming shortwave radiation decreases, and longwave radiation is released by the earth's surface causing surface cooling. This leads to equivalent cooling of the overlying air parcels and decreases the temperatures of air closer to the surface. This results in a temperature inversion that extends a few meters above the surface. The presence of cool near-surface air mass indicates decreasing density of air with increasing height. In such an atmospheric state, weak buoyancy forces inhibit the rising of thermals and restrict vertical turbulent mixing in ABL (Smedman, 1988). This results in the formation of a stably stratified layer defined as a nocturnal boundary layer or stable boundary layer (SBL) (Figure 1.3). The depth of SBL varies typically between 50 to 500 m (Mahrt, 1998a). SBLs are not only formed during nighttime but also observed in regions of weak solar forcing or cloudy/overcast conditions. SBL is

prominently observed in mid-latitudes during wintertime, where the developed nighttime SBL sustains throughout the next day due to weaker solar insolation.

The diurnal cycle of the boundary layer discussed above is an idealized cycle that holds over a homogenous land surface, but these conditions are rarely observed in reality. Real boundary layers depart from idealized boundary layers based upon surface topography and heterogeneity of land and water surfaces. Also, clouds and synoptic surface forcing complicates real atmospheric boundary layer structure. Therefore, understanding the structure and characteristics of ABL over regions of land having distinct topographic features as well as over global open ocean water surfaces has been an important topic of research for few decades (Avissar and Pielke, 1989; Mahrt, 2010).

1.2.2. Features of Atmospheric Boundary Layer over varying geographic domains

1.2.2.1. Coastal Atmospheric Boundary Layer

The coast is the boundary seperating two drastically different surfaces i.e., land and ocean surfaces. Due to the differential diurnal heating/cooling occurring over these surfaces the coastal atmospheric boundary layer represents an inhomogeneous atmospheric boundary layer. Because of its inhomogeneity several meso-scale processes such as land-sea breeze circulation, formation of mesoscale eddies and the typical structure of winds are common phenomenon within coastal ABL. Due to these phenomena, a complex pattern of air flow occurs within the coastal ABL (Wilczak et al., 1991; Ulrickson, 1992). The structure of ABL over the coast largely depends upon the shoreline curvature and coastal topography (i.e., mountains near the coast) (Klipp and Mahrt, 2003). The characteristics of coastal ABL are observed to be distinct from an inland boundary layer because of the unique nature of the local atmospheric circulation (Prakash et al., 1992; Ramachandran et al., 1994a; Miller et al., 2003; Venkata Ramana et al., 2004; Wichink Kruit et al., 2004; Porson et al., 2007b; Talbot et al., 2007; Kala et al., 2010b; Muppa et al., 2012; Anurose et al., 2018; Pal and Lee, 2019). Depending upon the unique air

circulation within the coastal ABL, occurrence of land-sea breeze occurs on the diurnal scale. Land-sea breeze is a local convective circulation formed due to the differential heating of the land and sea surface, and on account of which sea breeze occurs during the daytime while land breeze during the nighttime. The intensity and the horizontal as well as vertical range of land-sea breeze largely depends upon several factors i.e., synoptic flow, the temperature difference between the land-sea surface, air temperature, and moisture profile of the boundary layer (Garratt, 1990; Reddy et al., 2021). Another unique layer peculiarly formed within coastal atmospheric boundary layer is the formation of thermal internal boundary layer (TIBL) which results due to the occurrence of land-sea breeze circulation. Although during the last few decades, the significance of land-sea breeze has been understood over coastal ABL, but the proper knowledge required to accurately model the effects of land-sea breeze interaction with the coastal ABL and associated large-scale weather system has still remains inadequate, and needs more attention (Melecio-Vázquez et al., 2018; Pal and Lee, 2019).

1.2.2.2. Marine Atmospheric Boundary Layer

The marine atmospheric boundary layer is formed above the surface of open oceans where within few meters of ocean water significant homogeneity of temperature exists on spatial and temporal scale (Smith and Reynolds, 2004b). The interaction between atmosphere and the ocean surface is much deeper with its effect penetrating to several tens of meters unlike the interaction between atmosphere and land surface which is limited to few meters or within the canopy (de Boyer Montégut et al., 2004b; Holte et al., 2017). Also, unlike over land, over the ocean surfaces, due to higher heat capacity of ocean and the deeper oceanic mixing, the diurnal variation of sea surface temperature (*SST*) is less and limited to < 1℃ to 2 ℃ in shorter spatial scales, but on considering larger spatial scales, upwelling regions, seasonal and interannual scales, the variation in *SST* is significant (Sandeep et al., 2014b). Thus, on short spatial scales, the diurnal pattern of ABL over ocean i.e., MABL is much weaker than the diurnal pattern of

ABL over land (Liu and Liang, 2010; Johnson and Ciesielski, 2017). In open ocean regions that experiences unique weather systems and large-scale circulations the temporal variations in MABL are much prominent (Augstein et al., 1974; Bhat et al., 2003; Ramana et al., 2004b; Alappattu and Kunhikrishnan, 2010; de Szoeke et al., 2017; Johnson and Ciesielski, 2017; Lang et al., 2018; Truong et al., 2020a). In general, the typical variation of MABL height is from < 500 m to about 1,000 m which depends upon the atmospheric stability conditions, presence of clouds and nature of weather pattern specific to that region (Bhat et al., 2003; Morwal and Seetaramayya, 2003; Subrahamanyam and Radhika 2003a; Ramana et al., 2004b; Alappattu and Kunhikrishnan, 2010; Liu and Liang, 2010; Ratnam and Basha, 2010; Guo et al., 2011; Jones et al., 2011; Ao et al., 2012; Johnson and Ciesielski, 2017). At the top of the MABL, common presence of boundary layer marine stratocumulus clouds occurs (Albrecht et al., 1995; Bony and Dufresne, 2005). These boundary layer clouds vary significantly on diurnal scale with variations in their frequency of occurrences and thickness and have substantial influence in determining the thermal structure and mixing within the MABL (Bony and Dufresne, 2005). The structural characteristics of MABL can be accurately understood using ship-based radiosonde observations (Bhat et al., 2000; Seidel et al., 2010; Lang et al., 2018; Truong et al., 2020a) and lidar profiles (Melfi et al., 1985; Luo et al., 2014). Also, remote measurements and GPS radio occultation techniques have been used in recent years to understand the structure of MABL over global oceans (Von Engeln et al., 2005; Ratnam and Basha, 2010; Guo et al., 2011; Ao et al., 2012; Luo et al., 2014; Winning et al., 2017).

1.3. Characteristics of Atmospheric Surface Layer (ASL)

The atmospheric surface layer (ASL) is defined as the lowest layer within ABL wherein momentum flux lies within 90% of its surface estimates (Stull, 1988; Arya, 2001). As a result, this layer is also referred to as a nearly constant flux layer. This layer is characterized by an increase in wind speed with height caused due to surface frictional effects Figure 1.4. Thus, in

this layer shear-induced turbulence strongly controls the transfer of heat, momentum, and mass within the air column. In addition, turbulence in this layer is dependent on characteristics such as atmospheric stability and surface roughness (Stull, 1988). In ASL, elements of surface roughness (such as forests, houses, buildings, etc.) plays a vital role in shaping wind and temperature profiles specific to regions, which in turn influences the magnitude of surface layer fluxes of energy and momentum. Atmospheric stability in this layer plays a distinct role. Unstable stratification caused by excess surface heating from the solar radiation supports the rising of buoyant thermals and high energy eddies and augments turbulent air

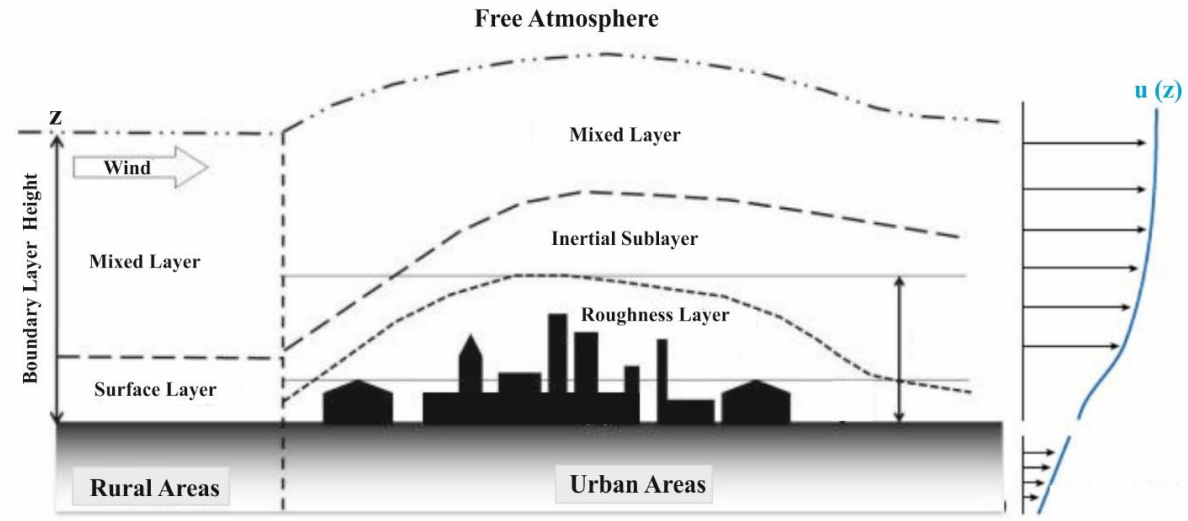

Figure 1.4 The ABL includes an atmospheric surface layer (ASL) that comprises of a roughness layer and an inertial sub-layer, where the classical Monin-Obukhov Similarity Theory (MOST) could be applied for surface layer micrometeorological studies (Modified after Kohler et al., 2012).

motions in this layer. At nighttime, the intensity of thermal eddies is negligible which leads to stably stratified conditions with reduced turbulent air motions. Thus, a time series of mean airflow and turbulent fluctuations of wind and temperature over a fixed surface of a particular region is widely examined to determine the regional airflow characteristic of ASL.

The surface layer turbulence and fluxes have been mathematically represented by the Naiver-Stokes equation. For practical application, the nature of surface-layer turbulence is given by the equation of the budget of turbulent kinetic energy (e),

$$\frac{\partial \bar{e}}{\partial t} = -U\frac{\partial \bar{e}}{\partial x} - \overline{u'w'}\frac{\partial U}{\partial z} - \frac{\partial \overline{w'e'}}{\partial z} - \frac{1}{\rho}\frac{\partial \overline{w'p'}}{\partial z} + \frac{g}{T_v}\frac{\partial \overline{w'T'_v}}{\partial z} - \nu\frac{\overline{\partial u'_\iota u'_\iota}}{\overline{\partial x_J \partial x_J}} \quad 1.1$$

Here, u', v', and w' represent the fluctuation of zonal (x-direction), meridional (y-direction) and vertical (z-direction) wind velocity components. $\bar{e}$ represents turbulent kinetic energy (e) normalized by air density (ρ) while e' represents the instantaneous contribution to e. These variables are given as,

$$\bar{e} = \frac{E}{\bar{\rho}} = \frac{1}{2}\overline{u'_\iota u'_\iota} \quad 1.2$$

$$e' = \frac{1}{2}u'_\iota u'_\iota \quad 1.3$$

T_v represents virtual temperature, is defined as $T(1 + 0.61q)$ where T is the air temperature and q are specific humidity. In the equation, 1.1, the first term on the right side indicates the rate of change of turbulent kinetic energy due to advection, the second term indicates the shear production term, the third term represents flux divergence of turbulent kinetic energy, and the fourth term is the pressure flux divergence, the fifth term is buoyancy loss or turbulent energy production, and the last term indicates loss of turbulent energy due to viscosity.

The complication of this equation, however, prohibits its applicability to direct use. Hence, a simplified version of this equation is formulated which eliminates a few independent parameters for readily accessible solutions. Among the introduced simplifications, an assumption of steady-state, horizontally homogenous, lateral symmetry in turbulence and flux variations w.r.t average meridional wind direction are considered. Considering this assumption, a modified form of the above equation appears as follows,

$$-\overline{u'w'}\frac{\partial U}{\partial z} = \frac{g}{T_v}\frac{\partial \overline{w'T'_v}}{\partial z} - \varepsilon + \bar{I} \qquad 1.4$$

Here, $\bar{I}$, the last term on the right side of equation 1.4 is the imbalance term which is the sum of pressure flux divergence and energy flux terms. Generally, this imbalance term is neglected during most of the conditions for surface layer turbulence and flux studies (Geernaert, 2003).

1.3.1. Theoretical framework for the turbulence characteristics of Atmospheric Surface Layer

Monin-Obukhov 1941, has proposed a robust theoretical framework referred as Monin-Obukhov Similarity Theory (MOST) to better understand the turbulent characteristics of ASL (Pahlow et al., 2001; Foken, 2006). This theory was partly developed for important applications such as pollutant dispersion calculations, and modelling regional weather and climate (Leelőssy et al., 2014). The basis for the formulation of this theory was laid on the assumption that groups of dimensional variables can be arranged in terms of the functional form of relationship with the airflow. Also, another assumption of the surface layer to be nearly a constant flux layer for exchange of heat, moisture, momentum, and mass. According to this theory, the fundamental variables needed to depict surface layer processes are the surface heat flux ($-\overline{u'w'}$), buoyancy factor ($w'T'_v$), frictional velocity (u^*) and the height above the ground surface. According to this theory, any bulk quantity (X) satisfying assumptions of MOST can be written in the form of,

$$\frac{\partial X}{\partial z} = \frac{X^*}{kz}\phi_x \qquad 1.5$$

Here, X can be U, T_v, q and other such variables. X^* represents the vertical turbulent flux of quantity X normalized by scaling parameter u^* and ϕ_x is a quantity representing stratification. This equation when used for wind speed and temperature can be written in the form of,

$$\frac{\partial U}{\partial z} = \frac{U^*}{kz}\phi_U \qquad 1.6a$$

$$\frac{\partial T}{\partial z} = \frac{T^*}{kz}\,\phi_T \qquad 1.6b$$

Here, κ is the von Karman constant having a value of 0.4. The functions ϕ_U and ϕ_T are presented in terms of the dimensionless parameter (*z/L*), where *z* represents the height of measurements and *L* is the Monin-Obukhov length. This stability parameter is defined as the ratio of shear-induced turbulent energy to buoyancy induced turbulent energy written in the form of,

$$z/L = \frac{gkz\,\overline{w'T'_v}}{T_v\,u^{*3}} \qquad 1.7$$

Integrating equation 1.7 to equation 1.6a will give a logarithmic wind speed profile upon assigning wind speed at a small height (z_0) above the surface as zero. This height is generally referred to as roughness length.

Another application of MOST is in deriving co-efficient for variation of surface layer fluxes with respect to varying conditions of surface layer stability. These coefficients are mostly derived using time series field observations conducted on fixed stable platforms having minimum distortion to surface layer airflow. The significance of deriving flux coefficients is that theoretically they negligibly depend on wind speed but show relatively higher dependence on surface roughness, height, and ranges of atmospheric stability conditions based on the region's topographic features. These coefficients are obtained during near-neutral conditions with a height of around 10 m or above, to compare with other region datasets as well as to integrate these parameterizations in regional models.

1.4. Aerosols and their impact on earth's climate

Aerosols are small solid, or liquid or mixed phased particles dispersed in the atmosphere. Their size varies in the range between a few nanometres to 100 μm (Albrecht, 1989). Depending upon the generation mechanism, aerosols are classified as primary and secondary aerosols, where both are produced from natural as well as anthropogenic sources. Primary anthropogenic

aerosols are composed of anthropogenic dust released from land cover, burning of fossil fuel, biomass, and agricultural remains and secondary aerosols are generated by homogenous nucleation of gases and condensation of vapors released from combustion process (Seinfeld and Pandis, 1998). These suspended aerosols are removed from the atmosphere mainly by two processes, i.e., dry and wet removal mechanisms (Slinn and Slinn, 1981). Dry removal is accomplished by the transport of aerosols through gravitational settling, impaction, and diffusion (Zhang and Vet, 2006). These processes are dependent upon surface characteristics and the state of the atmosphere (Hoppel et al., 2002). The wet removal process involves cloud scavenging (below- and in-cloud) (Seinfeld and Pandis, 1998). These aerosols once released to the atmosphere can remain suspended according to their residence time. Their residence time is dependent upon aerosol size, altitude of occurrence, optical properties, production mechanism, dry or wet deposition, growth and transformation defined by meteorological conditions (Pruppacher and Klett, 1978; Jaenicke, 1980; Hofmann and Rosen, 1981).

These aerosols are known to affect life on earth, weather, and global climate (IPCC, 2014). The climate implication of aerosols can be classified into two categories i.e., climate forcing and climate feedback (Hansen et al., 1997). Aerosol-induced climate forcing is the alterations in the earth's total radiation balance caused by abnormal absorption and scattering of irradiances. This forcing is strongly dependent upon the optical properties of aerosols. Climate feedback on the other end is the atmospheric response to these climate forcing. These responses are mainly meteorological responses such as changes in atmospheric and surface temperatures, and the pattern of wind and precipitation across the globe (IPCC, 2013; Pörtner et al., 2022). Such climatic implications of aerosols are often quantified using the concept of atmospheric radiative forcing, which provides the change in net solar flux at the top of the atmosphere, surface, and its resultant within the column of atmosphere with and without the presence of aerosols (Hansen et al., 1997). Using this quantification, a negative radiative

forcing implies that the present aerosols induce cooling of the atmosphere while a positive radiative forcing implies warming relative to the initial state of the atmosphere without aerosols (Ramaswamy et al., 2019).

Important climate implications of these aerosols are over mid-and high latitude regions. Over these regions, in-situ generation of anthropogenic aerosols is negligible hence presently serves as a natural laboratory on the earth's surface. However, from the past few years, increased urbanization has been attributed to the deposition of anthropogenic aerosols over these regions through long-range advective mechanisms (Noone and Clarke, 1988). These advected aerosols strongly influences the radiative balance of these pristine regions by direct and indirect interactions with solar radiation (Clarke and Noone, 1985; Chýlek et al., 1996). In addition, they tend to alter the surface albedo over poles (Clarke and Noone, 1985; Warren and Clarke, 1990). For example, the deposition of absorbing aerosols over higher reflecting surfaces such as ice or snow reduces overall albedo causing the melting of ice shelves, which is an another major climate concern in the mid-and high latitude regions (Hansen and Nazarenko, 2004).

1.5. Previous studies

1.5.1. On the micrometeorological characteristics of the Atmospheric Surface Layer (ASL) over continental regions of different geographical and meteorological settings

In 1941, Kolmogorov proposed a significant contribution towards understanding the structure of microscale turbulence and energy exchange processes occurring within ASL. In the same year, Obukhov 1941, proposed the distribution of spectral energy in a turbulent airflow in ASL. Monin 1970, further contributed to the field of ASL studies and the contribution is now known as the Monin-Obukhov Similarity Theory (MOST) (Foken, 2006). The period from 1960 to 1970 was a golden age for boundary layer studies when conditions of several boundary layers

(such as convective, stable, and neutral layers) were studied, and more importantly, the verification of surface layer similarity theory was conducted. One of the pioneering turbulence studies was carried out in an international experiment known as International Turbulence Comparison Experiment (ITCE-1976 & 1981). This experiment illustrated that more reliable observations are required on the variances of surface layer variables to examine errors associated with point measurement techniques (Francey and Garratt, 1981; Dyer et al., 1982; Tsvang et al., 1985). Other major land-based surface layer experiments were the Kansas experiment in 1968 and the Minnesota experiment conducted in 1973 (Kaimal and Wyngaard, 1990), the Wangara experiments in 1967 (Clarke et al., 1971), First International Satellite Land Surface Climatology Project (ISLSCP), field Experiments (FIFE) in 1983 (Sellers et al., 1988; Betts, 1992), boundary layer experiment in 1983 (Stull and Eloranta, 1984), Amazon and Arctic Boundary layer Experiment (ABLE) in 1985; 1987 (Harriss et al., 1990), Hydrological and Atmospheric Boundary Layer Experiment (HAPEX) in 1986 (André et al., 1986). These experiments improved the understanding of the spectral and co-spectral behavior of ASL (Kaimal et al., 1972; Wyngaard and Coté, 1972; Kaimal, 1973). Also, the terms contributing to turbulent kinetic energy equations were defined (Wyngaard and Coté, 1972; Deardorff and Willis, 1985; Moeng and Wyngaard, 1989). (Högström, 1996) examined the prime issues in the then understanding of surface layer physics. (Al-Jiboori et al., 2001; Zhang, L. et al., 2001) presented the importance of similarity theory over regions of varying topographic features. Following the importance, several studies were proposed that tested the applicability of the Monin-Obukhov similarity theory over homogeneous surfaces (Monin and Yaglom, 1975; Sorbjan, 1989a; Wyngaard, 2010), complex terrains (Moraes et al., 2005; Yue et al., 2015), heterogeneous terrains (Babić et al., 2016), Greenland, Arctic pack ice and Antarctica (Forrer and Rotach, 1997; Grachev et al., 2007, 2013). On the foundation laid by MOST, globally several statistical-based turbulence studies were also carried out over urban land-based regions

(Grimmond and Oke, 1999; Roth, 2000; Wood et al., 2010; Trini Castelli and Falabino, 2013; Trini Castelli et al., 2014). Notably, most of these experiments were conducted over oceanic domains and over mid-latitude regions whereas such studies over coastal land-based regions were comparatively sparse (Singha and Sadr, 2012; Grachev et al., 2014; Grachev et al., 2015; Grachev et al., 2018b; Grachev et al., 2021).

Over tropical regions, similar experimental campaigns and field measurements quantifying turbulence of ASL were least. However, over the tropical Indian sub-continent, a such studies were conducted at different geographical locations like inland regions (Goel and Srivastava, 1990; Sivaramakrishnan et al., 1992; Kailas and Goel, 1996; Rao et al., 1996), semi-arid regions (Krishnan and Kunhikrishnan, 2002; Solanki et al., 2016a; Solanki et al., 2019a; Nagi Reddy et al., 2021), complex terrains (Solanki et al., 2016a; Barman et al., 2019; Solanki et al., 2019a; Solanki et al., 2021) and coastal regions (Prakash et al., 1992; Kunhikrishnan et al., 1993; Ramachandran et al., 1994a; Ramana et al., 2004a). Most of the above-mentioned studies were carried out in campaign mode during a particular season, but a study by Ramachandran et al. (1994a); Namboodiri et al. (2014); Prasad et al. (2019) has demonstrated that surface layer parameters varies with seasons over Indian sub-continent. To better understand surface layer turbulence over a specific region, it becomes essential to know the seasonal surface layer turbulence characteristics. These kinds of studies hold important applications for modelling regional-scale turbulent exchanges and pollutant dispersion in numerical models over regions of varying geography, topography, and meteorology.

Among different geographical regions, coastal boundary/surface layers are of great interest considering the occurrence of strong mesoscale circulations and diurnal advection of heat and moisture across the land-sea interface (Kunhikrishnan et al., 1993; Ramachandran et al., 1994a; Miller and Keim, 2003; Miller et al., 2003; De Tomasi et al., 2011; Anurose et al., 2018; KiranKumar et al., 2019; Pal and Lee, 2019; Davis et al., 2020). Several national and

international studies have been conducted in the past to understand the structure and dynamics of coastal boundary layers. Results from these studies highlighted that coastal ABL exhibits significant spatial variations in the nature of surface transfers due to variations in surface roughness, vegetation, soil temperature, and soil moisture (Shao et al., 1991; Shao, 1992; Angevine, 2008; Crosman and Horel, 2010; De Tomasi et al., 2011; Rajeev et al., 2016; Melecio-Vázquez et al., 2018; Wei et al., 2018; Davis et al., 2020). Among unique features of coastal ABL is the formation of thermal internal boundary layer which forms because of the advection of cold and moist marine air over the coastal regions (Garratt, 1990; Lyons et al., 1995; Ramana et al., 1999; Wei et al., 2018). This layer inhibits development of convective boundary layer and vertical mixing of aerosols over coastal regions (Parameswaran, 2001). Studies have highlighted the crucial role of sea and land breeze circulation on the evolving structure of boundary layer and pollutant dispersions in coastal regions (Neumann and Mahrer, 1971; Parameswaran et al., 1997; Parameswaran, 2001; Miller and Keim, 2003; Srinivas et al., 2007; Talbot et al., 2007; Reddy et al., 2021). Ramachandran et al. (1994b) have conducted a study over western coastal station for different wind directions (northeast monsoon & southwest monsoon) and have reported that the variation of frictional velocity with height was mainly attributed to variation of surface roughness which varied with the wind direction associated with the sea breeze. The flow structure of the coastal ABL strongly depends on the curvature of the shoreline and the topography of the coast like the presence of mountains along the coast (Klipp and Mahrt., 2003). Nair et al. (2018) presented in detail the variability of mixed boundary layer height over Thiruvananthapuram, one of the tropical coastal sites of India. This study has also reported seasonal variability in the thickness of three different sublayers of the coastal boundary layer, namely, mixed layer, turbulent flow, and sea breeze flow over Thumba region. Renju et al. (2017) highlighted the potential of microwave radiometer profiler observations to investigate the continuous diurnal evolution of boundary layer height over a

tropical coastal region manifested by a thermal internal boundary layer (TIBL) at much better time resolution. Using two-years of field observations, a reliable climatology on the diurnal evolution of the vertical thickness of sea breeze flow and vertical thickness of ABL in association with the altitudes of lifting condensation level have been provided over Thiruvananthapuram (8.5°N, 76.9°E), a coastal station on the western coastline of the Indian sub-continent (Anurose et al., 2018). Detailed studies focused on boundary layer have been carried out at 18 different coastal locations in United States along the Gulf of Mexico and the Atlantic and Pacific Oceans which revealed the impact of the advection of marine airmass on the boundary-layer height at coastal areas during onshore flow (Pal and Lee, 2019). The ABL height during offshore and onshore flow differed by 100 – 1500 m, depending on location and season (Pal and Lee, 2019). In recent years, model simulations involving inputs of surface physics such as surface temperature, soil moisture, evaporation, and evapotranspiration has significantly improved the representation of coastal ABL development, structure, and onset timings of land-sea breeze circulation (Zhang et al., 2008).

1.5.2. On the characteristics of Marine Atmospheric Boundary Layer and its interactions with aerosols in Southern Ocean and Antarctica

Southern Ocean (SO) is one of the unique oceans on earth due to remarkable differences in geographic location and extreme weather conditions driven by the strong Antarctic Circumpolar Current (ACC) (Carslaw. et al., 2013; Ghan et al., 2013). This massive current causes water mass to flow from west to east around Antarctica. Thus, Antarctica forms the southern boundary of SO while the southern extent of the Pacific, Atlantic, and Indian Oceans forms the northern boundary of SO. ACC is also associated with several fronts that separate tropical, sub-tropical, sub-Antarctic, and polar water masses (Belkin and Gordon, 1996). Among other oceans, SO constitutes about 20% of global waters (Haumann et al., 2020). SO is widely reported to have a crucial impact on global climate, beginning from energy

distribution across the globe, signatures of temperature anomalies, and influence on global rainfall pattern to huge storage of carbon dioxide in the atmosphere (Rintoul, 2018). A detailed review of the climate system of the Antarctic and the Southern Ocean is provided in Mayewski et al. (2009). Despite its strong effect on global climate, SO remains largely under-explored due to fewer field observation. Conducting frequent year-round field experiments are hindered by the remoteness and harsh weather conditions of this oceanic region. Hence, poses a great challenge for weather and climate models to accurately simulate SO atmosphere, which is known to be highly distinct from the atmosphere across the globe. For instance, the absence of terrestrial inhabitants and anthropogenically produced aerosols results in a highly pristine atmosphere over SO. Thus, the likelihood of natural aerosols is prominently high while long-range advection is likely to feed anthropogenic aerosols over SO. Such conditions make SO a natural laboratory to study the dynamics of the boundary layer, its interaction with aerosols, and the effect of their coupled dynamics on the SO radiation budget. In this context, during the last two-decades several field campaigns have been conducted that sampled different sectors of SO (such as Australian and African sectors) however, the Indian Ocean sector of SO (ISSO) is still under-sampled for boundary layer and aerosol based studies (McFarquhar et al., 2021).

Previous campaigns conducted in different sectors of SO (mostly were in the Australasian sector) with a major focus on understanding the dynamics, structure, and characteristics of the boundary layer are provided in Table 1 in (Schmale et al., 2019). The observations from these campaigns have greatly helped in improving understanding of the climatology of MABL over SO as well as in identifying biases in satellite retrievals and climate models projecting SO (Haynes et al., 2011; Huang et al., 2014; Naud et al., 2014; Hande et al., 2015). These observations revealed the complex structure of the boundary layer aggravated by the dominance of multilayer low-level clouds (Russell et al., 1998; Jensen et al., 2000; Mace et al., 2009; Chubb et al., 2016). Specifically, revealed the presence of shallow low-level

boundary layer clouds at altitudes as low as 500 m (Haynes et al., 2011; Huang et al., 2012; Lang et al., 2018; Roh et al., 2020; Truong et al., 2020a). These clouds were reported to be highly saturated in mixed supercooled water or ice phase (Russell et al., 1998; Alexander and Protat, 2018; Mace and Protat, 2018a; Alexander et al., 2021; Humphries et al., 2021; Mace et al., 2021; Vignon et al., 2021). These studies also revealed the presence of large biases in the shortwave radiation budget attributed to such unique low-level cloud coverage which generates anomalies in the absorption of irradiance and limits the accuracy of remote measurements (Haynes et al., 2011; Huang et al., 2012; Muhlbauer et al., 2014; Huang et al., 2015a; Huang et al., 2015b; Mace and Protat, 2018a; Lang et al., 2020; Mace et al., 2020; Roh et al., 2020; Mace et al., 2021). These biases were particularly reported over SO storm track region where extra-tropical fronts and cyclones have been associated with the occurrence of low altitude clouds (Orsi et al., 1995; Belkin and Gordon, 1996; Simmonds., 2003; Hoskins and Hodges, 2005; Haynes et al., 2011). These biases can be minimized by improving the parameterization of boundary layer structure, cloud microphysics, and low-level thermodynamic characteristics based on well-resolved in-situ measurements (Huang et al., 2015a; Furtado and Field, 2017).

In addition to the characterization of SO boundary layer, campaigns have been executed on studying aerosol dynamics over SO (mostly in the Australasian sector). Details on these campaigns are provided in Table 1 of Kremser et al. (2021). However, the Indian Ocean sector of SO has been explored to some extent in terms of aerosol characterization during a series of Indian expeditions to the Southern Ocean (Menon et al., 2015; Hulswar et al., 2020; Srivastava et al., 2021). Observations from all these campaigns revealed large spatiotemporal variability in the concentration, and optical and radiative properties of aerosols over SO (Quinn et al., 2000; Moorthy et al., 2003; Moorthy et al., 2005a; Moorthy et al., 2008). These observations also revealed that natural aerosols predominantly act as cloud condensation nuclei (CCNs) (Gras, 1995; Yum and Hudson, 2005). However, studies across the globe have revealed that

the distribution and characteristics of residing aerosols and their ability to alter climate are strongly governed by atmospheric dynamics controlled by prevailing meteorology and regional/long-range advective mechanisms (Alroe et al., 2020; Zhang et al., 2021). These governing dynamical variables are majorly marine atmospheric boundary layer (MABL), physical processes (such as convection and advection), state of atmospheric stability, characteristics of clouds and inversions unique to the SO region (Groß et al., 2015; Rittmeister et al., 2017; Thomas et al., 2022). Thus, to examine alterations induced by aerosols on radiation budget, weather pattern and climate systems of SO and Antarctica, accurate quantification of aerosol-boundary layer interactions are required (McFarquhar et al., 2021).

1.6. Research Gap, motivation, and aims of the present study

As described in the earlier sections, extensive studies have been carried out on the ABL characteristics, structure, and their changes at various spatial and temporal scales, along with its crucial role in governing regional weather and global climate based on field observations and modelling approaches (Ramdas and Atmanathan, 1932; Monin and Obukhov, 1954; Lenschow, 1973; Deardorff, 1974; Willis and Deardorff, 1974; Kaimal et al., 1976; Deardorff, 1980; Deardorff et al., 1980; Kaimal and Finnigan, 1994; Narasimha and Prasad, 1994; Atkins et al., 1995; Wilczak, J.M. et al., 1996; Luhar et al., 1998b; Rao and Fuelberg, 2000; Angevine et al., 2001; Miller et al., 2003; Hogan et al., 2009; Lothon et al., 2009; Mahrt, 2010; Tucker et al., 2010; Barlow et al., 2011; De Tomasi et al., 2011; Busse and Knupp, 2012; Harvey et al., 2013; Lothon et al., 2014; Jensen et al., 2016; Solanki et al., 2016a; Wang and Wang, 2016; Mahrt et al., 2018a; Manninen et al., 2018; Segal Rozenhaimer et al., 2018b; Barman et al., 2019; Chandra et al., 2019a; LeMone et al., 2019; Pal and Lee, 2019; Solanki et al., 2019b; Truong et al., 2020a; Barman et al., 2021). However, despite substantial progress made in these areas, major gaps still exist in proper understanding of the characteristics of ABL/ASL, its diurnal evolution, the nature of ABL/ASL under conditions of varying background

meteorological, topographical, and geographical conditions in regions across the globe. Coupled variations between these factors affects the characteristics of ABL/ASL such as., solar radiative flux, soil moisture, turbulent air-land/sea interactions, tropospheric stability and clouds. The impact of these boundary layer characteristics in regulating the diurnal and seasonal evolution of turbulence over several regions across the globe are less explored. Particularly, the role of these factors in shaping the spatiotemporal variations of the thermodynamic characteristics of ABL over open Southern Indian Ocean and Antarctic regions sufficiently lacks field observation-based studies. Mostly studies focused on providing more accurate and reliable quantifications on the vertical structure of MABL in these regions. For a better understanding of the structure and dynamics of ABL/ASL and its role in governing regional weather systems and aerosols/pollutant dispersion over these regions, combination of theoretical, observational, and numerical modelling studies is required.

Among these approaches, observational studies are particularly important as they provide direct means for analyzing, validating, and improving model results for more accurate visualization of physical processes governing the dynamic structure of ABL/ASL on varying spatial and temporal scales. Mostly such studies are needed in data sparce regions such as Southern Ocean, where continuous monitoring using field measurements are challenging. So, to understand the role played by ABL of such remote regions on global climate, accurate remotely retrieved datasets from these regions becomes important. In particular, by using a combination of field measurements and remotely retrieved datasets from SO region, more studies are needed on the dynamics behind development of SO ABL, and its influence on the atmospheric stability state, transport of moisture to the free troposphere, nature of atmospheric inversions and stable layers, and distribution of clouds. Currently, less studies are available that describes the spatial and temporal variation of ABL/ASL, with its effects on regulating the aerosols dynamics along with their radiative effects covering large spatial domains i.e., from

tropics to subtropics to polar Antarctic regions. Such kind of studies are important over tropics, as well as Southern Ocean and Antarctica regions as these regions plays a key role in regulating the global heat, water vapor, and radiation budget. Such kind of observational based quantifications on boundary layer properties when incorporated in regional and global climate models will serve as an essential tool to improve its accuracies in projecting ABL/ASL over tropics, subtropics, and Antarctica regions.

Further, if compared to the sparce knowledge on MABL of Indian sector of Southern Ocean, significant literature is available on the ABL/ASL over coastal tropical Indian regions and surrounding oceanic domains (Prakash et al., 1992; Sivaramakrishnan et al., 1992; Kunhikrishnan et al., 1993; Ramachandran et al., 1994b; Sikka and Narasimha, 1995; Satyanarayana et al., 2000; Miller et al., 2003; Pillai et al., 2004; Ramana et al., 2004a; De Tomasi et al., 2011; Hariprasad et al., 2014; Namboodiri et al., 2014; Pal and Haeffelin, 2015; Lee and Pal, 2017; Melecio-Vázquez et al., 2018; Pal and Lee, 2019; Davis et al., 2020). As, it is well known that dynamic physical processes within ABL/ASL are unique to a particular location with specific geographic and topographic settings. Considering this aspects, in past several field campaigns such as., Monsoon Experiment (MONEX) - December 1978 to November 1979 (Holt and Sethuraman, 1985); Monsoon Trough Boundary Layer Experiment (MONTBLEX) - 1987 to 1990 (Goel and Srivastava, 1990; Sikka and Narasimha, 1995; Gera et al., 1996; Kailas and Goel, 1996; Rao et al., 1996); Land Surface processes Experiments (LASPEX) – 1997 (Vernekar et al., 2003; Sanjay, 2008); Bay of Bengal and Monsoon Experiment (BOBMEX) – 1999 (Mitra et al., 2003; Jain et al., 2010); Indian Ocean Experiment (INDOX-IFP 99) – 1999 (Subrahamanyam, D. et al., 2003; Subrahamanyam, D.B. et al., 2003); Integrated Campaign for Aerosol, Trace Gases and Radiation Budget (ICARB) – 2006-2009 (Moorthy et al., 2008) have been conducted that covered different parts of India and surrounding oceans. Studies from these campaigns has provided significant knowledge on the

detail structure and characteristics of ABL/ASL in different land-based regions of India as well as in oceans surrounding the India i.e., Arabian Sea, Bay of Bengal, and Indian Ocean. Among different coastal tropical Indian regions, the Goa region, lying in the west of India, has very few studies focused on providing an understanding on ASL using field-based measurements. In 2003-2004, a national filed experiment called the ARabian Sea Monsoon EXperiment (ARMEX-I and ARMEX-II) was conducted in the west coast of India at NCPOR, Goa, India using 9 m high micro-meteorological tower-based datasets (Murthy and Sivaramakrishnan, 2005; Rao, 2005; Babu et al., 2008; Murthy et al., 2009; Yashvant and Uma Charan, 2021). The measurement of meteorological variables was made to understand the characteristics of coastal ABL, the interaction of mesoscale with micro-meteorological scales turbulent processes, and development of thermal internal boundary layer. Results from this study highlighted that some of the aspects of surface layer turbulence showed different features unlike predicted by Monin-Obkhov Similarity Theory during light winds conditions and has emphasized the need to study these results with another new set of field observations. Also, indicated the need to provide observation-based quantifications on diurnal and seasonal turbulent dynamics for improving the parametrizations schemes which uses similarity theory to predicts surface layer fluxes during low wind conditions in global climate models. Further, quantifications on the diurnal variations of surface layer fluxes of sensible heat, turbulent kinetic energy, and momentum fluxes under varying stages of surface layer stability conditions during different seasons from Goa region was limited.

Considering these aspects, the goal of this thesis is to address the above scientific issues and to bring down the knowledge gap in these areas particularly in the tropical coastal atmosphere and the atmosphere over the Indian Ocean sector of Southern Ocean and Antarctica. To achieve this, a combination of ground based, remote, and modelled observations collected over land i.e., over a tropical coastal region of Goa, India (15.46°N, 73.83°E) and over oceanic domain

i.e., in the region of ISSO up to Antarctica between 24°S to 68°S along 57°E to 79°E have been collected and analyzed. Over these study regions, characteristics of ASL and ABL, and the role of ABL in the distribution of aerosols, and the effect of their coupled interaction on radiative forcing and atmospheric heating due to aerosols have been investigated. The objectives specifically addressed in this thesis are,

1. To analyze turbulence and flux (heat and momentum) exchange processes to study surface energy balance.
2. To investigate vertical thermodynamic profile of atmospheric boundary layer over an oceanic domain.
3. To study spatiotemporal heterogeneity and long-range transport of aerosols in association with boundary layer dynamics and their radiative impact.

1.7. Thesis outline

Chapter 1 details the characteristic of ABL, its evolution, and associated dynamics over regions of varying geography and topography. Also, the properties of ASL have been briefly discussed along with the theoretical background used for studying turbulence within ASL. An introduction to aerosols and its properties together with its role in altering weather and climate have been provided. A brief literature review, research gaps, and the significance of the present work have been discussed.

Chapter 2 This chapter describes two different study regions i.e., one over continent (a tropical coastal region of Goa, India) and other over an open oceanic domain (Indian Ocean sector of Southern Ocean and Antarctica). This chapter also describes the technical specification of instruments used, details of field experiments, atmospheric models, and novel database generated and examined in the present study.

Chapter 3 presents micrometeorological characteristics of atmospheric surface layer (ASL) over a tropical coastal region of Goa, India. The diurnal variability of surface layer fluxes of heat (i.e., sensible heat flux), energy (i.e., turbulent kinetic energy), momentum (i.e., momentum flux), and associated stability conditions (i.e., stability parameter) of ASL on a seasonal scale have been described. Also, unique results based on the analysis of surface layer turbulence by using the formulations of Monin-Obukhov Similarity Theory (MOST) has been presented. New records of the empirical variance relationships established for surface layer parameters under varying stability conditions unique to the study site have been provided.

Chapter 4 investigates the boundary layer of poorly sampled remote marine atmosphere i.e., MABL of the Indian Ocean sector of the Southern Ocean (ISSO) from 24°S to the Prydz Bay region of coastal Antarctica, nearly 68°S along 57°E to 79°E based on in-situ measurements collected during three field campaigns carried out in 2017, 2018, and 2020 (i.e., SOE-IX, SOE-X, and SOE-XI). The investigation involved understanding the thermodynamic stability state of MABL in response to synoptic meteorology. Also, the cloud macrophysical properties (i.e., heights of cloud top and cloud base, total cloud geometric thickness, and probability of cloud occurrence), and the properties of boundary layer inversions (i.e., the height of significant inversions, the strength of these inversions, and probability of occurrence of significant inversions), as well as dominant low level thermodynamic (physical) processes investigated using conserved variable analysis (CVA) have been discussed.

Chapter 5 examines the spatial and vertical distribution of aerosols in association with atmospheric boundary layer dynamics over ISSO, using set of in-situ as well as remotely derived observations on aerosols and meteorological parameters collected during X^{th} Southern Ocean Expedition (SOE -X) conducted from December 2017 to February 2018. Moreover, the effect of their coupled interaction on total clear sky direct shortwave radiative forcing and rate of atmospheric heating have also been discussed in this chapter.

Chapter 6 summarizes the major outcomes from the study and discusses the scope for future work on aerosols - boundary layer studies.

Chapter 2

Study Regions, Instruments, and Experimental Data

2.1. Introduction

An overview of globally conducted field experiments on investigating the characteristics of ABL, and its role in regulating the dynamics of aerosols and radiative forcing described in the previous chapter, has clearly emphasized the need for conducting more such studies over other underexplored regions of the globe (Garratt et al., 1996; IPCC, 2013; Li et al., 2021). From these experiments, it has been known that distinct variability exists in characteristics of ABL over land to that over the ocean (Stull, 1988; Garratt, 1993). It has also emerged that the interaction of ABL meteorology with natural as well as anthropogenic aerosols occurring across the globe as among the major factors responsible for the formation of different weather patterns, alteration in earth's radiation budget, and global climate change (Bender, 2020; Li et al., 2017). Therefore, to address such climate concerns, continuous monitoring the dynamics of climatically important ABL and its interaction with aerosol species over different geographic regions becomes crucial (Li et al., 2017). To achieve this, continuous real-time measurements are required by deploying sophisticated instruments over land-based sites as well as over oceans. Over land, year around time-series measurements is more feasible than over the ocean where campaign mode data retrievals are the only means of obtaining measurements via mobile platforms (ships and aircraft). In addition, remote sensing measurements are accessed to alleviate the lack of in-situ data. In-situ measurements are costlier, limited to lower heights, and require proper maintenance, but are the only source for providing highly accurate measurements. While remote sensing measurements are readily available and could provide measurements at higher altitudes but are less accurate due to poor signal-to-noise ratio. Thus,

this chapter describes a series of instruments that were utilized for collecting in-situ as well as remote measurements at two geographically unique regions to study the features of atmospheric boundary layer and aerosols. The first study region was over coastal land, where microscale turbulence characteristics of ASL specific to this region have been analyzed using data from a 32 m tall meteorological tower stationed on the campus of Goa University, Goa, India. The measurements from these instruments were continuously collected for a period of 1 year (March 2015 to February 2016). Using these observations, novel set of quantifications on surface layer turbulent fluxes of heat, energy, and momentum along with the empirical coefficients were estimated based on the local scaling and similarity relationships under the framework of MOST over the coastal Goa site. Another study region was over a climatically important and unexplored oceanic domain of the Indian Ocean sector of the Southern Ocean (ISSO) reaching up to Antarctica (24°S to 68°S). Over this oceanic region, a set of instruments were operated during the austral summer of 2017, 2018, and 2020 (i.e., the period of three campaigns to ISSO) to collect measurements on aerosols and meteorology. These measurements over ISSO provided detailed insight into the prevailing climatology of ISSO and dynamic processes governing the thermodynamic structure of ISSO boundary layer, clouds, and inversions. In addition, coupled interaction of aerosols and meteorology occurring over ISSO has been studied using a combination of in-situ and remote measurements. A detailed description of the key instruments used to collect in-situ and remote measurements over these regions followed by details on unique database generated to address the objectives of this thesis are described in this chapter. Table 2.1 presents a brief overview of measurements analyzed in this thesis work.

2.2. Study over a coastal station in India

2.2.1. Study site

The region selected over land for studying the micro-meteorological characteristics of ASL is a tropical coastal region, Goa (15.46°N, 73.83°E, and 50 m above mean sea level), India (Figure 2.1a). This region is bordered along the western side by the Arabian Sea (≈1.3 km away) and is at a distance of 6 km from the capital city Panaji. The site falls under the tropical monsoon climate zone. Based on the ambient meteorological conditions prevailing in this region, the study has been carried out by classifying the entire year into four seasons viz., pre-monsoon season (March to May), summer-monsoon season (June to September), post-monsoon season (October and November), and winter season (December to February) respectively. The southwest monsoon onset around early June and the downpour contribute to maximum rainfall in this region. The reversal of wind takes place during October-November and north-east winds flow from December. Over this region, a 32 m meteorological tower is installed within the campus of Goa University. Inside the campus, the location for establishing this tower has been chosen in a way that there is no hindrance to a free flow of wind. The nearest building (32.5 m length and 44 m breadth and 8 m height) is located at a distance of 17 m in the south-east direction from the tower, while the bushes, about 3 m high, at the north, are at a distance of 7.2 m (Figure 2.1b). Another building (8 m high) located in the southwest direction is at a distance of about 10 m from the tower. There is an open field on the opposite side of the buildings. This tower is equipped with different sensors that provide continuous time series monitoring and collection of meteorological variables.

Table 2.1 Summary of key measurements used in this thesis work.

Techniques	Instruments	Measured Variables	
In-situ Measurements	Sensors instrumented on 32 m tall Meteorological Tower	High frequency sonic sensors	Orthogonal components of wind (*u*, *v*, and w*)* and virtual temperature (T_v) at 10 m and 20 m heights at a frequency of 10 Hz
		Low frequency sensors	Air temperature (*AT*), relative humidity (*RH*), winds speed (*WS*), wind direction (*WD*), atmospheric pressure (*P*) at 4 m, 18 m, and 30 m heights at an hourly interval
	Pisharoty Radiosondes	Vertical profiles of meteorological variables (1 Hz) from surface up to nearly 32,000 m altitude	
	Aethalometer	Mass concentration of Black Carbon (*BC*) aerosols near the surface	
	MICROTOPS-II Sunphotometer	Columnar Aerosol Optical Depth (*AOD*) of composite aerosols.	
Re-analysis Datasets	ECMWF-ERA5 re-analysis	2 m air temperature (T_{air}), sea surface temperature (*SST*), wind components (10 m *u*- and *v*- component)	
Satellite Measurements	CALIPSO retrievals	Vertical features of aerosol sub-types and clouds from surface up to 5,000 m altitude	
Model Simulations	OPAC Model	Aerosol Optical Depth (*AOD*), Single Scattering Albedo (*SSA*), and Asymmetric Parameter (*ASY*)	
	SBDART Model	Clear sky Direct Aerosol Radiative Forcing (*DARF*) and atmospheric Heating Rate (*HR*)	
	HYSPLIT Model	Air mass history	

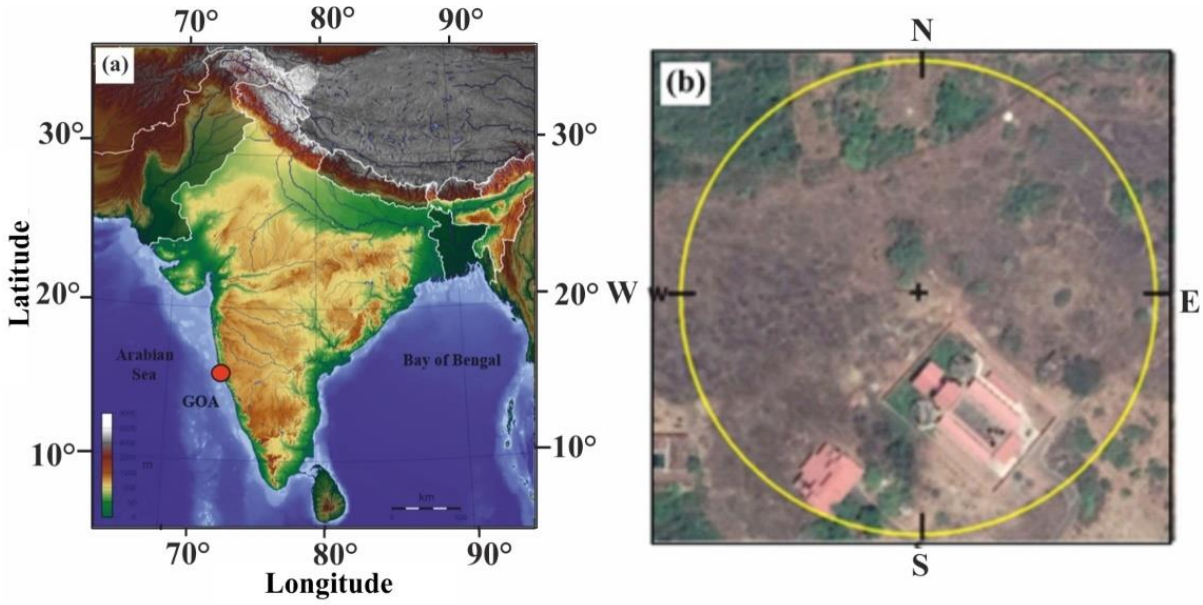

Figure 2.1 (a) Topographic map of India locating study area (Goa) and (b) Aerial image (taken from Google Maps) of the area surrounding the tower (indicated with a cross). The circle represents a radius of 100 m around the tower.

2.2.2. Instrumentation

The installed 32 m meteorological tower was equipped with fast response sensors as well as slow response sensors which were operated at different frequencies (Figure 2.2a, b). Such meteorological towers are widely used for highly accurate measurements of small-scale atmospheric fluctuations occurring within the ASL. Slow response sensors measured atmospheric parameters that vary in scales of a few hours, while fast response sensors measured micro-scale fluctuations that involve turbulent fluxes of heat and momentum as well as the nature of region-specific turbulence based upon its surface roughness characteristics (Markowski et al., 2019). These sensors were mounted on this tower at different pre-defined heights above the earth's surface. The slow response sensors provided continuous

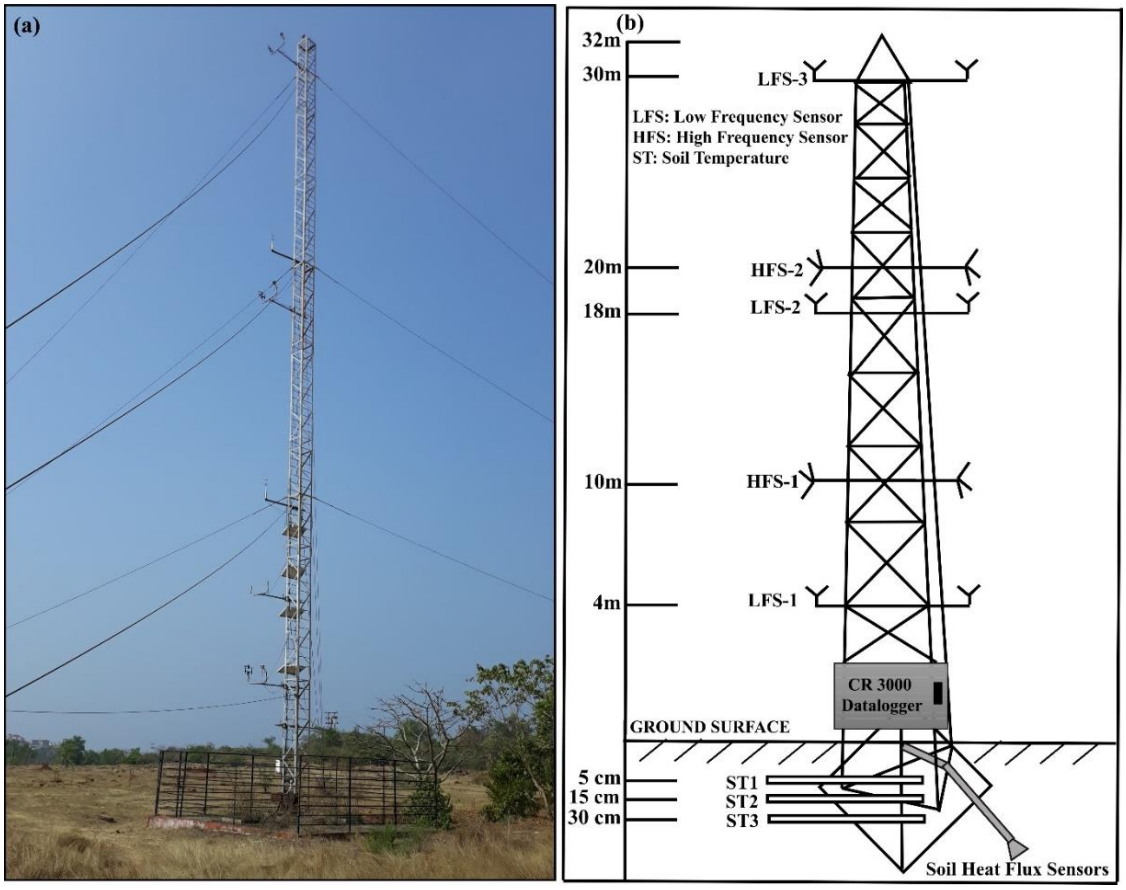

Figure 2.2 (a) Photograph of on-site installed 32 m tall meteorological tower and (b) Schematic represents different sensors mounted at respective heights on the tower.

measurements of air temperature (*T*), relative humidity (*RH*), wind speed (*WS*), and wind direction (*WD*) at three heights above the surface (i.e., 4 m, 18 m, 30 m) at every 1 hour interval. Also, measurements of atmospheric pressure and rainfall were obtained every 1 hour using pressure probes and a rain gauge installed at 4 m above the surface. In addition, fast response sensors (i.e., 3D sonic anemometers) operating at a frequency of 10 Hz measured orthogonal component of wind (*u*, *v*, and *w*) and sonic derived air temperature (*T*) at two heights (i.e., 10

Table 2.2 Technical details of the sensors equipped on the instrumented meteorological tower.

Sensors	Sensor Specifications			Measured Parameters	Sampling Frequency
Fast Response Sensors	Heights: 10 m and 20 m				10 Hz
3 Axis-Sonic Anemometer Gill	Wind speed	Range	0 to 65 m s^{-1}	Orthogonal components of wind ($u, v,$ and w)	
		Accuracy	< 1.5 % RMS @ 12 m s^{-1}		
	Temperature	Range	- 40 ℃ to + 70 ℃	Sonic temperature (T)	
		Accuracy	- 20 ℃ to + 30℃ within ±0.5℃ of ambient temperature		
Slow Response Sensor	Heights: 4 m, 18 m, and 30 m				1 hour
Automatic Weather Station (AWS)	032002-L-PT RM Young Wind sentry set	*WS* range	0 to > 50 m s^{-1}	Wind speed (*WS*) and wind direction (*WD*)	
		WS accuracy	±0.5 m s^{-1}		
		WD range	0°- 360°		
		WD accuracy	±5°		
	CS215-L-PT	Range	- 40 ℃ to + 70 ℃	Air temperature (*AT*)	
		Accuracy	±0.3℃ (at 25 ℃) ±0.4℃ (5℃ to 40℃) ±0.9℃ (- 40℃ to + 70℃)		
	CS215-L-PT	Range	0 to 100 % *RH* (- 20 ℃ to + 60 ℃)	Relative humidity (*RH*)	
		Accuracy	±2% (10 ℃ to 90 % range) at 25℃ ±4% (0 ℃ to 100 % range) at 25℃		
	Barometric Pressure Sensor-CS100	Range	600 to 1100 hPa	Atmospheric pressure (*P*)	
	Tipping bucket rain gauge-TE525MM	Rainfall/tip	0.1 mm (0.004 in.)	Rainfall	
		Accuracy	1.0 % up to 2 in./h (50 mm/h)		

m and 20 m) above the surface. To minimize the misalignment of sensors, the sonic anemometers were positioned in the prominent direction of the wind. All sensors were factory calibrated. Details of the sensors used in this study are given in Table 2.2

2.2.2.1. Fast response sensor

For the turbulence-related study, measurements using a sonic anemometer are widely used due to their efficiency in providing highly accurate microscale temporal resolution. Sonic anemometers are preferred for long-term usage in outdoor weather system and buoys for studying turbulence as compared to traditionally used vane anemometer and cup anemometers, whose reliability and accuracy is significantly affected by dust or salty air. A close preview of the ultrasonic anemometer is shown in Figure 2.3a. In a sonic anemometer, the measurement of air temperature is strongly dependent upon the measure of the speed of sound. The equation assessed for measuring air temperature using a sonic anemometer is,

$$c^2 = 403.T(1 + 0.32\,e/p) \qquad 2.1$$

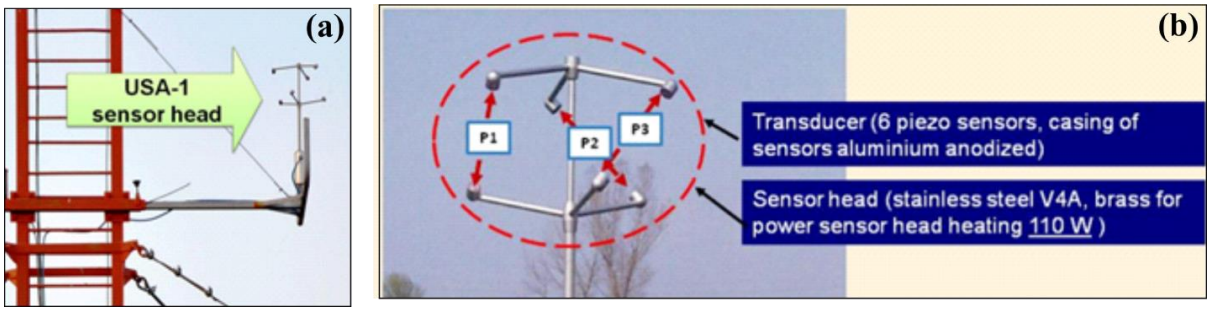

Figure 2.3 (a) A close view of ultrasonic anemometer (USA-1) and (b) signal paths.

Here, T is the air temperature in K, and c is the sound velocity in m s^{-1}, e and p are the water vapor pressure and ambient pressure respectively (Kaimal and Gaynor, 1991). In addition to air temperature, an ultrasonic anemometer provides highly accurate measurements of 3 dimensional winds. These wind components are measured using six transducers (i.e., 6 piezo sensors having a casing of aluminum anodized) and sensors head (made up of stainless steel V4A, power sensor made of brass with head heating of 110W) as depicted in Figure 2.3b. It

utilizes ultrasonic pulses to measure wind speed and direction alternatively three orthogonal components of wind: *u*, *v*, and *w* along zonal (x), meridional (y), and vertical (z) wind direction respectively. These sonic pulses are transmitted through transducers along three non-coplanar paths of sonic pulse P1, P2, and P3 which are again received by the transducers. The nominal time of travel for a sonic pulse along the path is nearly 0.5 m sec, while the alignment of pulse paths is 120° steps in azimuth and 45° tilt in title angle. Each pulse is transmitted by maintaining a fixed time interval between the chains of pulses. Hence, the measurement of the three-dimensional wind speed and direction are obtained by placing three transducer pairs on three distinct axes.

The working principle of a sonic anemometer is the measurement of travel time taken by one sonic pulse to traverse between a pair of transducers. This travel time varies depending upon the distance between transducers, and the speed of air and sound along the transducer axis. This variation when written in the form of an equation appears as follows,

$$T_t = L/(c + v) \tag{2.2}$$

Here, T_t is the travel time of the sonic pulse, L is the distance between the transducers, and c and v are the speed of air and sound along the axis of the transducer.

The speed of air between the transducers is obtained in a way that each transducer acts as a transmitter and receiver to manage the transfer of sonic pulse in both directions between each transducer. Thus, using the time a pulse takes to travel in both the directions speed of air is calculated using the formula,

$$v = 0.5L\ (1/t1 - 1/t2) \tag{2.3}$$

The speed of sound in the air varies with the variation in air temperature, pressure, and atmospheric components suspended in the air. The air temperature is calculated using the travel time of sonic pulse using the following equation,

$$c = 0.5L\ (1/t1 + 1/t2) \quad 2.4$$

Here, *t1* and *t2* are transit times for ultrasonic sound signal to travel over the path length *L* in each direction between the transducers while *c* represents the sonic speed in still air. Further, the three-dimensional wind vector is estimated by combining the velocities of sounds propagating from different directions. Later, the velocity of sound is estimated for the atmospheric conditions having a negligible motion of air which represents the virtual temperature of the air. However, the velocity of sound is dependent on the air temperature as well as on the relative humidity of the atmosphere. The measured temperature is derived by sonic anemometer using the following equations,

$$c_0 = \frac{L}{2}\left(\frac{1}{(t1 - t_{T1} - t_{R2})} + \frac{1}{(t2 - t_{T2} - t_{R1})}\right) \quad 2.5$$

$$T_s = (c_0/20.05)^2 \quad 2.6$$

Here, c_0 is the acoustic velocity, T_s is the sonic sensor-derived temperature, and *L* is the path length between the two transducers, and t_{T1}, t_{T2}, t_{R1}, and t_{R2} are transit times taken for ultrasonic sound signal to travel towards and return between transducer *T1* and *T2* respectively. The sonic temperature, T_s (in Kelvin), may differ from the ambient temperature by an amount nearly equal to the water vapor content in the air measured. This difference is closely around ±1°C at 20°C and decreases as the temperature decreases (Campbell Scientific, Inc., 1998).

2.2.2.2. Slow response sensors

Cup anemometer: Cup Anemometers were used for measuring mean wind speed. This anemometer starts at the initial speed of 0.5 m s^{-1} having a constant distance between 1.5 and 5 m. The cup anemometer commonly tends to over speed hence it has a partial non-linear response characteristic (Camp et al., 1970). The advantage of using a cup anemometer is that no alignment is required in the direction of the wind. Its basic working principle depends upon

the differential drag of load on the cup which makes the rotating speed of the 3-cup rotor directly proportional to the speed of wind in the rotor plane (Figure 2.4a).

Wind vane: A wind vane was used to obtain the orientation of the wind (i.e., wind direction). It works upon the precise balance of the wind vane with respect to the corresponding counter load. On achieving the balance, the wind vane rotates freely in the wind and soon after comes to equilibrium, by positioning in the direction of the mean wind. The shaft is rotated by the wind vane having a coupled resistance of 360 turn pot. The direction of wind frequently takes a complete turn from a reference direction between 0° to 360° which is then indicated in the pot output. This resistance pot output from the sensor is then converted into an analog output

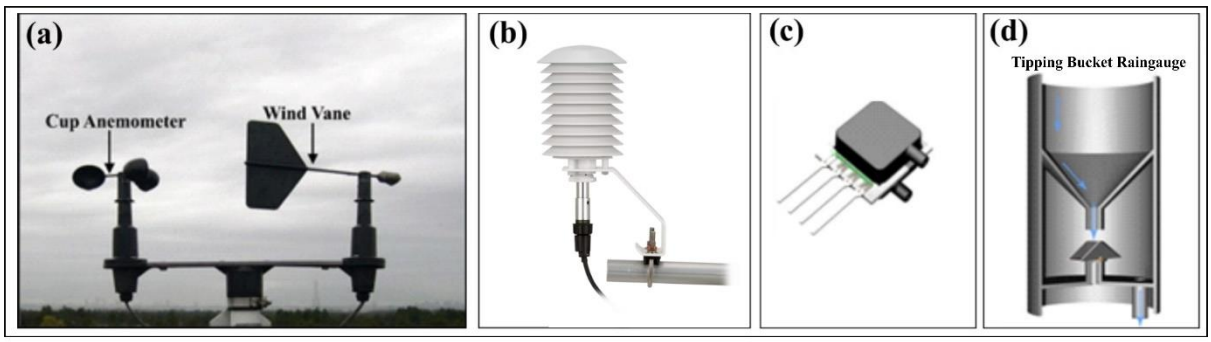

Figure 2.4 A close view of (a) cup anemometer and wind vane, (b) combined temperature and humidity sensor, (c) pressure sensor, and (d) the interior of tipping bucket rain gauge.

voltage by the inbuilt electronics in the translator of the wind vane. The configuration of the wind vane incorporated with the translator is configured in a way that the final output provides a voltage between 0 to 3.6 volts depending upon the varying direction of wind between 0° to 360° (Figure 2.4a).

Temperature sensor: The slow response temperature sensor is the resistance thermometer that provides direct and appropriate temperature measurements. These thermometers comprise of a platinum wire which is coated with ceramic. The time constant of these thermometers is quite large (orders of some tens of seconds) and configured to have a standard resistance. The

standard resistance is dependent upon the surrounding temperature. Thus, the resistance fluctuation is transformed into appropriate voltage by connecting the elements of the temperature sensor to the bridge network. The recorded voltage is amplified into DC output voltage. This variation of DC voltage is directly proportional to the temperature variation. Later this DC voltage is converted into standard temperature using a suitable electronic circuit. The temperature sensor is configured in a way that the voltage between 0 to 5 volt is given in terms of the temperature range between 0℃ to 50℃ (Figure 2.4b)

Humidity sensor: Humicap, a hygroscopic sensor, was used to measure humidity. This sensor comprised of a thin element that responds within nearly one-second. In this sensor, the capacitance of the element varies with the relative humidity, thereby making it as a capacitance type of sensor. The variation of the capacitance depends upon the variation in relative humidity which is transformed to appropriate frequency. This conversion is achieved when the humicap sensor is connected to a multi vibrator in the form of a capacitance element. The frequency of the multivibrator is inversely proportional to the relative humidity. Thus, the sensor output is configured in a way that corresponds to 0 to1 volt, and relative humidity is recorded between 0 to 100% (Figure 2.4b).

Pressure sensor: The pressure sensor uses diaphragm technology in which the pressure difference is measured between the two sides of the diaphragm. The pressure sensor consists of a micro-machined silicon diaphragm equipped with piezoresistive strain gauges which are diffused to a silicon or glass plate. These resistors are connected in the form of a Wheatstone bridge whose output is proportional to pressure at another end. In the atmosphere, as the reference medium is vacuum, recorded pressure is termed atmospheric pressure (Figure 2.4c)

Rain gauge: A tipping bucket rain gauge device is used to measure the amount of rain received on the ground. As the rain falls on the surface, it enters the funnel of the tipping bucket rain gauge. As soon as the marked amount of water gets collected into the funnel, the magnet within

it will release its hold slowing the bucket to tip. As water tips down, the other bucket is positioned for the next reading. Every time a bucket tips and switches position an electronic signal is sent by a tiny switch. The number of times this signal is sent, the knowledge of the defined catchment area of each bucket, provides a reliable calculation for total rainfall (Figure 2.4d)

2.2.3. Database over land

The database generated over the land domain is a combination of slow and fast response measurements retrieved for the period from March 2015 to February 2016. These measurements were obtained using respective sensors mounted at different heights above the ground surface. These generated raw measurements were at first screened and all rainy days were discarded. This elimination was done by identifying the number of rainy days from rain gauge data. After adopting this criterion, the remaining number of available days of data were considered for further analysis presented in chapter 3 of this thesis. The detailed statistics on data availability at distinct heights from these sensors, observed rainy days, and the actual number of days of data considered in the present work are provided in Table 2.3.

Table 2.3 Criteria adopted for considering data from low and high-frequency sensors equipped at different heights in the present study.

Season	Month	Number of days of available low-frequency data	Number of days of available high-frequency data	Number of rainy days	Number of days considered for surface-based meteorological study	Number of days considered for micro-scale turbulence study
		At 4 m, 18 m, and 30 m height	At 10 m and 20 m height			
Pre-monsoon	March (2015)	31	18	1	30	17
	April (2015)	30	24	0	30	24
	May (2015)	17	14	1	16	13
Data considered for Pre-Monsoon Season		78	56	2	76	54
Summer-monsoon	June (2015)	30	11	16	14	9
	July (2015)	31	23	15	16	18
	August (2015)	29	17	16	11	11
	September (2015)	19	11	7	15	10
Data considered for Summer-Monsoon Season		109	62	54	56	48
Post-monsoon	October (2015)	31	22	1	30	21
	November (2015)	17	14	1	17	17
Data considered for Post-Monsoon Season		48	36	2	47	38
Winter	December (2015)	NA	NA	0	NA	NA
	January (2016)	NA	NA	0	NA	NA
	February (2016)	18	10	0	18	10
Data considered for Winter Season		18	10	0	18	10

2.3. Study over oceanic region

2.3.1. Study region and details of campaigns

The other region considered for the study is a climatically important and unexplored remote oceanic domain of the Indian Ocean sector of the Southern Ocean (ISSO) extending up to Antarctica, encompassing latitudes between 24°S to 68°S and longitudes between 57°E to 79°E. Over this region, in-situ measurements on meteorology and aerosols were performed during three consecutive Southern Ocean (SO) field campaigns conducted during the austral summers of 2017, 2018, and 2020 (Figure 2.5a). These campaigns were numbered as IXth (SOE-IX), Xth (SOE-X), and XIth (SOE-XI) Indian expedition to Southern. All three campaigns had been conducted on a ship-based platform onboard an oceanographic research vessel *S. A. Agulhas*. These campaigns were flagged off from Port Louis, Mauritius (20°S), and covered a large spatial domain reaching up to the edge of Antarctica's Prydz Bay region (68°S). The details of these campaigns are listed in Table 2.4. All three campaigns have successfully sampled three major oceanic frontal regions of ISSO (i.e., Sub-Tropical Front (STF), Antarctic Circumpolar Current (ACC), and Antarctic Zone (AZ)) (Figure 2.5). STF marks the region separating tropical waters from sub-Antarctic waters (Deacon, 1937; Lutjeharms and Valentine, 1984; Sokolov and Rintoul, 2002; Hamilton, 2006). The region north and south of STF was identified as NSTF and Southern Subtropical Front (SSTF, after Belkin and Gordon (1996)). Further south of SSTF, the frontal systems of the strong Antarctic Circumpolar Current (ACC) were identified as Sub-Antarctic Front (SAF), Polar Front (PF), and Southern ACC Front (SACCF), and the southern boundary of ACC (SB). The ACC exhibited enhanced mesoscale circulations induced by intensive eddy activities caused by high-speed jets (Lutjeharms and Valentine, 1988; Stammer, 1998; Phillips and Rintoul, 2000; Morrow et al., 2004; Sallée et al., 2008). Beyond SB, the southernmost region was in the coastal waters of the Antarctic Zone, termed as Coastal Antarctic (CA). In this manner, a total of 10 frontal regions

Table 2.4 Details of Measurements Collected During Three Southern Ocean Field Campaigns.

Campaign	Period of Campaign	Latitude Range	Longitude Range	Number of Soundings	Onboard Aerosol Measurements	Time / Height Resolution
SOE-IX	6th January 2017 – 28th February 2017	30°S to 68°S	57.4°E to 75°E	18	*BC* observations using Aethalometer AE-42 *AOD* measurements using MICROTOPS – II Sunphotometer	1 sec / 0.1 m
SOE-X	8th December 2017 – 4th February 2018	28°S to 66.6°S	57.4°E to 76.5°E	30	*BC* observations using Aethalometer AE-42 *AOD* measurements using MICROTOPS – II Sunphotometer	1 sec / 0.1 m
SOE-XI	10th January 2020 – 8th March 2020	24°S to 67.5°S	57.4°E to 79°E	27	*BC* observations using Aethalometer AE-42 *AOD* measurements using MICROTOPS – II Sunphotometer	1 sec / 0.1 m

*Note: *BC represents Black Carbon aerosols and AOD represents Columnar Aerosol Optical Depth.*

Table 2.5 Regional classification of study area and distribution of 75 atmospheric soundings.

Sr. No.	Regions	Frontal regions in ISSO	The classification adopted for the present study	Indicator Variable	Total RL count
				Sea Surface Temperature (°C)	
1	Sub-Tropical Indian Ocean (STIO)	Northern Subtropical Front (NSTF1)	24°S–32°S	26 - 22°C	8
2		Northern Subtropical Front (NSTF2)	32°S–40°S	21 - 22°C	8
3		Agulhas Return Front (ARF) + Southern Subtropical Frontal (SSTF)	40°S–41°30′S	19 - 17°C, 17 - 11°C	3
4	Indian sector of Southern Ocean (ISSO)	Northern Sub-Antarctic Frontal (SAF1)	41°30′S–44°S	11 - 9°C	6
5		Southern Sub-Antarctic Frontal (SAF2)	46°30′S–48°S	7 - 6°C	1
6		Northern Polar Frontal (PF1)	50°S–52°30′S	5 - 4°C	5

7		Southern Polar Frontal (PF2)	54°30′S–59°30′S	3 - 2°C	8
8	High-Latitude Southern Ocean (High-Latitude SO)	Southern Antarctic Circumpolar Current Front (SACCF)	60°S–61°S	Increased Temperature, $T_{max} > 1.8$°C	6
9		Southern Boundary of ACC (SB)	64°S–65°S	Isotherm of 1.5°C	10
10		Coastal Antarctic (CA)	65°S–68.5°S	-0.5 - 1.5°C	20

were examined based on the location of measurements and regional characteristics, which broadly fall into three major oceanic frontal regions, (a) Sub-Tropical Indian Ocean (STIO) includes three regions, NSTF1, NSTF2, and SSTF; (b) ISSO includes four regions, northern SAF (SAF1), southern SAF (SAF2), northern PF (PF1) and southern PF (PF2); and (c) High-Latitude Southern Ocean includes three regions, SACCF, SB, and CA. Details of each frontal region classified here are also provided in Table 2.5. Approximate demarcation of each ISSO frontal region has been adopted from Anilkumar et al. (2015).

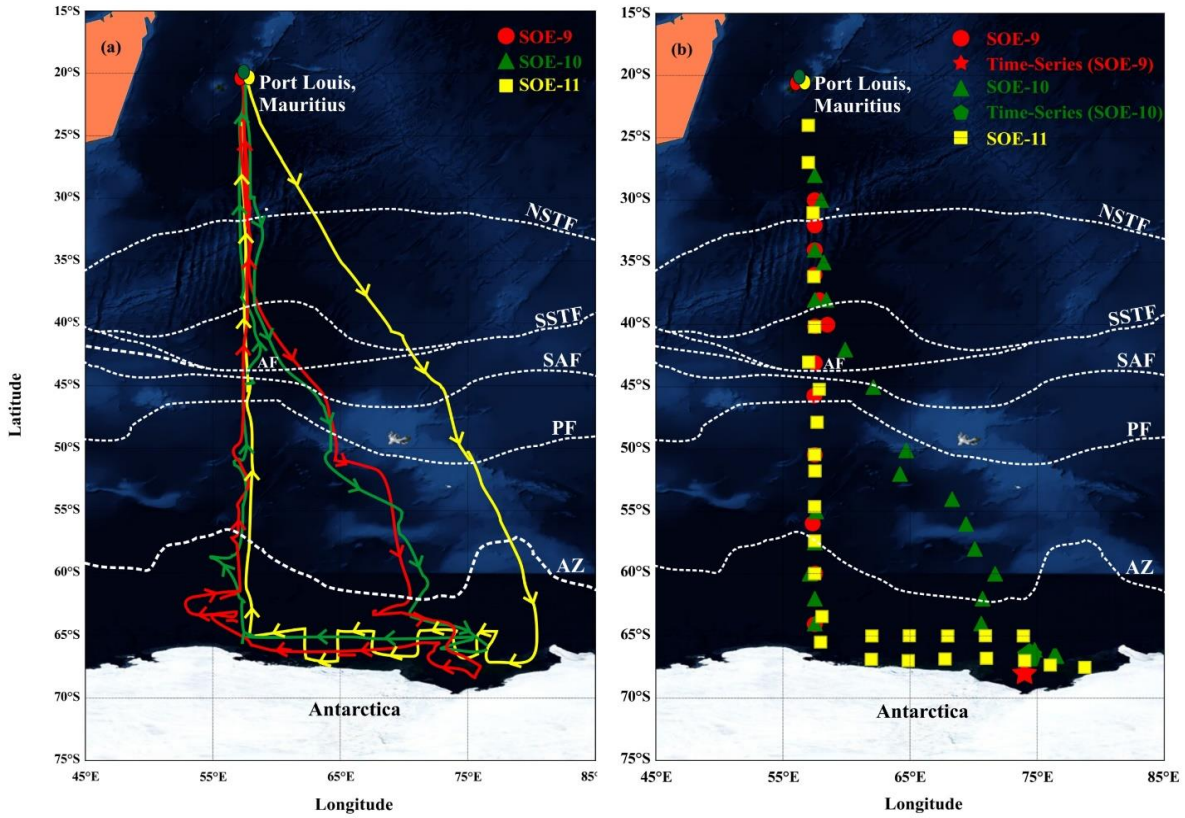

Figure 2.5 (a) Cruise track along which atmospheric measurements were made during three campaigns (SOE-IX (red color track), SOE-X (green color track), and SOE-XI (yellow color track)) over the Indian sector of Southern Ocean (ISSO). Arrows indicate onward and return track journeys. Approximate location of various fronts are marked by white dotted lines from Belkin and Gordon (1996) and Anilkumar et al. (2015): [NSTF and SSTF, Northern and Southern Sub-Tropical Fronts; SAF, Sub-Antarctic Front; PF, Polar Front; and AZ, Antarctic Zone]. (b) The distribution of 75 atmospheric soundings launched during SOE-IX (red circles), SOE-X (green triangles), and SOE-XI (yellow squares). Location for time series measurements made during SOE-IX (red star) and SOE-X (green pentagon) are shown.

2.3.2. Instruments for in-situ measurements

2.3.2.1. Automatic Weather Station (AWS)

The surface meteorological dataset comprises of air temperature (T_{air}), relative humidity (*RH*), mean sea level pressure (*MSLP*), wind speed (*WS*), and wind direction (*WD*) at respective locations and times. During the first two campaigns (2017 and 2018), these variables were collected using a standard per-calibrated Automatic Weather Station AWS (WeatherPak®-2000 v3; Coastal Environment Systems Inc., 2006) equipped with GPS specifically designed for ocean-based applications to provide true *WS* and *WD* (Figure 2.6). During these campaigns, datasets were collected at a frequency of every 1 minute, as well as the manual record of these variables were maintained at every 1-hour interval. The AWS was installed on the front side of the ship at a height of 10 m above MSL, and its alignment was corrected as the campaigns progressed. During the third campaign (2020), AWS failed to provide continuous data, therefore, data was manually logged every 6 hours. Also, *SST* was measured using a standard Bucket Thermometer (Theodor Friedrichs & Co.) at every 6-hour interval during all the campaigns. Details on this instrument are provided in Table 2.6.

Figure 2.6 On-board installed Automatic Weather Station (WeatherPak®-2000 v3).

2.3.2.2. Atmospheric sounding

For upper-air meteorological measurements, several high-resolution atmospheric profiles were obtained using *Pisharoty* radiosonde system version 'B3' developed by Vikram Sarabhai Space Centre of ISRO. The details on radiosonde performance, technical information, and validation can be assessed in Divya et al. (2014) (Figure 2.7a). It provided vertical profiles of *T, MSLP, RH, WS*, and *WD* at respective latitudes, longitude, altitude, and time up to an altitude of nearly 32,000 m.

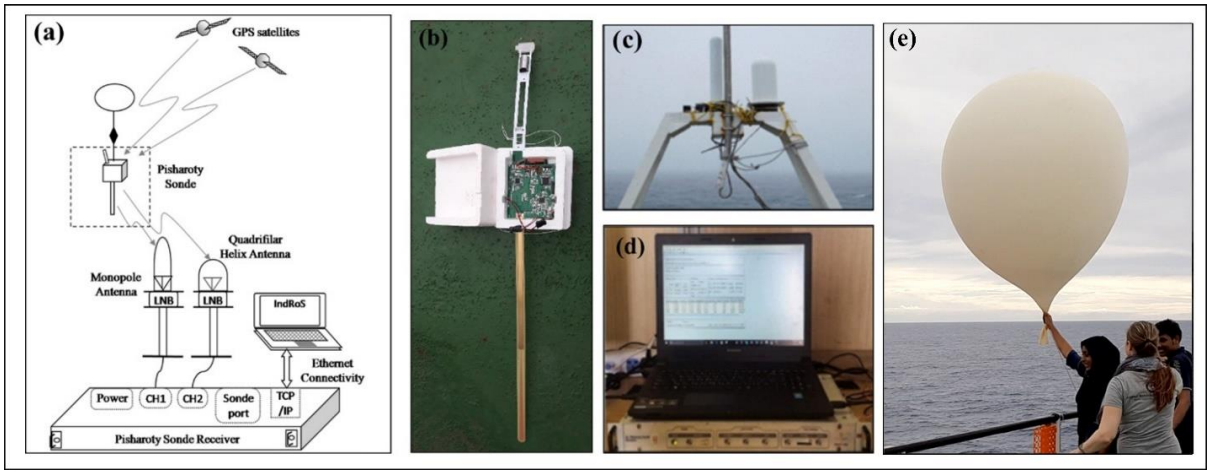

Figure 2.7 (a) Schematic of the *Pisharoty* sonde system. Courtesy: (Divya et al., 2014), (b) *Pisharoty* sonde payload, (c) LNB antennas, (d) ground control station, and (e) release of hydrogen-filled weather balloon on board ORV *S. A. Agulhas*.

All launches were made from approximately 12 m above MSL and from the stern side of the ship to minimize the influence of the ship structure or atmospheric conditions. An onboard setup of the radiosonde launch is shown in Figure 2.7 (b-e). During all three campaigns, a total of 75 radiosondes were launched in this region (Table 2.7). To check the reliability of the *Pisharoty* radiosonde, a comparison of these radiosondes was made with Vaisala, Meisei, and Graw make radiosondes by Divya et al. (2014). The comparison showed a correlation of 0.99 for *T* and *MSLP*, 0.97 for *RH*, and 0.998 and 0.976 for east-west and north-south components of *WS* respectively.

Table 2.6 Specification of instruments used over oceanic domain.

Instruments	Parameters	Height	Details	Sensor Specifications
[a]*Pisharoty* Radiosondes (PS01 version B3) (Manufacturer: Indian Space Research Organization (ISRO)'s -Vikram Sarabhai Space Centre (VSSC), India)	Air temperature (*T*)	From 10 m to 32,000 m	Range	-90° to 60℃
			Resolution	0.1℃
			Accuracy	±1℃
			Response time	< 1s
			Sampling rate	1 Hz
			Correlation with other radiosondes [b]	R 0.999
	Atmospheric pressure (*P*)	From 10 m to 32,000 m	Accuracy	±1.4 hPa (>100 hPa), ±0.5 hPa (≤ 100 hPa)
			Sampling rate	1 Hz
			Correlation with other radiosondes [b]	R 0.999
	Relative humidity (*RH*)	From 10 m to 32,000 m	Range	0% to 100%
			Resolution	0.1 %
			Accuracy	±5 %
			Response time	<5 s
			Sampling rate	1 Hz
			Correlation with other radiosondes [b]	R 0.966
	Wind speed (*WS*)	From 10 m to 32,000 m	Range	0-500 m s^{-1}
			Resolution	0.01 m s^{-1}
			Accuracy	0.1 m s^{-1}
			Sampling rate	1 Hz
			Correlation with other radiosondes [b]	R 0.998 (EW)

				0.976 (NS)
[c] Bucket Thermometer	Sea surface temperature (*SST*)	A sampling near the sea surface	Range	- 10 to + 40 ℃
			Scaling	0.5 ℃
			Accuracy	± 0.5 ℃

[a] *Details on Pisharoty Radiosonde System is detailed in an article by Divya et al. (2014)*
[b] *Other radiosondes refers to Vaisala, Meisei, and Graw radiosondes*
[c] *Theodor Friedrichs & Co., Outboard thermometer (Navy Bucket)*
Coastal Environment Systems, Inc., 2006; WEATHERPAK®-2000 user manual for specifications of surface measurement

2.3.2.3. Aethalometer

Aethalometer (Make: M/s Magee Scientific, model AE-42), a self-contained, automatic instrument operating at seven wavelength channels (370, 470, 520, 590, 660, 880, and 950 nm) was used for real-time measurements of mass concentrations of *BC* aerosols (Hansen et al., 1984). This instrument was installed on the bow side of the ship to obtain headwinds and prevent contamination from the ship's exhaust (Figure 2.8a). During installation, the focus was on maintaining an unobstructed airflow towards the instrument to minimize the effects of the vessel on measurements. Using factory set calibration coefficients, *BC* mass concentrations were estimated in ng m^{-3} from the absorbance at 880 nm using filtration on quartz fiber and optical transmission techniques. The ambient particles were aspirated through the inlet through a heated sample line which was fixed at a height of 12 m at the bow of the ship. This heated sample line maintained the relative humidity of the airflow to be approximately 60% within the air stream entering into the sampling channel of the instrument (Figure 2.8b). The instrument was operated continuously along the cruise track at every 5 minutes interval with a flow rate of 5 litres per minute (litres per minute) (Figure 2.8c).

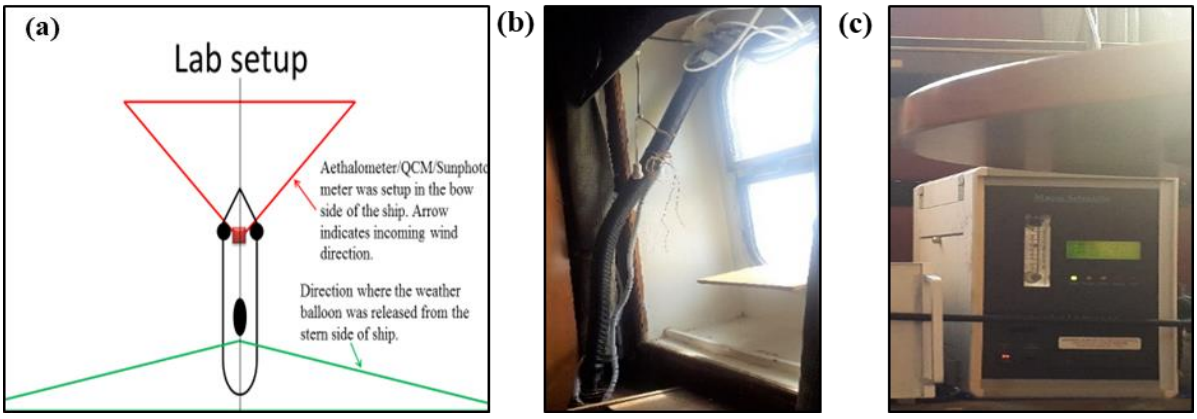

Figure 2.8 (a) schematic of on-board installation of Aethalometer (b) heated sample line connected to Aethalometer, (c) Aethalometer (AE-42) on-board ORV *S. A. Agulhas*.

2.3.2.4. MICROTOPS-II Sunphotometer

The MICROTOPS-II Sunphotometer as shown in Figure 2.9a, is a hand-held, compact, and portable device manufactured by Solar Light Company Inc., USA especially designed for *AOD* measurements on fixed as well as mobile ship-based platforms (Figure 2.9b). This instrument operates at five wavelengths, i.e., 380, 440, 500, 675, and 870 nm and provides measurements of total columnar aerosol optical depths at each wavelength (Morys et al., 2001). The field of view of the Sunphotometer is 2.51° at full-width half maximum, and the pointing accuracy is more than 0.1°. By following the principle of Beer-Lambert law, this instrument, after measuring the direct solar flux computes *AOD* using internal factory-calibrated coefficients and local coordinates. The overall instrumental uncertainties introduced in the *AOD* measurements were 0.005. More technical details can be found in its user manual (MICROTOPS-II Sunphotometer, Version 2.43).

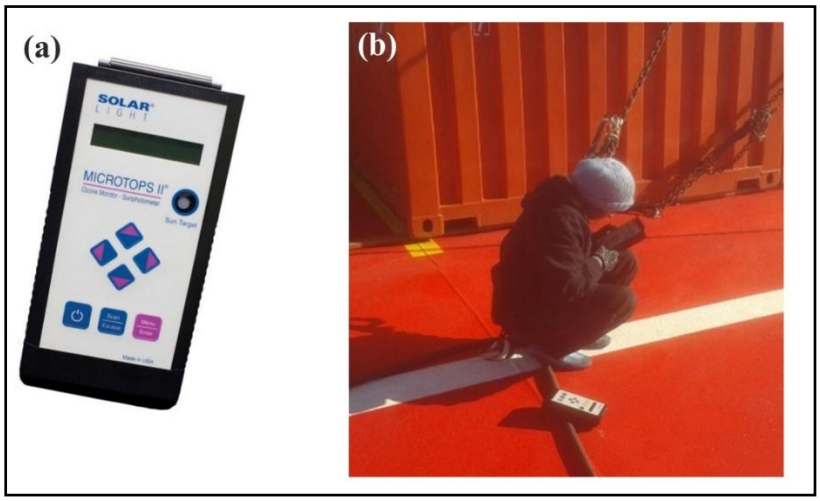

Figure 2.9 (a) Photograph of MICROTOPS-II Sunphotometer (b) Photograph while collecting Sunphotometer measured *AOD* readings onboard ORV *S. A. Agulhas*.

2.3.3. Satellite retrieved measurements

2.3.3.1. ECMWF–ERA5 reanalysis data

ERA5, a fifth-generation atmospheric reanalysis data product developed by European Centre for Medium-Range Weather Forecasts (ECMWF) covers global regions on a latitudinal-longitudinal grid resolution of 0.25° × 0.25° since 1950 till the present day (Hersbach et al., 2019; Hersbach et al., 2020). From this product, datasets have been extracted to evaluate background synoptic surface forcing (*SST*-T_{air}) conditions and wind circulation patterns. An hourly dataset of wind fields (10 m *u*- and 10 m *v*- component), 2 m air temperature, and surface *SST* were retrieved in this study. These datasets were used to examine synoptic surface forcing around each sounding location examined in this thesis. Details on this product can be found at https://cds.climate.copernicus.eu/.

2.3.3.2. CALIPSO data

Cloud-aerosol Lidar and infrared pathfinder satellite observation (CALIPSO), a two-wavelength polarization-sensitive near nadir-viewing lidar are used globally to provide high-resolution vertical profiles of aerosols and clouds (Proestakis et al., 2018). Its retrieval algorithm is detailed in Winker et al. (2009). It orbits at a height of 705 km with an inclination

of 98.05º. The cloud and aerosol layers are detected by comparing the signal return measured at 532 nm with the signal expected from molecular components of the atmosphere. After calibration and range correction, cloud and aerosol layers are identified. The work presented in this thesis analyses CALIOP level 2 Version 4.10x data products to investigate the vertical features of aerosol sub-types and cloud phase (ice/water) over the study region. Details on CALIPSO derived data products can be found on https://www-calipso.larc.nasa.gov/.

2.3.4. Atmospheric models

2.3.4.1. HYSPLIT model

Air mass back trajectories computed using National Oceanic and Atmospheric Administration - Air Resources Laboratory (NOAA-ARL) Hybrid Single-Particle Lagrangian Integrated Trajectory (HYSPLIT, version 4) model were accessed in this thesis work. This model is provided with NCEP Global Data Assimilation System (GDAS) meteorological datasets obtained from data archives of NOAA-ARL (http://arlftp.arlhq.noaa.gov/pub/archives/gdas1). This model involves a hybrid calculation method that uses the Lagrangian approach to calculate the advection and diffusion of aerosols when transported from their initial source locations. This model has been used to determine air mass history to examine prominent sources of prevailing aerosol species based on the back-trajectory analysis.

2.3.4.2. OPAC model

The aerosol and cloud model, OPAC (Optical Properties of Aerosols and Clouds), a software package comprising of microphysical properties of aerosols and clouds developed by Hess et al. (2014) has been used for estimating the optical properties of aerosols i.e., aerosol optical depth (*AOD*), single scattering albedo (*SSA*), and asymmetry parameter (*ASY*) of a mixture of defined aerosol species prevailing over the study region. Estimates of which were obtained by running the OPAC model with the user-defined inputs such as type of aerosol species such as total water-soluble components, sea salt (accumulation mode), sea salt (coarse mode), sulphate,

BC soot, sulfates, nitrates, and dust as well as vertical mixing height, wavelengths, and range of relative humidity from 0% to 100% (Hess et al., 1998). More details on the methods for simulating the optical properties of aerosols using OPAC can be found in Singh et al. (2016). The output of aerosol optical properties (i.e., *AOD*, *SSA*, and *ASY*) from OPAC were fed as an input to the SBDART model for radiative forcing estimations.

2.3.4.3. SBDART model

Santa Barbara DISORT Atmospheric Radiative Transfer (SBDART) model was used to estimate the direct aerosol radiative forcing (*DARF*). To accurately estimate *DARF*, OPAC simulated optical properties of composite aerosols (i.e., *AOD*, *SSA*, and *ASY*) was fed as an input in SBDART model to compute clear-sky direct shortwave *DARF*. In addition to the aforementioned input, other inputs given to SBDART model was surface reflectance which was derived from MODIS product. A vertical profile of neutral atmosphere of 10, 000 m has been considered. Along with these paraments, for water vapor content in the atmosphere, the regional average *RH* values have been used over the large latitudinal span covered in this study. Total columnar concentration of ozone expressed in Dobson Unit (DU), measured from Microtops-II Sunphotometer at 380 μm channel was used to obtain the optical depths due to ozone absorptions. The SBDART model, developed by Ricchiazzi et al. (1998), is a parallel plane discrete ordinate model which calculates radiative fluxes with and without aerosols. The estimates of *DARF* at top of the atmosphere (*TOA*), surface (*SFC*), and within the atmosphere (*ATM*) can be obtained within a the short-wavelength range of 0.2–4.0 μm as well as within long-wavelength range of 4.0–40 μm. A proportional amount of atmospheric *DARF* is known to heat the atmospheric column resulting in atmospheric radiative heating (*HR*) (Srivastava et al., 2011).

2.3.5. Database over ocean

Database over the ocean was the combination of surface as well as vertical meteorological parameters and aerosol-based measurements. Real-time measurements of surface meteorological parameters were continuously obtained using onboard installed AWS throughout the cruise period between 24°S to 68°S during the forward track, return track, and time series location of all three campaigns. The quality of the AWS collected measurements was compared to those with variables measured using ORV's sensors used for navigational purposes. The collected AWS dataset was in close approximation with ORV's dataset. Additionally, from the measured *WD* and *WS*, true magnitude and direction were computed using ORV's heading, course, and speed. Similarly, 75 high-resolution atmospheric profiling were done using *Pisharoty* radiosonde ascents which provided upper air meteorological measurements over the unexplored study region (Table 2.6). All radiosondes were preferably launched at 00:00, 16:00, 12:00, and 18:00 UTC. However, few launches were made at discrete intervals to record any severe weather event or frontal activity. All the launches were made only when the wind speed at the location did not exceed 30 knots. The launch locations were selected to target crucial atmospheric and oceanic fronts. During the third campaign (in 2020), discrete launches were made over the latitudinal transit track at a longitudinal interval of every 3°. The distribution of 75 radiosondes released during three campaigns is tabulated in Table 2.7. During SOE-IX (in 2017), a total of 18 radiosondes were launched along the complete cruise track, among which 2 were made during the ongoing track followed by a time-series observation where 4 launches were made at 00:00, 06:00, 12:00, and 18:00 UTC at 68°03′S, 74°04′E. The remaining 12 launches were made during the return track from $68°S$ to $30°S$. During the SOE-X campaign (in December 2017- February 2018), 46 radiosondes had been launched, among which 19 radiosondes were released during the forward track, while 18 other sondes were released during the return track, and the remaining 8 radiosondes were released at

the time series location at at 68°03′S, 74°04′E. During the SOE-XI campaign (in 2020), radiosondes were released along the longitudinal transit track as well as the latitudinal transit track. A total of 28 radiosondes were released, wherein 13 radiosondes were released along the longitudinal transit track and 15 radiosondes were released along the latitudinal transit track (Table 2.7). In addition to surface and upper air meteorological measurements, the real-time surface concentration of *BC* aerosols was measured continuously during the entire cruise period sampling the complete cruise track from 24°S to 68°S, except at time series locations where measurements were stopped to avoid contamination from the ship's exhaust.

Table 2.7 Details of radiosonde measurements analyzed.

Sr. No.	Campaigns	Radiosonde Launch No.	Cruise Track	Date	Julian Day / 1 Jan	Time (UTC)	Latitude	Longitude	Frontal Regions
1	IXth Southern Ocean Expedition (SOE-IX)	RL1	OT1	9-Jan-17	9	22:29	30^{o}S	57.51^{o}E	NSTF1
2		RL2	OT2	12-Jan-17	12	06:09	40^{o}S	58.48^{o}E	SSTF
3		RL3	TS1	27-Jan-17	27	00:53	68.05^{o}S	74.07^{o}E	CA
4		RL4	TS2	27-Jan-17	27	05:54	68^{o}S	73.99^{o}E	CA
5		RL5	TS3	27-Jan-17	27	11:50	68.01^{o}S	73.93^{o}E	CA
6		RL6	TS4	27-Jan-17	27	17:51	68^{o}S	73.98^{o}E	CA
7		RL7	RT1	11-Feb-2017	42	05:53	64.05^{o}S	57.51^{o}E	SB
8		RL8	RT2	14-Feb-2017	45	03:58	59.98^{o}S	57.52^{o}E	SACCF
9		RL9	RT3	16-Feb-2017	47	03:35	55.97^{o}S	57.33^{o}E	PF2
10		RL10	RT4	18-Feb-2017	49	05:45	50.46^{o}S	57.51^{o}E	PF1
11		RL11	RT5	20-Feb-2017	51	09:09	45.71^{o}S	57.45^{o}E	SAF1
12		RL12	RT6	21-Feb-2017	52	05:47	43.08^{o}S	57.51^{o}E	SAF1
13		RL13	RT7	22-Feb-2017	53	11:53	40.14^{o}S	57.52^{o}E	SSTF
14		RL14	RT8	23-Feb-2017	54	03:50	38.03^{o}S	57.84^{o}E	NSTF2
15		RL15	RT9	23-Feb-2017	54	12:23	35.98^{o}S	57.49^{o}E	NSTF2

16		RL16	RT10	23-Feb-2017	54	23:11	34.01°S	57.51°E	NSTF2
17		RL17	RT11	24-Feb-2017	55	10:23	32.03°S	57.5°E	NSTF1
18		RL18	RT12	24-Feb-2017	55	22:00	30.02°S	57.51°E	NSTF1
19	Xth Southern Ocean Expedition (SOE-X)	RL19	OT	12-Dec-2017	346	04:00	30°S	58°E	NSTF1
20		RL20	OT	13-Dec-2017	347	09:00	35°S	58.2°E	NSTF2
21		RL21	OT	14-Dec-2017	348	01:00	38°S	58.4°E	NSTF2
22		RL22	OT	18-Dec-2017	352	03:00	42°S	59.9°E	SAF1
23		RL23	OT	19-Dec-2017	353	06:00	45°S	62.1°E	SAF1
24		RL24	OT	21-Dec-2017	355	03:00	50.1°S	64.7°E	PF1
25		RL25	OT	22-Dec-2017	356	22:00	52°S	64.2°E	PF1
26		RL26	OT	23-Dec-2017	357	06:00	54°S	68.3°E	PF2
27		RL27	OT	24-Dec-2017	358	08:00	56°S	69.4°E	PF2
28		RL28	OT	25-Dec-2017	359	06:10	58°S	70.1°E	PF2
29		RL29	OT	26-Dec-2017	360	11:11	60°S	71.7°E	SACCF
30		RL30	OT	27-Dec-2017	361	03:00	62°S	70.7°E	SACCF
31		RL31	OT	28-Dec-2017	362	06:00	64°S	70.6°E	SB
32		RL32	OT	29-Dec-2017	363	05:00	66.1°S	74.8°E	CA
33		RL33	TS	3-Jan-2018	3	06:00	66.6°S	76.4°E	CA
34		RL34	TS	3-Jan-2018	3	10:00	66.6°S	76.4°E	CA

35		RL35	TS	3-Jan-2018	3	18:00	66.6ºS	76.4ºE	CA
36		RL36	TS	3-Jan-2018	3	22:00	66.6ºS	76.5ºE	CA
37		RL37	TS	4-Jan-2018	4	02:00	66.6ºS	76.4ºE	CA
38		RL38	TS	4-Jan-2018	4	06:00	66.6ºS	76.4ºE	CA
39		RL39	TS	4-Jan-2018	4	14:18	66.6ºS	76.4ºE	CA
40		RL40	TS	5-Jan-2018	5	02:00	66.6ºS	76.3ºE	CA
41		RL41	RT	16-Jan-2018	16	06:00	64ºS	57.5ºE	SB
42		RL42	RT	17-Jan-2018	17	06:00	62ºS	57.5ºE	SACCF
43		RL43	RT	19-Jan-2018	19	12:00	60ºS	57.1ºE	SACCF
44		RL44	RT	21-Jan-2018	21	02:00	57.5ºS	57.5ºE	PF2
45		RL45	RT	22-Jan-2018	22	09:00	55ºS	57.6ºE	PF2
46		RL46	RT	30-Jan-2018	30	11:30	38ºS	57.5ºE	NSTF2
47		RL47	RT	31-Jan-2018	31	11:00	34ºS	57.5ºE	NSTF2
48		RL48	RT	2-Feb-2018	33	06:00	28ºS	57.5ºE	NSTF1
49	XIth Southern Ocean Expedition (SOE-XI)	RL49	LT1	7-Feb-2020	38	12:00	67.52ºS	78.75ºE	CA
50		RL50	LT2	8-Feb-2020	39	12:00	67.35ºS	76.05ºE	CA
51		RL51	LT3	10-Feb-2020	41	12:00	65ºS	73.93ºE	SB
52		RL52	LT4	11-Feb-2020	42	12:00	66.99ºS	74.02ºE	CA
53		RL53	LT5	12-Feb-2020	43	06:00	66.8ºS	71.03ºE	CA

54	RL54	LT6	13-Feb-2020	44	12:00	64.99°S	70.93°E	SB
55	RL55	LT7	14-Feb-2020	45	12:00	65°S	67.98°E	SB
56	RL56	LT8	15-Feb-2020	46	11:00	66.86°S	67.77°E	CA
57	RL57	LT9	16-Feb-2020	47	06:00	66.98°S	64.86°E	CA
58	RL58	LT10	17-Feb-2020	48	12:00	64.98°S	64.95°E	SB
59	RL59	LT11	18-Feb-2020	49	12:00	65°S	62°E	SB
60	RL60	LT12	19-Feb-2020	50	12:00	66.88°S	61.95°E	CA
61	RL61	RT1	20-Feb-2020	51	12:00	65.5°S	57.96°E	SB
62	RL62	RT2	22-Feb-2020	53	12:00	63.46°S	58.07°E	SB
63	RL63	RT3	24-Feb-2020	55	12:00	60°S	57.5°E	SACCF
64	RL64	RT4	25-Feb-2020	56	12:00	57.37°S	57.5°E	PF
65	RL65	RT5	26-Feb-2020	57	18:00	54.62°S	57.51°E	PF2
66	RL66	RT6	27-Feb-2020	58	12:00	51.76°S	57.52°E	PF1
67	RL67	RT7	28-Feb-2020	59	12:00	50.43°S	57.51°E	PF1
68	RL68	RT8	29-Feb-2020	60	12:00	47.85°S	57.7°E	SAF2
69	RL69	RT9	1-Mar-2020	61	18:00	45.2°S	57.85°E	SAF1
70	RL70	RT10	2-Mar-2020	62	12:00	43.02°S	57.02°E	SAF1
71	RL71	RT11	3-Mar-2020	63	12:00	40.19°S	57.51°E	SSTF
72	RL72	RT12	4-Mar-2020	64	12:00	36.15°S	57.43°E	NSTF2

73		RL73	RT13	5-Mar-2020	65	12:00	31.02°S	57.38°E	NSTF1
74		RL74	RT14	6-Mar-2020	66	12:00	27°S	57°E	NSTF1
75		RL75	RT15	7-Mar-2020	67	12:00	24°S	57°E	NSTF1

Note. RL refers to radiosonde launch; OT refers to onward track and RT refers to return track

Chapter 3

Micrometeorological Characteristics of Atmospheric Surface Layer over a Tropical Coastal Region of Goa, India

3.1. Introduction

The surface layer is defined as the lowest part (about 10%) of the atmospheric boundary layer (Högström, 1996). This layer exhibits turbulent characteristics due to radiative heating, cooling and mesoscale motions which are augmented due to surface heterogeneities of the earth's surface. This eventually controls heat, moisture, and momentum transport within the surface layer (Stull, 1988; Sorbjan, 1989b; Garratt, 1992; Kaimal and Finnigan, 1994) . The transport of heat and moisture fluxes varies over a broad range of spatial domains, especially for forest ecosystems, terrains with complex topography, inland, semi-arid, coastal, urban, and rural areas. This makes it difficult to draw a comparative analysis of statistics of estimated values with that of other locations and from the numerical models.

The turbulence fluxes in the surface layer are well described by the Monin-Obukhov similarity theory (MOST) (Monin and Obukhov, 1954), which provides suitable and acceptable empirical relations associated with variances of wind and temperature along with stability and scaling parameters. Fundamentally, MOST can suggest plausible universal functions between fluxes and mean quantities and the exact forms of these relations are to be verified from accurate observations under different stability conditions (Monin and Yaglom, 1971; Kaimal and Finnigan, 1994; Pahlow et al., 2001). Though MOST is not 'universal' when it comes to heterogeneity of the surface conditions (Wilson, 2008), it is used in airflow and air dispersion studies even in urban locations. In modelling the transport of air pollutants, knowledge of the airflow and its turbulent characteristic close to the ground are extremely crucial. Thus, an improved understanding of this is based on the surface roughness parameter. This parameter is

unique for different regions and must be estimated using a series of data generated from experimental observations. Such statistical studies have been carried out in many other urban regions (Grimmond and Oke, 1999; Roth, 2000; Wood et al., 2010; Trini Castelli and Falabino, 2013; Trini Castelli et al., 2014). Literature on these studies particularly in coastal regions is comparatively less (Lange et al., 2004; Singha and Sadr, 2012; Grachev et al., 2018a). Experimental campaigns and field measurements to quantify the turbulence statistics of the surface layer over tropical regions are rare. Over the Indian sub-continent a few studies have been carried out at different geographical locations like inland regions (Goel and Srivastava, 1990; Sivaramakrishnan et al., 1992; Kailas and Goel, 1996; Rao et al., 1996), semi-arid regions (Krishnan and Kunhikrishnan, 2002; Reddy and Rao, 2016; Siva Kumar et al., 2021), complex terrains (Solanki et al., 2016b; Barman et al., 2019; Solanki et al., 2019b) and coastal regions (Prakash et al., 1992; Kunhikrishnan et al., 1993; Ramachandran et al., 1994a; Ramana et al., 2004b) .

An improved understanding of the surface layer processes requires knowledge of the turbulence characteristics during different seasons. In view of this, several studies have been conducted in past focused on improving the present understanding of the surface layer processes and the nature of the turbulence characteristics during different seasons. For instance, studies by Ramachandran et al. (1994a); Namboodiri et al. (2014); Prasad et al. (2019) have demonstrated the seasonal variability of surface layer parameters. Such studies attain important implications for modelling the turbulent exchange coefficients in regional-scale numerical models and pollutant dispersion studies. Understanding the surface characteristics and associated energy exchange process is essential for the knowledge of local climate, and modelling of the turbulent exchange in regional scale numerical models. In view of this, the study presented in this chapter partially addresses this prerequisite based on observations generated from a 32 m tall meteorological tower installed at a fixed location within the Goa

University campus. The details on the experimental site and the instrumental setup used for conducting this study are discussed in section 2.2.1. and section 2.2.2. of chapter 2 of this thesis. By accessing the data generated using the on-site instrumental setup, the study described in this chapter aimed to address the following questions,

1. How does the fluxes of heat and momentum, and associated stability conditions vary on the diurnal and seasonal scales over the study region?
2. How well does MOST perform under different stability conditions over the present experimental site that represents a tropical coastal region?
3. To establish an empirical relationship of variances of wind components and temperature with varying stability conditions.

Several studies have been carried out over different climatic regions across the globe and limited locations over the Indian regions. Experimental studies by Prasad et al. (2019) over east coast of India and Ramachandran et al. (1994) over the west coast of India showed a seasonal variability in the empirical relations and they attributed to the surface roughness associated with the varying wind direction over the seasons. However, Ramana et al. (2004) showed that turbulent statistics are nearly independent of seasons in a region in Lucknow, India. It is evident from these studies that turbulence statistics depend on the terrain and meteorology. In Chapter 2, it is described that the coastal experimental site i.e., a station in Goa region is influenced by the varying wind patterns and wind intensities over various seasons. Under these conditions, the variation of surface turbulence statistics was not explored. The understanding and quantification of turbulence intensities - specifically normalized velocity variances and correlation coefficients are important because these measurements over this study location is first of its kind and aims to provide an understanding on turbulent nature of surface layer during different tropical seasons. The uniqueness of the present study lies in establishing suitable empirical equations over this least explored coastal region which are crucial for modelling

studies. The empirical fitting relations obtained from the present study can be used to validate the representation of surface layer turbulence in regional weather models developed for terrains of similar characteristics. Realizing these aspects, Geosphere, Biosphere Programme of Indian Space Research Organization (ISRO-GBP) under the aegis of Network of Boundary Layer Experiments (NOBLE) project has established a boundary layer experimental setup at Goa University campus for conducting the present work.

3.2. Data and method

The data generated for fair weather days collected during the period from March 2015 - February 2016 were considered for the study. Rainy and cloudy days were discarded to obtain close estimates of surface layer fluxes under clear sky conditions with minimum effect of clouds (if any) while collecting observations over this study region. The complete data statistics used for undertaking this study are listed in Table 2.3. in chapter 2 of this thesis. The primary dataset constitutes time-series measurements of low frequency (hourly) data i.e., air temperature (*AT*), relative humidity (*RH*), wind speed (*WS*), and wind direction (*WD*) from slow response sensors installed on the meteorological tower at 4 m, 18 m, and 30 m heights respectively. Additionally, low frequency data from pressure probe and rain gauge equipped at 4 m height have been used. A set of 3D sonic anemometers installed at 10 m and 20 m heights provided high frequency (10 Hz) data of sonic temperature (*T*) and components of wind (*u*, *v*, and *w*). Low frequency data were utilized to understand the diurnal and seasonal pattern of surface layer meteorological conditions and wind pattern. High frequency data measuring the fluctuations of wind components in the horizontal and vertical direction and sonic temperature were utilized to study diurnal and seasonal variations in the surface layer fluxes of heat and momentum, and associated stability conditions. Thus, high frequency data were used to compute friction velocity (u_*), sensible heat flux (H), momentum flux (τ), turbulent kinetic energy (e) and stability (z/L), where z is the height of observation and L is the Obukhov

length). These dynamical parameters have been estimated using the eddy correlation technique (Kaimal and Finnigan, 1994; Aubinet et al., 2012).

The friction velocity (u_*) was estimated from,

$$u_* = \sqrt[4]{(\overline{u'w'})^2 + (\overline{v'w'})^2} \quad 3.1$$

where the bar and the prime average over time and fluctuations from the mean value respectively (Stull, 1988), ($u'w'$) and ($v'w'$) are the kinematic momentum fluxes in the along and cross-wind directions. The temperature scaling parameter (T_*) and the Obukhov length (L) were computed from,

$$T_* = \overline{w'T'}/u_* \quad 3.2$$

$$L = -\frac{u_*^3 \bar{T}}{(k.g\,\overline{w'T'})} \quad 3.3$$

where k is von Karman constant (=0.4), g is the acceleration due to gravity, u_* is frictional velocity and $\overline{w'T'}$ is the heat flux. The quantities e, τ, and H are computed using the following equations,

$$e = \frac{1}{2}\left[\overline{u'^2} + \overline{v'^2} + \overline{w'^2}\right] \quad 3.4$$

$$\tau = \rho\sqrt{(\overline{u'w'})^2 + (\overline{v'w'})^2} \quad 3.5$$

$$H = \rho.C_p(\overline{w'T'}) \quad 3.6$$

where ρ is the density of air and C_p is the specific heat of air at constant pressure.

The normalized standard deviation of wind components (σ_u/u_*, σ_v/u_*, and σ_w/u_*) and temperature (σ_T/T_*) are computed for every 30 minute time interval using high frequency data. Variation of these estimations with the stability parameter is obtained by averaging corresponding values at uniform intervals of z/L.

The correlation coefficients of momentum and heat flux had been computed using the equations given below,

$$|r_{uw}| = \frac{\overline{u'w'}}{\sigma_u \sigma_w} \quad 3.7$$

$$|r_{wT}| = \frac{\overline{w'T'}}{\sigma_w \sigma_T} \quad 3.8$$

where, r_{uw} and r_{wT} are correlation coefficients for momentum and heat flux respectively.

The surface roughness length (z_o) was calculated for the data at 10 m height using the following equation (Panofsky and Dutton, 1984; Sorbjan, 1989b).

$$lnz_0 = lnz - k\ \frac{U}{u_*} -\ \psi_m\ (z/L) \quad 3.9$$

where, $\psi_m\ \left(\frac{z}{L}\right) = 2\ ln\left(\frac{1+x}{2}\right) + ln\left(\frac{1+x^2}{2}\right) - 2tan^{-1}(x) +\ \pi/2$

where, $x = \left(1 - \gamma_1 \frac{z}{L}\right)^{1/4}$ for $z/L < 0$ with $\gamma_1 = 16$

$\psi_m\ \left(\frac{z}{L}\right) = -5\frac{z}{L}$ for $z/L > 0$

where $\psi_m\ \left(\frac{z}{L}\right)$ is the momentum stability correction factor (Paulson, 1970; Panofsky and Dutton, 1984; Sorbjan, 1989b).

3.2.1. Quality check

The sonic anemometer data was collected at every 0.1s and a total of 11232 half-an-hour data samples were obtained for this study. To eliminate the unrealistic values arising out of instrument error such as jitter, data points outside the absolute limits set for u, v, w and T were removed. This was performed for both horizontal (u, v) (-50 m s^{-1} to +50 m s^{-1}) and vertical (w) components of wind speed (-10 m s^{-1} to +10 m s^{-1}). A moving window method given by Vickers and Mahrt (1997) was applied to identify the spikes while a linear detrending method was applied to remove any long-term trend present in unprocessed u, v, w, and T. While doing this, care has been taken not to consider data points outside 3.5 times the standard deviation limits. Further, to minimize the effect of any misalignment of sensors, quality checks such as double rotation and tilt corrections had been performed on data (Wilczak et al., 2001). This

facilitates the alignment of the axes of the coordinate system to mean stream-wise wind direction. In addition, a stationary test was performed as a part of a quality check (Foken and Wichura, 1996).

3.2.1.1. Stationary test

The non-stationarity of the data arises due to the diurnal variation in heating and cooling of Earth's surface and mesoscale variation of winds (Večenaj and De Wekker, 2015). The application of MOST assumes that the time series data must be stationary (i.e., statistics of the turbulence do not vary with time), but the non-stationarity nature of the data becomes a key issue in the estimation of turbulence (Mahrt, 1998b). Thus, it is pertinent to correct the data by eliminating the non-stationary components of data from the stationary datasets before considering the applicability of MOST (Mahrt, 1998b). To achieve this, the methodology proposed by Foken and Wichura (1996), which is reported to effectively identify a large number of stationary data among other reported stationary tests, has been adopted to generate a stationary dataset (Foken and Wichura, 1996; Večenaj and De Wekker, 2015; Babić et al., 2016). Adopting this method, stationary components have been extracted by taking mean values of the covariance for every 30 minute interval (18000 data in 30 minutes, sampling at the frequency of 10 Hz) and are compared with the values calculated at every 5 minute sub-interval (3000 data in every 5 minutes). If the difference between these values is less than 30% then the time series data was considered to be stationary. After incorporating this test, a quality check proposed by Agarwal et al. (1995) was adopted so that all wind speed values less than 0.5 m s^{-1} were discarded. Owing to this, a total of 7609 and 7745 half an hour of data generated from 10 m and 20 m heights respectively were used for further analysis.

3.2.1.2. Gap filling method

By adopting the above-mentioned quality checks, some data points that did not meet the quality criteria were eliminated. This resulted in a gap/missing data point for certain periods, which

was filled in this study by adopting the look-up table (LUT) method (Falge et al., 2001) . LUTs were generated such that missing flux values were identified based on similar meteorological conditions associated with the missing flux data (Falge et al., 2001; Reichstein et al., 2005). LUTs were binned by temperature class defined by 2°C intervals ranging from 10°C to 50°C. In each class interval, mean and standard deviation of temperature and corresponding fluxes were calculated. If the gap still exists in the defined class interval in LUT then it was filled by linear interpolation. Thus, LUTs were created to reproduce the mean values of fluxes based on seasonal meteorological conditions. On average, about 32% and 31% of missing data could be identified for the heights of 10 m and 20 m respectively. This ultimately resulted in 3623 and 3487 missing data points to be looked up and filled at 10 m and 20 m respectively.

3.2.1.3. Self-correlation analysis

Without evaluating the role of self-correlation of data, the validity of MOST becomes incomplete (Mahrt, 1998b). The self-correlation arises due to the appearance of a common friction velocity u_* in σ_w/u_*, σ_T/T_*, and z/L. To evaluate self-correlation in the present dataset, a random sampling approach described in Klipp and Mahrt (2004) was adopted. From the observed datasets of u_*, $\overline{(\mathrm{w}'T')}$, σ_w, and σ_T, a new 1000 random datasets have been generated at each measurement height. Subsequently, the linear correlation coefficient was estimated between z/L and σ_w/u_* and thereafter between z/L and σ_T/T_*. The coefficients thus obtained were averaged and then $\langle R^2_{Random} \rangle$ was calculated, this indicated the measure of self-correlation due to a common variable. Similarly, R^2_{data} for the original datasets were estimated and the difference $R^2_{diff} = R^2_{data} - \langle R^2_{Random} \rangle$ was computed. The R^2_{diff} is indicative of true physical variance associated with processes governing turbulence (Klipp and Mahrt, 2004). Negative values of R^2_{diff} indicate that self-correlation has a significant influence on the total variance, while as it tends to unity, the effect of self-correlation becomes less

prominent (Babić et al., 2016). Results of the assessment of self-correlation are presented in Table 3.1. attributed to the limitation of this method in the stable atmospheric boundary layers.

Table 3.1 Self-correlation analysis of the variations in σ_w/u_* and of σ_T/T_* with stability. R^2_{data} is defined as square of the correlation coefficient for the original dataset, R^2_{Random} is the coefficient of determination from self-correlation, and $R^2_{diff} = R^2_{data} - \langle R^2_{Random} \rangle$ is the fraction of true physical variance associated with processes governing the turbulence.

Measurement heights	Stability	Variables	No. of data points	R^2_{data}	$\langle R^2_{Random} \rangle$	$R^2_{diff} = R^2_{data} - \langle R^2_{Random} \rangle$
10 m	Unstable	*w*	2044	0.63	0.36	0.27
		T	2044	0.37	0.01	0.36
	Stable	*w*	743	0.17	0.18	-0.01
		T	743	0.01	0.05	-0.04
20 m	Unstable	*w*	2010	0.76	0.40	0.34
		T	2010	0.37	0.02	0.35
	Stable	*w*	950	0.34	0.25	0.09
		T	950	0.01	0.02	-0.01

During unstable conditions, the self-correlation for the dataset *w* is found to be higher compared to that of *T*. In present data, the value of R^2_{diff} is found to be higher (>0.25) at both heights indicating self-correlation under unstable conditions. However, for stable conditions, the values of self-correlation coefficients for *w* and *T* are found to be very small and negative. Babić et al. (2016) has also reported smaller and negative values of self-correlation coefficients during stable conditions, and it was attributed to the limitation of this method in the stable atmospheric boundary layers.

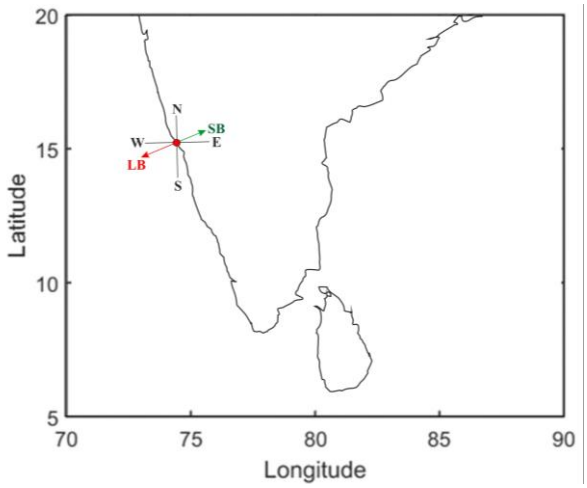

Figure 3. 1 A schematic site map of Goa region, showing the study location with respect to the coastline, and the land/sea breeze direction with respect to it.

3.3. Results and Discussion

This section describes the diurnal and seasonal variability of surface layer meteorological parameters, fluxes of heat, momentum and associated stability conditions over a tropical coastal site, Goa. As the observational site is located near the Arabian Sea, it experiences land/sea breeze circulation, arising due to the differential heating of land and adjoining sea. The breeze originating from the sea brings the cool air over the heated coastal region and subsequent formation of the thermal internal boundary layer (TIBL) during the daytime (Kunhikrishnan et al., 1993; Davis et al., 2020; Davis et al., 2022). Thus, the diurnal evolution of thermal structure and surface characteristics of the coastal atmospheric boundary layer (CABL) is modulated by the sea/land breeze. Studies also showed that the height of CABL is lowered with the advection of sea breeze (Miller and Keim, 2003; Miller et al., 2003). Furthermore, flux-variance relationships in the atmospheric surface layer are defined by MOST, which assumes homogeneity of the surface, including surface fluxes as well as surface roughness (Stull, 1988) Hence, in subsequent sections below, by adopting MOST, flux-variance relationships obtained over the study site have been discussed.

3.3.1. Diurnal mean and seasonal variation of surface layer parameters

Figure 3.1 depicts the seasonal mean diurnal variation of slow response sensor-measured air temperature (*AT*), relative humidity (*RH*), wind speed (*WS*), and wind direction (*WD*) at 18 m height during winter, pre-monsoon, summer-monsoon, and post-monsoon seasons respectively over the experimental site. The air temperature starts increasing from around 07:00 IST (IST = UTC + 05:30 hrs) and showed a systematic diurnal variation. The average value of maximum air temperature (AT_{max}) observed during winter, pre-monsoon, summer-monsoon, and post-monsoon seasons are 29.9 ± 1.8 ℃, 29.5 ± 1.5 ℃, 28.8 ± 0.4 ℃ and 30.9 ± 1.6 ℃ with a difference in the time of occurrence [around 13:00 IST, 12:00 IST, 14:00 IST and 13:00 IST] respectively. Similarly, the average value of RH_{mean}, during each season was 62%, 75%, 88% and 75% respectively during daytime while 81%, 84%, 92% and 90% during nighttime respectively. Variation of winds revealed the prevalence of high-speed winds dominantly from a west-northwest direction (270°-315°) during the summer monsoon season followed by pre-monsoon and low wind prevails in the winter season. Statistics of the wind are not only important in determining the travel period of pollutants from the source region but also control the surface concentration. Over this region, poor dispersal of pollutants is expected in the

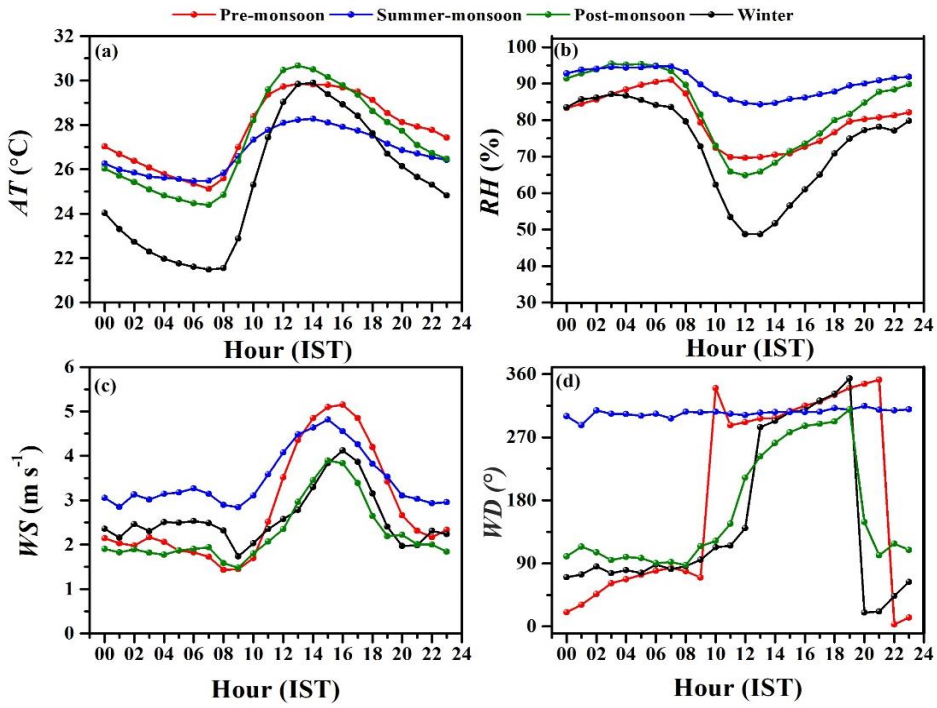

Figure 3.2 Diurnal mean seasonal fluctuations of (a) air temperature (AT), (b) relative humidity (RH), (c) wind speed (WS), and (d) wind direction (WD) observed at 18 m heights during winter (black), pre-monsoon (red), summer-monsoon (blue), and post-monsoon (green) seasons.

winter season. The occurrence of the land/sea breeze system was observed with wind speeds typically <6-7 m s^{-1} during daytime (sea breeze) and less than 3 m $s^{-1,}$ during nighttime (land breeze) (Figure 3.1). Data reveals that the dominant land breeze comes from east direction whereas, the sea breeze originates from west/northwest direction over the experimental site. The winds are from the west/northwest direction during the monsoon season (Figure 3.1).

3.3.2. Wind characteristics at the study site

The wind-rose diagram in Figure 3.2a, b depicts the variability of hourly averaged wind speeds obtained from the slow response sensor at 18 m and a sonic anemometer at 10 m height for the study period. The dominant wind directions at the site were mainly from the northwest to the west (wind direction is mostly within 292° and 330°) and from northeast to east directions (wind direction is mostly within a cone of 67° and 97°). In general, wind speeds greater than 3

m s^{-1} were frequently observed from the northwest and west, while wind speeds with magnitudes less than 3 m s^{-1} were observed less frequently from the east and northeast directions. Seasonal wind variability observed over the study site is represented in Figure 3.2 (c-f). The dominant direction of winds during winter asnd pre-monsoon were north westerlies while during post-monsoon season north easterlies and during summer-monsoon south westerlies winds were prominently observed.

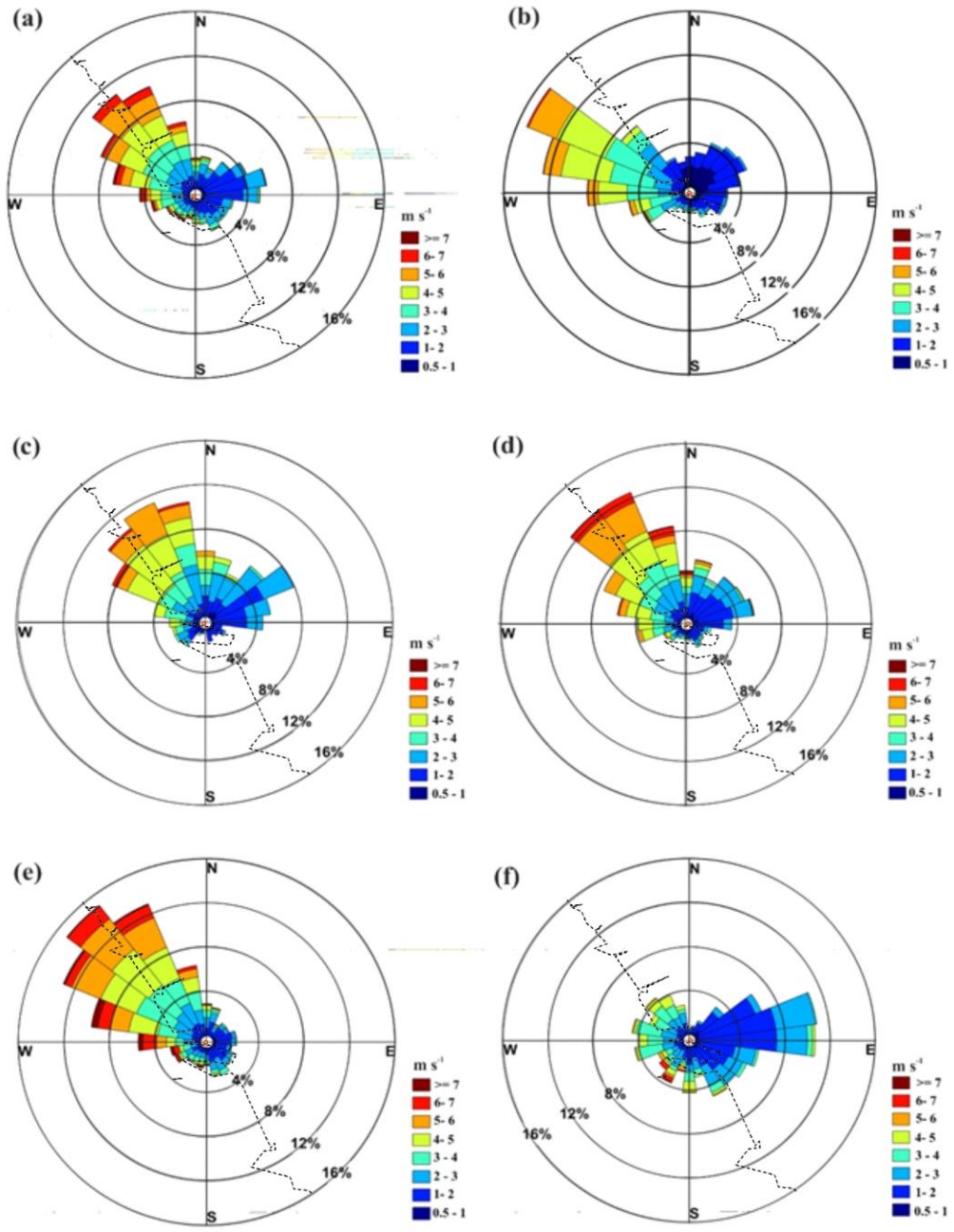

Figure 3.3 (a-b) represents wind rose diagram observed for varying wind speed thresholds over the experimental site with on an average over all seasons at (a) 18 m height using slow response sensors and (b) 10 m height using a sonic anemometer for the period from March 2015 to February 2016. (c-f) represents wind rose diagram depicting wind variation observed over the site during different seasons i.e., (c) winter d) pre-monsoon, (e) summer-monsoon and (f) post-monsoon at the 18 m height during the study period. The coastline geometry is shown in black dotted line.

3.3.3. Estimation of surface roughness length

A better understanding of the surface layer lies on the surface homogeneity. However, any heterogeneities prevailing at the surface affect the length scales. As already mentioned, the surface heterogeneity over the coastal environment leads to the formation of complex vertical structures such as TIBL and roughness sub-layers where turbulence parameters become the function of winds. Conventionally, the surface roughness length (z_0) is estimated using the observations of wind speed at two or more height levels in neutral stability conditions. The z_0 at a site does not change with wind speed, stability, or stress. It can be changed only if the roughness elements over the surface change such as caused by an increase in the vegetation, construction of buildings etc. (Stull, 1988). Also, z_0 is strongly dependent on wind direction, as this variation is the result of different surface features and obstacles that affect wind flow in different directions. In this study, z_0 has been calculated using the methodology described by Panofsky and Dutton (1984) (equation 3.9). The results of which are mentioned in Table 3.2 for six wind sectors and all wind directions around the experimental site. The data obtained at this location were categorized into each of these sectors based on wind directions encountered at 10 m height: 330–30◦ (524 data), 30–90◦ (1049 data), 90-150◦ (587 data), 150–210◦ (229 data), 210–270◦ (1267 data) and 270–330◦ (2916 data) respectively. From the values estimated over different wind sectors, it is evident that the maximum values of roughness length were

found in sectors; 150-210° and 330-30° and minimum values were in sectors 30-90° and 270-330° respectively during all seasons. These high and low values portrayed varying geometry surrounding the experimental site (refer Figure 2.1 of chapter 2). Over the study site, from all considered wind direction sectors, the value of z_0 ranged from 0.08 m to 0.97 m. The high roughness length associated with the 330-30° sector is attributed to the daytime winds originating from the sea, while the easterly winds are dominant during the nighttime (Figure 3.1d). For easterly wind directions, the lowest roughness lengths were estimated. The data also confirms that the roughness length is independent of the wind speed. Larger values of z_0 in the wind direction of 150-210° is due to the presence of buildings (Figure 2.1b, 2.2a). Considering all sectors, mean values of z_0 varied between 0.19 m and 0.37 m. On the seasonal scale, the value of z_0 was found to be highest (reaching nearly 0.37 m) in pre-monsoon season. The larger values are mainly attributed to the dominant wind originating from the sectors 150° - 210° (presence of building) and 330° - 30° (presence of 3m high trees) (Figure 2.1). The lowest values of z_0 were observed during post-monsoon season (reaching nearly 0.19 m), where the dominant wind from east direction (Figure 3.3f), where there is no obstruction (open space) (Figure 2.1).

Table 3.2 Roughness length values are estimated at a height of 10 m for different wind sectors and in all directions.

Seasons	All Directions	330°-30°	30°-90°	90°-150°	150°-210°	210°-270°	270°-330°
Winter	0.32 m	0.74 m	0.15 m	0.10 m	0.48 m	0.28 m	0.16 m
Pre-monsoon	0.37 m	0.97m	0.13 m	0.26 m	0.48 m	0.21 m	0.17 m
Summer-monsoon	0.24 m	0.94 m	0.15 m	0.21 m	0.49 m	0.31 m	0.17 m
Post-monsoon	0.19 m	0.41 m	0.08 m	0.26 m	0.51 m	0.27 m	0.13 m

All seasons	0.25 m	0.85 m	0.11 m	0.25 m	0.50 m	0.28 m	0.26 m

3.3.4. Seasonal mean variation of turbulent energy and heat flux parameters

Turbulence in the atmosphere is the coupled effect of buoyancy-induced thermals and mechanical eddies. In this study, an approximation for thermal turbulence is studied using sensible heat fluxes (H) while mechanical turbulence is studied using momentum fluxes (τ). The effect of both buoyancies, as well as mechanical shear, are illustrated using turbulent kinetic energy (e). As discussed, (in section 3.2.1.2 of this chapter), estimation of fluxes was obtained after adopting a look-up method for filling missing data gaps (Falge et al., 2001). Figure 3.3a, b shows seasonal mean diurnal variations observed at 10 m and 20 m height. Variation of sensible heat flux showed negative values during nighttime (H directed towards the surface) and increases to positive values around 07:00 IST (H directed away from the surface). Later, it showed a systematic increase and reaches a peak value between 13:00 to 14:00 IST followed by a further decrease to attain negative values after 17:30 IST. It is observed that sensible heat flux at 10 m attains maximum seasonal mean value during pre-monsoon ($76\ \mathrm{W\ m^{-2}}$) followed by winter ($61\ \mathrm{W\ m^{-2}}$), post-monsoon ($51\ \mathrm{W\ m^{-2}}$) and minimum during the summer monsoon season ($11\ \mathrm{W\ m^{-2}}$) respectively. Seasonal mean values of sensible heat flux at 10 m lie within 15% of the data obtained at 20 m. Lower values of heat flux during summer-monsoon showed the prevalence of weak heat flux exchanges due to cloud coverage during this season. Seasonal mean values of turbulent kinetic energy (e) were dominantly high during the summer monsoon season due to prevailing strong winds (Figure 3.1; 3.3a, b). Systematic diurnal variation in$e$ showing noontime enhancement was observed during all seasons at both heights. The highest seasonal mean values of e were observed during the summer monsoon season ($\approx 0.76 \pm 0.33\ \mathrm{m^2\ s^{-2}}$ at 10 m height). Variation of momentum flux (τ) exhibits a typical diurnal cycle in phase with turbulent kinetic energy (e) during all the

seasons. The highest seasonal mean stress (τ) at 10 m was observed during summer-monsoon ($\approx 0.17 \pm 0.09$ N m^{-2}) followed by moderate during pre-monsoon ($\approx 0.11 \pm 0.04$ N m^{-2}) and lowest during post-monsoon ($\approx 0.07 \pm 0.03$ N m^{-2}) respectively. On the diurnal scale, the highest momentum flux transfer occurred during noon hours while the lowest was during the night. The observed fluctuations in these atmospheric fluxes (heat and momentum) are associated with variability in temperature and wind speed which are responsible for altering the stability of the atmosphere within the surface layer. Thus, this study further examined *z/L* to understand the changes in the atmospheric state due to mesoscale processes which induce or diffuse the vertical motion of eddies. The observed diurnal variation of *z/L* at 10 m height showed that during the evening and nocturnal hours highly stable conditions prevailed while during daytime highly unstable conditions were dominant. Nighttime stable stratification was due to the suppressed vertical mixing by buoyancy. Similar diurnal variation of stability parameter (*z/L*) was also observed at 20 m with slight variations in its magnitude (Figure 3.3b).

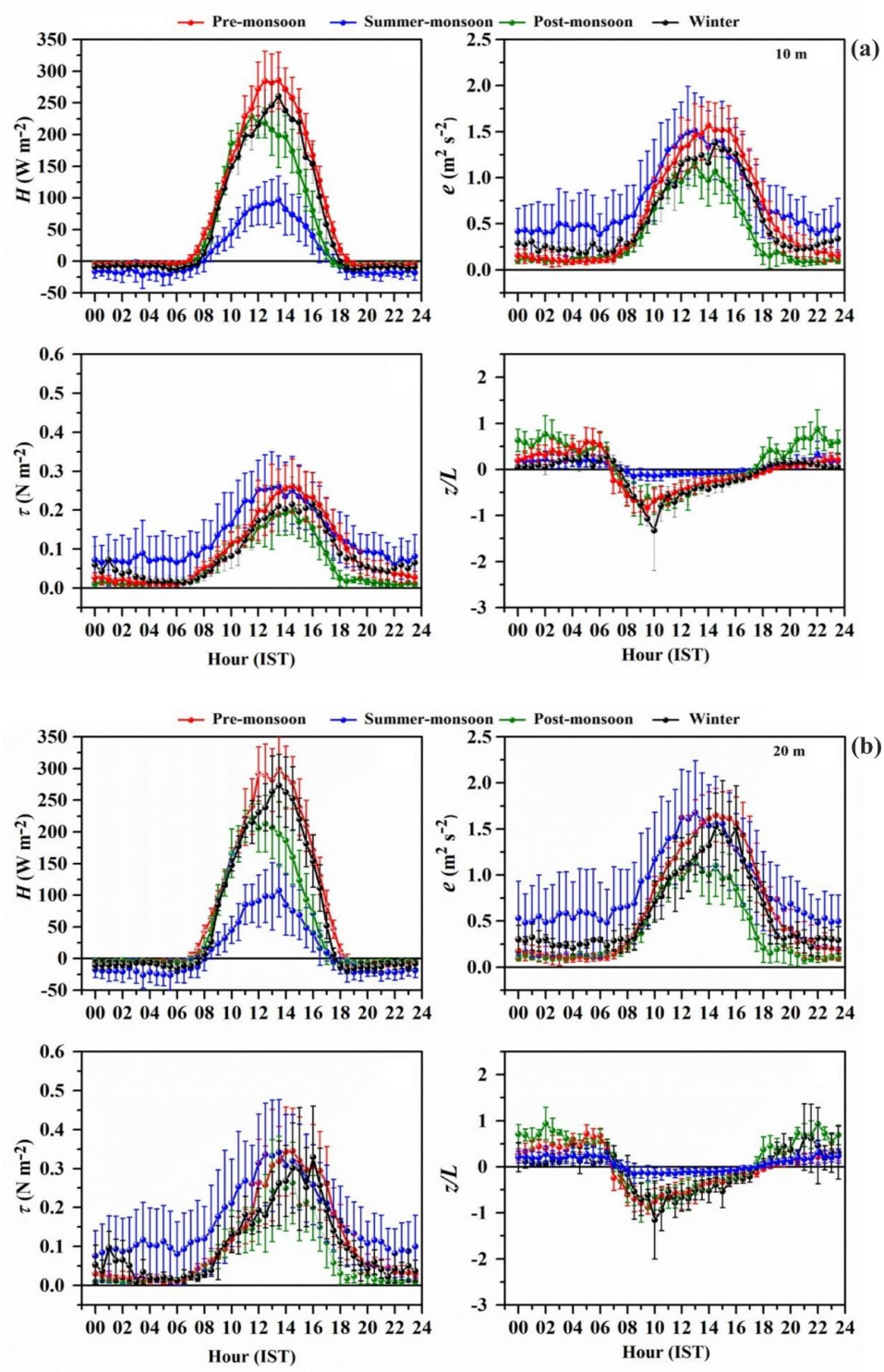

Figure 3.4 Diurnal mean seasonal fluctuations of sensible heat flux (H)**,** turbulent kinetic energy (e), momentum flux (τ), and stability parameter (z/L) observed at (a) 10 m and (b) 20 m hegith during different seasons i.e., winter (black), pre-monsoon (red), summer-monsoon (blue) and post-monsoon (green) seasons. Error bars indicate standard deviations.

3.3.5. Turbulent statistics

This section evaluates the universal functions of MOST over inhomogeneous terrain of coastal site Goa by comparing our data with those observed over other flat, homogeneous, and heterogeneous locations. According to the MOST, the normalized standard deviation of velocity components (i.e., $\sigma_{i=u,v,w}$) are functions of z/L within the surface layer. Equation 3.10 proposed by Panofsky and Dutton (1984) was used to investigate the validity of MOST over the experimental site.

$$\sigma_{i=u,v,w}/u_* = C1(1 + C2\, z/L)^{C3} \quad 3.10$$

In general, the coefficients $C1$,$C2$ and $C3$ experimentally determined. The universal function (Equation 3.10) is valid for vertical fluctuations over homogenous terrains under unstable and stable conditions (Moraes et al., 2005). However, in recent years, data obtained from heterogeneous terrains showed good general agreement with equation 3.10 for horizontal variances under unstable and stable conditions (Smedman, 1988; Mahrt, 1998b; Roth, 2000; Al-Jiboori et al., 2001; Yusup et al., 2008; Weber and Kordowski, 2010; Wood et al., 2010; Fortuniak et al., 2013; Trini Castelli et al., 2014). In this study, the coefficients $C1$ and $C2$ are determined by using least-squares regression. The empirical fit using equation 3.10 is applied to the data assuming $C3$=1/3 for both unstable and stable conditions. The stability conditions were defined as neutral: -0.1< $z/L < 0.1$ for which $z/L \rightarrow 0$; unstable: z/L <-0.1; stable: z/L>0.1.

3.3.5.1. The normalized standard deviation of horizontal (σ_u/u_* and σ_v/u_*) and vertical (σ_w/u_*) components of wind with stability parameter (z/L)

Figure 3.4 shows the variation of normalized standard deviations of along wind (σ_u/u_*), cross wind (σ_v/u_*), and vertical wind components as a function of z/L at 10 m and 20 m heights for z/L<0 and z/L>0 conditions respectively. Data points in Figure 3.4 represent bin averaged

$\sigma_{i=u,v,w}/u_*$ collected with *z/L*, where the vertical error bar of each data point represents the standard deviation of data points within a particular bin. In Figure 3.4 the curves (solid black line) are estimated using the best fits of the $\sigma_{i=u,v,w}/u_*$ over the Goa site using equation 3.10 and are plotted with the observed data. For comparison, the curves generated using the function given by Xu et al. (1997); Trini Castelli et al. (2014) representing sub-urban reference sites, and Fortuniak et al. (2013) representing urban reference are presented in Figure 3.4 and Table 3.3. Table 3.3 also report the standard deviations of coefficients of *C1* and *C2* observed in this study to present the related uncertainties.

The curves of $\sigma_{i=u,v}/u_*$ produced with reference locations, lie within the variability range of the observed data for the Goa site. The data of $\sigma_{i=u,v}/u_*$ are close to the observations of Xu et al. (1997); Trini Castelli et al. (2014) compared to the observations of Fortuniak et al. (2013). The curves corresponding to Fortuniak et al. (2013).are found to be consistently lower compared to our data for -0.2 <*z/L*<0, but the data from Xu et al. (1997); Trini Castelli et al. (2014) agree well. Results during unstable conditions show that $\sigma_{i=u,v}/u_*$ fits reasonably well with the MOST free-convection prediction of the '1/3' slope for *z/L*<-0.2, the same as observed with the urban/suburban reference locations. Data of $\sigma_{i=u}/u_*$ compares well with the function given by Roth (1993) over a suburban region (not shown). As can be noticed from Table 3.3, the constant *C2* of *u* in unstable conditions are less than those obtained over reference locations. The values of *C2* of $\sigma_{i=u,v}/u_*$ over Goa location is lower than over semi-arid regions like Anand (Dharmaraj et al., 2009) and Anantapur (Sivakumar Reddy et al., 2021). Indicating that the surface characteristics over the Goa is less unstable compared to the semi-arid regions. A possible explanation is the following: the data observed over Goa site during the unstable conditions (daytime) are of sea breeze, originating from west/northwest direction with wind speed greater than 3 m s^{-1} (Figure 3.2). The daytime coastal atmospheric boundary layer

is lowered with the onset of sea breeze and subsequent formation of TIBL (Kunhikrishnan et al., 1993). The reduction in the contribution of convective activity and mesoscale wind during daytime lowers the boundary layer height. This may be the reason for the lower value of the constant *C2* of σ_u in equation 3.10. Interestingly, the observed values C2 are lower than the reported values over Kalpakkam, east-coast (Prasad et al., 2018). This shows that its growth rate with the instability is slower over Goa location compared to that of Kalpakkam, which depends on heat flux and friction velocity. In this study, the effect is observed for both the data points.

The stable data of $\sigma_{i=u,v}/u_*$ as a function of z/L depicted in Figure 3.4 shows that Goa site observations of $\sigma_{i=u,v}/u_*$ lies between suburban and urban locations, indicating the turbulence during stable conditions over the Goa site has similar features as that of the reference locations. As supported by Trini Castelli and Falabino (2013), turbulence has common features under low wind conditions irrespective of locations and this is confirmed by Trini Castelli et al. (2014). As already stated, present data during the stable conditions (nighttime) are of land breeze, originating from easterly direction, with wind speed less than 2 m s^{-1} (except in monsoon season) (Figure 3.2). The present results show that the turbulence in low wind conditions has common features as that of the reference locations during the stable conditions. Studies have shown that $\sigma_{i=u,v}/u_*$ are better scaled with mixed-layer similarity variables. Due to the non-availability of direct information on mixed-layer depth (z_i), the variations of $\sigma_{i=u,v}/u_*$ on z_i/L cannot be verified. Regardless of the scaling details, present results show dependency of $\sigma_{i=u,v}/u_*$ on z/L and follow '1/3' power law. Similar behavior was reported by several researchers over different regions across the world i.e., Moraes et al. (2005) over rough and forest terrain, Quan and Hu (2009); Wood et al. (2010) in London and Siva Kumar Reddy et al. (2021) in semi-arid region, Anantapur, India.

The curves of σ_w/u_* produced with reference locations, lie within the variability range of the observed σ_w/u_* data for the Goa site. The curves increase with instability and follow '1/3' power law. The agreement of $\sigma_w/u_*$with the suburban results of Trini Castelli et al. (2014) is good at large instabilities (z/L<-1) but for small negative values of z/L, the present data lie below their curve. Whereas present observations agree with the curve of Xu et al. (1997) for z/L>-0.2 but lie below their curve for z/L<-0.2. The variability between locations, however, was quite considerable. Further, it was found that the mean values of σ_w/u_* from the present study were lower than the values reported over semi-arid region (Krishnan and Kunhikrishnan 2002; Dharmaraj et al., 2009), but higher than values reported over inland (Ramana et al., 2004) and coastal regions (Ramachandran et al., 1994; Prasad et al., 2019). These results revealed that the vertical transport of turbulence at present study site is higher than that over two coastal stations (Thumba and Kalpakkam) which could be due to differences in the distribution of turbulence associated with the intensity of vertical wind.

The observations from Fortuniak et al. (2013) compare well with the present data. The σ_w/u_*values are constant up to $z/L \approx 0.7 - 0.8$, after which an increase was observed. The present results agree well with the data of Fortuniak et al. (2013); Trini Castelli et al. (2014). Similar behavior has been reported over other urban locations Al-Jiboori et al. (2001); Weber and Kordowski (2010) and natural surfaces by Pahlow et al. (2001). The present data follows the data of Xu et al. (1997) for z/L<0.1, afterwards, their data revealed an increase. Present results are consistent with the observations of Nieuwstadt (1984), who found σ_w/u_* to be approximately constant at 1.4. Nieuwstadt's observations (refer their Figure 2) are concentrated on the range 0.1<z/L<2.0. Our data agree well with their data up to z/L≈0.8, after which departs slightly from a constant value. According to Pahlow et al. (2001), an increase in σ_w/u_* in strongly stable conditions might be an effect of turbulence damping. In such situations, only small turbulence eddies exist, which are no longer directly influenced by the surface and

u_*becomes small. Results show the dependence on *z/L* as described by equation 3.10. Table 3.4 provides a comparison of near-neutral values of σ_u/u_* , σ_v/u_*, and σ_w/u_* obtained from the present study with other reported studies. From Table 3.4, one can see that the mean values of $\sigma_u/u_* > \sigma_v/u_* > \sigma_w/u_*$ in the neutral regime agree well with other suburban and urban locations (Högström et al., 1982; Yersel and Goble, 1986; Roth, 1993; Zhang, H. et al., 2001; Chang et al., 2009). The neutral values of $\sigma_{i=u,v,w}/u_*$observed over Goa site are slightly higher than the values reported by Panofsky and Dutton (1984). Further, the mean σ_w/u_*value (≈ 1.21) lies within the values (1.1–1.4) reported by Panofsky and Dutton (1984) over flat and complex terrains.

It is noteworthy to mention the standard deviation of the coefficients C1 and C2 (Equation 3.10) for different seasons, presented in Table 3.5. It clearly indicates that the seasonal differences are well within the limits of uncertainties and hence turbulence statistics are nearly independent of seasons. The recommended functions of $\sigma_{i=u,v,w}/u_*$ for the Goa site with related uncertainty are given in Table 3.3, and Table 3.4 for near-neutral conditions. Ramana et al. (2004b) also showed that turbulent statistics are nearly independent of seasons in a region in Lucknow, India. The functional forms developed over Goa region describes the turbulent nature of surface layer specific to this site and has significant implications in regional air pollution studies. As in air quality calculations, observational estimates of meteorological parameters, frictional velocity, Obukhov length, and surface roughness under varying conditions of stability are considered as useful parameters. Thus, the empirical coefficients which are estimated based on the local scaling and similarity relationships under the framework of MOST over coastal Goa site can be applied in regional dispersion models to improve surface layer parameterization schemes for this site and regions of similar terrain characteristics.

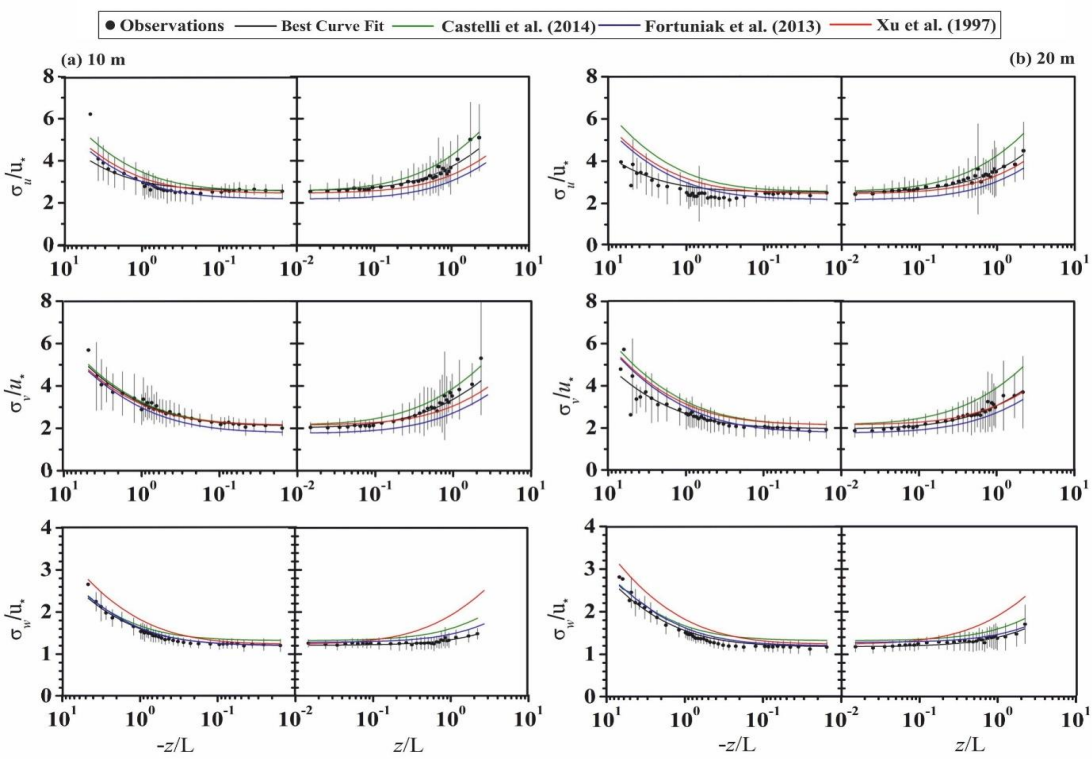

Figure 3.5 Variations of normalized standard deviations of wind velocities $\sigma_{i=u,v,w}/u_*$ studied as a function of *z/L* for unstable (*z/L*<0) and stable conditions (*z/L*>0) over the observational site at 10 m height (left panel) and 20 m height (right panel). Error bars indicate standard deviations. The black solid curve represents functional fit using equation 3.10; the green, blue, and red curves represent the function curves of Xu et al. (1997); Fortuniak et al. (2013); Trini Castelli et al. (2014) respectively.

Table 3.3 Comparison of coefficients of normalized standard deviations of wind components with stability obtained from the present study at 10 m and 20 m heights during the unstable (z/L<0) and stable (z/L>0) conditions with the coefficients reported from studies over other locations. Also, presents the uncertainty in the coefficients (Equation 3.10).

Locations	Unstable			Stable		
	σ_u/u_*	σ_v/u_*	σ_w/u_*	σ_u/u_*	σ_v/u_*	σ_w/u_*
Nanjing (urban) Xu et al. (1997)	$2.46(1 - 1.20z/L)^{1/3}$	$2.15(1 - 2.17z/L)^{1/3}$	$1.23(1 - 2.30z/L)^{1/3}$	$2.46(1 + 1.50z/L)^{1/3}$	$2.15(1 + 1.91z/L)^{1/3}$	$1.23(1 + 2.80z/L)^{1/3}$
Łód´z—Narutowicza, Urban Fortuniak et al. (2013)	$2.18(1 - 1.62z/L)^{1/3}$	$1.79(1 - 3.75z/L)^{1/3}$	$1.20(1 - 1.50z/L)^{1/3}$	$2.17(1 + 1.78z/L)^{1/3}$	$1.70(1 + 2.76z/L)^{1/3}$	$1.28(1 + 0.52z/L)^{1/3}$
Turin in Northern Italy, Suburban Trini Castelli et al. (2014) 09 m	$2.41(1 - 3.06z/L)^{1/3}$	$2.09(1 - 5.09z/L)^{1/3}$	$1.29(1 - 2.01z/L)^{1/3}$	$2.41(1 + 5.69z/L)^{1/3}$	$2.09(1 + 7.42z/L)^{1/3}$	$1.29(1 + 0.84z/L)^{1/3}$
25 m	$2.56(1 - 1.49z/L)^{1/3}$	$2.14(1 - 2.60z/L)^{1/3}$	$1.32(1 - 1.04z/L)^{1/3}$	$2.56(1 + 3.69z/L)^{1/3}$	$2.14(1 + 5.14z/L)^{1/3}$	$1.32(1 + 0.79z/L)^{1/3}$
Goa, Coastal, India (Present study) Total data at 10 m	$2.59(1 - 0.58z/L)^{1/3}$	$2.11(1 - 2.55z/L)^{1/3}$	$1.21(1 - 1.34z/L)^{1/3}$	$2.57(1 + 2.09z/L)^{1/3}$	$2.01(1 + 3.79z/L)^{1/3}$	$1.21(1 + 0.36z/L)^{1/3}$
	2.59±0.12 0.58±0.24	2.11±0.10 2.55±0.24	1.21±0.03 1.34±0.01	2.57±0.12 2.09±0.25	2.01±0.13 3.79±0.46	1.21±0.01 0.36±0.01
Total data at 20 m	$2.54(1 - 0.38z/L)^{1/3}$	$1.97(1 - 1.57z/L)^{1/3}$	$1.18(1 - 1.33z/L)^{1/3}$	$2.52(1 + 1.89z/L)^{1/3}$	$1.95(1 + 2.91z/L)^{1/3}$	$1.18(1 + 0.69z/L)^{1/3}$
	2.54±0.12 0.38±0.07	1.97±0.20 1.57±0.30	1.18±0.04 1.33±0.11	2.52±0.08 1.89±0.17	1.95±0.07 2.91±0.11	1.18±0.02 0.69±0.07

Table 3.4 Comparison of coefficients of normalized standard deviations of wind components obtained during near-neutral conditions from the present study at 10 m and 20 m heights with the coefficients reported from studies over other locations.

Author	Place (Surface)	σ_u/u_*	σ_v/u_*	σ_w/u_*
Högström et al. (1982)	Uplandia (Urban location)	2.5	2.2	1.5
Panofsky and Dutton (1984)	Kansas, USA (Flat and uniform terrain)	2.39±0.03	1.92± 0.05	1.25± 0.03
Yersel and Goble (1986)	Urban location	2.7	2.2	1.2
Roth (1993)	Suburban location	2.3	2.5	1.2
Krishnan and Kunhikrishnan (2002)	Ahmedabad (Semi-arid) Southwest monsoon (Daytime)	2.32±0.39	2.29±0.22	1.37
Ramana et al. (2004b)	Lucknow (Inland)	2.63±0.36	2.19±0.06	1.0±0.04
Chang et al. (2009)	Oklahoma City (7.8 – 83.2 m)	2.4-1.8	2.2-1.4	1.5-1.2
Fortuniak et al. (2013)	Narutowicza (Urban location)	2.28±0.20	1.79±0.23	1.27±0.09
Goa, Coastal, India (Present Study)	Total data at 10 m	2.59±0.23	2.11±0.20	1.21±0.08
	Total data at 20 m	2.52±0.28	1.97±0.26	1.19±0.10

Table 3.5 Coefficients of *C1* and *C2* for the equation 3.9 with 95% confidence level for the mean for the data obtained during different seasons at 10 m and 20 m heights.

Goa, Coastal, India (Present study)	Co-efici-ents	Unstable $C1(1-C2z/L)^{1/3}$			Stable $C1(1+C2z/L)^{1/3}$		
		σ_u/u_*	σ_v/u_*	σ_w/u_*	σ_u/u_*	σ_v/u_*	σ_w/u_*
Winter season (10 m)	*C1*	2.50±0.11	2.08±0.1	1.22±0.05	2.45±0.15	1.99±0.09	1.20±0.05
	C2	0.45±0.24	3.08±0.68	1.30±0.39	1.65±0.7	3.01±0.7	0.61±0.15
Pre-monsoon (10 m)	*C1*	2.55±0.09	2.15±0.05	1.22±0.04	2.51±0.09	2.11±0.06	1.21±0.04
	C2	0.73±0.5	3.03±0.17	1.38±0.18	1.8±0.05	2.97±0.17	0.45±0.05
Summer-monsoon (10 m)	*C1*	2.59±0.15	2.12±0.19	1.24±0.07	2.56±0.21	2.07±0.14	1.23±0.05
	C2	0.65±0.33	3.01±0.63	0.65±0.2	2.5±0.55	3.37±0.64	0.25±0.08
Post-monsoon (10 m)	*C1*	2.61±0.09	2.14±0.07	1.18±0.03	2.58±0.12	2.12±0.07	1.17±0.04
	C2	0.49±0.15	2.01±0.17	1.06±0.12	2.19±0.41	3.72±0.01	0.59±0.03
Total data (10 m)	*C1*	2.59±0.12	2.11±0.10	1.21±0.03	2.57±0.12	2.01±0.13	1.21±0.01
	C2	0.58±0.24	2.55±0.24	1.34±0.01	2.09±0.25	3.79±0.46	0.36±0.01
Winter season (20 m)	*C1*	2.48±0.1	1.93±0.03	1.19±0.03	2.44±0.1	1.90±0.08	1.17±0.05
	C2	0.44±0.01	1.51±0.21	1.15±0.15	1.50±0.49	1.99±0.36	0.59±0.16
Pre-monsoon (20 m)	*C1*	2.50±0.09	1.92±0.1	1.20±0.03	2.45±0.1	1.91±0.06	1.19±0.03
	C2	0.49±0.15	1.63±0.35	1.46±0.17	1.70±0.41	1.96±0.26	0.44±0.11
Summer-monsoon (20 m)	*C1*	2.59±0.12	1.99±0.1	1.21±0.1	2.57±0.19	1.92±0.1	1.20±0.11
	C2	0.60±0.25	2.33±0.5	0.94±0.29	2.37±0.32	2.83±0.62	0.45±0.18
Post-monsoon (20 m)	*C1*	2.55±0.08	2.03±0.01	1.17±0.03	2.49±0.07	1.97±0.07	1.16±0.03
	C2	0.38±0.08	1.69±0.12	1.29±0.15	2.11±0.08	3.50±0.12	0.22±0.09
Total data (20 m)	*C1*	2.54±0.12	1.97±0.20	1.18±0.04	2.52±0.08	1.95±0.07	1.18±0.02
	C2	0.38±0.07	1.57±0.30	1.33±0.11	1.89±0.17	2.91±0.11	0.69±0.07

3.3.5.2. The normalized standard deviation of temperature (σ_T/T_*) with stability parameter (z/L)

The functional form of relationship applied to present observations of temperature are given below,

$$\sigma_T/T_* = C1(1 - C2\, z/L)^{-1/3} \quad (z/L < 0) \qquad 3.11$$

$$\sigma_T/T_* = C1(1 + C2\, z/L)^{-1} \quad (z/L > 0) \qquad 3.12$$

$$\sigma_T/T_* = C1(-z/L)^{-1/3} \quad (z/L < 0) \qquad 3.13$$

where $C1$ and $C2$ are the coefficients estimated in the present study. Equations 3.11 and 3.12 are considered following the studies carried out over the Indian region (Sivaramakrishnan et al., 1992; Krishnan and Kunhikrishnan, 2002; Ramana et al., 2004b; Dharmaraj et al., 2009), while equation 3.13 was considered following Wyngaard et al. (1971). Figure 3.5 depicts bin averaged normalized standard deviations of temperature (σ_T/T_*) plotted against stability parameter (z/L) for unstable and stable conditions at 10 m and 20 m heights. It is observed that temperature variations followed the "-1/3 power law" during thermally unstable conditions as proposed by Wyngaard et al. (1971) while during stable conditions, σ_T/T_*showed a slight decrease with an increase in *z/L*.

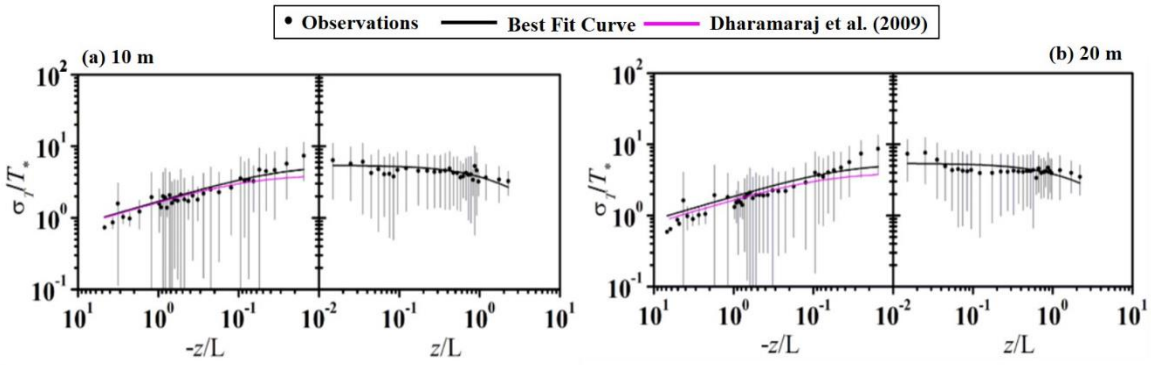

Figure 3.6 Variations of normalized standard deviations of air temperature σ_T/T_* studied as a function of *z/L* for unstable (*z/L*<0) and stable conditions (*z/L*>0) over the observational site at 10 m height (left panel) and 20 m height (right panel). Error bars indicate standard deviations.

The black solid curve represents functional fit using equation 3.11 and 3.12; the magenta curve represents the function curves using equation provided by Dharmaraj et al. (2009).

In Figure 3.5 solid black lines represent the empirical fitting curves obtained from the present study using the relations given in equations 3.11 and 3.12. This fitted curve agrees well with the curves obtained by Dharmaraj et al. (2009) over Indian locations. During unstable conditions, the values $C1$ and $C2$ defined in equations 3.11 and 3.12 are respectively low and high over this location when compared with the measurements from other Indian locations like Ahmedabad (semi-arid) and Lucknow (inland) (Table 3.6). In stable conditions, values of σ_T/T_* attains a constant value of about 5.4 which is close to the values reported by Fortuniak et al. (2013) over the urban location. However, as z/L approaches highly stable conditions, a small decrease in σ_T/T_* is observed. The value of the constant *C1* in equation 13 as suggested by Wyngaard et al. (1971) was 9.5 for unstable conditions. Our results show that the constant value is around 1.6 for both 10 m and 20 m heights respectively, which is very close to the values reported by Quan and Hu (2009); Fortuniak et al. (2013) (Table 3.6). The variation of (σ_T/T_*) follows $(z/L)^{-1/3}$ during unstable conditions and approaches constant value in stable conditions.

Table 3.6 Comparison of coefficients of normalized standard deviations of temperature obtained from the present study at 10 m and 20 m heights during the unstable (z/L< 0) and stable (z/L> 0) conditions with the coefficients reported in studies over other locations.

Locations	Unstable (z/L< 0)	Stable (z/L>0)
	σ_T/T_*	σ_T/T_*
MONTBLEX-90, inland, southwest monsoon, Sivaramakrishnan et al. (1992)	$5.12(1-8z/L)^{-1/3}$	$8.0(1+0.67z/L)^{-1}$
Rural, Andreas et al. (1998)	$3.2(1-28.4z/L)^{-1/3}$	3.2
Beijing, Al-Jiboori et al. (2001)	$2.23(-z/L)^{-1/3}$	3.1
Ahmedabad, Semi-arid, India, Southwest monsoon, Krishnan and Kunhikrishnan (2002)	$6.5(1-9.5z/L)^{-1/3}$	$6.5(1+0.8z/L)^{-1}$
Lucknow, India, Inland Ramana et al. (2004b)	$6.56(1-9.5z/L)^{-1/3}$	$6.45(1+0.25z/L)^{-1}$
Beijing, Quan and Hu (2009)	$1.5(-z/L)^{-1/3}$	$3.0(z/L)^{-1/3}$
Łódz-Lipowa, Poland, urban, Fortuniak et al. (2013)	$1.60(-z/L)^{-1/3}$	$4.18+0.15z/L^{-0.69}$
Łódz-Narutowicz, Poland, urban, Fortuniak et al. (2013)	$1.61(-z/L)^{-1/3}$	$3.60+0.13z/L^{-0.74}$
Goa, Coastal, India (Present study)		
Total data at 10 m	$5.42(1-33z/L)^{-1/3}$ $1.60(-z/L)^{-1/3}$	$5.42(1+0.50z/L)^{-1}$
Total data at 20 m	$5.40(1-25z/L)^{-1/3}$ $1.65(-z/L)^{-1/3}$	$5.40(1+0.41z/L)^{-1}$

3.3.6. Correlation coefficient

Figure 3.6a, b shows correlation coefficients of momentum ($|r_{uw}|$) and heat flux ($|r_{wT}|$) as a function of stability (z/L) estimated at 10 m and 20 m heights respectively. The values of $|r_{uw}|$ and $|r_{wT}|$ were respectively small and large during strong unstable conditions, whereas during neutral conditions the values of $|r_{uw}|$ becomes large (greater than 0.3) (Figure 3.6). Results indicate that the value of momentum flux is larger in neutral conditions and decreases with instability. This could be attributed to the enhancement of convection due to significantly high heat flux during highly unstable conditions. The values of $|r_{uw}|$ and $|r_{wT}|$ at both heights during unstable conditions were respectively greater or lesser than 0.1 and 0.55. A similar trend was reported in other locations such as coastal Singha and Sadr (2012); urban (Al-Jiboori et al., 2001; Wood et al., 2010) and rural regions (Kaimal and Finnigan, 1994). The mean values of $|r_{uw}|$ obtained for unstable and stable conditions were 0.29 and 0.20 respectively at 10 m, which lies within the range between 0.1-0.4 as reported for other urban locations (Roth, 1993). The mean values of $|r_{wT}|$ during unstable conditions (z/L<-0.1) were about 0.48 and 0.46 at 10 m and 20 m respectively, which were slightly higher than those reported over London ($|r_{wT}|$ ≈ 0.4) by Wood et al. (2010). Whereas, during stable conditions (z/L >0.1) the values of $|r_{wT}|$ remained almost constant ≈ 0.22 and 0.24 at 10 m and 20 m respectively which were found to be similar to the values of r_{wT} (≈0.24) reported by Nieuwstadt (1984). During neutral conditions,the obtained value of these measurements was 0.29 and 0.33 for $|r_{uw}|$ at 10 m and 20 m heights respectively. These turbulent correlation coefficients are crucial for dispersion models in estimating fluxes where mean temperature and wind data are fed as input Quan and Hu (2009).

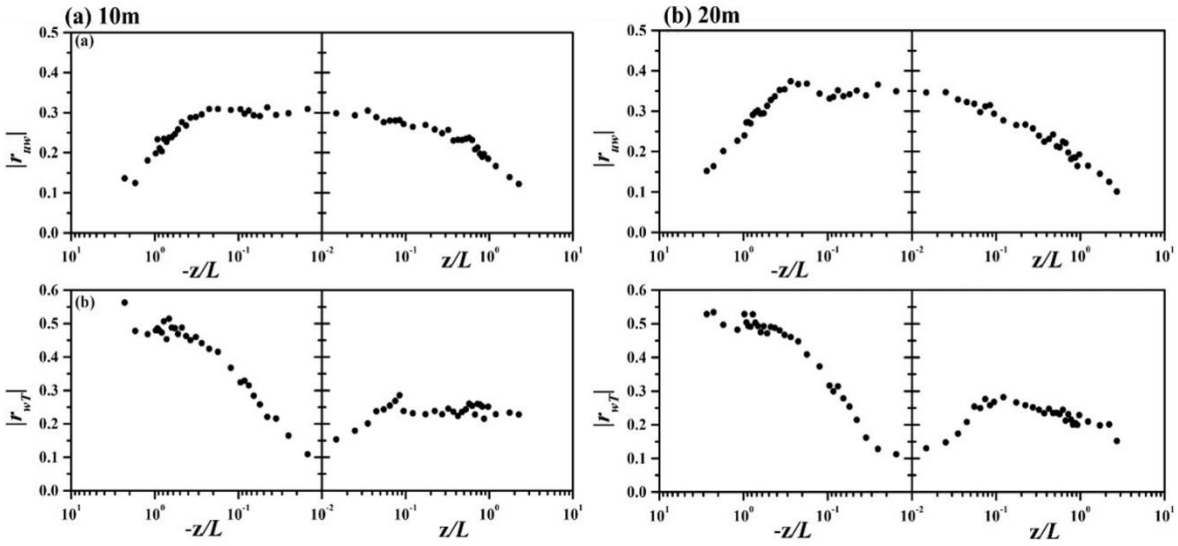

Figure 3.7 Variations of $|r_{uw}|$ and $|r_{wT}|$ studied as a function of z/L for unstable (z/L<0) and stable conditions (z/L>0) at 10 m (left panel) and 20 m height (right panel) respectively.

3.4. Concluding remarks

The analysis presented in this chapter aims at understanding the micrometeorological turbulence characteristics of atmospheric surface layer (ASL) over a tropical coastal region in Goa (15.46°N, 73.83°E, and 50 m a.s.l.), India. This has been achieved based on the computations of time-series collected using high as well as low frequency meteorological dataset. The distinct features of ASL observed from this study for Goa region are the following,

1. Data revealed that the low offshore wind speed (< 3 m s^{-1}) dominates during nighttime, while onshore wind speed greater than 3 m s^{-1} dominates during daytime. This aspect along with the urban geometry of the location represents the distinct characteristics of the database.
2. The normalized standard deviations of wind components analyzed within the framework of Monin–Obukhov similarity theory (MOST) showed that $\sigma_{i-u,v,w}/u_*$, follow the '1/3' power law in the free convection limit, and approach constant value for neutral stratifications, and follow '1/3' power law during stable conditions.

3. The power function provided in equation 3.10 can be used to model for both stable and unstable conditions.
4. The suburban and urban functions proposed by Xu et al. (1997); Fortuniak et al. (2013); Trini Castelli et al. (2014) lies within the variability range of the Goa observations.
5. The mean values of $\sigma_u/u_* > \sigma_v/u_* > \sigma_w/u_*$ in the neutral regime agree well with other suburban and urban locations. These results confirm that the surface turbulence characteristics observed over this experimental site obey similarity relations.
6. Analysis revealed that the turbulence statistics are independent of seasons.
7. The normalized temperature variances σ_T/T_* follow $(z/L)^{-1/3}$ during unstable conditions and approach a constant value in the stable limit.
8. The correlation coefficients for momentum and heat flux observed over the study site were respectively small and high under strong unstable and stable conditions, while the mean values of momentum flux increased steeply as it approached neutral conditions. This characteristic pattern was in line with the results reported over urban/cities and rural locations.
9. Upon comparing the coefficients and empirical relationships derived in our study with those reported for various non-coastal locations in India and the reference locations presented in our work, it becomes evident that the turbulence intensity for horizontal winds over the Goa region is notably lower, particularly during unstable atmospheric conditions. This is attributed to the reduction in the contribution of convective activity and mesoscale wind during daytime and subsequent formation of Thermal Internal boundary layer.
10. On comparing the observations from coastal stations in India, results showed a similar patterns of turbulence intensities. Results showed that the turbulence statistics are independent of seasons on contrast to other coastal locations. The observed coefficients (C2) during unstable conditions show lower values indicating the slow growth rate of

instability over this site. Further, the mean values of σ_w/u_* observed in this study are lower than the values reported over semi-arid region (Krishnan and Kunhikrishnan 2002; Dharmaraj et al. 2009) but higher than values reported over inland (Ramana et al. 2004) and coastal regions (Ramachandran et al. 1994; Prasad et al. 2019). This result revealed that the vertical transport of turbulence at present study site is higher than that over two coastal stations (Thumba and Kalpakkam) which could be due to differences in the distribution of turbulence associated with the intensity of vertical wind.

PUBLICATION

S. Neha Salim, Harilal B. Menon, N. V. P. Kiran Kumar, K. Rajeev, (2023) Study of micrometeorological characteristics of the atmospheric surface layer over a tropical coastal station in Goa. ***Meteorology and Atmospheric Physics***, 135, 3, *https://doi.org/10.1007/s00703-022-00940-3*

Chapter 4

Thermodynamic Characteristics of Marine Atmospheric Boundary Layer over Indian Ocean sector of Southern Ocean (ISSO)

4.1. Introduction

Among the global oceans, the role played by Southern Ocean (SO) in regulating earth's climatic perturbations are extremely crucial (Sallée, 2018; Swart et al., 2018). The SO covers nearly a twentieth of the earth's water (Webb, 2021) and uptakes more than 40% of the global heat (Sallée et al., 2008), and 30-40% of globally released carbon dioxide (CO_2) by fossil fuel burning (Long et al., 2021). Such a significant uptake of heat and CO_2 is linked to an increase in ocean acidification, declining ice-cover, and alterations in wind and precipitation patterns across the globe (Sen Gupta et al., 2009; Hopkins et al., 2020). These perturbations relating to extremities in weather are the result of dynamic exchange of water vapor, momentum, energy, mass and other atmospheric constituents regulated through a complex ocean-atmospheric interaction occurring across the globe (Edson et al., 1999). Moreover, these perturbations are projected to amplify in future warming scenarios (Lee et al., 2021), thereby, highlighting the need to improve the understanding of SO atmosphere in order to better predict its influence on the global climate. Thus, this chapter focuses on better understanding the atmosphere prevailing in the Indian Ocean sector of Southern Ocean (ISSO).

Among world oceans, SO serves a distinctively unique ocean composed of numerous oceanic fronts formed by a sharp gradient in sea surface temperatures (*SST*) and salinity. These fronts are embedded within the massive circulating Antarctic Circumpolar Current (ACC) that connects the Atlantic, Pacific, and Indian oceanic basins as well as strongly links exchanges

between tropics and poles (Talley et al., 2011). The oceanic fronts embedded within ACC are the Sub-Tropical Front (STF), Sub-Antarctic Front (SAF), Polar Front (PF), Southern Antarctic Circumpolar Current Front (SACCF), and Southern boundary of ACC (SB) (Orsi et al., 1995; Belkin and Gordon, 1996). On a temporal scale, a shift in the locations of these fronts occurs which is reflected in the changes in *SST* gradients (Thompson and Richards, 2011). Past studies have recorded the most substantial *SST* gradients in the Indian Ocean sector of the Southern Ocean (ISSO) compared to other sectors of SO (Small et al., 2014). Depending on the magnitude of the *SST* gradient, enhancement in the activities of oceanic eddies and amplification/suppression of air-sea exchanges are observed specifically in the vicinity of oceanic fronts and regions of strong mesoscale activities (Rouault and Lutjeharms, 2000; Chelton et al., 2001; Small et al., 2008). Equivalent to air-sea exchanges which are regulated by *SST* gradient and air temperature differences (SST-T_{air}), an input of surface layer heat fluxes (positive/negative) are fed into the low-level atmosphere which regulates the structure and dynamics of the marine atmospheric boundary layer (MABL) via the flow of low-level warm air advection (LLWAA) or low-level cold air advection (LLCAA) (Zheng and Li, 2019b; Zheng et al., 2018b). In the case of LLWAA ($SST<T_{air}$), the negative surface heat flux weakens vertical atmospheric mixing and enhances lower atmospheric stability (Martin et al., 1995; Wood and Bretherton, 2004; O et al., 2018; Zheng et al., 2018b). On the contrary, during LLCAA ($SST>T_{air}$), the positive surface heat flux supports the development of a well-mixed MABL capped by clouds, thereby forming a strongly coupled MABL (Zheng et al., 2018b). Across the ISSO fronts, the frequent transitional flow of LLWAA and LLCAA prevails mainly due to strong baroclinic instabilities laid by varying *SST* gradients and changing SST-T_{air} (Pierrehumbert and Swanson, 1995; Moore et al., 1999b). As a result of the advection, such different types of air masses across multiple oceanic fronts account for the formation of numerous atmospheric fronts (warm, cold, and occluded). Typically, warm (cold) fronts are

associated with LLCAA (LLWAA) which supports the development of high-pressure anticyclonic (low-pressure cyclonic) area and are commonly associated with the formation of coupled (decoupled) MABL's over SO. Moreover, the isolation of warm air mass between two adjacent cold air masses commonly accounts formation of occluded front where highly stabilized MABL's are common (Li et al., 2015). Past studies have identified a higher frequency of decoupled MABL's associated with LLWAA particularly in SO (Boers et al., 1998; Russell et al., 1998; Jensen et al., 2000; Hande et al., 2012; Chubb et al., 2016; Zheng et al., 2018b; Zheng and Li, 2019b). These aforementioned unique SO conditions mainly driven by dynamic ocean-atmospheric exchanges contribute to a higher frequency of stormy low-pressure cyclonic systems, and are majorly responsible for making SO one of the stormiest cyclonic regions of the globe and is, therefore, referred to as the SO storm track region (Bischoff and Thompson, 2014; Chapman et al., 2015; Huang et al., 2015b).

The source of the present knowledge of SO is based on in-situ data collected from a few scientific campaigns conducted in different sectors of SO e.g., the Australian (McFarquhar et al., 2021) and African (Messager et al., 2012) sector of SO (Table 1 in Schmale et al., 2019). These in-situ datasets were also employed for validating remotely retrieved data and model-simulated results over SO, where large uncertainties in remote and modeled datasets were identified (Sallée. et al., 2013; Bodas-Salcedo et al., 2014; Hyder et al., 2018; Schuddeboom et al., 2019). For example, significant misrepresentation of cloud properties, underestimation of atmospheric inversions, and biases in radiative estimates (Lang et al., 2018; McFarquhar et al., 2021; Vignon et al., 2021) were observed in frequently accessed satellite retrievals e.g., ERA-Interim and MERRA (Naud et al., 2014), particularly over extra-tropical fronts and stormy regions (Hoskins and Hodges, 2005; Haynes et al., 2011; Catto et al., 2012). Recent investigations revealed that one of the major causes of these uncertainties is the significant cloud coverage over SO for nearly 80% of the year (Haynes et al., 2011; Huang et al., 2012;

Mace and Protat, 2018b; Mace et al., 2020; Mace et al., 2021; McFarquhar et al., 2021). Thus, to properly understand SO atmosphere via improved space borne SO monitoring for better predicting its role in altering global climate, it's crucial to have more field measurements and improved quantification of low-level atmosphere of SO.

Particularly, in-situ data that represents the spatial and vertical structure of SO atmosphere with an emphasis on the dynamic processes governing the distribution of clouds and inversions are required. Recognizing its significance, this chapter aims to examine the dynamic structure and characteristics of low-level atmosphere prevailing over the frontal regions of the Indian Ocean sector of Southern Ocean (ISSO), a least sampled SO sector. Few studies, conducted with similar aims are available from the African sector of SO (Messager et al., 2012) and the Australasian sector of SO (McFarquhar et al., 2021). However, no records were available from the ISSO. Hence, this chapter presents the novel set of ship-based meteorological observations utilized to address three major questions i.e., (i) Does the exchanges occurring at the air-sea interface effects the vertical thermodynamic stability state of low-level atmosphere (in this study, from surface up to 4,000 m altitude) in the ISSO? (ii) How does the characteristics of clouds and inversions vary in response to the varying thermodynamic stability and synoptic meteorological conditions? (iii) What were the dominant physical processes driving the conditions of low-level atmosphere in the ISSO?

The chapter is structured as follows. In section 4.2, a detailed account of the field campaigns, sampled study region, the dataset generated, and the method of data processing used for the study mentioned in this chapter are provided. The unique observations and results obtained in the present study are discussed in sub-sections of section 4.3. In sub-section 4.3.1, the low-level thermodynamic conditions over the ISSO frontal regions are discussed. The macrophysical characteristics of clouds and inversions are discussed in section 4.3.2. Section 4.3.3 discusses the dominant physical processes occurring in the low-level atmosphere of

ISSO. Section 4.3.4 describes three typical case studies (each lying in three major oceanic domains) illustrating the effect of synoptic meteorology in altering the state of MABL. Lastly, the variability of metrics i.e., estimated inversion strength (*EIS)* and lower tropospheric stability (*LTS)* across different frontal regions are evaluated in section 4.3.5. Also, by utilizing these metrics the applicability of relationship given by Wood and Bretherton (2006) for estimating *CF* have been tested for these regions. A brief discussion based on obtained observations and results are elaborated in section 4.4. The major conclusions drawn from the present study are discussed in section 4.5.

4.2. Data and method

4.2.1. Data

In this chapter, a set of meteorological datasets collected during three scientific field campaigns executed onboard *S. A. Agulhas* from Port Louis, Mauritius (20°S) to Prydz Bay of Antarctica (68°S) have been analyzed and discussed. The cruise track of each campaign is shown in Figure 2.5 and the details of each are provided in Table 2.4 of chapter 2 of the thesis. This way spatial extend of the study region successfully captured major oceanic fronts of the ISSO during all the campaigns (Table 2.5). All cruises had been conducted during the southern hemispheric austral summers of 2017 (January-March), 2018 (December-February), and 2020 (January-March). The study discussed here is based on the dataset of near surface as well as vertical profiles of meteorological variables collected across the study region. The near-surface meteorological dataset comprised of air temperature (T_{air}), relative humidity (*RH*), mean sea level pressure (*MSLP*), wind speed (*WS*), and wind direction (*WD*) recorded using a standard pre-calibrated automatic weather station (AWS, WeatherPak®-2000 v3, Coastal Environment Systems Inc., 2006) at every 30 minutes interval. These near-surface observations were successfully made during the first two campaigns (i.e., in 2017 and 2018), while during the third campaign (in 2020), AWS failed to store data and atmospheric conditions was manually

logged at every 6-hour intervals. Surface based dataset also included measurements of *SST* recorded using a bucket thermometer (T. Friedrichs & Co.) at 6 hour intervals during all the campaigns. Dataset based on vertical profiles of meteorological parameters were recorded by releasing high-resolution atmospheric soundings (*Pisharoty* radiosonde; ISRO, 2011) at pre-determined locations. A total of 75 high-resolution sounding datasets collected during three campaigns have been analyzed and discussed in this study. The location of radiosonde launches is depicted in Figure 2.5b and the detail of each sounding is provided in Table 2.7.

4.2.2. Method of data analysis

Measurements from ship-based platforms are commonly subjected to issues because of ship's structure, sensor failures, rain showers or sea sprays. To minimize the effect of such issues on the measurements, the AWS was installed on the ship's deck at a height of ≈10 m above mean sea level and as the campaign progressed, its alignment was regularly corrected to ensure quality data collection. Also, radiosonde measurements were subjected to initial corrections before considering for actual analysis. At first, all anomalous data-values i.e., random value in an increasing or decreasing trend of data were eliminated from each profile. Further, profiles of all meteorological variables were vertically averaged for every 20 m intervals followed by smoothening using a five-point moving average technique (Subrahamanyam and Radhika 2003b). This method has been widely adopted in the Australasian sectors of SO to examine the thermodynamic structure of low-level atmosphere (Hande et al., 2012; Lang et al., 2018; Truong et al., 2020a). Later, the data from surface ≈12 m to 4,000 m altitude were only used for analysis presented in this chapter.

After employing these criteria, the thermodynamic stability of low-level atmosphere was examined using profiles of conserved variables i.e., virtual potential temperature (θ_v) and water vapor mixing ratio (r). Profiles of these variables are commonly accessed for evaluating

lower atmospheric stability (Messager et al., 2012; Lang et al., 2018). The estimation of these variables were obtained following Stull (1988),

$$\theta_v = \theta(1 + 0.61r) \quad (4.1)$$

$$r = [0.623e/P - 0.377e] \quad (4.2)$$

where, θ is the potential temperature, P is the atmospheric pressure, and e represents vapor pressure.

In addition, the frequency of occurrences of cloud and inversions along with their macrophysical properties such as the height of cloud base, cloud top, total cloud geometric thickness, the height of inversions, and its strength were estimated following the method described by Truong et al. (2020a). The cloud layers were identified as single, multilayer, or complete clouds by computing the difference between T_{air} and dew point temperature (T_d). In this study, a larger dewpoint depression threshold of T_{air}-T_d (< 2.0°C) has been chosen than the threshold of 1.5°C used in Truong et al. (2020), to reflect clouds from MODIS and CALIPSO observations qualitatively. The cloud layers were detected if this threshold was met for an altitude thickness of at least 60 m or more. These criteria were applied in altitudes between 500 and 4,000 m, and the presence of clouds was ascertained. Following the method of Mace et al. (2009), a "multi-layered cloud" was recorded, if at least two or more cloud layers were identified in a radiosonde profile. Also, the macrophysical cloud characteristics included the total geometric cloud thickness which was estimated as a sum of dew point depression among cloud layers in each profile Truong et al. (2020a). The cloud-base and cloud-top heights were identified as the altitudes of cloud base of lowest cloud layer and top of the highest cloud layer.

Further, the inversions in each radiosonde profile were considered as significant, if $d\theta_v/dz$ was greater than or equal to a limiting threshold of 0.14 K m^{-1} and every next significant inversion was at least 300 m away from the previous inversion (Zeng et al., 2004;

Hande et al., 2012; Lang et al., 2018; Truong et al., 2020a). Between 500 – 4,000 m, a number of significant inversions were recorded as no inversion, single, or multiple inversions depending on their occurrence. A "multi-level inversion" was recorded in a sounding if at least two or more inversions were identified between 500 and 4,000 m altitudes.

In addition to cloud layers and inversions, lower tropospheric stability (*LTS* after Klein and Hartmann (1993)) and estimated inversion strength (*EIS* after Wood and Bretherton (2006)) were also analyzed. According to Wood and Bretherton (2006), these metrics indicates the measure of inversion strength within MABL and a higher estimates of these metrics are indicators of strong low-lying inversions. Stronger inversions are more likely to trap moisture within MABL and result in higher coverage of low-level clouds. The estimation of *EIS* and *LTS* in other sectors of SO as well as parts of world oceans have been correlated well with the in-situ records of low-level cloud cover (Muhlbauer et al., 2014; Naud et al., 2016; Lang et al., 2018; Truong et al., 2020a).

$$LTS = \theta_{700} - \theta_{surface} \tag{4.3}$$

The estimation of *EIS* has been computed using the equation reported by given as,

$$EIS = LTS - \Gamma_m^{850}(z_{700} - LCL) \tag{4.4}$$

where, Γ_m^{850} is the moist adiabatic potential temperature gradient at 850 hPa, calculated using the average of T_{air} at the surface and at 700 hPa,

$$\Gamma_m^{850} = \Gamma_m([T_0 + T_{700}]/2), 850hPa \tag{4.5}$$

Γ_m was calculated following Wood and Bretherton (2006), after applying the simplified approximation suggested by Bolton (1980),

$$\Gamma_m(T,p) = \frac{g}{c_p}\left[1 - \frac{1 + L_v r_s(T,p)/R_a T}{1 + L_v^2 r_s(T,p)/c_p R_v T^2}\right] \tag{4.6}$$

where g is the acceleration due to gravity, $c_p$is the specific heat of air at constant pressure, L_v is the latent heat of vaporization, $r_s(T,p)$ is the saturation mixing ratio at respective altitudes having temperature (T) and pressure (P), R_a and R_v are the gas constants for dry air and water vapor respectively. *LCL* is the lifting condensation level and z_{700} is the altitude of 700 hPa. Standard procedure for calculating *LCL* height have been obtained from Bolton (1980).

Lastly, the diagnosis of the boundary layer processes within the lower 4,000 m atmospheric column was performed using conserved variable analysis (CVA). CVA is based on Saturation Point (SP) concept introduced by Betts (1982). According to this concept, when an air parcel is lifted dry adiabatically with the same mixing ratio, it attains saturation at a certain level known as level of saturation point. SP of air parcel remains unchanged change during dry/moist adiabatic ascent/descent, but it can be modified due to the influence of processes such as convection, radiative cooling/warming and precipitation/evaporation. An ideal schematic of conserved variable diagram which shows the modifications of mixing line under the influence of these physical processes is provided in Betts (1982). In this diagram, conserved variables i.e., equivalent potential temperature (θ_e) is plotted on X axis and specific humidity (q) is plotted on Y axis and the Y axis is reversed so that it superficially resembles vertical air column from surface to higher altitude. The vertical variability of these conserved variables were examined following Betts and Albrecht (1987) and estimated as follows,

$$\theta_e = \theta e^{2.67.q/T_{LCL}} \quad 4.7$$

$$q = (0.622 \times e)/(p - (0.378 \times e)) \quad 4.8$$

where, T_{LCL} is the temperature at *LCL*.

In addition to the in-situ meteorological dataset, reanalysis data retrieved from ERA5 was accessed to visualize the features of synoptic *dT (SST-T_{air})* and wind circulation patterns prevailing near the surface and in the vicinity of radiosonde launch locations. Details on this

data product is provided in section 2.3.3.1. From this data product, wind fields (10 m *u*- and 10 m *v*- component), 2 m air temperature (T_{air}), and surface *SST* data were retrieved with date, time, and location coinciding with 75 radiosondes launched during the three campaigns.

4.3. Observations and Results

Being first records on the characterization of ISSO MABL and considering the large extent of the study region, the results of each oceanic frontal regions are grouped into regions lying in three major oceanic domains. These three oceanic domains are, (a) Sub-Tropical Indian Ocean (STIO) covering NSTF1, NSTF2, and SSTF, (b) ISSO covering SAF1, SAF2, PF1, and PF2, and (c) High Latitudes of SO (HLSO) covering SACCF, SB, and CA.

4.3.1. Thermodynamic conditions of low-level atmosphere

The continuous measurements of surface-based meteorological parameters, i.e., *SST*, T_{air}, *RH*, *WS*, and *WD* collected across the entire cruise track traversed during two consecutive field campaigns (in 2017 and 2018) showed significant variability in near-surface meteorological conditions across the ISSO fronts irrespective of the campaigning period (Figure 4.1). In addition to near-surface meteorology, prominent spatial variability was observed in the air-sea coupling (SST-T_{air}) and it was observed to strongly regulate the thermodynamic stability/instability state of MABL. Thus, this subsection sequentially describes the thermodynamic state of the low-level atmosphere over ten frontal regions grouped in three major oceanic domains by analyzing vertical profiles of conserved variables, i.e., θ_v and r generated from 75 atmospheric soundings (Figure A1-A13) in the appendices.

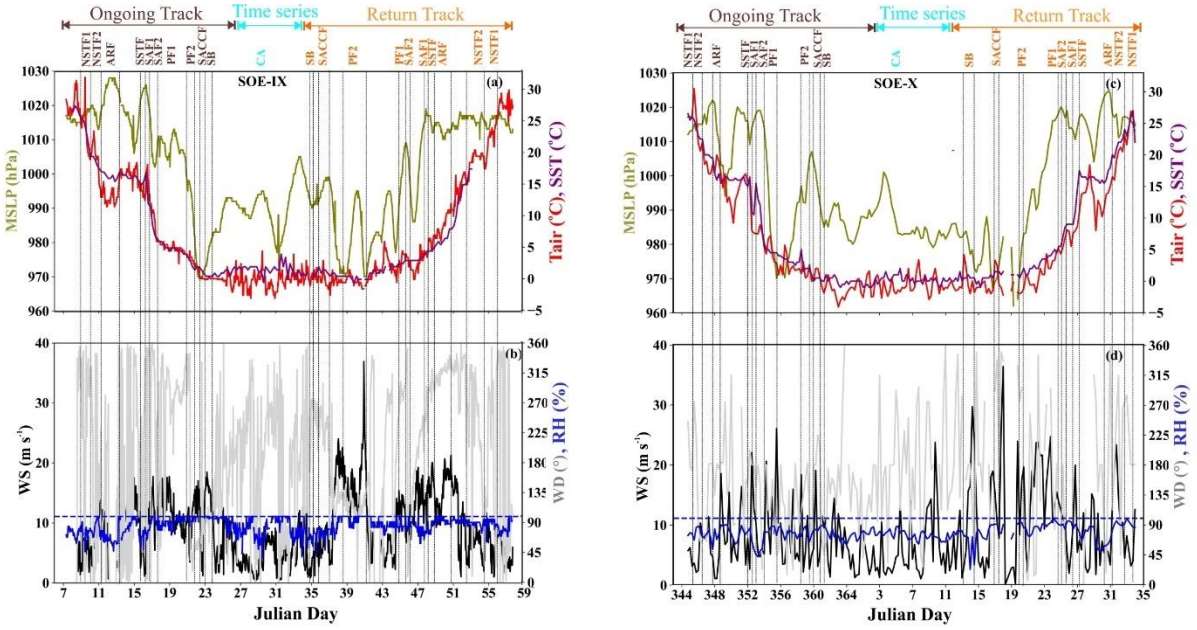

Figure 4.1 Time series surface measurements of: (a, c) *MSLP*, the mean sea level pressure in hPa (green lines); T_{air} and *SST*, the air temperature and sea surface temperature in ℃ (red and magenta lines respectively); (b, d) *WS*, wind speed in m s^{-1} (black lines); *WD*, wind direction in degrees (grey lines) and *RH*, relative humidity in % (blue lines) were measured while crossing ISSO oceanic fronts during SOE-IX (left panel [a, b]) and SOE-X (right panel [c, d]) campaigns respectively. In panel (a, c), the left vertical scale is for *MSLP*, and right vertical scale is for temperatures (T_{air} and *SST*). In panel (b, d), the left vertical scale is for *WS*, and right vertical scale is for *WD* and *RH*. The maximum limit of *RH* (100%) is marked in panel (b, d) with blue dotted line. For all panels, the horizontal axis is the Julian day number according to the campaign periods of SOE-IX (left panels) and SOE-X (right panels). The vertical dashed black lines mark the approximate locations of encountered oceanic fronts while crossing ISSO during campaigns adopting the demarcation provided by Belkin and Gordon (1996); Anilkumar et al. (2015). The fronts encountered during the forward track (brown), time series region (cyan), and return track (orange) are mentioned on the top of panel (a, c).

4.3.1.1. Sub-Tropical Indian Ocean (STIO)

Out of 19 soundings released over STIO, 12 atmospheric soundings (RL2, RL13, RL14, RL17, RL19, RL20, RL46, RL47, RL48, RL72, RL73, and RL74) suggest high-pressure regions (Figure A1-A13). The *SST* was higher than T_{air} which revealed positive surface heat flux and the occurrence of LLCAA. This warm front region favored convective destabilization of the low-level atmosphere leading to the formation of a well-evolved mixed layer structure evident in r and θ_v profiles (Figure A1-A3). The average mixed-layer height during unstable conditions reached altitudes of 1,153 m, 1,240 m, and 1,270 m over NSTF1, NSTF2, and SSTF, respectively (Figure 4.2a, c, e). The mixed layer was capped by stratocumulus clouds, indicating a thermodynamically coupled boundary layer structure. The formation of such coupled boundary layer structures in the NSTF region was due to higher *MSLP*, $SST > T_{air,}$ and the advection of cold air masses supported the formation of warm fronts in this region. Moreover, the region also encountered clear sky conditions accompanied by weak winds carrying dry air masses (RH<83%) (Table 4.1). These conditions over NSTFs were attributed to the prevalence of sub-tropical ridges that generally prevailed at 30 ° S (Timbal and Drosdowsky, 2013). The SSTF region revealed strongly coupled and highly destabilized MABL due to an intense warm front caused by the action of convectively active oceanic eddies formed over meandering Agulhas Retroflection Current (ARC) (Figure 4.2e).

In contrast, at the remaining seven soundings (RL1, RL15, RL16, RL18, RL21, RL71, and RL75), *SST's* were less than T_{air}, which indicated negative surface heat flux associated with the cold front region. It showed the prevalence of LLWAA that inhibited vertical mixing in the low-level atmosphere and promoted a decoupled MABL. A more stably stratified low-level atmosphere was evident as r and θ_v gradually increased with altitude (Figure A1-A3). The formation of stable and decoupled MABL over NSTF1 (RL1, RL18, and RL75) may be associated with the developing monsoon conditions over Mauritius, as well as due to the

influence of continentally advected warm and moist air masses by westerlies in the low-level atmosphere (higher values of *r* and *RH)* (Figure 4.2b). However, stable MABL conditions recorded in soundings over NSTF2 (RL15, RL16, and RL21) were associated with the nighttime conditions and development of the cold front region (Figure A5). The weakly unstable conditions observed in soundings over SSTF (RL13 and RL71) were associated with the weakening of oceanic eddies induced by the ARC, which augmented negative surface heat flux inputs and promoted stability within the boundary layer (Figure A1, A3).

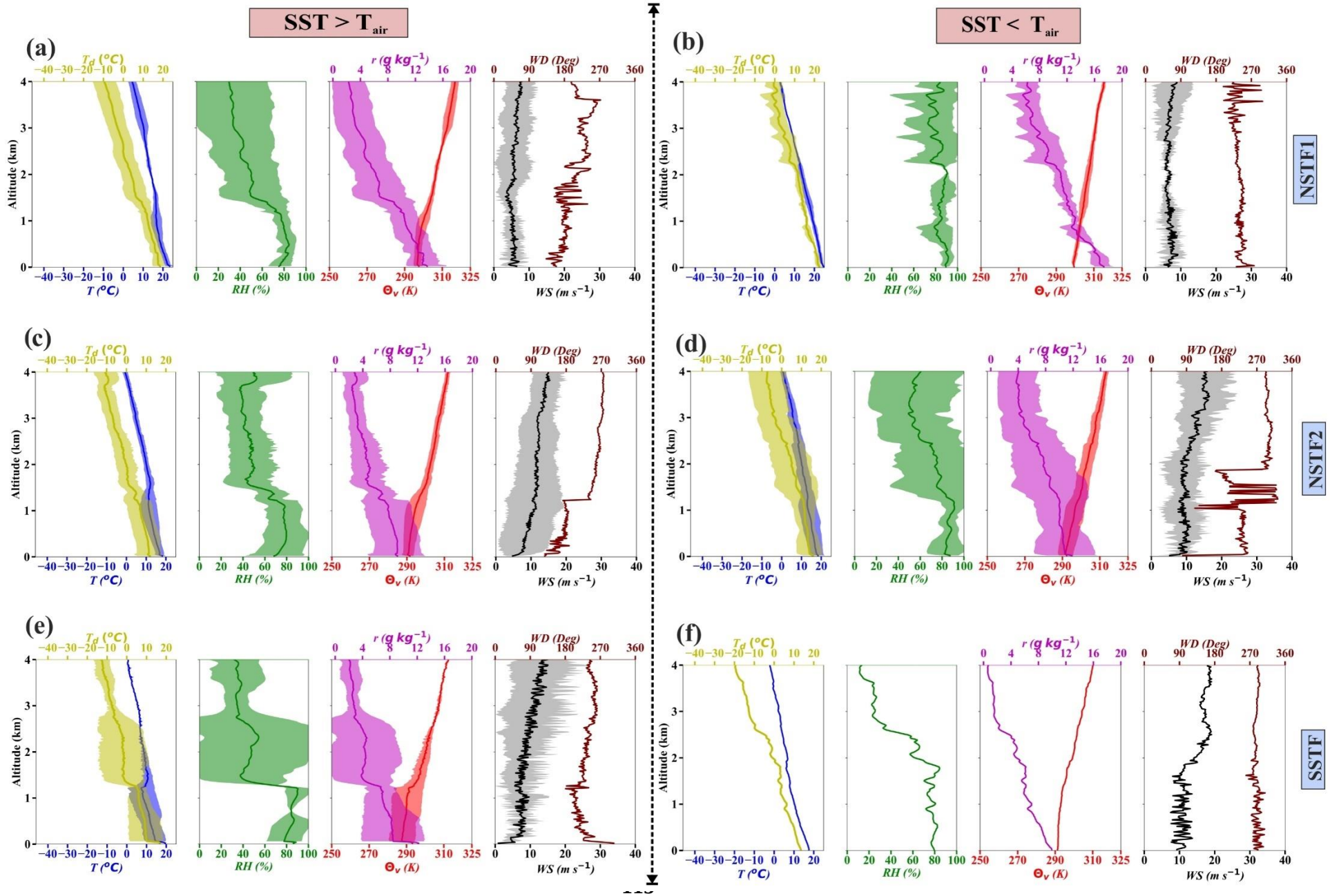
SST > T air
SST < T air
(a)
(b)
(c)
(d)
(e)
(f)
NSTF1
NSTF2
SSTF
Altitude (km)
T (°C)
Td (°C)
RH (%)
r (g kg−1)
Θv (K)
WD (Deg)
WS (m s−1)

Figure 4.2 Mean vertical thermodynamic profiles of air temperature (T in ℃, blue line), dew point temperature (T_d in ℃, yellow line), relative humidity (RH in %, green line), virtual potential temperature (θ_v in K, red line bottom x-axis), mixing ratio (r in g kg^{-1}, magenta line, and upper magenta x-axis), wind speed (WS in m s^{-1}, black line bottom x-axis), and wind direction (WD in degrees, brown line, and upper brown x-axis) up to 4,000 m altitude for upper air soundings released in frontal regions of Sub-Tropical Indian Ocean (STIO) (i.e., NSTF1, NSTF2, and SSTF). The left panel indicates sounding profiles where $SST>T_{air}$ in (a) NSTF1, (c) NSTF2, and (e) SSTF while the right panel indicates sounding profiles where $SST<T_{air}$ in (b) NSTF1, (d) NSTF2, and (f) SSTF. The shaded area represents 1 standard deviation (except for wind direction). In these frontal regions lying in STIO domains, conditions when $SST>T_{air,}$ formation of well-evolved mixed layer structures are clearly seen from nearly uniform variation of θ_v and r, whereas during conditions of $SST<T_{air,}$ significantly stable boundary layers were observed. Owing to increased boundary layer stabilization, formation of well developed mixed layers are significatly reduced and higher stabilization is clearly depicted with gradual increasing (decreasing) tendency of θ_v and r. Highest MABL destabilization was observed in SSTF region, leading to formation of well-mixed layer extending up to the height of nearly 1,270 m altitude.

4.3.1.2. Indian Ocean sector of Southern Ocean (ISSO)

The unique characteristic of this region is the prominent advection of distinct air masses which induces frequently changing atmospheric cold, warm, or occluded fronts. This makes ISSO the stormiest region of SO. Of the total 20 launches, at 11 soundings (RL9, RL10, RL22, RL23, RL24, RL27, RL28, RL44, RL45, RL68, and RL69) *SST* was higher than T_{air} (Figure A1-A3). However, a decrease in *MSLP* was observed which accounted for the weakening of the intensity of positive heat flux inputs to the lower atmosphere. Thus, low-level instability was noticed from the profiles of *r* and θ_v in these soundings which revealed the formation of a well-developed mixed layer capped by cumulus clouds (Miller and Albrecht, 1995; Bretherton, 1997; Zheng et al., 2018a). The averaged mixed layer height during unstable conditions were ~1630 m, ~720 m, ~412 m, and ~920 m at SAF1, SAF2 (low confidence), PF1, and PF2 respectively. The destabilized MABL over SAF1 (RL22 and RL23) were attributed to convectively active oceanic eddies in the nearest vicinity of soundings that led to the development of a warm atmospheric frontal region. In RL69, an active warm front region was observed with *SST* as 3.0℃ higher than T_{air} (Figure A7). Similarly, in RL68, the formation of a warm front region (SST-T_{air} = 2.4℃) resulted in destabilized MABL (Figure A8).

The remaining 9 soundings (RL11, RL12, RL25, RL26, RL64, RL65, RL66, RL67, and RL70) showed $SST<T_{air}$ (A1-A3). This indicates the formation of cold/occluded fronts to initiate LLWAA, thereby promoting the development of highly stratified decoupled MABL (Zheng et al., 2018b). The stabilized low-level atmosphere was also evident from a gradual increase in *r* and θ_v up to 4,000 m (Figure 4.3b, e, g). A combined effect of stable conditions, high-speed winds (>32 m s^{-1} within 4,000 m), and the formation of multiple cold/occluded fronts supported the formation of frequent low-pressure stormy cyclonic systems in these mid-latitude regions of ISSO (manual weather records). Similar atmospheric conditions were recorded in the soundings (RL11, RL12, and RL70) made in SAF1 where the cold front formed

due to the advection of warm and moist air masses via strong northwesterly is evident (Figure A7). However, highly stable conditions over PF (RL25, RL26, RL64, RL65, RL66, and RL67) were attributed to low *MSLP* (~995 hPa), T_{air}>*SST*, polar jet streams inducing strong westerly winds exceeding 32 m s^{-1} within ~4,000 m altitudes, and presence of strong baroclinicity (Figure A9, A10). All soundings over PF2 showed an abrupt increase in wind speeds at altitudes between 700 m and 1,500 m, which indicates the presence of distinct air mass that may act as a barrier between the well-developed low-level downdraft precipitation core and the upper-level storms. As a result of these conditions, numerous localized low-pressure stormy cyclones were experienced. Also, significant saturation in the form of snowfall and foggy conditions was observed within the low-level atmosphere of PF1 and PF2 (Trenberth, 2011).

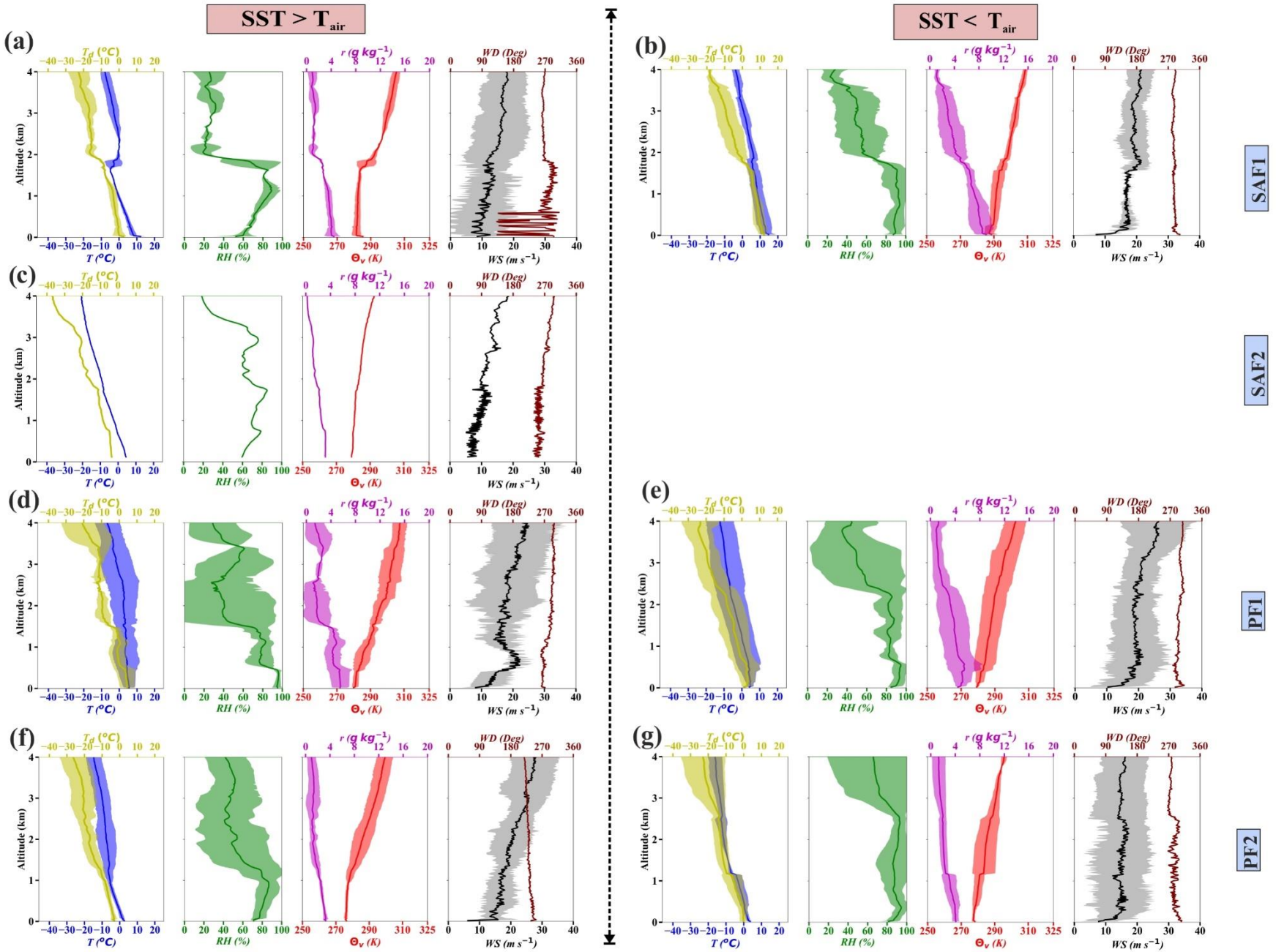
SST > T air
SST < T air
(a)
(b)
(c)
(d)
(e)
(f)
(g)
SAF1
SAF2
PF1
PF2
Altitude (km)
T (°C)
Td (°C)
RH (%)
r (g kg−1)
Θv (K)
WD (Deg)
WS (m s−1)

Figure 4.3 Mean vertical thermodynamic profiles of air temperature (T in ℃, blue line), dew point temperature (T_d in ℃, yellow line), relative humidity (RH in %, green line), virtual potential temperature (θ_v in K, red line bottom x-axis), mixing ratio (r in g kg^{-1}, magenta line, and upper magenta x-axis), wind speed (WS in m s^{-1}, black line bottom x-axis), and wind direction (WD in degrees, brown line, and upper brown x-axis) up to 4,000 m altitude for upper air soundings released in frontal regions of the Indian Ocean sector of Southern Ocean (ISSO). The left panel represents sounding profiles where $SST > T_{air}$ in (a) SAF1, (c) SAF2, (d) PF1, (f) PF2, and the right panel represents sounding profiles where $SST < T_{air}$ in (b) SAF1, (e) PF1, (g) PF2. The shaded area represents 1 standard deviation (except for wind direction). In these frontal regions of ISSO, significant stabilization of MABL could be observed, and in consequence, formation of well-developed mixed layers structures was observed to be significantly suppressed. A combined effect of highly stable boundary layer conditions, coupled with high-speed winds (>32 m s^{-1} within 4,000 m) advecting multiple types of air masses (cold/warm), aided by the formation of multiple cold/occluded fronts significantly enhances the frequent occurrences of low-pressure stormy cyclonic systems in these mid-latitude regions of ISSO. Polar jet streams inducing strong westerly winds exceeding 32 m s^{-1} within ~4,000 m altitudes could be observed in this figure.

4.3.1.3. High-Latitude Southern Ocean (HLSO)

In this region, a significant decrease in wind intensities and reduced atmospheric stabilities were recorded. Out of 36 soundings, 19 showed weak low-level atmospheric instability, while the remaining indicated stable low-level atmosphere (Figure 4.4a, c, e). The profiles of *r* and θ_v showed weak and shallow mixed layers with weak low-level instability induced by positive surface heat flux (RL5, RL6, RL31, RL32, RL33, RL34, RL35, RL36, RL40, RL42, RL51, RL52, RL55, RL56, RL57, RL58, RL59, RL60, RL61, and RL62) (Figure A1-A3). The weak positive heat flux was observed (i.e., $SST > T_{air}$), however, the difference ($SST\text{-}T_{air}$) was observed to be lowest than that observed over STIO and ISSO regions. The condition with $SST > T_{air}$ was predominantly noticed in SB and CA regions which were due to the potential warming of Antarctic waters caused by the enhanced oceanic eddy activities associated with the closed mesoscale polar gyres. Particularly, the convective activities of Weddell Sea gyre (west of SB) and Prydz Bay gyre (east of SB and in the CA region) (Orsi et al., 1995; Orsi et al., 1999; Meijers et al., 2010; Couldrey et al., 2013) were characterized by the presence of a closed cyclonic gyre centered at Amery depression, off Amery Ice Shelf (Smith et al., 1984) (Figure A12, A13). The warming of Antarctic waters coupled with the outflow of cold polar air masses by easterly winds over SB (Figure 4.4b, 4.4c) and strong katabatic winds originating from Antarctica over CA (low *RH* and *r*; Figure 4.4d; Figure A13) (Parish and Cassano, 2003b, 2003a) has initiated LLCAA-induced destabilization and coupled boundary layer structure (Zheng et al., 2018b). The average height of the mixed layer formed due to destabilization varied from ~512 m and ~562 m in the SB and CA regions, respectively (Figure 4.4b, d). A slight increase in *MSLP* was noticed in SB and CA regions, contributing to MABL destabilization (Table 4.1). The atmospheric dynamics over the CA region differs from the SB region with less intensity of polar mesoscale cyclones owing to the geographic constraint imposed by the coast. The destabilized MABL over SB and CA were associated with the closer

proximity of the gyre and the time of soundings (i.e., daytime, afternoon, and evening times profiles). In cases of sounding further away from the active gyre and nighttime or early morning launches, $T_{air}>SST$ accounted for the formation of the cold front region that promoted stability within MABL caused by LLWAA. The highly stable boundary layer was evident from gradually increasing r and θ_v profiles (RL3, RL4, RL7, RL37, RL 38, RL39, RL41, RL49, RL50, RL53, and RL54) (Figure A1-A3). Also, the SACCF region represented a significantly stabilized state of vertical atmosphere evident in the gradually increasing trend of r and θ_v in all soundings (RL8, RL29, RL30, RL42, RL43, and RL63). The T_{air} higher than *SST* indicated initiation of LLWAA that inhibited vertical mixing within MABL. This promoted the formation of a decoupled boundary layer structure over SACCF. This post-cold frontal region of ISSO is positioned in the southernmost extent of meandering ACC, where weak westerly winds (13.1 m s^{-1}), lowest *MSLP* (983.2 hPa), highest *RH* (95.77 %), and $T_{air}>SST$ were ubiquitous, and led to the frequent development of low-pressure polar cyclonic systems (Carleton and Song, 1997; Irving et al., 2010).

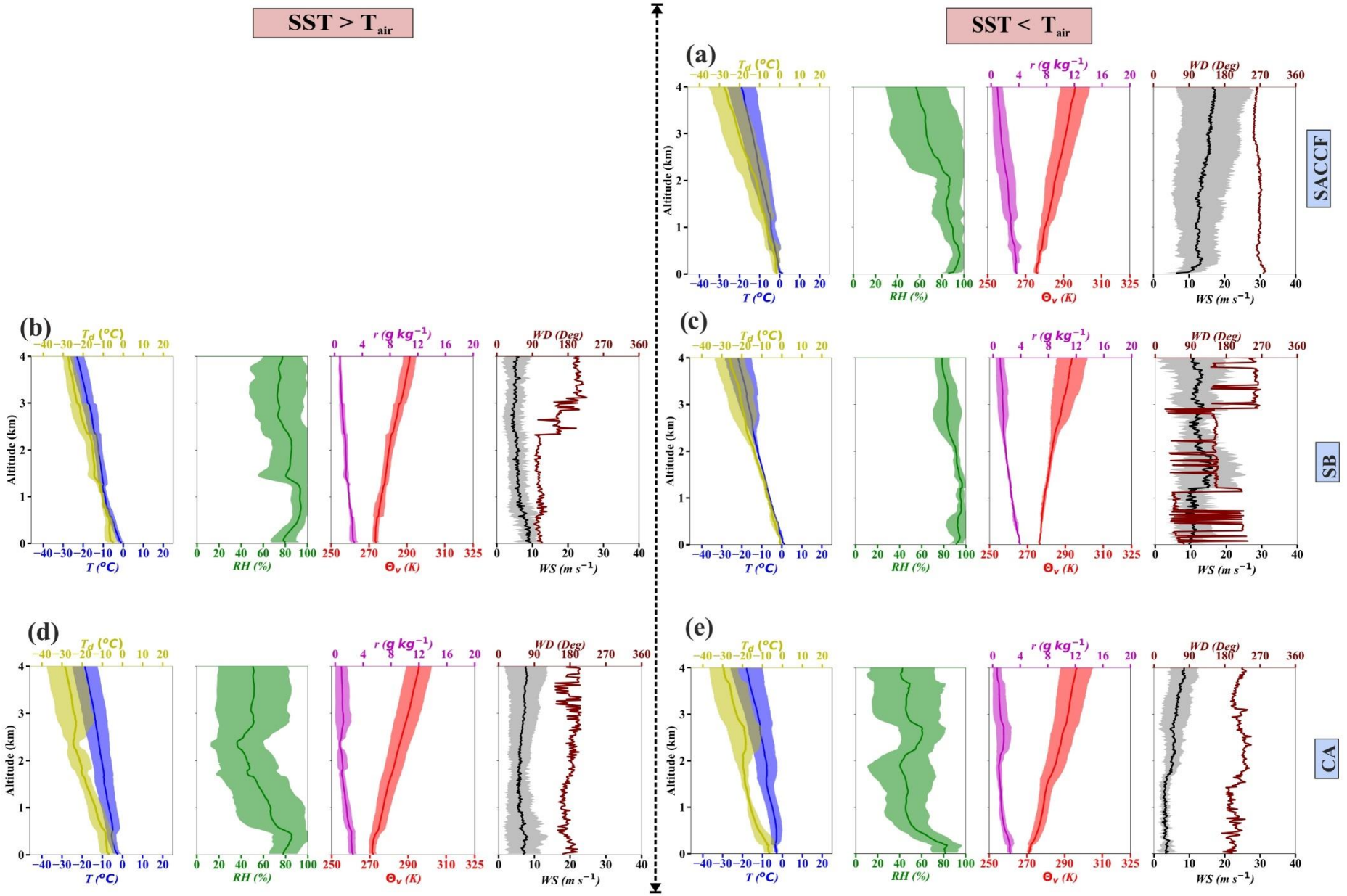
SST > T air
SST < T air
(a)
(b)
(c)
(d)
(e)
SACCF
SB
CA
Altitude (km)
T (°C)
Td (°C)
RH (%)
r (g kg−1)
Θv (K)
WD (Deg)
WS (m s−1)

Figure 4.4 Mean vertical thermodynamic profiles of air temperature (*T* in ℃, blue line), dew point temperature (T_d in ℃, yellow line), relative humidity (*RH* in %, green line), virtual potential temperature (θ_v in K, red line bottom x-axis), mixing ratio (r in g kg^{-1}, magenta line, and upper magenta x-axis), wind speed (*WS* in m s^{-1}, black line bottom x-axis), and wind direction (*WD* in degrees, brown line, and upper brown x-axis) up to 4,000 m altitude for upper air soundings released in frontal regions of High-latitude Southern Ocean (HLSO). The left panel represents sounding profiles where $SST > T_{air}$ in (b) SB and (d) CA while the right panel represents sounding profiles where $SST < T_{air}$ in (a) SACCF, (c) SB, and (e) CA. The shaded area represents 1 standard deviation (except for wind direction). In these frontal regions of HLSO, significant decrease in the heat and water vapor content within MABL could be seen with large decrease in the values of *T* and *RH* from close to surface to 5000 m altitude. Significant boundary layer stratification could be observed in SB region mainly due to different air masses advected by wind flow from differing directions near 60°S. In coastal Antarctic region of Prydz Bay, during conditions of $SST > T_{air}$ formation of shallow mixed layer structures could be observed with nearly uniform variation of θ_v and r up to few meters above the sea surface.

Table 4.1 Characteristics of classified regions in terms of Campaigns, Thermodynamics, Clouds, Inversions, and their Macrophysical properties.

Oceanic Domains	Subtropical Indian Ocean (STIO)			Indian Ocean sector of Southern Ocean (ISSO)				High-Latitude Southern Ocean (HLSO)		
Frontal Regions	NSTF1	NSTF2	SSTF	SAF1	SAF2	PF1	PF2	SACCF	SB	CA
I. Campaign										
SOE-IX	3	3	2	2	-	1	1	1	1	4
SOE-X	2	4	-	2	-	2	5	4	2	9
SOE-XI	3	1	1	2	1	2	2	1	7	7
Total Count	8	8	3	6	1	5	8	6	10	20
II. Thermodynamics										
SST mean (℃): Oceanic domains	20.10 ± 3.04			7.70 ± 4.27				1.01 ± 0.38		
SST mean (℃): Frontal regions	24.19	19.21	16.92	13.15	10.38	4.85	2.43	1.45	1.06	0.52
SST gradient (℃/degree latitude): Oceanic domains	1.43 ± 0.98			0.74 ± 0.17				1.05 ± 0.18		
SST gradient (℃/degree latitude): Frontal regions	0.94	0.56	2.80	0.92	0.73	0.84	0.48	0.93	1.30	0.93
SST boundaries (℃)	27.5 – 20.5	23.6 – 19.1	18.5 – 14.3	12.8 – 10.5	8.3 – 7.2	5.8 – 3.7	3.6 – 1.2	1.9 – 0.5	2.2 – -0.4	2.18 – -1.1
SST - T_{air} (℃)	-0.55	0.43	0.80	-0.71	2.38	-0.67	0.12	-0.23	1.33	2.43
MSLP (hPa)	1016.2	1017.8	1019.3	1010.3	1011.1	994.7	995.3	983.2	984.3	990.6
WS (m s^{-1})	5.66	9.82	9.07	14.68	7.94	21.05	15.44	13.10	8.91	5.15
WD (°)	215.9	196.3	232.3	279.5	247.9	278.7	255.9	265.7	86.74	185.3
RH (%)	79.64	80.77	81.2	87.23	77.04	86.04	85.57	95.77	91.78	66.96
EIS (K)	8.46	9.89	8.61	8.29	2.41 (LC)	9.45	7.65	7.51	5.19	9.82
LTS (K)	16.32	17.86	16.34	15.52	7.23 (LC)	18.63	14.26	13.63	11.47	17.63
III. Cloud Layer										
No cloud (%)	37.5	50	33.33	0	100 (LC)	60	50	16.66	20	55
1 layer (%)	37.5	37.5	33.33	100	0 (LC)	0	12.5	33.33	40	40
2 layer (%)	25	12.5	33.33	0	0 (LC)	20	25	33.33	20	5
3 or more layer (%)	0	0	0	0	0 (LC)	20	0	16.66	10	0

Complete cloud (%)	0	0	0	0	0 (LC)	0	12.5	0	10	0
IV. Cloud Macro characteristics										
Total cloud thickness (m)	808± 575	1015± 571	450± 90	593± 374	NC (LC)	1360± 320	1750± 1181	1556± 614	1925± 880	602± 321
Cloud top height (m)	2612±1 183	2445± 998	1870± 650	1383± 387	NC (LC)	2790± 590	2430± 990	2548± 873	2807± 1067	2122± 1193
Cloud base height (m)	1196± 651	615± 199	680± 180	840± 415	NC (LC)	500±0	575± 129	500±0	632± 224	1326± 952
V. Inversion (INV)										
No INV (%)	25	37.5	33.33	0	100 (LC)	20	50	50	90	50
1 INV (%)	50	25	0	33.33	0 (LC)	40	25	16.66	0	25
2 INV (%)	12.5	0	0	66.67	0 (LC)	0	12.5	16.66	0	5
3 or more inversion (%)	12.5	37.5	66.67	0	0 (LC)	40	12.5	16.66	10	20
VI. INV Macro characteristics										
Main INV height (m)	1206± 704	1600± 1112	650± 90	2244± 680	NI (LC)	1840± 1347	1950± 1241	1313± 670	500±0	1632± 1061
Main INV strength (K m^{-1})	0.23± 0.05	0.34± 0.12	0.35± 0.15	0.30± 0.11	NI (LC)	0.40± 0.21	0.25± 0.05	0.24± 0.09	0.20± 0.00	0.23± 0.1
Second INV height (m)	2390± 790	2087± 227	2210± 1070	2325± 1628	NI (LC)	1890± 450	2410± 1250	3420± 80	1200± 0	2263± 1149
Second INV strength (K m^{-1})	0.20± 0.00	0.37± 0.12	0.55± 0.05	0.33± 0.19	NI (LC)	0.65± 0.45	0.27± 0.00	0.23± 0.00	0.20± 0.00	0.25± 0.08

Note: A total number of atmospheric soundings available in each region during the respective campaign is summarized under subheading I. EIS and LTS stand for Estimated Inversion Strength and Lower Tropospheric Stability. NC denotes No Cloud, LC denotes Low in Confidence, and NI denotes No Inversion. The wind speed (WS), wind direction (WD), and relative humidity (RH) in subheading II are mean values observed at 925 hPa

4.3.2. Cloud and inversion characteristics

This section describes the characteristics of clouds (i.e., frequency of cloud occurrences, the height of the cloud base and cloud top along with total cloud thickness) and inversions properties (i.e., frequency of occurrences of inversion, height, and strength of primary and secondary inversions) observed over frontal regions lying in three major oceanic domains, i.e., STIO, ISSO, and HLSO.

4.3.2.1. Sub-Tropical Indian Ocean (STIO)

Out of a total of 19 soundings available in this region, no cloud layers were observed in 8 soundings. While single-layer and double-layer clouds were witnessed in 7 and 4 soundings respectively (Table 4.1). The mean base of the lowest cloud was at 1,196 m elevation over NSTF1 which decreased to 615 m and 680 m over NSTF2 and SSTF, respectively. Similarly, the mean cloud top height of the highest cloud layer was 2,612 m and 2,445 m over NSTF1 and NSTF2 which gradually decreased to 1,870 m over SSTF. The mean cloud thickness observed over NSTF1 was 880 m, which increased to 1,015 m over NSTF2 and dropped to 450 m over SSTF. The decrease in the total cloud thickness over SSTF was due to the convective activities of ARC. Over SSTF, the coverage of thin low-level stratocumulus clouds was attributed to the formation of closed mesocyclonic systems at the top of the convective boundary layer (Muhlbauer et al., 2014; Truong et al., 2020a).

The primary inversions over frontal regions, i.e., NSTF1 and NSTF2, were located at higher than 1,200 m altitude having a strength of 0.23 K m^{-1} over NSTF1 and 0.34 K m^{-1} over NSTF2. These primary inversions over both NSTF regions were likely associated with the advection of warmer air mass from the African continent and strong subsidence due to the anti-cyclonic circulation of diverging winds, respectively. The secondary inversions over NSTF1 and NSTF2 were noticed at altitudes higher than 2,000 m having the strength of 0.20 K m^{-1} and 0.37 K m^{-1}, respectively. Compared to NSTF1 and NSTF2, the strongest primary inversions were observed over SSTF at a lower altitude (650 m) with a strength of 0.35 K m^{-1}, while the secondary inversions were observed at a height of 2,250 m with a strength of 0.55 K m^{-1}. The lowest primary inversions in SSTF are likely to cap the convective boundary layer (CBL) formed due to enhanced low-level mixing caused due to eddies ejected from ARC (Lutjeharms and Valentine, 1988; Lutjeharms and Van Ballegooyen, 1988; Figure A6; Boebel et al., 2003).

4.3.2.2. Indian Ocean sector of Southern Ocean (ISSO)

The presence of high cloud cover and multiple inversions were noticed in ISSO. This was attributed to the mixing of distinct air masses regulated by multiple atmospheric fronts, i.e., cold/warm/occluded fronts over shorter spatial scales. Of the 20 soundings, 12 recorded the presence of clouds over ISSO. The six soundings launched over SAF1 showed the presence of low-level clouds. Whereas only one sounding over the SAF2 region shows cloud-free conditions. However, based on single sounding, it is difficult to provide a statistically significant interpretation for the SAF2 region. A recent study by Behrangi and Song (2020) reported more cloud occurrences over the SAF region than in PF. Significant low-level clouds with heights as low as 500 m and as high as 4,000 m were observed in the ISSO region. Data showed the presence of multi-layered and complete clouds over PF1 and PF2, respectively. Over SAF1, the clouds had an average thickness of 593 m, while over PF1 and PF2, it was 1,360 m and 1,750 m, respectively. Average cloud top heights were observed to be higher in PF1 (2,790 m) and PF2 (2,430 m) regions. The low-level stratus clouds over these regions experienced air mass temperatures as low as -3.79°C at 500 m. The second cloud layer was identified at an average altitude of 3,360 m recording temperatures as low as -18.82°C (Figure 4.3). This is consistent with previous studies highlighting the presence of multilayered clouds in mixed phases (Huang et al., 2012; Mace et al., 2020; Mace et al., 2021). Over the ISSO, the low-level stratus clouds commonly precipitate due to strong advection-induced mixing of multiple air masses. This triggers snowfall and foggy conditions over PF, while precipitation as rain over SAF (Kawai et al., 2015).

Inversions over ISSO were primarily due to advective motions induced mixing between different air masses by stronger winds (Hande et al., 2012). Two-thirds of the soundings made over SAF1 and SAF2 show the presence of double inversions followed by single inversions. The average height of the primary and secondary inversions were 2,244 m and 2,325 m, with

a strength of 0.30 K m^{-1} and 0.33 K m^{-1}, respectively. Over PF1 and PF2, three or more inversions of significant strengths were detected, which were likely induced by polar jet streams forcing strong baroclinic instabilities (Simmonds and Lim, 2009; Figure A9, A10). Here, the average height of primary and secondary inversions were 1,840 m and 1,890 m in PF1 and 1,950 m and 2,410 m in PF2, respectively. However, relatively stronger inversions were observed over PF1, i.e., 0.40 K m^{-1} (primary) and 0.65 K m^{-1} (secondary), than compared to PF2, i.e., 0.25 K m^{-1} (primary) and 0.27 K m^{-1} (secondary).

4.3.2.3. High-Latitude Southern Ocean (HLSO)

Approximately half of the soundings over SACCF revealed two or more layered clouds, which decreased to two-fifth over SB and one-twentieth over CA. Low-level multilayer thick clouds over SACCF were attributed to the frequent formation of low-pressure mesoscale cyclonic systems. In contrast, the decreased frequency of multilayered clouds over SB and CA was due to increased convective activity of polar gyres (i.e., Weddell Sea gyre and Prydz Bay gyre) (Table 4.1). The average cloud thickness over SACCF was 1,556 m, which increased further over SB (1,925 m) and decreased to 602 m over CA. Over SACCF and SB, clouds were noticed at significantly low altitudes (i.e., at average cloud base height of 500 m and 632 m), having air temperatures as low as -2.81°C. At higher altitudes (>2,000 m), the air temperature within the cloud layer was as low as -23°C. As indicated with air masses of such low temperature, mixed-phased clouds, i.e., low-level supercooled water droplets and mid-level ice crystals within 4,000 m have been consistently reported in other areas of HLSO (Huang et al., 2012; Mace et al., 2020). The average cloud base height over the CA region was recorded at a relatively higher altitude (1,326 m) than that over SACCF and SB. Distinctively, ice virga (precipitation not reaching the surface) was noticed over SB and CA, consistent with previous studies (Wang et al., 2018; Vignon et al., 2019b; Jullien et al., 2020; Alexander et al., 2021).

Concerning inversions over SACCF, no significant inversions were observed among half of the soundings (Table 4.1). The other half constituted single-inversion, double-inversion, and three or more than three inversions, in equal counts. The recorded inversions were generally associated with strong convergence and prominent low-pressure cyclonic systems in the low-level atmosphere. Regardless, the primary and secondary inversions were weak (0.24 and 0.23 K m^{-1}) and were observed at ~1,313 m and ~3,420 m, respectively. The presence of multi-level inversions (three or more) was dominant over SB and CA. However, these inversions were weak over SB (0.20 K m^{-1}) due to lower *MSLP* and slowly evolving low-level convection at low altitudes. It can be anticipated that weak unstable conditions might form for a small duration and promote cloud formation. These clouds generally appear beneath weaker inversions, which could be easily eroded through radiation or even by weak easterlies. Compared to SB, inversion strength slightly increased over CA. Over CA, average primary inversions of strength 0.23 K m^{-1} were observed at higher altitudes (1,632 m), and secondary inversions of strength 0.25 K m^{-1}, if observed, were at ~2,263 m. The inversions were associated with an increase in the temperature of Antarctic surface waters, a slight increase in *MSLP*, and katabatic winds advecting dry and cold air mass across mid-altitudes.

4.3.3. Physical and dynamic atmospheric processes

In this section, the dominant physical processes such as convection, advection, precipitation, and radiative heating/cooling were investigated between altitudes 500 m and 4,000 m following Betts (1982); Betts and Albrecht (1987). The modification in air mass saturation was traced by analysing conserved variables (i.e., θ_e and q) in the form of $\theta_e - q$ diagram representing frontal regions lying in three major oceanic domains examined in the present study.

4.3.3.1. Sub-Tropical Indian Ocean (STIO)

Over NSTF1 and SSTF, the presence of near-surface convective mixing was evident with a clear mixing line structure indicated by a gradual decreasing tendency of θ_e and q with

increasing altitude (Figure 4.5b, c). Instability caused due to convective mixing accounted for the formation of shallow CBL with the top of the surface-based mixed layer extending up to 840 m (925 hPa) over NSTF1 and 1,200 m (887 hPa) over SSTF. The presence of shallow CBL is anticipated (if CBL tops ≥ 800 hPa) (Betts and Albrecht, 1987). However, the convective mixing was not only restricted to surface based CBL but extended in intermediate altitudes (simultaneous decrease in θ_e and q) splitted by radiative process (change in θ_e with constant q) (Figure 4.5b). This demonstrates that CBL thermally-coupled to surface promotes internal convective mixing due to re-stratification (Nicholls, 1984; Betts and Albrecht, 1987) and splits up single well-mixed air-column into different convectively mixed layers at higher altitudes (simultaneous decrease in θ_e and q*;* NSTF1 and SSTF; Figure 4.5b). Thus, this indicates coupled CBL in NSTF1 and SSTF, which is consistent with studies reporting the common presence of coupled boundary layers over high-pressure regions (Nicholls, 1984; Bretherton and Wyant, 1997; Stevens, 2000; Jones et al., 2011; Dong et al., 2015; McGibbon and Bretherton, 2017; Zheng et al., 2018a). Radiative heating was the regulatory process in altitudes between the intermediately decoupled layer (Figure 4.5b, c). Interestingly, at the top of CBL over SSTF, weak precipitation signature (near uniform variation of θ_e and q) accompanied by radiative heating underneath and above was evident (Figure 4.5b). Thus, anticipates presence of a thin stratocumulus clouds layer above the CBL top associated with a closed mesoscale convective system, which is concurrent with few reported studies (Muhlbauer et al., 2014; Truong et al., 2020a). In NSTF1 and SSTF, irrespective of $SST > T_{air}$ ($SST < T_{air}$), signatures of these processes were observed with differences in the increased (decreased) intensity of convective mixing leading to a highly (weakly) evolved mixed layer structure. Noticeably, the most robust low-level convective mixing occurred over SSTF, driven by ARC's convective activities (Figure 4.5b, c). Compared to physical processes over NSTF1 and SSTF, over NSTF2, low-level advection of cool air-mass followed by precipitation (from ~220 m to

~1,080 m) was anticipated as the dominant process (NSTF2; Figure 4.5b, c). Above the precipitation signature, advection due to changing wind directions (south to west) appears to drift the atmospheric moisture content (Figure 4.2c, d).

4.3.3.2. Indian Ocean sector of Southern Ocean (ISSO)

Over SAF1 and SAF2, signatures of low-level convection were significantly suppressed, while strong advective motions of multiple air masses were likely to be a regulatory process. This anticipation is supported by the abruptly changing wind direction that portrays this region as a dynamic storm track region constructed of multiple air masses (Figure 4.3a, b). For the atmospheric conditions, when $SST > T_{air}$, the $\theta_e - q$ diagram in these regions showed vertical lines which may readily indicate advection-induced mixing between different air masses mainly enforced by the prevalence of multiple atmospheric fronts. However, when $SST < T_{air}$, in addition to advection induced-mixing, the likelihood of substantial precipitation was indicated in $\theta_e - q$ diagram by a larger decrease in q with a nearly uniform variation of θ_e up to 4,000 m altitude in SAF1 (Figure 4.5c). Further ahead, the $\theta_e - q$ diagram observed over PF1 showed stronger low-level advection caused due to merging of multiple air masses by high-speed winds as well as due to the impact of the intense polar jet stream (Figure 4.3d-g). This strong advection-induced air mass mixing was favorable during both conditions (i.e., $SST > T_{air}$ and $SST < T_{air}$) throughout the vertical 4,000 m altitude over PF1 (Figure 4.5b, c). In contrast, in conditions when $SST < T_{air}$, the likelihood of precipitation/condensation of falling precipitation at higher altitudes (beyond 1,500 m) was another dynamic process in PF1. In PF2, the $\theta_e - q$ diagram depicted the dominant signature of precipitation/condensation of falling precipitation up to nearly 2,000 m altitude irrespective of the conditions (i.e., $SST > T_{air}$ and $SST < T_{air}$), which indicates a meteorologically highly stable atmosphere formed due to stronger advection of multiple air masses (Figure 4.5b, c).

4.3.3.3. High-Latitude Southern Ocean (HLSO)

Over SACCF, the low-level atmosphere was influenced by advective processes, while weak convection prevailed over SB and CA. Over SACCF, although the intensity of advective motions decreased, strong low-level convergence and continuous advection of cold polar air mass induce a highly stable atmosphere ($SST<T_{air}$) and a system of intensified low-pressure cyclones. As a result, in the $\theta_e - q$ diagram of SACCF, low-level advection was likely, above which precipitation occurred (uniformity in θ_e and decrease in q) with the occurrence of radiative heating above and below this precipitation (SACCF; Figure 4.5c). This falling precipitation tends to condense faster, causing foggy and snowy conditions in the near-surface atmosphere, while in intermediate and higher altitudes supported the formation of low-level thicker clouds. However, at higher altitudes, no clear signature of precipitation was observed (Figure 4.5b). This indicated the occurrence of closed mesoscale cyclonic systems due to strong low-level convergence.

Over SB and CA, the $\theta_e - q$ diagram observed during conditions of $SST>T_{air}$ depicted shallow convective mixing line structure (decline in θ_e and q) up to ~60 m over SB and ~220 m over CA due to an increase in the temperature of Antarctic surface waters linked to the activity of sub-polar gyres, i.e., Weddell Sea gyre and Prydz Bay gyre (SB and CA; Figure 4.5b). With increasing altitudes, a decline in convection and occurrence of prominent precipitation (uniformity in θ_e and a significant declining q) was observed at intermediate and high altitudes in both regions (Figure 4.5b). In these regions, sublimation of precipitation to support virga conditions was anticipated as a regulatory process commonly in the intermediate altitudes. Occurrence of sublimation-supported virga conditions have been reported in a few studies poleward of 64°S (Forbes and Hogan, 2006; Alexander et al., 2021) and over Antarctica (Forbes and Hogan, 2006; Jullien et al., 2020). Interestingly, significant precipitation in intermediate altitudes and prominent radiative heating at higher altitudes were observed over

CA than that over SB (Figure 4.5b). However, in conditions when $SST < T_{air}$, the convective mixing signature was not pronounced over both SB and CA; weak advection was likely followed by stronger precipitation at mid and high altitudes (Figure 4.5c).

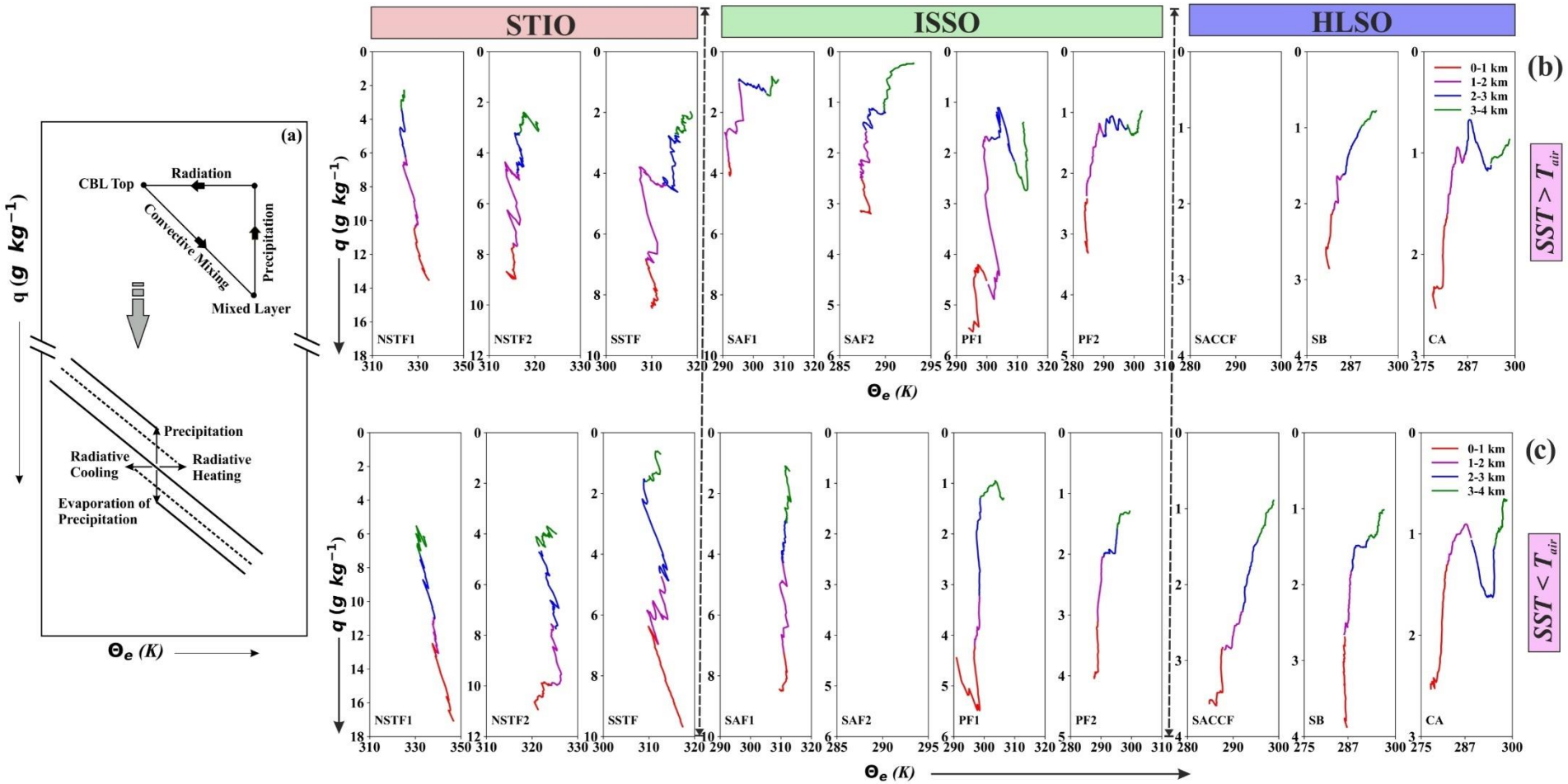

Figure 4.5 (a) Schematic diagram of conserved variables ($\theta_e - q$) depicting the effect of physical processes such as convective mixing, precipitation/evaporation, and radiative heating/cooling in modifying the mixing line structure. (b) The $\theta_e - q$ diagram obtained over ten frontal

regions of ISSO. Obtained structure of air parcel motion in all frontal regions are colored as: surface – 1,000 m (in red), 1,000 – 2,000 m (in magenta), 2,000 – 3,000 m (in blue), and 3,000 – 4,000 m (in green). (c) The $\theta_e - q$ diagram obtained over ten frontal regions of ISSO but for clear variability of structure of air parcel motion, scales for x and y axis are varied accordingly for each frontal regions with altitudes marked in km. In STIO region, instability induced by convective activities were prominent, and is depicted with fluctuations in both θ_e and q, however in ISSO regions, dominance of precipitation process is evident with large decrease in θ_e with nearly uniform varying trend of q. In HLSO regions, precipitation, and sublimation of falling precipitation were the dominant regulatory processes.

4.3.4. Case studies in frontal regions of three major oceanic domains

In addition to low-level thermodynamics, clouds, and inversion characteristics, the effect of synoptic scale meteorology in altering the state of MABL has been presented in the form of case studies in this section. Three typical case studies were chosen i.e., from SSTF, SAF1, and CA regions lying in STIO, ISSO, and HLSO respectively. A sounding selected in SSTF was aimed to highlight the effect of Agulhas Retroflection Current (ARC) to regulate the vertical state of MABL, while the selection of sounding in SAF1 region was aimed to demonstrate the effect of common multiple atmospheric fronts (i.e., cold, and warm front) in SO region to alter the state of MABL. Also, a sounding selected in the CA region aims to depict the influence of the convective activities over the Prydz Bay gyres as well as the effect of katabatic winds on the structure of MABL in the coastal region of Antarctica.

4.3.4.1. Sub-Tropical Indian Ocean (STIO)

A sounding launched at 40°S, 58.48°E on 12th January 2017 at 06:00 UTC is presented in Figure 4.6a. The synoptic view around this sounding depicted a warm front region indicated by $SST > T_{air}$ and increased activity of oceanic eddies associated with the ARC (Lutjeharms and Van Ballegooyen, 1988). The *SST* at the location of sounding was 3.02°C higher than T_{air} and recorded *MSLP* at 1027 hPa. The advection of LLCAA was evident from the prominent southerly winds bringing cold polar air mass to the region (Figure 4.6a). These conditions led to an unstable MABL leading to the formation of a well-evolved thermodynamically coupled mixed layer structure (Zheng et al., 2018b, 2018a; Zheng and Li, 2019b). This was also evident in the nearly uniform variation in profiles of θ_v and r up to 1,220 m. At the top, vertical mixing was suppressed by a strong primary inversion (0.73 K m^{-1}), followed by multiple inversions (>3) to an altitude of 4,000 m (Figure 4.6a). In unstable conditions, the formation of a single cloud layer was noticed with a cloud base height of ~980 m, cloud top height of ~1,220 m, and total cloud thickness of ~240 m. These observations concur with the records about thin

low-level stratocumulus cloud coverage at the top of the convective boundary layer (Muhlbauer et al., 2014; Truong et al., 2020a).

4.3.4.2. Indian Ocean sector of Southern Ocean (ISSO)

A sounding launched at 43.02°S, 57.02°E on 2nd March 2020 at 12:00 UTC is presented in Figure 4.6b. The synoptic illustration depicted both the warm front region ($SST > T_{air}$) and cold front region ($SST < T_{air}$) in the nearest proximity of the sounding location, with considered sounding lying in the cold front region. Being in a cold front region, inputs of weak negative surface heat fluxes were evident with $SST < T_{air}$ by 1.75°C. Also, prominent synoptic LLWAA could be seen from strong north-westerly winds advecting warm moist air masses over this region. LLWAA, which is one of the characteristic features commonly reported in the SO region, can be observed in this typical sounding (Wall et al., 2017). The LLWAA coupled with inputs of weak negative fluxes ($SST < T_{air}$) and decreased *MSLP* (1011 hPa) accounted for highly stabilized and thermodynamically decoupled MABL in this sounding. Also, previous studies have frequently reported the presence of decoupled boundary layer in this SO region (Mace and Protat, 2018b; Zheng and Li, 2019a; Truong et al., 2020a). A highly stabilized boundary layer can be observed with a gradually increasing tendency of θ_v and r within 4,000 m altitude (Figure 4.6b). Due to high low-level stabilization, the formation of a thick cloud layer was observed with cloud base height (~760 m), cloud top height (~1,720 m), and total cloud thickness (~960 m). The main inversion having significant strength (~0.55 K m^{-1}) was recorded at the height of ~1,840 m (Figure 4.6b). Interestingly, profiles of θ_v, r, and *RH* depicted the presence of air masses of distinct properties within the 4,000 m air column. This is indicated by the presence of highly saturated air mass in the low-level atmosphere (up to ~1,720 m) below the main inversion and by the prevalence of relatively dry air mass above this inversion up to 4,000 m altitude (Figure 4.6b). The presence of such varying property air masses together with highly stabilized conditions is attributed to the frequent formation of

multiple cold (warm) fronts at shorter spatial scales mainly driven by LLWAA (LLCAA) in the SO region (Zheng and Li, 2019b).

4.3.4.3. High-Latitude Southern Ocean (HLSO)

A sounding launched at 66.98°S, 64.86°E on 16th February 2020 at 06:00 UTC lying in the CA region, was used as a representative sounding in HLSO (Figure 4.6c). The synoptic conditions depicted the occurrence of a warm front ($SST > T_{air}$) at and around the sounding location (Figure 4.6c). The formation of a warm front in this region is attributed to the potential warming of coastal Antarctic waters due to the convective activity of polar mesocyclones regulated by the Prydz Bay gyre near the Antarctic coast (Smith et al., 1984). As a result, at this typical sounding, the inputs of positive surface heat fluxes were indicated from $SST > T_{air}$ by 3.76°C and the recorded *MSLP* as 988 hPa. Also, the presence of prominent LLCAA of cold, dry polar air mass through strong katabatic south easterly winds mainly originated from the Antarctic continent was observed (Figure 4.6c). The combined effect of increased surface heat fluxes and strong LLCCA at and in the vicinity of the sounding location has induced low-level atmospheric instability. This instability resulted in the formation of a well-mixed layer (indicated by nearly uniform variation of θ_v and r) capped by a weak inversion recorded at ~820 m of strength ~ 0.24 K m^{-1}, which marks the limit of vertical mixing at this sounding (Figure 4.6c). Thus, the LLCAA induced destabilization resulted in the formation of thermodynamically coupled MABL, supporting the occurrence of a thin cloud layer with a cloud base height of ~920 m and a total cloud thickness of ~440 m formed at the top of the mixed layer. Above the cloud layer, a significant stable atmosphere composed of dry and cold air mass was observed in the sounding launched in this region (Figure 4.6c).

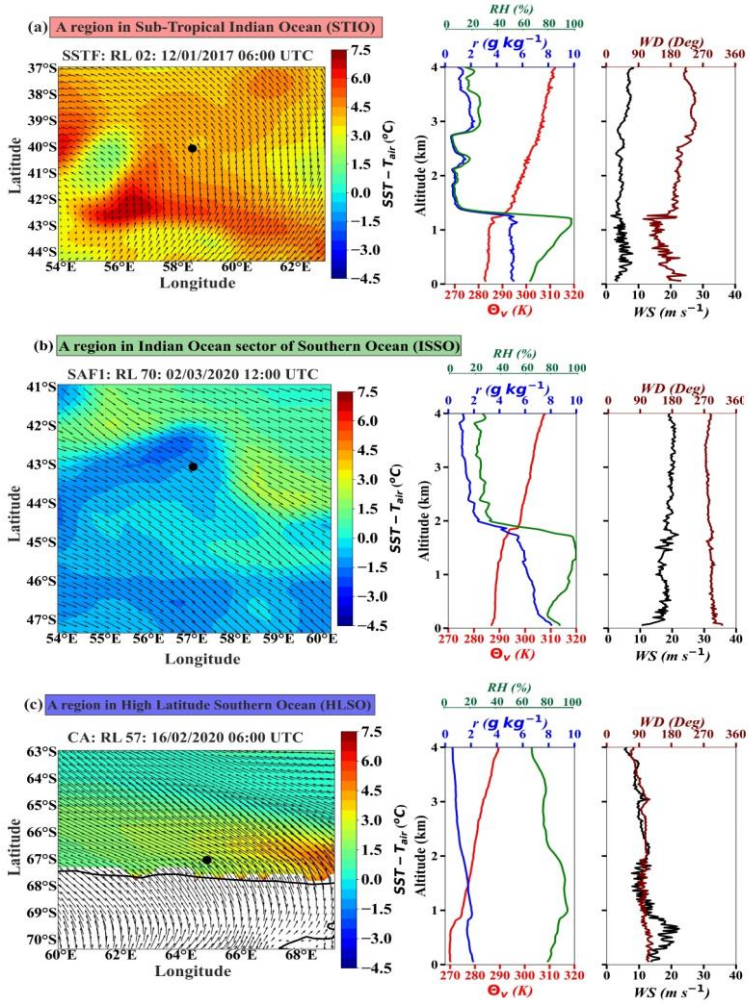

Figure 4.6 Case studies using three typical soundings launched in three distinct frontal regions lying in three major oceanic domains i.e., (a) In the Sub-tropical Indian Ocean (STIO) over the Southern Sub-Tropical Front (SSTF) (b) In the Indian Ocean sector of Southern Ocean (ISSO) over Northern Sub-Antarctic Front (SAF1), and (c) In High Latitude Southern Ocean (HLSO) over Coastal Antarctica (CA). The Upper, middle, and lower left panel represents synoptic near-surface air-sea temperature difference (SST-T_{air} in ℃) and wind circulation pattern observed in the vicinity of soundings launched in SSTF, SAF1, and CA respectively. This synoptic view was generated using data on surface-based SST, T_{air} at 2 m, and wind fields (10 m *u*- and *v*- component) obtained from ECMWF-ERA5 reanalysis. The sounding locations are marked with a black circular dot and color bars are shown. The Upper, middle, and lower right panel represents a 4,000 m vertical profile of virtual potential temperature (θ_v in red), *mixing*

ratio (*r* in blue), relative humidity (*RH* in green), wind speed (*WS* in black), and wind direction (*WD* in brown) for radiosonde launched at 40.00°S, 58.48°E on 12-01-2017 at 06:00 UTC in the SSTF, at 43.02°S, 57.02°E on 02-03-2020 at 12:00 UTC in the SAF1, and at 66.98°S, 64.86°E on 16-02-2020 at 06:00 UTC in CA region respectively.

4.3.5. Estimated Inversion Strength (*EIS*) and Lower Tropospheric Stability (*LTS*)

This is the first document reporting the estimates of *EIS* and *LTS* over ISSO region, especially over higher latitudes. The estimates for *LTS* were comparable with estimates reported over regions of the Australasian sector of the Southern Ocean (ASSO) by Truong et al. (2020a). However, slight differences in the estimates were obtained over a few frontal regions of ISSO (Table 4.1). This could be attributed to the differences in the ISSO's regional, seasonal, and meteorological conditions to that of the ASSO. Further, the variability of fractional cloud cover (1-'no cloud frequency') with *EIS/LTS* showed a good fit with respect to the linear relationship proposed by Wood and Bretherton (2006), particularly over post-cold frontal regions of ISSO, i.e., over SACCF and SB. These observations for the linear relationship of Wood and Bretherton (2006) closely estimate *CF* using estimated *EIS/LTS* over post-cold frontal regions of SO are consistent with the findings of Naud et al. (2016) and Wood and Bretherton (2006). However, in the other regions of the study area, this relationship poorly served to provide estimates of *CF*.

4.4. Discussion

The observations presented in this chapter provides first time understanding with respect to the characteristics of low-level atmosphere over the least examined region of the Indian Ocean sector of Southern Ocean (ISSO). In the results section of this chapter, the effects of synoptic air-sea coupling i.e., air-sea temperature gradient (*dT*) in shaping the vertical thermodynamic structure of low-level atmosphere (MABL), and the macrophysical characteristics of clouds and inversions associated with the dynamic physical processes occurring over frontal regions

lying in three major oceanic domains i.e., Sub-Tropical Indian Ocean (STIO), Indian sector of Southern Ocean (ISSO), and High Latitudes of Southern Ocean (HLSO) have been elaborated. In continuation to the obtained results, a brief discussion on these results and observations are presented in this section.

Across the frontal regions from sub-tropics to high latitudes, four major processes could be delineated; these are convection, advection, precipitation, and radiative heating/cooling. Among these processes, over STIO regions (NSTF1, NSTF2, and SSTF), major inputs of positive surface heat fluxes were observed to initiate convection in the low-level atmosphere. As a result, prominent low-level atmospheric mixing formed a well-evolved convective mixed layer. This convective mixed layer thermodynamically coupled to the surface was observed to decouple (weakened) in mid-altitudes, but due to the re-stratification, continued internal convective mixing resulted in the formation of a coupled mixed layer structure. Compared to NSTF1 and NSTF2 regions, in SSTF, which represented a high-pressure region experienced strong convection-induced low-level convective mixing formed a deeper mixed layer structure accompanied by multiple strong inversions and higher proximity of no clouds to very thin clouds. These conditions observed over SSTF were because of active oceanic eddies associated with ARC (Lutjeharms and Gordon, 1987; Lutjeharms and Van Ballegooyen, 1988). Overall, in sub-tropical regions, strong convection and high-pressure formations accounted for the formation of thermodynamically coupled MABL capped by thin mid-altitude clouds followed by strong low-level inversions. In addition to convection, advection in intermediate altitudes was seasonal because of changing wind patterns. Also, prominent advection of cold air masses and few instances of weak precipitation caused weak radiative heating in intermediate altitudes.

Further southwards, in the regions of ISSO, the prominence of advection-induced mixing of multiple air masses and precipitation were regulatory processes. Strong advective mixing was induced by a frequently changing system of atmospheric fronts (i.e.,

cold/warm/occluded). A dynamic system of multiple atmospheric fronts over shorter spatial scales was experienced by these regions. These systems aided significant precipitation, mainly in conditions when $SST < T_{air}$. Moreover, in the PF1 and PF2 regions of ISSO, a unique system of intensified winds hinted at the impact of the polar jet stream, while the presence of baroclinic instabilities was depicted by a system of multiple cold and warm fronts. The combined effect of this causes rigorous advective mixing of air masses of varying properties in ISSO regions. Such an advection aided faster condensation of falling precipitation in these regions, which is consistent with past reported studies (Jensen et al., 2000; Wang et al., 2015; Lang et al., 2021). This condensation is likely to be in the form of fog and snow in PF regions while in the form of rain in SAF regions. At mid- and higher altitudes, condensation accounted for the formation of thicker multi-layered clouds, which were as low as 500 m and as high as 4,000 m. In the ISSO regions, the frequency of low-level inversions was relatively less than multiple inversions that occurred at higher altitudes, mainly led by stronger advection of multiple air masses by intense winds.

Further southwards in one of the HLSO region, i.e., over SACCF, prominent low-level precipitation was observed to be associated with the formation of intensified low-pressure cyclonic systems formed due to the convergence of north-westerly and south-easterly winds. This precipitation cum condensation accounted for low-level multi-layered clouds, while strong advection at higher altitudes caused multiple high-level inversions even in this HLSO region. Notably, the action of high-speed winds that continually advected cold and warm air-masses through a dynamic system of formation of multiple atmospheric fronts in PF1, PF2, and SACCF has accounted for enhancing the severity of stormy low-pressure cyclones in these regions. These observations are consistent with reports on the occurrence of mid-latitude stormy cyclones over other sectors of SO, i.e., the Australasian sector of the Southern Ocean (Carleton and Song, 1997; Field and Wood, 2007; Irving et al., 2010; Truong et al., 2020a).

Formation of such systems supported prominent precipitation and condensation of descending precipitation at different altitudes. The occurrences of aforementioned processes in these regions of ISSO were highlighted by Srivastava et al. (2007) over ISSO, and some studies have documented it over the Australasian sector of the Southern Ocean (Wang et al., 2015; Lang et al., 2018; Lang et al., 2021). The dominance of these processes over ISSO regions and SACCF has accounted for the presence of low-level multilayered cloud structures. The presence of such types of clouds in these regions is consistent with the previous records using in-situ observations (Jensen et al., 2000; Lang et al., 2018; Mace and Protat, 2018b; Truong et al., 2020a; Alexander et al., 2021; Lang et al., 2021) and remote sensing observations made in other sectors of SO (Mace et al., 2009; Huang et al., 2012; Huang et al., 2015a; McCoy et al., 2015; Kuma et al., 2020). However, recorded high-level inversions in these regions comply well with past reports in the Australasian sector of the Southern Ocean (Jensen et al., 2000; Truong et al., 2020a).

Further towards southernmost regions of HLSO, i.e., over SB and CA, low-level dynamics were regulated by weak and shallow convection coupled with the advection of cold and dry polar air mass via strong katabatic winds originating from the Antarctic continent in the intermediate and high altitudes. Results revealed multiple weak inversions induced by the action of katabatic winds, while the strength of these winds regulated the strength of occurring inversions. Similar observation on inversions in Antarctica were reported by Connolley (1996). Moreover, weak precipitation in intermediate altitudes was anticipated to undergo a sublimation process resulting in ice virga conditions. Similar conditions were reported in regions of similar characteristics in the Australasian sector of the Southern Ocean (Wang et al., 2018; Vignon et al., 2019b; Jullien et al., 2020; Alexander et al., 2021).

Further, results on *EIS/LTS* provided better estimates of low-level fractional cloud cover (*CF*) over dynamically active post-cold frontal regions of ISSO, i.e., over SACCF and

SB, which are in line with the findings of Naud et al. (2016) and Wood and Bretherton (2006), wherein they highlighted the applicability of this linear relationship, particularly in mid-latitudes. Thus, this study based on a large set of in-situ meteorological measurements presents useful information on the vertical thermodynamic structure of low-level atmosphere, characteristics of cloud (layers) and inversions, and the associated physical processes occurring over yet unexplored regions of ISSO.

4.5. Concluding remarks

By covering a large spatial domain from 24°S to 68°S during three field campaigns, the study presented in this chapter records for novel observations based on the vertical thermodynamic structure of low-level atmosphere, exhibiting clouds and inversions of unique properties driven by dynamical physical processes occurring over one of the least explored ISSO region. The new findings of this study are noted below,

1. The thermodynamic stability and the vertical structure of low-level atmosphere were strongly dependent on the synoptic conditions and continually varying air-sea coupling i.e., air-sea temperature gradient (*dT)* across system of multiple oceanic fronts of the study region.

2. Over sub-tropical frontal regions (NSTF1, NSTF2, and SSTF), low-level convection caused low-level convective mixing and supported formation of a well-developed mixed layer. This surface-based mixed layer that was thermodynamically coupled to the surface appeared to be decoupled in mid-altitudes, however, re-stratification process caused internal convective mixing at mid-altitudes which regulated convective mixing in the decoupled mixed layer just above the surface-based mixed layer. Thus, decoupled mixed layer structure was commonly noticed.

3. Over SSTF, an increase in the convective activities of oceanic eddies associated with Agulhas Retroflection Current (ARC) accounted for enhanced convective mixing in low-level

atmosphere. This resulted in deeper mixed layer structure capped by low-lying multilevel strong inversion with prominent cloud free sky or very thin single layer clouds.

4. The regions in the Indian Ocean sector of Southern Ocean (SAF1, SAF2, PF1, and PF2), exhibited significant precipitation and condensation/evaporation of descending precipitation at different altitudes. This was attributed to frequent formation of multiple atmospheric fronts (i.e., cold, warm, and occluded fronts) due to stronger advection of multiple air masses by high-speed winds. Such an advection caused faster condensation of falling precipitation. At low altitudes, this supported foggy and snowy conditions few meters above the surface while in altitudes as low as 500 m and as high as 3,500 m presence of thick multi-layered clouds were noticed. These clouds were likely to be in mixed phase (i.e., SLW/IWC) clouds with temperatures as low as -18.43℃.

5. In ISSO, due to the presence of thick multi-layered clouds, radiative heating process was noticed in intermediate altitudes likely occurring above the top and below the base of the multi-layered clouds. However, at higher altitudes, advection was the dominant process accounting for multiple high-level inversions in the ISSO.

6. In ISSO, frequent occurrences of low-pressure stormy cyclonic systems were witnessed.

7. Over SACCF, significant precipitation was associated with the formation of intensified low-pressure cyclonic systems caused by convergence of north-westerly and south-easterly winds. Precipitation cum condensation of this precipitation accounted for thicker low-level multilayered clouds in mixed phase (i.e., SLW/IWC). Complete clouds from 500 m to 4,000 m altitudes were commonly observed. Followed by precipitation, occurrence of radiative heating in intermediate altitudes above and below the multilayered clouds was seen. At high altitudes, prominent advection supported multiple high-level inversions.

8. Over high-latitude Southern Ocean regions (SB and CA), low-level dynamics were regulated by weak and shallow convection coupled with the advection of cold continental dry air-mass advected by strong katabatic winds in the intermediate altitudes. In intermediate altitudes, weak precipitation goes through an abrupt sublimation process mostly due to the action of katabatic winds resulting in ice virga conditions. Thus, the presence of prominent ice clouds over SB and CA could be anticipated.

9. Collectively, four dominant processes i.e., convective mixing, advection, precipitation/condensation of falling precipitation, and radiative heating/cooling were the common regulatory process driving atmospheric conditions over three major oceanic domains described in this study.

PUBLICATION

S. Neha Salim, Arjun Adhikari, Harilal B. Menon, N. V. P. Kiran Kumar, K. Rajeev, (2023) Thermodynamic characteristics of Marine Atmospheric Boundary Layer across frontal regions of the Indian Ocean Sector of Southern Ocean based on three field campaigns, ***Atmospheric Research***, 106678, *https://doi.org/10.1016/j.atmosres.2023.106678*

Chapter 5

Aerosol-Boundary Layer Dynamics and its Effect on Aerosol Radiative Forcing and Atmospheric Heating Rate in the Indian Ocean sector of Southern Ocean (ISSO)

5.1. Introduction

Aerosols are significant contributors to poor air quality (IPCC, 2014) and influence the climate and weather patterns by either scattering or absorbing irradiance (McCormick and Ludwig, 1967; Charlson and Pilat, 1969) and also by acting as nuclei for cloud formation (Sassen, 2002). Heterogeneous in their global distribution, aerosols of natural and anthropogenic origins are characterized by their shapes, sizes, and chemical compositions. Due to the differences in the properties of different aerosol species, a larger impact of their interaction with irradiance has important implications on Earth's radiative balance. For example, (Bellouin et al., 2020) reported global mean aerosol radiative forcing estimates in the range between -0.65 and -1.6 W m^{-2} at 68% confidence intervals. The global scale assessment of aerosol radiative forcing poses severe challenges concerning aerosol-radiation and aerosol-cloud processes (Bender, 2020) in remote regions, particularly over the Southern Ocean (SO).

Studies have reported a large spatiotemporal variability in the concentrations and optical properties of aerosols over different regions of the World Ocean (Krishnamurti et al., 1998; Ramanathan et al., 2001; IPCC, 2014; Menon et al., 2015). The key factor driving such an aerosol variability is the dynamic state of the marine atmospheric boundary layer (MABL) and its characteristics feature, i.e., state of atmospheric stability, physical processes (such as convection and advection), characteristics of clouds and inversions (Groß et al., 2015; Turner, 2020; Prasad et al., 2021). Broadly, MABL acts as a shield to updraft of near-surface in-situ

generated/long-range advected aerosols (Stull, 1988; Zhang et al., 2018; Ma et al., 2020; Su et al., 2020). The coupled interaction of aerosols and MABL shows significant heterogeneity depending on regions, seasons, diurnal/time, and aerosol types and their vertical distribution (Guo et al., 2019; Lou et al., 2019). This makes it challenging to quantify the effects of aerosols on the evolution and thermodynamic stability of MABL. It results in uncertainties in satellite retrievals of aerosol-associated radiative forcing (Ramanathan et al., 2001), specifically over the SO where predominant cloud coverage (80%) adds additional difficulties in accurate simulations of aerosols as well as boundary layer properties.

Field measurements in different parts of SO have reported various mechanisms of interactions of aerosols with clouds, with varying MABL characteristics (Kremser et al., 2021). In the Australian Sector of SO (ASSO), (Alexander and Protat, 2019) showed a decoupled layer (separated from the surface mixed layer and free troposphere) within MABL with low backscattering wherein the presence of clouds was capped by weak temperature inversions at the mid-latitudes. Using various observations from the Australian Sector of SO, McFarquhar et al. (2021) reported the zonal variability in aerosol compositions within MABL. The droplet-nucleation was primarily influenced by the origin (source) of aerosols. These studies and several others (Quinn et al., 1998; Alexander and Protat, 2019; Schmale et al., 2019; Landwehr et al., 2020; Kremser et al., 2021) have improved the understanding of clouds, aerosols, and the thermodynamical structure of MABL and their interactions in the respective sectors of SO. However, a knowledge gap exists in the ISSO due to the unavailability of in-situ observations, which ultimately leads to bias in climate models and satellite retrievals (Trenberth and Fasullo, 2010; Bodas-Salcedo et al., 2014).

To address the gap, several studies based on in-situ measurements (Menon et al., 2015; McFarquhar et al., 2021) reported the presence of anthropogenic aerosols in the remote regions of SO. The presence of sea-salt and non-sea-salt aerosols acting as CCN was also explained

(Quinn et al., 2017; Fossum et al., 2018). Few reports from ISSO were concentric on the spatial and temporal variability of aerosols and associated radiative forcing (Menon et al., 2015; Hulswar et al., 2020; Srivastava et al., 2021). However, there was no attempt to understand the thermodynamic state of MABL and its boundary layer features (such as inversions and clouds) attributing to its role in regulating the distribution of aerosols, clear sky direct shortwave radiative forcing, and atmospheric heating rate vital for Earth's radiative balance. Hence, study described in this chapter presents the first-time understanding of the boundary layer features in conjugation with the dynamics of aerosols over the ISSO fronts lying between 24°S-68°S along 57°E-79°E. Focusing on this aspect, this chapter is to address the following questions,

1. How is the spatial heterogeneity of surface and vertical meteorological conditions across the ISSO fronts?

2. What is the role played by the thermodynamic structure of low-level atmosphere (up to 5,000 m altitude), characteristic nature of clouds and inversions in regulating the distribution of aerosols over the ISSO fronts?

3. How is the spatial variability of aerosols i.e., black carbon aerosols (*BC*) and composite aerosols (using aerosol optical depth (*AOD*)), and the resultant aerosol induced clear sky direct aerosol radiative forcing (DARF) and rate of atmospheric heating (HR) across the ISSO fronts.

5.2 Data and method

5.2.1. Data

In this chapter, a combination of in-situ, re-analyzed, modelled, and satellite datasets obtained between 24°S-68°S along 57°E-79°E covering the frontals regions of ISSO during the onward cruise track of the Xth Southern Ocean Expedition (SOE-X), from 8th December 2017 to 05th January 2018 have been utilized (Figure 5.1). The details on the classification of different frontal regions of the ISSO identified as STF, SAF, PF, SACCF, SB, and CA are provided in

Table 2.5 of chapter 2 (Belkin and Gordon, 1996; Anilkumar et al., 2015). The in-situ measurements accessed in this chapter includes surface meteorological measurements, surface-based mass concentration of *BC* aerosols, and columnar *AOD* while the vertical thermodynamic structure of the atmospheric column was examined using atmospheric soundings measurements. The re-analysis data were used to understand synoptic near-surface temperature gradient (i.e., air-sea temperature gradient, $dT=SST-T_{air}$) and wind circulation patterns. The modelled data comprised of columnar *AOD* using Optical Properties of Aerosols and Clouds (OPAC) model, whereas satellite data was used for examining the vertical spread of aerosols and cloud phases derived from CALIPSO retrievals.

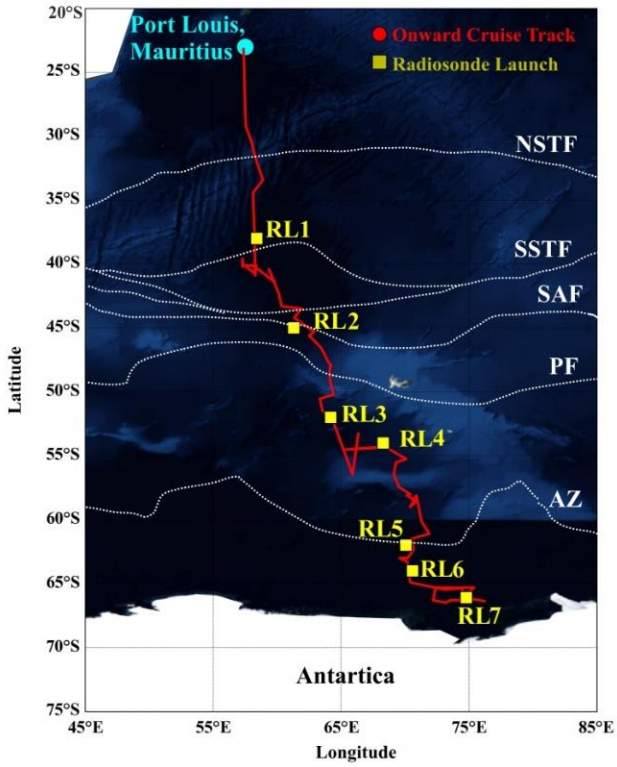

Figure 5.1 The cruise track (in red) is shown along with atmospheric measurements, performed during the forward track of the Xth Indian Expedition to the Indian Ocean sector of Southern Ocean (SOE-X) flagged off from Port Louis, Mauritius, 20 °S to Prydz Bay region of Antarctica, 69°S. Locations of seven radiosondes considered in each ISSO region are marked (yellow markers). Demarcation of the approximate location of oceanic fronts (white dotted

lines) was adopted from Belkin and Gordon (1996) and Anilkumar et al. (2015) (namely, NSTF and SSTF - Northern and Southern Sub-Tropical Fronts; SAF - Sub-Antarctic Front; PF - Polar Front; and AZ -Antarctic Zone).

5.2.1.1. Surface meteorology

The in-situ surface meteorological parameters utilized for this study were observations of air temperature (T_{air}), relative humidity (*RH*), mean sea level pressure (*MSLP*), wind speed (*WS*), and wind direction (*WD*). An automatic weather station (WeatherPak®-2000 v3) equipped with GPS provided the true *WS* and *WD* at ≈10 m above mean-sea-level height. The measurements stored at every 1-minute average throughout the onward track of the cruise were used. In addition, a standard bucket thermometer was used at 6 hours intervals to measure sea-surface temperature (*SST*). More details on the instrumentation related to automatic weather station and bucket thermometer have been provided in Table 2.6 of chapter 2.

5.2.1.2. *B*C aerosols

The in-situ measurements of *BC* mass concentrations were carried out using an automated self-contained Aethalometer (AE-42) manufactured by M/s Magee Scientific (Hansen et al., 1984). The instrument was operating at seven different wavelengths i.e., 370, 470, 520, 590, 660, 880, and 950 nm (refer section 2.3.2.3 for instrumentation). During all the cruises, the ambient air particles were aspirated from an inlet through a heated sample line fixed at the height of nearly 12 m above ocean level. Data was collected at every 5-minute intervals at a flow rate of 5 liters per minute. The *BC* mass concentrations (in ng m^{-3}) were estimated from the absorbance estimates recorded at 880 nm using the factory-set calibration coefficients.

5.2.1.3. Aerosol Optical Depth (*AOD*)

The *AOD* measurements were performed using a MICROTOPS-II Sunphotometer (Solar Light Co., USA) operating at five wavelengths, i.e., 380, 440, 500, 675, and 870 nm following (Morys et al., 2001)). Technical details of this instrument are provided in section 2.3.2.4 of

chapter 2 of the thesis. The *AOD* measurements carried out along the forward cruise track of SOE-X campaign during clear sky conditions were only used for the study.

5.2.1.4. Atmospheric soundings

For the representation of the vertical thermodynamic structure of low-level atmosphere above ISSO fronts, a total of 7 sounding profiles generated during the onward cruise period of SOE-X campaign have been used. The details of soundings considered in this study are provided in Table 5.1. These atmospheric soundings were *Pisharoty* type developed by Vikram Sarabhai Space Centre of the Indian Space Research Organization. Details on *Pisharoty* soundings are provided in section 2.3.2.2 of chapter 2 and can also be accessed in Divya et al. (2014). The vertical profiles of air temperature (*T*), atmospheric pressure (*P*), *RH*, *WS*, and *WD* collected at 1 Hz from the surface (≈12 m above the sea surface) have been utilized for this study.

5.2.1.5. Synoptic winds and surface temperature gradient (*dT*)

ERA5 (Hersbach et al., 2019; Hersbach et al., 2020), a fifth-generation atmospheric reanalysis data product developed by ECMWF (European Centre for Medium-Range Weather Forecasts) has been used in this study. A comparison made between in-situ measured and ERA5-derived measurements of meteorological parameters, i.e., *SST*, T_{air}, and *WS* obtained at 7 sounding locations showed a correlation for *SST* ($r = 0.982$), T_{air} ($r = 0.980$), *dT* ($r = 0.977$), and moderate correlation for *WS* ($r = 0.657$). Hence, in the present study ERA-5 derived estimates were used to calculate hourly averaged winds (10 m *u*- and 10 m *v*- component), 2 m T_{air}, and *SST* at a resolution of 0.25° × 0.25°. Subsequently, *dT* for each frontal region was estimated to depict synoptic background in the vicinity of each sounding location.

5.2.1.6. Vertical distribution of aerosols

Based on the in-situ atmospheric sounding locations, the CALIOP orbit track closest to the coordinates of the radiosonde measurements were acquired. The locations marked as pointers

in CALIPSO retrievals lie within 0.5°-1° with respect to the in-situ atmospheric-sounding location. The resolution was comparable to the standard resolution used in climate and regional models (Christian et al., 2019). From these satellite retrievals, clouds and aerosol properties are evaluated and identified after the calibration and range corrections incorporated into the signal return measured at 532 nm (Winker et al., 2009). In this study, CALIOP Level 2 Version 4.10x has been used to portray the distribution of aerosol types and cloud phases over ISSO frontal regions.

5.2.2. Methods of analysis

5.2.2.1. Air mass history

For this study, in order to discern the likely source of aerosols, air mass back-trajectories up to 120 hours have been modelled using HYSPLIT model version 4, available with NOAA-ARL (Draxler and Rolph, 2003). The model uses NCEP Global Data Assimilation System (GDAS) meteorological data at different altitudes and for this study, back-trajectories of air mass arriving at different altitudes at respective sounding locations were computed. For more details on HYSPLIT model refer to section 2.3.4.1 of chapter 2.

5.2.2.2. Estimation of thermodynamic variables

The radiosonde based thermodynamic parameters used in this study comprised of dew point temperature (T_d), virtual potential temperature (θ_v), equivalent potential temperature (θ_e), and water vapor mixing ratio (r). The estimation of these parameters was done after introducing appropriate corrections to the mean profiles of *T, RH, P, WS,* and *WD* of raw sounding data. The corrections employed to the raw sounding profiles and the equations used for the estimation of these variables are provided in section 4.2.2 of chapter 4 of this thesis.

5.2.2.3. Clear sky Direct Shortwave Aerosol Radiative Forcing (*DARF*)

The aerosols present in the atmosphere alter the incoming solar radiation by either direct or indirect interactions, thus accounting for direct or indirect aerosol-induced radiative forcing.

Direct aerosol radiative forcing (*DARF*) involves the scattering and absorption of solar radiation by atmospheric aerosols and is influenced by the type of aerosols and surface reflectance. Depending upon these properties, a negative or positive *DARF* is estimated at the surface (Vinoj et al., 2004; Ganguly et al., 2005; Li et al., 2010). However, the indirect *DARF* involves the modification of microphysical properties, amount, and the lifetime of clouds and hence, the variability in the incoming solar radiation (Parry et al., 2007, and the references therein). In view of this, in the present study, only clear sky *DARF* has been estimated.

For the estimation of clear sky *DARF*, estimates of aerosol optical properties such as *AOD*, single scattering albedo (*SSA*), and asymmetry parameter (*ASY*) were required. Direct measurements of these parameters (*SSA* and *ASY*) were not available. Hence, estimates of these parameters were simulated using the OPAC model. Details on the OPAC model has been provided in section 2.3.4.2 of chapter 2. These estimations were obtained by accessing the Sunphotometer-measured *AODs* only during clear sky conditions. The clear sky conditions imply that the sun was completely visible, and the atmosphere was cloud-free or the daytime intervals that were cloud-free. A minimum of five continuous observations were carried out every time the instrument was directed toward the sun. Further, the average *AOD* was calculated for locations at which at least four clear sky readings were available. Thus, in all the locations where the Sunphotometer-measured *AOD* values were available, the OPAC model was run to obtain the *AOD*, *SSA*, and *ASY* estimates for deriving clear sky *DARF*. In this study, of the total 7 examined frontal regions, Sunphotometer-measured *AOD*s were available at a few locations in five frontal regions (NSTF, PF1, PF2, SB, and CA), while *AOD* measurements could not be collected in regions of SAF and SACCF due to persistent cloud cover.

For obtaining a clear sky *DARF*, the inputs given to the OPAC model were five aerosol types, i.e., total water-soluble components, sea salt (accumulation mode), sea salt (coarse mode), sulphate, and *BC*, height profile, five standard Sunphotometer wavelengths, and *RH*

following Hess et al. (1998). Among these inputs, at first, the *BC* number concentrations were estimated from the Aethalometer measured *BC* mass concentrations. This was done in a way that in OPAC model, number density of *BC* aerosols was varied by keeping the number densities of water-soluble aerosols and of insoluble unchanged until iterations closely matched the measured value of *BC* mass concentration. Upon estimating the number concentrations of *BC*, iterations were then performed by keeping *BC* number concentrations fixed while the remaining four naturally occurring aerosol types were then iterated. These iterations were performed until the OPAC simulated *AOD* was corroborated closely (±0.05) with the Sunphotometer-measured *AOD*. The comparison between the Sunphotometer-measured *AOD* and OPAC simulated *AOD* represented a correlation, r = 0.981. Such a hybrid approach to estimate *SSA* and *ASY* for obtaining clear sky *DARF* has been reported over the Arabian Sea, Bay of Bengal (Vinoj et al., 2004; Ganguly et al., 2005), and over the Saharan dust (Li et al., 2010). Thus, OPAC simulated *SSA*, *ASY*, and *AOD* under clear sky conditions were given as inputs for *DARF* estimations performed using Santa Barbara DISORT Atmospheric Radiative Transfer Model (SBDART, Ricchiazzi et al., 1998). More details on the SBDART model are provided in section 2.3.4.3 of chapter 2. In addition to the aforementioned input, another input was surface reflectance which was derived from MODIS. The *DARF* was computed in the shortwave range of 0.25 to 4.0 µm. The *DARF* represents the net change in the incoming and outgoing irradiance with and without aerosols in the atmospheric column. To estimate net radiative forcing, two scenarios were considered at the top of the atmosphere (*TOA)* and the surface (*SFC),* (i) without aerosols representing clean air and (ii) with aerosols. The difference between the two scenarios gives the total radiative forcing (*ARF*) due to aerosols (Stamnes et al., 2000). Thus, the *ARF* is calculated using,

$$ARF = Flux\ (net)_{TOA/SFC\ with\ aerosols} - Flux\ (net)_{TOA/SFC\ without\ aerosols} \quad 5.1$$

Thus, the total atmospheric forcing was,

$$ARF_{ATM} = ARF_{TOA} - ARF_{SFC} \quad 5.2$$

5.2.2.4. Atmospheric Heating Rate (*HR*)

A measure of the total radiative effect induced due to the absorption by aerosols present in the atmosphere is quantified in terms of the rate of atmospheric radiative heating (K day^{-1}),

$$\frac{\partial T}{\partial t} = \frac{g}{c_p}\left[\frac{ARF_{ATM}}{\triangle P}\right] \times (hr/day) \times 3600\ (sec/hr) \quad 5.3$$

where, $\partial T/\partial t$ is the atmospheric heating rate, g is the acceleration due to gravity (9.8 m s^{-2}), c_p is the specific heat capacity of air at constant pressure (1006 J kg^{-1} K^{-1}), and *P* represents atmospheric pressure (hPa). $\triangle P$ is calculated as the difference in pressure between the surface and 10,000 m altitude, considering the maximum extent of the tropospheric air column.

5.3. Results

This section presents the meteorological conditions near the surface as well as in the vertical low-level atmosphere, the vertical thermodynamic structure of MABL, and the observations on aerosol obtained in the ISSO regions.

5.3.1. Synoptic meteorology

There was a distinct spatial variability in the meteorological conditions observed near the surface and at different altitudes in atmosphere over each frontal region (Figure 5.2, 5.3). It was primarily due to the sharp gradients in meteorological parameters caused by the oceanic frontal systems, thereby developing distinct features in the atmospheric column. The regions north of the PF (i.e., NSTF and SAF) showed a convectively driven atmosphere with higher θ_e (307 K <θ_e< 323 K) up to 5,000 m altitude. However, a sharp wind reversal in mid-altitude (≈1,800 m) accounted for separating low-level convectively mixed moist air mass (5.6 g kg^{-1} < *r* < 8.2 g kg^{-1}; 52% < *RH* < 78%) from dry air mass (1.8 g kg^{-1} < *r* < 3.3 g kg^{-1}; 12% < *RH* < 35%) at high altitudes. This reversal was caused by the easterly wind. In the PF regions, distinct meteorological conditions comprised of strong high-speed westerly winds (>28 m s^{-1}) that

advected highly saturated cold air mass with temperatures < 1^{o}C and *RH* > 94%, from surface to ≈5,000 m (Figure 5.2, 5.3). The advection accounted for the development of a low-pressure system with *MSLP*<973 hPa. In consequence, the occurrence of low-pressure cyclonic systems suppressed the strength of convective potential (lower values of 284 K< θ_e < 307 K) in the lower atmosphere of PF region (Figure 5.3). The SACCF region is located south of PF and forms at the boundaries of the Ferrell and Polar cells at ≈60°S. In SACCF, the weakening of strong polar westerly winds was observed due to the convergence of cold-dry air mass by south-easterly winds and relatively warm moist air mass by north-westerly winds. This convergence accounted for a lower *MSLP* (987 hPa) and intensified low-level cyclone formation. In consequence, high moisture content (1.3 g kg^{-1} < *r* < 4.3 g kg^{-1}), and highest *RH* (97%) were noticed throughout 5,000 m altitude (Figure 5.3). Further, at the extreme south of all frontal regions, the regions SB and CA showed significantly dry-colder air mass (lowest values of 0.4 g kg^{-1} < *r* < 2.3 g kg^{-1}) advected by weak easterly winds (*WS* < 6 m s^{-1}) from Antarctic continent. Low-level atmospheric conditions, however, had highly saturated air mass compared to the air column at mid and upper altitudes. The presence of drier air in mid and high altitudes can be attributed to prevailing katabatic winds near the coast of the Antarctic continent. Overall, the region was characterized by weak unstable conditions, as indicated by the lowest values of θ_e (282 K < θ_e < 294 K) in 5,000 m altitude.

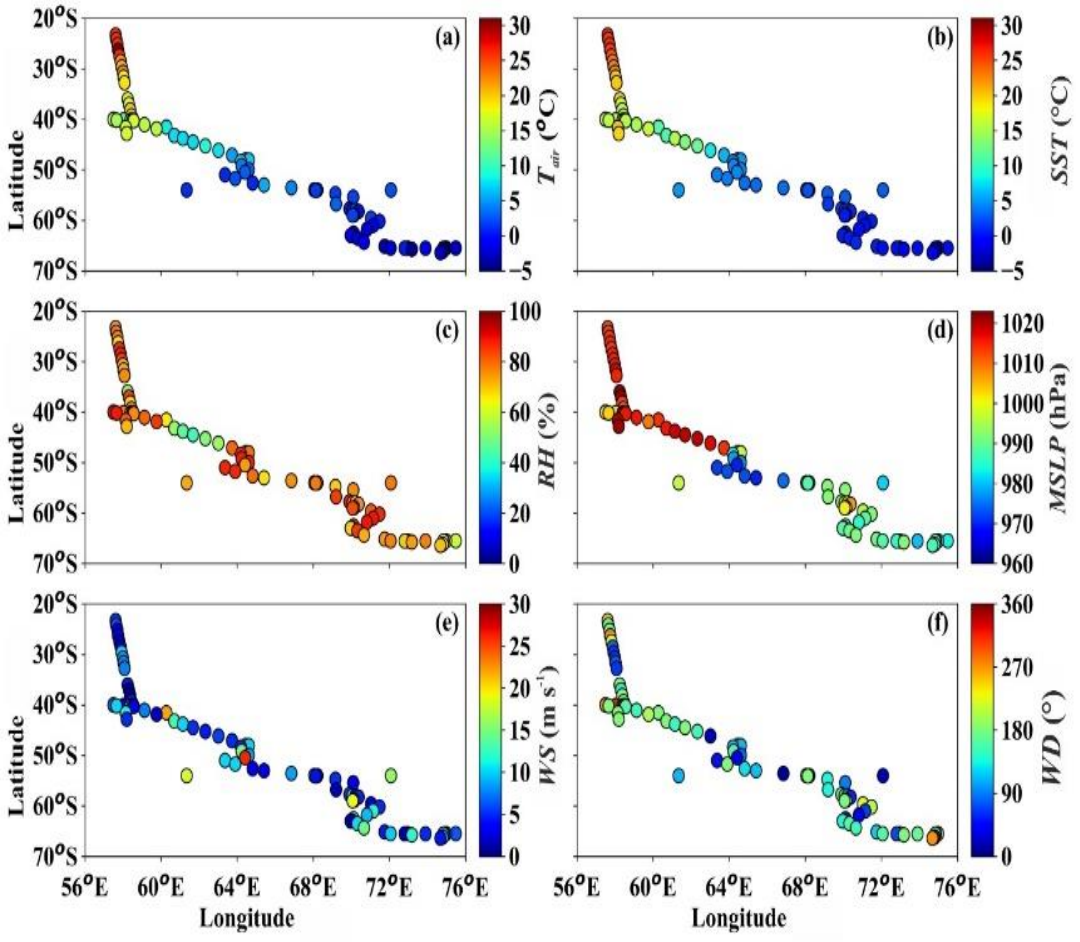

Figure 5.2 The measurements conducted along the forward cruise track of the Xth Indian Expedition to the Southern Ocean (SOE-X) from 35°S to 66°S along 56°E to 76°E. Along this cruise track, a 2D variation of measured meteorological parameters, (a) air temperature (T_{air}), (b) sea surface temperature (*SST*), (c) relative humidity (*RH*), (d) mean sea level pressure (*MSLP*), (e) wind speed (*WS*), and (f) wind direction (*WD*) are shown. Approximate locations of oceanic fronts are acquired from Belkin and Gordon (1996) and Anilkumar et al. (2015) (grey dotted lines).

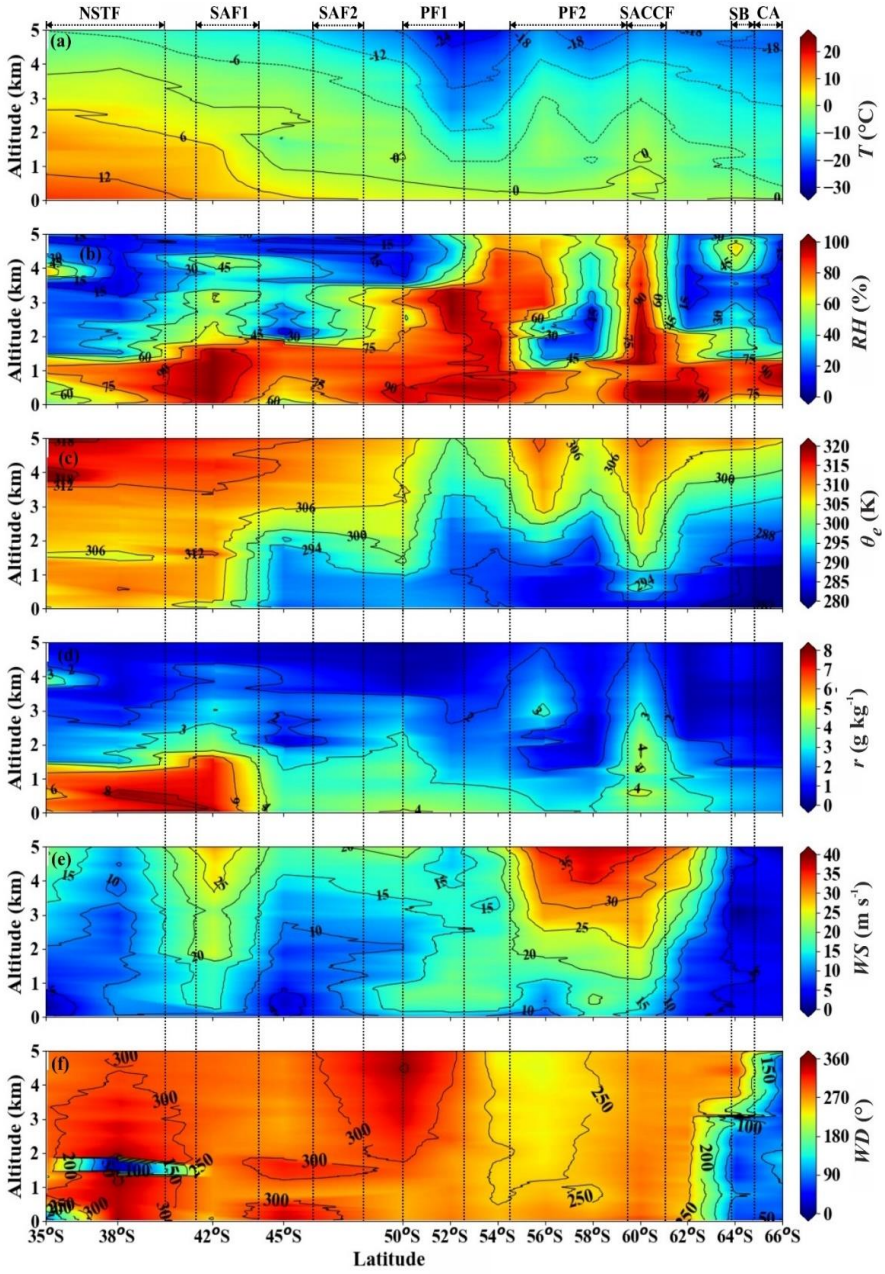

Figure 5.3 Contour plots of (a) atmospheric temperature (*T*), (b) relative humidity (*RH*), (c) equivalent potential temperature (θ_e), (d) mixing ratio (*r*), (e) wind speed (*WS*), and (f) wind direction (*WD*), representing vertical thermodynamic structure of the atmosphere from 0 - 5,000 m altitude over the latitudinal range from 35°S to 66°S during the forward track of Xth Southern Ocean Expedition (SOE-X) are shown. Approximate locations of oceanic fronts are acquired from Belkin and Gordon (1996) and Anilkumar et al. (2015) (grey dotted lines).

5.3.2. Observations on aerosols and MABL characteristics

Aerosol-boundary layer observations recorded in each frontal region is described in this section.

5.3.2.1. Over Sub-Tropical Front (NSTF)

Data from the radiosonde launched at 38.00°S, 58.40°E on 14th December 2017 at 01:00 UTC (06:30 LT) were used as a representative sounding in NSTF region (Figure 5.4a, b). This early morning (local time) sounding was associated with a weak positive near-surface air-sea temperature gradient (dT = 0.1℃; Figure 5.4c). Weak dT had a negligible effect in altering the stable state of nighttime MABL, which was evident with a gradual increase (decrease) in $\theta_e(r)$ with increasing altitude (Figure 5.4b). However, despite stable profiles of θ_e and r, three significant inversions, and with no cloud layers were noticed (Figure 5.4a, b). These observations were attributed to the subsidence associated with high *MSLP* (1013 hPa) as well as the advection of warmer air mass from its northern region with higher dT > 0.4℃. These conditions supported significant inversions near the surface (660 m) and at mid-altitudes (2,440 m), having gradients 0.27 K m^{-1} and 0.89 K m^{-1}, respectively (Figure 5.4b). Additionally, a weaker inversion (0.19 K m^{-1}) was observed at a higher altitude (4,660 m) (Figure 5.4b). Out of these three significant inversions, the height of the mixed layer (≈2,440 m) was identified as the height where the maximum gradient was observed in θ_v and r profiles (Ramana et al., 2004b) . Under these thermodynamical conditions, the vertical aerosol features derived from CALIPSO revealed the presence of naturally produced marine aerosols, such as sea salt, dimethyl sulfate (DMS), and other organic aerosols (O'Dowd et al., 1997). Noticeably, the higher loading of marine aerosols was confined below 1,500 m altitude (Figure 5.4d). Additionally, in-situ measurements of *BC* aerosols at this location recorded were higher *BC* estimates (46 ± 21 ng m^{-3}). Such an accumulation of these aerosols' species is attributed to the unique meteorology specific to this region mainly driven by high-pressure formations. As a

result of this, strong subsidence capped by significant atmospheric inversions were observed, and this played a crucial role in restricting the further vertical dispersion of these aerosols and increasing their concentrations in few meter above the oceanic surface. Moreover, the prevalence of anthropogenic aerosols (elevated smoke) at higher altitudes (≈3,700 m) was also noticed (Figure 5.4d), which is likely to be remotely originated and advected from the South African continent (3,500 m; Figure 5.4d, f).

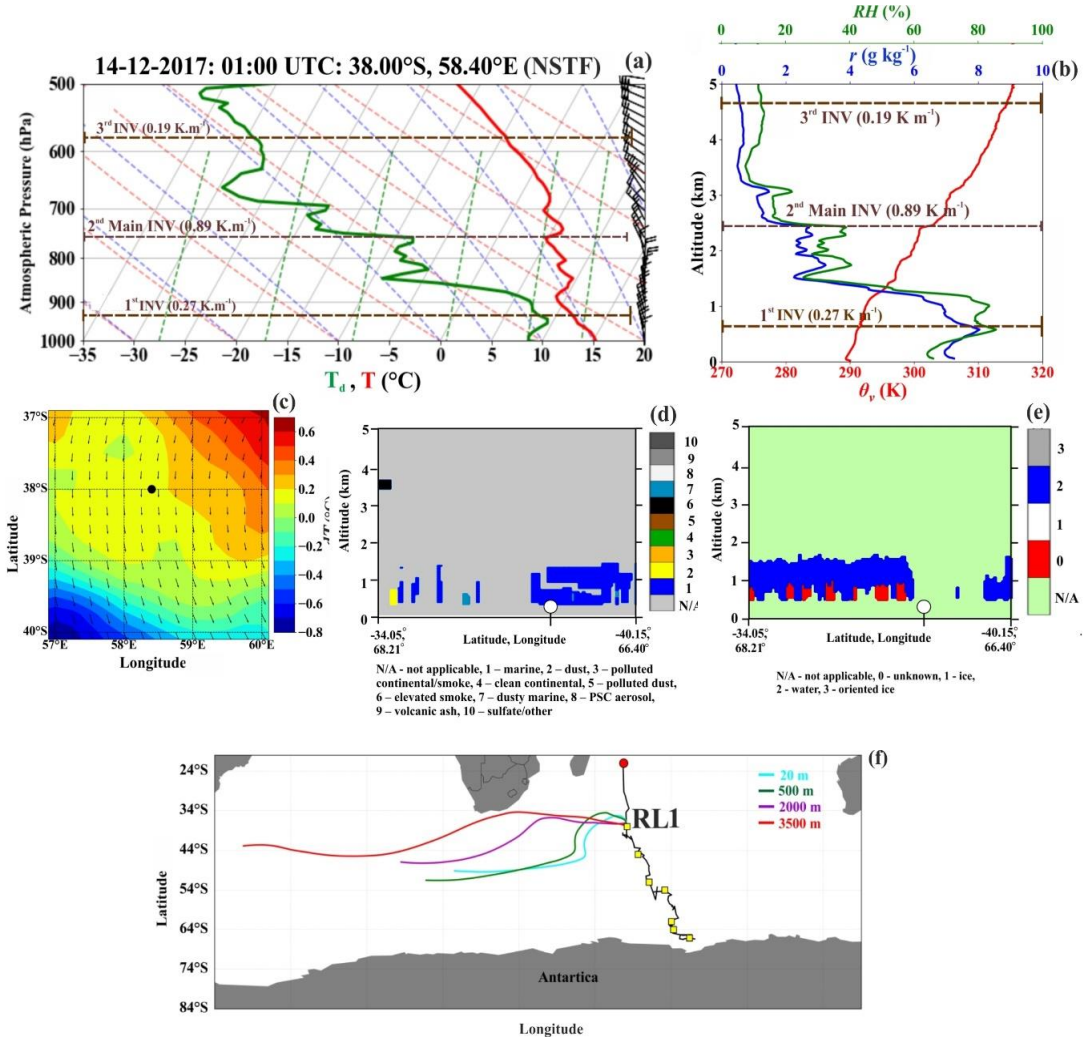

Figure 5.4 The figure depicts the region lying to the north of the Polar Front (PF), i.e., region of the Northern Sub-Tropical Front (NSTF). Panel (a) a Skew-T diagram plotted for the sounding launched in this region. For the respective sounding, profile of air temperature (*T* in red) and dew point temperature (T_d in green) from surface up to 5,000 m altitude have been

shown. Wind barbs are overlaid (in black on the right side of the panel) to depict the magnitude and direction of winds. Panel (b) shows a 5,000 m vertical profile of virtual potential temperature (θ_v in red), mixing ratio (r in blue), and relative humidity (RH in green) for radiosonde launched at 38.00°S, 58.40°E on 14-12-2017 at 01:00 UTC in the NSTF region. The estimated altitudes of inversions (brown) (inversion strength in K m^{-1}) and cloud layers (blue) (cloud thickness in m) are marked. Panel (c) represents synoptic near-surface air-sea temperature gradient (dT in ℃) and wind circulation pattern in the vicinity of this sounding obtained using ECMWF-ERA5 reanalysis dataset, where *SST* values at the surface, T_{air} at 2 m, wind fields (10 m *u*- and *v*- component) are considered. The launch location is marked with a black circular dot. The respective color bar is shown. Panel (d) represents CALIPSO standard daytime 0 – 5,000 m vertical products of aerosol sub-types derived for 14-12-2017, 20:36 to 20:50 UTC during its orbit between 34.05°S, 68.21°E to 40.15°S, 66.40°E. Panel (e) represents CALIPSO standard daytime profile of 0 – 5,000 m vertical products of ice/water cloud phase derived for 14-12-2017, 20:36 to 20:50 UTC profile while it is orbiting between 34.05°S, 68.21°E to 40.15°S, 66.40°E. Panel (f) represents NOAA HYSPLIT model calculated air mass back trajectories for preceding 120 hours at different heights (selected based on CALIPSO-derived aerosol loading) for sounding (RL1) launched in NSTF region.

5.3.2.2. Over Sub-Antarctic Front (SAF1)

Data from radiosonde launched at 45.00°S, 61.30°E on 19th December 2017 at 06:00 UTC (11:30 LT) was used as a representative sounding in SAF1 region (Figure 5.5a, b). There was a formation of a warm front evident with the air-sea temperature gradient (dT = 5.5℃ at sounding location and >5.5℃ around this location; red shaded region; Figure 5.5c). The formation of this warm front was caused due to the active oceanic eddies induced by the strong ARC (Lutjeharms and Van Ballegooyen, 1988). An associated effect of this current at the air-sea interface strongly shaped the vertical thermodynamic structure of MABL in this region

(Figure 5.5a, b). The high *dT* and *MSLP* (1019 hPa) enhanced atmospheric mixing at lower altitudes. The near-uniform variation in θ_v and *r* profiles indicated of a well-developed mixed layer up to 1,860 m capped by a strong inversion of strength 3.17 K m^{-1} (Figure 5.5b).

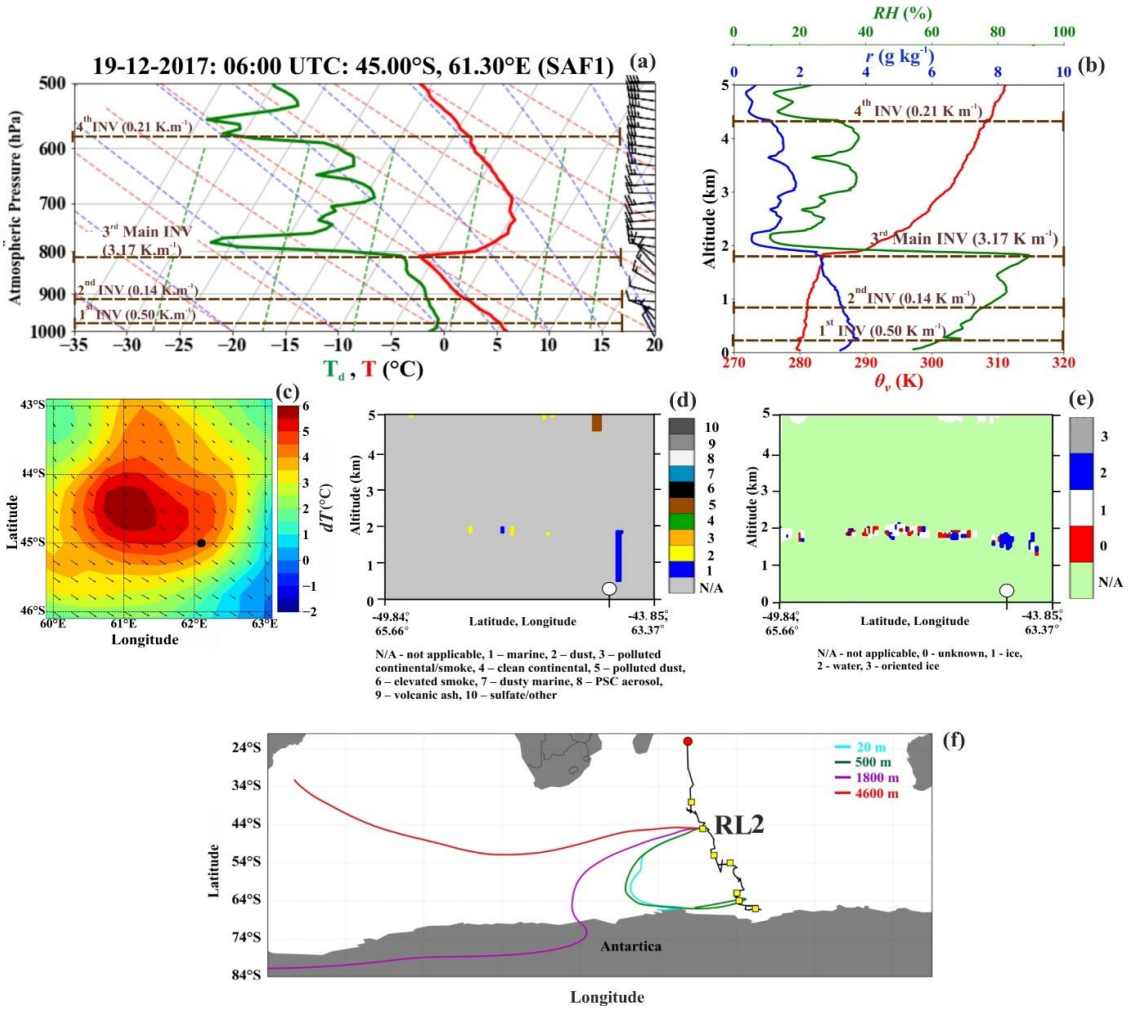

Figure 5.5 The figure depicts the region lying to the north of the Polar Front (PF), i.e., region of the Northern Sub-Antarctic Front (SAF1). Panel (a) represents the same as Figure 5.4 (a) but for sounding launched in SAF1 region. Panel (b) represents same as Figure 5.4 (b) but for sounding launched at 45.00°S, 61.30°E on 19-12-2017 at 06:00 UTC in SAF1 region. Panel (c) represents same as Figure 5.4 (c) but for sounding launched in SAF1 region. Panel (d) represents CALIPSO standard daytime 0 – 5,000 m vertical products of aerosol sub-types derived for 19-12-2017, 09:56 to 10:09 UTC during its orbit between 49.84°S, 65.66°E to 43.85°S, 63.37°E. Panel (e) represents CALIPSO standard daytime profile of 0 – 5,000 m

vertical products of ice/water cloud phase derived for 19-12-2017, 09:56 to 10:09 UTC while it is orbiting between 49.84°S, 65.66°E to 43.85°S, 63.37°E. Panel (f) represents same as Figure 5.4 (f) but for sounding (RL2) launched in SAF1 region.

These unstable conditions supported the formation of four significant inversions and the absence of cloud layers (Table 5.1). The aerosols were primarily of marine origin at lower altitudes (<2,000 m), while polluted dust was noticed at higher altitudes (>4,500 m) (Figure 5.5d). From air mass back-trajectories, the marine aerosols at lower altitudes were locally generated or long-range advected from open SO region at altitudes 20 m and 500 m, respectively (Figure 5.5f). In comparison, the likelihood of polluted dust at high altitudes (4,600 m) was attributed to long-range transport from the South American continent (Figure 5.5f). Interestingly, aerosol loading was weak in the region due to the unstable atmospheric conditions that mixed and dispersed aerosols, thereby limiting accumulation of aerosols in within the well-mixed boundary layer. In contrast, in-situ measurements on near surface mass concentration of *BC* aerosols showed relatively higher estimates (54 ± 6 ng m^{-3}) in this region if compared to near surface *BC* mass concentration (46 ± 21 ng m^{-3}) observed in NSTF region. Such an increase of near surface concentration of *BC* aerosols in this case is likely attributed to relatively reduced dispersion of surface-based *BC* aerosols due to low-speed winds close to the oceanic surface in SAF1 (3.06 m s^{-1}) case compared to higher wind magnitudes (10.19 m s^{-1}) in case for NSTF region. Also, can be due to the formation of system of multiple oceanic and atmospheric fronts.

5.3.2.3. Over Polar Front (PF1)

Data from radiosonde launched at 52.00°S, 64.20°E on 22nd December 2017 at 22:00 UTC (03:30 LT) represents the atmospheric conditions over PF1 (Figure 5.6a, b). The synoptic near-surface air-sea temperature gradient increased from -1.0 to 1.5℃, while at the sounding location, *dT* equals to 0.9℃ was observed (Figure 5.6c). In this region, the combined effect of

weak *dT*, the lowest recorded *MSLP* (973 hPa), and the advection of colder air masses by westerly winds (> 19.16 m s^{-1}) caused significant stability as well as supported the formation of an intense low-pressure cyclonic system. The stable state of the lower atmosphere is evident with a gradual increasing (decreasing) tendency of θ_v (r) profiles with increasing altitudes up to 5,000 m (Figure 5.6b). In these atmospheric conditions, the presence of low-level multi-layer clouds (decreased gradient of T and T_d, RH > 90%) were observed (Figure 5.6a, b). The lowest cloud layer was as low as 340 m (cloud base) with a thickness of 320 m, while the second thicker cloud layer was present at 2,200 m with a thickness of 1,160 m and extending up to 3,360 m (Figure 5.6a, b). The temperature at the top of the first cloud layer was -0.4°C

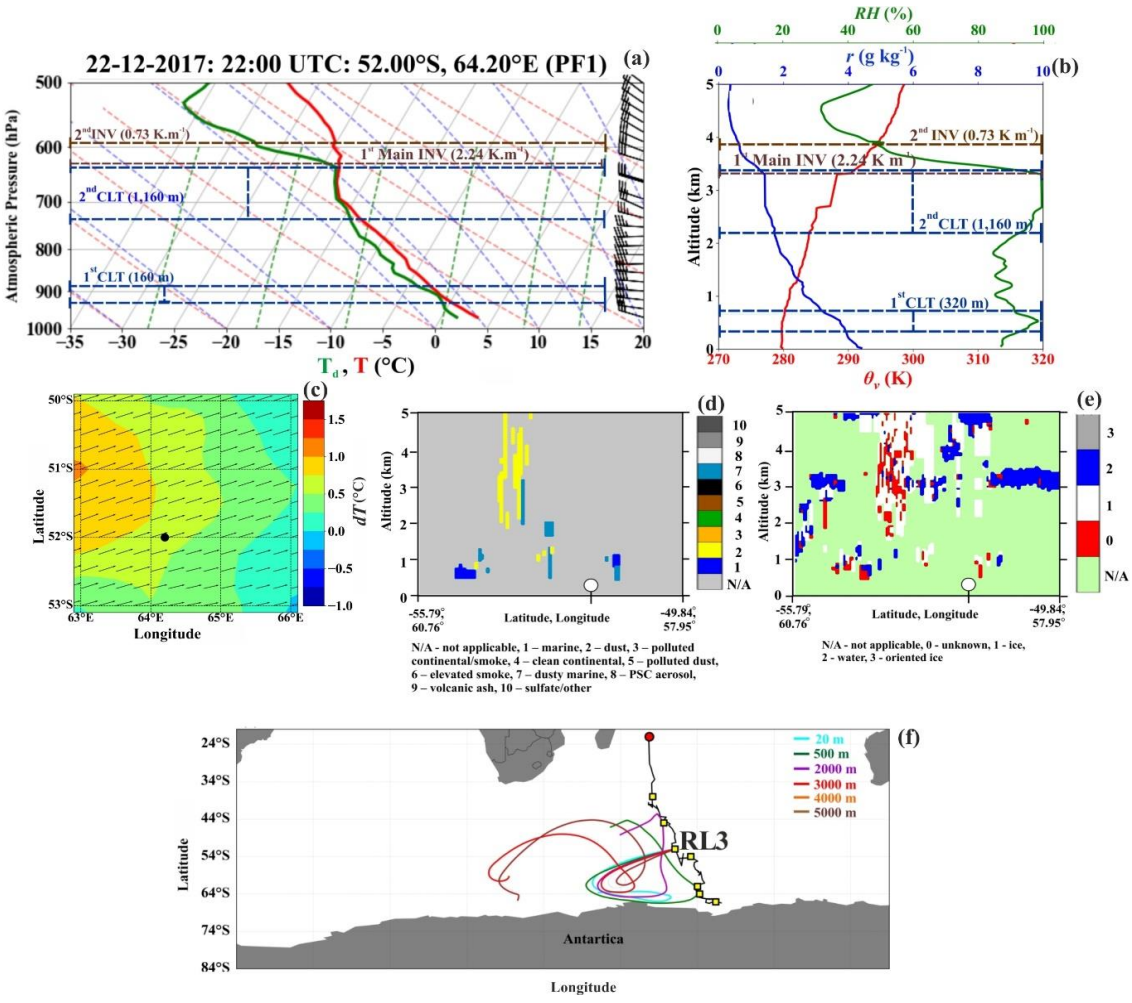

Figure 5.6 The figure depicts the region lying in the Polar Front (PF), i.e., region of the Northern Polar Front (PF1). Panel (a) represents the same as Figure 5.4 (a) but for sounding

launched in PF1 region. Panel (b) represents same as Figure 5.4 (b) but for sounding launched at 52.00°S, 64.20°E on 22-12-2017 at 22:00 UTC in the PF1 region. Panel (c) represents same as Figure 5.4 (c) but for sounding launched in PF1 region. Panel (d) represents CALIPSO standard daytime 0 – 5,000 m vertical products of aerosol sub-types derived for 22-12-2017, 10:26 to 10:40 UTC during its orbit between 55.79°S, 60.76°E to 49.84°S, 57.95°E. Panel (e) represents CALIPSO standard daytime profile of 0 – 5,000 m vertical products of ice/water cloud phase derived for 22-12-2017, 10:26 to 10:40 UTC while it is orbiting between 55.79°S, 60.76°E to 49.84°S, 57.95°E. Panel (f) represents same as Figure 5.4 (f) but for sounding (RL3) launched in PF1 region.

which indicated the presence of highly saturated supercooled water (SLW). However, at the base and top of the second cloud layer, the temperature dropped abruptly from -8.2℃ to -9.7℃, indicating that condensation may have resulted in the formation of mixed-phased SLW or ice-phased clouds (Figure 5.6a). SLW/IWC clouds in this region were also noticed in the CALIPSO water phase feature (Figure 5.6e). The significant stability in the low-level atmosphere accounted for multiple stronger inversions at higher altitudes (Figure 5.6b). In this sounding, the top of the second cloud layer was capped by the first inversion of strength 2.24 K m^{-1} at 3,300 m, while a weaker second inversion of strength 0.73 K m^{-1} was observed at 3,880 m. Overall, the presence of thick clouds prevented identifying the top of the mixed layer height. Significant loading of dust and dusty marine aerosols prevailed within intermediate and higher altitudes (1,000 m to 5,000 m; Figure 5.6d). At lower altitudes (< 2,000 m), marine origin aerosols were observed. The back-trajectories showed the clockwise circulation of air mass associated with an intensified cyclonic system (Figure 5.6f).

5.3.2.4. Over Polar Front (PF2)

Data from radiosonde launched at 54.00°S, 68.30°E on 23rd December 2017 at 06:00 UTC (11:30 LT) was used as a representative sounding for PF2 (Figure 5.7a, b). The atmospheric

conditions over PF2 were like PF1 and recorded the lowest *MSLP* in this study (980 hPa), lowest freezing temperatures (-1℃), and the highest percentage of *RH* (97.71%). Also, strong winds (>17.98 m s^{-1}) induced by the polar jet stream were noticed up to 5000 m altitude that constantly advected colder and highly saturated air masses from the west direction (245.73^{o}; Figure 5.7a, c). The only distinction observed in the PF2 region was the strong barrier generated by winds at mid-latitudes (at 500 m to 1,600 m altitude), which separated low-level low-pressure cyclonic precipitation core from the high-level updraft storms. The cyclonic precipitation core was evident by the formation of the cold front region exhibiting negative *dT* ranging from -0.15℃ to 0.15℃ (blue shaded area in Figure 5.7c). The radiosonde

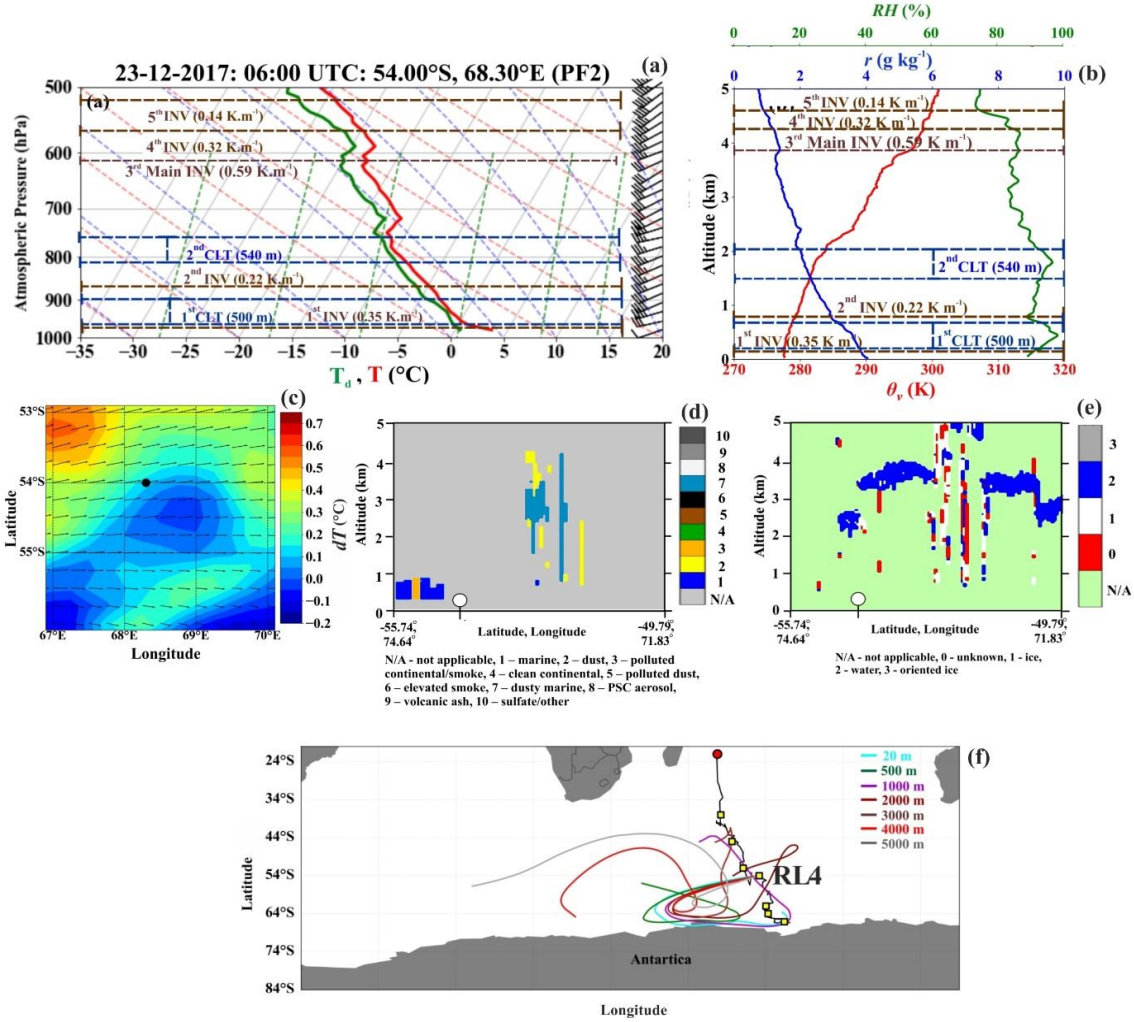

Figure 5.7 The figure depicts the region lying in the Polar Front (PF), i.e., region of the Southern Polar Front (PF2). Panel (a) represents the same as Figure 5.4 (a) but for sounding

launched in PF2 region. Panel (b) represents same as Figure 5.4 (b) but for sounding launched at 54.00°S, 68.30°E on 23-12-2017 at 06:00 UTC in PF2 region. Panel (c) represents the same as Figure 5.4 (c) but for sounding launched in PF2 region. Panel (d) represents CALIPSO standard daytime 0 – 5,000 m vertical products of aerosol sub-types derived for 23-12-2017, 09:31 to 09:44 UTC during its orbit between 55.74°S, 74.64°E to 49.79°S, 71.83°E. Panel (e) represents CALIPSO standard daytime profile of 0 – 5,000 m vertical products of ice/water cloud phase derived for 23-12-2017, 09:31 to 09:44 UTC while it is orbiting between 55.74°S, 74.64°E to 49.79°S, 71.83°E. Panel (f) represents same as Figure 5.4 (f) but for sounding (RL4) launched in PF2 region.

the lowest dT (-0.2℃), and its coupling with prevailing atmospheric parameters accounted for the stable conditions. This was evident with the gradually increasing (decreasing) tendency of θ_v (r) throughout 5,000 m altitude (Figure 5.7b). In addition, the condensation also accounted for the saturated first cloud layer from just a few meters above the surface (40 m), having a thickness of 520 m (Figure 5.7a, b). In comparison, the second cloud layer was noticed up to 2,020 m having a thickness of 540 m. These low-level clouds were likely in the form of SLW or IWC, with temperatures ranging between -5℃ and -12℃ (Figure 5.7a, b). The presence of SLW/ICE clouds was also observed in the CALIPSO water phase feature (Figure 5.7e). Of the total, five significant inversions were observed, i.e., three high altitude inversions at 3,780 m, 4,260 m, and 4,600 m of strength 0.59 K m^{-1}, 0.32 K $m^{-1,}$ and 0.14 K m^{-1}, respectively. Another two low-altitude inversions at 160 m and 800 m of strength 0.35 K m^{-1} and 0.22 K m^{-1}, respectively, were also observed at the base and top of the first cloud layer (Figure 5.7b). In PF2, identification of mixed layer height was not possible due to higher cloud coverage at low altitudes. Akin to PF1, the vertical aerosol features in PF2 also showed higher loading of dust and dusty marine-type aerosols within 5,000 m altitude (Figure 5.7d). In addition, polluted

continental/smoke and marine aerosols were observed in lower altitudes (< 1,000 m). A cyclonic circulation was evident in the back-trajectory analysis (Figure 5.7f).

5.3.2.5 Over Southern Antarctic Circumpolar Current Front (SACCF)

Data from radiosonde launched at 62.00°S, 70.07°E on 27th December 2017 at 03:00 UTC (08:30 LT) is used to represents the conditions over SACCF (Figure 5.8a, b). The region lies in the trough of ACC and is characterized by the formation of mesoscale polar cyclonic systems due to the strong convergence of cold-dry air mass by southeast winds and relatively warm moist air mass by northwest winds. It accounts for the convergence that weakens the wind (5.01 m s^{-1}). The winds continuously advect colder and drier polar air masses in the region (Figure 5.8a). Thereby, it supports the formation of the cold front as observed from dT (blue-shaded region; Figure 5.8c). The radiosonde was launched in the cold front during the early morning time (local), and a weak dT (0.1℃), low *MSLP* (987 hPa), and high *RH* (95.06%) were recorded (Table 5.1). The gradual increase (decrease) in $\theta_v(r)$ accounted for higher stability of the atmospheric column (Figure 5.8b). It supported an intense cyclonic system that caused significant low-level precipitation resulting in low-level multi-layered clouds (Figure 5.8b). The base of the first cloud layer was observed to be as low as 40 m with a thickness of 520 m, while the second cloud layer was only a few meters above the first cloud layer extending from 860 m to 920 m with thickness 60 m (Figure 5.8a, b). The low-level cloud formation was due to the mesoscale convergence. At mid and higher altitudes above 920 m, the weakening of convergence updrafts caused cloud-free conditions. The strong winds at high altitudes also resulted in multiple inversions (Figure 5.8b). The first significant inversion was observed at 1,100 m with a strength of 1.78 K m^{-1}, which capped the top of the second cloud layer (Figure 5.8b). This inversion marked the top of the mixed layer (1,100 m), above which the presence of dry tropospheric air mass (the larger decreasing tendency of r and *RH*; Figure 5.8b) prevailed. There was a decrease in aerosol species (notably dust aerosols) within a 5,000 m

atmosphere compared to the aerosol loading observed in PF (Figure 5.8d). However, in lower altitudes (< 1500 m), aerosols of marine origin, i.e., sea salt, non-sea salt aerosols, such as dimethyl sulfate (DMS), and other organic aerosols, were observed. Additionally, some dust aerosols were also noticed at higher altitudes (4,500 m to 5,000 m).

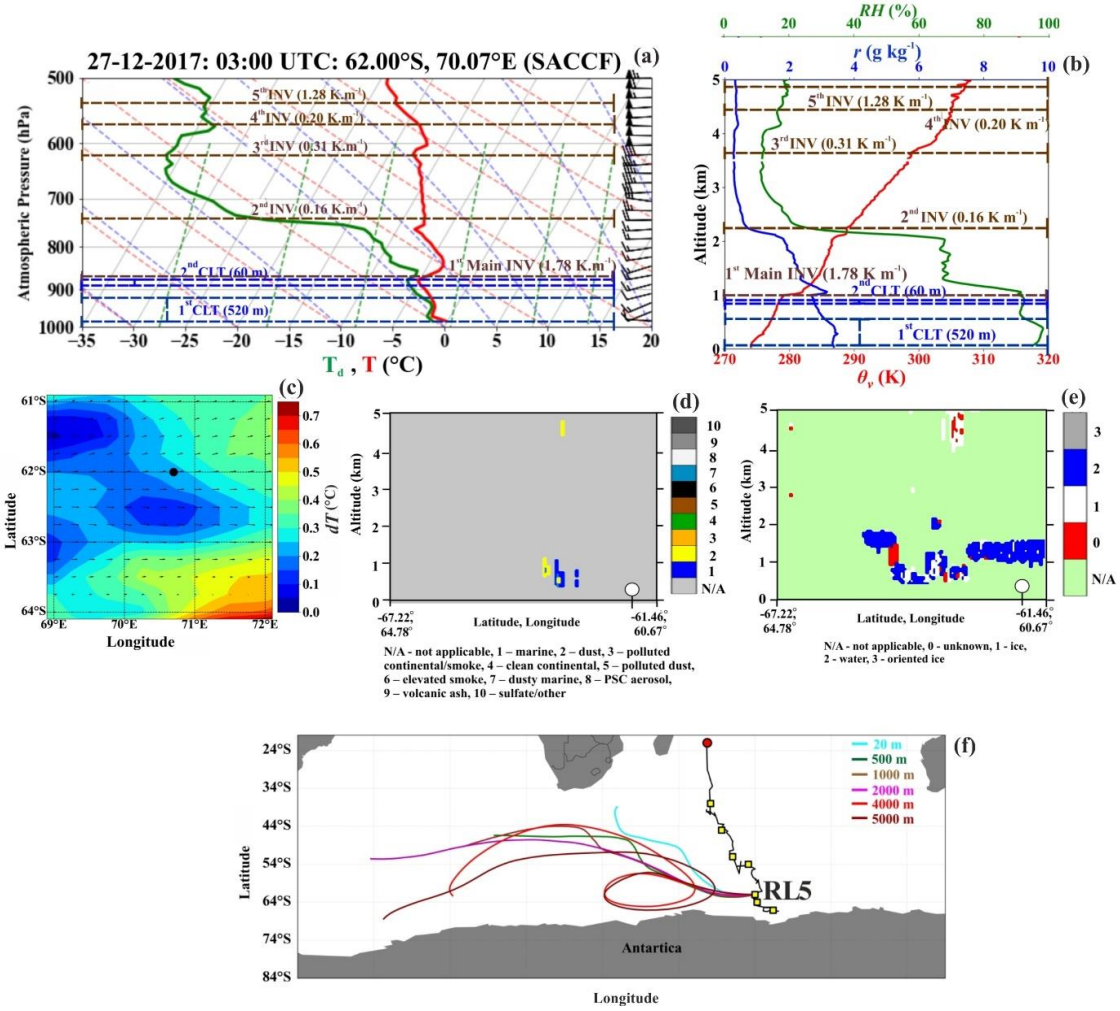

Figure 5.8 The figure depicts the region lying in the south of the Polar Front (PF), i.e., region of Southern Antarctic Circumpolar Current Front (SACCF). Panel (a) represents the same as Figure 5.4 (a) but for sounding launched in SACCF region. Panel (b) represents same as Figure 5.4 (b) but for sounding launched at 62.00°S, 70.07°E on 27-12-2017 at 03:00 UTC in SACCF region. Panel (c) represents the same as Figure 5.4 (c) but for sounding launched in SACCF region. Panel (d) represents CALIPSO standard daytime 0 – 5,000 m vertical products of aerosol sub-types derived for 27-12-2017, 10:45 to 10:59 UTC while it is orbiting between

67.22°S, 64.78°E to 61.46°S, 60.67°E. Panel (e) represents CALIPSO standard daytime profile of 0 – 5,000 m vertical products of ice/water cloud phase derived for 27-12-2017, 10:45 to 10:59 UTC while it is orbiting between 67.22°S, 64.78°E to 61.46°S, 60.67°E. Panel (f) represents same as Figure 5.4 (f) but for sounding (RL5) launched in SACCF region.

5.3.2.6. Over Southern Boundary of ACC (SB)

Data from radiosonde launched at 64.40°S, 70.60°E on 28th December 2017 at 06:00 UTC (11:30 LT) represents the SB region (Figure 5.9a, b). The atmospheric conditions were controlled by the potential warming of Antarctic waters regulated by two sub-polar gyres (Weddell gyre to its west and Prydz Bay gyre to its east). This induced higher *dT* (2.0℃) and resulted in a weak warmer frontal region (orange-yellow shaded region in Figure 5.9c). It enhanced the surface air-sea temperature gradient accounted for unstable MABL conditions. The destabilization of MABL resulted in a higher atmospheric mixing leading to a well-developed shallow mixed layer capped by a single inversion observed at 1,220 m of strength 1.57 K m^{-1} (Figure 5.9b). Above this inversion, drier air mass with lower values of *RH* and *r* (also a more significant difference in *T* and T_d; Figure 5.9a, b) prevailed. The absence of cloud layers was observed over SB (Figure 5.9b). Based on the vertical profile of aerosols, a natural atmosphere, primarily composed of marine aerosols prevails; however, a small amount of dusty marine aerosol was also noticed at lower altitudes below 1,500 m (Figure 5.9d). The major vertical spread of the aerosols was confined below 1,100 m where strong inversion may be a restrictive factor (Figure 5.9b, d). In this region, clean maritime air mass prevailed at mid and higher altitudes (>1,500 m to 5,000 m; Figure 5.9d, f).

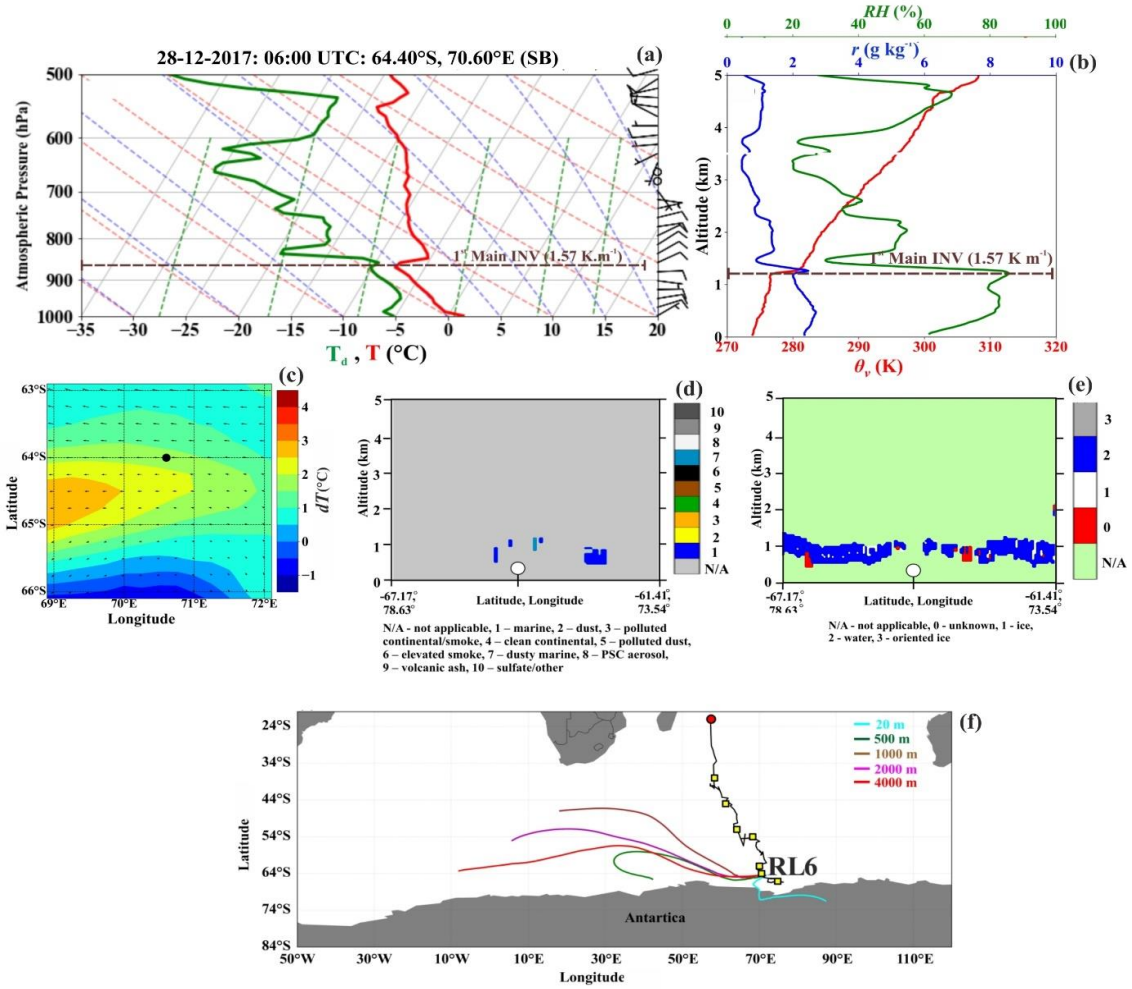

Figure 5.9 The figure depicts the region lying in the south of the Polar Front (PF), i.e., region of Southern boundary of ACC (SB). Panel (a) represents the same as Figure 5.4 (a) but for sounding launched in SB region. Panel (b) represents same as Figure 5.4 (b) but for sounding launched at 64.40°S, 70.60°E on 28-12-2017 at 06:00 UTC in SB region. Panel (c) represents the same as Figure 5.4 (c) but for sounding launched in SB region. Panel (d) represents CALIPSO standard daytime 0 – 5,000 m vertical products of aerosol sub-types derived for 28-12-2017, 09:49 to 10:03 UTC during its orbit between 67.17°S, 78.63°E to 61.41°S, 73.54°E. Panel (e) represents CALIPSO standard daytime profile of 0 – 5,000 m vertical products of ice/water cloud phase derived for 28-12-2017, 09:49 to 10:03 UTC while it is orbiting between 67.17°S, 78.63°E to 61.41°S, 73.54°E. Panel (f) represents same as Figure 5.4 (f) but for sounding (RL6) launched in SB region.

5.3.2.7. Over Coastal Antarctica (CA)

Data from radiosonde launched at 66.10°S, 74.80°E on 29th December 2017 at 05:00 UTC (10:30 LT) was used to depict conditions over CA (Figure 5.10a, b). The atmospheric dynamics This region was influenced by the activity of Prydz Bay gyre (Smith et al., 1984). It induced stronger convective eddies near the sea-surface, evident from higher *dT* forming a warmer front (red shaded region; Figure 5.10c). The higher *dT* at the location of radiosonde sounding (2.1℃) triggered unstable conditions resulting in a well-evolved mixed layer (Figure 5.10b, c). The mixing was capped by a significant low-level inversion at 1,200 m height of strength, 1.34 K m^{-1}. Below this inversion, condensation occurred due to the advection of cold continental air mass (*RH*> 90 % below 1,200 m; Figure 5.10a). This supported the formation of a low-level single cloud layer with a base at ≈580 m and a thickness of 540 m (Figure 5.10a, b). Above this inversion, cold-dry air mass prevailed (larger difference in *T* and T_d, lowest *RH* and *r*; Figure 5.10a, b). The vertical aerosol features showed a negligible fraction of dust aerosols in lower altitudes (<2,000 m), while clean maritime air masses were more likely (Figure 5.10d). Thus, nearly natural atmospheric conditions were observed in this region.

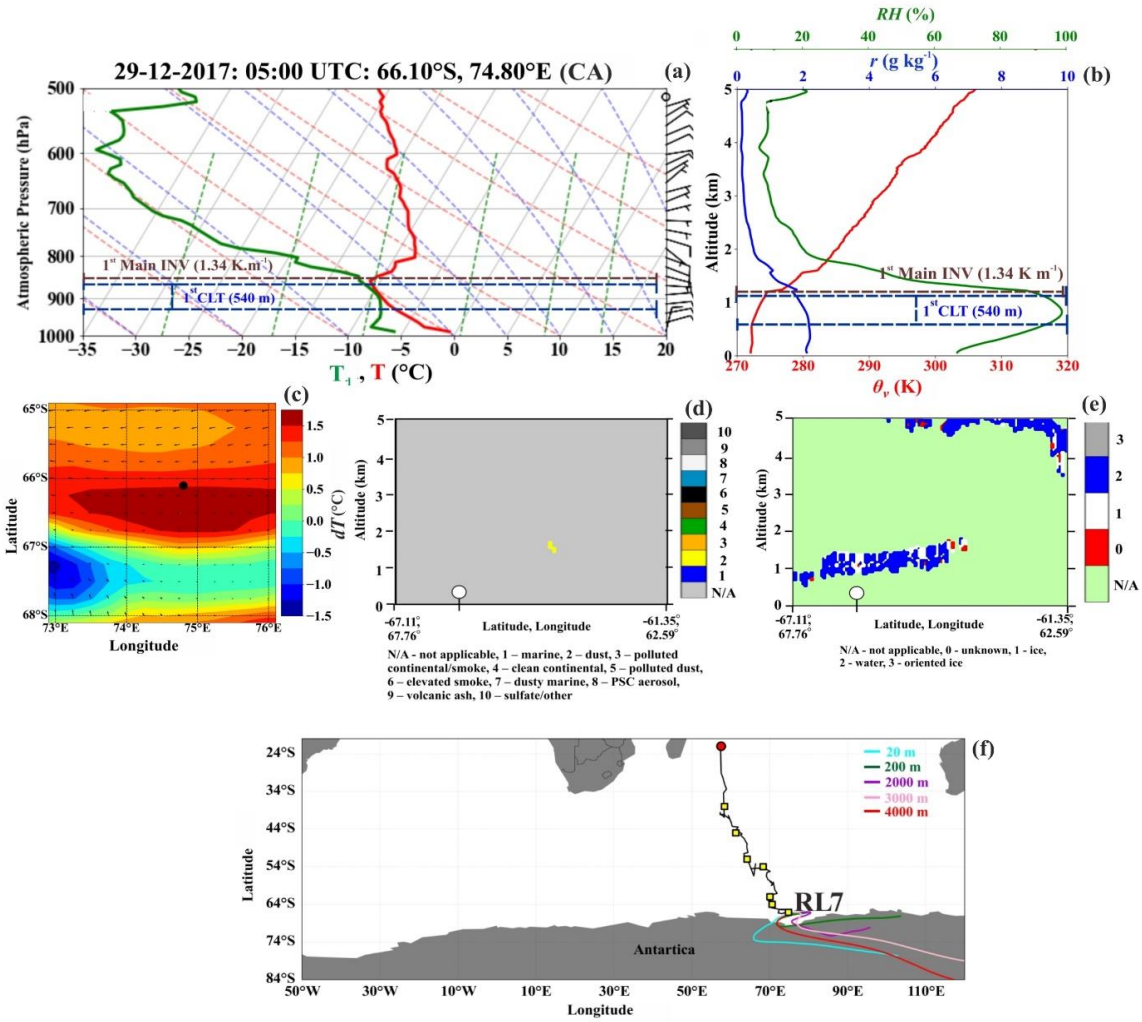

Figure 5.10 The figure depicts the region lying in the south of the Polar Front (PF), i.e., region of Coastal Antarctica (CA). Panel (a) represents the same as Figure 5.4 (a) but for sounding launched in CA region. Panel (b) represents same as Figure 5.4 (b) but for sounding launched at 66.10°S, 74.80°E on 29-12-2017 at 05:00 UTC in CA region. Panel (c) represents the same as Figure 5.4 (a) but for sounding launched in CA region. Panel (d) represents CALIPSO standard daytime 0 – 5,000 m vertical products of aerosol sub-types derived for 29-12-2017, 10:33 to 10:46 UTC during its orbit between 67.11°S, 67.76°E to 61.35°S, 62.59°E. Panel (e) represents CALIPSO standard daytime profile of 0 – 5,000 m vertical products of ice/water cloud phase derived for 29-12-2017, 10:33 to 10:46 UTC while it is orbiting between 67.11°S, 67.76°E to 61.35°S, 62.59°E. Panel (f) represents same as Figure 5.4 (f) but for sounding (RL7) launched in CA region.

5.3.3. Variability of aerosols, direct shortwave aerosol radiative forcing and rate of atmospheric heating due to aerosols

5.3.3.1. Variation of Black Carbon (*BC*) mass concentration

The *BC* mass concentrations measured along the cruise track are shown in Figure 5.11a. Measurements revealed significantly higher values of *BC* (prominently > 250 ng m^{-3}) in the PF regions (PF1 and PF2) lying between 47°S to 60°S. The highest *BC* concentration was at 59.00°S, 70.04°E, with a 297 ng m^{-3}. The regions north of the PF between 30°S to 46°S (i.e., NSTF and SAF) showed moderate *BC* values ranging from 21 ng m^{-3} to 85 ng m^{-3}. Estimates of *BC* mass concentrations in regions of NSTF and SAF1 were 45.56±21.49 and 54±6.48 ng m^{-3} respectively. In the region south of PF, between 60°S and 65°S (i.e., SACCF and SB), BC concentrations varied from 24 ng m^{-3} to 155 ng m^{-3}. Towards the extreme south near the coast of Antarctica (CA), a decrease in *BC* mass concentrations was observed with values as low as 43 ng m^{-3}. A previous study by Moorthy et al. (2005a) has also reported lower values of *BC* mass concentration (< 50 ng m^{-3}) between 20°S to 56°S, whereas (Menon et al., 2015; Hulswar et al., 2020) reported values ranging between 49 and 300 ng m^{-3}. However, a recent study by Srivastava et al. (2021) reported relatively higher estimates of *BC* mass (>200 ng m^{-3}) till 57°S.

5.3.3.2. Variation of Aerosol Optical Depth (*AOD)*

High variability in the Sunphotometer-measured *AOD* values were observed across the study region (Figure 5.11b). From this variability, it is evident that over PF (PF1 and PF2), significantly higher values of *AOD* varied from 0.123 to 0.088 (Figure 5.11b). In PF1, the mean estimates of *AOD* were 0.111±0.016, while in PF2, the values were 0.108±0.001 (Table 5.1). The regions north of the PF (NSTF and SAF) showed values of *AOD* varying between 0.083 and 0.103, with mean estimates of 0.095±0.006. In contrast, the regions south of PF to the coast of Antarctica (SACCF, SB, and CA) showed lower estimates of *AOD*, reaching as low as 0.067. A similar range of *AOD* values were reported in previous studies in the ISSO (Menon

et al., 2015; Hulswar et al., 2020) as well as in the Australian sector of the SO (Alexander and Protat, 2019). In this study, a large oceanic region has been covered (30°S to 67°S), and across such a large spatial area, a wide range of *AOD* values prevailed. These values highlighted the large spatial contrast over the study area due to varying sources, sinks, and transport pathways.

5.3.3.3. Comparison Between Aerosol Distribution Observed from Varied Sources

As discussed in sections above, vertical distribution of aerosol species has been examined using CALIPSO datasets for seven different case studies conducted in seven unique frontal regions of ISSO. Corresponding to these seven case study locations and timing, mass concentration of *BC* aerosols and columnar *AOD* was measured. Inferences drawn on aerosol loading observed from CALIPSO datasets closely corroborated with in-situ measured *BC* aerosols concentrations and columnar *AOD* estimates. In polar front region, CALIPSO data revealed significant higher loading of aerosols (i.e., dust and dusty marine) in vertical 5000 m atmosphere. Such a significant aerosol loading in this region was also observed in in-situ measured near surface *BC* aerosols (275.5 ± 23.5 ng m^{-3}) and in-situ measured columnar *AOD* (0.1095 ± 0.0085) in this region. Thus, remotely retrieved as well as in-situ aerosol measurements obtained from different sources clearly highlighted the presence of anomalously higher aerosol concentrations near the surface as well as within MABL in this remote polar front region of ISSO. In contrast, further in regions south of polar front, data from CALIPSO as well as from in-situ measurements i.e., near surface mass concentration of *BC* aerosols (240.3 ± 18.3 ng m^{-3}) and columnar *AOD* (0.0705) highlighted a relative decline in aerosol loading in this region, if compared to that observed in polar front region. This decrease is attributed to prevailing unique meteorological conditions in this region such as., significant decline in the baroclinic instabilities due to weaking of horizontal pressure gradient force which was strongest in regions of polar front. The strong baroclinic instabilities in polar front region has thereby caused higher accumulation by increasing the residence time of aerosols in that

region. Moreover, lowest aerosols loading was observed in region north of polar front if compared to that observed in polar front region and region south of polar front. Both CALIPSO data and in-situ measured *BC* aerosols (50.0 ± 13.5 ng m^{-3}) and columnar *AOD* (0.095 ± 0.006) data revealed significantly lower aerosols in this region. Such a decreased aerosol loading in this region is attributed to drastically distinct boundary layer dynamics observed in these regions. Mainly higher *SST* and air temperatures accounts for increased turbulent air-sea exchanges within MABL's which, coupled with common high-pressure formations results in destabilizing boundary layer and accounting for strong boundary layer mixing. The results of enhanced boundary layer mixing are likely to cause increased dispersion of aerosols and consequently decreases the proximity of increased aerosols accumulation or higher residence of aerosols within the MABL's in these regions.

5.3.3.4. Clear sky Direct Shortwave Aerosol Radiative Forcing (*DARF*)

The *DARF* variation at top of the atmosphere (*TOA)*, surface (*SFC)*, and atmosphere (*ATM)* depicted an irregular varying trend over ISSO fronts (Figure 5.11c). This variation depicted different distributions of aerosols attributed to the resultant irregular variability of *DARF*. The interpretation of aerosol-induced *DARF* was such that consistently high *ATM* forcing was observed over PF regions (PF1 and PF2) varying from 1.33 to 1.98 W m^{-2}, where mean estimates at PF1 were 1.75±0.29 W m^{-2} and in PF2 was 1.71±0.01 W m^{-2}. However, relatively lower values of *DARF* were observed over the frontal regions north and south of PF. The *DARF* over the northern regions of PF (NSTF and SAF) varied from 1.14 to 1.43 W $m^{-2,}$ while regions south of PF (SACCF, SB, and CA) showed lowest values of *DARF* varying between 1.10 and 1.21 W m^{-2} (Table 5.1). Over PF regions, the *DARF* at *TOA* varied between -5.5 and -8.16 W m^{-2} and at *SFC* was between -6.89 and -10.14 W m^{-2}, leading to the resultant *DARF*. The *TOA* forcing in the regions north of PF varied between -4.55 and -4.99 W m^{-2}, and the corresponding forcing at *SFC* between -4.57 and -6.38 W m^{-2}. However, in the regions south of PF, the *TOA*

forcing varied between -6.60 and -7.05 W $m^{-2,}$ and *SFC* forcing varied between -7.77 and -8.27 W m^{-2}, respectively.

5.3.3.5. Variation of atmospheric Heating Rate (*HR*)

The *HR* estimates varied between 0.021 to 0.032 K day^{-1} over PF1 and PF2. In contrast, lower *HR* estimates were obtained in regions south of PF (SACCF, SB, and CA), with values as low as 0.018 and 0.019 K day^{-1}. In the regions north of PF (NSTF and SAF), *HR* values varied between 0.018 and 0.023 K day^{-1}.

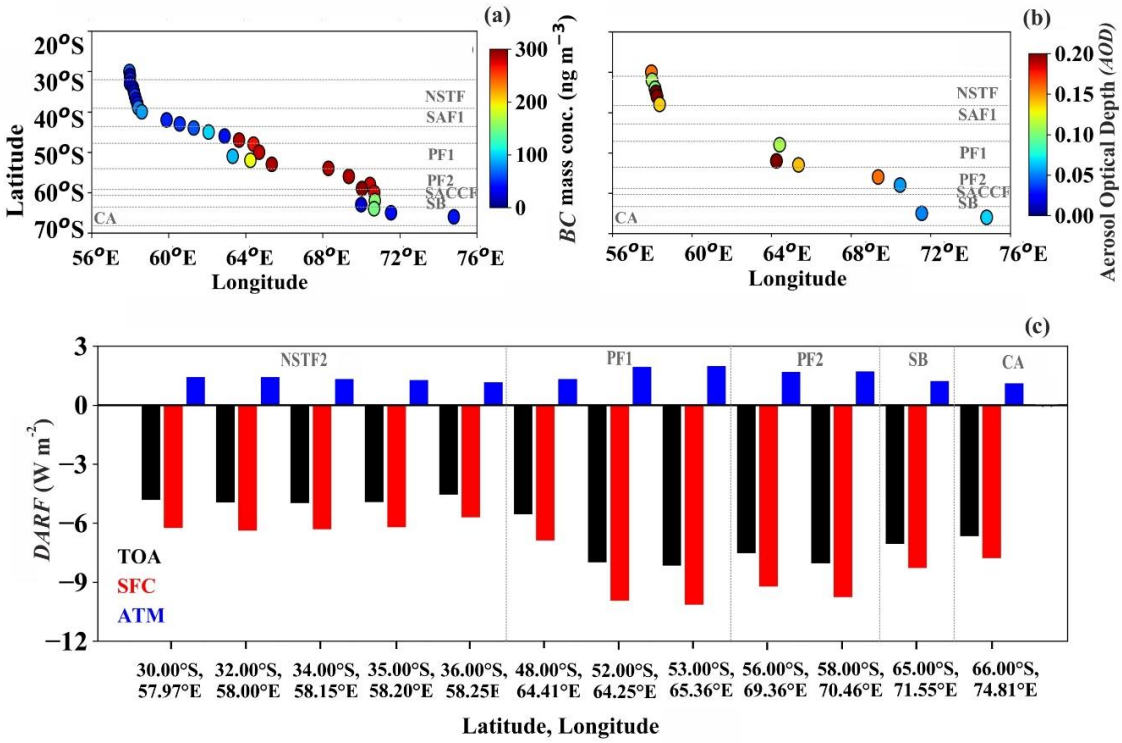

Figure 5.11 Aerosol measurements carried along the forward cruise track of the X^{th} Indian Expedition to the Southern Ocean (SOE-X) from 35°S to 66°S along 56°E to 76°E. Along this cruise track, a 2D variation of (a) mass concentration of black carbon (*BC*) aerosols, (b) aerosol optical depth (*AOD*), and (c) total shortwave clear sky direct aerosol radiative forcing (*DARF*) observed at the surface (*SFC* in red), top of atmosphere (*TOA* in black), and atmosphere (*ATM* in blue) are depicted. Approximate locations of oceanic fronts are acquired from Belkin and Gordon (1996) and Anilkumar et al. (2015) (grey dotted lines).

Table 5.1 The characteristics of clouds, inversions, aerosols, direct shortwave radiative forcing, and atmospheric heating rate over ISSO regions from measurements collected during forward track of the Xth Southern Ocean Expedition.

I. Frontal Regions of the Indian Ocean sector of Southern Ocean (ISSO)	Regions North of Polar Front		Polar Front Regions		Regions South of Polar Front		
	Sub-Tropical Front (NSTF)	Sub-Antarctic Front (SAF1)	Northern Polar Front (PF1)	Southern Polar Front (PF2)	Southern Antarctic Circumpolar Current Front (SACCF)	Southern Boundary of ACC (SB)	Coastal Antarctica (CA)
*Adopted frontal-based classification of the study area	32°S to 40°S	41°30′S to 44°S	47°S to 52°30′S	54°30′S to 59°30′S	60°S to 62°S	64°S to 65°S	65°S to 68.5°S
II. Details of Atmospheric Sounding at Seven Case Study Locations							
Launch Number	RL1	RL2	RL3	RL4	RL5	RL6	RL7
Launch Date	14 Dec 2017	19 Dec 2017	22 Dec 2017	23 Dec 2017	27 Dec 2017	28 Dec 2017	29 Dec 2017
Launch Time (UTC)	01:00	06:00	22:00	06:00	03:00	06:00	05:00
Launch Location	38.00°S, 58.40°E	45.00°S, 61.30°E	52.00°S, 64.20°E	54.00°S, 68.30°E	62.00°S, 70.07°E	64.40°S, 70.60°E	66.10°S, 74.80°E
III. Thermodynamic Metrics							
SST (K)	17.1	13.3	3.1	1.2	0.1	0.5	-1.2
SST - T_{air} (K)	0.1	5.5	0.9	-0.2	0.34	2.0	2.1

MSLP (hPa)	1013	1019	973	980	987	990	987
***WS* (m s^{-1})	10.19	3.06	19.16	17.98	5.01	5.18	6.14
***WD* (°)	338.74	289.64	270.78	245.73	251.51	91.1	69.88
***RH* (%)	79.01	73.93	95.32	97.71	95.06	82.66	91.58
IV. Inversion Characteristics (Surface - 5,000 m)							
Inversions (INV)	3 INV	4 INV	2 INV	5 INV	5 INV	1 INV	1 INV
First INV height (m)	660	220	3,300	160	1,100	1,220	1,200
First INV strength (K m^{-1})	0.27	0.50	2.24	0.35	1.78	1.57	1.34
Second INV height (m)	2,440	840	3,880	800	2,220	-	-
Second INV strength (K m^{-1})	0.89	0.14	0.73	0.22	0.16	-	-
Third INV height (m)	4,660	1,860	-	3,780	3,640	-	-
Third INV strength (K m^{-1})	0.19	3.17	-	0.59	0.31	-	-
Fourth INV height (m)	-	4,320	-	4,260	4,440	-	-
Fourth INV strength (K m^{-1})	-	0.12	-	0.32	0.2	-	-
Fifth INV height (m)	-	-	-	4,600	4,880	-	-
Fifth INV strength (K m^{-1})	-	-	-	0.14	1.28	-	-
V. Cloud Characteristics (Surface - 5,000 m)							
Cloud layer (CL)	No CL	No CL	2 CL	2 CL	2 CL	No CL	1 CL
1^{st} CL: base height (m)	-	-	340	180	40	-	580

1st CL: top height (m)	-	-	660	680	560	-	1,120
1st CL: Total cloud thickness (m)	-	-	320	500	520	-	540
2nd CL: base height (m)	-	-	2,200	1,480	860	-	-
2nd CL: top height (m)	-	-	3,360	2,020	920	-	-
2nd CL: Total cloud thickness (m)	-	-	1,160	540	60	-	-
VI. Aerosol Characteristics							
Dominant aerosol type	Marine, dust, and elevated smoke	Marine, dust, and polluted dust	Marine, dust, and dusty marine	Marine, dust, dusty marine, and smoke	Marine and dust	Marine and dusty marine	Dust
Measured Aerosol Optical Depth	0.095± 0.006	-	0.111± 0.016	0.108± 0.001	-	0.074	0.067
Black Carbon mass conc. (ng m^{-3})	46±21	54±6	269±42	282±5	155	71±55	43
Clear sky Direct Aerosol Radiative Forcing (W m^{-2})	1.32± 0.11	-	1.75± 0.30	1.71± 0.01	-	1.22	1.11
Atmospheric Heating Rate (K day^{-1})	0.022± 0.002	-	0.029± 0.005	0.028± 0.001	-	0.002	0.018

Note: ** Identification of oceanic fronts over ISSO were adopted from Belkin and Gordon, 1996 and Anil Kumar et al., 2015. * * The wind speed (WS), wind direction (WD), and relative humidity (RH) in subheading II are mean values at 925 hPa.*

5.4. Discussion

5.4.1. Regions of Polar Front (PF1 and PF2)

The atmosphere over PF revealed a significant loading of dust aerosols. Also, elevated surface *BC* aerosols were noticed in these regions. Because of higher aerosol loading, the estimated clear sky shortwave *DARF* and atmospheric *HR* were maximum. Thus, it can be inferred that the only possible origin of anthropogenic aerosols was long-range transport from the neighboring continent. Examination of back-trajectories revealed prominent advection from the open SO region, while strong winds in this region might be able to transport dust particles advected from longer distances mainly generated from the western African continent and other far away continents as well (Figure A14). Thus, due to strong wind, these long-range advected dust particles are most likely to be in fine mode range (O'Dowd et al., 1997; Murphy et al., 1998; Menon et al., 2015). This increases the possibility for higher suspension and increased residence time of these aerosols. Moreover, the higher near-surface mass concentration of *BC* aerosols was most likely advected from the Kerguelen Island (49.50°S, 69.50°E), being in the closest proximity to PF (Srivastava et al., 2021). However, in addition to long-range transport, the pertinent factor for such an enormous dust loading was the thermodynamic properties of low-level MABL, which regulate the cycle of these aerosols.

Firstly, this region experienced strong winds due to the polar jet stream. The polar jet stream typically witnessed in the proximity of 60°S induces strong winds having average magnitudes greater than 23 m s^{-1}, wherein the intensities were dependent upon factors such as the location of high and low-pressure systems, development of warm and cold fronts, and seasonal changes (Nakamura et al., 2004). Such an intense wind rapidly mixes air masses of distinct properties. Hence, a strong temperature-pressure gradient was built that separated these air masses. This separation is commonly referred as the formation of baroclinic instabilities which occurred at

shorter distances in the atmosphere of polar front region (Reed, 1979; Moore et al., 1999a). Any small fraction of aerosols (dust, *BC,* and other anthropogenic aerosols) advected or (marine aerosols) produced in this region were forced into these thermal boundaries by high-speed gusty winds. Once trapped, the meteorological conditions of freezing temperatures, decreased *MSLP*, highest *RH*, and continuous flow of colder air masses accounted for the confinement of these aerosols within the atmosphere. The meteorological conditions were also conducive to forming numerous intensified mid-latitude cyclonic systems (Carleton and Song, 1997; Field and Wood, 2007; Irving et al., 2010). These cyclonic cores also accounted for enhanced trapping and, thereby, decreased the dispersion of these aerosols. The coupled role of these two dynamics specific to PF accounted for higher confinement and accumulation, thus, increasing the residence time of aerosols over the PF.

5.4.2. Regions North of Polar Front (NSTF and SAF)

The subtropical frontal regions (NSTF and SAF) showed prominence of marine aerosols in the low-level atmosphere, while some fractions of continentally originated aerosols were noticed at higher altitudes (>3,500 m). Also, a moderate concentration of near-surface *BC* aerosols and *AOD* were observed in this region. Thus, the clear sky *DARF* in this region was governed by naturally originated aerosols and, to a lesser extent, by anthropogenically produced aerosols. Due to this, the clear sky *DARF* and atmospheric *HR* were less in this region compared to the PF. In this region, marine aerosols comprised sea salt particles produced in-situ from sea spray, bubble bursting, or wave breaking induced by surface winds, as well as other organic particles produced by conversion from gas to particles (O'Dowd et al., 1997). The origin of these aerosols, when traced by back-trajectories, indicated their long-range transport from the open SO region to the lower atmosphere. However, at higher altitudes (>3,500 m), anthropogenic aerosols comprised particles of polluted dust and elevated smoke, which were long-range

advected from the western South African continent. Interestingly, a higher loading of marine aerosols was observed in the NSTF region, while relatively negligible aerosols were observed in the SAF region. Although both regions represented a high-pressure zone where strong subsidence was a prominent dynamic feature, the influence of strong subsidence was evident over NSTF. It accounted for a higher accumulation of aerosols in the lower atmosphere, like the results over land from Hu et al. (2021). These aerosols were strongly mixed and confined well within a mixed layer capped by a stronger temperature inversion that prevented further dispersion of aerosols in altitudes above this inversion (Prasad et al., 2021). However, over SAF, the occurrence of subsidence was weakened by strong convection in the lower atmosphere. This convection was induced by ARC (Lutjeharms and Gordon, 1987; Lutjeharms and Ansorge, 2001). The effect of strongest convection was evident in the atmospheric column evident with uniform mixing that formed a well-evolved deeper mixed layer over SAF. Hence, a convective updraft of air mass has accounted for the higher dispersion of low-lying aerosols. This may have led to reduced suspension and lesser accumulation of aerosols in the SAF region.

5.4.3. Regions South of Polar Front (SACCF, SB, and CA)

Over SACCF, the distinct atmospheric condition included forming an intensified low-pressure mesoscale cyclonic system regulated by the convergence of air mass of varying properties of winds from different directions. The intensification of this system was supported by the lowest temperatures and atmospheric pressure conditions. These cyclonic systems were responsible for significant precipitation leading to snowfall or foggy conditions, followed by clouds nearer to the surface. These clouds were low-level multi-layered SLW/ICE. In contrast to PF, distinct lower aerosol variability was observed. Here, the aerosol concentrations were negligible throughout the vertical column of the atmosphere compared to those over PF. A small fraction

of in-situ produced marine aerosols advected from the open SO and dust advected from active research stations in eastern Antarctica were observed in the lower atmosphere. At the same time, a clean maritime air mass was prominently seen at different altitudes. Also, a reduction in the surface concentration of *BC* aerosols and *AOD* were noticed. Because of the lower aerosol loading, clear sky *DARF* and *HR* were also lower than that at the PF. Thus, probing the reason for such a distinct aerosol variability in SACCF, despite similar meteorology as that of PF could be attributed to the weakening of westerly winds (5.01 m s^{-1}). As a result, this has ultimately decreased the temperature-pressure gradient, eroding the baroclinic boundaries' intensity throughout the atmospheric column over SACCF. The likelihood of higher aerosol dispersion was high, thus preventing any aerosol accumulation. It can also be noted that a small fraction of aerosols confined in the lower atmosphere was mainly within the convergence over the mesoscale cyclonic core.

Further, towards the SB and CA regions, minimum aerosol loading was observed. The predominant aerosols were naturally produced marine aerosols and more likely naturally or anthropogenically produced dust aerosols. Dust aerosols and a small amount of *BC* aerosols were advected from long range transport from active research stations in Antarctica (Srivastava et al., 2021). However, the atmospheric dynamics specific to this region have accounted for lower accumulation and higher dispersion of advected aerosols. The warming of Antarctic waters controlled these dynamics due to strong convective activities occurring over the Weddell Sea gyre and Prydz Bay gyre (Smith et al., 1984). The proximity forming low-pressure cyclonic systems was the least, indicating less probability of an increase in aerosols within the cyclonic cores. However, shallow convection spreads aerosols in this region. Thus, in resonating with such atmospheric dynamics, the formation of clouds was inhibited, leading to

clear sky/cloud-free conditions. However, convective instability induced a single low-level inversion that restricted the convective updrafts above MABL in these regions.

5.5. Concluding remarks

The study described in this chapter provided a novel set of measurements presenting first-time understanding of the effect of oceanic fronts in shaping the vertical thermodynamic structure of MABL and its role in regulating aerosol dynamics and associated clear sky *DARF* and *HR* in the ISSO region. Some of the major findings of this study are listed below,

1. A significant accumulation of dust and *BC* aerosols were observed over the PF and hence resulted in higher estimates of clear sky *DARF* and *HR*. The long-range advected anthropogenic origin aerosols (from continent) as well as in-situ produced natural origin aerosols, likely trapped within the baroclinic instability and intense mid-latitude low pressure cyclonic system were likely the primary cause of higher aerosol loading and increased residence and accumulation of aerosols in the atmosphere of polar front region.
2. The pattern of wind circulation over polar front region i.e., PF1, PF2, and SACCF depicted strong cyclonic clockwise curling of winds indicating occurrence of mid-latitude cyclones.
3. Much of the atmospheric column over the Antarctic coast was pristine, and thereby accounted for lowest clear sky *DARF* and *HR* in this region. However, there was evidence of long-range transport of dust and *BC* aerosols in small fractions over the Antarctic coast, where shallow convection enhanced the spread of aerosols at lower altitudes.
4. An extreme contrast in aerosol loading and thermodynamic state was observed in the subtropical frontal regions. Over NSTF region, higher loading of marine aerosols confined at lower altitudes has contributed to the resultant *DARF* and *HR*, while negligible aerosol loading over SAF1 was associated with the strong convective updrafts induced due to the

convective activities associated with the ARC and thus, a reduced *DARF* and *HR* was observed.

5. In subtropical frontal regions i.e., NSTF and SAF1 region, marine aerosols were confined in lower atmosphere while respectively small fraction of elevated smoke and polluted dust advected by long range transport from South African continent were noticed at higher altitudes.
6. There was considerable loading of continental aerosols over the polar front region, and two scenarios can be implied. In the first scenario, hygroscopic growth of dust aerosols can potentially serve as cloud condensation nuclei/ice nucleating particles, i.e., (CCN/INP), and initiate excess cloud formation, resulting in anomalous cloud coverage. Secondly, an increase in dust and *BC* aerosols increases the absorption of shortwave radiation (its optical property) and may enhance *HR*. Both scenarios are also applicable to the Antarctic coast, where a small fraction of dust and *BC* aerosols were also deposited by long range transport. Because of these scenarios, *DARF* and *HR* are altered locally as well as on a larger scale, and these alterations have direct effect on Earth's climate and radiative balance.

PUBLICATION

S. Neha Salim, Arjun Adhikari, Atiba A. Shaikh, Harilal B. Menon, N. V. P. Kiran Kumar, K. Rajeev, (2023) Aerosol-boundary layer dynamics and its effect on aerosol radiative forcing and atmospheric heating rate in the Indian Ocean sector of Southern Ocean. ***Science of The Total Environment***, 858: 159770, *http://dx.doi.org/10.1016/j.scitotenv.2022.159770*

Chapter 6

Conclusions and Future Scope

6.1. Conclusions

This thesis explored in detail the boundary layer dynamics occurring in tropics, southern mid-latitudes, and Antarctica regions, regions which lie among climatically sensitive regions of the globe. The uniqueness of investigation presented in this thesis lies in the fact that it addresses crucial aspects of atmospheric boundary layer, beginning with air-sea exchanges, surface layer turbulence characteristics, structure of marine atmospheric boundary layer, properties of clouds, occurrence of inversions, physical processes (i.e., convection, advection, precipitation, and radiative heating/cooling), aerosol distribution, radiative forcing, and atmospheric heating. Knowledge of these aspects are of crucial importance to underpin key atmospheric dynamics and its role in regulating distribution of aerosols and associated radiative forcing unique to geographically and topographically distinct regions of the globe with a broader aim to evaluate its effect on global climate. Thus, using multidisciplinary techniques, theoretical formulations, and a combination of in-situ, remote, and modelled datasets, the study conducted in this thesis provided records of new quantifications and surprising results. Major findings obtained in this thesis are summarized as follows,

This thesis begins by analyzing diurnal and seasonal variability of micrometeorological turbulence characteristics of atmospheric surface layer (ASL) over a tropical coastal region of Goa (15.46^{o}N, 73.83^{o}E), India using measurements from 32 m meteorological tower installed in the campus of Goa University. Analysis of these measurements revealed strong diurnal and seasonal variations in the meteorological conditions and associated surface layer fluxes of sensible heat (H), turbulent kinetic energy (e), and momentum flux (τ) resulting in

perturbations in the surface layer stability conditions. The results highlighted that over this tropical coastal site, seasons of pre-monsoon, post-monsoon, and winter were favorable for highly diffusive conditions for the dispersion of aerosols compared to the summer-monsoon season. Presence of mesoscale phenomenon peculiar over coastal regions i.e., the onset of land and sea breeze circulation during pre-monsoon, post-monsoon, and winter, while the prevalence of strong sea breeze throughout 24-hour cycle during summer monsoon season was observed over this study region. Analysis based on the application of Monin-Obukhov Similarity Theory (MOST) showed prominent variation in the variances of wind components and temperature with stability conditions during different seasons. The fitting relationships obtained between these variances and stability conditions, empirical coefficients, as well as estimations for surface layer fluxes on diurnal and seasonal scales are novel quantifications representing this region have been recorded in this thesis. The functional forms developed over Goa region describe the turbulent nature of surface layer specific to this location and have significant implications in regional air pollution studies. As in air quality calculations, observational estimates of meteorological parameters, frictional velocity, Obukhov length, and roughness length under varying conditions of stability are considered as a very useful parameter. Also, the empirical coefficients which are estimated based on the local scaling and similarity relationships under the framework of MOST over the coastal Goa site could be included in dispersion models to improve its boundary layer parameterization schemes specific for this region.

Apart from exploring diurnal and seasonal ASL characteristics of a tropical coastal region of Goa, India, this thesis presents first novel spatiotemporal records on MABL structure, properties of clouds, inversions, and physical processes over least examined sector of SO i.e., ISSO, based on 75 high resolution atmospheric sounding measurements collected by participating in three ISSO field campaigns. The obtained records described in detail the

vertical thermodynamic stability structure of MABL in response to varying air-sea coupling over a system of multiple oceanic and atmospheric fronts encountered over three major oceanic domains i.e., STIO, ISSO, and HLSO examined in this study. Analysis revealed that frequently varying air-sea coupling strongly regulated the vertical thermodynamic structure of MABL over wide spatial domain (24°S to 68°S) investigated in this thesis. In STIO region, prominent low-level convection was observed to cause prominent destabilization and low-level mixing which supported formation of well-developed mixed layer commonly thermodynamically coupled to the surface but weakened in mid-latitudes. This was linked to the occurrence of internal convective mixing at higher altitudes resulting in a decoupled mixed layer structure. In these regions, the strongest convective mixing resulted in deep mixed layer structure capped by multilevel strong inversion and no cloud to very thin single layer clouds in intermediate altitudes. In ISSO, precipitation was the dominant driving process which was attributed to the frequent formation of multiple atmospheric fronts due to the advection of multiple types of air masses by high-speed winds. This caused faster condensation of falling precipitation at intermediate altitudes. The condensation of precipitation accounted for the presence of thicker low-level multilayered clouds which were as low as 500 m and as high as 3,000 m. These clouds were prominently in the form of mixed phased super-cooled liquid water or ice-water (SLW/IWC) clouds. However, at high altitudes, strong advection of dry air mass was the dominant process that caused strong multiple inversions over ISSO. Aided by these processes, frequent formation of low pressure stormy cyclonic systems was common in ISSO region. In HLSO region, low-level atmospheric dynamics were driven by weak and shallow convection influenced by colder continental drier air mass advected by strong katabatic winds from the intermediate and higher altitudes. These katabatic winds generated multiple inversions. The strength of katabatic winds modulated the strength of inversions. Moreover, the weak

precipitation in intermediate altitudes went through an abrupt sublimation process due to katabatic winds resulting in ice virga conditions.

Further, these unique atmospheric dynamics observed in each oceanic domain played a major role in controlling the vertical distribution of aerosols and associated radiative forcing. Surprisingly, higher estimates of dust, dusty marine, and black carbon aerosols, and associated radiative forcing were observed in the remote pristine region of polar front (50°S to 60°S). This was attributed to unique boundary layer dynamics specific to polar front region and mainly to three major factors; (a) strong convergence associated with frequent low-pressure cyclonic systems possessed strong potential of trapping long-range advected aerosols (b) presence of strong baroclinic instabilities, a peculiar feature of polar front region which formed strong thermal boundaries separating air masses of varying properties, thereby exhibits more likelihood of higher confinement of aerosols within these boundaries (c) The highly stabilized vertical thermodynamic structure of MABL over polar front region. Thus, boundary layer dynamics-driven higher aerosol loading in this region is alarming in terms of its potential to alter regional weather and climatic pattern of SO, as exhibits a tendency to strongly alter the radiative balance of this remote pristine oceanic region. Mostly by suppressing cloud formation or promoting anomalous cloud cover by serving as a cloud condensation nucleus (CCN's), depending upon the optical properties of aerosols advected in this region. Anomalously excess cloud coverage impedes the accuracies of satellite retrieved measurements and simulations from climate models projecting SO. This in turn significantly impairs the ability of scientists to continually monitor through remote measurements all-round the year for the changes in SO atmosphere and its role in altering global climate. This weakens the constant efforts of climate communities to access climate risks and develop mitigation plans to address climate change. So, in present time the observation-based quantifications on vertical thermodynamic stability structure of MABL, macrophysical properties of clouds, inversions, dominant physical

processes, radiative forcing, and atmospheric heating rate presented in this thesis are of crucial importance in terms of addressing some of these climate concerns as well as validating and improving satellite retrieved and model simulated datasets for ISSO region. Particularly, the quantifications recorded in this thesis are first of its kind and unique as it has covered a wide spatial domain of one the least explored sector of SO i.e., ISSO (24°S to 68°S) in terms of aerosols and boundary layer meteorology.

6.2. Scope for future research

6.2.1. Improvements in the characterization of the turbulent nature of ASL

The first part of this thesis (chapter 3) provided an enhanced understanding of the diurnal and seasonal turbulent properties of the atmospheric surface layer over a coastal region of the tropical Indian sub-continent. However, the variation of surface layer fluxes and turbulence during an offshore and onshore wind circulation, which is one among the unique features of the coastal regions, has been poorly explored. Hence, such a study will help in understanding the role of diurnal wind reversals to shape the evolution of coastal boundary layer. In the light of the findings presented in this study, the diurnal and seasonal evolution of the turbulence spectra can be an interesting future research work. The nature of the surface layer turbulence characteristics during the nocturnal hours still requires proper understanding. The influence of surface topographic properties in determining the intensity of turbulence under varying stability conditions and seasonal changes together with its role in the dispersion of pollutants within the boundary layer can be potential area for future research. As these studies have direct applications in modelling regional-scale weather pattern and mechanisms driving pollutant dispersion.

6.2.2. Improvements in observational, remote, and modelled based quantification of the thermodynamic properties of MABL, clouds, inversions, and dynamic processes over Southern Ocean and Antarctica

A challenge with research in the Southern Ocean is the sparse in-situ observations due to remote and harsh weather conditions. As a result, particularly ISSO, lack observational analysis compared to other sectors of SO (i.e., Australasian sector (McFarquhar et al., 2021) and African sector (Messager et al., 2012)), where such studies are relatively well documented. In view of this, a significant contribution has been made in this thesis by presenting for the first time an observational analysis on the thermodynamics of MABL, clouds, inversions, and dynamic processes occurring in the STIO, ISSO, HLSO regions (chapter 4). These findings highlighted the unique system of low-level thick multi-layered and mixed phased clouds, multiple strong high-altitude inversions, and dominant precipitation over ISSO. The presence of such clouds was reported in studies conducted in sectors of SO (Mace and Protat, 2018a; McFarquhar et al., 2021). These studies have reported that these clouds are majorly responsible for introducing large biases in the data retrievals from satellite and climate models specifically over SO regions compared to other regions across the globe (Trenberth and Fasullo, 2010; Bodas-Salcedo et al., 2014). However, with the perspective of the crucial role played by SO atmosphere in regulating the global climate, it becomes essential to have proper knowledge on the MABL structure and dynamics which can only be achieved through a combination of accurate observational, remote, and modelling approaches. Thus, a fruitful area of future research could be employing the observation-based quantifications provided in this thesis work in numerical models to accurately parameterize and project boundary layer structure, cloud and inversion properties, and precipitation dynamics over ISSO. Also, these quantifications can be used for validating frequently accessed remote sensing retrievals and model evaluation. The results presented in this thesis represents the detailed thermodynamics of MABL during southern hemispheric

austral summers, while similar understanding of MABL during austral winters can be a future field work, that can serve for studying seasonal variations in the ISSO boundary layer.

6.2.3. Improved understanding on the coupled-effect of aerosol-boundary layer dynamics in shaping the structure of clouds, inversions, and shortwave radiative forcing over Southern Ocean and Antarctica

Followed by the detailed characterization of the ISSO boundary layer, clouds, inversions, and processes (chapter 4), work presented in this thesis also dealt with the coupled interaction of aerosols and boundary layer dynamics in the ISSO up to Antarctica (chapter 5). From this examination, a new highlighted finding was the significant loading of anthropogenic origin long-range advected dust and black carbon (*BC*) aerosols in the atmosphere of polar front. This loading was attributed to long-range advection, significant stability of MABL, cyclonic formations, and meteorological conditions supporting baroclinicity to cause higher accumulation by increasing the residence time of aerosol suspension in the atmosphere. Carrying forward to this finding, an important area for future research could be to identify other factors responsible for such an anomalous aerosol loading in this region. Also, physio-chemical characterization of aerosols prevailing in ISSO and the possible effect of these aerosol properties in determining the stability and the vertical development of ISSO MABL could be an interesting topic for future investigation.

Appendices

Appendix 1: Vertical thermodynamic profiles obtained from 75 atmospheric soundings launched in the Indian Ocean sector of Southern Ocean (ISSO) and the synoptic near sea-surface meteorological conditions observed in the vicinity of 75 sounding locations.

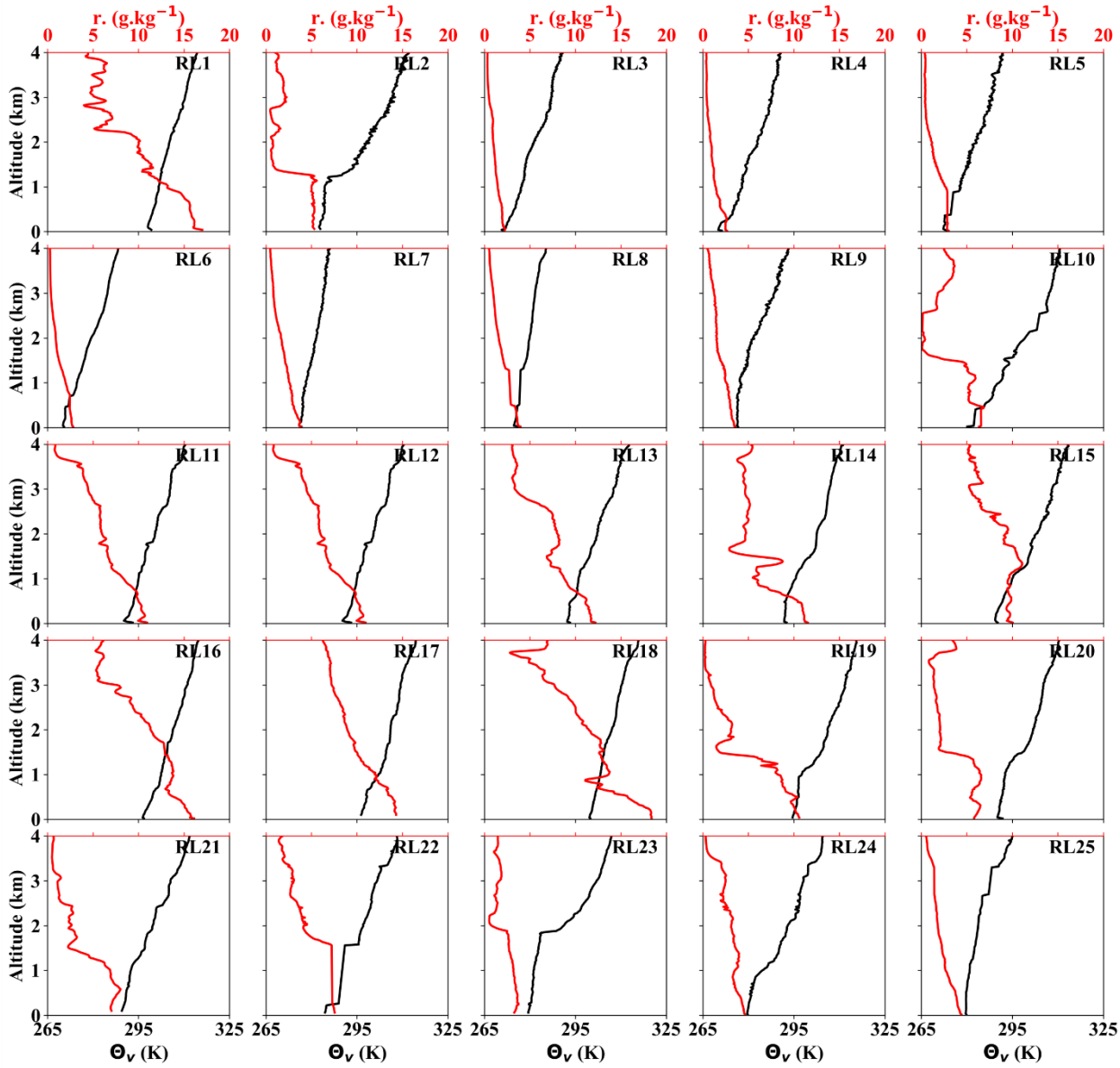

Figure A1 Thermodynamic profiles of virtual potential temperature (θ_v) in K (black line – bottom x-axis) and mixing ratio (r) in g kg^{-1} (red line – top x-axis) up to 4,000 m altitude for 25 atmospheric soundings (RL1 to RL25).

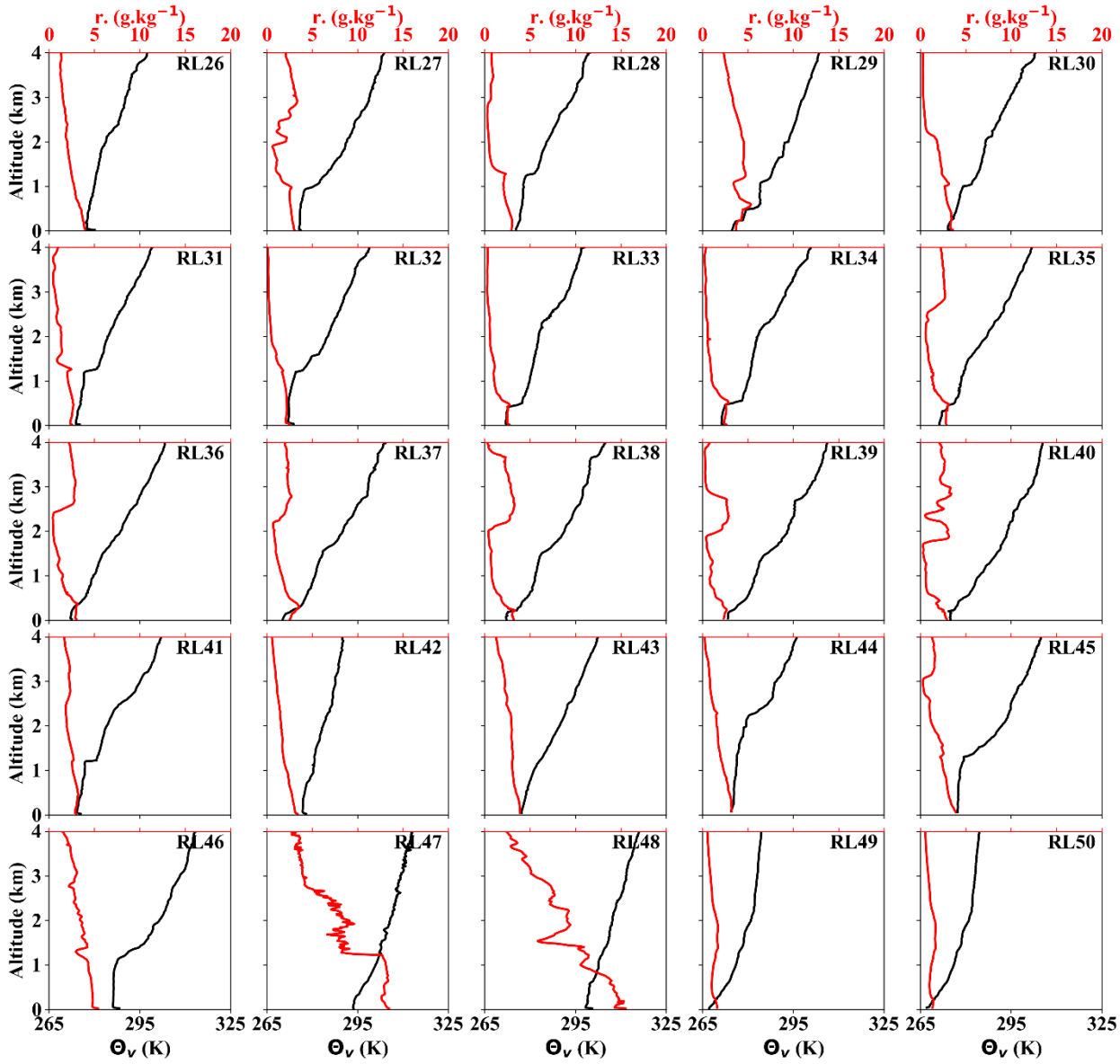

Figure A2 Thermodynamic profiles of virtual potential temperature (θ_v) in K (black line – bottom x-axis) and mixing ratio (r) in g kg^{-1} (red line – top x-axis) up to 4,000 m altitude for the next 25 atmospheric soundings (RL26 to RL50).

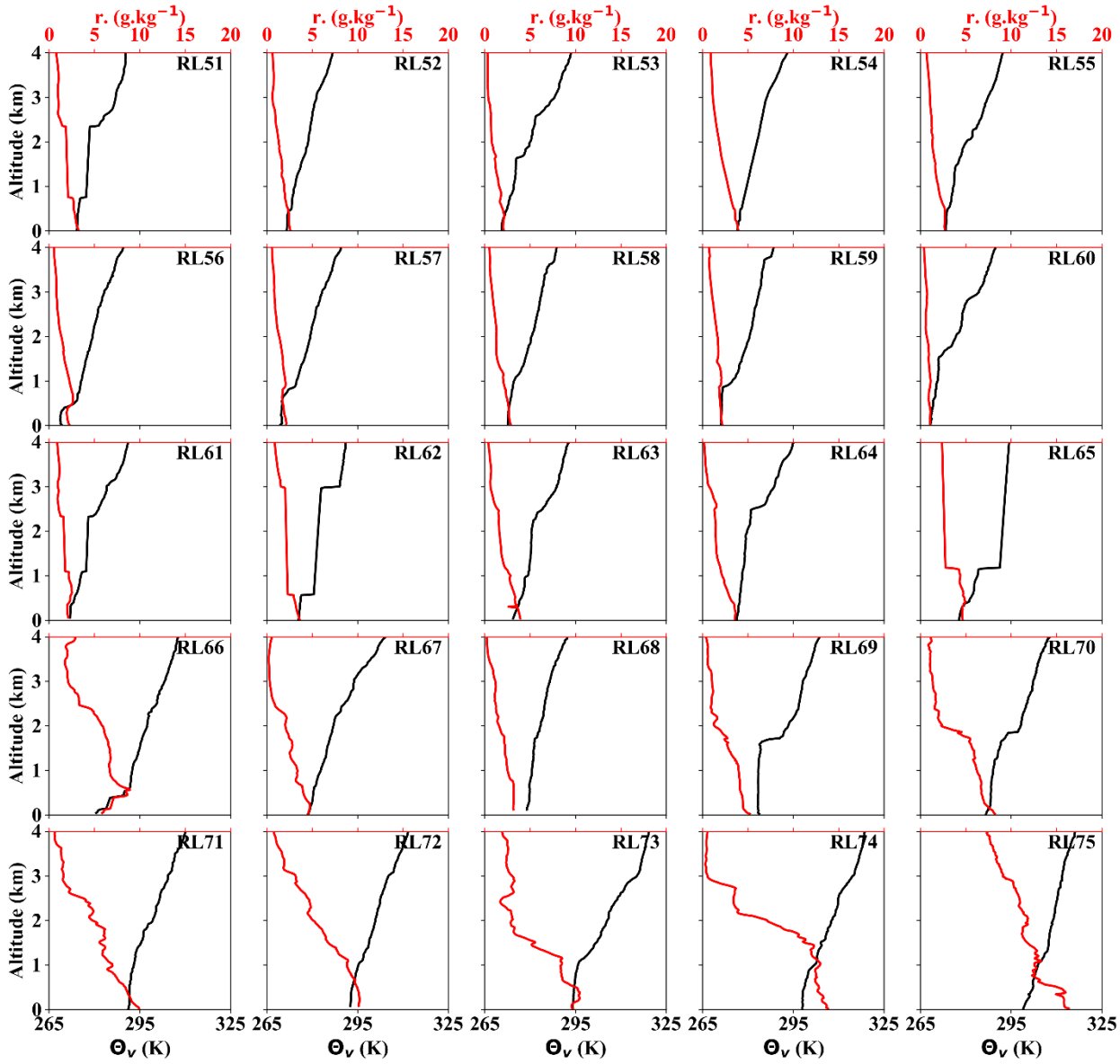

Figure A3 Thermodynamic profiles of virtual potential temperature (θ_v) in K (black line – bottom x-axis) and mixing ratio (r) in g kg^{-1} (red line – top x-axis) up to 4,000 m altitude for the next 25 atmospheric soundings (RL51 to RL75).

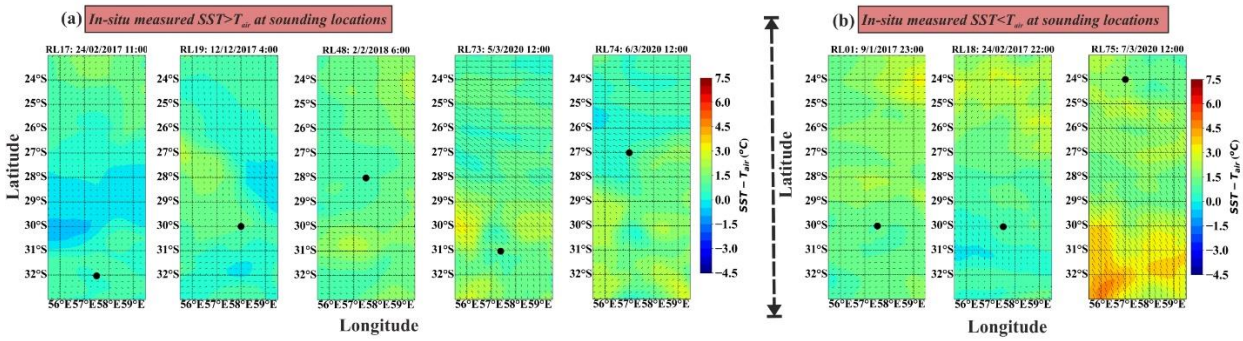

Figure A4 Synoptic conditions of near-surface air-sea temperature difference (*SST*-T_{air}) around radiosondes launched in NSTF1 during the conditions when in-situ measured (a) *SST*>T_{air} and (b) *SST*<T_{air} at respective sounding locations. Sounding locations are marked as black dots. Plotted y-axis are a latitudinal range for NSTF1 (with $\pm$1° latitudes). The colored background represents the near-surface air-sea temperature difference in ℃ obtained from ECMWF ERA5 reanalysis. The color bar (towards the right) indicates the range of *SST*-T_{air}. Wind vectors (knots) are overlaid. Details of each sounding location are mentioned on top of each synoptic panel.

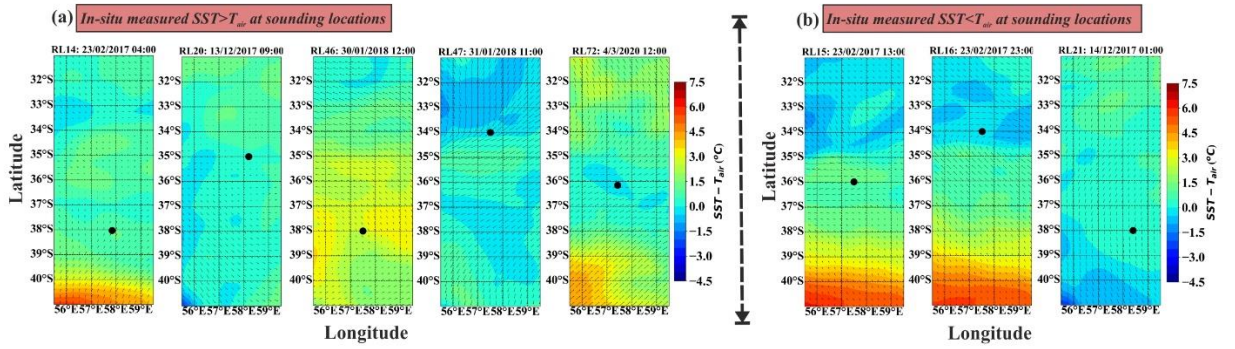

Figure A5 Same as Figure A4 but for upper air soundings launched in NSTF2.

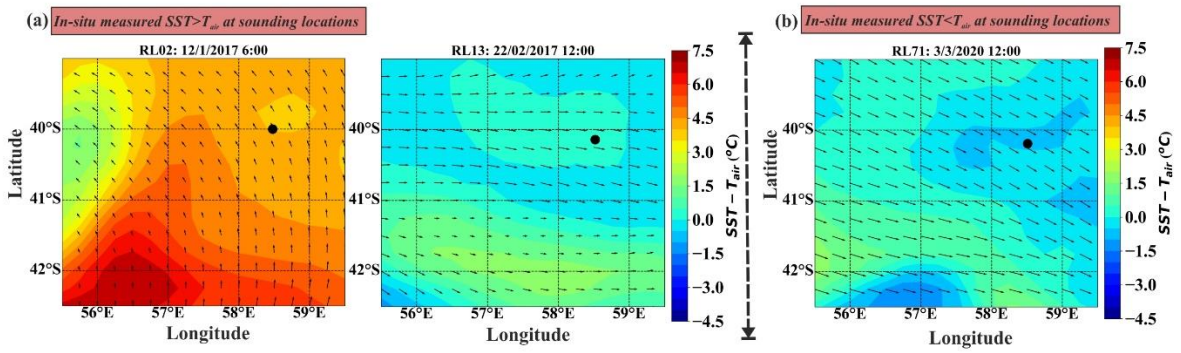

Figure A6 Same as Figure A4 but for upper air soundings launched in SSTF.

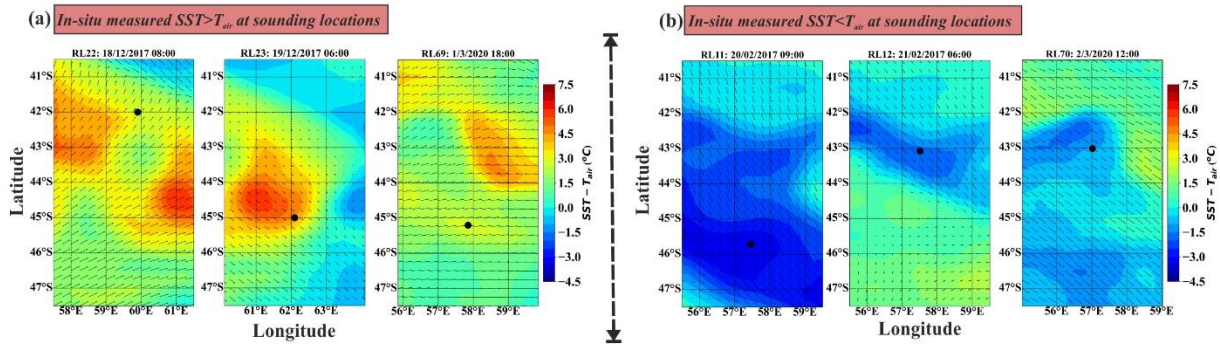

Figure A7 Same as Figure A4 but for upper air soundings launched in SAF1.

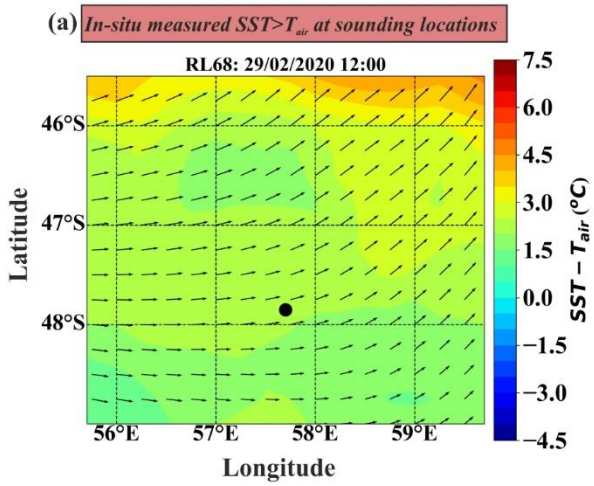

Figure A8 Same as Figure A4 but for upper air soundings launched in SAF2.

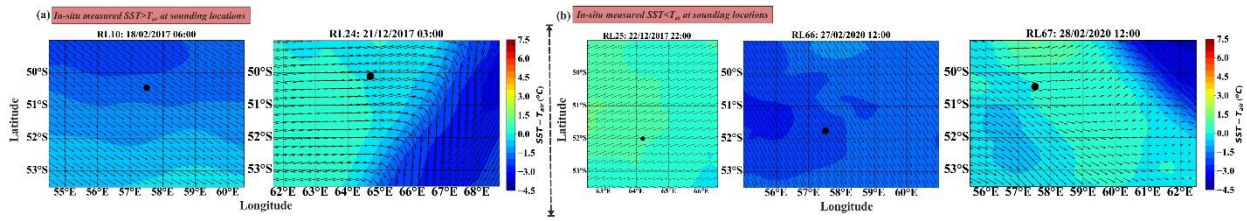

Figure A9 Same as Figure A4 but for upper air soundings launched in PF1.

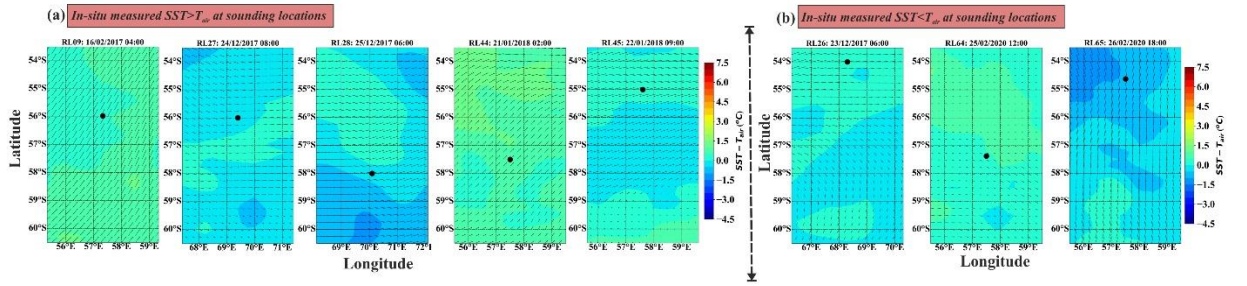

Figure A10 Same as Figure A4 but for upper air soundings launched in PF2.

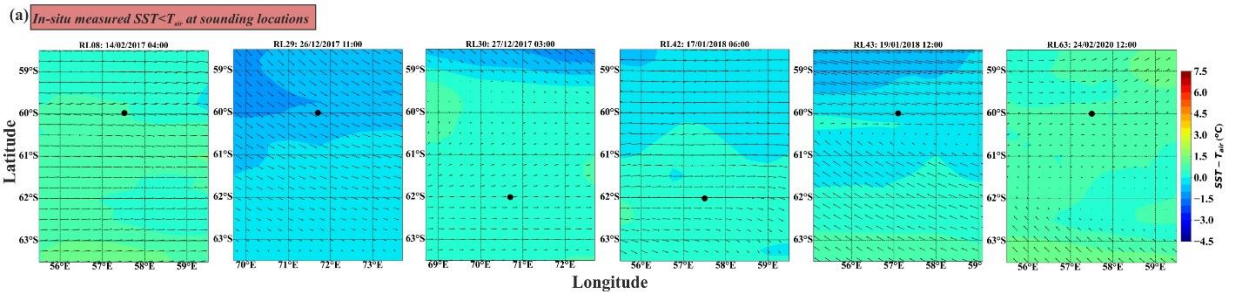

Figure A11 Same as Figure A4 but for upper air soundings launched in SACCF.

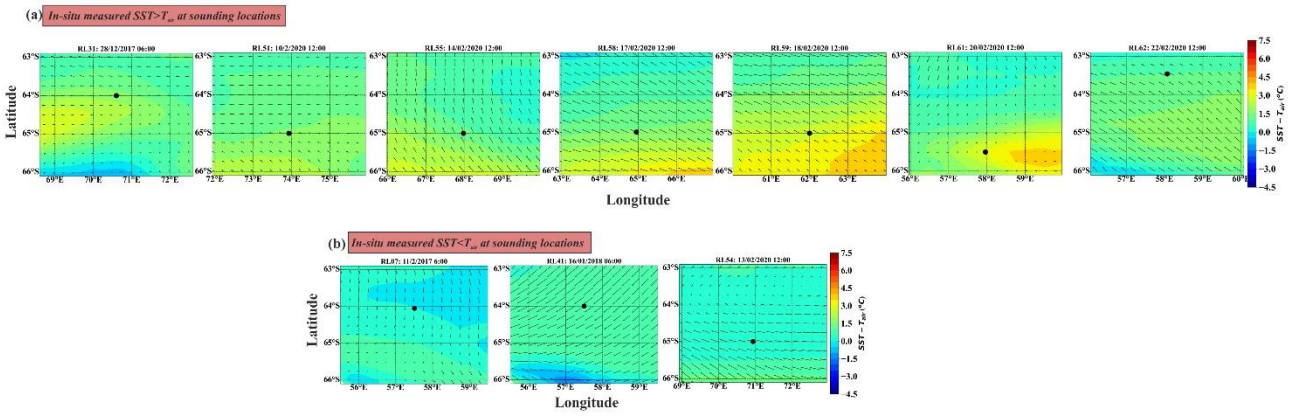

Figure A12 Same as Figure A4 but for upper air soundings launched in SB.

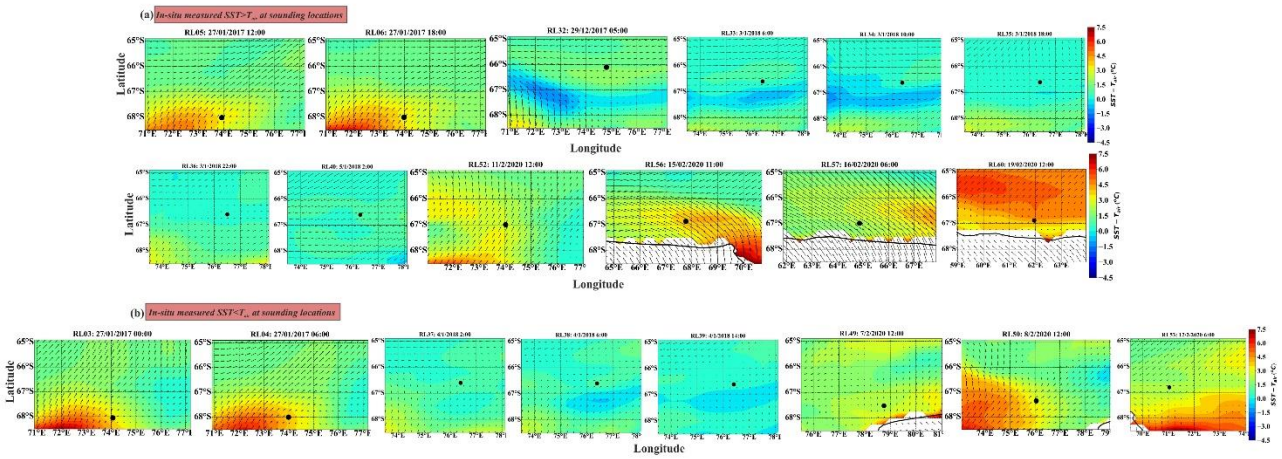

Figure A13 Same as Figure A4 but for upper air soundings launched in CA.

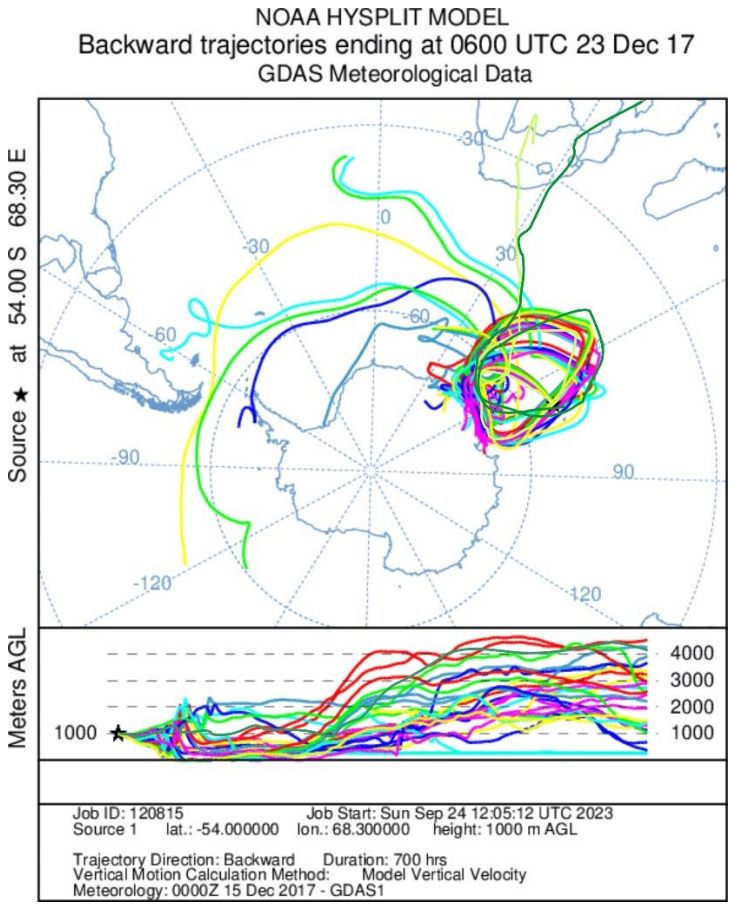

Figure A14 represents NOAA-HYSPLIT model calculated air mass back trajectories for preceding 700 hours at different heights for sounding (RL4) launched in polar front region at 54.00°S, 68.30°E around 06:00 UTC. Back-trajectories depicts prominent wind advection from the open SO region, while strong winds in this region are likely to have transported dust

aerosols from longer distances mainly originated from the western African continent and other far away continents as well as seen from air mass movement in this figure.

Meteorology and Atmospheric Physics (2023) 135:3
https://doi.org/10.1007/s00703-022-00940-3

ORIGINAL PAPER

Study of micrometeorological characteristics of the atmospheric surface layer over a tropical coastal station in Goa

Shaikh Neha Salim[1,2] · Harilal B. Menon[1,2] · N. V. P. Kiran Kumar[3] · K. Rajeev[3]

Received: 1 March 2022 / Accepted: 8 November 2022
© The Author(s), under exclusive licence to Springer-Verlag GmbH Austria, part of Springer Nature 2022

Abstract
This study presents turbulence characteristics of the atmospheric surface layer (ASL) observed during March 2015 to February 2016 over a tropical coastal site in Goa (15.46°N, 73.83°E), India. The primary datasets utilized are the 3D wind components and sonic temperature from sensors mounted on a 32-m meteorological tower at 10 and 20 m heights respectively. Eddy correlation technique has been adopted to study turbulence characteristics and is investigated under the framework of Monin–Obukhov Similarity Theory (MOST). Results revealed that normalized wind variances ($\sigma_{i=u,v,w}/u_*$) follow the '1/3' power law in highly unstable and stable conditions and approach constant values close to near-neutral conditions. In the neutral limit, it is found that $\sigma_u/u_* > \sigma_v/u_* > \sigma_w/u_*$. The normalized temperature variances (σ_T/T_*) followed $(z/L)^{-1/3}$ during unstable conditions and approach a constant value in the stable limit. The correlation coefficients for momentum (heat) flux with stability were small (high) under strong unstable and stable conditions. Also, the values of momentum flux increased as it approaches neutral conditions which are consistent with studies reported over coastal/urban locations.

1 Introduction

The surface layer is defined as the lowest part (about 10%) of the atmospheric boundary layer (Högström 1996). This layer exhibits turbulent characteristics due to radiative heating, cooling and mesoscale motions which are augmented due to surface heterogeneities of the earth's surface. This eventually controls heat, moisture and momentum transport within the surface layer (Stull 1988; Sorbjan 1989; Garratt 1992; Kaimal and Finnigan 1994). The transport of heat and moisture fluxes varies over a broad range of spatial domains, especially for forest ecosystems, terrains with complex topography, inland, semi-arid, coastal, urban and rural areas. This makes it difficult to draw a comparative analysis of statistics of estimated values with that of other locations and also from the numerical models.

The turbulence fluxes in the surface layer are well described by the Monin–Obukhov similarity theory (MOST) (Monin and Obukhov 1954), which provides suitable and acceptable empirical relations associated with variances of wind and temperature along with stability and scaling parameters. Fundamentally, MOST can suggest plausible universal functions between fluxes and mean quantities and the exact forms of these relations are to be verified from accurate observations under different stability conditions (e.g., Monin and Yaglom 1971; Kaimal and Finnigan 1994; Pahlow et al. 2001). There are many studies explaining the applicability of MOST over homogeneous surfaces (e.g., Monin and Yaglom 1971; Sorbjan 1989; Garratt 1992; Wyngaard 2010), complex terrains (Moraes et al. 2005; Yue et al. 2015), heterogeneous terrains (e.g., Babić et al. 2016) and over Greenland, Arctic pack ice and Antarctica (Forrer and Rotach, 1997; Grachev et al. 2007, 2013).

Though MOST is not 'universal' when it comes to the heterogeneity of the surface conditions (Wilson 2008), it is used in airflow and air dispersion studies even in urban locations. In modelling the transport of air pollutants, knowledge of the airflow and its turbulent characteristic close to the ground are extremely crucial. Thus, an improved understanding of this is based on the surface roughness parameter.

Responsible Editor: Clemens Simmer, Ph.D.

✉ Harilal B. Menon
harilalm@gmail.com; hbmenon@unigoa.ac.in

[1] Remote Sensing Laboratory, Goa University, Goa 403206, India

[2] School of Earth, Ocean and Atmospheric Sciences, Goa University, Goa 403206, India

[3] Space Physics Laboratory, Vikram Sarabhai Space Centre, Indian Space Research Organization, Trivandrum 695022, India

Published online: 22 November 2022

This parameter is unique for different regions and must be estimated using a series of data generated from experimental observations. Such statistical studies have been carried out in many other urban regions (Grimmond and Oke 1999; Roth 2000; Wood et al. 2010; Trini Castelli and Falabino 2013; Trini Castelli et al. 2014). Literature on these studies, particularly in coastal regions, is comparatively less (Lange et al. 2004; Singha and Sadr 2012; Grachev et al. 2018).

The experimental campaigns and field measurements to quantify the turbulence statistics of the surface layer over tropical regions are rare. Over the Indian sub-continent a few studies have been carried out at different geographical locations like inland regions (Goel and Srivastava 1990; Sivaramakrishnan et al. 1992; Kailas and Goel 1996; Rao et al. 1996; Ramana et al. 2004), semi-arid regions (Krishnan and Kunhikrishnan 2002; Reddy and Rao 2016; Sivakumar Reddy et al. 2021) complex terrains (Solanki et al. 2016, 2019; Barman et al. 2019) and coastal regions (Prakash et al. 1992; Kunhikrishnan et al. 1993; Ramachandran et al. 1994).

Most of the studies mentioned above were carried out in campaign mode during a particular season. An improved understanding of the surface layer processes requires knowledge of the turbulence characteristics during different seasons. Studies by Ramachandran et al. (1994), Namboodiri et al. (2014) and Prasad et al. (2019) have demonstrated the seasonal variability of surface layer parameters. Such studies attain important implications for modelling the turbulent exchange coefficients in regional-scale numerical models and pollutant dispersion studies.

Understanding the surface characteristics and associated energy exchange process is essential for the knowledge of local climate and modelling of the turbulent exchange in regional scale numerical models. These studies also attain relevance in addressing the problems related to pollution transport. The present study partially addresses this prerequisite and is based on yearlong observations over tropical coastal location Goa. This work has been conducted under the project 'Network of Observatories for Boundary Layer Experiments (NOBLE)' linked to the Geosphere, Biosphere Programme of the Indian Space Research Organization (ISRO-GBP), under the aegis of which boundary layer experimental setup has been established at the Goa University campus. The main objective of the study was to investigate (1) the seasonal variations of fluxes of momentum and heat, (2) the applicability of MOST under different stability conditions, and (3) to establish the empirical relationships of variances of wind components and temperature with stability.

2 Observation site, instrumentation, data and methodology

2.1 Characteristic regional meteorology

The observational site is a coastal location at Goa University Campus, Goa (15.46 N°, 73.83° E, and 50 m a.s.l), along the west is bordered by the Arabian Sea (≈ 1.3 km away) (Fig. 1). This site is located approximately 6 km from the capital city Panaji and falls under the tropical monsoon climate zone. Based upon the regional ambient meteorological conditions, the region experiences four seasons viz., pre-monsoon season (March to May), summer-monsoon season (June to September), post-monsoon season (October and November), and winter season (December to February), respectively. Since the onset of the monsoon is in the first week of June, the region receives maximum downpour during this season. All the observations were carried out from a 32-m meteorological tower installed at Goa University Campus. While choosing the study site, care has been taken

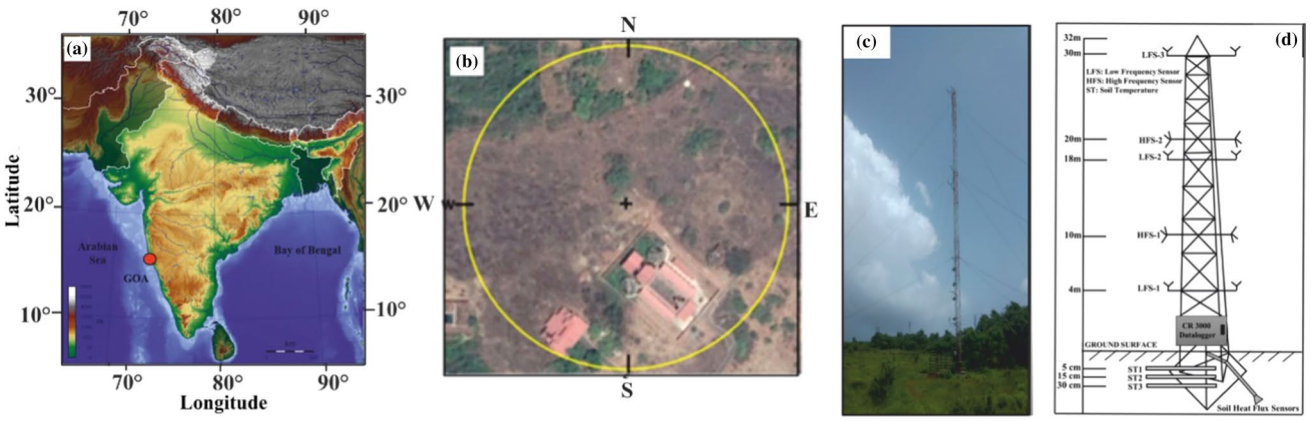

Fig. 1 **a** Topographic map of India locating study area (Goa), **b** Aerial image (taken from Google Maps) of the area surrounding the tower (indicated with a cross). The circle represents the radius of 100 m around the tower **c** the on-site installed meteorological tower (32 m tall) and **d** the schematic representing different sensors mounted at respective heights on the tower

to avoid any hindrance to the free flow of wind. The nearest building (32.5 m length and 44 m breadth and 8 m height) is located at a distance of 17 m in the south-east direction (Fig. 1) from the tower, while the bushes of about 3 m high are at a distance of 7.2 m at the northern side. Another building, 8 m high, located in the southwest direction, is at a distance of about 100 m from the tower. Moreover, on opposite sides of buildings, there is an open space.

2.2 Instrumentation, data and methodology

The data generated from 234 fair weather days during March 2015—February 2016 were considered for the study. It constitutes time-series measurements of air temperature, relative humidity, wind speed, and wind direction from slow response sensors installed on the meteorological tower at 4, 18, and 30 m heights, respectively. Additionally, data from pressure probe, rain gauge equipped at 4 m height and 3D sonic anemometer at 10 and 20 m heights, respectively, have been supplemented to the above data. The Sonic anemometer is a high-frequency sensor that measures the orthogonal components of wind and sonic temperature (T). To minimize the wake, the sonic anemometer was oriented in the direction of the prevailing wind. Details of factory-calibrated sensors are provided in Table 1. The fluctuations of wind components in the horizontal and vertical direction and sonic temperature were utilized to compute friction velocity (u_*), sensible heat flux (H), momentum flux (τ), turbulent kinetic energy (e) and stability (z/L, where z is the height of observation and L is the Obukhov length). These dynamical parameters have been estimated using the eddy correlation technique (Kaimal and Finnigan 1994; Aubinet et al. 2012).

The friction velocity (u_*) was estimated from

$$u_* = \sqrt[4]{\left(\overline{u'w'}\right)^2 + \left(\overline{v'w'}\right)^2}, \quad (1)$$

where the bar and the prime average over time and fluctuations from the mean value, respectively (Stull 1988), $\left(\overline{u'w'}\right)$ and $\left(\overline{v'w'}\right)$, are the kinematic momentum fluxes in the along and cross-wind directions. The temperature scaling parameter (T_*) and the Obukhov length (L) were computed from

Table 1 Technical details of the sensors equipped on 32 m meteorological tower

Sensors	Sensor specifications			Measured parameters	Sampling frequency
Fast response sensors		Heights: 10 m and 20 m			10 Hz
3 axis-sonic anemometer gill	Wind speed	Range	0 to 65 m s^{-1}	Orthogonal components of wind (u, $v$and$w$)	
		Accuracy	< 1.5% RMS @ 12 ms^{-1}		
	Temperature	Range	− 40 °C to + 70 °C	Sonic temperature (T)	
		Accuracy	− 20 °C to + 30 °C within ±0.5°C of ambient temperature		
Slow response sensors	Heights: 4, 18, and 30 m				1 h
Automatic weather station (AWS)	032,002-L-PT RM Young Wind sentry set	WS range	0 to > 50 m s^{-1}	Wind speed (WS) and wind direction (WD)	
		WS accuracy	± 0.5 m s^{-1}		
		WD range	0–360 °		
		WD accuracy	±5°		
	CS215-L-PT (Air temperature)	Range	− 40 °C to + 70 °C	Air temperature (AT)	
		Accuracy	±0.3°C (at 25 °C) ±0.4°C (5 °C to 40 °C) ±0.9°C (− 40 °C to + 70 °C)		
	CS215-L-PT (Relative humidity)	Range	0 to 100% RH (− 20 °C to + 60 °C)	Relative humidity (RH)	
		Accuracy	±2% (10 °C to 90% range) at 25 °C ±4% (0 °C to 100% range) at 25 °C		
	Barometric pressure sensor-CS100	Range	600 to 1100 hPa	Atmospheric pressure (P)	
	Tipping bucket rain gauge-TE525MM	Rainfall/tip	0.1 mm (0.004 in.)	Rainfall	
		accuracy	1.0% up to 2 in./h (50 mm/h)		

$$T_* = \overline{w'T'}/u_* \tag{2}$$

$$L = -\frac{u_*^3 \overline{T}}{\left(k.g\,\overline{w'T'}\right)}, \tag{3}$$

where k is von Karman constant (=0.4), g is the acceleration due to gravity, u_* is frictional velocity, and $\overline{w'T'}$ is the heat flux. The quantities e, τ, and H are computed using the following equations:

$$e = \frac{1}{2}\left[\overline{u'^2} + \overline{v'^2} + \overline{w'^2}\right] \tag{4}$$

$$\tau = \rho\sqrt{\overline{(u'w')}^2 + \overline{(v'w')}^2} \tag{5}$$

$$H = \rho.C_p\left(\overline{w'T'}\right), \tag{6}$$

where ρ is the density of air and C_p is the specific heat of air at constant pressure.

The normalized standard deviation of wind components (σ_u/u_*, σ_v/u_* and σ_w/u_*) and temperature (σ_T/T_*) are computed for every 30-min time interval using high-frequency data. Variation of these estimations with the stability parameter is obtained by averaging corresponding values at uniform intervals of z/L.

The correlation coefficients of momentum and heat flux had been computed using the following equations:

$$|r_{uw}| = \frac{\overline{uw'}}{\sigma_u \sigma_w} \tag{7}$$

$$|r_{wT}| = \frac{\overline{w'T'}}{\sigma_w \sigma_T}, \tag{8}$$

where r_{uw} and r_{wT} are correlation coefficients for momentum and heat flux, respectively.

The surface roughness length (z_o) was calculated for the data at 10 m height using the following equation (Sorbjan, 1989; Panofsky and Dutton, 1984):

$$nz_0 = lnz - k\frac{U}{u_*} - \psi_m(z/L), \tag{9}$$

where

$$\psi_m\left(\frac{z}{L}\right) = 2\ln\left(\frac{1+x}{2}\right) + \ln\left(\frac{1+x^2}{2}\right) - 2tan^{-1}(x) + \pi/2,$$

where

$$x = \left(1 - \gamma_1 \frac{z}{L}\right)^{1/4} \quad \text{for } z/L < 0 \text{ with } \gamma_1 = 16$$

$$\psi_m\left(\frac{z}{L}\right) = -5\frac{z}{L} \quad \text{for } z/L > 0,$$

where $\psi_m\left(\frac{z}{L}\right)$ is the momentum stability correction factor (Paulson, 1970; Sorbjan 1989; Panofsky and Dutton 1984).

2.3 Quality check

The sonic anemometer data have been obtained at every 0.1 s and a total of 11,232 half-an-hour data points are obtained for the present study. To eliminate the unrealistic values arising out of instrument error such as jitter, data points outside the absolute limits set for u, v, w and T were removed. This was performed for both horizontal (u, v) (− 50 m s^{-1} to + 50 m s^{-1}) and vertical (w) components of wind speed (− 10 m s^{-1} to + 10 m s^{-1}). A moving window method given by Vickers and Mahrt (1997) was applied to identify the spikes while a linear detrending method was applied to remove any long-term trend present in unprocessed u, v, w and T. While doing this, care has been taken not to consider data points outside 3.5 times the standard deviation limits. Further, to minimize the effect of any misalignment of sensors, quality checks such as double rotation and tilt corrections had been performed on data (Wilczack et al. 2001). This facilitates the alignment of the axes of the coordinate system to mean stream-wise wind direction. In addition, a stationary test was performed as a part of a quality check (Foken and Wichura 1996).

2.3.1 Stationary test

The non-stationarity of the data arises due to the diurnal variation in heating and cooling of Earth's surface and mesoscale variation of winds (e.g., Večenaj and De Wekker 2015). The application of MOST assumes that the time series data must be stationary (i.e., statistics of the turbulence do not vary with time), but the non-stationarity nature of the data becomes a key issue in the estimation of turbulence (Mahrt 1998). Thus, it is pertinent to correct the data by eliminating the non-stationary components of data from the stationary datasets before considering the applicability of MOST (Mahrt 1998). To achieve this, the methodology proposed by Foken and Wichura (1996), which is reported to effectively identify a large number of stationary data among other reported stationary tests, has been adopted to generate a stationary dataset in this study (Večenaj and De Wekker 2015; Babić et al. 2016; Foken and Wichura 1996). Adopting this method, stationary components have been extracted by taking mean values of the covariance for

every 30-min interval (18,000 data in 30 min, sampling at the frequency of 10 Hz) and are compared with the values calculated at every 5-min sub-interval (3000 data in every 5 min). If the difference between these values is less than 30% then the time series data were considered to be stationary. After incorporating this test, a quality check proposed by Agarwal et al. (1995) was adopted wherein from the data all wind speed values less than 0.5 m s^{-1} were discarded. Owing to this, a total of 7609 and 7745 half an hour of data generated from 10 and 20 m heights, respectively, were used for further analysis.

2.3.2 Gap filling method

By adopting the above-mentioned quality checks, some data points that did not meet the quality criteria were eliminated. This resulted in a gap/missing data point for certain periods, which was filled in this study by adopting the look-up table (LUT) method (Falge et al. 2001b). LUTs were generated such that missing flux values were identified based on similar meteorological conditions associated with that missing flux data (Falge et al. 2001a, b; Reichstein et al. 2005). LUTs were binned by temperature class defined by 2 °C intervals ranging from 10 to 50 °C. In each class interval mean and standard deviation of temperature and corresponding fluxes were calculated. If the gap still exists in the defined class interval in LUT then it was filled by linear interpolation. Thus, LUTs were created to reproduce the mean values of fluxes based on seasonal meteorological conditions. On average, about 32% and 31% of missing data could be identified for the heights of 10 and 20 m respectively. This ultimately resulted in 3623 and 3487 missing data points to be looked up and filled at 10 and 20 m respectively.

2.3.3 Self-correlation analysis

Without evaluating the role of self-correlation of data, the validity of MOST becomes incomplete (Mahrt 1998). The self-correlation arises due to the appearance of a common friction velocity u_* in σ_w/u_*, σ_T/T_* and z/L. To evaluate self-correlation in the present dataset, a random sampling approach described in Klipp and Mahrt (2004) was adopted. From the observed datasets of u_*, $(w'T')$, σ_w and σ_T, a new 1000 random datasets have been generated at each measurement height. Subsequently, the linear correlation coefficient was estimated between z/L and σ_w/u_* and thereafter between z/L and σ_T/T_*. The coefficients thus obtained were averaged and then $\langle R^2_{Random} \rangle$ was calculated, this indicated the measure of self-correlation due to a common variable. Similarly, R^2_{data} for the original datasets were estimated and the difference $R^2_{diff} = R^2_{data} - \langle R^2_{Random} \rangle$ was computed. The R^2_{diff} is indicative of true physical variance associated with processes governing turbulence (Klipp and Mahrt 2004). Negative values of R^2_{diff} indicate that self-correlation has a significant influence on the total variance, while as it tends to unity, the effect of self-correlation becomes less prominent (Babić et al. 2016). Results of the assessment of self-correlation are presented in Table 2. It can be seen that during unstable conditions, the self-correlation for the dataset w is found to be higher compared to that of *T*. In present data, the value of R^2_{diff} is found to be higher (> 0.25) at both heights indicating self-correlation under unstable conditions. However, for stable conditions, the values of self-correlation coefficients for w and T are found to be very small and negative. Babic et al. (2016) has also reported smaller and negative values of self-correlation coefficients during stable conditions, and it was attributed to the limitation of this method in the stable atmospheric boundary layers.

Table 2 Self-correlation analysis of the variations in σ_w/u_* and of σ_T/T_* with stability

Measurement heights	Stability	Variables	No. of data points	R^2_{data}	$\langle R^2_{Random} \rangle$	$R^2_{diff} = R^2_{data} - \langle R^2_{Random} \rangle$
10 m	Unstable	w	2044	0.63	0.36	0.27
		T	2044	0.37	0.01	0.36
	Stable	w	743	0.17	0.18	− 0.01
		T	743	0.01	0.05	− 0.04
20 m	Unstable	w	2010	0.76	0.40	0.34
		T	2010	0.37	0.02	0.35
	Stable	w	950	0.34	0.25	0.09
		T	950	0.01	0.02	− 0.01

R^2_{data} is defined as square of the correlation coefficient for the original dataset, R^2_{Random} is the coefficient of determination from self-correlation, and $R^2_{diff} = R^2_{data} - \langle R^2_{Random} \rangle$ is the fraction of true physical variance associated with processes governing the turbulence

It is noteworthy to mention that there exists a relatively low correlation (coefficient 0.63 of *w*) in R^2_{data} at 10 m height as compared to that at 20 m height (Table 2). This indicates the presence of large scatters of data points at lower heights. The self-correlation assessment which is based on linear correlation resulted in small correlations of similar magnitudes for both physical and random data. This, resulted in smaller values and exhibited a strong positive fit in a way that σ_w/u_* increases with increasing stability. In the stable regime, the correlation coefficient is small (< 0.4) for R^2_{data} and very small values of $\langle R^2_{Random} \rangle$. This resulted in very small values of R^2_{diff}.

3 Results and discussion

This section describes the diurnal and seasonal variability of surface layer meteorological parameters, fluxes of heat, momentum and associated stability conditions over a tropical coastal site, Goa. As the observational site being located near the Arabian Sea experiences land/sea breeze circulation, arising due to the differential heating of land and adjoining sea. The breeze originating from the sea brings the cool air over the heated coastal region and subsequent formation of the thermal internal boundary layer (TIBL) during the daytime (Kunhikrishnan et al. 1993; Davis et al. 2020, 2021). Thus, the diurnal evolution of thermal structure and surface characteristics of the coastal atmospheric boundary layer (CABL) is modulated by the sea/land breeze. Studies also showed that the height of CABL is lowered with the advection of sea breeze (Miller et al. 2003). Furthermore, flux-variance relationships in the atmospheric surface layer are defined by MOST, which assumes homogeneity of the surface, including surface fluxes as well as surface roughness (Stull 1988). Hence, in subsequent sections below, by adopting MOST, flux-variance relationships obtained over the study site have been discussed.

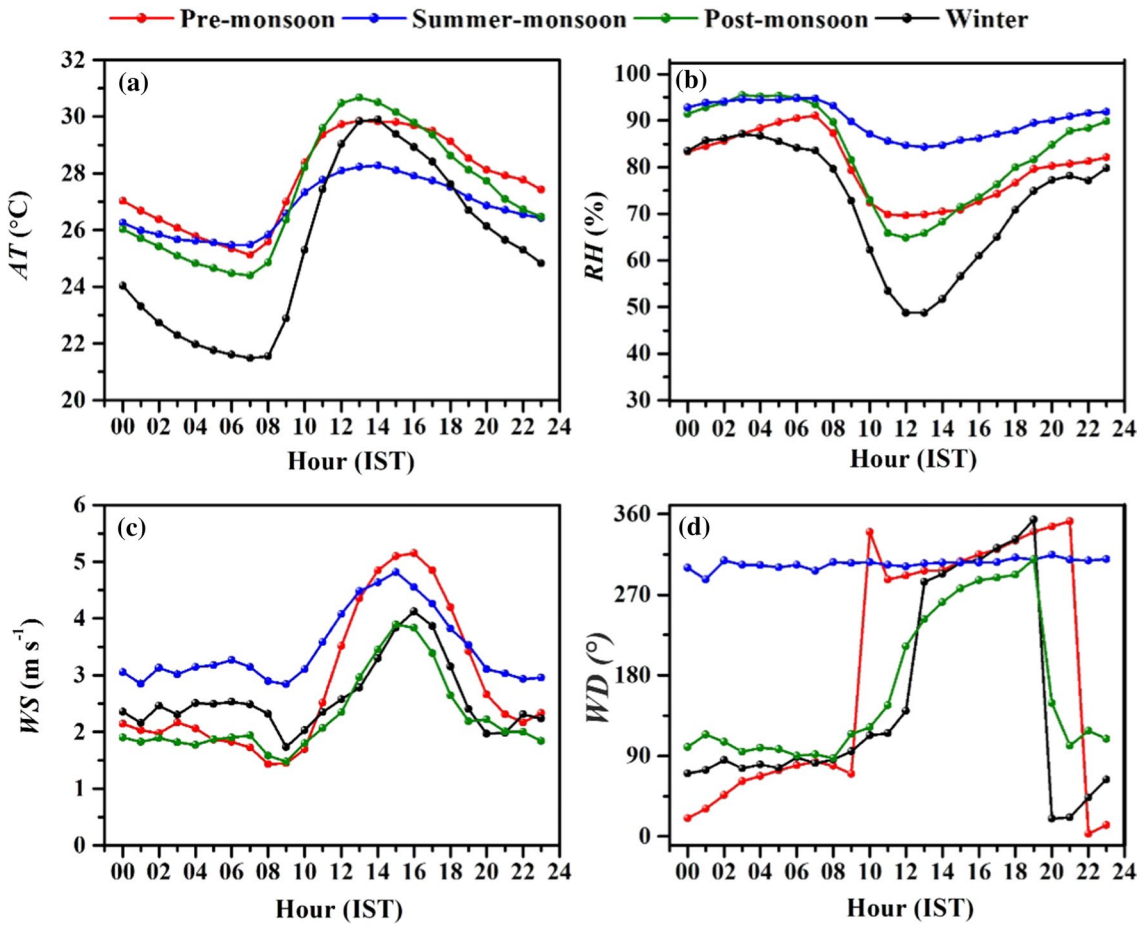

Fig. 2 Diurnal mean seasonal fluctuations of **a** air temperature (*AT*), **b** relative humidity (RH), **c** wind speed (WS) and **d** wind direction (WD) observed at 18 m heights during winter (black), pre-monsoon (red), summer-monsoon (blue) and post-monsoon (green) seasons

3.1 Diurnal mean and seasonal variation of surface layer parameters

Figure 2 depicts the seasonal mean diurnal variation of air temperature (*AT*), relative humidity (*RH*), wind speed (*WS*) and wind direction (*WD*) at 18 m height during winter, pre-monsoon, summer-monsoon, and post-monsoon seasons respectively over the experimental site. The air temperature starts increasing around 07:00 IST (IST = UTC + 05:30 h) and showed a systematic diurnal variation. The average value of maximum air temperature (AT_{max}) observed during winter, pre-monsoon, summer-monsoon and post-monsoon seasons are 29.9 ± 1.8, 29.5 ± 1.5, 28.8 ± 0.4 and 30.9 ± 1.6 ℃ with a difference in the time of occurrence [around 13:00 IST, 12:00 IST, 14:00 IST and 13:00 IST] respectively. Similarly, the average value of RH_{mean}, during each season was 62, 75, 88 and 75% respectively during daytime while 81, 84, 92 and 90% during nighttime respectively. Variation of winds revealed the prevalence of high-speed winds dominantly from a west-northwest direction (270–315°) during the summer monsoon season followed by pre-monsoon and low wind prevails in the winter season. Statistics of the wind are not only important in determining the travel period of pollutants from the source region but also control the surface concentration. Over this region, poor dispersal of pollutants is expected in the winter season.

The occurrence of the land/sea breeze system was observed with wind speeds typically < 6–7 ms^{-1} during daytime (sea breeze) and less than 3 ms^{-1}, during nighttime (land breeze) (Fig. 2). Data reveals that the dominant land breeze comes from east direction whereas, the sea breeze originates from west/northwest direction over the experimental site. The winds are from the west/northwest direction during the monsoon season (Fig. 2).

3.2 Wind characteristics at the study site

The wind-rose diagram in Fig. 3 depicts the variability of hourly averaged wind speeds obtained from the slow response sensor at 18 m and a sonic anemometer at 10 m height for the study period. The dominant wind directions at the site were mainly from the northwest to the west (wind direction is mostly within 292 and 330°) and from northeast to east directions (wind direction is mostly within a cone of 67 and 97°). In general, wind speeds greater than 3 m s^{-1} were frequently observed from the northwest and west, while wind speeds with magnitudes less than 3 m s^{-1} were observed less frequently from the east and northeast directions. Seasonal winds variability observed during the study period over the study site is represented in Supplementary Fig. 8. Dominant direction of winds during all seasons were north westerlies, except during post-monsoon season where northeast-easterlies were prominently observed.

3.3 Estimation of surface roughness length

A better understanding of the surface layer lies on the surface homogeneity. However, any heterogeneities prevailing at the surface affect the length scales. As already mentioned, the surface heterogeneity over the coastal environment leads to the formation of complex vertical structures such as TIBL and roughness sub-layers where turbulence parameters become the function of wind direction. Conventionally, the surface roughness length (z_0) is estimated using the observations of wind speed at two or more height levels in neutral stability conditions. The z_0 at a site does not change with wind speed, stability or stress. It can be changed only if the roughness elements over the surface change such as caused by an increase in the vegetation, construction of buildings

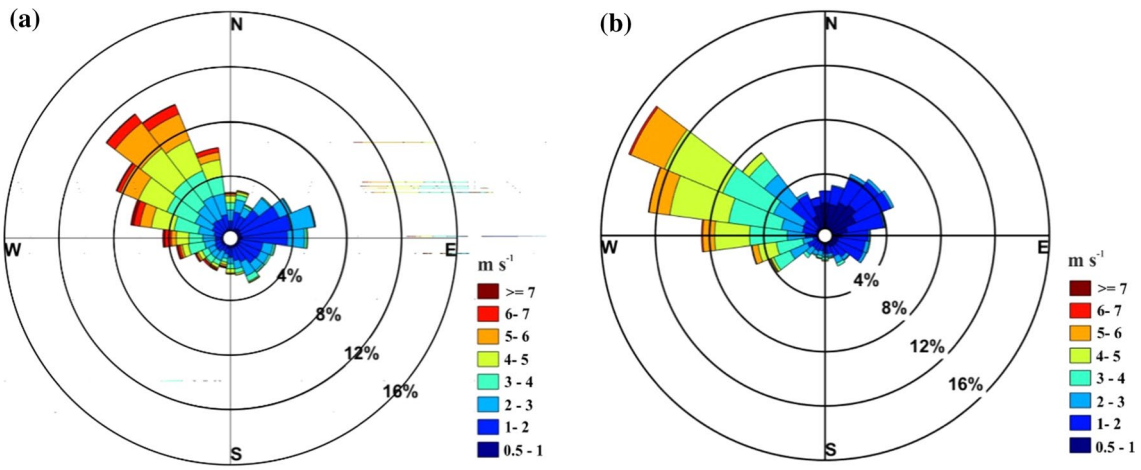

Fig. 3 Wind rose diagram observed for varying wind speed thresholds over the experimental site at **a** 18 m height using slow response sensors and **b** 10 m height using a sonic anemometer for the period from March 2015 to February 2016

Table 3 Roughness length values are estimated at a height of 10 m for different wind sectors and in all directions

Seasons	All directions (m)	330–30° (m)	30–90° (m)	90–150° (m)	150–210° (m)	210–270° (m)	270–330° (m)
Winter	0.32	0.74	0.15	0.10	0.48	0.28	0.16
Pre-monsoon	0.37	0.97	0.13	0.26	0.48	0.21	0.17
Summer-monsoon	0.24	0.94	0.15	0.21	0.49	0.31	0.17
Post-monsoon	0.19	0.41	0.08	0.26	0.51	0.27	0.13
All seasons	0.25	0.85	0.11	0.25	0.50	0.28	0.26

etc. (Stull 1988). In this study, z_0 has been calculated using the methodology described by Panofsky and Dutton (1984) (Eq. 9), the results of which are mentioned in Table 3 for six wind sectors and all wind directions around the experimental site. The data obtained at this location were categorized into each of these sectors based on wind directions encountered at 10 m height: 330–30◦ (524 data), 30–90◦ (1049 data), 90–150◦ (587 data), 150–210◦ (229 data), 210–270◦ (1267 data) and 270–330◦ (2916 data), respectively. From the values estimated over different wind sectors, it is evident that the maximum values of roughness length were found in sectors; 150–210 and 330–30° and minimum values were in sectors 30–90 and 270–330°, respectively. These high and low values portrayed varying geometry surrounding the experimental site (see Sect. 2.1).

Over the study site, from all considered wind direction sectors, the value of z_0 ranged from 0.08 m to 0.97 m. The high roughness length associated with the 330–30° sector is attributed to the daytime winds originating from the sea, while the easterly winds are dominant during the nighttime (Fig. 2). For easterly wind directions, the lowest roughness lengths were estimated. The data also confirm that the roughness length is independent of the wind speed. Larger values of z_0 in the wind direction of 150–210° is due to the presence of buildings (Fig. 1). Considering all sectors, mean values of z_0 varied between 0.19 and 0.37 m.

3.4 Seasonal mean variation of turbulent energy and heat flux parameters

Turbulence in the atmosphere is the coupled effect of buoyancy-induced thermals and mechanical eddies. In this study, an approximation for thermal turbulence is studied using sensible heat fluxes (H) while mechanical turbulence is studied using momentum fluxes (τ). The effect of both buoyancy, as well as mechanical shear, is illustrated using turbulent kinetic energy (e). As discussed, (in Sect. 2.3.2), estimation of fluxes was obtained after adopting a look-up method for filling missing data gaps (Falge et al. 2001a, b). Figure 4 shows the seasonal mean diurnal variations observed at 10 m height (For variations at 20 m height refer to Supplementary Fig. 9a). Variation of sensible heat flux showed negative values during nighttime (H directed towards the surface) and increases to positive values around 07:00 IST (H directed away from the surface). Later, it showed a systematic increase and reaches a peak value between 13:00 and 14:00 IST followed by a further decrease to attain negative values after 17:30 IST. It is observed that sensible heat flux at 10 m attains maximum seasonal mean value during pre-monsoon ($76 \mathrm{Wm}^{-2}$), followed by winter ($61 \mathrm{Wm}^{-2}$), post-monsoon ($51 \mathrm{Wm}^{-2}$) and minimum during the summer monsoon season ($11 \mathrm{Wm}^{-2}$), respectively. Seasonal mean values of sensible heat flux at 10 m lie within 15% of the data obtained at 20 m. Lower values of heat flux during summer-monsoon show the prevalence of weak heat flux exchanges due to cloud coverage during this season. Seasonal mean values of turbulent kinetic energy (e) were dominantly high during the summer monsoon season due to prevailing strong winds (Fig. 2 and Supplementary Fig. 9b). Systematic diurnal variation in e showing noontime enhancement was observed during all seasons at both heights. The highest seasonal mean values of e were observed during the summer monsoon season ($\approx 0.76 \pm 0.33 \mathrm{m}^2\mathrm{s}^{-2}$ at 10m height). Variation of momentum flux (τ) exhibits a typical diurnal cycle in phase with turbulent kinetic energy (e) during all the seasons. The highest seasonal mean stress (τ) at 10 m was observed during summer-monsoon ($\approx 0.17 \pm 0.09 \mathrm{Nm}^{-2}$) followed by moderate during pre-monsoon ($\approx 0.11 \pm 0.04\ \mathrm{Nm}^{-2}$) and lowest during post-monsoon ($\approx 0.07 \pm 0.03\ \mathrm{Nm}^{-2}$), respectively. On the diurnal scale, the highest momentum flux transfer occurred during noon hours while the lowest was during the night. The observed fluctuations in these atmospheric fluxes (heat and momentum) are associated with variability in temperature and wind speed which are responsible for altering the stability of the atmosphere within the surface layer. Thus, in this study, we further examined z/L to understand the changes in the atmospheric state due to mesoscale processes which induce or diffuse the vertical motion of eddies. The observed diurnal variation of z/L at 10 m height showed that during the evening and nocturnal hours highly stable conditions prevailed while during daytime highly unstable conditions were dominant. Nighttime stable stratification

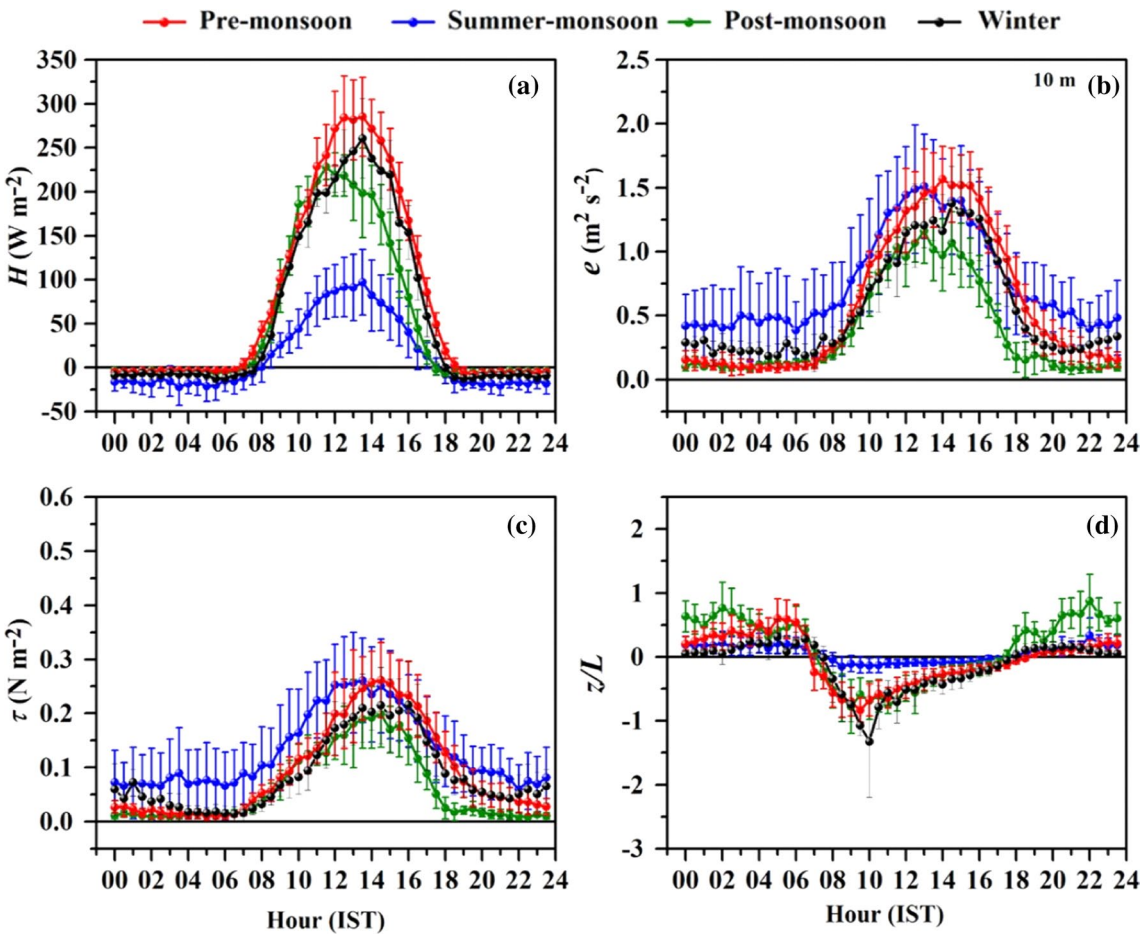

Fig. 4 Diurnal mean seasonal fluctuations of **a** sensible heat flux (H), **b** turbulent kinetic energy (e), **c** momentum flux (τ), and **d** stability parameter (z/L) observed at 10 m winter (black), pre-monsoon (red), summer-monsoon (blue) and post-monsoon (green) seasons. Error bars indicate standard deviations

was due to the suppressed vertical mixing by buoyancy. Similar diurnal variation of stability parameter (z/L) was also observed at 20 m with slight variations in its magnitude (see Supplementary Fig. 9d).

3.5 Turbulent statistics

In this section, we evaluate the universal functions of MOST over inhomogeneous terrain of coastal site Goa by comparing our data with those observed over flat, homogeneous and heterogeneous locations. According to the MOST, the normalized standard deviation of velocity components (i.e., $\sigma_{i=u,v,w}$) are functions of z/L within the surface layer. Equation 10 proposed by Panofsky and Dutton (1984) was used to investigate the validity of MOST over the experimental site.

$$\sigma_{i=u,v,w}/u_* = C1(1 + C2z/L)^{C3} \quad (10)$$

In general, the coefficients C1,C2 and C3 experimentally determined. The universal function (Eq. 10) is valid for vertical fluctuations over homogenous terrains under unstable and stable conditions (Moraes et al. 2005). However, in recent years, data obtained from heterogeneous terrains show good general agreement with Eq. 10 for horizontal variances under unstable and stable conditions (Xu et al. 1993; Smedman 1988; Mahrt 1998; Roth 2000; Al-Jiboori et al. 2002; Yusup et al. 2008; Weber and Kordowski 2010; Wood et al. 2010; Fortuniak et al. 2013; Trini Castelli et al. 2014). In this study, the coefficients C1 and C2 are determined using least-squares regression. The empirical fit using Eq. 10 is applied to the data assuming C3=1/3 for both unstable and stable conditions. The following stability conditions are defined as neutral: $-0.1<z/L<0.1$ for which $z/L\rightarrow 0$; unstable: $z/L<-0.1$; stable:$z/L>0.1$.

3.5.1 The normalized standard deviation of horizontal (σ_u/u_* and σ_v/u_*) and vertical (σ_w/u_*) components of wind with stability parameter (z/L)

Figure 5 shows the variation of normalized standard deviations of along wind (σ_u/u_*), cross wind (σ_v/u_*), and vertical wind components as a function of z/L at 10 m and 20 m heights for z/L<0 and z/L>0 conditions, respectively. Data points in Fig. 5 represent bin averaged $\sigma_{i=u,v,w}/u_*$ collected with z/L, where the vertical error bar of each data point represents the standard deviation of data points within a particular bin. In Fig. 5 the curves (solid black line) are estimated using the best fits of the $\sigma_{i=u,v,w}/u_*$ over the Goa site using Eq. 10 and are plotted with the observed data. For comparison, the curves generated using the function given by Xu et al. (1997), Trini Castelli et al. (2014) representing sub-urban reference sites and Fortuniak et al. (2013) representing urban reference are presented in Fig. 5 and Table 4. In Table 4, we also report the standard deviations of coefficients of C1 and C2 observed in this study to present the related uncertainties.

The curves of $\sigma_{i=u,v}/u_*$ produced with reference locations, lie within the variability range of the observed data for the Goa site. The data of $\sigma_{i=u,v}/u_*$ are close to the observations of Xu et al. (1997) and Trini Castelli et al. (2014) compared to the observations of Fortuniak et al. (2013). The curves corresponding to Fortuniak et al. (2013) are found to be consistently lower compared to our data for $-0.2 < z/L < 0$, but the data from Xu et al. (1997) and Trini Castelli et al. (2014) agree well. Results during unstable conditions show that $\sigma_{i=u,v}/u_*$ fits reasonably well with the MOST free-convection prediction of the '1/3' slope for $z/L < -0.2$, the same as observed with the urban/suburban reference locations. Data of $\sigma_{i=u}/u_*$ compares well with the function given by Roth (1993) over a suburban region (not shown). As can be noticed from Table 4, the constant C2 of u in unstable conditions are less than those obtained over reference locations. A possible explanation is the following: the data observed over the Goa site during the unstable conditions (daytime) are of sea breeze, originating from west/northwest direction with wind speed greater than 3 ms^{-1} (Fig. 3). The daytime

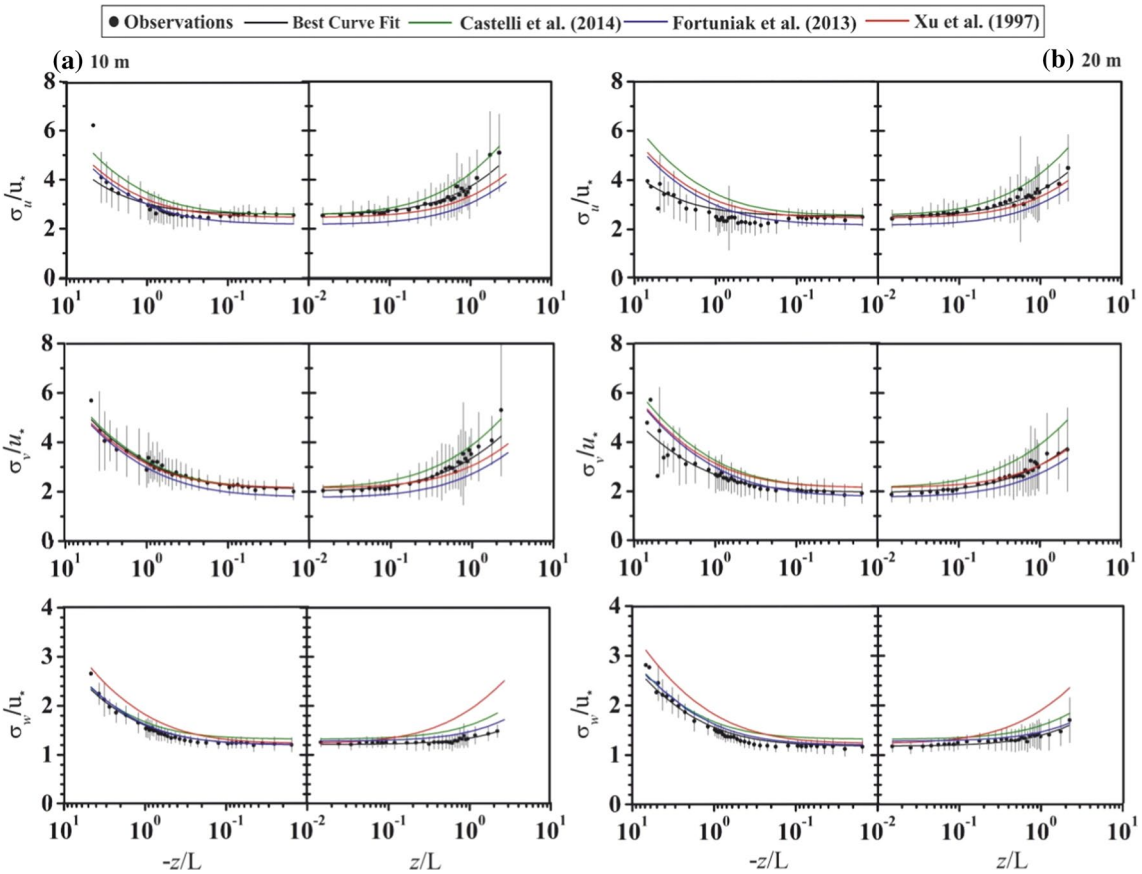

Fig. 5 Variations of normalized standard deviations of wind velocities $\sigma_{i=u,v,w}/u_*$ studied as a function of z/L for unstable (z/L < 0) and stable conditions (z/L > 0) over the observational site at 10 m height (left panel) and 20 m height (right panel). Error bars indicate standard deviations. The black solid curve represents functional fit using Eq. 10; the green, blue and red curves represent the function curves of Trini Castelli et al. (2014), Fortuniak et al. (2013) and Xu et al. (1997) respectively

Table 4 Comparison of coefficients of normalized standard deviations of wind components with stability obtained from the present study at 10 and 20 m heights during the unstable (z/L< 0) and stable (z/L> 0) conditions with the coefficients reported from studies over other locations

Locations	Unstable			Stable		
	σ_u/u_*	σ_v/u_*	σ_w/u_*	σ_u/u_*	σ_v/u_*	σ_w/u_*
Nanjing (urban) Xu et al. (1997)	$2.46(1-1.20z/L)^{1/3}$	$2.15(1-2.17z/L)^{1/3}$	$1.23(1-2.30z/L)^{1/3}$	$2.46(1+1.50z/L)^{1/3}$	$2.15(1+1.91z/L)^{1/3}$	$1.23(1+2.80z/L)^{1/3}$
Łód´z—Narutowicza, Urban Furtunaik et al. (2013)	$2.18(1-1.62z/L)^{1/3}$	$1.79(1-3.75z/L)^{1/3}$	$1.20(1-1.50z/L)^{1/3}$	$2.17(1+1.78z/L)^{1/3}$	$1.70(1+2.76z/L)^{1/3}$	$1.28(1+0.52z/L)^{1/3}$
Turin in Northern Italy, Suburban Trini Castelli et al. (2014) 09 m	$2.41(1-3.06z/L)^{1/3}$	$2.09(1-5.09z/L)^{1/3}$	$1.29(1-2.01z/L)^{1/3}$	$2.41(1+5.69z/L)^{1/3}$	$2.09(1+7.42z/L)^{1/3}$	$1.29(1+0.84z/L)^{1/3}$
25 m	$2.56(1-1.49z/L)^{1/3}$	$2.14(1-2.60z/L)^{1/3}$	$1.32(1-1.04z/L)^{1/3}$	$2.56(1+3.69z/L)^{1/3}$	$2.14(1+5.14z/L)^{1/3}$	$1.32(1+0.79z/L)^{1/3}$
Goa, Coastal, India (Present study)	$2.59(1-0.58z/L)^{1/3}$	$2.11(1-2.55z/L)^{1/3}$	$1.21(1-1.34z/L)^{1/3}$	$2.57(1+2.09z/L)^{1/3}$	$2.01(1+3.79z/L)^{1/3}$	$1.21(1+0.36z/L)^{1/3}$
Total data at 10 m	2.59 ± 0.12	2.11 ± 0.10	1.21 ± 0.03	2.57 ± 0.12	2.01 ± 0.13	1.21 ± 0.01
	0.58 ± 0.24	2.55 ± 0.24	1.34 ± 0.01	2.09 ± 0.25	3.79 ± 0.46	0.36 ± 0.01
Total data at 20 m	$2.54(1-0.38z/L)^{1/3}$	$1.97(1-1.57z/L)^{1/3}$	$1.18(1-1.33z/L)^{1/3}$	$2.52(1+1.89z/L)^{1/3}$	$1.95(1+2.91z/L)^{1/3}$	$1.18(1+0.69z/L)^{1/3}$
	2.54 ± 0.12	1.97 ± 0.20	1.18 ± 0.04	2.52 ± 0.08	1.95 ± 0.07	1.18 ± 0.02
	0.38 ± 0.07	1.57 ± 0.30	1.33 ± 0.11	1.89 ± 0.17	2.91 ± 0.11	0.69 ± 0.07

We also present the uncertainty in the coefficients (Eq. 10)

coastal atmospheric boundary layer is lowered with the onset of sea breeze and subsequent formation of TIBL (Kunhikrishnan et al. 1993). The reduction in the contribution of convective activity and mesoscale wind during daytime lowers the boundary layer height. This may be the reason for the lower value of the constant C2 of σ_u in Eq. 10. In this study, the effect is observed for both the data points.

The stable data of $\sigma_{i=u,v}/u_*$ as a function of z/L depicted in Fig. 5 show that Goa site observations of $\sigma_{i=u,v}/u_*$ lie between suburban and urban locations, indicating the turbulence during stable conditions over the Goa site has similar features as that of the reference locations. As supported by Trini Castelli and Falabino (2013), turbulence has common features under low wind conditions irrespective of locations and this is confirmed by Trini Castelli et al. (2014). As already stated, present data during the stable conditions (nighttime) are of land breeze, originating from easterly direction, with wind speed less than 2 ms^{-1} (except in monsoon season) (Fig. 3). The present results show that the turbulence in low wind conditions has common features as that of the reference locations during the stable conditions.

Studies have shown that the $\sigma_{i=u,v}/u_*$ are better scaled with mixed-layer similarity variables. Due to the non-availability of direct information on mixed-layer depth (z_i), the variations of $\sigma_{i=u,v}/u_*$ on z_i/L cannot be verified. Regardless of the scaling details, present results show dependency of $\sigma_{i=u,v}/u_*$ on z/L and follow '1/3' power law. Similar behavior was reported by several researchers over different regions across the world such as by Moraes et al. (2005) over rough and forest terrain, Quan and Hu (2009) in Beijing, Wood et al. (2010) in London and Sivakumar Reddy et al. (2021) in semi-arid region Ananthapur, India.

The curves of σ_w/u_* produced with reference locations lie within the variability range of the observed σ_w/u_* data for the Goa site. The curves increase with instability and follow '1/3' power law. The agreement of σ_w/u_* with the suburban results of Trini Castelli et al. (2014) is good at large instabilities (z/L < − 1) but for small negative values of z/L, the present data lie below their curve, whereas present observations agree with the curve of Xu et al. (1997) for z/L > − 0.2 but lie below their curve for z/L < − 0.2. Variability between locations, however, was quite considerable. The observations from Fortuniak et al. (2013) compare well with the present data.

The σ_w/u_* values are constant up to z/L ≈ 0.7−0.8, after which an increase was observed. The present results agree well with the data of Trini Castelli et al. (2014) and Fortuniak et al. (2013). Similar behavior has been reported over other urban locations (Al-Jiboori et al. 2002; Weber and Kordowski 2010) and natural surfaces by Pahlow et al. (2001). The present data follow the data of Xu et al. (1997) for z/L < 0.1; afterwards, their data show an increase. Present results are consistent with the observations of Nieuwstadt (1984), who found σ_w/u_* to be approximately constant at 1.4. Nieuwstadt's observations (see their Fig. 2) are concentrated on the range 0.1 < z/L < 2.0. Our data agree well with their data up to z/L≈0.8, after which they depart slightly from being constant. According to Pahlow (2001), the increase of σ_w/u_* in strongly stable conditions might be an effect of turbulence damping. In such situations, only small turbulence eddies exist, which are no longer directly influenced by the surface and u_* becomes small. Results show the dependence on z/L as described by Eq. 10.

Table 5 provides a comparison of near-neutral values of σ_u/u_*, σ_v/u_* and σ_w/u_* obtained from the present study with other reported studies. From Table 5, one can see that the mean values of $\sigma_u/u_* > \sigma_v/u_* > \sigma_w/u_*$ in the neutral regime agree well with other suburban and urban locations (Högström et al. 1982; Yersel and Goble 1982; Roth 1993; Zhang et al. 2001; Change et al. 2009). The neutral values

Table 5 Comparison of coefficients of normalized standard deviations of wind components obtained during near-neutral conditions from the present study at 10 and 20 m heights with the coefficients reported from studies over other locations

Author	Place (Surface)	σ_u/u_*	σ_v/u_*	σ_w/u_*
Högström et al. (1982)	Uplandia (Urban location)	2.5	2.2	1.5
Panofsky and Dutton (1984)	Kansas, USA (Flat and uniform terrain)	2.39 ± 0.03	1.92 ± 0.05	1.25 ± 0.03
Yersel and Goble (1986)	Urban location	2.7	2.2	1.2
Roth (1993)	Suburban location	2.3	2.5	1.2
Krishnan and Kunhikrishnan (2002)	Ahmedabad (Semi-arid) Southwest monsoon (Daytime)	2.32 ± 0.39	2.29 ± 0.22	1.37
Ramana et al. (2004)	Lucknow (Inland)	2.63 ± 0.36	2.19 ± 0.06	1.0 ± 0.04
Chang et al. (2009)	Oklahoma City (7.8–83.2 m)	2.4-1.8	2.2-1.4	1.5-1.2
Fortuniak et al. (2013)	Narutowicza (urban location)	2.28 ± 0.20	1.79 ± 0.23	1.27 ± 0.09
Goa, Coastal, India (Present Study)	Total data at 10 m	2.59 ± 0.23	2.11 ± 0.20	1.21 ± 0.08
	Total data at 20 m	2.52 ± 0.28	1.97 ± 0.26	1.19 ± 0.10

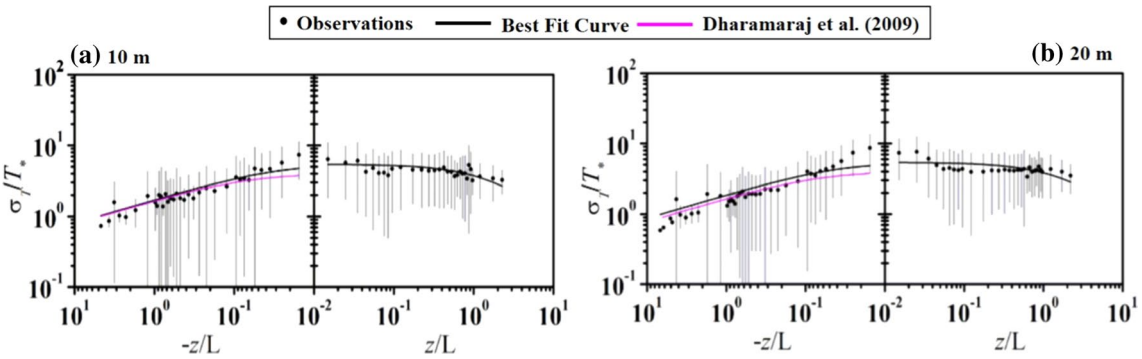

Fig. 6 Same as Fig. 5 but for the variations of σ_T/T_*

of $\sigma_{i=u,v,w}/u_*$ observed over the Goa site are slightly higher than the consensus values reported by Panofsky and Dutton (1984). Further, the mean σ_w/u_* value (≈ 1.21) lies within the values (1.1–1.4) as reported by Panofsky and Dutton (1984) over flat and complex terrains.

It is noteworthy to mention the standard deviation of the coefficients C1 and C2 (Eq. 10) for different seasons are presented in Supplementary Table 7. From this, it is clear that the seasonal differences are well within the limits of uncertainties and hence turbulence statistics are nearly independent of seasons. The recommended functions of $\sigma_{i=u,v,w}/u_*$ for the Goa site with related uncertainty are given in Tables 4, 5 for near-neutral conditions. Ramana et al. (2003) also showed that turbulent statistics are nearly independent of seasons in Lucknow, India. As suggested by Falabino and Trini Castelli (2017), the functional forms developed over certain location describes the turbulent quantities of the location and could be of interest to air pollution studies. In air quality calculation, in addition to the meteorological parameters, frictional velocity, Obukhov length and roughness length are often considered. Thus, the empirical coefficients which are estimated based on the local scaling and similarity relationships under the framework of MOST over the coastal Goa site could be applied in dispersion models and boundary layer parameterization schemes for this region.

Table 6 Comparison of coefficients of normalized standard deviations of temperature obtained from the present study at 10 and 20 m heights during the unstable ($z/L< 0$) and stable ($z/L> 0$) conditions with the coefficients reported in studies over other locations

Locations	Unstable ($z/L< 0$) σ_T/T_*	Stable ($z/L>0$) σ_T/T_*
MONTBLEX-90, inland, southwest monsoon (Sivaramakrishnan et al. 1992)	$5.12(1-8z/L)^{-1/3}$	$8.0(1+0.67z/L)^{-1}$
Rural (Andreas et al. 1998)	$3.2(1-28.4z/L)^{-1/3}$	3.2
Beijing (Al-Jiboori et al. 2002)	$2.23(-z/L)^{-1/3}$	3.1
Ahmedabad, Semi-arid, India, Southwest monsoon (Krishnan and Kunhikrishnan 2002)	$6.5(1-9.5z/L)^{-1/3}$	$6.5(1+0.8z/L)^{-1}$
Lucknow, India, Inland (Ramana et al. 2004)	$6.56(1-9.5z/L)^{-1/3}$	$6.45(1+0.25z/L)^{-1}$
Beijing (Quan and Hu 2009)	$1.5(-z/L)^{-1/3}$	$3.0(z/L)^{-1/3}$
Łódz-Lipowa, Poland, urban (Fortuniak et al. 2013)	$1.60(-z/L)^{-1/3}$	$4.18+0.15z/L^{-0.69}$
Łódz-Narutowicz, Poland, urban (Fortuniak et al. 2013)	$1.61(-z/L)^{-1/3}$	$3.60+0.13z/L^{-0.74}$
Goa, Coastal, India (Present study)		
Total data at 10 m	$5.42(1-33z/L)^{-1/3}$ $1.60(-z/L)^{-1/3}$	$5.42(1+0.50z/L)^{-1}$
Total data at 20 m	$5.40(1-25z/L)^{-1/3}$ $1.65(-z/L)^{-1/3}$	$5.40(1+0.41z/L)^{-1}$

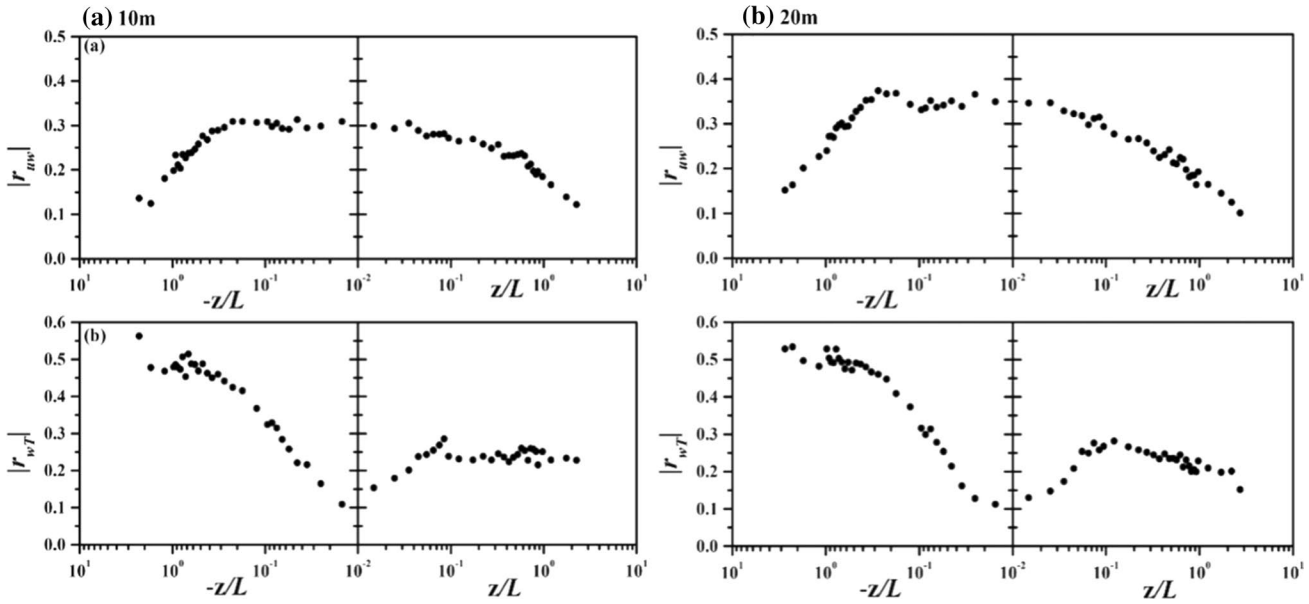

Fig. 7 Variations of $|r_{uw}|$ and $|r_{wT}|$ studied as a function of z/L for unstable (z/L<0) and stable conditions (z/L>0) at 10 m (left panel) and 20 m height (right panel), respectively, dispersion models in estimating fluxes where mean temperature and wind data are fed as input (e.g., Quan and Hu 2009)

3.5.2 The normalized standard deviation of temperature (σ_T/T_*) with stability (z/L)

The functional form of relationship applied to present observations of temperature are given as follows:

$$\sigma_T/T_* = C1(1 - C2z/L)^{-1/3} \quad (z/L < 0) \tag{11}$$

$$\sigma_T/T_* = C1(1 - C2z/L)^{(-1/3)} \quad (z/L < 0) \tag{12}$$

$$\sigma_T/T_* = C1(-z/L)^{(-1/3)} \quad (z/L < 0), \tag{13}$$

where C1 and C2 are the coefficients estimated in the present study. Equations 11 and 12 are considered following the studies carried out over the Indian region (Sivaramakrishnan et al. (1992); Krishnan and Kunhikrishnan (2002); Ramana et al. (2004); Dharmaraj et al. (2009)), while Eq. 13 was considered following Wyngard et al. (1971).

Figure 6 depicts bin averaged normalized standard deviations of temperature (σ_T/T_*) plotted against stability parameter (z/L) for unstable and stable conditions at 10 and 20 m heights. It is observed that temperature variations followed the "− 1/3 power law" during thermally unstable conditions as proposed by Wyngaard et al. (1971) while during stable conditions, σ_T/T_* showed a slight decrease with an increase in z/L.

In Fig. 6 solid black lines represent the empirical fitting curves obtained from the present study using the relations given in Eqs. 11 and 12. This fitted curve agrees well with the curves obtained by Dharamraj et al. (2009) over Indian locations. During unstable conditions, the values C1 and C2 defined in Eqs. 11 and 12 are respectively low and high over this location when compared with the measurements from other Indian locations like Ahmedabad (semi-arid) and Lucknow (inland) (Table 6). In stable conditions, values of σ_T/T_* attains a constant value of about 5.4 which is close to the values reported by Fortuniak et al. (2013) over the urban location. However, as z/L approaches highly stable conditions, a small decrease in σ_T/T_* is observed.

The value of the constant C1 in Eq. 13 as suggested by Wyngard (1971) was 9.5 for unstable conditions. Our results show that the constant value is around 1.6 for both 10 and 20 m heights respectively, which is very close to the values reported by Fortuniak et al. (2013) and Quan and Hu (2009) (Table 6). The variation of (σ_T/T_*) follows $(z/L)^{-1/3}$ during unstable conditions and approaches constant value in stable conditions.

3.6 Correlation coefficient

Figure 7a, b show correlation coefficients of momentum ($|r_{uw}|$) and heat flux ($|r_{wT}|$) as a function of stability (z/L) estimated at 10 m and 20 m heights respectively. The values of $|r_{uw}|$ and $|r_{wT}|$ were respectively small and large during strong unstable conditions, whereas during neutral conditions the values of $|r_{uw}|$ becomes large (greater than 0.3) (Fig. 7). Results indicate that the value of momentum flux is larger in neutral conditions and decreases with instability.

This could be attributed to the enhancement of convection due to significantly high heat flux during highly unstable conditions. The values of $|r_{uw}|$ and $|r_{wT}|$ at both heights during unstable conditions were, respectively, greater or lesser than 0.1 and 0.55. A similar trend was reported in other locations such as coastal (Singha and Sadr 2012), urban (e.g., Al-Jiboori et al. 2002; Wood et al. 2010) and rural regions (e.g., Kaimal and Finnigan 1994). The mean values of $|r_{uw}|$ obtained for unstable and stable conditions were 0.29 and 0.20, respectively, at 10 m, which lies within the range between 0.1 and 0.4 as reported for other urban locations (Roth 1993). The mean values of $|r_{wT}|$ during unstable conditions ($z/L<-0.1$) were about 0.48 and 0.46 at 10 and 20 m, respectively, which were slightly higher than those reported over London ($|r_{wT}| \approx 0.4$) by Wood et al. (2010), whereas during stable conditions ($z/L>0.1$) the values of $|r_{wT}|$ remained almost constant ≈ 0.22 and 0.24 at 10 and 20 m, respectively, which were found to be similar to the values of r_{wT} (≈ 0.24) reported by Nieuwstadt (1984). During neutral conditions, the obtained value of these measurements was 0.29 and 0.33 for $|r_{uw}|$ at 10 and 20 m heights, respectively. These turbulent correlation coefficients are crucial for dispersion models in estimating fluxes where mean temperature and wind data are fed as input (e.g., Quan and Hu 2009).

4 Summary and conclusions

This paper describes turbulence characteristics of the atmospheric surface layer over a tropical coastal site in Goa (15.46°N, 73.83°E, and 50 m a.s.l.), India. The datasets used were retrieved from slow and fast response sensors mounted at different heights on a 32 m meteorological tower. The observed data revealed that the low offshore wind speed (<3 ms^{-1}) dominates during nighttime, while onshore wind speed greater than 3 ms^{-1} dominates during daytime. This aspect along with the urban geometry of the location represents the distinct characteristics of the database.

The normalized standard deviations of wind components were analyzed within the framework of Monin–Obukhov similarity theory (MOST). Results show that $\sigma_{i=u,v,w}/u_*$, follow the '1/3' power law in the free convection limit, and approach constant value for neutral stratifications. Results also confirm that normalized wind components follow '1/3' in stable conditions. Thus, the power function (Eq. 10) can be used to model for both stable and unstable conditions. The suburban and urban functions proposed by Xu et al. (1997), Fortuniak et al. (2013), and Trini Castelli et al. (2014) lie within the variability range of the Goa observations.

The mean values of $\sigma_u/u_* > \sigma_v/u_* > \sigma_w/u_*$ in the neutral regime agree well with other suburban and urban locations. The present results confirm that the surface turbulence characteristics observed over this experimental site obey similarity relations. Present results also show that turbulence statistics are independent of seasons.

Additionally, the normalized temperature variances (σ_T/T_*) follow $(z/L)^{-1/3}$ during unstable conditions and approach a constant value in the stable limit.

The correlation coefficients for momentum and heat flux observed over the study site were, respectively, small and high under strong unstable and stable conditions, while the mean values of momentum flux increased steeply as it approached neutral conditions. This characteristic pattern was in line with the results reported over urban/cities and rural locations.

Supplementary Information The online version contains supplementary material available at https://doi.org/10.1007/s00703-022-00940-3.

Acknowledgements This study has been conducted under Project Network of Observatories for Boundary Layer Experiments (NOBLE) as a part of the Geosphere-Biosphere Programme funded by the Space Physics Lab of Indian Space Research Organization (ISRO-SPL). The authors acknowledge the Vice-Chancellor of Goa University for rendering the facilities to successfully conduct this experiment. Valuable support extended by Dr. Siva Kumar Reddy Nagi Reddy from Space Physics Lab of Vikram Sarabhai Space Centre (VSSC-SPL) is greatly acknowledged. Author's express their sincere gratitude to all the anonymous reviewers for contributing significantly for improving this manuscript.

Author contributions Not applicable.

Funding The study has been funded under the project 'Network of Observatories for Boundary Layer Experiments' (NOBLE) funded by the Space Physics Lab of Indian Space Research Organization (ISRO-SPL) with project sanction number NO.DS_2B-13015/12019.

Data availability Data belongs to the Space Physics Lab of the Indian Space Research Organization (ISRO-SPL); hence any sharing of data requires their prior permission.

Code availability Not applicable.

Declarations

Conflict of interest The authors declare no competing interests.

References

Agarwal P, Yadav AK, Gulati A, Raman S, Rao SM, Singh MP, Nigam S, Reddy N (1995) Surface-layer turbulence processes in low wind speeds over land. Atmos Environ 29:2089–2098. https://doi.org/10.1016/1352-2310

Al-Jiboori MH, Xu Y, Qian Y (2002) Local similarity relationships in the urban boundary layer. Boundary-Layer Meteorol 102:63–82. https://doi.org/10.1023/a:1012745322728

Andreas EL, Hill RJ, Gosz JR, Moore DI, Otto WD, Sarma AD (1998) Statistics of surface-layer turbulence over terrain with metre-scale heterogeneity. Boundary-Layer Meteorol 86:379–408. https://doi.org/10.1023/A:1000609131683

Aubinet M, Vesala T, Papale D (2012) Eddy covariance: a practical guide to measurement and data analysis. Springer Science & Business Media. Springer, Netherlands

Babić K, Rotach MW, Klaić ZB (2016) Evaluation of local similarity theory in the wintertime nocturnal boundary layer over heterogeneous surface. Agric for Meteorol 228:164–179. https://doi.org/10.1016/j.agrformet.2016.07.002

Barman N, Borgohain A, Kundu SS, Roy R, Saha B, Solanki R, Kumar NVPK, Raju PLN (2019) Daytime temporal variation of surface-layer parameters and turbulence kinetic energy budget in topographically complex terrain around Umiam, India. Boundary-Layer Meteorol 172:149–166. https://doi.org/10.1007/s10546-019-00443-6

Chang S, Huynh G, Tofsted D (2009) Turbulence characteristics in Oklahoma City measured from an 83-meters pseudo tower. In: Boundary Layers and Turbulence Committee (ed) Eighth symposium on the urban environment, Phoenix, Arizona, 12–15 January

Davis EV, Rajeev K, Mishra MK (2020) Effect of clouds on the diurnal evolution of the atmospheric boundary-layer height over a tropical coastal station. Bound-Layer Meteorol 175:135–152. https://doi.org/10.1007/s10546-019-00497-6

Dharmaraj T, Chinthalu G, Raj PE (2009) Turbulence characteristics in the atmospheric surface layer during of 1997 over a semi-arid location in India. Meteorol Atmos Phys 104:113–123. https://doi.org/10.1007/s00703-009-0022-y

Falabino S, Castelli ST (2017) Estimating wind velocity standard deviation values in the inertial sublayer from observations in the roughness sublayer. Meteorol Atmos Phys 129(1):83–98

Falge E, Baldocchi D, Olson R, Anthoni P, Aubinet M, Bernhofer C, Burba G, Ceulemans R, Clement R, Dolman H et al (2001a) Gap filling strategies for long term energy flux data sets. Agric for Meteorol 107:71–77. https://doi.org/10.1016/S0168-1923(00)00235-5

Falge E, Baldocchi D, Olson R, Anthoni P, Aubinet M, Bernhofer C, Burba G, Ceulemans R, Clement R, Dolman H et al (2001b) Gap filling strategies for defensible annual sums of net ecosystem exchange. Agric for Meteorol 107:43–69. https://doi.org/10.1016/S0168-1923(00)00225-2

Foken T, Wichura B (1996) Tools for quality assessment of surface-based flux measurements. Agric for Meteorol 78:83–105. https://doi.org/10.1016/0168-1923

Forrer J, Rotach MW (1997) On the turbulence structure in the stable boundarylayer over the greenland ice sheet. Boundary-Layer Meteorl 85:111–136. https://doi.org/10.1023/A:1000466827210

Fortuniak K, Pawlak W, Siedlecki MJ (2013) Integral turbulence statistics over a central European city centre. Boundary-Layer Meteorol 146:257–276. https://doi.org/10.1007/s10546-012-9762-1

Garratt JR (1992) The atmospheric boundary layer. Cambridge University Press, Cambridge, UK

Goel M, Srivastava HN (1990) Monsoon trough boundary layer experiment (MONTBLEX). Bull Am Meteor Soc 71(11):1594–1600. https://doi.org/10.1175/1520-0477(1990)071%3c1594:MTBLE%3e2.0.CO;2

Grachev AA, Andreas EL, Fairall CW, Guest PS, Persson POG (2007) On the turbulent Prandtl number in the stable atmospheric boundary layer. Boundary-Layer Meteorol 125(2):329–341. https://doi.org/10.1007/s10546-007-9192-7

Grachev AA, Andreas EL, Fairall CW, Guest PS, Persson POG (2013) Thecritical Richardson number and limits of applicability of local similarity theoryin the stable boundary layer. Boundary-Layer Meteorol 147:51–82. https://doi.org/10.1007/s10546-012-9771-0

Grachev AA, Leo LS, Fernando HJ, Fairall CW, Creegan E, Blomquist BW, Christman AJ, Hocut CM (2018) Air–sea/land interaction in the coastal zone. Boundary-Layer Meteorol 167(2):181–210. https://doi.org/10.1007/s10546-017-0326-2

Grimmond CSB, Oke TR (1999) Aerodynamic properties of urban areas derived from analysis of surface form. J Appl Meteorol 38(9):1262–1292

Högström U (1996) Review of some basic characteristics of the atmospheric surface layer. Boundary-Layer Meteorol 78:215–246. https://doi.org/10.1007/BF00120937

Högström U, Bergström H, Alexandersson H (1982) Turbulence characteristics in a near neutrally stratified urban atmosphere. Bound-Layer Meteorol 23:449–472. https://doi.org/10.1007/BF00116272

Kailas SV, Goel M (1996) Planning MONTBLEX - an overview. Proc Indian Acad Sci - Earth PLanet Sci 105(3):209–225

Kaimal JC, Finnigan JJ (1994) Atmospheric boundary layer flows: their structure and measurement. Oxford University Press, Oxford, UK

Klipp C, Mahrt L (2004) Flux-gradient relationship, self-correlation and intermittency in the stable boundary layer. Q J R Meteorol Soc 130:2087–2104. https://doi.org/10.1256/qj.03.161

Krishnan P, Kunhikrishnan P (2002) Some characteristics of atmospheric surface layer over a tropical inland region during southwest monsoon period. Atmos Res 62:111–124. https://doi.org/10.1016/S0169-8095(02)00004-2

Kunhikrishnan PK, Gupta KS, Ramachandran R, Prakash WJ, Narayanan Nair K (1993) Study on thermal internal boundary layer structure over Thumba, India. Ann Geophys 11:52–60

Lange B, Larsen S, Hojstrup J, Barthelmie R (2004) Theinfluence of thermal effects on the wind speed profile of the coastal marine boundary layer. Boundary-Layer Meteorol 112:587–617. https://doi.org/10.1023/B:BOUN.0000030652.20894.83

Mahrt L (1998) Stratified atmospheric boundary layers and breakdown of models. Theor Comput Fluid Dyn 11:263–279. https://doi.org/10.1007/s001620050093

Monin AS, Yaglom AM (1971) Statistical fluid mechanics: mechanics of turbulence, vol 1. MIT Press, Cambridge

Moninobukhovam AS (1954) Basic laws of turbulent mixing in the surfacelayer of the atmosphere. Contrib Geophys Inst Acad Sci USSR 151:163–187

Moraes OL, Acevedo OC, Degrazia GA, Anfossi D, da Silva R, Anabor V (2005) Surface layer turbulence parameters over a complex terrain. Atmos Environ 39:3103–3112. https://doi.org/10.1016/j.atmosenv.2005.01.046

Namboodiri KVS, Krishnan DP, Nileshwar RK, Mammen K, Kiran Kumar N (2014) Coastal boundary layer characteristics of wind, turbulence, and surface roughness parameter over the Thumba equatorial rocket launching station. India J Climatol 504178:1–21. https://doi.org/10.1155/2014/504178

Nieuwstadt FTM (1984) The turbulent structure of the stable, nocturnal boundary layer. J Atmos Sci 41:2202–2216. https://doi.org/10.1175/1520-0469(1984)041%3c2202:TTSOTS%3e2.0.CO;2

Pahlow M, Parlange MB, Porté-Agel F (2001) On Monin-Obukhov similarity in the stable atmospheric boundary layer. Boundary-Layer Meteorol 99:225–248. https://doi.org/10.1023/A:1018909000098

Panofsky HA, Dutton J (1984) Atmospheric turbulence: models and methods for engineering applications. John Wiley, Hoboken, New Jersey

Prakash JWJ, Ramachandran R, Nair KN, Gupta KS, Kunhikrishnan P (1992) On the structure of sea-breeze fronts observed near the coastline of Thumba. India Bound-Layer Meteorol 59:111–124. https://doi.org/10.1007/BF00120689

Prasad KH, Srinivas CV, Singh AB, Naidu CV, Baskaran R, Venkatraman B (2019) Turbulence characteristics of surface boundary layer over the Kalpakkam tropical coastal station. India Meteorol Appl 131(4):827–843. https://doi.org/10.1007/s00703-018-0605-6

Quan L, Hu F (2009) Relationship between turbulent flux and variance in the urban canopy. Meteorol Atmos Phys 104:29–36. https://doi.org/10.1007/s00703-008-0012-5

Ramachandran R, Prakash JWJ, Gupta KS, Nair KN, Kunhikrishnan P (1994) Variability of surface roughness and turbulence intensities at a coastal site in India. Boundary-Layer Meteorol 70:385–400. https://doi.org/10.1007/BF00713777

Ramana MV, Krishnan P, Kunhikrishnan P (2004) Surface boundary-layer characteristics over a tropical inland station: seasonal features. Boundary-Layer Meteorol 111:153–175. https://doi.org/10.1023/B:BOUN.0000010999.25921.1a

Rao KG, Narasimha R, Prabhu A (1996) Estimation of drag coefficient at low wind speeds over the monsoon trough land region during MONTBLEX-90. Geophys Res Lett 23:2617–2620. https://doi.org/10.1029/96GL02368

Reddy NN, Rao KG (2016) Roughness lengths at four stations within the micrometeorological network over the Indian Monsoon Region. Bounda-Layer Meteorol 158(1):151–164. https://doi.org/10.1007/s10546-015-0080-2

Riechstein M, Falge E, Baldocchi D, Papale D, Aubinet M, Berbigier P, Bernhofer C, Buchmann N, Gilmanov T, Granier A et al (2005) On the separation of net ecosystem exchange into assimilation and ecosystem respiration: review and improved algorithm. Globlal Change Biol 11:1424–1439. https://doi.org/10.1111/j.1365-2486.2005.001002.x

Roth M (1993) Turbulent transfer relationships over an urban surface. II: Integral statistics. Q J Roy Meteor Soc 119:1105–1120. https://doi.org/10.1002/qj.49711951312

Roth M (2000) Review of atmospheric turbulence over cities. Q J R Meteor Soc 126:941–990. https://doi.org/10.1002/qj.49712656409

Singha A, Sadr R (2012) Characteristics of surface layer turbulence in coastal area of Qatar. Environ Fluid Mech 12:515–531. https://doi.org/10.1007/s10652-012-9242-7

Siva Kumar Reddy N, Kiran Kumar NVP, Rama Gopal K, Balakrishnaiah G, Rajaobul Reddy K (2021) Characteristics of atmospheric surface layer during winter season over Anantapur (14.62°N, 77.65°E), a semi-arid location in peninsular India. J Atmos Sol Terr Phys 216:105554. https://doi.org/10.1016/j.jastp.2021.105554

Sivaramakrishnan S, Saxena S, Vernekar K (1992) Characteristics of turbulent fluxes of sensible heat and momentum in the surface boundary layer during the Indian summer monsoon. Boundary-Layer Meteorol 60:95–108. https://doi.org/10.1007/BF00122063

Smedman A-S (1988) Observations of a multi-level turbulence structure in a very stable atmospheric boundary layer. Bound-Layer Meteorol 44:231–253. https://doi.org/10.1007/BF00116064

Solanki R, Singh N, Kiran Kumar NVP, Rajeev K, Dhaka SK (2016) Time variability of surface-layer characteristics over a mountain ridge in the central himalayas during the spring season. Bound-Layer Meteorol 158:453–471. https://doi.org/10.1007/s10546-015-0098-5

Solanki R, Singh N, Kumar NK, Rajeev K, Imasu R, Dhaka SK (2019) Impact of mountainous topography on surface-layer parameters during weak mean-flow conditions. Bound-Layer Meteorol 172(1):133–148. https://doi.org/10.1007/s10546-019-00438-3

Sorbjan Z (1989) Structure of the atmospheric boundary layer. Prentice Hall, New Jersey

Stull R (1988) An introduction to boundary layer meteorology. Springer Science & Business Media, Germany

Trini Castelli S, Falabino S (2013) Analysis of the parameterization for the wind-velocity fluctuation standard deviations in the surface layer in low-wind conditions. Meteorol Atmos Phys 119(1):91–107

Trini Castelli S, Falabino S, Mortarini L, Ferrero E, Richiardone R, Anfossi D (2014) Experimental investigation of surface-layer parameters in low wind-speed conditions in a suburban area. Q J R Meteorol Soc 140(683):2023–2036

Večenaj Ž, De Wekker SF (2015) Determination of non-stationarity in the surface layer during the T-REX experiment. Q J R Meteorol Soc 141(690):1560–1571. https://doi.org/10.1002/qj.2458

Vickers D, Mahrt L (1997) Fetch limited drag co-efficients. Bound-Layer Meteorol 85(1):53–79

Weber S, Kordowski K (2010) Comparison of atmospheric turbulence characteristics and turbulent fluxes from two urban sites in Essen, Germany. Theor Appl Climatol 102:61–74. https://doi.org/10.1007/s00704-009-0240-8

Wilczak JM, Oncley SP, Stage S (2001) Sonic anemometer tilts correction algorithms. Bound-Layer Meteorol 99:127–150. https://doi.org/10.1023/A:1018966204465

Wilson JD (2008) Monin-Obukhov functions for standard deviations of velocity. Bound-Layer Meteorol 129(3):353–369. https://doi.org/10.1007/s10546-008-9319-5

Wood CR, Lacser A, Barlow JF, Padhra A, Belcher SE, Nemitz E, Helfter C, Famulari D, Grimmond CSB (2010) Turbulent flow at 190 m height above london during 2006–2008: a climatology and the applicability of similarity theory. Bound-Layer Meteorol 137:77–96. https://doi.org/10.1007/s10546-010-9516-x

Wyngaard JC (2010) Turbulence in the Atmosphere. CambridgeUniversity Press, New York, NY

Wyngaard J, Coté O, Izumi Y (1971) Local free convection, similarity, and the budgets of shear stress and heat flux. J Atmos Sci 28:1171–1182. https://doi.org/10.1175/1520-0469

Xu Y, Zhou C, Li Z, Zhang W (1997) Turbulent structure and local similarity in the tower-layer over the nanjing area. Bound-Layer Meteorol 82:1–21. https://doi.org/10.1023/A:1000111431036

Yersel M, Goble R (1986) Roughness effects on urban turbulence parameters. Bound-Layer Meteorol 37:271–284. https://doi.org/10.1007/BF00122989

Yue P, Zhang Q, Wang RY, Li YH, Wang S (2015) Turbulence intensity and turbulent kinetic energy parameters over a heterogeneous terrain of the Loess Plateau, China. Adv Atmos Sci 32:1291–1302. https://doi.org/10.1007/s00376-015-4258-9

Yusup YB, Daud WR, Zaharim A, Talib MZ (2008) Structure of the atmospheric surface layer over an industrialized equatorial area. Atmos Res 90:70–77. https://doi.org/10.1016/j.atmosres.2008.04.003

Zhang H, Chen J, Park S-J (2001) Turbulence structure in unstable conditions over various surfaces. Bound-Layer Meteorol 100:243–261. https://doi.org/10.1023/A:1019223316895

Publisher's Note Springer Nature remains neutral with regard to jurisdictional claims in published maps and institutional affiliations.

Springer Nature or its licensor (e.g. a society or other partner) holds exclusive rights to this article under a publishing agreement with the author(s) or other rightsholder(s); author self-archiving of the accepted manuscript version of this article is solely governed by the terms of such publishing agreement and applicable law.

Atmospheric Research 286 (2023) 106678

Contents lists available at ScienceDirect

Atmospheric Research

journal homepage: www.elsevier.com/locate/atmosres

Thermodynamic characteristics of marine atmospheric boundary layer across frontal regions of the Indian Ocean Sector of the Southern Ocean based on three field campaigns

Shaikh Neha Salim [a,b], Arjun Adhikari [a,b], Harilal B. Menon [a,b,*], N.V.P. Kiran Kumar [c], Rajeev Kunjukrishnapillai [c]

[a] Remote Sensing Laboratory, Goa University - 403206, Goa, India
[b] School of Earth, Ocean and Atmospheric Sciences, Goa University - 403206, Goa, India
[c] Space Physics Laboratory, Vikram Sarabhai Space Centre, Indian Space Research Organisation, Thiruvananthapuram 695022, India

ARTICLE INFO

Keywords:
Thermodynamic stability
Clouds
Inversions
Low-level atmospheric process
Conserved variable analysis

ABSTRACT

The Southern Ocean (SO) marine atmospheric boundary layer (MABL), regulated by continuous air-sea exchanges, plays a key role in transporting exchanges between tropics and poles. Among SO sectors, the Indian Ocean sector of SO (ISSO) remained least explored in terms of MABL characterization and is examined in this study. In ISSO, occurrence of sharp oceanic thermohaline fronts regulates the vertical thermodynamic structure of MABL, clouds, and inversions. In this study, these properties of ISSO MABL are investigated over three oceanic domains (Sub-Tropical Indian Ocean (STIO), ISSO, and High-Latitude SO (HLSO)). To achieve this, near-sea surface air-sea exchanges along with profiles of meteorological parameters generated between 25°S and 68°S and 57°E to78°E during three field campaigns conducted in the austral summers of 2017, 2018, and 2020 were utilized. Results showed strong $SST\text{-}T_{air}$ variability across the study region. In STIO, positive $SST\text{-}T_{air}$ indicated Low-Level Cold Air Advection (LLCAA)-induced destabilized and coupled MABLs capped by multiple inversions (>3INV's of strength~0.35 K m^{-1} above~1200 m) and thin mid/high-altitudes clouds (cloud-base~830 m, cloud-top~2309 m, and cloud-thickness~758 m). Over ISSO and northern HLSO, weak and negative $SST\text{-}T_{air}$ indicated Low-Level Warm Air Advection (LLWAA)-induced stratified and decoupled MABLs. Aided by advective mixing of multiple air-masses, low-level thick multilayered clouds (>2 layers, average cloud-base~604 m, cloud-top~2288 m, and cloud-thickness~1314 m) and multiple strong high-level inversions (>2INV's, strength>0.4 K m^{-1},~1836 m) was observed. In HLSO, weakly positive $SST\text{-}T_{air}$ indicated LLCAA-induced weakly destabilized MABLs capped by mid-altitude inversions (strength~0.22 K m^{-1},~1632 m) and mid-altitude clouds (cloud-base~979 m, cloud-top~2465 m, and cloud-thickness~1263 m) supported by sublimation leading to virga conditions.

1. Introduction

The anomalous geophysical circulation patterns are widely associated with anthropogenic inputs (Stott et al., 2010; IPCC, 2014). Collectively, these inputs account for global climate perturbations via changes in atmospheric and oceanic circulation patterns, such as increased global temperatures, rising sea levels, melting polar ice caps and ice sheets, and changing wind patterns (Fawzy et al., 2020). On a local to regional scale, these climatic perturbations have profoundly affected human health and survival (Falga and Wang, 2022). The occurrence of these perturbations results from the dynamic exchange of water vapor, energy, mass, momentum, atmospheric constituents, and naturally and anthropogenically released emissions on diurnal, seasonal, and annual scales (Stull, 1988). These exchanges regulated via continuously occurring coupled land-ocean-atmospheric interactions drives the earth's climate, radiation budget, and water cycle (Edson et al., 1999). From the perspective of present-time global warming and the faster-changing earth's climate, ocean-atmosphere exchanges hold the key to addressing rising future climate concerns (Liu et al., 2013). Recognizing its significance, numerous studies are available from the

* Corresponding author at: Remote Sensing Laboratory, Goa University - 403206, Goa, India.
E-mail address: hbmenon@unigoa.ac.in (H.B. Menon).

https://doi.org/10.1016/j.atmosres.2023.106678
Received 5 October 2022; Received in revised form 17 February 2023; Accepted 19 February 2023
Available online 23 February 2023
0169-8095/© 2023 Published by Elsevier B.V.

world oceans e.g., the Atlantic Ocean (Huang and Shukla, 2005; Nobre et al., 2012), the Pacific Ocean (Xie et al., 2001; Smirnov et al., 2014), Indian Ocean (Webster et al., 1999), and the Arctic Ocean (Deser et al., 2015; Petrie et al., 2015), but Southern Ocean (SO) is relatively one of the least explored ocean (Sallée, 2018; Swart et al., 2018). Its least exploration is attributed to the challenge of continuous monitoring due to its distant continental proximity, extreme remoteness, and harsh weather conditions. However, in the recent past, efforts to generate in situ data by conducting SO field expeditions have improved the understanding of SO (McFarquhar et al., 2021). Based on past studies, SO is observed to act as a sink for >40% of the global heat content (Sallée et al., 2008), and 30–40% of anthropogenic carbon dioxide (CO_2) released in the atmosphere (Long et al., 2021). This record highlights the major contribution of SO in regulating climate perturbations such as declining ice cover, increasing ocean acidification, and changing global wind and precipitation patterns (Sen Gupta et al., 2009; Hopkins et al., 2020). These perturbations are projected to amplify in future warming scenarios (Lee et al., 2021), thereby indicating the need for an improved understanding of SO-atmosphere interactions.

Among world oceans, SO serves a distinctively unique ocean composed of numerous oceanic fronts formed by a sharp gradient in sea surface temperatures (*SST*) and salinity. These fronts are embedded within the massive circulating Antarctic Circumpolar Current (ACC) that connects the Atlantic, Pacific, and Indian oceanic basins as well as strongly links exchanges between tropics and poles (Talley et al., 2011). The oceanic fronts embedded within ACC are the Sub-Tropical Front (STF), Sub-Antarctic Front (SAF), Polar Front (PF), Southern Antarctic Circumpolar Current Front (SACCF), and Southern boundary of ACC (SB) (Orsi et al., 1995; Belkin and Gordon, 1996). On a temporal scale, a shift in the locations of these fronts occurs which is reflected in the changes in *SST* gradients (Thompson and Richards, 2011). Past studies have recorded the most substantial *SST* gradients in the Indian Ocean sector of the Southern Ocean (ISSO) compared to other sectors of SO (Small et al., 2014). Depending on the magnitude of the *SST* gradient, enhancement in the activities of oceanic eddies and amplification/suppression of air-sea exchanges are observed specifically in the vicinity of oceanic fronts and regions of strong mesoscale activities (Rouault and Lutjeharms, 2000; Chelton et al., 2001; Small et al., 2008). Equivalent to air-sea exchanges which are regulated by *SST* gradient and air temperature differences (SST-T_{air}), an input of surface layer heat fluxes (positive/negative) are fed into the low-level atmosphere which regulates the structure and dynamics of the marine atmospheric boundary layer (MABL) via the flow of low-level warm air advection (LLWAA) or low-level cold air advection (LLCAA) (Zheng and Li, 2019b; Zheng et al., 2018b). In the case of LLWAA ($SST < T_{air}$), the negative surface heat flux weakens vertical atmospheric mixing and enhances lower atmospheric stability (Martin et al., 1995; Wood and Bretherton, 2004; Wood et al., 2018; Zheng et al., 2018b). On the contrary, during LLCAA ($SST > T_{air}$), the positive surface heat flux supports the development of a well-mixed MABL capped by clouds, thereby forming a strongly coupled MABL (Zheng et al., 2018b). Across the ISSO fronts, the frequent transitional flow of LLWAA and LLCAA prevails mainly due to strong baroclinic instabilities laid by varying *SST* gradients and changing SST-T_{air} (Pierrehumbert and Swanson, 1995; Moore et al., 1999). As a result of the advection, such different types of air masses across multiple oceanic fronts account for the formation of numerous atmospheric fronts (warm, cold, and occluded). Typically, warm (cold) fronts are associated with LLCAA (LLWAA) which supports the development of the high-pressure anticyclonic (low-pressure cyclonic) area and are commonly associated with the formation of coupled (decoupled) MABL's over SO. Moreover, the isolation of warm air mass between two adjacent cold air masses commonly accounts formation of occluded front where highly stabilized MABL's are common (Li et al., 2015). Past studies have identified a higher frequency of decoupled MABL's associated with LLWAA particularly in SO (Boers et al., 1998; Russell et al., 1998; Jensen et al., 2000; Hande et al., 2012; Chubb et al., 2016; Zheng et al., 2018b; Zheng and Li, 2019a). These aforementioned unique SO conditions mainly driven by dynamic ocean-atmospheric exchanges contribute to a higher frequency of stormy low-pressure cyclonic systems, and are majorly responsible for making SO one of the stormiest cyclonic regions of the globe and is, therefore, referred to as the SO storm track region (Bischoff and Thompson, 2014; Chapman et al., 2015; Huang et al., 2015b).

The source of the present knowledge of SO is based on in-situ data collected from a few scientific campaigns conducted in different sectors of SO e.g., the Australian (McFarquhar et al., 2021) and African (Messager et al., 2012) sector of SO (Table 1 in Schmale et al., 2019). These in-situ datasets were also employed for validating remotely retrieved data and model-simulated results over SO, where large uncertainties in remote and modeled datasets were identified (Sallée et al., 2013; Bodas-Salcedo et al., 2014). (Sallée et al., 2013; Bodas-Salcedo et al., 2014; Hyder et al., 2018; Schuddeboom et al., 2019). For example, significant misrepresentation of cloud properties, underestimation of atmospheric inversions, and biases in radiative estimates (Lang et al., 2018; McFarquhar et al., 2021; Vignon et al., 2021) were observed in frequently accessed satellite retrievals e.g., ERA-Interim and MERRA (Naud et al., 2014), particularly over extra-tropical fronts and stormy regions (Hoskins and Hodges, 2005; Haynes et al., 2011; Catto et al., 2012). Recent investigations revealed that one of the major causes of these uncertainties is the significant cloud coverage over SO for nearly 80% of the year (Haynes et al., 2011; Huang et al., 2012; Mace and Protat, 2018; Mace et al., 2020; Mace et al., 2021; McFarquhar et al., 2021). Thus, to properly understand SO and to improve SO monitoring using space-borne observations, it becomes crucial to increase in situ observations over poorly sampled SO regions (e.g., ISSO).

Particularly, in situ data that presents the spatial and vertical structure of the SO atmosphere with an emphasis on the dynamic processes governing the distribution of clouds and inversions is required. Thus, recognizing its significance, the present study is carried out to understand the coupled air-sea exchanges occurring over a system of multiple ISSO fronts and their effect on the thermodynamics of ISSO MABL. For this purpose, in situ data generated during three consecutive field campaigns conducted during the austral summers of 2017 (January–March), 2018 (December–February), and 2020 (January–March) have been used. A dataset comprising 75 high-resolution atmospheric soundings and near-surface meteorological parameters has been used to achieve the following objectives,

- Understand low-level thermodynamic stability conditions in response to prevailing synoptic meteorology
- Assess the cloud's macrophysical properties

Table 1
Details of atmospheric soundings collected during three Southern Ocean field campaigns.

Campaign	Period of Campaign	Latitude Range	Longitude Range	Number of Soundings	Time / Height Resolution
[a] SOE-IX	6th January 2017 – 28th February 2017	30°S to 68°S	57.4°E to 75°E	18	1 s / 0.1 m
[a] SOE-X	8th December 2017 – 4th February 2018	28°S to 66.6°S	57.4°E to 76.5°E	30	1 s / 0.1 m
[a] SOE-XI	10th January 2020 – 8th March 2020	24°S to 67.5°S	57.4°E to 79°E	27	1 s / 0.1 m

Note: [a] SOE denotes Southern Ocean Expeditions conducted in the Indian Ocean sector.

- Examine boundary layer inversions
- Investigate dominant physical processes in the low-level atmosphere

2. Study region, data, and method

The study is based on a set of meteorological measurements carried out during three scientific campaigns executed in the ISSO during the austral summers of 2017, 2018, and 2020 onboard research vessel *S.A. Agulhas* from Port Louis, Mauritius (20°S) to Prydz Bay region of coastal Antarctica (68°S). The cruise track of each campaign is shown in Fig. 1a, and the details are provided in Table 1.

2.1. Study region

The oceanic domains examined in this study cover the oceanic fronts of the ISSO up to the Prydz Bay region of coastal Antarctica. The approximate locations of ISSO fronts are discussed in Orsi et al. (1995); Belkin and Gordon (1996); Kostianoy et al. (2004). For this study, measurements began from STF, an oceanic front that is known to separate tropical waters from sub-Antarctic waters (Deacon, 1937; Lutjeharms and Valentine, 1984; Sokolov and Rintoul, 2002; Hamilton, 2006). The region north and south of STF are termed NSTF1, NSTF2, and SSTF. Further south of SSTF, the frontal regions SAF1, SAF2, PF1, and PF2 embedded within ACC represent the ISSO region (Lutjeharms and Valentine, 1988; Stammer, 1998; Phillips and Rintoul, 2000; Morrow et al., 2004; Sallée et al., 2008). Beyond PF2, the region of SACCF is marked around 60°S, which represents a region of stronger convergence of winds. Ahead of SACCF, a region of SB is marked which lies near two sub-polar gyres i.e., Weddell Sea gyre and Prydz Bay gyre. Lastly, the measurements towards the southernmost extent were collected in the coastal waters of the Prydz Bay region of Antarctica, termed CA (Coastal Antarctica). The meteorological measurements used in this study describe these ten frontal regions, which lie in three major oceanic domains, i.e., (i) Sub-tropical Indian Ocean (STIO) comprising of NSTF1, NSTF2, and SSTF, (ii) ISSO comprising of SAF1, SAF2, PF1, and PF2, and (iii) High-Latitude SO (HLSO) comprising of SACCF, SB, and CA (see Table 2 for details).

2.2. Data

The primary data used for this study comprised measurements of near-surface and vertical profiles of meteorological variables generated over the study region. The near-surface measurements included air temperature (T_{air}), relative humidity (*RH*), mean sea level pressure (*MSLP*), wind speed (*WS*), and wind direction (*WD*) recorded using a standard pre-calibrated automatic weather station (AWS, WeatherPak®-

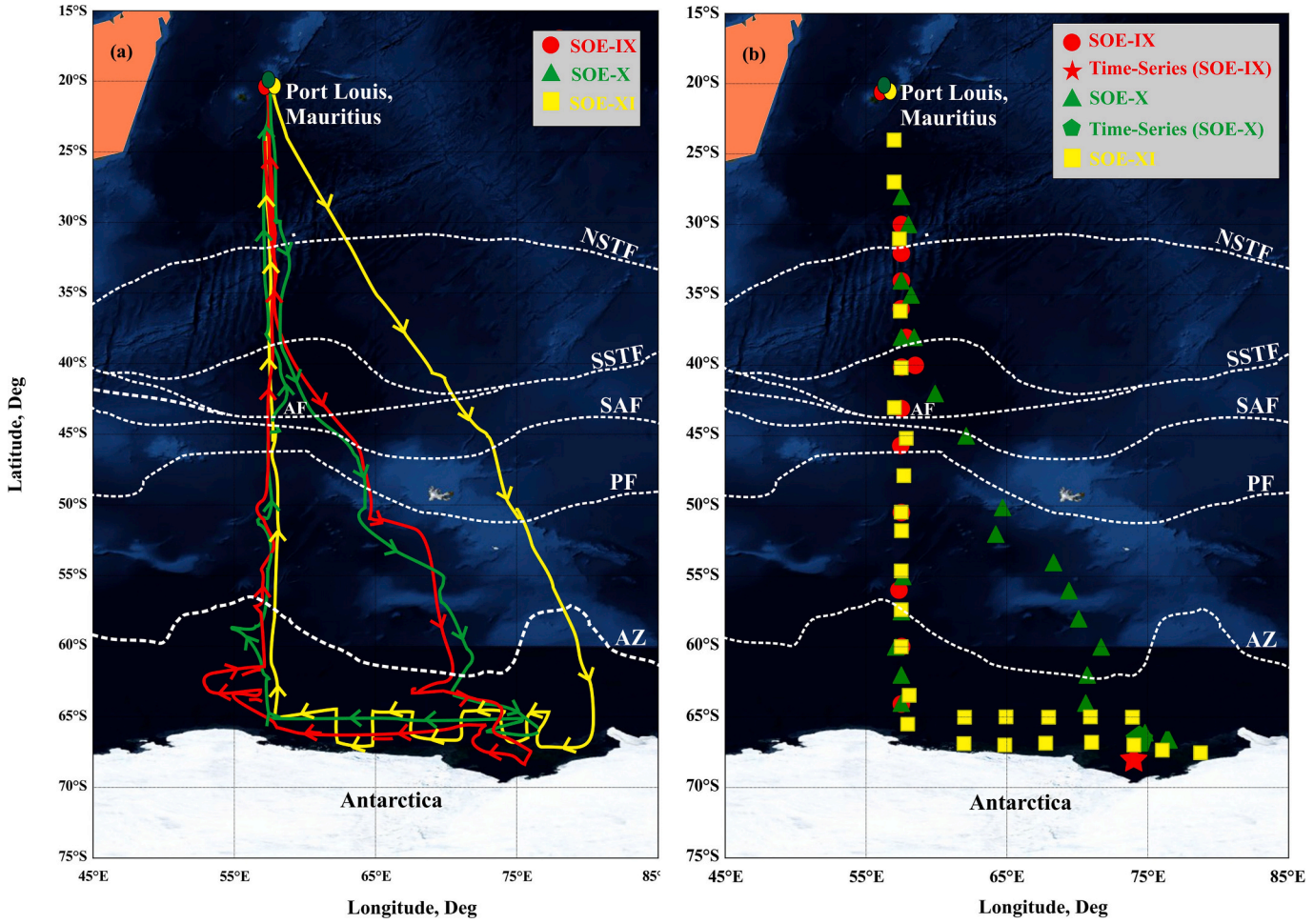

Fig. 1. (a) Cruise track along which atmospheric measurements were made during three campaigns (SOE-IX (red colour track), SOE-X (green colour track), and SOE-XI (yellow colour track)) over the Indian Ocean sector of Southern Ocean (ISSO). Arrows indicate onward and return track journeys. The approximate location of major fronts marked by white dotted lines are adopted from (Belkin and Gordon, 1996; Anil Kumar et al., 2015): [NSTF and SSTF, Northern and Southern Sub-Tropical Fronts; SAF, Sub-Antarctic Front; PF, Polar Front; and AZ, Antarctic Zone]. (b) The distribution of 75 atmospheric soundings launched during SOE-IX (red circles), SOE-X (green triangles), and SOE-XI (yellow squares) campaigns. Locations for time series measurements made during SOE-IX (red star) and SOE-X (green pentagon) campaigns are shown. (For interpretation of the references to colour in this figure legend, the reader is referred to the web version of this article.)

Table 2
Regional classification of the study area and the distribution of 75 atmospheric soundings.

Sr. No.	Oceanic Domains	Frontal regions of ISSO	Classification adopted for present study	Indicator Variable	Criteria for considered soundings		Total RL count
				SST (°C)	$SST > T_{air}$	$SST < T_{air}$	
1	Sub-Tropical Indian Ocean (STIO)	Northern Subtropical Front (NSTF1)	24°S–32°S	26 to 22 °C	RL17, RL19, RL48, RL73, RL74	RL1, RL18, RL75	8
2		Northern Subtropical Front (NSTF2)	32°S–40°S	22 to 21 °C	RL14, RL20, RL46, RL47, RL72	RL15, L16, RL21	8
3		Agulhas Return Front (ARF) + Southern Subtropical Front (SSTF)	40°S–41°30′S	19 to 17 °C, 17 to 11 °C	RL2, RL13	RL71	3
4	Indian Ocean sector of Southern Ocean (ISSO)	Northern Sub-Antarctic Front (SAF1)	41°30′S–44°S	11 to 9 °C	RL22, RL23, RL69	RL11, RL12, RL70	6
5		Southern Sub-Antarctic Front (SAF2)	46°30′S–48°S	7 to 6 °C	RL68	–	1
6		Northern Polar Front (PF1)	50°S–52°30′S	5 to 4 °C	RL10, RL24	RL25, RL66, RL67	5
7		Southern Polar Front (PF2)	54°30′S–59°30′S	3 to 2 °C	RL9, RL27, RL28, RL44, RL45	RL26, RL64, RL65	8
8	High-Latitude Southern Ocean (HLSO)	Southern Antarctic Circumpolar Current Front (SACCF)	59°30′S–61°S	Increased Temperature, $T_{max} > 1.8$ °C	–	RL8, RL29, RL30, RL42, RL43, RL63	6
9		Southern Boundary of ACC (SB)	63°S–65°S	Isotherm of 1.5 °C	RL31, RL51, RL55, RL58, RL59, RL61, RL62	RL7, RL41, RL54	10
10		Coastal Antarctic (CA)	65°S–68.5°S	1.5 to −0.5 °C	RL5, RL6, RL32, RL33, RL34, RL35, RL36, RL40, RL52, RL56, RL57, RL60	RL3, RL4, RL37, RL38, RL39, RL49, RL50, RL53	20

Note: Identification of oceanic fronts in the ISSO was adopted from Belkin and Gordon (1996); Anil Kumar et al. (2015).

2000 v3, Coastal Environment Systems Inc.) at every 30 min interval. This AWS was installed on the ship's deck at a height of ~10 m above mean sea level, and its alignment was regularly corrected as the campaign progressed. These observations were successfully made during the first two cruises (i.e., in 2017 and 2018), while AWS failed to store data during the third cruise (in 2020). The data was manually logged at 6-h intervals. The measurements of *SST* were recorded using a bucket thermometer (T. Friedrichs & Co.) at 6-h intervals during all campaigns. The vertical profiles of meteorological parameters were generated using *Pisharoty* radiosondes developed by Vikram Sarabhai Space Centre (VSSC) of the Indian Space Research Organization (ISRO) (Divya et al., 2014). A total of 75 high-resolution atmospheric soundings were released during the three campaigns (Fig. 1b) and details of these launches are provided in Table S2. During all campaigns, radiosondes were released at pre-determined locations to target oceanic fronts and preferably around 00:00, 16:00, 12:00, and 18:00 UTC. Although, a few radiosondes were also released at discrete timings. During the third campaign in 2020, atmospheric soundings were performed across the latitudinal transit track at a 3°longitudinal interval. A comparison of measurements between *Pisharoty* radiosonde and from *Vaisala*, *Meisei*, and *Graw* make radiosondes were reported by Divya et al. (2014). It revealed a correlation of 0.99 for *T* and *MSLP*, 0.97 for *RH*, 0.998 for east-west (*u*), and 0.976 for the north-south (*v*) component of *WS*, making it suitable for the present study. The technical details of the sensors equipped on the *Pisharoty* radiosonde are provided in Table S1.

2.3. Methodology

Before analyzing radiosonde measurements, the anomalous values (random values in an increasing or decreasing order) had been flagged and removed. Further, the profiles of all meteorological variables were averaged at 20 m intervals, followed by smoothening using a five-point moving average technique (Subrahamanyam and Radhika, 2003). A similar method was adopted to examine the thermodynamic structure of the low-level atmosphere (near-surface to 4000 m altitude) in the Australasian sectors of SO (Hande et al., 2012; Lang et al., 2018; Truong et al., 2020). Hence, in this study, data from the surface (~12 m) to 4000 m altitude were only used to examine the thermodynamic properties of MABL across the study region. After employing these criteria, the thermodynamic stability of low-level atmosphere was investigated using profiles of conserved variables, i.e., virtual potential temperature (θ_v) and mixing ratio (r) (Messager et al., 2012; Lang et al., 2018). These variables were obtained following Stull, 1988,

$$\theta_v = \theta(1 + 0.61r) \quad (1)$$

$$r = 0.623e/P - 0.377e \quad (2)$$

where θ is the potential temperature, P is the atmospheric pressure, and e represents vapor pressure.

In addition, the frequency of occurrences of cloud and inversions along with their macrophysical properties such as the height of cloud base, cloud top, total cloud geometric thickness, the height of inversions, and its strength were estimated following the method described by Truong et al. (2020). The cloud layers were identified as single, multi-layer, or complete clouds by computing the difference between T_{air} and dew point temperature (T_d). In this study, a larger dewpoint depression threshold of T_{air}-T_d (< 2.0°C) has been chosen than the threshold of 1.5°C used in Truong et al. (2020), to reflect clouds from MODIS and CALIPSO observations qualitatively. The cloud layers were detected if this threshold was met for an altitude thickness of at least 60 m or more. These criteria were applied in the altitudes between 500 and 4000 m, and the presence of clouds was ascertained. Following the method of Mace et al. (2009), a "multi-layered cloud" was recorded if at least two or more cloud layers were identified in a radiosonde profile. Further, the total geometric cloud thickness was estimated as a sum of T_{air}-T_d among cloud layers (Truong et al., 2020). The cloud base and cloud top heights were identified as the altitudes of the cloud base of the lowest cloud layer and the top of the highest cloud layer.

Further, the inversions from each radiosonde profile were considered significant, if $d\theta_v/dz$ was greater than or equal to a limiting threshold of 0.14 K $m^{-1}$and subsequent significant inversion was at least 300 m away from the previous inversion (Zeng et al., 2004; Hande et al., 2012; Lang et al., 2018; Truong et al., 2020). Between 500 and 4000 m, the number of significant inversions was recorded as no inversion, single, or multiple inversion. A "multi-level inversion" was recorded in a sounding if at least two or more inversions were identified between 500 and 4000 m altitudes.

In addition to cloud layers and inversions, Lower Tropospheric

Stability (*LTS* after Klein and Hartmann (1993) and Estimated Inversion Strength (*EIS* after Wood and Bretherton (2006) were estimated. According to Wood and Bretherton (2006), these metrics indicate the measure of inversion strength within MABL, and higher estimates of these metrics are indicators of strong low-lying inversions. Stronger inversions are more likely to trap moisture within MABL, resulting in higher coverage of low-level clouds. The estimation of *EIS* and *LTS* in other sectors of SO have been correlated well with the in-situ records of low-level cloud cover (Muhlbauer et al., 2014; Naud et al., 2016; Lang et al., 2018; Truong et al., 2020).

The estimation of *LTS* was computed as a difference between θ at 700 mb pressure level and the surface (Klein and Hartmann, 1993),

$$LTS = \theta_{700} - \theta_{surface} \tag{3}$$

The estimation of *EIS* has been computed using the following equation,

$$EIS = LTS - \Gamma_m^{850}(z_{700} - LCL) \tag{4}$$

where, Γ_m^{850} is the moist adiabatic potential temperature gradient at 850 hPa, calculated using the average of T_{air} at the surface and 700 hPa,

$$\Gamma_m^{850} = \Gamma_m([T_0 + T_{700}]/2), 850hPa \tag{5}$$

In Eq. (5), Γ_m was calculated following Wood and Bretherton (2006), after applying the simplified approximation suggested by Bolton (1980),

$$\Gamma_m(T,p) = \frac{g}{c_p}\left[1 - \frac{1 + L_v r_s(T,p)/R_a T}{1 + L_v^2 r_s(T,p)/c_p R_v T^2}\right] \tag{6}$$

where g is the acceleration due to gravity, $c_p$is the specific heat of air at constant pressure, L_v is the latent heat of vaporization, $r_s(T,p)$ is the saturation mixing ratio at respective altitudes having temperature (T) and pressure (P), and R_a and R_v represent the gas constants for dry air and water vapor, respectively. The *LCL* is the lifting condensation level and z_{700} is the altitude of 700 hPa. The standard procedures for calculating *LCL* height were adopted by Bolton (1980).

Lastly, the boundary layer processes were diagnosed within the lower 4000 m atmospheric column using conserved variable analysis (CVA). The conserved variables, i.e., equivalent potential temperature (θ_e) and specific humidity (q) were examined following Betts and Albrecht (1987). The conserved variable θ_e and q were estimated as follows,

$$\theta_e = \theta e^{2.67 q/T_{LCL}} \tag{7}$$

$$q = (0.622 \times e)/(p - (0.378 \times e)) \tag{8}$$

where, T_{LCL} is the temperature at *LCL*.

3. Results

The results are discussed in the subsections below, beginning with low-level thermodynamic conditions in section 3.1. In sections 3.2 and 3.3, the characteristics of clouds and inversions, and dominant physical processes are presented. In section 3.4, we describe three typical case studies illustrating the effect of synoptic meteorology in altering the state of MABL. Lastly, in section 3.5, the variability of *EIS* and *LTS* across

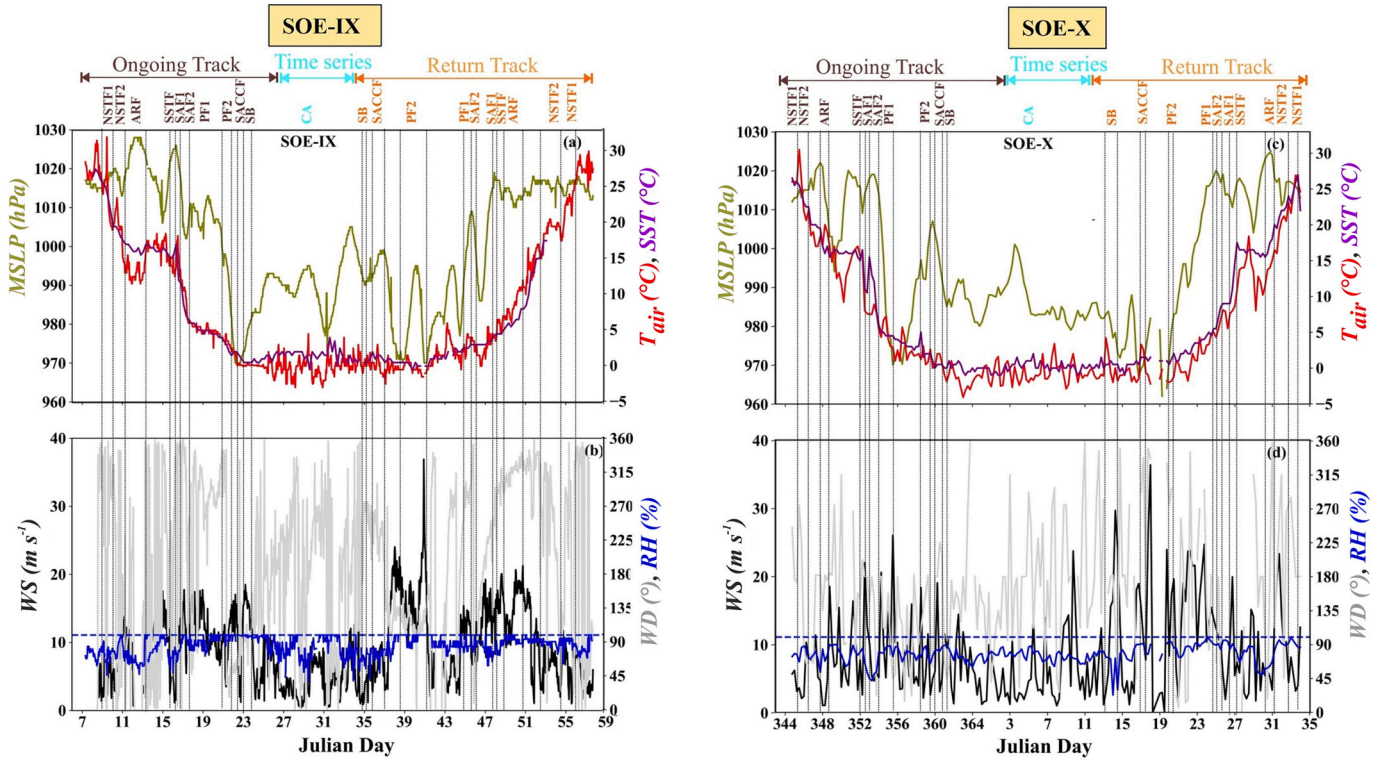

Fig. 2. Time series of surface measurements of (a, c) MSLP, the mean sea level pressure in hPa (green lines); T_{air} and SST, the air temperature and sea surface temperature in °C (red and magenta lines respectively); (b, d) WS, wind speed in m s^{-1} (black lines); WD, wind direction in degrees (grey lines) and RH, relative humidity in % (blue lines) were measured while crossing ISSO oceanic fronts during SOE-IX (left panel [a, b]) and SOE-X (right panel [c, d]) campaigns respectively. In panels (a, c), the left vertical scale is for MSLP, and the right vertical scale is for temperatures (T_{air} and SST). In panels (b, d), the left vertical scale is for WS, and the right vertical scale is for WD and RH. The maximum limit of RH (100%) is marked in panels (b, d) with a blue dotted line. For all panels, the horizontal axis is the Julian day number according to the campaign periods of SOE-IX (left panels) and SOE-X (right panels). The vertical dashed black lines mark the approximate locations of encountered oceanic fronts while crossing ISSO during the campaigns adopting the markation provided by (Belkin and Gordon, 1996; Anil Kumar et al., 2015). The fronts encountered during the forward track (brown), time series region (cyan), and return track (orange) are mentioned on the top of the panel (a, c). (For interpretation of the references to colour in this figure legend, the reader is referred to the web version of this article.)

the study region is discussed.

3.1. the thermodynamic state of the low-level atmosphere

The continuous measurements of surface-based meteorological parameters, i.e., *SST*, T_{air}, *RH*, *WS*, and *WD* collected across the entire cruise track traversed during two consecutive field campaigns (in 2017 and 2018) showed significant variability in near-surface meteorological conditions across the ISSO fronts irrespective of the campaigning period (Fig. 2). In addition to near-surface meteorology, prominent spatial variability was observed in the air-sea coupling (SST-T_{air}) and it was observed to strongly regulate the thermodynamic stability/instability state of MABL. Thus, in this subsection, we have sequentially described the thermodynamic state of the low-level atmosphere over ten frontal regions grouped in three major oceanic domains by analyzing vertical profiles of conserved variables, i.e., θ_v and r generated from 75 atmospheric soundings (Fig. S1-S3).

3.1.1. STIO

Out of 19 soundings released over STIO, 12 atmospheric soundings (RL2, RL13, RL14, RL17, RL19, RL20, RL46, RL47, RL48, RL72, RL73, and RL74) suggest high-pressure regions (Table 1). The *SST* was higher than T_{air} which revealed positive surface heat flux and the occurrence of LLCAA. This warm front region favored convective destabilization of the low-level atmosphere leading to the formation of a well-evolved mixed layer structure evident in r and θ_v profiles (Fig. S1-S3). The average mixed-layer height during unstable conditions reached altitudes of 1153 m, 1240 m, and 1270 m over NSTF1, NSTF2, and SSTF, respectively (Fig. 3a,c,e). The mixed layer was capped by stratocumulus clouds, indicating a thermodynamically coupled boundary layer structure. The formation of such coupled boundary layer structures in the NSTF region was due to higher *MSLP*, $SST > T_{air}$, and the advection of cold air masses supported the formation of warm fronts in this region. Moreover, the region also encountered clear sky conditions accompanied by weak winds carrying dry air masses ($RH < 83\%$) (Table 3). These conditions over NSTFs were attributed to the prevalence of sub-tropical ridges that generally prevailed at 30°S (Timbal and Drosdowsky, 2013). The SSTF region revealed strongly coupled and highly destabilized MABL due to an intense warm front caused by the action of convectively active oceanic eddies formed over meandering Agulhas Retroflection Current (ARC) (Fig. 3e).

In contrast, at the remaining seven soundings (RL1, RL15, RL16, RL18, RL21, RL71, and RL75), *SSTs* were less than T_{air}, which indicated negative surface heat flux associated with the cold front region. It showed the prevalence of LLWAA that inhibited vertical mixing in the low-level atmosphere and promoted a decoupled MABL. A more stably stratified low-level atmosphere was evident as r and θ_v gradually increased with altitude (Fig. S1-S3). The formation of stable and

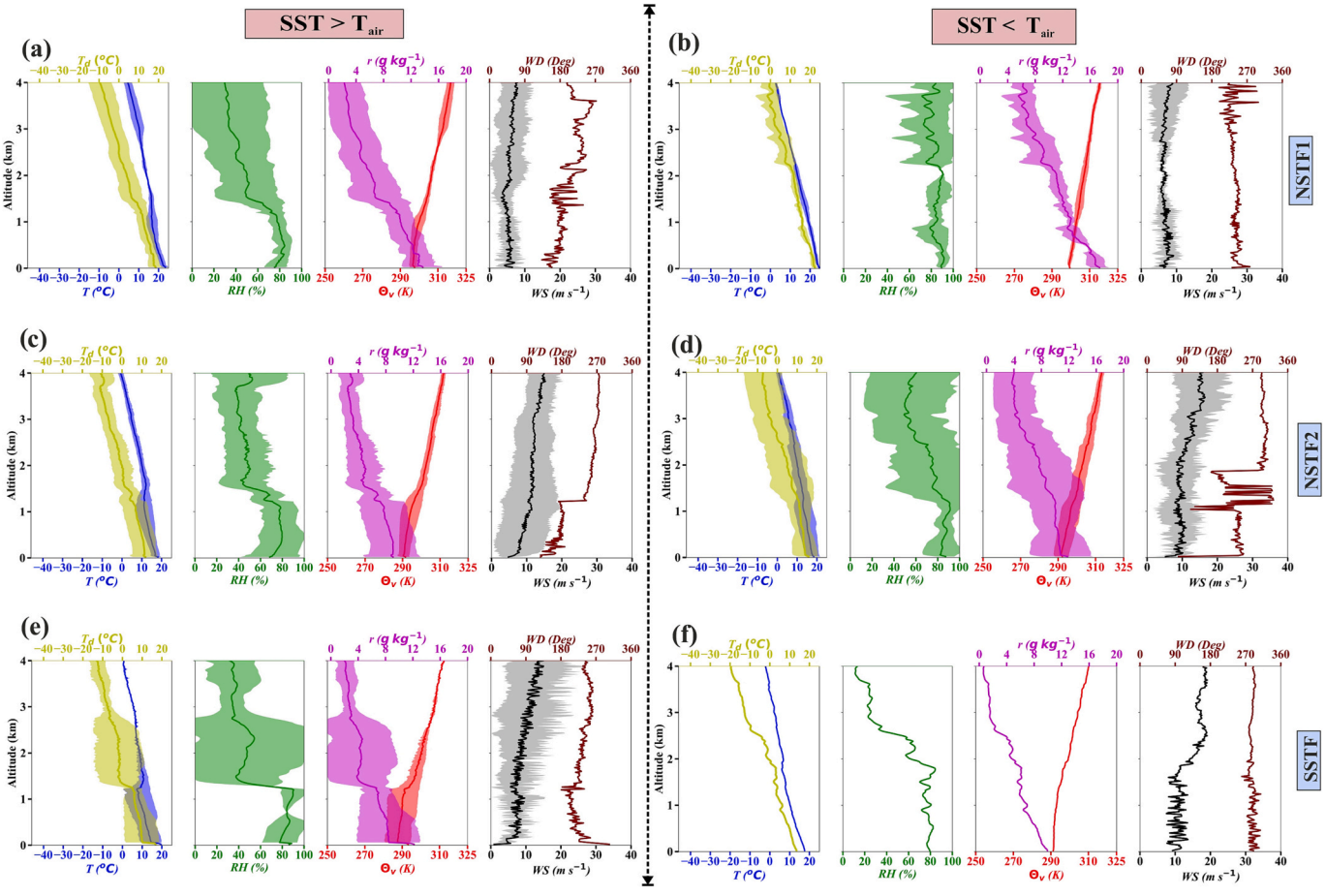

Fig. 3. Mean vertical thermodynamic profiles of air temperature (T in °C, blue line), dew point temperature (T_d in °C, yellow line), relative humidity (RH in %, green line), virtual potential temperature (θ_v in K, red line bottom x-axis), mixing ratio (r in g kg^{-1}, magenta line, and upper magenta x-axis), wind speed (WS in m s^{-1}, black line bottom x-axis), and wind direction (WD in degrees, brown line, and upper brown x-axis) up to 4000 m altitude for upper air soundings released in frontal regions of Sub-Tropical Indian Ocean (STIO) (i.e., NSTF1, NSTF2, and SSTF). The left panel indicates sounding profiles where $SST > T_{air}$ in (a) NSTF1, (c) NSTF2, and (e) SSTF while the right panel indicates sounding profiles where $SST < T_{air}$ in (b) NSTF1, (d) NSTF2, and (f) SSTF. Details of soundings considered for mean profiles in each region are provided in Table S2. The shaded area represents 1 standard deviation (except for wind direction). (For interpretation of the references to colour in this figure legend, the reader is referred to the web version of this article.)

Table 3
Characteristics of classified regions in terms of Campaigns, Thermodynamics, Clouds, Inversions, and their Macrophysical properties.

Oceanic Domains	Subtropical Indian Ocean (STIO)			Indian Ocean sector of Southern Ocean (ISSO)				High-Latitude Southern Ocean (HLSO)		
Frontal Regions	NSTF1	NSTF2	SSTF	SAF1	SAF2	PF1	PF2	SACCF	SB	CA
I. Campaign										
SOE-IX	3	3	2	2	–	1	1	1	1	4
SOE-X	2	4	–	2	–	2	5	4	2	9
SOE-XI	3	1	1	2	1	2	2	1	7	7
Total Count	8	8	3	6	1	5	8	6	10	20
II. Thermodynamics										
mean *SST* (°*C*): Oceanic domains	20.10 ± 3.04			7.70 ± 4.27				1.01 ± 0.38		
mean *SST* (°*C*): Frontal regions	24.19	19.21	16.92	13.15	10.38	4.85	2.43	1.45	1.06	0.52
SST gradient (°*C*/degree latitude): Oceanic domains	1.43 ± 0.98			0.74 ± 0.17				1.05 ± 0.18		
SST gradient (°*C*/degree latitude): Frontal regions	0.94	0.56	2.80	0.92	0.73	0.84	0.48	0.93	1.30	0.93
SST boundaries (°*C*)	27.5–20.5	23.6–19.1	18.5–14.3	12.8–10.5	8.3–7.2	5.8–3.7	3.6–1.2	1.9–0.5	2.2 – −0.4	2.18 – −1.1
SST - T_{air} (°*C*)	−0.55	0.43	0.80	−0.71	2.38	−0.67	0.12	−0.23	1.33	2.43
MSLP (hPa)	1016.2	1017.8	1019.3	1010.3	1011.1	994.7	995.3	983.2	984.3	990.6
WS (m s^{-1})	5.66	9.82	9.07	14.68	7.94	21.05	15.44	13.10	8.91	5.15
WD (°)	215.9	196.3	232.3	279.5	247.9	278.7	255.9	265.7	86.74	185.3
RH (%)	79.64	80.77	81.2	87.23	77.04	86.04	85.57	95.77	91.78	66.96
EIS (K)	8.46	9.89	8.61	8.29	2.41 (LC)	9.45	7.65	7.51	5.19	9.82
LTS (K)	16.32	17.86	16.34	15.52	7.23 (LC)	18.63	14.26	13.63	11.47	17.63
III. Cloud Layer										
No cloud (%)	37.5	50	33.33	0	100 (LC)	60	50	16.66	20	55
1 layer (%)	37.5	37.5	33.33	100	0 (LC)	0	12.5	33.33	40	40
2 layer (%)	25	12.5	33.33	0	0 (LC)	20	25	33.33	20	5
3 or more layer (%)	0	0	0	0	0 (LC)	20	0	16.66	10	0
Complete cloud (%)	0	0	0	0	0 (LC)	0	12.5	0	10	0
IV. Cloud Macro characteristics										
Total cloud thickness (m)	808± 575	1015± 571	450± 90	593± 374	NC (LC)	1360 ± 320	1750 ± 1181	1556± 614	1925 ± 880	602± 321
Cloud top height (m)	2612 ± 1183	2445± 998	1870 ± 650	1383 ± 387	NC (LC)	2790 ± 590	2430 ± 990	2548± 873	2807 ± 1067	2122± 1193
Cloud base height (m)	1196± 651	615± 199	680± 180	840± 415	NC (LC)	500 ± 0	575± 129	500 ± 0	632± 224	1326± 952
V. Inversion (INV)										
No INV (%)	25	37.5	33.33	0	100 (LC)	20	50	50	90	50
1 INV (%)	50	25	0	33.33	0 (LC)	40	25	16.66	0	25
2 INV (%)	12.5	0	0	66.67	0 (LC)	0	12.5	16.66	0	5
3 or more inversion (%)	12.5	37.5	66.67	0	0 (LC)	40	12.5	16.66	10	20
VI. INV Macro characteristics										
Main INV height (m)	1206± 704	1600± 1112	650± 90	2244 ± 680	NI (LC)	1840 ± 1347	1950 ± 1241	1313± 670	500 ± 0	1632± 1061
Main INV strength (K m^{-1})	0.23± 0.05	0.34± 0.12	0.35± 0.15	0.30± 0.11	NI (LC)	0.40± 0.21	0.25± 0.05	0.24± 0.09	0.20 ± 0.00	0.23± 0.1
Second INV height (m)	2390± 790	2087± 227	2210 ± 1070	2325 ± 1628	NI (LC)	1890 ± 450	2410 ± 1250	3420± 80	1200 ± 0	2263± 1149
Second INV strength (K m^{-1})	0.20± 0.00	0.37± 0.12	0.55± 0.05	0.33± 0.19	NI (LC)	0.65± 0.45	0.27± 0.00	0.23± 0.00	0.20 ± 0.00	0.25± 0.08

Note: A total number of atmospheric soundings available in each region during the respective campaign is summarized under subheading I. EIS and LTS stand for Estimated Inversion Strength and Lower Tropospheric Stability. NC denotes No Cloud, LC denotes Low in Confidence, and NI denotes No Inversion. The wind speed (WS), wind direction (WD), and relative humidity (RH) in subheading II are mean values observed at 925 hPa

decoupled MABL over NSTF1 (RL1, RL18, and RL75) may be associated with the developing monsoon conditions over Mauritius, as well as due to the influence of continentally advected warm and moist air masses by westerlies in the low-level atmosphere (higher values of *r* and *RH)* (Fig. 3b). However, stable MABL conditions recorded in soundings over NSTF2 (RL15, RL16, and RL21) were associated with the nighttime conditions and development of the cold front region (Fig. S5). The weakly unstable conditions observed in soundings over SSTF (RL13 and RL71) were associated with the weakening of oceanic eddies induced by the ARC, which augmented negative surface heat flux inputs and promoted stability within the boundary layer (Fig. S1, S3).

3.1.2. ISSO

The unique characteristic of this region is the prominent advection of distinct air masses which induces frequently changing atmospheric cold, warm, or occluded fronts. This makes ISSO the stormiest region of SO. Of the total 20 launches, at 11 soundings (RL9, RL10, RL22, RL23, RL24, RL27, RL28, RL44, RL45, RL68, and RL69) *SST* was higher than T_{air}.

However, a decrease in *MSLP* was observed which accounted for the weakening of the intensity of positive heat flux inputs to the lower atmosphere. Thus, low-level instability was noticed from the profiles of r and θ_v in these soundings which revealed the formation of a well-developed mixed layer capped by cumulus clouds (Miller and Albrecht, 1995; Bretherton, 1997; Zheng et al., 2018a). The averaged mixed layer height during unstable conditions were ~ 1630 m, ~720 m, ~412 m, and ~ 920 m at SAF1, SAF2 (low confidence), PF1, and PF2 respectively. The destabilized MABL over SAF1 (RL22 and RL23) were attributed to convectively active oceanic eddies in the nearest vicinity of soundings that led to the development of a warm atmospheric frontal region. In RL69, an active warm front region was observed with *SST* as 3.0°**C** higher than T_{air} (Fig. S7). Similarly, in RL68, the formation of a warm front region (*SST*-T_{air} = 2.4°**C**) resulted in destabilized MABL (Fig. S8).

The remaining 9 soundings (RL11, RL12, RL25, RL26, RL64, RL65, RL66, RL67, and RL70) showed *SST* < T_{air}. This indicates the formation of cold/occluded fronts to initiate LLWAA, thereby promoting the development of highly stratified decoupled MABL (Zheng et al., 2018b). The stabilized low-level atmosphere was also evident from a gradual increase in r and θ_v up to 4000 m (Fig. 4b,e,g). A combined effect of stable conditions, high-speed winds (>32 m s^{-1} within 4000 m), and the formation of multiple cold/occluded fronts supported the formation of frequent low-pressure stormy cyclonic systems in these mid-latitude regions of ISSO (manual weather records). Similar atmospheric conditions were recorded in the soundings (RL11, RL12, and RL70) made in SAF1 where the cold front formed due to the advection of warm and moist air masses via strong northwesterly is evident (Fig. S7). However, highly stable conditions over PF (RL25, RL26, RL64, RL65, RL66, and RL67) were attributed to low *MSLP* (~995 hPa), T_{air} > *SST*, polar jet streams inducing strong westerly winds exceeding 32 m s^{-1} within ~4000 m altitudes, and presence of strong baroclinicity (Fig. S9, S10). All soundings over PF2 showed an abrupt increase in wind speeds at altitudes between 700 m and 1500 m, which indicates the presence of distinct air mass that may act as a barrier between the well-developed low-level downdraft precipitation core and the upper-level storms. As a result of these conditions, numerous localized low-pressure stormy cyclones were experienced. Also, significant saturation in the form of snowfall and foggy conditions was observed within the low-level atmosphere of PF1 and PF2 (Trenberth, 2011).

3.1.3. HLSO

In this region, a significant decrease in wind intensities and reduced atmospheric stabilities were recorded. Out of 36 soundings, 19 showed weak low-level atmospheric instability, while the remaining indicated stable low-level atmosphere (Fig. 5a,c,e). The profiles of r and θ_v showed weak and shallow mixed layers with weak low-level instability induced by positive surface heat flux (RL5, RL6, RL31, RL32, RL33, RL34, RL35, RL36, RL40, RL42, RL51, RL52, RL55, RL56, RL57, RL58, RL59, RL60, RL61, and RL62). The weak positive heat flux was observed (i.e., *SST* >

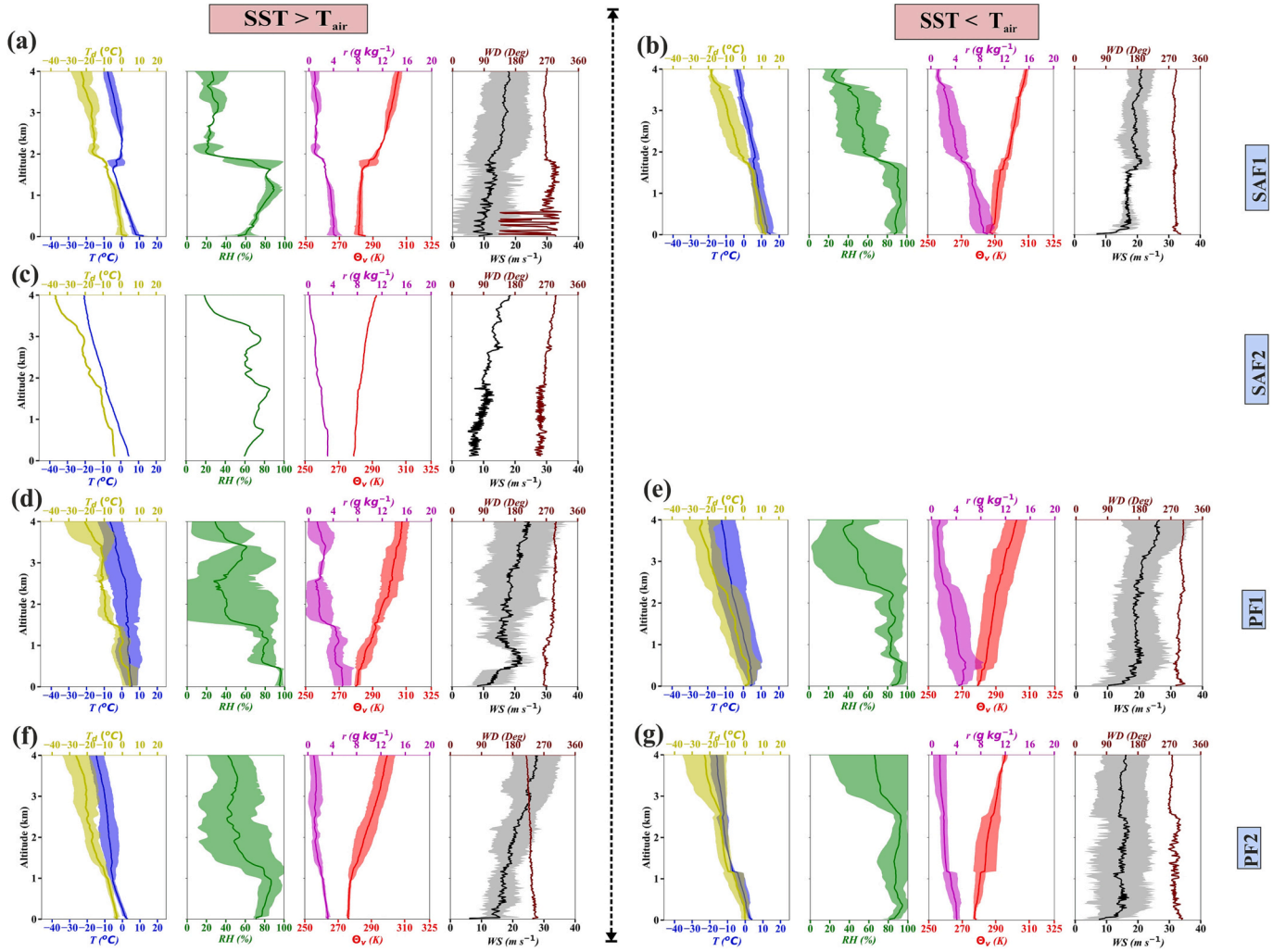

Fig. 4. Same as Fig. 3 but for the regions of the Indian Ocean sector of Southern Ocean (ISSO). The left panel represents sounding profiles where SST > T_{air} in (a) SAF1, (c) SAF2, (d) PF1, (f) PF2, and the right panel represents sounding profiles where SST < T_{air} in (b) SAF1, (e) PF1, (g) PF2.

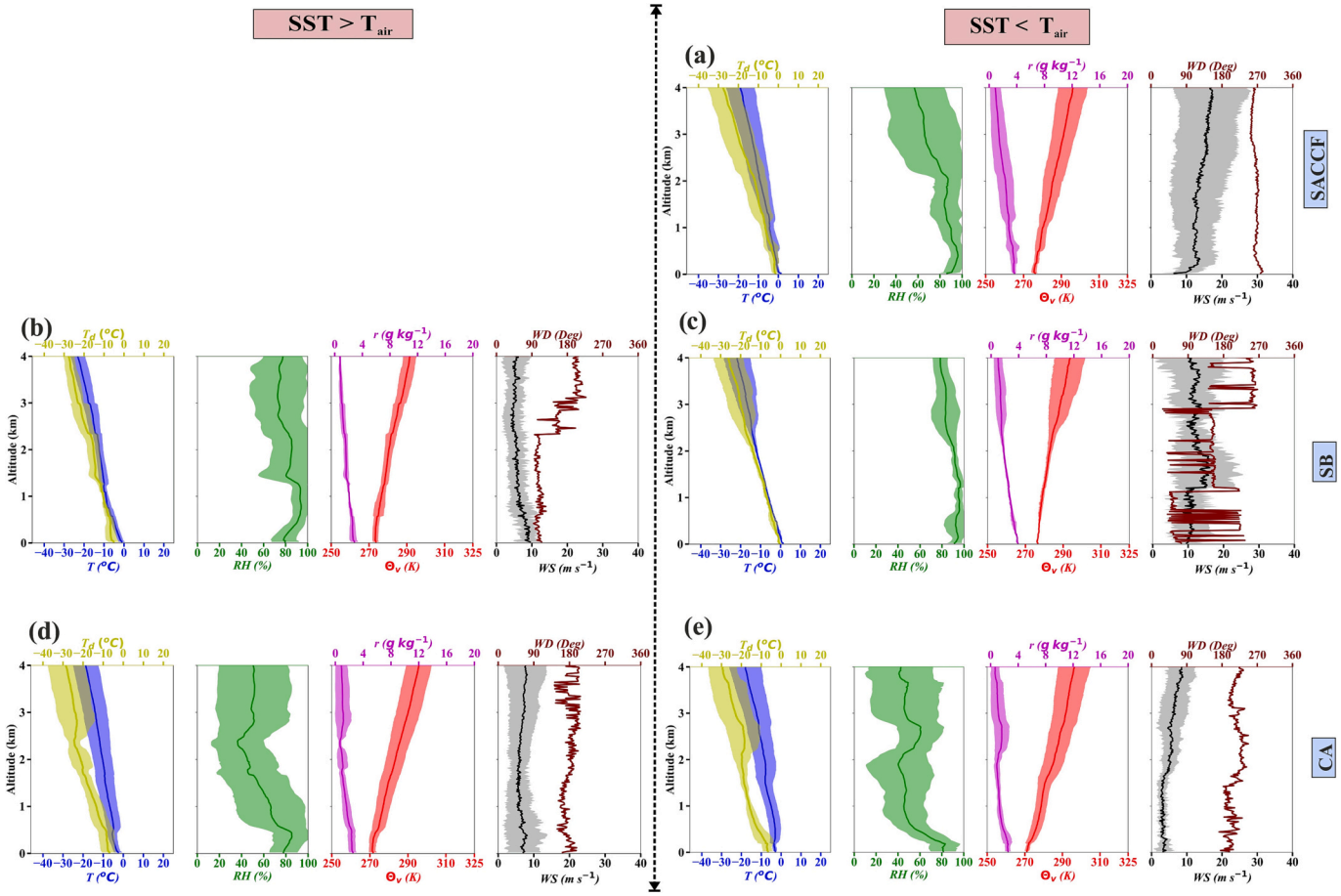

Fig. 5. Same as Fig. 3 but for regions High-latitude Southern Ocean (HLSO). The left panel represents sounding profiles where SST > T_{air} in (b) SB and (d) CA while the right panel represents sounding profiles where SST < T_{air} in (a) SACCF, (c) SB, and (e) CA.

T_{air}), however, the difference (*SST*-T_{air}) was observed to be lowest than that observed over STIO and ISSO regions. The condition with $SST > T_{air}$ was predominantly noticed in SB and CA regions which were due to the potential warming of Antarctic waters caused by the enhanced oceanic eddy activities associated with the closed mesoscale polar gyres. Particularly, the convective activities of Weddell Sea gyre (west of SB) and Prydz Bay gyre (east of SB and in the CA region) (Orsi et al., 1995; Orsi et al., 1999; Meijers et al., 2010; Couldrey et al., 2013) were characterized by the presence of a closed cyclonic gyre centered at Amery depression, off Amery Ice Shelf (Smith et al., 1984) (Fig. S12, S13). The warming of Antarctic waters coupled with the outflow of cold polar air masses by easterly winds over SB (Fig. 5b, 5c) and strong katabatic winds originating from Antarctica over CA (low *RH* and *r*; Fig. 5d, Fig. S13) (Parish and Cassano, 2003b; Parish and Cassano, 2003a) has initiated LLCAA-induced destabilization and coupled boundary layer structure (Zheng et al., 2018b). The average height of the mixed layer formed due to destabilization varied from ~512 m and ~ 562 m in the SB and CA regions, respectively (Fig. 5b,d). A slight increase in *MSLP* was noticed in SB and CA regions, contributing to MABL destabilization (Table 3). The atmospheric dynamics over the CA region differs from the SB region with less intensity of polar mesoscale cyclones owing to the geographic constraint imposed by the coast. The destabilized MABL over SB and CA were associated with the closer proximity of the gyre and the time of soundings (i.e., daytime, afternoon, and evening times profiles). In cases of sounding further away from the active gyre and nighttime or early morning launches, $T_{air} > SST$ accounted for the formation of the cold front region that promoted stability within MABL caused by LLWAA. The highly stable boundary layer was evident from gradually increasing *r* and θ_v profiles (RL3, RL4, RL7, RL37, RL 38, RL39, RL41, RL49, RL50, RL53, and RL54). Also, the SACCF region represented a significantly stabilized state of vertical atmosphere evident in the gradually increasing trend of *r* and θ_v in all soundings (RL8, RL29, RL30, RL42, RL43, and RL63). The T_{air} higher than *SST* indicated initiation of LLWAA that inhibited vertical mixing within MABL. This promoted the formation of a decoupled boundary layer structure over SACCF. This post-cold frontal region of ISSO is positioned in the southernmost extent of meandering ACC, where weak westerly winds (13.1 m s^{-1}), lowest *MSLP* (983.2 hPa), highest *RH* (95.77%), and $T_{air} > SST$ were ubiquitous, and led to the frequent development of low-pressure polar cyclonic systems (Carleton and Song, 1997; Irving et al., 2010).

3.2. Cloud and inversion characteristics

This section describes the characteristics of clouds (i.e., frequency of cloud occurrences, the height of the cloud base and cloud top along with total cloud thickness) and inversions properties (i.e., frequency of occurrences of inversion, height, and strength of primary and secondary inversions) observed over three major oceanic domains, i.e., STIO, ISSO, and HLSO.

3.2.1. STIO

Out of a total of 19 soundings available in this region, no cloud layers were observed in 8 soundings. While single-layer and double-layer clouds were witnessed in 7 and 4 soundings respectively (Table 3). The mean base of the lowest cloud was at 1196 m elevation over NSTF1 which decreased to 615 m and 680 m over NSTF2 and SSTF, respectively. Similarly, the mean cloud top height of the highest cloud layer

was 2612 m and 2445 m over NSTF1 and NSTF2 which gradually decreased to 1870 m over SSTF. The mean cloud thickness observed over NSTF1 was 880 m, which increased to 1015 m over NSTF2 and dropped to 450 m over SSTF. The decrease in the total cloud thickness over SSTF was due to the convective activities of ARC. Over SSTF, the coverage of thin low-level stratocumulus clouds was attributed to the formation of closed mesocyclonic systems at the top of the convective boundary layer (Muhlbauer et al., 2014; Truong et al., 2020).

The primary inversions over frontal regions, i.e., NSTF1 and NSTF2, were located at higher than 1200 m altitude having a strength of 0.23 K m^{-1} over NSTF1 and 0.34 K m^{-1} over NSTF2. These primary inversions over both NSTF regions were likely associated with the advection of warmer air mass from the African continent and strong subsidence due to the anti-cyclonic circulation of diverging winds, respectively. The secondary inversions over NSTF1 and NSTF2 were noticed at altitudes higher than 2000 m having the strength of 0.20 K m^{-1} and 0.37 K m^{-1}, respectively. Compared to NSTF1 and NSTF2, the strongest primary inversions were observed over SSTF at a lower altitude (650 m) with a strength of 0.35 K m^{-1}, while the secondary inversions were observed at a height of 2250 m with a strength of 0.55 K m^{-1}. The lowest primary inversions in SSTF are likely to cap the convective boundary layer (CBL) formed due to enhanced low-level mixing caused due to eddies ejected from ARC (Lutjeharms and Valentine, 1988; Lutjeharms and Van Ballegooyen, 1988; Fig. S6; Boebel et al., 2003).

3.2.2. ISSO

The presence of high cloud cover and multiple inversions were noticed in ISSO. This was attributed to the mixing of distinct air masses regulated by multiple atmospheric fronts, i.e., cold/warm/occluded fronts over shorter spatial scales. Of the 20 soundings, 12 recorded the presence of clouds over ISSO. The six soundings launched over SAF1 showed the presence of low-level clouds. Whereas only one sounding over the SAF2 region shows cloud-free conditions. However, based on single sounding, it is difficult to provide a statistically significant interpretation for the SAF2 region. A recent study by Behrangi and Song (2020) reported more cloud occurrences over the SAF region than in PF. Significant low-level clouds with heights as low as 500 m and as high as 4000 m were observed in the ISSO region. Data showed the presence of multi-layered and complete clouds over PF1 and PF2, respectively. Over SAF1, the clouds had an average thickness of 593 m, while over PF1 and PF2, it was 1360 m and 1750 m, respectively. Average cloud top heights were observed to be higher in PF1 (2790 m) and PF2 (2430 m) regions. The low-level stratus clouds over these regions experienced air mass temperatures as low as −3.79°C at 500 m. The second cloud layer was identified at an average altitude of 3360 m recording temperatures as low as −18.82°C (Fig. 4). This is consistent with previous studies highlighting the presence of multilayered clouds in mixed phases (Huang et al., 2012; Mace et al., 2020; Mace et al., 2021). Over the ISSO, the low-level stratus clouds commonly precipitate due to strong advection-induced mixing of multiple air masses. This triggers snowfall and foggy conditions over PF, while precipitation as rain over SAF (Kawai et al., 2015).

Inversions over ISSO were primarily due to advective motions induced mixing between different air masses by stronger winds (Hande et al., 2012). Two-thirds of the soundings made over SAF1 and SAF2 show the presence of double inversions followed by single inversions. The average height of the primary and secondary inversions were 2244 m and 2325 m, with a strength of 0.30 K m^{-1} and 0.33 K m^{-1}, respectively. Over PF1 and PF2, three or more inversions of significant strengths were detected, which were likely induced by polar jet streams forcing strong baroclinic instabilities (Simmonds and Lim, 2009; Fig. S9, S10). Here, the average height of primary and secondary inversions were 1840 m and 1890 m in PF1 and 1950 m and 2410 m in PF2, respectively. However, relatively stronger inversions were observed over PF1, i.e., 0.40 K m^{-1} (primary) and 0.65 K m^{-1} (secondary), than compared to PF2, i.e., 0.25 K m^{-1} (primary) and 0.27 K m^{-1} (secondary).

3.2.3. HLSO

Approximately half of the soundings over SACCF revealed two or more layered clouds, which decreased to two-fifth over SB and one-twentieth over CA. Low-level multilayer thick clouds over SACCF were attributed to the frequent formation of low-pressure mesoscale cyclonic systems. In contrast, the decreased frequency of multilayered clouds over SB and CA was due to increased convective activity of polar gyres (i.e., Weddell Sea gyre and Prydz Bay gyre) (Table 3). The average cloud thickness over SACCF was 1556 m, which increased further over SB (1925 m) and decreased to 602 m over CA. Over SACCF and SB, clouds were noticed at significantly low altitudes (i.e., at average cloud base height of 500 m and 632 m), having air temperatures as low as −2.81°C. At higher altitudes (>2000 m), the air temperature within the cloud layer was as low as −23°C. As indicated with air masses of such low temperature, mixed-phased clouds, i.e., low-level supercooled water droplets and mid-level ice crystals within 4000 m have been consistently reported in other areas of HLSO (Huang et al., 2012; Mace et al., 2020). The average cloud base height over the CA region was recorded at a relatively higher altitude (1326 m) than that over SACCF and SB. Distinctively, ice virga (precipitation not reaching the surface) was noticed over SB and CA, consistent with previous studies (Wang et al., 2018; Vignon et al., 2019; Jullien et al., 2020; Alexander et al., 2021).

Concerning inversions over SACCF, no significant inversions were observed among half of the soundings (Table 3). The other half constituted single-inversion, double-inversion, and three or more than three inversions, in equal counts. The recorded inversions were generally associated with strong convergence and prominent low-pressure cyclonic systems in the low-level atmosphere. Regardless, the primary and secondary inversions were weak (0.24 and 0.23 K m^{-1}) and were observed at ~1313 m and ~ 3420 m, respectively. The presence of multi-level inversions (three or more) were dominant over SB and CA. However, these inversions were weak over SB (0.20 K m^{-1}) due to lower *MSLP* and slowly evolving low-level convection at low altitudes. It can be anticipated that weak unstable conditions might form for a small duration and promote cloud formation. These clouds generally appear beneath weaker inversions, which could be easily eroded through radiation or even by weak easterlies. Compared to SB, inversion strength slightly increased over CA. Over CA, average primary inversions of strength 0.23 K m^{-1} were observed at higher altitudes (1632 m), and secondary inversions of strength 0.25 K m^{-1}, if observed, were at ~2263 m. The inversions were associated with an increase in the temperature of Antarctic surface waters, a slight increase in *MSLP,* and katabatic winds advecting dry and cold air mass across mid-altitudes.

3.3. Signatures of dynamic physical processes

In this section, the dominant physical processes such as convection, advection, precipitation, and radiative heating/cooling were investigated between altitudes 500 m and 4000 m following (Betts, 1982; Betts and Albrecht, 1987). The modification in air mass saturation was traced by analyzing conserved variables (i.e., $\theta_e$and q) in the form of θ_e−q diagram representing three oceanic domains examined in the present study.

3.3.1. STIO

Over NSTF1 and SSTF, the presence of near-surface convective mixing was evident with a clear mixing line structure indicated by a gradual decreasing tendency of $\boldsymbol{\theta_e}$ and q with increasing altitude (Fig. 6b,c). Instability caused due to convective mixing accounted for the formation of shallow CBL with the top of the surface-based mixed layer extending up to 840 m (925 hPa) over NSTF1 and 1200 m (887 hPa) over SSTF. The presence of shallow CBL is anticipated (if CBL tops ≥ 800 hPa) (Betts and Albrecht, 1987). However, the convective mixing was not only restricted to surface-based CBL but extended in intermediate altitudes (simultaneous decrease in $\boldsymbol{\theta_e}$ and q) splitted by radiative process (change in $\boldsymbol{\theta_e}$ with constant q) (Fig. 6b). This demonstrates that CBL

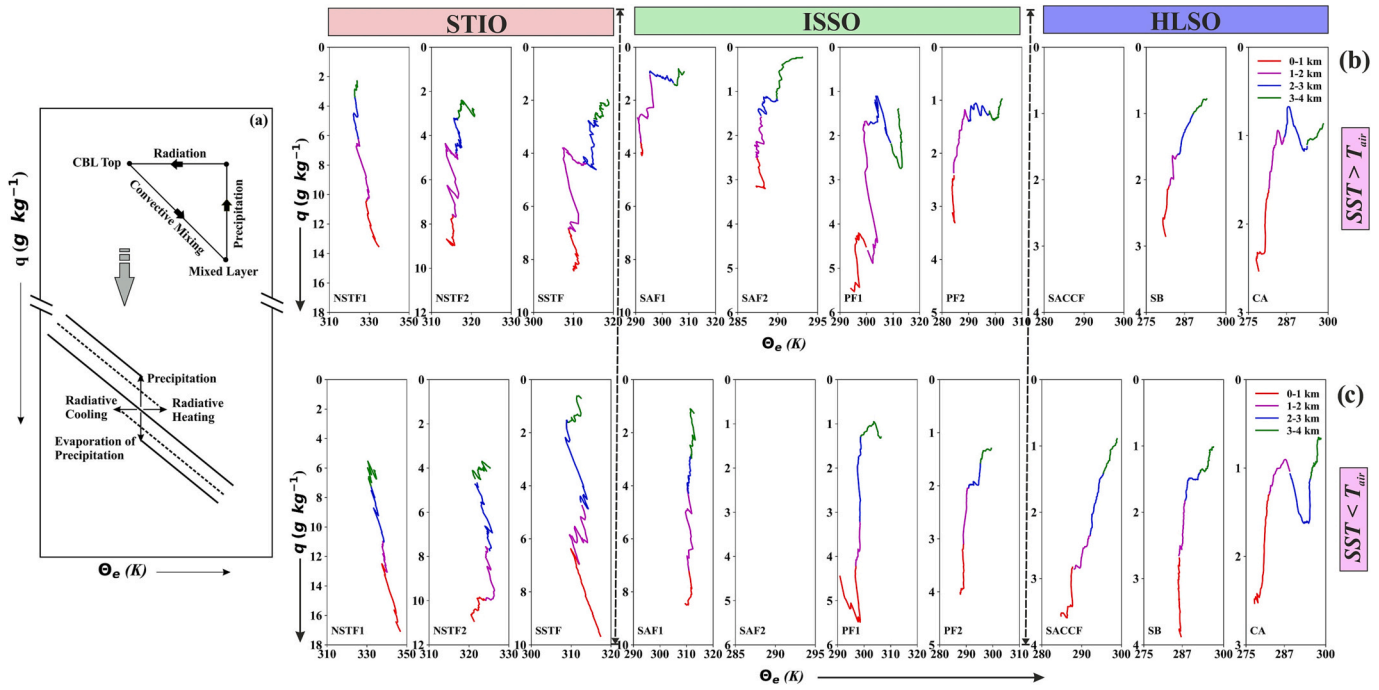

Fig. 6. (a) Schematic diagram of conserved variables ($\theta_e - q$) depicting the effect of physical processes such as convective mixing, precipitation/evaporation, and radiative heating/cooling in modifying the mixing line structure. The $\theta_e - q$ diagram obtained over each frontal region of three major oceanic domains (i.e., STIO, ISSO, and HLSO) when (b) SST > T_{air} and (c) SST < T_{air} at soundings considered in each region. Obtained structure of air parcel motion in all frontal regions is colored as surface – 1000 m (in red), 1000–2000 m (in magenta), 2000–3000 m (in blue), and 3000–4000 m (in green). For clear variability of the structure of air parcel motion, scales for the x and y axis are varied accordingly for each region. (For interpretation of the references to colour in this figure legend, the reader is referred to the web version of this article.)

thermally-coupled to surface promotes internal convective mixing due to re-stratification (Nicholls, 1984; Betts and Albrecht, 1987) and splits up single well-mixed air-column into different convectively mixed layers at higher altitudes (simultaneous decrease in $\boldsymbol{\theta_e}$ and *q;* NSTF1 and SSTF; Fig. 6b). Thus, this indicates coupled CBL in NSTF1 and SSTF, which is consistent with studies reporting the common presence of coupled boundary layers over high-pressure regions (Nicholls, 1984; Bretherton and Wyant, 1997; Stevens, 2000; Jones et al., 2011; Dong et al., 2015; McGibbon and Bretherton, 2017; Zheng et al., 2018a). Radiative heating was the regulatory process in altitudes between the intermediately decoupled layer (Fig. 6b,c). Interestingly, at the top of CBL over SSTF, weak precipitation signature (near uniform variation of $\boldsymbol{\theta_e}$ and *q*) accompanied by radiative heating underneath and above was evident (Fig. 6b). Thus, anticipates presence of a thin stratocumulus clouds layer above the CBL top associated with a closed mesoscale convective system, which is concurrent with few reported studies (Muhlbauer et al., 2014; Truong et al., 2020). In NSTF1 and SSTF, irrespective of $SST > T_{air}$ ($SST < T_{air}$), signatures of these processes were observed with differences in the increased (decreased) intensity of convective mixing leading to a highly (weakly) evolved mixed layer structure. Noticeably, the most robust low-level convective mixing occurred over SSTF, driven by ARC's convective activities (Fig. 6b,c). Compared to physical processes over NSTF1 and SSTF, over NSTF2, low-level advection of cool air-mass followed by precipitation (from ~220 m to ~1080 m) was anticipated as the dominant process (NSTF2; Fig. 6b,c). Above the precipitation signature, advection due to changing wind directions (south to west) appears to drift the atmospheric moisture content (Fig. 3c,d).

3.3.2. ISSO

Over SAF1 and SAF2, signatures of low-level convection were significantly suppressed, while strong advective motions of multiple air masses were likely to be a regulatory process. This anticipation is supported by the abruptly changing wind direction that portrays this region as a dynamic storm track region constructed of multiple air masses (Fig. 4a,b). For the atmospheric conditions, when $SST > T_{air}$, the $\boldsymbol{\theta_e} - q$ diagram in these regions showed vertical lines which may readily indicate advection-induced mixing between different air masses mainly enforced by the prevalence of multiple atmospheric fronts. However, when $SST < T_{air}$, in addition to advection induced-mixing, the likelihood of substantial precipitation was indicated in $\boldsymbol{\theta_e} - q$ diagram by a larger decrease in q with a nearly uniform variation of $\boldsymbol{\theta_e}$ up to 4000 m altitude in SAF1 (Fig. 6c). Further ahead, the $\boldsymbol{\theta_e} - q$ diagram observed over PF1 showed stronger low-level advection caused due to merging of multiple air masses by high-speed winds as well as due to the impact of the intense polar jet stream (Fig. 4d-g). This strong advection-induced air mass mixing was favorable during both conditions (i.e., $SST > T_{air}$ and $SST < T_{air}$) throughout the vertical 4000 m altitude over PF1 (Fig. 6b,c). In contrast, in conditions when $SST < T_{air}$, the likelihood of precipitation/condensation of falling precipitation at higher altitudes (beyond 1500 m) was another dynamic process in PF1. In PF2, the $\boldsymbol{\theta_e}$–q diagram depicted the dominant signature of precipitation/condensation of falling precipitation up to nearly 2000 m altitude irrespective of the conditions (i.e., $SST > T_{air}$ and $SST < T_{air}$), which indicates a meteorologically highly stable atmosphere formed due to stronger advection of multiple air masses (Fig. 6b,c).

3.3.3. HLSO

Over SACCF, the low-level atmosphere was influenced by advective processes, while weak convection prevailed over SB and CA. Over SACCF, although the intensity of advective motions decreased, strong low-level convergence and continuous advection of cold polar air mass induce a highly stable atmosphere ($SST < T_{air}$) and a system of intensified low-pressure cyclones. As a result, in the $\boldsymbol{\theta_e}$– q diagram of SACCF, low-level advection was likely, above which precipitation occurred (uniformity in $\boldsymbol{\theta_e}$and decrease in q) with the occurrence of radiative heating above and below this precipitation (SACCF; Fig. 6c). This falling

precipitation tends to condense faster, causing foggy and snowy conditions in the near-surface atmosphere, while in intermediate and higher altitudes supported the formation of low-level thicker clouds. However, at higher altitudes, no clear signature of precipitation was observed (Fig. 6b). This indicated the occurrence of closed mesoscale cyclonic systems due to strong low-level convergence.

Over SB and CA, the θ_e−q diagram observed during conditions of $SST > T_{air}$ depicted shallow convective mixing line structure (decline in θ_e and q) up to ~60 m over SB and ~220 m over CA due to an increase in the temperature of Antarctic surface waters linked to the activity of subpolar gyres, i.e., Weddell Sea gyre and Prydz Bay gyre (SB and CA; Fig. 6b). With increasing altitudes, a decline in convection and occurrence of prominent precipitation (uniformity in θ_e and a significant declining q) was observed at intermediate and high altitudes in both regions (Fig. 6b). In these regions, we anticipate sublimation of precipitation to support virga conditions as a regulatory process commonly in the intermediate altitudes. Occurrence of sublimation-supported virga conditions have been reported in a few studies poleward of 64°S (Forbes and Hogan, 2006; Alexander et al., 2021) and over Antarctica (Forbes and Hogan, 2006; Jullien et al., 2020). Interestingly, significant precipitation in intermediate altitudes and prominent radiative heating at higher altitudes were observed over CA than that over SB (Fig. 6b). However, in conditions when $SST < T_{air}$, the convective mixing signature was not pronounced over both SB and CA; weak advection was likely followed by stronger precipitation at mid and high altitudes (Fig. 6c).

3.4. Case studies in frontal regions of three major oceanic domains

In addition to low-level thermodynamics, cloud, and inversion characteristics, the effect of synoptic scale meteorology in altering the state of MABL has been presented in the form of case studies in this section. Three typical case studies were chosen from SSTF, SAF1, and CA regions lying in STIO, ISSO, and HLSO respectively. A sounding selected in SSTF was aimed to highlight the effect of Agulhas Retroflection Current (ARC) to regulate the vertical state of MABL, while the selection of sounding in SAF1 region was aimed to demonstrate the effect of common multiple atmospheric fronts (i.e., cold, and warm front) in SO region to alter the state of MABL. Also, a sounding selected in the CA region aims to depict the influence of the convective activities over the Prydz Bay gyres as well as the effect of katabatic winds on the structure of MABL in the coastal region of Antarctica.

3.4.1. In STIO (SSTF)

A sounding launched at 40°S, 58.48°E on 12th January 2017 at 06:00 UTC is presented in Fig. 7a. The synoptic view around this sounding depicted a warm front region indicated by $SST > T_{air}$ and increased activity of oceanic eddies associated with the ARC (Lutjeharms and Van Ballegooyen, 1988). The *SST* at the location of sounding was 3.02°C higher than T_{air} and recorded *MSLP* at 1027 hPa. The advection of LLCAA was evident from the prominent southerly winds bringing cold polar air mass to the region (Fig. 7a). These conditions led to an unstable MABL leading to the formation of a well-evolved thermodynamically coupled mixed layer structure (Zheng et al., 2018b; Zheng et al., 2018a; Zheng and Li, 2019a). This was also evident in the nearly uniform variation in profiles of $\boldsymbol{\theta_v}$ and r up to 1220 m. At the top, vertical mixing was suppressed by a strong primary inversion (0.73 K m^{-1}), followed by multiple inversions (>3) to an altitude of 4000 m (Fig. 7a). In unstable conditions, the formation of a single cloud layer was noticed with a cloud base height of ~980 m, cloud top height of ~1220 m, and total cloud thickness of ~240 m. These observations concur with the records about thin low-level stratocumulus cloud coverage at the top of the convective boundary layer (Muhlbauer et al., 2014; Truong et al., 2020).

3.4.2. In ISSO (SAF1)

A sounding launched at 43.02°S, 57.02°E on 2nd March 2020 at 12:00 UTC is presented in Fig. 7b. The synoptic illustration depicted both the warm front region ($SST > T_{air}$) and cold front region ($SST < T_{air}$) in the nearest proximity of the sounding location, with considered sounding lying in the cold front region. Being in a cold front region, inputs of weak negative surface heat fluxes were evident with $SST < T_{air}$ by 1.75°C. Also, prominent synoptic LLWAA could be seen from strong north-westerly winds advecting warm moist air masses over this region. LLWAA, which is one of the characteristic features commonly reported in the SO region, can be observed in this typical sounding (Wall et al., 2017). The LLWAA coupled with inputs of weak negative fluxes ($SST < T_{air}$) and decreased *MSLP* (1011 hPa) accounted for highly stabilized and thermodynamically decoupled MABL in this sounding. Also, previous studies have frequently reported the presence of decoupled boundary layer in this SO region (Mace and Protat, 2018; Zheng and Li, 2019b; Truong et al., 2020). A highly stabilized boundary layer can be observed with a gradually increasing tendency of $\boldsymbol{\theta_v}$ and r within 4000 m altitude (Fig. 7b). Due to high low-level stabilization, the formation of a thick cloud layer was observed with cloud base height (~760 m), cloud top height (~1720 m), and total cloud thickness (~960 m). The main inversion having significant strength (~0.55 K m^{-1}) was recorded at the height of ~1840 m (Fig. 7b). Interestingly, profiles of $\boldsymbol{\theta_v}$, r, and *RH* depicted the presence of air masses of distinct properties within the 4000 m air column. This is indicated by the presence of highly saturated air mass in the low-level atmosphere (up to ~1720 m) below the main inversion and by the prevalence of relatively dry air mass above this inversion up to 4000 m altitude (Fig. 7b). The presence of such varying property air masses together with highly stabilized conditions is attributed to the frequent formation of multiple cold (warm) fronts at shorter spatial scales mainly driven by LLWAA (LLCAA) in the SO region (Zheng and Li, 2019a).

3.4.3. In HLSO (CA)

A sounding launched at 66.98°S, 64.86°E on 16th February 2020 at 06:00 UTC lying in the CA region, was used as a representative sounding in HLSO (Fig. 7c). The synoptic conditions depicted the occurrence of a warm front ($SST > T_{air}$) at and around the sounding location (Fig. 7c). The formation of a warm front in this region is attributed to the potential warming of coastal Antarctic waters due to the convective activity of polar mesocyclones regulated by the Prydz Bay gyre near the Antarctic coast (Smith et al., 1984). As a result, at this typical sounding, the inputs of positive surface heat fluxes were indicated from $SST > T_{air}$ by 3.76°C and the recorded *MSLP* as 988 hPa. Also, the presence of prominent LLCAA of cold, dry polar air mass through strong katabatic south easterly winds mainly originated from the Antarctic continent was observed (Fig. 7c). The combined effect of increased surface heat fluxes and strong LLCCA at and in the vicinity of the sounding location has induced low-level atmospheric instability. This instability resulted in the formation of a well-mixed layer (indicated by nearly uniform variation of $\boldsymbol{\theta_v}$ and r) capped by a weak inversion recorded at ~820 m of strength ~ 0.24 K m^{-1}, which marks the limit of vertical mixing at this sounding (Fig. 7c). Thus, the LLCAA induced destabilization resulted in the formation of thermodynamically coupled MABL, supporting the occurrence of a thin cloud layer with a cloud base height of ~920 m and a total cloud thickness of ~440 m formed at the top of the mixed layer. Above the cloud layer, a significant stable atmosphere composed of dry and cold air mass was observed in the sounding launched in this region (Fig. 7c).

3.5. Estimated inversion strength (EIS) and lower tropospheric stability (LTS)

To the best of the authors' knowledge, it is the first-time reporting the estimates of *EIS* and *LTS* over a least explored ISSO, especially over high polar latitudes. The estimates for *LTS* were comparable with estimates reported over regions of the Australasian sector of the Southern

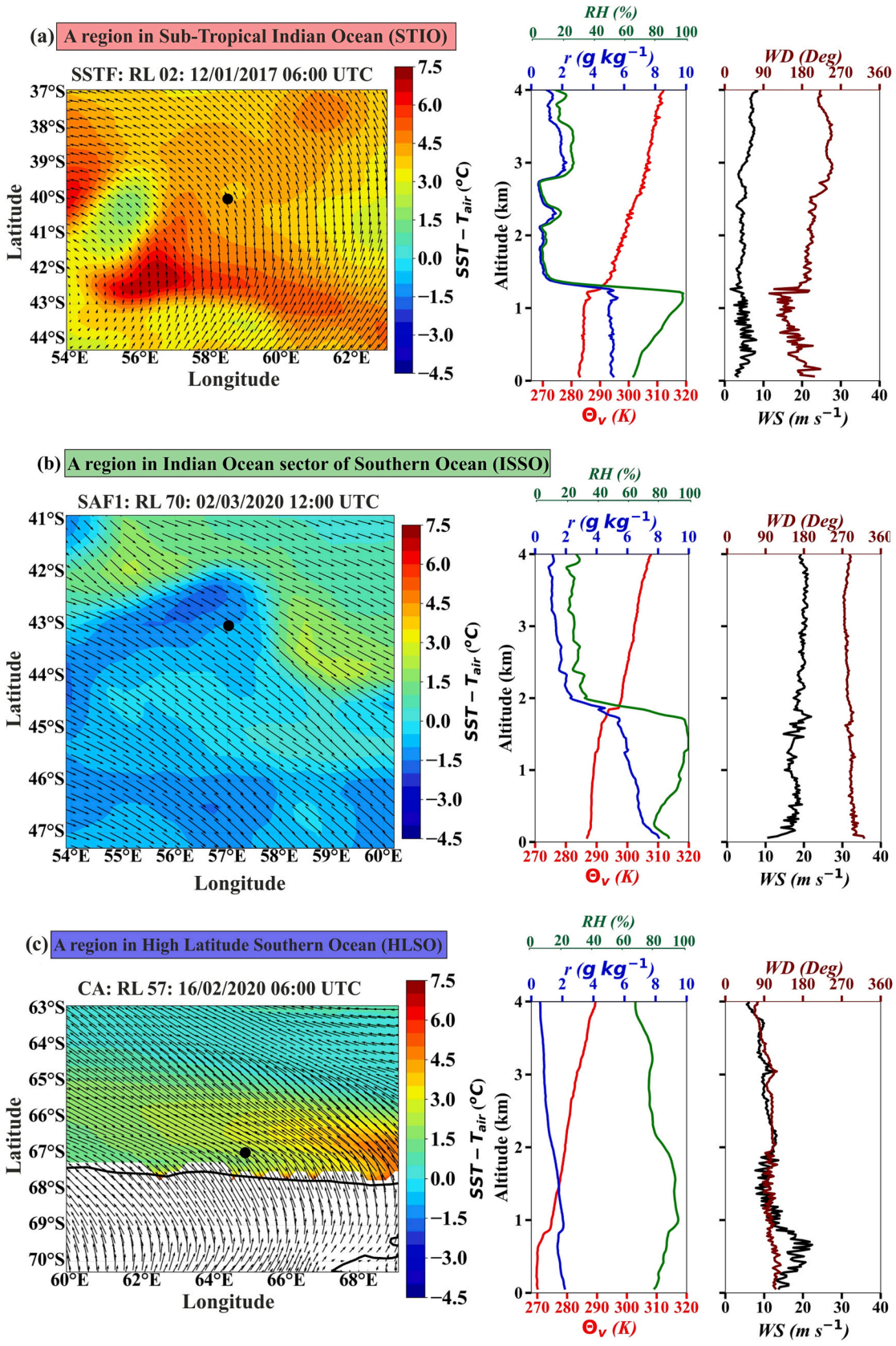

(caption on next page)

Fig. 7. Case studies using three typical soundings launched in three distinct frontal regions lying in three major oceanic domains i.e., (a) In the Sub-tropical Indian Ocean (STIO) over the Southern Sub-Tropical Front (SSTF) (b) In the Indian Ocean sector of Southern Ocean (ISSO) over Northern Sub-Antarctic Front (SAF1), and (c) In High Latitude Southern Ocean (HLSO) over Coastal Antarctica (CA). The Upper, middle, and lower left panel represents synoptic near-surface air-sea temperature difference (SST-T_{air} in °C) and wind circulation pattern observed in the vicinity of soundings launched in SSTF, SAF1, and CA respectively. This synoptic view was generated using data on surface-based SST, T_{air} at 2 m, and wind fields (10 m u- and v- component) obtained from ECMWF-ERA5 reanalysis. The sounding locations are marked with a black circular dot and colour bars are shown. The Upper, middle, and lower right panel represents a 4000 m vertical profile of virtual potential temperature (θ_v in red), mixing ratio (r in blue), relative humidity (RH in green), wind speed (WS in black), and wind direction (WD in brown) for radiosonde launched at 40.00°S, 58.48°E on 12-01-2017 at 06:00 UTC in the SSTF, at 43.02°S, 57.02°E on 02-03-2020 at 12:00 UTC in the SAF1, and at 66.98°S, 64.86°E on 16-02-2020 at 06:00 UTC in CA region respectively. (For interpretation of the references to colour in this figure legend, the reader is referred to the web version of this article.)

Ocean (ASSO) by Truong et al. (2020). However, slight differences in the estimates were obtained over a few frontal regions of ISSO (Table 3). This could be attributed to the differences in the ISSO's regional, seasonal, and meteorological conditions to that of the ASSO. Further, the variability of fractional cloud cover (1-'no cloud frequency') with *EIS/LTS* showed a good fit with respect to the linear relationship proposed by Wood and Bretherton (2006), particularly over post-cold frontal regions of ISSO, i.e., over SACCF and SB. These observations for the linear relationship of Wood and Bretherton (2006) closely estimate CF using estimated *EIS/LTS* over post-cold frontal regions of SO are consistent with the findings of Naud et al. (2016) and Wood and Bretherton (2006). However, in the other regions of the study area, this relationship poorly served to provide estimates of CF.

4. Discussion and conclusion

The Indian Ocean sector of the Southern Ocean (ISSO) is one of the least studied regions concerning the thermodynamic characterization of low-level atmosphere, clouds, inversions, and physical processes. This study presents the first set of meteorological measurements covering a large geographical area between 25°S to 68°S along 57°E to 78°E while crossing numerous oceanic fronts of three major oceanic domains (STIO, ISSO, and HLSO). This study explores the effects of air-sea coupling (i.e., air-sea temperature difference, $SST\text{-}T_{air}$) in shaping the vertical thermodynamic structure of low-level atmosphere (in particular, MABL), and its influence on the characteristics of clouds and inversions associated with the dynamic physical processes occurring over the frontal regions of STIO, ISSO, and HLSO. Our finding highlights that the thermodynamic stability, and the associated structure of the low-level atmosphere were strongly affected by synoptic meteorological conditions and continually varying air-sea coupling, i.e., the air-sea temperature difference across frontal regions of the study area.

Across the frontal regions from sub-tropics to high latitude polar regions, four significant processes, namely convection, advection, precipitation, and radiative heating/cooling were observed. Among these processes, over STIO regions (NSTF1, NSTF2, and SSTF), major inputs of positive surface heat fluxes were observed to initiate convection in the low-level atmosphere. As a result, prominent low-level atmospheric mixing formed a well-evolved convective mixed layer. This convective mixed layer thermodynamically coupled to the surface was observed to decouple (weakened) in mid-altitudes, but due to the re-stratification, continued internal convective mixing resulted in the formation of a coupled mixed layer structure. Compared to NSTF1 and NSTF2 regions, in SSTF, strong convection-induced low-level convective mixing formed a deeper mixed layer structure accompanied by multiple strong inversions and higher proximity of no clouds to very thin clouds. These conditions observed over SSTF were because of active oceanic eddies associated with ARC (Lutjeharms and Gordon, 1987; Lutjeharms and Van Ballegooyen, 1988). Overall, in sub-tropical regions, strong convection and high-pressure formations accounted for the formation of thermodynamically coupled MABL capped by thin mid-altitude clouds followed by strong low-level inversions. In addition to convection, advection in intermediate altitudes was seasonal because of changing wind patterns. Also, prominent advection of cold air masses and few instances of weak precipitation caused weak radiative heating in intermediate altitudes.

Further southwards, in the regions of ISSO, the prominence of advection-induced mixing of multiple air masses and precipitation were regulatory processes. Strong advective mixing was induced by a frequently changing system of atmospheric fronts (i.e., cold/warm/occluded). A dynamic system of multiple atmospheric fronts over shorter spatial scales was experienced by these regions. These systems aided significant precipitation, mainly in conditions when $SST < T_{air}$. Moreover, in the PF1 and PF2 regions of ISSO, a unique system of intensified winds hinted at the impact of the polar jet stream, while the presence of baroclinic instabilities was depicted by a system of multiple cold and warm fronts. The combined effect of this causes rigorous advective mixing of air masses of varying properties in ISSO regions. Such an advection aided faster condensation of falling precipitation in these regions, which is consistent with past reported studies (Jensen et al., 2000; Wang et al., 2015; Lang et al., 2021). This condensation is likely to be in the form of fog and snow in PF regions while in the form of rain in SAF regions. At mid- and higher altitudes, condensation accounted for the formation of thicker multi-layered clouds, which were as low as 500 m and as high as 4000 m. In the ISSO regions, the frequency of low-level inversions was relatively less than multiple inversions that occurred at higher altitudes, mainly led by stronger advection of multiple air masses by intense winds.

Further southwards in one of the HLSO region, i.e., over SACCF, prominent low-level precipitation was observed to be associated with the formation of intensified low-pressure cyclonic systems formed due to the convergence of north-westerly and south-easterly winds. This precipitation cum condensation accounted for low-level multi-layered clouds, while strong advection at higher altitudes caused multiple high-level inversions even in this HLSO region.

Notably, the action of high-speed winds that continually advected cold and warm air-masses through a dynamic system of formation of multiple atmospheric fronts in PF1, PF2, and SACCF has accounted for enhancing the severity of stormy low-pressure cyclones in these regions. These observations are consistent with reports on the occurrence of mid-latitude stormy cyclones over other sectors of SO, i.e., the Australasian sector of the Southern Ocean (Carleton and Song, 1997; Field and Wood, 2007; Irving et al., 2010; Truong et al., 2020). Formation of such systems supported prominent precipitation and condensation of descending precipitation at different altitudes. The occurrences of aforementioned processes in these regions of ISSO were highlighted by (Srivastava et al., 2007) over ISSO, and some studies have documented it over the Australasian sector of the Southern Ocean (Wang et al., 2015; Lang et al., 2018; Lang et al., 2021). The dominance of these processes over ISSO regions and SACCF has accounted for the presence of low-level multi-layered cloud structures. The presence of such types of clouds in these regions is consistent with the previous records using in-situ observations (Jensen et al., 2000; Lang et al., 2018; Mace and Protat, 2018; Truong et al., 2020; Alexander et al., 2021; Lang et al., 2021) and remote sensing observations made in other sectors of SO (Mace et al., 2009; Huang et al., 2012; Huang et al., 2015a; McCoy et al., 2015; Kuma et al., 2020). However, recorded high-level inversions in these regions comply well with past reports in the Australasian sector of the Southern Ocean (Jensen et al., 2000; Truong et al., 2020).

Further towards southernmost regions of HLSO, i.e., over SB and CA,

low-level dynamics were regulated by weak and shallow convection coupled with the advection of cold and dry polar air mass via strong katabatic winds originating from the Antarctic continent in the intermediate and high altitudes. Results revealed multiple weak inversions induced by the action of katabatic winds, while the strength of these winds regulated the strength of occurring inversions. Similar observation on inversions in Antarctica were reported by Connolley (1996). Moreover, weak precipitation in intermediate altitudes was anticipated to undergo a sublimation process resulting in ice virga conditions. Similar conditions were reported in regions of similar characteristics in the Australasian sector of the Southern Ocean (Wang et al., 2018; Vignon et al., 2019; Jullien et al., 2020; Alexander et al., 2021).

Further, results on *EIS/LTS* provided better estimates of low-level fractional cloud cover (CF) over dynamically active post-cold frontal regions of ISSO, i.e., over SACCF and SB, which are in line with the findings of Naud et al. (2016) and Wood and Bretherton (2006), wherein they highlighted the applicability of this linear relationship, particularly in mid-latitudes.

Thus, this study presents the first novel record on the variability of low-level thermodynamic structure of MABL, clouds, inversions, and signatures of dominant physical processes regulated by continually varying air-sea temperature differences over regions of three major oceanic domains (STIO, ISSO, and HLSO). Although the crucial role played by the SO atmosphere in modulating the earth's climate has been highlighted in a series of IPCC reports, fewer in-situ observations over SO challenge our present-time abilities to continuously monitor changes in the SO atmosphere. Also, recent approaches to understanding SO atmosphere through satellite retrievals or model simulations have indicated significant uncertainties in these datasets. Past reports have attributed these uncertainties to the complicated SO boundary layer structure with multiple inversions and thick low-level multi-layered clouds. Hence, the present study based on in-situ meteorological measurements can serve to provide useful information on the vertical thermodynamic structure of the low-level atmosphere, characteristics of cloud (layers) and inversions, and the associated physical processes occurring over least explored regions of ISSO (STIO, ISSO, and HLSO).

CRediT authorship contribution statement

Shaikh Neha Salim: Data curation, Conceptualization, Formal analysis, Writing – original draft, Writing – review & editing. **Arjun Adhikari:** Writing – review & editing. **Harilal B. Menon:** Conceptualization, Funding acquisition, Project administration, Resources, Supervision, Writing – review & editing. **N.V.P. Kiran Kumar:** Conceptualization, Formal analysis. **Rajeev Kunjukrishnapillai:** Project administration.

Declaration of Competing Interest

The authors declare the following financial interests/personal relationships which may be considered as potential competing interests:

Harilal B. Menon reports financial support was provided by Vikram Sarabhai Space Centre.

Data availability

ECMWF-ERA5 data used in this study are available at https://cds.climate.copernicus.eu/. Data can be obtained after request from the corresponding author.

Acknowledgments

This financial support was given by the Space Physics Laboratory of Vikram Sarabhai Space Centre, ISRO. The grant was received under A-38 (7) by Goa University, India. The authors greatly acknowledge the National Center for Polar and Oceanic Research (NCPOR) of Ministry of Earth Sciences (MoES) for providing the ship to execute campaigns in the ISSO. We duly acknowledge the entire team of officers, crew members, and all scientific personnel for their support in data collection during all campaigns, particularly Dr. Shrivardhan Hulswar (IITM), Ms. Atiba Shaikh (Goa University), Mr. Mohd. Tarique (University of Cambridge), Mr. Satya Chanakya, and Mr. Thamizharasan Sakthivel (IISc) and Dr. Aditya Narayanan (University of Gothenburg).

Appendix A. Supplementary data

Supplementary data to this article can be found online at https://doi.org/10.1016/j.atmosres.2023.106678.

References

Alexander, S.P., McFarquhar, G.M., Marchand, R., Protat, A., Vignon, É., Mace, G.G., Klekociuk, A.R., 2021. Mixed-phase clouds and precipitation in Southern Ocean cyclones and cloud systems observed poleward of 64°S by ship-based cloud radar and lidar. J. Geophys. Res. Atmos. 126 https://doi.org/10.1029/2020JD033626.

Anil Kumar, N., George, J.V., Chacko, R., Nuncio, N., Sabu, P., 2015. Variability of fronts, freshwater input, and chlorophyll in the Indian Ocean sector of the Southern Ocean. N. Z. J. Mar. Freshw. Res. 49, 20–40. https://doi.org/10.1080/00288330.2014.924972.

Behrangi, A., Song, Y., 2020. A new estimate for oceanic precipitation amount and distribution using complementary precipitation observations from space and comparison with GPCP. Environ. Res. Lett. 15, 124042 https://doi.org/10.1088/1748-9326/abc6d1.

Belkin, I.M., Gordon, A.L., 1996. Southern Ocean fronts from the Greenwich meridian to Tasmania. J. Geophys. Res. Oceans 101, 3675–3696. https://doi.org/10.1029/95JC02750.

Betts, A.K., 1982. Saturation point analysis of moist convective overturning. J. Atmos. Sci. 39, 1484–1505. https://doi.org/10.1175/1520-0469(1982)039%3C1484:SPAOMC%3E2.0.CO;2.

Betts, A.K., Albrecht, B.A., 1987. Conserved variable analysis of the convective boundary layer thermodynamic structure over the tropical oceans. J. Atmos. Sci. 44, 83–99. https://doi.org/10.1175/1520-0469(1987)044%3C0083:CVAOTC%3E2.0.CO;2.

Bischoff, T., Thompson, A.F., 2014. Configuration of a Southern Ocean Storm Track. J. Phys. Oceanograph. 44, 3072–3078. https://doi.org/10.1175/jpo-d-14-0062.1.

Bodas-Salcedo, A., Williams, K.D., Ringer, M.A., Beau, I., Cole, J.N.S., Dufresne, J.-L., Koshiro, T., Stevens, B., Wang, Z., Yokohata, T., 2014. Origins of the solar radiation biases over the Southern Ocean in CFMIP2 models. J. Clim. 27, 41–56. https://doi.org/10.1175/JCLI-D-13-00169.1.

Boebel, O., Lutjeharms, J., Schmid, C., Zenk, W., Rossby, T., Barron, C., 2003. The Cape Cauldron: a regime of turbulent inter-ocean exchange. Deep-Sea Res. II Top. Stud. Oceanogr. 50, 57–86. https://doi.org/10.1016/S0967-0645(02)00379-X.

Boers, R., Jensen, J.B., Krummel, P.B., 1998. Microphysical and short-wave radiative structure of stratocumulus clouds over the Southern Ocean: Summer results and seasonal differences. Q. J. R. Meteorol. Soc. 124, 151–168. https://doi.org/10.1002/qj.49712454507.

Bolton, D., 1980. The computation of equivalent potential temperature. Mon. Weather Rev. 108, 1046–1053.

Bretherton, C., 1997. Convection in stratocumulus-topped atmospheric boundary layers. In: The Physics and Parameterization of Moist Atmospheric Convection. Springer, pp. 127–142. https://doi.org/10.1007/978-94-015-8828-7_5.

Bretherton, C.S., Wyant, M.C., 1997. Moisture transport, lower-tropospheric stability, and decoupling of cloud-topped boundary layers. J. Atmos. Sci. 54, 148–167. https://doi.org/10.1175/1520-0469(1997)054%3C0148:MTLTSA%3E2.0.CO;2.

Carleton, A.M., Song, Y., 1997. Synoptic climatology, and intrahemispheric associations, of cold air mesocyclones in the Australasian sector. J. Geophys. Res.-Atmos. 102, 13873–13887. https://doi.org/10.1029/96JD03357.

Catto, J.L., Jakob, C., Berry, G., Nicholls, N., 2012. Relating global precipitation to atmospheric fronts. Geophys. Res. Lett. 39 https://doi.org/10.1029/2012GL051736.

Chapman, C.C., Hogg, A.M., Kiss, A.E., Rintoul, S.R., 2015. The Dynamics of Southern Ocean Storm Tracks. J. Phys. Oceanograph. 45, 884–903. https://doi.org/10.1175/jpo-d-14-0075.1.

Chelton, D.B., Esbensen, S.K., Schlax, M.G., Thum, N., Freilich, M.H., Wentz, F.J., Gentemann, C.L., McPhaden, M.J., Schopf, P.S., 2001. Observations of coupling between surface wind stress and sea surface temperature in the eastern Tropical Pacific. J. Clim. 14, 1479–1498. https://doi.org/10.1175/1520-0442(2001)014%3C1479:OOCBSW%3E2.0.CO;2.

Chubb, T., Huang, Y., Jensen, J., Campos, T., Siems, S., Manton, M., 2016. Observations of high droplet number concentrations in Southern Ocean boundary layer clouds. Atmos. Chem. Phys. 16, 971–987. https://doi.org/10.5194/acp-16-971-2016.

Connolley, W.M., 1996. The Antartic temperature inversion. Int. J. Climatol. 16, 1333–1342. https://doi.org/10.1002/(SICI)1097-0088(199612)16:12<1333::AID-JOC96>3.0.CO;2-6.

Couldrey, M.P., Jullion, L., Naveira Garabato, A.C., Rye, C., Herráiz-Borreguero, L., Brown, P.J., Meredith, M.P., Speer, K.L., 2013. Remotely induced warming of Antarctic Bottom Water in the eastern Weddell gyre. Geophys. Res. Lett. 40, 2755–2760. https://doi.org/10.1002/grl.50526.

Deacon, G., 1937. The Hydrology of the Southern Ocean. Cambridge University Press, Macmillan, London; New York.

Deser, C., Tomas, R.A., Sun, L., 2015. The Role of Ocean–Atmosphere Coupling in the Zonal-Mean Atmospheric Response to Arctic Sea Ice Loss. J. Clim. 28, 2168–2186. https://doi.org/10.1175/jcli-d-14-00325.1.

Divya, U.S., Girija, J., Satyanarayana, S., Zachariah, J.P., 2014. An advanced radiosonde system for aerospace applications. J. Atmos. Ocean. Technol. 31, 2067–2077. https://doi.org/10.1175/JTECH-D-13-00050.1.

Dong, X., Schwantes, A.C., Xi, B., Wu, P., 2015. Investigation of the marine boundary layer cloud and CCN properties under coupled and decoupled conditions over the Azores. J. Geophys. Res.-Atmos. 120, 6179–6191. https://doi.org/10.1002/2014JD022939.

Edson, J., Paluszkiewicz, T., Sandgathe, S., Vincent, L., Goodman, L., Curtin, T., Hollister, J., Colton, M., Anderson, S., Andreas, E., 1999. Coupled Marine Boundary Layers and Air-Sea Interaction Initiative: Combining Process Studies, Simulations, and Numerical Models. Office of Naval Reasearch.

Falga, R., Wang, C., 2022. The rise of Indian summer monsoon precipitation extremes and its correlation with long-term changes of climate and anthropogenic factors. Sci. Rep. 12, 11985. https://doi.org/10.1038/s41598-022-16240-0.

Fawzy, S., Osman, A.I., Doran, J., Rooney, D.W., 2020. Strategies for mitigation of climate change: a review. Environ. Chem. Lett. 18, 2069–2094. https://doi.org/10.1007/s10311-020-01059-w.

Field, P.R., Wood, R., 2007. Precipitation and cloud structure in midlatitude cyclones. J. Clim. 20, 233–254. https://doi.org/10.1175/jcli3998.1.

Forbes, R.M., Hogan, R.J., 2006. Observations of the depth of ice particle evaporation beneath frontal cloud to improve NWP modelling. Q. J. R. Meteorol. Soc. 132, 865–883. https://doi.org/10.1256/qj.04.187.

Hamilton, L.J., 2006. Structure of the subtropical front in the Tasman Sea. Deep-Sea Res. I Oceanogr. Res. Pap. 53, 1989–2009. https://doi.org/10.1016/j.dsr.2006.08.013.

Hande, L.B., Siems, S.T., Manton, M.J., Belusic, D., 2012. Observations of wind shear over the Southern Ocean. J. Geophys. Res.-Atmos. 117 https://doi.org/10.1029/2012JD017488.

Haynes, J.M., Jakob, C., Rossow, W.B., Tselioudis, G., Brown, J., 2011. Major characteristics of Southern Ocean cloud regimes and their effects on the energy budget. J. Clim. 24, 5061–5080. https://doi.org/10.1175/2011JCLI4052.1.

Hopkins, F.E., Suntharalingam, P., Gehlen, M., Andrews, O., Archer, S.D., Bopp, L., Buitenhuis, E., Dadou, I., Duce, R., Goris, N., Jickells, T., Johnson, M., Keng, F., Law, C.S., Lee, K., Liss, P.S., Lizotte, M., Malin, G., Murrell, J.C., Naik, H., Rees, A.P., Schwinger, J., Williamson, P., 2020. The impacts of ocean acidification on marine trace gases and the implications for atmospheric chemistry and climate. Proceed. Royal Soc. A. 476 https://doi.org/10.1098/rspa.2019.0769.

Hoskins, B.J., Hodges, K.I., 2005. A new perspective on southern hemisphere storm tracks. J. Clim. 18, 4108–4129. https://doi.org/10.1175/JCLI3570.1.

Huang, B., Shukla, J., 2005. Ocean–Atmosphere Interactions in the Tropical and Subtropical Atlantic Ocean. J. Clim. 18, 1652–1672. https://doi.org/10.1175/jcli3368.1.

Huang, Y., Siems, S.T., Manton, M.J., Hande, L.B., Haynes, J.M., 2012. The structure of low-altitude clouds over the Southern Ocean as seen by CLOUDSAT. J. Clim. 25, 2535–2546. https://doi.org/10.1175/JCLI-D-11-00131.1.

Huang, Y., Franklin, C.N., Siems, S.T., Manton, M.J., Chubb, T., Lock, A., Alexander, S., Klekociuk, A., 2015a. Evaluation of boundary-layer cloud forecasts over the Southern Ocean in a limited-area numerical weather prediction system using in situ, space-borne and ground-based observations. Q. J. R. Meteorol. Soc. 141, 2259–2276. https://doi.org/10.1002/qj.2519.

Huang, Y., Protat, A., Siems, S.T., Manton, M.J., 2015b. A-Train observations of maritime midlatitude storm-track cloud systems: comparing the Southern Ocean against the North Atlantic. J. Clim. 28, 1920–1939. https://doi.org/10.1175/JCLI-D-14-00169.1.

Hyder, P., Edwards, J.M., Allan, R.P., Hewitt, H.T., Bracegirdle, T.J., Gregory, J.M., Wood, R.A., Meijers, A.J.S., Mulcahy, J., Field, P., Furtado, K., Bodas-Salcedo, A., Williams, K.D., Copsey, D., Josey, S.A., Liu, C., Roberts, C.D., Sanchez, C., Ridley, J., Thorpe, L., Hardiman, S.C., Mayer, M., Berry, D.I., Belcher, S.E., 2018. Critical Southern Ocean climate model biases traced to atmospheric model cloud errors. Nat. Commun. 9, 3625. https://doi.org/10.1038/s41467-018-05634-2.

IPCC, 2014. Climate Change 2013 – The Physical Science Basis: Working Group I Contribution to the Fifth Assessment Report of the Intergovernmental Panel on Climate Change. Cambridge University Press, Cambridge. https://doi.org/10.1017/CBO9781107415324.

Irving, D., Simmonds, I., Keay, K., 2010. Mesoscale cyclone activity over the ice-free Southern Ocean: 1999–2008. J. Clim. 23, 5404–5420. https://doi.org/10.1175/2010JCLI3628.1.

Jensen, J.B., Lee, S., Krummel, P.B., Katzfey, J., Gogoasa, D., 2000. Precipitation in marine cumulus and stratocumulus.: part I: Thermodynamic and dynamic observations of closed cell circulations and cumulus bands. Atmos. Res. 54, 117–155. https://doi.org/10.1016/S0169-8095(00)00040-5.

Jones, C.R., Bretherton, C.S., Leon, D., 2011. Coupled vs. decoupled boundary layers in VOCALS-REx. Atmos. Chem. Phys. 11, 7143–7153. https://doi.org/10.5194/acp-11-7143-2011.

Jullien, N., Vignon, É., Sprenger, M., Aemisegger, F., Berne, A., 2020. Synoptic conditions and atmospheric moisture pathways associated with virga and precipitation over coastal Adélie Land in Antarctica. Cryosphere 14, 1685–1702. https://doi.org/10.3929/ethz-b-000418970.

Kawai, H., Yabu, S., Hagihara, Y., Koshiro, T., Okamoto, H., 2015. Characteristics of the cloud top heights of marine boundary layer clouds and the frequency of marine fog over mid-latitudes. J. Meteorol. Soc. Japan Ser. II. 93, 613–628. https://doi.org/10.2151/jmsj.2015-045.

Klein, S.A., Hartmann, D.L., 1993. The seasonal cycle of low stratiform clouds. J. Clim. 6, 1587–1606. https://doi.org/10.1175/1520-0442(1993)006%3C1587:TSCOLS%3E2.0.CO;2.

Kostianoy, A.G., Ginzburg, A.I., Frankignoulle, M., Delille, B., 2004. Fronts in the Southern Indian Ocean as inferred from satellite sea surface temperature data. J. Mar. Syst. 45, 55–73. https://doi.org/10.1016/j.jmarsys.2003.09.004.

Kuma, P., McDonald, A.J., Morgenstern, O., Alexander, S.P., Cassano, J.J., Garrett, S., Halla, J., Hartery, S., Harvey, M.J., Parsons, S., Plank, G., Varma, V., Williams, J., 2020. Evaluation of Southern Ocean cloud in the HadGEM3 general circulation model and MERRA-2 reanalysis using ship-based observations. Atmos. Chem. Phys. 20, 6607–6630. https://doi.org/10.5194/acp-20-6607-2020.

Lang, F., Huang, Y., Siems, S.T., Manton, M.J., 2018. Characteristics of the marine atmospheric boundary layer over the Southern Ocean in response to the synoptic forcing. J. Geophys. Res.-Atmos. 123, 7799–7820. https://doi.org/10.1029/2018JD028700.

Lang, F., Huang, Y., Protat, A., Truong, S.C.H., Siems, S.T., Manton, M.J., 2021. Shallow convection and precipitation over the Southern Ocean: a case study during the CAPRICORN 2016 field campaign. J. Geophys. Res.-Atmos. 126 https://doi.org/10.1029/2020JD034088.

Lee, J.-Y., Marotzke, J., Bala, G., Cao, L., Corti, S., Dunne, J.P., Engelbrecht, F., Fischer, E., Fyfe, J.C., Jones, C., 2021. Future global climate: scenario-based projections and near-term information. In: IPCC. https://doi.org/10.1017/9781009157896.006.

Li, X., Yang, X., Zheng, W., Zhang, J.A., Pietrafesa, L.J., Pichel, W.G., 2015. Synergistic use of Satellite Observations and Numerical Weather Model to Study Atmospheric Occluded Fronts. IEEE Trans. Geosci. Remote Sens. 53, 5269–5279. https://doi.org/10.1109/TGRS.2015.2420312.

Liu, Z., Wu, S., Zhang, S., Liu, Y., Rong, X., 2013. Ensemble data assimilation in a simple coupled climate model: the role of ocean-atmosphere interaction. Adv. Atmos. Sci. 30, 1235–1248. https://doi.org/10.1007/s00376-013-2268-z.

Long, M.C., Stephens, B.B., McKain, K., Sweeney, C., Keeling, R.F., Kort, E.A., Morgan, E. J., Bent, J.D., Chandra, N., Chevallier, F., Commane, R., Daube, B.C., Krummel, P.B., Loh, Z., Luijkx, I.T., Munro, D., Patra, P., Peters, W., Ramonet, M., Rödenbeck, C., Stavert, A., Tans, P., Wofsy, S.C., 2021. Strong Southern Ocean carbon uptake evident in airborne observations. Science. 374, 1275–1280. https://doi.org/10.1126/science.abi4355.

Lutjeharms, J.R.E., Gordon, A.L., 1987. Shedding of an Agulhas ring observed at sea. Nature. 325, 138–140. https://doi.org/10.1038/325138a0.

Lutjeharms, J.R.E., Valentine, H.R., 1984. Southern Ocean thermal fronts south of Africa. Deep Sea Res. Part A Oceanograph. Res. Papers. 31, 1461–1475. https://doi.org/10.1016/0198-0149(84)90082-7.

Lutjeharms, J.R.E., Valentine, H.R., 1988. Eddies at the subtropical convergence south of Africa. J. Phys. Oceanogr. 18, 761–774. https://doi.org/10.1175/1520-0485(1988)018%3C0761:EATSCS%3E2.0.CO;2.

Lutjeharms, J.R.E., Van Ballegooyen, R.C., 1988. The Retroflection of the Agulhas current. J. Phys. Oceanogr. 18, 1570–1583. https://doi.org/10.1175/1520-0485(1988)018%3C1570:TROTAC%3E2.0.CO;2.

Mace, G., Protat, A., 2018. Clouds over the Southern Ocean as observed from the R/V investigator during CAPRICORN. Part I: Cloud Occurrence and phase Partitioning. J. Appl. Meteorol. Climatol. 57, 1783–1803. https://doi.org/10.1175/JAMC-D-17-0194.1.

Mace, G., Zhang, Q., Vaughan, M., Marchand, R., Stephens, S., Trepte, C., Winker, D., 2009. A description of hydrometeor layer occurrence statistics derived from the first year of merged Cloudsat and CALIPSO data. J. Geophys. Res.-Atmos. 114 https://doi.org/10.1029/2007JD009755.

Mace, G., Benson, S., Hu, Y., 2020. On the frequency of occurrence of the ice phase in supercooled Southern Ocean low clouds derived from CALIPSO and CLOUDSAT. Geophys. Res. Lett. 47 https://doi.org/10.1029/2020GL087554.

Mace, G., Protat, A., Benson, S., 2021. Mixed-phase clouds over the Southern Ocean as observed from satellite and surface based lidar and radar. J. Geophys. Res.-Atmos. 126 https://doi.org/10.1029/2021JD034569.

Martin, G.M., Johnson, D.W., Rogers, D.P., Jonas, P.R., Minnis, P., Hegg, D.A., 1995. Observations of the Interaction between Cumulus Clouds and Warm Stratocumulus Clouds in the Marine Boundary Layer during ASTEX. J. Atmos. Sci. 52, 2902–2922. https://doi.org/10.1175/1520-0469(1995)052%3C2902:OOTIBC%3E2.0.CO;2.

McCoy, D.T., Hartmann, D.L., Zelinka, M.D., Ceppi, P., Grosvenor, D.P., 2015. Mixed-phase cloud physics and Southern Ocean cloud feedback in climate models. J. Geophys. Res.-Atmos. 120, 9539–9554. https://doi.org/10.1002/2015JD023603.

McFarquhar, G.M., Bretherton, C.S., Marchand, R., Protat, A., DeMott, P.J., Alexander, S. P., Roberts, G.C., Twohy, C.H., Toohey, D., Siems, S., Huang, Y., Wood, R., Rauber, R.M., Lasher-Trapp, S., Jensen, J., Stith, J.L., Mace, J., Um, J., Järvinen, E., Schnaiter, M., Gettelman, A., Sanchez, K.J., McCluskey, C.S., Russell, L.M., McCoy, I. L., Atlas, R.L., Bardeen, C.G., Moore, K.A., Hill, T.C.J., Humphries, R.S., Keywood, M. D., Ristovski, Z., Cravigan, L., Schofield, R., Fairall, C., Mallet, M.D., Kreidenweis, S. M., Rainwater, B., D'Alessandro, J., Wang, Y., Wu, W., Saliba, G., Levin, E.J.T., Ding, S., Lang, F., Truong, S.C.H., Wolff, C., Haggerty, J., Harvey, M.J., Klekociuk, A. R., McDonald, A., 2021. Observations of clouds, aerosols, precipitation, and surface radiation over the Southern Ocean: an overview of CAPRICORN, MARCUS, MICRE, and SOCRATES. Bull. Am. Meteorol. Soc. 102, 894–928. https://doi.org/10.1175/BAMS-D-20-0132.1.

McGibbon, J., Bretherton, C.S., 2017. Skill of ship-following large-eddy simulations in reproducing MAGIC observations across the Northeast Pacific stratocumulus to cumulus transition region. J. Adv. Model. Earth Sys. 9, 810–831. https://doi.org/10.1002/2017MS000924.

Meijers, A.J.S., Klocker, A., Bindoff, N.L., Williams, G.D., Marsland, S.J., 2010. The circulation and water masses of the Antarctic shelf and continental slope between

30◦E and 80◦E. Deep-Sea Res. II Top. Stud. Oceanogr. 57, 723–737. https://doi.org/10.1016/j.dsr2.2009.04.019.
Messager, C., Speich, S., Key, E., 2012. Marine atmospheric boundary layer over some Southern Ocean fronts during the IPY BGH 2008 cruise. Ocean Sci. 8, 1001–1023. https://doi.org/10.5194/os-8-1001-2012.
Miller, M.A., Albrecht, B.A., 1995. Surface-based observations of Mesoscale Cumulus–Stratocumulus Interaction during ASTEX. J. Atmos. Sci. 52, 2809–2826. https://doi.org/10.1175/1520-0469(1995)052<2809:Sboomc>2.0.Co;2.
Moore, J.K., Abbott, M.R., Richman, J.G., 1999. Location and dynamics of the Antarctic Polar Front from satellite sea surface temperature data. J. Geophys. Res. Oceans 104, 3059–3073. https://doi.org/10.1029/1998JC900032.
Morrow, R., Birol, F., Griffin, D., Sudre, J., 2004. Divergent pathways of cyclonic and anti-cyclonic ocean eddies. Geophys. Res. Lett. 31 https://doi.org/10.1029/2004GL020974.
Muhlbauer, A., McCoy, I.L., Wood, R., 2014. Climatology of stratocumulus cloud morphologies: microphysical properties and radiative effects. Atmos. Chem. Phys. 14, 6695–6716. https://doi.org/10.5194/acp-14-6695-2014.
Naud, C.M., Booth, J.F., Del Genio, A.D., 2014. Evaluation of ERA-Interim and MERRA cloudiness in the Southern Ocean. J. Clim. 27, 2109–2124. https://doi.org/10.1175/JCLI-D-13-00432.1.
Naud, C.M., Booth, J.F., Del Genio, A.D., 2016. The relationship between boundary layer stability and cloud cover in the post-cold-frontal region. J. Clim. 29, 8129–8149. https://doi.org/10.1175/JCLI-D-15-0700.1.
Nicholls, S., 1984. The dynamics of stratocumulus: Aircraft observations and comparisons with a mixed layer model. Q. J. R. Meteorol. Soc. 110, 783–820. https://doi.org/10.1002/qj.49711046603.
Nobre, P., De Almeida, R.A., Malagutti, M., Giarolla, E., 2012. Coupled Ocean–Atmosphere Variations over the South Atlantic Ocean. J. Clim. 25, 6349–6358. https://doi.org/10.1175/jcli-d-11-00444.1.
Orsi, A.H., Whitworth, T., Nowlin, W.D., 1995. On the meridional extent and fronts of the Antarctic Circumpolar current. Deep-Sea Res. I Oceanogr. Res. Pap. 42, 641–673. https://doi.org/10.1016/0967-0637(95)00021-W.
Orsi, A.H., Johnson, G.C., Bullister, J.L., 1999. Circulation, mixing, and production of Antarctic Bottom Water. Prog. Oceanogr. 43, 55–109. https://doi.org/10.1016/S0079-6611(99)00004-X.
Parish, T.R., Cassano, J.J., 2003a. Diagnosis of the katabatic wind influence on the wintertime Antarctic surface wind field from numerical simulations. Mon. Weather Rev. 131, 1128–1139. https://doi.org/10.1175/1520-0493(2003)131%3C1128:DOTKWI%3E2.0.CO;2.
Parish, T.R., Cassano, J.J., 2003b. The role of katabatic winds on the Antarctic surface wind regime. Mon. Weather Rev. 131, 317–333. https://doi.org/10.1175/1520-0493(2003)131%3C0317:TROKWO%3E2.0.CO;2.
Petrie, R.E., Shaffrey, L.C., Sutton, R.T., 2015. Atmospheric impact of Arctic Sea Ice Loss in a Coupled Ocean–Atmosphere Simulation. J. Clim. 28, 9606–9622. https://doi.org/10.1175/jcli-d-15-0316.1.
Phillips, H.E., Rintoul, S.R., 2000. Eddy variability and energetics from direct current measurements in the Antarctic circumpolar current south of Australia. J. Phys. Oceanogr. 30, 3050–3076. https://doi.org/10.1175/1520-0485(2000)030%3C3050:EVAEFD%3E2.0.CO;2.
Pierrehumbert, R., Swanson, K., 1995. Baroclinic instability. Annu. Rev. Fluid Mech. 27, 419–467.
Rouault, M., Lutjeharms, J.R.E., 2000. Air-sea exchange over an Agulhas eddy at the subtropical convergence. Glob. Atmosp. Ocean Syst. 7, 125–150.
Russell, L.M., Lenschow, D.H., Laursen, K.K., Krummel, P.B., Siems, S.T., Bandy, A.R., Thornton, D.C., Bates, T.S., 1998. Bidirectional mixing in an ACE 1 marine boundary layer overlain by a second turbulent layer. J. Geophys. Res.-Atmos. 103, 16411–16432. https://doi.org/10.1029/97JD03437.
Sallée, J.B., 2018. Southern Ocean Warming. Oceanography. 31, 52–62. https://www.jstor.org/stable/26542651.
Sallée, J.B., Speer, K., Morrow, R., 2008. Response of the Antarctic Circumpolar current to atmospheric variability. J. Clim. 21, 3020–3039. https://doi.org/10.1175/2007JCLI1702.1.
Sallée, J.B., Shuckburgh, E., Bruneau, N., Meijers, A.J.S., Bracegirdle, T.J., Wang, Z., Roy, T., 2013. Assessment of Southern Ocean water mass circulation and characteristics in CMIP5 models: Historical bias and forcing response. J. Geophys. Res. Oceans 118, 1830–1844. https://doi.org/10.1002/jgrc.20135.
Schmale, J., Baccarini, A., Thurnherr, I., Henning, S., Efraim, A., Regayre, L., Bolas, C., Hartmann, M., Welti, A., Lehtipalo, K., Aemisegger, F., Tatzelt, C., Landwehr, S., Modini, R.L., Tummon, F., Johnson, J.S., Harris, N., Schnaiter, M., Toffoli, A., Derkani, M., Bukowiecki, N., Stratmann, F., Dommen, J., Baltensperger, U., Wernli, H., Rosenfeld, D., Gysel-Beer, M., Carslaw, K.S., 2019. Overview of the Antarctic Circumnavigation Expedition: Study of preindustrial-like aerosols and their climate effects (ACE-SPACE). Bull. Am. Meteorol. Soc. 100, 2260–2283. https://doi.org/10.1175/BAMS-D-18-0187.1.
Schuddeboom, A., Varma, V., McDonald, A.J., Morgenstern, O., Harvey, M., Parsons, S., Field, P., Furtado, K., 2019. Cluster-based evaluation of model compensating errors: a case study of cloud radiative effect in the Southern Ocean. Geophys. Res. Lett. 46, 3446–3453. https://doi.org/10.1029/2018GL081686.
Sen Gupta, A., Santoso, A., Taschetto, A.S., Ummenhofer, C.C., Trevena, J., England, M. H., 2009. Projected changes to the Southern Hemisphere Ocean and sea ice in the IPCC AR4 climate models. J. Clim. 22, 3047–3078. https://doi.org/10.1175/2008JCLI2827.1.
Simmonds, I., Lim, E.-P., 2009. Biases in the calculation of Southern Hemisphere mean baroclinic eddy growth rate. Geophys. Res. Lett. 36 https://doi.org/10.1029/2008GL036320.
Small, R.J., deSzoeke, S.P., Xie, S.P., O'Neill, L., Seo, H., Song, Q., Cornillon, P., Spall, M., Minobe, S., 2008. Air–sea interaction over ocean fronts and eddies. Dyn. Atmos. Oceans 45, 274–319. https://doi.org/10.1016/j.dynatmoce.2008.01.001.
Small, R.J., Tomas, R.A., Bryan, F.O., 2014. Storm track response to ocean fronts in a global high-resolution climate model. Clim. Dyn. 43, 805–828. https://doi.org/10.1007/s00382-013-1980-9.
Smirnov, D., Newman, M., Alexander, M.A., 2014. Investigating the Role of Ocean–Atmosphere Coupling in the North Pacific Ocean. J. Clim. 27, 592–606. https://doi.org/10.1175/jcli-d-13-00123.1.
Smith, N.R., Zhaoqian, D., Kerry, K.R., Wright, S., 1984. Water masses and circulation in the region of Prydz Bay, Antarctica. Deep Sea Res. Part A Oceanograph. Res. Papers. 31, 1121–1147. https://doi.org/10.1016/0198-0149(84)90016-5.
Sokolov, S., Rintoul, S.R., 2002. Structure of Southern Ocean fronts at 140°E. J. Mar. Syst. 37, 151–184. https://doi.org/10.1016/S0924-7963(02)00200-2.
Srivastava, R., Ramesh, R., Prakash, S., Anil Kumar, N., Sudhakar, M., 2007. Oxygen isotope and salinity variations in the Indian sector of the Southern Ocean. Geophys. Res. Lett. 34 https://doi.org/10.1029/2007GL031790.
Stammer, D., 1998. On eddy characteristics, eddy transports, and mean flow properties. J. Phys. Oceanogr. 28, 727–739. https://doi.org/10.1175/1520-0485(1998)028%3C0727:OECETA%3E2.0.CO;2.
Stevens, B., 2000. Cloud transitions and decoupling in shear-free stratocumulus-topped boundary layers. Geophys. Res. Lett. 27, 2557–2560. https://doi.org/10.1029/1999GL011257.
Stott, P.A., Gillett, N.P., Hegerl, G.C., Karoly, D.J., Stone, D.A., Zhang, X., Zwiers, F., 2010. Detection and Attribution of Climate Change: A Regional Perspective, 1, pp. 192–211. https://doi.org/10.1002/wcc.34.
Stull, R., 1988. An Introduction to Boundary Layer Meteorology. Kluwer Academic Publishers, Dordrecht, Netherlands.
Subrahamanyam, D., Radhika, R., 2003. Structural characteristics of marine atmospheric boundary layer (MABL) and its associated dynamics over the central Arabian Sea during INDOEX, ifp-99 campaign. Curr. Sci. 85, 1334–1340.
Swart, N.C., Gille, S.T., Fyfe, J.C., Gillett, N.P., 2018. Recent Southern Ocean warming and freshening driven by greenhouse gas emissions and ozone depletion. Nat. Geosci. 11, 836–841. https://doi.org/10.1038/s41561-018-0226-1.
Talley, L.D., Pickard, G.L., Emery, W.J., Swift, J.H., 2011. Southern Ocean. In: Talley, L. D., Pickard, G.L., Emery, W.J., Swift, J.H. (Eds.), Descriptive Physical Oceanography, Sixth edition. Academic Press, Boston, pp. 437–471. https://doi.org/10.1016/B978-0-7506-4552-2.10013-7.
Thompson, A.F., Richards, K.J., 2011. Low frequency variability of Southern Ocean jets. J. Geophys. Res. Oceans 116. https://doi.org/10.1029/2010JC006749.
Timbal, B., Drosdowsky, W., 2013. The relationship between the decline of Southeastern Australian rainfall and the strengthening of the subtropical ridge. Int. J. Climatol. 33, 1021–1034. https://doi.org/10.1002/joc.3492.
Trenberth, K.E., 2011. Changes in precipitation with climate change. Clim. Res. 47, 123–138. https://doi.org/10.3354/cr00953.
Truong, S.C.H., Huang, Y., Lang, F., Messmer, M., Simmonds, I., Siems, S.T., Manton, M. J., 2020. A climatology of the marine atmospheric boundary layer over the Southern Ocean from four field campaigns during 2016–2018. J. Geophys. Res.-Atmos. 125 https://doi.org/10.1029/2020JD033214.
Vignon, É., Traullé, O., Berne, A., 2019. On the fine vertical structure of the low troposphere over the coastal margins of East Antarctica. Atmos. Chem. Phys. 19, 4659–4683. https://doi.org/10.5194/acp-19-4659-2019.
Vignon, É., Alexander, S.P., DeMott, P.J., Sotiropoulou, G., Gerber, F., Hill, T.C.J., Marchand, R., Nenes, A., Berne, A., 2021. Challenging and improving the simulation of mid-level mixed-phase clouds over the high-latitude Southern Ocean. J. Geophys. Res.-Atmos. 126 https://doi.org/10.1029/2020JD033490.
Wall, C.J., Hartmann, D.L., Ma, P.-L., 2017. Instantaneous Linkages between Clouds and Large-Scale Meteorology over the Southern Ocean in Observations and a climate Model. J. Clim. 30, 9455–9474. https://doi.org/10.1175/jcli-d-17-0156.1.
Wang, Z., Siems, S.T., Belusic, D., Manton, M.J., Huang, Y., 2015. A climatology of the precipitation over the Southern Ocean as observed at Macquarie Island. J. Appl. Meteorol. Climatol. 54, 2321–2337. https://doi.org/10.1175/jamc-d-14-0211.1.
Wang, H., You, Y., Kulie, M., 2018. Global virga precipitation distribution derived from three spaceborne radars and its contribution to the false radiometer precipitation detection. Geophys. Res. Lett. 45, 4446–4455. https://doi.org/10.1029/2018GL077891.
Webster, P.J., Moore, A.M., Loschnigg, J.P., Leben, R.R., 1999. Coupled ocean–atmosphere dynamics in the Indian Ocean during 1997–98. Nature. 401, 356–360. https://doi.org/10.1038/43848.
Wood, R., Bretherton, C.S., 2004. Boundary layer depth, entrainment, and decoupling in the cloud-capped subtropical and tropical marine boundary layer. J. Clim. 17, 3576–3588. https://doi.org/10.1175/1520-0442(2004)017%3C3576:BLDEAD%3E2.0.CO;2.
Wood, R., Bretherton, C.S., 2006. On the relationship between stratiform low cloud cover and lower-tropospheric stability. J. Clim. 19, 6425–6432. https://doi.org/10.1175/JCLI3988.1.
Wood, O.K.-T., Tseng, R., Deeper, H.-H., 2018. Precipitating PBLs associated with optically thin veil clouds in the Sc-Cu transition. Geophys. Res. Lett. 45, 5177–5184. https://doi.org/10.1029/2018GL077084.
Xie, S.-P., Liu, W.T., Liu, Q., Nonaka, M., 2001. Far-reaching Effects of the Hawaiian Islands on the Pacific Ocean-Atmosphere System. Science. 292, 2057–2060. https://doi.org/10.1126/science.1059781.
Zeng, X., Brunke, M.A., Zhou, M., Fairall, C., Bond, N.A., Lenschow, D.H., 2004. Marine atmospheric boundary layer height over the eastern pacific: Data analysis and model evaluation. J. Clim. 17, 4159–4170. https://doi.org/10.1175/JCLI3190.1.

Zheng, Y., Li, Z., 2019a. Episodes of Warm-Air Advection Causing Cloud-Surface Decoupling during the MARCUS. J. Geophys. Res.-Atmos. 124, 12227–12243. https://doi.org/10.1029/2019JD030835.
Zheng, Y., Li, Z., 2019b. Episodes of warm-air advection causing cloud-surface decoupling during the MARCUS. J. Geophys. Res.-Atmos. 124, 12227–12243. https://doi.org/10.1029/2019JD030835.
Zheng, Y., Rosenfeld, D., Li, Z., 2018a. Estimating the Decoupling Degree of Subtropical Marine Stratocumulus Decks from Satellite. J. Geophys. Res.-Atmos. 45 https://doi.org/10.1029/2018GL078382, 12,560-512,568.
Zheng, Y., Rosenfeld, D., Li, Z., 2018b. The Relationships between Cloud Top Radiative Cooling rates, Surface Latent Heat Fluxes, and Cloud-Base Heights in Marine Stratocumulus. J. Geophys. Res.-Atmos. 123 https://doi.org/10.1029/2018JD028579, 11,678-611,690.

Science of the Total Environment 858 (2023) 159770

Contents lists available at ScienceDirect

Science of the Total Environment

journal homepage: www.elsevier.com/locate/scitotenv

Aerosol-boundary layer dynamics and its effect on aerosol radiative forcing and atmospheric heating rate in the Indian Ocean sector of Southern Ocean

S. Neha Salim [a,b], Arjun Adhikari [a,b], Atiba A. Shaikh [a,b], Harilal B. Menon [a,b,*], N.V.P. Kiran Kumar [c], K. Rajeev [c]

[a] Remote Sensing Laboratory, Goa University, 403206, India
[b] School of Earth, Ocean and Atmospheric Sciences, Goa University, 403206, India
[c] Space Physics Laboratory, Vikram Sarabhai Space Centre, Trivandrum 695022, India

HIGHLIGHTS

- First record of aerosol-boundary layer dynamics in the ISSO
- The frontal region-specific thermodynamic state of MABL governs aerosol distribution in the ISSO.
- High aerosol loading observed over polar front regions of ISSO
- Long-range advected anthropogenic aerosols prevailed over the polar front.
- Baroclinic boundaries formed over the polar front likely caused aerosols accumulation.

GRAPHICAL ABSTRACT

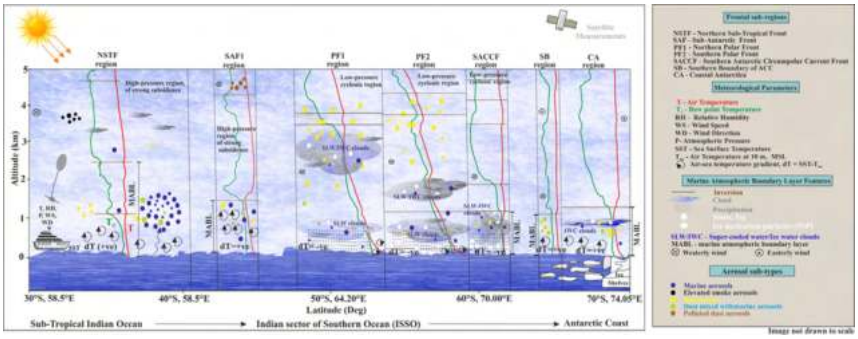

ARTICLE INFO

Editor: Anastasia Paschalidou

Keywords:
Marine atmospheric boundary layer (MABL)
Clouds
Inversions
Aerosols
Clear sky direct aerosol radiative forcing (*DARF*)
Atmospheric heating rate (*HR*)

ABSTRACT

The study examines the thermodynamic structure of the marine atmospheric boundary layer (MABL) and its effect on the aerosol dynamics in the Indian Ocean sector of Southern Ocean (ISSO) between 30°S-67°S and 57°E-77°E. It includes observations of aerosols and meteorology collected during the Xth Southern Ocean Expedition conducted in December 2017. The results revealed the effect of frontal-region-specific air-sea coupling on the thermodynamic structure of MABL and its role in regulating aerosols in ISSO. The MABL over the subtropical front was unstable and formed a well-evolved mixed layer (≈2400 m) capped by low-level inversions (≈660 m). Convective activities in the Sub-Antarctic Frontal region were associated with the Agulhas Retroflection Current, which supported the formation of a well-developed mixed layer (≈1860 m). The mean estimates of aerosol optical depth (*AOD*) and black carbon (*BC*) mass concentrations were 0.095 ± 0.006 and 50 ± 14 ng m^{-3}, respectively, and the resultant clear sky direct shortwave radiative forcing (*DARF*) and atmospheric heating rate (*HR*) were 1.32 ± 0.11 W m^{-2} and 0.022 ± 0.002 K day^{-1}, respectively. In the polar front (PF) region, frequent mid-latitude cyclones led to highly stabilized MABL, supported low-level multi-layered clouds (>3-layers) and multiple high-level inversions (strength > 0.5 K m^{-1} > 3000 m). The clouds were mixed-phased with temperatures less than −12 °C at 3000 m altitude. Interestingly, there was higher loading of dust and *BC* aerosols (276 ± 24 ng m^{-3}), maximum *AOD* (0.109 ± 0.009), clear sky *DARF* (1.73 ± 0.02 W m^{-2}), and *HR* (0.029 ± 0.005 K day^{-1}). This showed an accumulation of long-range advected anthropogenic aerosols within baroclinic-boundaries formed over the PF region. Specifically, in the region south of PF, weak convection caused weakly-unstable MABL with a single low-level inversion followed by no clouds/single-layer clouds. Predominant clean maritime air holding a small fraction of dust and *BC* accounted for lower estimates of *AOD* (0.071 ± 0.004), *BC* concentrations (90 ± 55 ng m^{-3}) and associated clear sky *DARF* and *HR* were 1.16 ± 0.06 W m^{-2} and 0.019 ± 0.001 K day^{-1}, respectively.

* Corresponding author at: School of Earth, Ocean and Atmospheric Sciences, Goa University, 403206, India.
E-mail address: hbmenon@unigoa.ac.in (H.B. Menon).

http://dx.doi.org/10.1016/j.scitotenv.2022.159770
Received 6 July 2022; Received in revised form 21 October 2022; Accepted 23 October 2022
Available online 26 October 2022
0048-9697/© 2022 Elsevier B.V. All rights reserved.

1. Introduction

Aerosols are significant contributors to poor air quality (Stocker et al., 2013) and influence the climate and weather patterns by either scattering or absorbing irradiance (Charlson and Pilat, 1969; McCormick and Ludwig, 1967) and also acting as nuclei for cloud formation (Sassen, 2002). Heterogeneous in their global distribution, aerosols of natural and anthropogenic origins are characterized by their shapes, sizes, and chemical compositions. Among different types of aerosols, EPS is a type of aerosol that creates biofouling which contributes to an increase in CO_2, particularly in the open ocean regions (Sepehri and Sarrafzadeh, 2018; Sepehri et al., 2020). Because of the differences in the properties of different aerosol species, a larger impact of their interaction with irradiance has important implications on Earth's radiative balance. For example, Bellouin et al. (2020) reported global mean aerosol radiative forcing estimates in the range between -0.65 and -1.6 W m^{-2} at 68 % confidence intervals. The global scale assessment of aerosol radiative forcing poses severe challenges concerning aerosol-radiation and aerosol-cloud processes (Bender, 2020) in remote regions, particularly over the Southern Ocean (SO).

Studies have reported a large spatiotemporal variability in the concentrations and optical properties of aerosols over different regions of the World Ocean (Stocker et al., 2013; Krishnamurti et al., 1998; Menon et al., 2015; Ramanathan et al., 2001; Chang et al., 2021; Doherty et al., 2021). The key factor driving such an aerosol variability is the dynamic state of the marine atmospheric boundary layer (MABL) and its characteristics feature, i.e., state of atmospheric stability, physical processes (such as convection and advection), characteristics of clouds and inversions (Groß et al., 2015; Prasad et al., 2021; Turner, 2020). Broadly, MABL acts as a shield to the vertical advection of near-surface in-situ generated/long-range advected aerosols (Ma et al., 2020; Stull, 1988; Su et al., 2020; Zhang et al., 2018). The coupled interaction of aerosols and MABL shows significant heterogeneity depending on regions, seasons, diurnal/time, and aerosol types and their vertical distribution (Guo et al., 2019; Lou et al., 2019). This makes it challenging to quantify the effects of aerosols on the evolution and thermodynamic stability of MABL. It results in uncertainties in satellite retrievals of aerosol-associated radiative forcing (Ramanathan et al., 2001), specifically over the SO where predominant cloud coverage (80 %) adds additional difficulties in accurate simulations of aerosols as well as boundary layer properties.

Field measurements in different parts of SO have reported various mechanisms of interactions of aerosols with clouds, with varying MABL characteristics (Kremser et al., 2021). In the Australian Sector of SO, Alexander and Protat (2019) showed a decoupled layer (separated from the surface mixed layer and free troposphere) within MABL with low backscattering wherein the presence of clouds was capped by weak temperature inversions at the mid-latitudes. Using various observations from the Australian Sector of SO, McFarquhar et al. (2021) reported the zonal variability in aerosol compositions within MABL. The droplet-nucleation was primarily influenced by the origin (source) of aerosols. These aforementioned studies and several others (Alexander and Protat, 2019; Kremser et al., 2021; Landwehr et al., 2020; Quinn et al., 1998; Schmale et al., 2019) improved the understanding of clouds, aerosols, and thermodynamical structure of MABL and their interactions in the respective sectors of SO. However, a knowledge gap exists in the ISSO due to the unavailability of in-situ observations, which leads to bias in modeling and satellite retrievals (Bodas-Salcedo et al., 2014; Trenberth and Fasullo, 2010).

To address the gap, several studies based on in-situ measurements (McFarquhar et al., 2021; Menon et al., 2015) reported the presence of anthropogenic aerosols in the remote regions of SO. The presence of sea-salt and non-sea-salt aerosols acting as cloud condensation nuclei (CCN) was also explained (Fossum et al., 2018; Quinn et al., 2017). Few reports from ISSO were concentric on the spatial and temporal variability of aerosols and associated radiative forcing (Hulswar et al., 2020; Menon et al., 2015; Srivastava et al., 2021). However, there was no attempt to understand the thermodynamic state of MABL and its boundary layer features (such as inversions and clouds) attributing to its role in regulating the distribution of aerosols, clear sky direct shortwave radiative forcing, and atmospheric heating rate vital of Earth's radiative balance.

The data reported in this study were collected between 30°S and 67°S along 57°E-77°E during the onward cruise track of the Xth Southern Ocean Expedition (SOE-X) from 8th December 2017 to 05th January 2018 (Fig. 1). The measurements were collected over the major oceanic frontals regions identified as the Sub-Tropical Front (STF), Sub-Antarctic Front (SAF), Polar Front (PF), Southern Antarctic Circumpolar Current Front (SACCF), Southern boundary of ACC (SB), and Coastal Antarctic (CA), by Anilkumar et al. (2015) and Belkin and Gordon (1996). The detailed classification adopted for each frontal region is provided in Table 1. With a focus on understanding the features of MABL and the distribution of aerosols, the study addresses,

(a) The effect of frontal-based air-sea coupling in shaping the thermodynamic structure of MABL,
(b) The role of MABL characteristics in regulating the vertical distribution of aerosols,
(c) The spatial variability of aerosol optical depth (*AOD*), black carbon (*BC*) mass concentrations, and associated clear sky direct shortwave radiative forcing (*DARF*) and heating rates.

2. Data and methods

2.1. Data

A combination of in-situ, re-analysis, modeled, and satellite data have been used. The in-situ measurements included surface meteorological

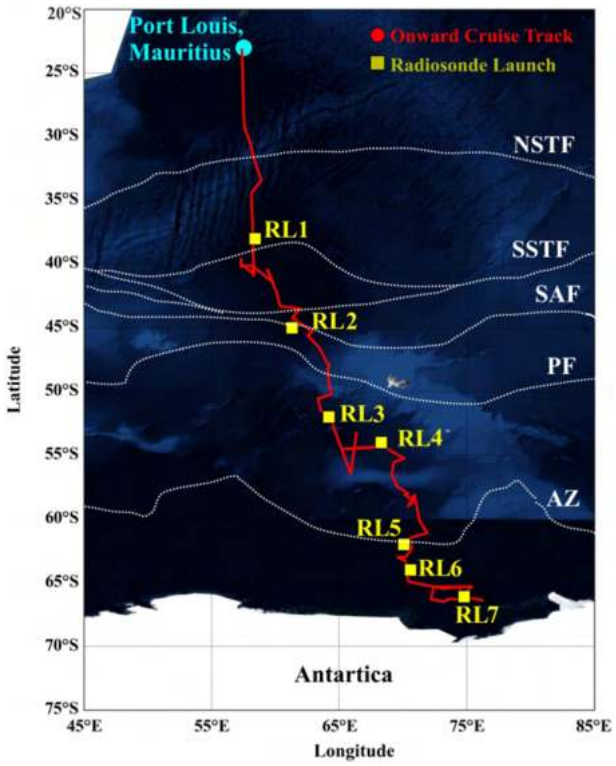

Fig. 1. The voyage track (in red) along which atmospheric measurements were performed during the forward track of the Xth Indian Expedition to the Indian Ocean sector of Southern Ocean (SOE-X) flagged from Port Louis, Mauritius, 20°S to Prydz Bay region of Antarctica, 69°S. Locations of seven radiosonde considered in each ISSO region are marked (yellow markers). Demarcation of the approximate location of oceanic fronts (white dotted lines) was adopted from Belkin and Gordon (1996) and Anilkumar et al. (2015) (namely, NSTF and SSTF - Northern and Southern Sub-Tropical Fronts; SAF - Sub-Antarctic Front; PF - Polar Front; and AZ -Antarctic Zone).

Table 1
The characteristics of clouds, inversions, aerosols, direct shortwave radiative forcing, and atmospheric heating rate over classified ISSO regions during the forward track of the Xth Southern Ocean Expedition.

	Regions north of Polar Front		Polar Front regions		Regions south of Polar Front		
	Subtropical Front (NSTF)	Sub-Antarctic Front (SAF1)	Northern Polar Front (PF1)	Southern Polar Front (PF2)	Southern Antarctic Circumpolar Current Front (SACCF)	Southern Boundary of ACC (SB)	Coastal Antarctica (CA)
I. Frontal Regions of the Indian Ocean sector of Southern Ocean (ISSO)							
Adopted frontal-based classification of the study area[a]	32°S to 40°S	41°30′S to 44°S	47°S to 52°30′S	54°30′S to 59°30′S	60°S to 62°S	64°S to 65°S	65°S to 68.5°S
II. Details of atmospheric sounding at 7 case study locations							
Launch number	RL1	RL2	RL3	RL4	RL5	RL6	RL7
Launch date	14 Dec 2017	19 Dec 2017	22 Dec 2017	23 Dec 2017	27 Dec 2017	28 Dec 2017	29 Dec 2017
Launch time (UTC)	01:00	06:00	22:00	06:00	03:00	06:00	05:00
Launch location	38.00°S, 58.40°E	45.00°S, 61.30°E	52.00°S, 64.20°E	54.00°S, 68.30°E	62.00°S, 70.07°E	64.40°S, 70.60°E	66.10°S, 74.80°E
III. Thermodynamic metrics							
SST (K)	17.1	13.3	3.1	1.2	0.1	0.5	−1.2
$SST - T_{air}$ (K)	0.1	5.5	0.9	−0.2	0.34	2.0	2.1
MSLP (hPa)	1013	1019	973	980	987	990	987
WS[b] ($m\ s^{-1}$)	10.19	3.06	19.16	17.98	5.01	5.18	6.14
WD[b] (°)	338.74	289.64	270.78	245.73	251.51	91.1	69.88
RH[b] (%)	79.01	73.93	95.32	97.71	95.06	82.66	91.58
IV. Inversion characteristics (surface - 5000 m)							
Inversions (INV)	3 INV	4 INV	2 INV	5 INV	5 INV	1 INV	1 INV
First INV height (m)	660	220	3300	160	1100	1220	1200
First INV strength ($K\ m^{-1}$)	0.27	0.50	2.24	0.35	1.78	1.57	1.34
Second INV height (m)	2440	840	3880	800	2220	–	–
Second INV strength ($K\ m^{-1}$)	0.89	0.14	0.73	0.22	0.16	–	–
Third INV height (m)	4660	1860	–	3780	3640	–	–
Third INV strength ($K\ m^{-1}$)	0.19	3.17	–	0.59	0.31	–	–
Fourth INV height (m)	–	4320	–	4260	4440	–	–
Fourth INV strength ($K\ m^{-1}$)	–	0.12	–	0.32	0.2	–	–
Fifth INV height (m)	–	–	–	4600	4880	–	–
Fifth INV strength ($K\ m^{-1}$)	–	–	–	0.14	1.28	–	–
V. Cloud characteristics (surface - 5000 m)							
Cloud layer (CL)	No CL	No CL	2 CL	2 CL	2 CL	No CL	1 CL
1st CL: base height (m)	–	–	340	180	40	–	580
1st CL: top height (m)	–	–	660	680	560	–	1120
1st CL: Total cloud thickness (m)	–	–	320	500	520	–	540
2nd CL: base height (m)	–	–	2200	1480	860	–	–
2nd CL: top height (m)	–	–	3360	2020	920	–	–
2nd CL: Total cloud thickness (m)	–	–	1160	540	60	–	–
VI. Aerosol characteristics							
Dominant aerosol type	Marine, dust, and elevated smoke	Marine, dust, and polluted dust	Marine, dust, and dusty marine	Marine, dust, dusty marine, and smoke	Marine and dust	Marine and dusty marine	Dust
Measured aerosol optical depth	0.095 ± 0.006	–	0.111 ± 0.016	0.108 ± 0.001	–	0.074	0.067
Black carbon mass conc. ($ng\ m^{-3}$)	46 ± 21	54 ± 6	269 ± 42	282 ± 5	155	71 ± 55	43
Clear sky direct aerosol radiative forcing ($W\ m^{-2}$)	1.32 ± 0.11	–	1.75 ± 0.30	1.71 ± 0.01	–	1.22	1.11
Atmospheric heating rate ($K\ day^{-1}$)	0.022 ± 0.002	–	0.029 ± 0.005	0.028 ± 0.001	–	0.002	0.018

[a] Identification of oceanic fronts over ISSO were adopted from Belkin and Gordon (1996) and Anilkumar et al. (2015).
[b] The wind speed (*WS*), wind direction (*WD*), and relative humidity (*RH*) in subheading II are mean values at 925 hPa.

parameters, measurements on *AOD*, and mass concentration of *BC*, while the vertical thermodynamic structure of the atmospheric column was analyzed using radiosonde measurements. The re-analysis data were used to understand synoptic surface gradient (air-sea temperature gradient, $dT = SST - T_{air}$) and wind circulation patterns. The satellite data comprises the vertical distribution of aerosols and cloud phases derived from CALIPSO (Cloud-Aerosol Lidar and Infrared Pathfinder Satellite Observation) retrievals. Details of data used, their mode of acquisition, instrumentation, and dynamic parameters are as follows.

2.1.1. Surface meteorology

The in-situ surface meteorological parameters included observations of air temperature (T_{air}), relative humidity (*RH*), mean sea level pressure (*MSLP*), wind speed (*WS*), and wind direction (*WD*). An automatic weather station (WeatherPak®-2000 v3) equipped with GPS provided the true *WS* and *WD* at ≈10 m above mean-sea-level height. The measurements were stored as 1-minute averages throughout the onward track of the cruise. In addition, a standard bucket thermometer was used at 6 hour intervals to measure sea-surface temperature (*SST*).

2.1.2. Black carbon (BC) aerosols

The in-situ measurements of *BC* mass concentrations were generated using an automatic self-contained Aethalometer (AE-42 manufactured by M/s Magee Scientific; Hansen et al., 1984) operating at seven wavelength channels (370, 470, 520, 590, 660, 880, and 950 nm). Data were collected at every 5-minute intervals operating at a flow rate of 5 l/min. The *BC* mass

concentrations were estimated in ng m^{-3} from the absorbance values at 880 nm involving quartz fiber filters and optical transmission using the factory-set calibration coefficients. The ambient particles were aspirated from the inlet through a heated sample line fixed at the height of 12 m at the ship's bow. The heated sample line maintained *RH* of the airflow at ≈60 % within the air stream entering the sampling channel of the instrument. More details about the instrument can be found elsewhere (Hansen et al., 1984; Hansen, 1996).

2.1.3. Aerosol optical depth (AOD)

The measurements of *AOD* were obtained using a MICROTOPS-II sunphotometer (Solar Light Co., USA) operating at five wavelengths, i.e., 380, 440, 500, 675, and 870 nm (Morys et al., 2001). The field of view of the sunphotometer is 2.51° at full-width half maximum, and the pointing accuracy is >0.1°. Following the principle of Beer-Lambert law, this instrument after measuring the direct solar flux computes *AOD* using internal factory-calibrated coefficients and local coordinates. All *AOD* measurements were collected along the cruise track only during clear sky conditions. The overall instrumental uncertainty in *AOD* is ±0.005.

2.1.4. Atmospheric soundings

A total of 7 radiosonde launches were used to present the vertical thermodynamical structure of the air column above each frontal region detailed in Table 1. The radiosonde was Pisharoty type developed by Vikram Sarabhai Space Centre of the Indian Space Research Organization. The vertical profiles of air temperature (*T*), atmospheric pressure (*P*), *RH*, *WS*, and *WD* were collected at 1 Hz from the surface to an altitude of nearly 32 km. A comparison of accuracy between Pisharoty radiosonde and other manufacturers (e.g., Vaisala) can be accessed in Divya et al. (2014). All radiosonde launches were conducted at 00:00, 12:00, 16:00, and 18:00 timings UTC.

2.1.5. Synoptic winds and surface temperature gradient (dT)

ERA5 (Hersbach et al., 2020) is a fifth-generation atmospheric reanalysis data product developed by ECMWF (European Centre for Medium-Range Weather Forecasts). A comparison made between in-situ measured and ERA5-derived measurements of meteorological parameters, i.e., *SST*, T_{air}, and *WS* obtained at 7 sounding locations showed a correlation for *SST* ($r = 0.982$), T_{air} ($r = 0.980$), *dT* ($r = 0.977$), and moderate correlation for *WS* ($r = 0.657$). Hence, in the present study ERA-5-derived estimates were used to calculate hourly averaged winds (10 m *u*- and 10 m *v*-component), 2 m T_{air}, and *SST* at a resolution of 0.25° × 0.25°. Subsequently, *dT* for each frontal region was estimated to represent a synoptic background in the vicinity of each sounding location.

2.1.6. Vertical aerosol profiles

Based on the in-situ atmospheric sounding locations, the CALIOP orbit track closest to the coordinates of the radiosonde measurements were acquired. The locations marked as pointers in CALIPSO retrievals lie within 0.5°-1° resolution with respect to the in-situ atmospheric-sounding location. The resolution was comparable to the standard resolution used in climate and regional models (Christian et al., 2019). From these satellite retrievals, clouds and aerosol properties were evaluated and identified after the calibration and range corrections incorporated into the signal return measured at 532 nm (Winker et al., 2009). The present study used CALIOP Level 2 Version 4.10 × to portray the distribution of aerosol types and cloud phases over ISSO frontal regions.

2.2. Methods and analysis

2.2.1. Air mass history

To discern the likely source of aerosols, air mass back-trajectories up to 120 h have been modeled using Hybrid Single-Particle Lagrangian Integrated Trajectory (HYSPLIT) version 4, available with NOAA-ARL (Draxler, 1992). The model uses NCEP Global Data Assimilation System (GDAS) meteorological data at different altitudes. For this study, back-trajectories of air mass arriving at different altitudes at respective sounding locations were computed.

2.2.2. Estimation of thermodynamic variables

From the radiosonde measurements, the computation of thermodynamic parameters comprised of (i) dew point temperature (T_d), (ii) virtual potential temperature (θ_v), (iii) equivalent potential temperature (θ_e), (iv) water vapor mixing ratio (*r*). Values >2.5 standard deviations from the mean vertical profile of the raw data (*T*, *RH*, *P*, *WS*, and *WD*) were considered outliers and discarded (Chandra et al., 2019). Owing to the irregularity of this data, an interpolation was performed for every 20 m height following Hande et al. (2012). This was followed by smoothening of the vertical profile using a 5-point moving average to eliminate small-scale fluctuations. These steps in generating smooth radiosonde profiles have been tested to preserve the thermodynamical characterization of MABL over SO (Lang et al., 2018; Truong et al., 2020).

Data ranging between 40 m and 5000 m were used in the analysis. Identification of mixed layer height has been delineated based on the sharp gradient in profiles of θ_v and *r* as these are conserved variables devoid of effects from dry and moist adiabatic processes (Betts, 1982). The estimation of θ_v and *r* were performed following (Stull, 1988),

$$\theta_v = \theta(1 + 0.61\, r) \tag{1}$$

$$\theta_e = \theta\, e^{2.67.q/T_{LCL}} \tag{2}$$

$$r = [0.623e/P - 0.377e] \tag{3}$$

In Eqs. (1)–(3), θ, the potential temperature and T_{LCL}, the temperature at LCL (lifting condensation level) had been computed following the equation of Bolton (1980), *q* is the specific humidity of the air, *P* is the atmospheric pressure, and *e* represents atmospheric vapor pressure.

From the smoothened radiosonde data, vertical cloud distribution was evaluated by examining the profiles of T_{air} and T_d from 40 m to 5000 m altitude of each sounding, and within this altitudinal range whenever the difference between T_{air} and T_d was <1.5 °C for an altitude thickness of at least 60 m or more, the presence of clouds were marked. Following this criterion, from each sounding, the presence of no cloud, single cloud layer, double cloud layer, more than three cloud layers, or complete cloud cover (up to 5000 m altitude) were marked. This criterion was adopted following the study conducted on cloud identification in the Australian sector of the Southern Ocean (ASSO) by Truong et al. (2020). A multi-layered cloud was identified if at least two or more cloud layers were recorded in each profile (Mace et al., 2009). Also, the cloud base and cloud top heights were determined. The cloud base height was identified as the base height of the first cloud layer (i.e., the lowest height at which $T_{air} - T_d < 1.5$ °C for at least 60 m or more for the first time in that sounding profile). The cloud total thickness was calculated as the altitude sum of the number of identified cloud layers where dew point depression was recorded (Truong et al., 2020).

The identification of significant temperature inversion was carried out from smoothened vertical profiles of virtual potential temperature (θ_v) with respect to altitude (*z*). If the gradient, $d\theta_v/dz$, was >1.4 K m^{-1} an inversion was recorded (Truong et al., 2020). In addition, after the first inversion is identified, a distance of 300 m was kept as a threshold for the subsequent inversion to be considered. Therefore, a "multi-level inversion" was reported when two or more inversions were marked in every vertical profile.

2.2.3. Clear sky direct atmospheric radiative forcing

The aerosols present in the atmosphere alter the incoming solar radiation by either direct or indirect interactions, thus, accounting for direct or indirect aerosol-induced radiative forcing. Direct aerosol radiative forcing (*DARF*) involves the scattering and absorption of solar radiation by atmospheric aerosols and is influenced by the type of aerosols and surface reflectance. Depending upon these properties, a negative or positive *DARF* is estimated at the surface (Ganguly et al., 2005; Li et al., 2004; Vinoj et al., 2004). However,

the indirect *DARF* involves the modification of microphysical properties, amount, and the lifetime of clouds and hence, the variability in the incoming solar radiation (Parry et al., 2007, and the references therein). In view of this, in the present study, only clear sky *DARF* has been estimated.

For the estimation of clear sky *DARF*, estimates of aerosol optical properties such as *AOD*, single scattering albedo (*SSA*), and asymmetry parameter (*ASY*) were required. Direct measurements of these parameters (*SSA* and *ASY*) were not available, hence, estimates of these parameters were simulated using the Optical Properties of Aerosols and Clouds (OPAC) model. These estimations were obtained by accessing the sunphotometer-measured *AODs* only in clear sky conditions. The clear sky conditions imply that the sun was completely visible and the atmosphere was cloud-free or the daytime intervals that were cloud-free. A minimum of five continuous observations were collected every time the instrument was directed towards the sun. Further, the average *AOD* was calculated for each location at which we had at least four clear sky readings. Thus, in all the locations where the sunphotometer-measured *AOD* values were available, the OPAC model was run to obtain the *AOD*, *SSA*, and *ASY* estimates for deriving clear sky *DARF*. In this study, of the total 7 examined frontal regions, sunphotometer-measured *AODs* were available at a few locations in five frontal regions (NSTF, PF1, PF2, SB, and CA), while *AOD* measurements could not be collected in regions of SAF and SACCF due to persistent cloud cover.

For obtaining a clear sky *DARF*, the inputs given to the OPAC model were five aerosol types, i.e., total water-soluble components, sea salt (accumulation mode), sea salt (coarse mode), sulfate, and *BC*, height profile, five standard sunphotometer wavelengths, and *RH* following by Hess et al. (1998). Among these inputs, the *BC* number concentration values were estimated from the Aethalometer measured *BC* mass concentration. Thus, the number concentrations of *BC* were kept fixed while the remaining four naturally occurring aerosol types were iterated. These iterations were performed until the OPAC simulated *AOD* was corroborated closely (± 0.05) with the sunphotometer-measured *AOD*. The comparison between the sunphotometer-measured *AOD* and OPAC simulated *AOD* represented a correlation, $r = 0.981$. Such a hybrid approach to estimate *SSA* and *ASY* for obtaining clear sky *DARF* has been reported over the Arabian Sea, Bay of Bengal (Vinoj et al., 2004; Ganguly et al., 2005), and over the Saharan dust (Li et al., 2004). Thus, OPAC simulated *SSA*, *ASY*, and *AOD* under clear sky conditions were given as inputs for *DARF* estimations performed using Santa Barbara DISORT Atmospheric Radiative Transfer Model (SBDART, Ricchiazzi et al., 1998). In addition to the aforementioned input, another input was surface reflectance which was derived from MODIS. The *DARF* was computed in the shortwave range of 0.25 to 4.0 μm. The *DARF* represents the net change in the incoming and outgoing irradiance with and without aerosols in the atmospheric column. To estimate net radiative forcing, two scenarios were considered at the top of the atmosphere (*TOA*) and the surface (*SFC*), (i) without aerosols representing clean air and (ii) with aerosols. The difference between the two scenarios gives the total radiative forcing (*ARF*) due to aerosols (Stamnes et al., 2000). Thus, the *ARF* is calculated using,

$$ARF = Flux\ (net)_{TOA/SFC\ with\ aerosols} - Flux\ (net)_{TOA/SFC\ without\ aerosols} \quad (4)$$

Thus, the total atmospheric forcing was,

$$ARF_{ATM} = ARF_{TOA} - ARF_{SFC} \quad (5)$$

2.2.4. Atmospheric heating rate (HR)

A measure of the total radiative effect induced due to the absorption by aerosols present in the atmosphere is quantified in terms of the rate of atmospheric radiative heating (K day^{-1}),

$$\frac{\partial T}{\partial t} = \frac{g}{c_p}\left[\frac{ARF_{ATM}}{\triangle P}\right] \times (\mathrm{h/day}) \times 3600\ (\mathrm{s/h}) \quad (6)$$

where, $\partial T/\partial t$ is the atmospheric heating rate, g is the acceleration due to gravity (9.8 m s^{-2}), c_p is the specific heat capacity of air at constant pressure (1006 J kg^{-1} K^{-1}), and P represents atmospheric pressure (hPa). ΔP is calculated as the difference in pressure between the surface and 10,000 m altitude, considering the maximum extent of the tropospheric air column.

3. Results

This section presents the atmosphere surface meteorological conditions, the vertical thermodynamic structure of MABL, and aerosol observations obtained over ISSO regions.

3.1. Synoptic meteorology

There was a distinct spatial variability in the meteorological conditions observed near the surface and at different altitudes in atmosphere over each frontal region (Figs. 2, 3). It was primarily due to the sharp gradients in meteorological parameters caused by the oceanic frontal systems, thereby developing distinct features in the atmospheric column.

The regions north of the PF (i.e., NSTF and SAF) showed a convectively driven atmosphere with higher θ_e (307 K < θ_e < 323 K) up to 5000 m altitude. However, a sharp wind reversal in mid-altitude (≈1800 m) accounted for separating low-level convectively mixed moist air mass (5.6 g kg^{-1} < r < 8.2 g kg^{-1}; 52 % < *RH* < 78 %) from dry air mass (1.8 g kg^{-1} < r < 3.3 g kg^{-1}; 12 % < *RH* < 35 %) at high altitudes. This reversal was set by the easterly wind. In the PF regions, distinct meteorological conditions comprised of strong high-speed westerly winds (>28 m s^{-1}) that advected highly saturated cold air mass with temperatures < 1 °C and *RH* > 94 %, from surface to ≈5000 m (Figs. 2–3). The advection accounted for the development of a low-pressure system with *MSLP* < 973 hPa. In consequence, the occurrence of low-pressure cyclonic systems suppressed the strength of convective potential (lower values of 284 < θ_e < 307) in the lower atmosphere of PF region (Fig. 3). The SACCF region is located south of PF and forms at the boundaries of the Ferrell and Polar cells at ≈60°S. In SACCF, the weakening of strong polar westerly winds was observed due to the convergence of cold-dry air mass by south-easterly winds and relatively warm moist air mass by north-westerly winds. This convergence accounted for a lower MSLP (987 hPa) and intensified low-level cyclone formation. In consequence, high moisture content (1.3 g kg^{-1} < r < 4.3 g kg^{-1}), and highest *RH* (97 %) were noticed throughout 5000 m altitude (Fig. 3). Further, at the extreme south of all frontal regions, the regions SB and CA showed significantly dry-colder air mass (lowest values of 0.4 g kg^{-1} < r < 2.3 g kg^{-1}) advected by weak easterly winds (*WS* < 6 m s^{-1}) from Antarctic continent. Low-level atmospheric conditions, however, had higher saturated air compared to the column at mid and upper altitudes. The presence of drier air in mid and high altitudes can be attributed to prevailing katabatic winds near the coast of the Antarctic continent. Overall, the region was characterized by weak unstable conditions, as indicated by the lowest values of θ_e (282 K < θ_e < 294 K) in 5000 m altitude.

3.2. Case studies based on observations on aerosols and MABL characteristics

Aerosol-boundary layer observations of each frontal region are reported in this section. A two-dimensional representation of meteorological parameters of each frontal region from surface to 5000 m is presented in a skew-T diagram in Fig. S1.

3.2.1. A case study over Sub-Tropical Front (NSTF)

Data from the radiosonde launched at 38.00°S, 58.40°E on 14th December 2017 at 01:00 UTC (06:30 LT) were used as a representative sounding to depict the NSTF2 region (Fig. 4a). This early morning (local time) sounding was associated with a weak positive near-surface air-sea temperature gradient (dT = 0.1 °C; Fig. 4a). Weak dT had a negligible effect in altering the stable state of night-time MABL, which was evident with a gradual

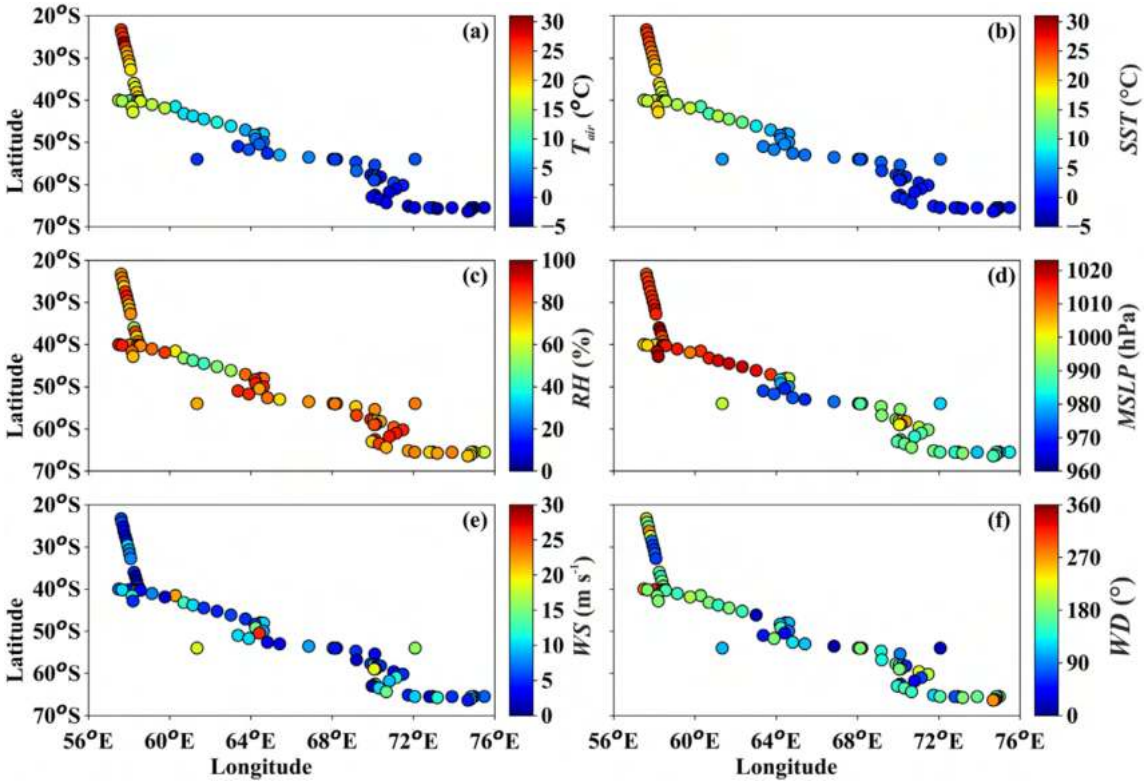

Fig. 2. The measurements conducted along the forward cruise track of the Xth Indian Expedition to the Southern Ocean (SOE-X) from 35°S to 66°S along 56°E to 76°E. Along this cruise track, a 2D variation of measured meteorological parameters, (a) air temperature (T_{air}), (b) sea surface temperature (*SST*), (c) relative humidity (*RH*), (d) mean sea level pressure (*MSLP*), (e) wind speed (*WS*), and (f) wind direction (*WD*) are shown. Approximate locations of oceanic fronts are acquired from Anilkumar et al. (2015) and Belkin and Gordon (1996) (grey dotted lines).

increase (decrease) in $\theta_e(r)$ with increasing altitude (Fig. 4b). However, despite stable profiles of θ_e and r, three significant inversions, and with no cloud layers were noticed (Figs. 4b, S1a). These observations were attributed to the subsidence associated with high MSLP (1013 hPa) as well as the advection of warmer air mass from its northern region with higher $dT > 0.4$ °C. The conditions supported significant inversions near the surface (660 m) and at mid-altitudes (2440 m), having gradients 0.27 K m^{-1} and 0.89 K m^{-1}, respectively (Fig. 4b). Additionally, a weaker inversion (0.19 K m^{-1}) was observed at a higher altitude (4660 m) (Fig. 4b). Out of these three significant inversions, the height of the mixed layer (≈2440 m) was identified as the height where the maximum gradient was observed in θ_v and r profiles (Ramana et al., 2004).

Under these thermodynamical conditions, the vertical aerosol features derived from CALIPSO revealed the presence of naturally produced marine aerosols, such as sea salt, dimethyl sulfate (DMS), and other organic aerosols (Fig. 4c; O'Dowd et al., 1997). Noticeably, the higher loading of marine aerosols was confined below 1500 m altitude (Fig. 4c). This indicated the role of inversions and subsidence in restricting the vertical dispersion of these aerosols. Moreover, the prevalence of anthropogenic aerosols (elevated smoke) at higher altitudes (≈3700 m) was also noticed (Fig. 4c), which is likely to be remotely originated and advected from the South African continent (3500 m; Fig. S2a).

3.2.2. A case study over Sub-Antarctic Front (SAF1)

Data from radiosonde launched at 45.00°S, 61.30°E on 19th December 2017 at 06:00 UTC (11:30 LT) was used as a representative sounding of SAF1 (Fig. 4d). There was a formation of a warm front evident in the air-sea temperature gradient (dT = 5.5 °C at sounding location and >5.5 °C around this location; red shaded region; Fig. 4d). The formation of this warm front was caused by the active oceanic eddies induced by the strong Agulhas Retroflection Current (Lutjeharms and Van Ballegooyen, 1988). An associated effect of this current at the air-sea interface shaped the vertical thermodynamic structure of MABL (Fig. 4e). The high dT and *MSLP* (1019 hPa) enhanced atmospheric mixing at lower altitudes. The near-uniform variation in θ_v and r profiles indicated of a well-developed mixed layer up to 1860 m capped by a strong inversion of strength 3.17 K m^{-1} (Fig. 4e). These unstable conditions supported the formation of four significant inversions and the absence of cloud layers (Table 1).

The aerosols were primarily of marine origin at lower altitudes (<2000 m), while polluted dust was noticed at higher altitudes (>4500 m) (Fig. 4f). From air mass back-trajectories, the marine aerosols at low altitudes were locally generated or long-range advected from open SO region at altitudes 20 m and 500 m, respectively (Fig. S2b). In comparison, the likelihood of polluted dust at high altitudes (4600 m) was attributed to long-range transport from the South American continent (Fig. S2b). Interestingly, aerosol loading was weak in the region due to the unstable atmospheric conditions that mix and disperse aerosols and limit accumulation.

3.2.3. A case study over Polar Front (PF1)

Data from radiosonde launched at 52.00°S, 64.20°E on 22nd December 2017 at 22:00 UTC (03:30 LT) represents the atmospheric conditions over PF1 (Fig. 5a). The synoptic near-surface air-sea temperature gradient increased from −1.0 to 1.5 °C, while at the sounding location, dT of 0.9 °C was observed (Fig. 5a). In this region, the combined effect of weak dT, the lowest recorded *MSLP* in this study (973 hPa), and the advection of colder air masses by westerly winds (>19.16 m s^{-1}) caused significant stability as well as supported the formation of an intense low-pressure cyclonic system. The stable state of the atmosphere is evident with a gradual increasing (decreasing) tendency of θ_v (r) profiles with increasing altitudes up to 5000 m (Fig. 5b). In these atmospheric conditions, the presence of low-level multi-layer clouds (the gradient of T and T_d, RH > 90 %) were observed (Figs. 5b, S1c). The lowest cloud layer was as low as 340 m

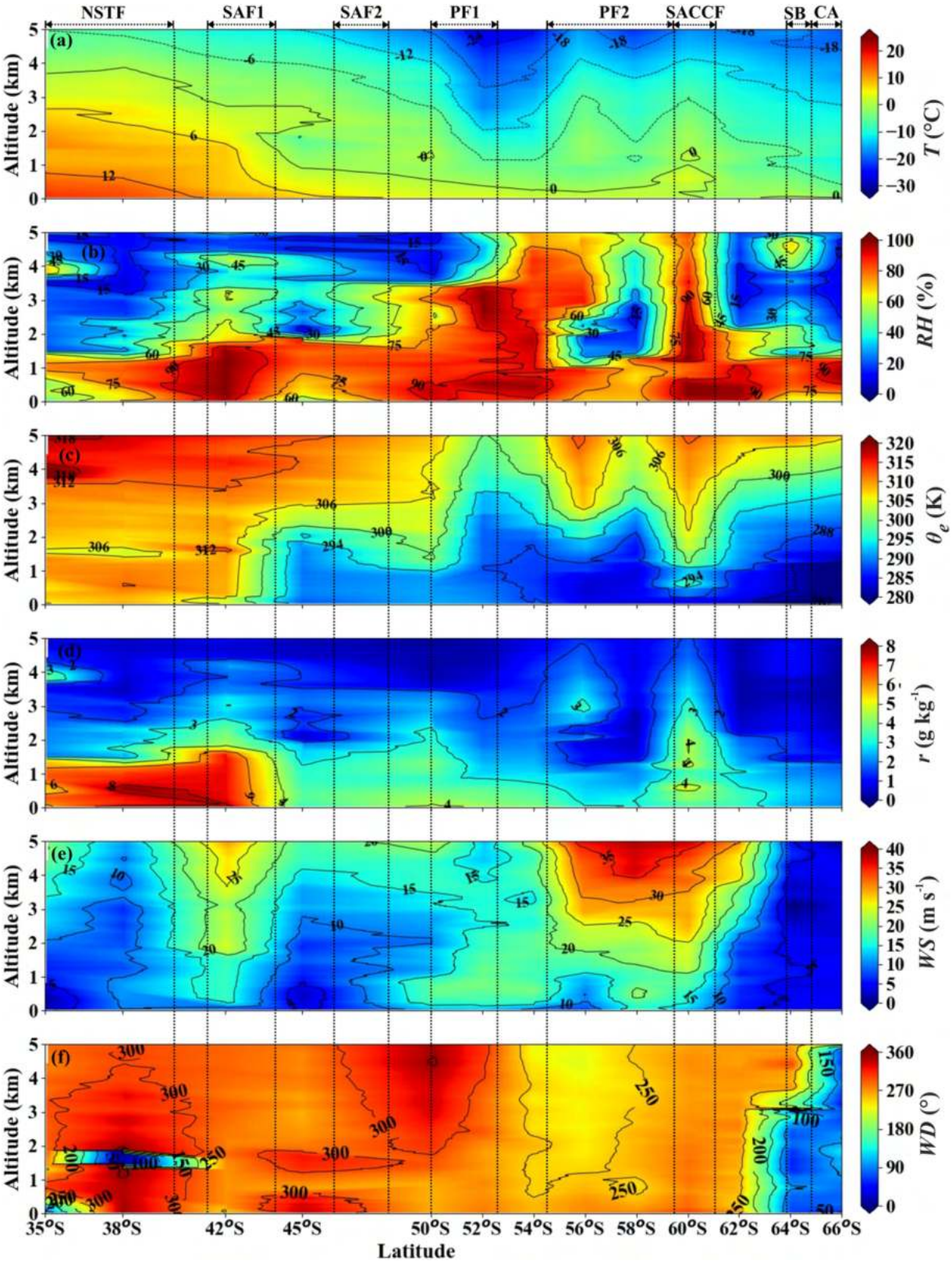

Fig. 3. Contour plots of, (a) atmospheric temperature (*T*), (b) relative humidity (*RH*), (c) equivalent potential temperature (θ_e), (d) mixing ratio (*r*), (e) wind speed (*WS*), and (f) wind direction (*WD*), representing observed vertical thermodynamic structure of the atmosphere from 0 to 5 km altitude over the latitudinal range from 35°S to 66°S during the forward track of Xth Southern Ocean Expedition (SOE-X) are shown. Approximate locations of oceanic fronts are acquired from Belkin and Gordon (1996) and Anilkumar et al. (2015) (grey dotted lines).

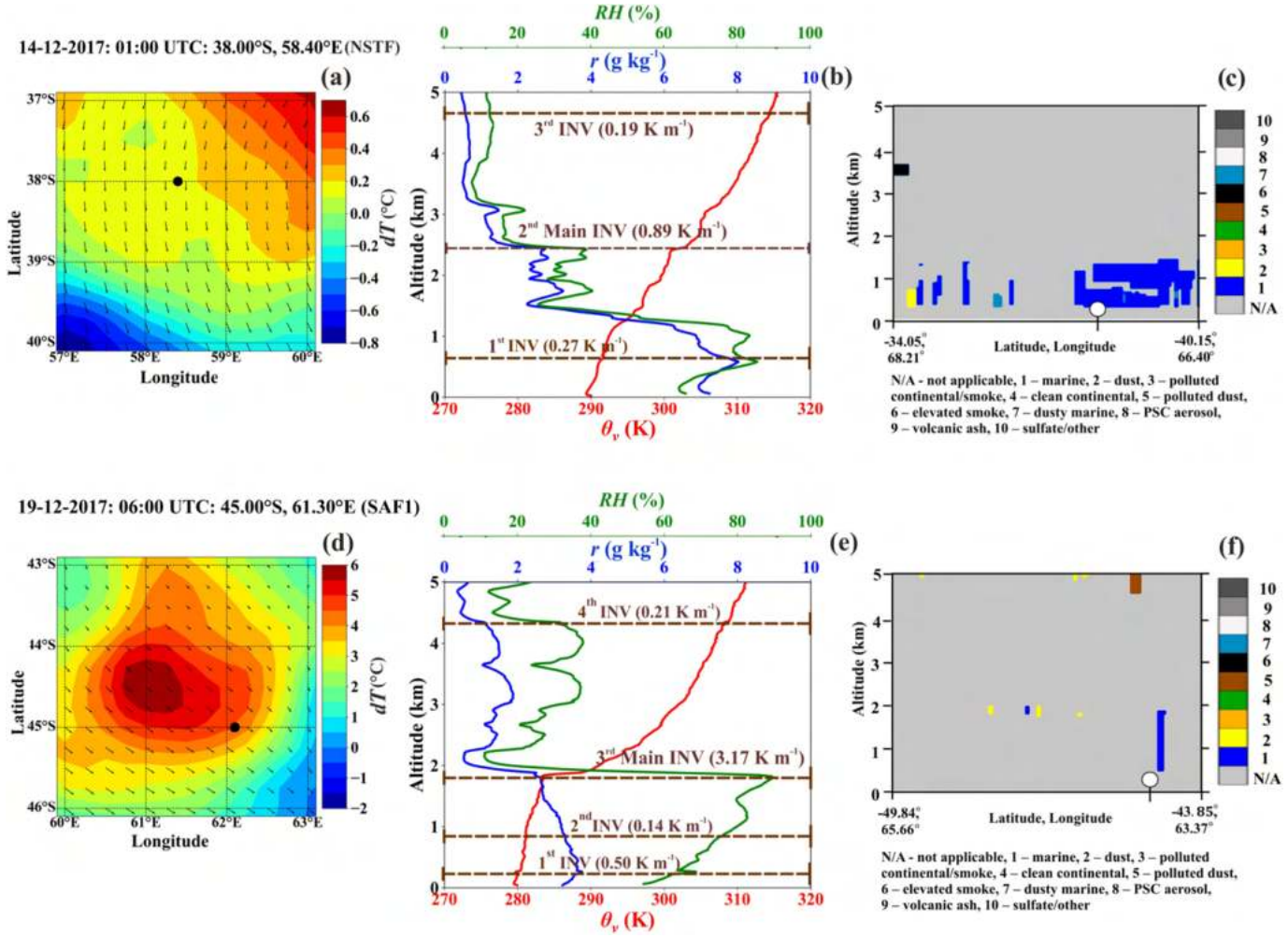

Fig. 4. The figure depicts the regions lying to the north of the Polar Front (PF), i.e., (a–c) region of the Sub-Tropical Front (NSTF) and (d–f) Sub-Antarctic Front (SAF1). Panel a represents synoptic near-surface air-sea temperature gradient (dT in °C) and wind circulation pattern in the vicinity of this sounding obtained using ECMWF-ERA5 reanalysis dataset, where *SST* values at the surface, T_{air} at 2 m, wind fields (10 m *u*- and *v*-component) are considered. The launch location is marked with a black circular dot. The respective colour bar is shown. Panel b shows a 5 km vertical profile of virtual potential temperature (θ_v in red), mixing ratio (r in blue), and relative humidity (*RH* in green) for radiosonde launched at 38.00°S, 58.40°E on 14-12-2017 at 01:00 UTC in the NSTF region. The estimated altitudes of inversions (brown) (inversion strength in K m^{-1}) and cloud layers (blue) (cloud thickness in m) are marked for respective launch locations. Panel c represents CALIPSO standard daytime 0–5 km vertical products of aerosol sub-types derived for 14-12-2017, 20:36 to 20:50 UTC during its orbit between 34.05°S, 68.21°E and 40.15°S, 66.40°E. Panels d and e represents the same as panels a and b, respectively, but for radiosonde launched at 45.00°S, 61.30°E on 19-12-2017 at 06:00 UTC in SAF1 region. Panel f represents CALIPSO standard daytime 0–5 km vertical products of aerosol sub-types derived for 19-12-2017, 09:56 to 10:09 UTC during its orbit between 49.84°S, 65.66°E and 43.85°S, 63.37°E.

(cloud base) with a thickness of 320 m, while the second thicker cloud layer was present at 2200 m with a thickness of 1160 m and extending up to 3360 m (Fig. 5b). The temperature at the top of the first cloud layer was −0.4 °C which indicated the presence of highly saturated supercooled water (SLW). However, at the base and top of the second cloud layer, the temperature dropped abruptly from −8.2 °C to −9.7 °C, indicating that condensation may have resulted in the formation of mixed-phased SLW or ice-phased clouds (Fig. 5b). SLW/IWC clouds in this region were also noticed in the CALIPSO water phase feature (Fig. S3c). The significant stability in the low-level atmosphere accounted for multiple stronger inversions at higher altitudes (Fig. 5b). In this sounding, the top of the second cloud layer was capped by the first inversion of strength 2.24 K m^{-1} at 3300 m, while a weaker second inversion of strength 0.73 K m^{-1} was observed at 3880 m. Overall, the presence of thick clouds prevented identifying the top of the mixed layer height.

Significant loading of dust and dusty marine aerosols prevailed within intermediate and higher altitudes (1000 m to 5000 m; Fig. 5c). At lower altitudes (<2000 m), marine origin aerosols were observed. The back-trajectories showed the clockwise circulation of air mass associated with an intensified cyclonic system (Fig. S2c).

3.2.4. A case study over Polar Front (PF2)

Data from radiosonde launched at 54.00°S, 68.30°E on 23rd December 2017 at 06:00 UTC (11:30 LT) was used as a representative sounding for PF2 (Fig. 5d). The atmospheric conditions over PF2 were similar to PF1 and recorded the lowest *MSLP* in this study (980 hPa), lowest freezing temperatures (−1 °C), and the highest percentage of *RH* (97.71 %). Also, strong winds (>17.98 m s^{-1}) induced by the polar jet stream were noticed up to 5000 m altitude that constantly advected colder and highly saturated air masses from the west direction (245.73°; Figs. 5d, S1d). The only distinction observed in the PF2 region was the strong barrier generated by winds at mid-latitudes (at 500 m to 1600 m altitude), which separated low-level low-pressure cyclonic precipitation core from the high-level updraft storms. The cyclonic precipitation core was evident by the formation of the cold front region exhibiting negative dT ranging from −0.15 °C to 0.15 °C (blue shaded area in Fig. 5d). The radiosonde measurements recorded the lowest dT (−0.2 °C), and its coupling with prevailing atmospheric parameters accounted for the stable conditions. This was evident with the gradually increasing (decreasing) tendency of θ_v (r) throughout 5000 m altitude (Fig. 5e). In addition, the condensation also accounted

for the saturated first cloud layer from just a few meters above the surface (40 m), having a thickness of 520 m (Fig. 5e). In comparison, the second cloud layer was noticed up to 2020 m having a thickness of 540 m. These low-level clouds were likely in the form of SLW or IWC, with temperatures ranging between −5 °C and −12 °C (Fig. S1d).

The presence of SLW/ICE clouds was also observed in the CALIPSO water phase feature (Fig. S3d). Of the total, five significant inversions were observed, i.e., three high altitude inversions at 3780 m, 4260 m, and 4600 m of strength 0.59 K m^{-1}, 0.32 K m^{-1}, and 0.14 K m^{-1}, respectively. Another two low-altitude inversions at 160 m and 800 m of strength 0.35 K m^{-1} and 0.22 K m^{-1}, respectively, were also observed at the base and top of the first cloud layer (Fig. 5e). In PF2, identification of mixed layer height was not possible due to higher cloud coverage at low altitudes.

Akin to PF1, the vertical aerosol features in PF2 also showed higher loading of dust and dusty marine-type aerosols within 5000 m altitude (Fig. 5f). In addition, polluted continental/smoke and marine aerosols were observed in lower altitudes (<1000 m). A cyclonic circulation was evident in the back-trajectory analysis (Fig. S2d).

3.2.5. A case study over Southern Antarctic Circumpolar Current Front (SACCF)

Data from radiosonde launched at 62.00°S, 70.07°E on 27th December 2017 at 03:00 UTC (08:30 LT) represents the conditions over SACCF (Fig. 6a). The region lies in the trough of ACC and is characterized by the formation of mesoscale polar cyclonic systems due to the strong convergence of cold-dry air mass by southeast winds and relatively warm moist air mass by northwest winds. It accounts for the convergence that weakens the wind (5.01 m s^{-1}). The winds continuously advect colder and drier polar air masses in the region (Fig. S1e). Thereby, it supports the formation of the cold front as observed from *dT* (blue-shaded region; Fig. 6a).

The radiosonde was launched in the cold front during the early morning time (local), and a weak *dT* (0.1 °C), low *MSLP* (987 hPa), and high *RH* (95.06 %) were recorded (Table 1). The gradual increase (decrease) in $\theta_v(r)$ accounted for higher stability of the atmospheric column (Fig. 6b). It supported an intense cyclonic system that caused significant low-level precipitation resulting in low-level multi-layered clouds (Fig. 6b). The base of the first cloud layer was observed to be as low as 40 m with a thickness of 520 m, while the second cloud layer was only a few meters above the first cloud layer extending from 860 m to 920 m with thickness 60 m (Fig. 6b). The low-level cloud formation was due to the mesoscale convergence. At mid and higher altitudes above 920 m, the weakening of convergence updrafts caused cloud-free conditions. The strong winds at high altitudes also resulted in multiple inversions (Fig. 6b). The first significant inversion was observed at 1100 m with a strength of 1.78 K m^{-1}, which capped the

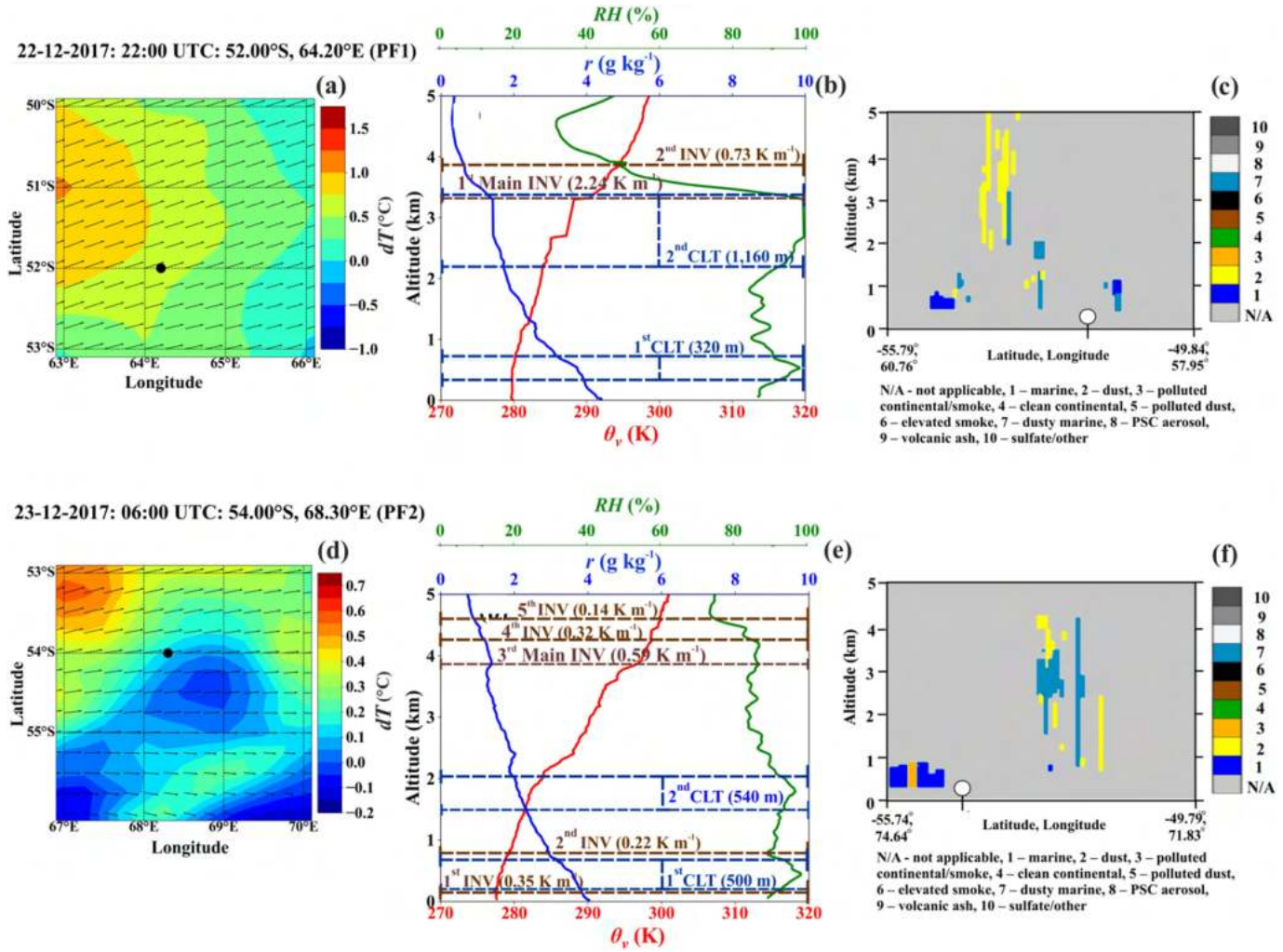

Fig. 5. The figure depicts the Polar Front (PF) regions, i.e., (a–c) Northern Polar Front (PF1) and (d–f) Southern Polar Front (PF2). Panels a and b represents the same as Fig. 4a, b, respectively, but for radiosonde launched at 52.00°S, 64.20°E on 22-12-2017 at 22:00 UTC in the PF1 region. Panel c represents the CALIPSO standard daytime 0–5 km vertical products of aerosol sub-types derived for 22-12-2017, 10:26 to 10:40 UTC during its orbit between 55.79°S, 60.76°E and 49.84°S, 57.95°E. Panels d and e represents the same as Fig. 4a, b, respectively, but for radiosonde launched at 54.00°S, 68.30°E on 23-12-2017 at 06:00 UTC in PF2 region. Panel f represents the CALIPSO standard daytime 0–5 km vertical products of aerosol sub-type derived for 23-12-2017, 09:31 to 09:44 UTC during its orbit between 55.74°S, 74.64°E and 49.79°S, 71.83°E.

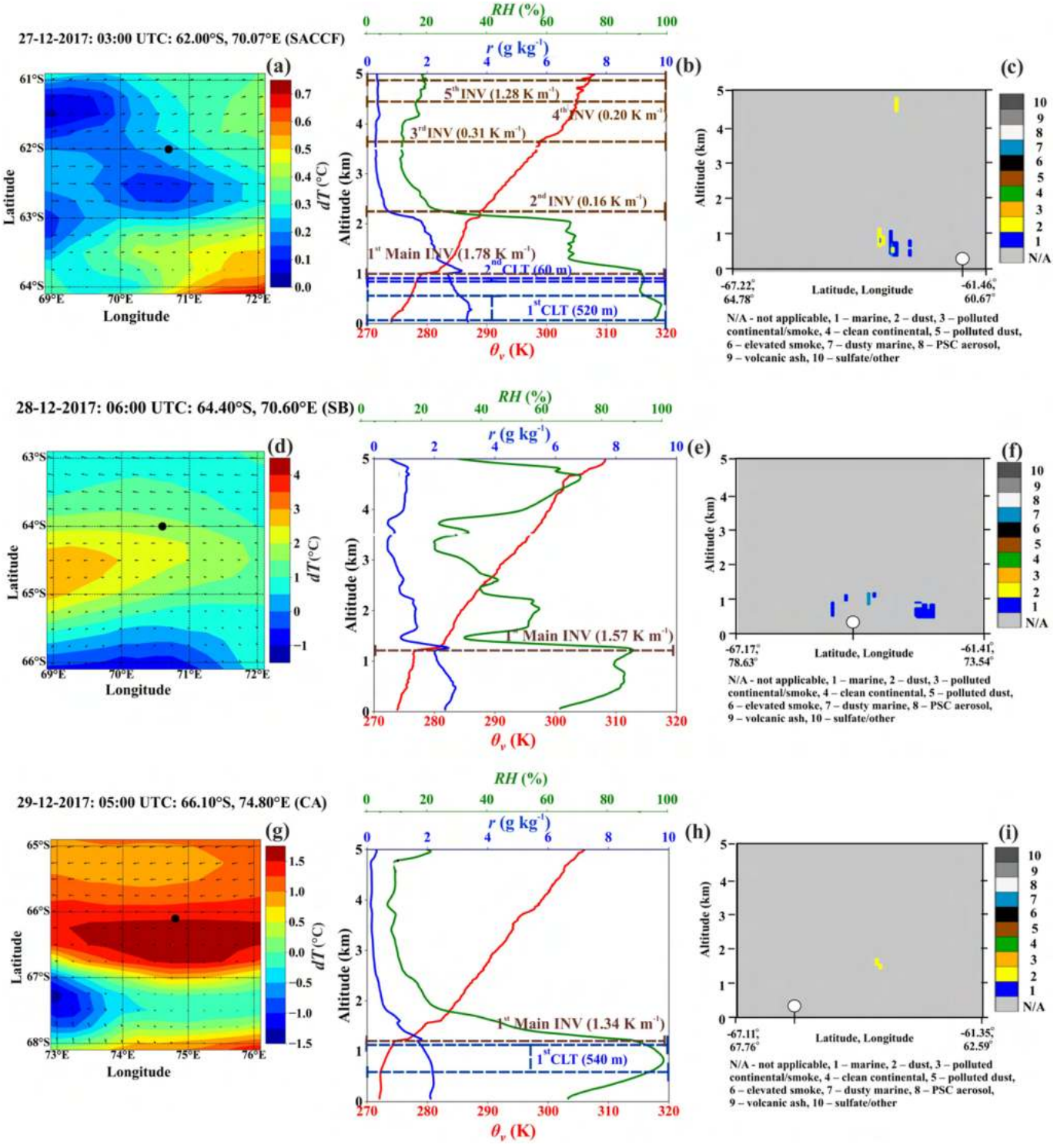

Fig. 6. The figure depicts the regions south of the polar front, i.e., (a–c) Southern Antarctic Circumpolar Current Front (SACCF), (d–f) Southern boundary of ACC (SB), and (g–i) Coastal Antarctica (CA). Panels a and b represents the same as Fig. 4a, b, respectively, but for radiosonde launched at 62.00°S, 70.07°E on 27-12-2017 at 03:00 UTC in SACCF region. Panel c represents the CALIPSO standard daytime 0–5 km vertical products of aerosol sub-type derived for 27-12-2017, 10:45 to 10:59 UTC while it is orbiting between 67.22°S, 64.78°E and 61.46°S, 60.67°E. Panels d and e represents the same as Fig. 4a, b, respectively, but for radiosonde launched at 64.40°S, 70.60°E on 28-12-2017 at 06:00 UTC in SB region. Panel f represents the CALIPSO standard daytime 0–5 km vertical products of aerosol sub-type derived for 28-12-2017, 09:49 to 10:03 UTC during its orbit between 67.17°S, 78.63°E and 61.41°S, 73.54°E. Panels g and h represents the same as Fig. 4a, b, respectively, but for radiosonde launched at 66.10°S, 74.80°E on 29-12-2017 at 05:00 UTC in CA region. Panel i represents the CALIPSO standard daytime 0–5 km vertical products of aerosol sub-type derived for 29-12-2017, 10:33 to 10:46 UTC during its orbit between 67.11°S, 67.76°E and 61.35°S, 62.59°E.

top of the second cloud layer (Fig. 6b). This inversion marked the top of the mixed layer (1100 m), above which the presence of dry tropospheric air mass (the larger decreasing tendency of *r* and *RH*; Fig. 6b) prevailed.

There was a decrease in aerosol species (notably dust aerosols) within a 5000 m atmosphere compared to the aerosol loading observed in PF (Fig. 6c). However, in lower altitudes (<1500 m), aerosols of marine origin,

i.e., sea salt, non-sea salt aerosols, such as dimethyl sulfate (DMS), and other organic aerosols, were observed. Additionally, some dust aerosols were also noticed at higher altitudes (4500 m to 5000 m).

3.2.6. A case study over Southern Boundary of ACC (SB)

Data from radiosonde launched at 64.40°S, 70.60°E on 28th December 2017 at 06:00 UTC (11:30 LT) represents the SB region (Fig. 6d). The atmospheric conditions were controlled by the potential warming of Antarctic waters regulated by two sub-polar gyres (Weddell gyre to its west and Prydz Bay gyre to its east). This induced higher *dT* (2.0 °C) and resulted in a weak warmer frontal region (orange-yellow shaded region in Fig. 6d). It enhanced the surface air-sea temperature gradient accounted for unstable MABL conditions. The destabilization of MABL resulted in a higher atmospheric mixing leading to a well-developed shallow mixed layer capped by a single inversion observed at 1220 m of strength 1.57 K m^{-1} (Fig. 6d). Above this inversion, drier air mass with lower values of *RH* and *r* (also a more significant difference in *T* and T_d; Fig. S1f) prevailed. The absence of cloud layers were observed over SB (Fig. 6e).

Based on the vertical profile of aerosols, it is clear that a natural atmosphere, primarily composed of marine aerosols prevails; however, a small amount of dusty marine aerosols were also noticed at lower altitudes below 1500 m (Fig. 6f). The major vertical spread of the aerosols was confined below 1100 m where strong inversion may be a restrictive factor (Fig. 6e, f). In this region, clean maritime air mass prevailed at mid and higher altitudes (>1500 m to 5000 m; Fig. 6f).

3.2.7. A case study over Coastal Antarctica (CA)

Data from radiosonde launched at 66.10°S, 74.80°E on 29th December 2017 at 05:00 UTC (10:30 LT) was used to depict conditions over CA (Fig. 6g). The atmospheric dynamics in this region were influenced by the activity of Prydz Bay gyre (Smith et al., 1984). It induced stronger convective eddies near the sea-surface, evident from higher *dT* forming a warmer front (red shaded region; Fig. 6g). The higher *dT* at the location of radiosonde sounding (2.1 °C) triggered unstable conditions resulting in a well-evolved mixed layer (Fig. 6h). The mixing was capped by a significant low-level inversion at 1200 m height of strength, 1.34 K m^{-1}. Below this inversion, condensation occurred due to the advection of cold continental air mass (*RH* > 90 % below 1200 m; Fig. S1g). This supported the formation of a low-level single cloud layer with a base at ≈580 m and a thickness of 540 m. Above this inversion, cold-dry air mass prevailed (larger difference in *T* and T_d, lowest *RH* and *r*; Figs. S1g, 6h).

The vertical aerosol features showed a negligible fraction of dust aerosols in lower altitudes (<2000 m), while clean maritime air masses were more likely (Fig. 6i). Thus, nearly natural atmospheric conditions were observed in this region.

3.3. Variability of aerosols, radiative forcing and heating rate

3.3.1. Variation of BC aerosols

BC mass concentrations measured along the cruise track are shown in Fig. 7a. Measurements revealed significantly higher values of *BC* (prominently >250 ng m^{-3}) in the PF regions (PF1 and PF2) lying between 47°S to 60°S. The highest *BC* concentration was at 59.00°S, 70.04°E, with a 297 ng m^{-3}. The regions north of the PF between 30°S to 46°S (i.e., NSTF and SAF) showed moderate *BC* values ranging from 21 ng m^{-3} to 85 ng m^{-3}.

Estimates of *BC* mass concentrations in regions of NSTF and SAF1 were 45.56 ± 21.49 and 54 ± 6.48 ng m^{-3}. In the region south of PF, between 60°S and 65°S (i.e., SACCF and SB), BC concentrations varied from 24 ng m^{-3} to 155 ng m^{-3}. Towards the extreme south near the coast of Antarctica (CA), a decrease in *BC* mass concentrations was observed with values as low as 43 ng m^{-3}. A previous study by Moorthy et al. (2005) has reported lower values of *BC* mass concentration (<50 ng m^{-3}) between 20°S to 56°S, whereas, Hulswar et al. (2020) and Menon et al. (2015) reported values ranging between 49 and 300 ng m^{-3}. However, a recent study by Srivastava et al. (2021) reported relatively higher estimates of *BC* mass (>200 ng m^{-3}) till 57°S.

3.3.2. Variation of AOD

High variability in the sunphotometer-measured *AOD* values was observed across the study region (Fig. 7b). From this variability, it is evident that over PF (PF1 and PF2), significantly higher values of *AOD* varied from 0.123 to 0.088 (Fig. 7b). In PF1, the mean estimates of *AOD* were 0.111 ± 0.016, while in PF2, the values were 0.108 ± 0.001 (Table 1). The regions north of the PF (NSTF and SAF) showed values of *AOD* varying between 0.083 and 0.103, with mean estimates of 0.095 ± 0.006. In contrast, the regions south of PF to the coast of Antarctica (SACCF, SB, and CA) showed lower estimates of *AOD*, reaching as low as 0.067. A similar range of *AOD* values were reported in previous studies in the ISSO (Suresh Babu et al., 2010; Hulswar et al., 2020; Menon et al., 2015) as well as in the Australian sector of the SO (Alexander and Protat, 2019). In this study, a large oceanic region has been covered (30°S to 67°S), and across such a large spatial area, a wide range of *AOD* values prevailed. These values highlighted the large spatial contrast over the study area due to varying sources, sinks, and transport pathways.

3.3.3. Variation of clear sky direct aerosol radiative forcing (DARF)

The *DARF* variation at *TOA*, *SFC*, and *ATM* depicted an irregular varying trend over ISSO fronts (Fig. 7c). This variation depicted different distributions of aerosols attributed to the resultant irregular variability of *DARF*. The interpretation of aerosol-induced *DARF* was such that consistently high *ATM* forcing was observed over PF regions (PF1, PF2) varying from 1.33 to 1.98 W m^{-2}, where mean estimates at PF1 were 1.75 ± 0.29 W m^{-2} and in PF2 was 1.71 ± 0.01 W m^{-2}. However, relatively lower values of *DARF* were observed over the frontal regions north and south of PF. The *DARF* over the northern regions of PF (NSTF and SAF) varied from 1.14 to 1.43 W m^{-2}, while regions in south of PF (SACCF, SB, and CA) showed the lowest values of *DARF* varying between 1.10 and 1.21 W m^{-2} (Table 1).

Over PF regions, the *DARF* at *TOA* varied between −5.5 and −8.16 W m^{-2} and at *SFC* was between −6.89 and −10.14 W m^{-2}, leading to the resultant *DARF*. The *TOA* forcing in the regions north of PF varied between −4.55 and −4.99 W m^{-2}, and the corresponding forcing at *SFC* between −4.57 and −6.38 W m^{-2}. However, in the regions south of PF, the *TOA* forcing varied between −6.60 and −7.05 W m^{-2}, and *SFC* forcing varied between −7.77 and −8.27 W m^{-2}, respectively.

3.3.4. Variation of atmospheric heating rate (HR)

The *HR* estimates varied between 0.021 and 0.032 K day^{-1} over PF1 and PF2. In contrast, lower *HR* estimates were obtained in regions south of PF (SACCF, SB, and CA), with values as low as 0.018 and 0.019 K day^{-1}. In the regions north of PF (NSTF and SAF), *HR* values varied between 0.018 and 0.023 K day^{-1}.

4. Discussion

4.1. Regions of Polar Front (PF1 and PF2)

The atmosphere over PF revealed a significant loading of dust aerosols. Also, elevated surface BC aerosols were noticed in these regions. Because of higher aerosol loading, the estimated clear sky shortwave *DARF* and atmospheric *HR* were maximum. Thus, it can be inferred that the only possible origin of anthropogenic aerosols was long-range transport from the neighboring continent. Examination of back-trajectories revealed prominent advection from the open SO region, while strong winds in this region might be able to transport dust particles for longer distances from the western African continent lying in closest proximity. Thus, due to the action of strong winds, these long-range advected dust particles are most likely to be in fine-mode (Menon et al., 2015; Murphy et al., 1998; O'Dowd et al., 1997). This increases the possibility for higher suspension and residence time of these aerosols. Moreover, the higher near-surface mass concentration of *BC* aerosols *was* most likely advected from the Kerguelen Island (49.50°S, 69.50°E), being in the closest proximity to PF (Srivastava et al., 2021). However, in addition to long-range transport, the pertinent factor

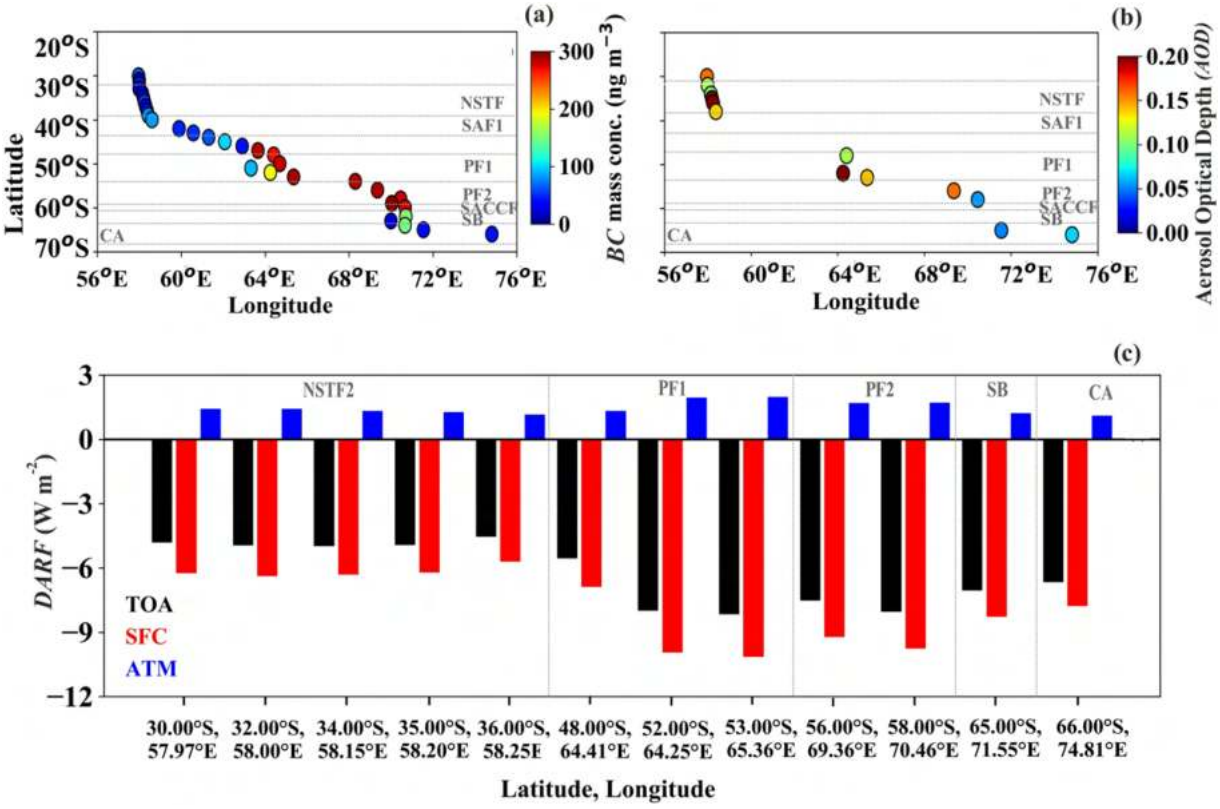

Fig. 7. Aerosol measurements carried along the forward cruise track of the Xth Indian Expedition to the Southern Ocean (SOE-X) from 35°S to 66°S along 56°E to 76°E. Along this cruise track, a 2D variation of (a) mass concentration of black carbon (*BC*) aerosols, (b) aerosol optical depth (*AOD*), and (c) total shortwave clear sky direct aerosol radiative forcing (*DARF*) was observed at the surface (*SFC* in red), top of atmosphere (*TOA* in black), and atmosphere (*ATM* in blue) are depicted. Approximate locations of oceanic fronts are acquired from Belkin and Gordon (1996) and Anilkumar et al. (2015) (grey dotted lines).

for such an enormous dust loading was the thermodynamic properties of low-level MABL.

Firstly, this region experienced strong winds due to the polar jet stream. The polar jet stream typically witnessed in the proximity of 60°S induces strong winds wherein the intensities are dependent upon factors such as the location of high and low-pressure systems, development of warm and cold fronts, and seasonal changes (Nakamura et al., 2004). This intense wind rapidly mixes air masses of distinct properties. Hence, a strong temperature-pressure gradient was built that separated these air masses. As a result, baroclinic instability occurred at shorter distances in the atmosphere (Moore et al., 1999; Reed, 1979). Any small fraction of aerosols (dust, *BC*, and other anthropogenic aerosols) advected or (marine aerosols) produced in this region were forced into these thermal boundaries by high-speed gusty winds. Once trapped, the meteorological conditions of freezing temperatures, decreased *MSLP*, highest *RH*, and continuous flow of colder air masses accounted for the confinement of these aerosols within the atmosphere.

The meteorological conditions were also conducive to forming numerous intensified mid-latitude cyclonic systems (Carleton and Song, 1997; Field and Wood, 2007; Irving et al., 2010). These cyclonic cores also accounted for enhanced trapping and, thereby, decreased the dispersion of these aerosols. The coupled role of these two dynamics specific to PF accounted for higher confinement and accumulation, thus, increasing the residence time of aerosols over the PF.

Regions North of PF (NSTF and SAF): The subtropical frontal regions (NSTF and SAF) showed prominence of marine aerosols in the low-level atmosphere, while some fraction of continental origin aerosols were noticed at higher altitudes (>3500 m). Also, a moderate concentration of near-surface *BC* aerosols and *AOD* were observed in this region. Thus, the clear sky *DARF* in this region was governed by naturally originated aerosols and, to a lesser extent, by anthropogenically produced aerosols. Due to this, the clear sky *DARF* and atmospheric *HR* were less in this region compared to the PF. In this region, marine aerosols comprised sea salt particles produced in-situ from sea spray, bubble bursting, or wave breaking induced by surface winds, as well as other organic particles produced by conversion from gas to particles (O'Dowd et al., 1997). The origin of these aerosols, when traced by back-trajectories, indicated their long-range transport from the open SO region to the lower atmosphere. However, at higher altitudes (>3500 m), anthropogenic aerosols comprised particles of polluted dust and elevated smoke, which were long-range advected from the western South African continent. Interestingly, a higher loading of marine aerosols was observed in the NSTF region, while relatively negligible aerosols were observed in the SAF region.

Although both regions represented a high-pressure zone where strong subsidence was a prominent dynamic feature, the influence of strong subsidence was evident over NSTF. It accounted for a higher accumulation of aerosols in the lower atmosphere, similar to the results over land from Hu et al. (2021). These aerosols were strongly mixed and confined well within a mixed layer capped by a stronger temperature inversion that prevented further dispersion of aerosols in altitudes above this inversion (Prasad et al., 2021). However, over SAF, the occurrence of subsidence was weakened by strong convection in the lower atmosphere. This convection was induced by ARC (Lutjeharms and Ansorge, 2001; Lutjeharms and Gordon, 1987). The effect of strongest convection was evident in the atmospheric column evident with uniform mixing that formed a well-evolved deeper mixed layer over SAF. Hence, a convective updraft of air mass has accounted for the higher dispersion of low-lying aerosols. This may have led to reduced suspension and accumulation of aerosols in the SAF region.

4.2. Regions south of PF (SACCF, SB, and CA)

Over SACCF, the distinct atmospheric condition included forming an intensified low-pressure mesoscale cyclonic system regulated by the

convergence of air mass of varying properties of winds from different directions. The intensification of this system was supported by the lowest temperatures and atmospheric pressure conditions. These cyclonic systems were responsible for significant precipitation leading to snowfall or foggy conditions, followed by clouds nearer to the surface. These clouds were low-level multi-layered SLW/ICE. In contrast to PF, distinct lower aerosol variability was observed. Here the aerosol concentrations were negligible throughout the vertical column of the atmosphere compared to those over PF. A small fraction of in-situ produced marine aerosols advected from the open SO and dust advected from active research stations in eastern Antarctica were observed in the lower atmosphere. At the same time, a clean maritime air mass was prominently seen at different altitudes. Also, a reduction in the surface concentration of *BC* aerosols and *AOD* were noticed. Because of the lower aerosol loading, clear sky *DARF* and *HR* were also lower than that in the PF. Thus, probing the reason for such a distinct aerosol variability in SACCF, despite similar meteorology as that of PF could be attributed to the weakening of westerly winds (5.01 m s^{-1}). As a result, this has ultimately decreased the temperature-pressure gradient, eroding the baroclinic boundaries' intensity throughout the atmospheric column over SACCF. The likelihood of higher aerosol dispersion was high, thus preventing any aerosol accumulation. It can also be noted that a small fraction of aerosols confined in the lower atmosphere was mainly within the convergence over the mesoscale cyclonic core.

Further, towards the SB and CA regions, minimum aerosol loading was observed. The predominant aerosols were naturally produced marine aerosols and more likely naturally or anthropogenically produced dust aerosols. Dust aerosols and a small amount of *BC* aerosols were advected from long range transport from active research stations in Antarctica (Srivastava et al., 2021). However, the atmospheric dynamics specific to this region have accounted for lower accumulation and higher dispersion of advected aerosols. The warming of Antarctic waters controlled these dynamics due to strong convective activities occurring over the Weddell Sea gyre and Prydz Bay gyre (Smith et al., 1984). The proximity forming low-pressure cyclonic systems was the least, indicating less probability of an increase in aerosols within the cyclonic cores. However, shallow convection spreads aerosols in this region. Thus, in resonating with such atmospheric dynamics, the formation of clouds was inhibited, leading to clear sky/cloud-free conditions. However, convective instability induced a single low-level inversion that restricted the convective updrafts above MABL in these regions.

5. Conclusions

This study provides a novel set of measurements presenting the first-time understanding of the effect of oceanic fronts in shaping the vertical thermodynamic structure of MABL and its role in regulating aerosol dynamics and associated clear sky *DARF* and *HR* in the ISSO region. A combination of in-situ, re-analysis, and remote sensing data of meteorological parameters and aerosols were used to achieve the objectives of this study. It revealed a significant accumulation of dust and *BC* aerosols over the PF and resulted in higher estimates of clear sky *DARF* and *HR*. The long-range transport of aerosols (from continent) associated with baroclinic instability and intense mid-latitude cyclonic system were the primary cause of aerosol loading over PF. Much of the atmospheric column over the Antarctic coast was pristine, and the lowest clear sky *DARF* and *HR* were recorded. However, there was evidence of long range transport of dust and *BC* aerosols in small fractions over the Antarctic coast, where shallow convection enhanced the spread of aerosols at low altitudes. An extreme contrast in aerosol loading and thermodynamic state was observed in the subtropical frontal regions. Over NSTF, higher loading of marine aerosols at low altitudes significantly contributed to *DARF* and *HR*, while negligible aerosol loading over SAF1 was associated with the strong convective updrafts by ARC and reduced *DARF* and *HR*.

6. Implications

There was considerable loading of continental aerosols over the PF, and two scenarios can be implied based on the results. In the first scenario, hygroscopic growth of dust aerosols can potentially serve as cloud condensation nuclei/ice nucleating particles, i.e., (CCN/INP), and initiate excess cloud formation, resulting in anomalous cloud coverage. Secondly, an increase in dust and *BC* aerosols increases the absorption of shortwave radiation (its optical property) and may enhance *HR*. Both scenarios are also applicable to Antarctic coast, where small fraction of dust and *BC* aerosols were also deposited by long range transport. It alters *DARF* and *HR* locally but affects Earth's climate and radiative balance on a large-scale.

Supplementary data to this article can be found online at https://doi.org/10.1016/j.scitotenv.2022.159770.

CRediT authorship contribution statement

S. Neha Salim: Data curation, Conceptualization, Formal analysis, Writing – original draft, Writing – review & editing. **Arjun Adhikari:** Writing – review & editing. **Atiba A. Shaikh:** Data curation, Formal analysis. **Harilal B. Menon:** Funding acquisition, Project administration, Resources, Conceptualization, Supervision, Writing – review & editing. **N.V.P. Kiran Kumar:** Formal analysis. **K. Rajeev:** Project administration.

Data availability statement

ECMWF Reanalysis 5th Generation (ERA5) dataset used in this study is available at https://cds.climate.copernicus.eu/. Cloud-aerosol Lidar and infrared pathfinder satellite observation (CALIPSO) data are available at https://www-calipso.larc.nasa.gov/. National Oceanic and Atmospheric Administration - Air Resources Laboratory (NOAA-ARL) Hybrid Single-Particle Lagrangian Integrated Trajectory (HYSPLIT, version 4) model is available at http://ready.arl.noaa.gov/HYSPLIT.php. In-situ data can be obtained after a request from the corresponding author.

Declaration of competing interest

The authors declare no competing interests.

Acknowledgments

This work is funded by the Space Physics Laboratory of the Indian Space Research Organisation (ISRO-SPL) under the Geosphere-Biosphere Programme for Project “Network of Observations for Boundary Layer Experiments”. The authors acknowledge the support of the National Centre for Polar and Oceanic Research, funded by the Ministry of Earth Sciences, for executing expeditions to ISSO. The authors thank all the officers, crew members, and scientists onboard ORV SA Agulhas during the SOE-X campaign for contributing to data collection.

References

Alexander, S.P., Protat, A., 2019. Vertical profiling of aerosols with a combined Raman-elastic backscatter lidar in the remote Southern Ocean marine boundary layer (43°S – 66°S, 132°E – 150°E). J. Geophys. Res. Atmos. 124.

Anilkumar, N., George, J.V., Chacko, R., Nuncio, N., Sabu, P., 2015. Variability of fronts, fresh water input and chlorophyll in the Indian Ocean sector of the Southern Ocean. N. Z. J. Mar. Freshw. Res. 49, 20–40.

Suresh Babu, S., Krishna Moorthy, K., Satheesh, S.K., 2010. Latitudinal gradient in aerosol properties over the indian and southern oceans during the austral summer. Curr. Sci. 99 (10), 1384–1389.

Belkin, I.M., Gordon, A.L., 1996. Southern Ocean fronts from the Greenwich meridian to Tasmania. J. Geophys. Res. Oceans 101, 3675–3696.

Bellouin, N., Quaas, J., Gryspeerdt, E., Kinne, S., Stier, P., Watson-Parris, D., Boucher, O., Carslaw, K.S., Christensen, M., Daniau, A.-L., Dufresne, J.-L., Feingold, G., Fiedler, S., Forster, P., Gettelman, A., Haywood, J.M., Lohmann, U., Malavelle, F., Mauritsen, T., McCoy, D.T., Myhre, G., Mülmenstädt, J., Neubauer, D., Possner, A., Rugenstein, M., Sato, Y., Schulz, M., Schwartz, S.E., Sourdeval, O., Storelvmo, T., Toll, V., Winker, D., Stevens, B., 2020. Bounding global aerosol radiative forcing of climate change. Rev. Geophys. 58, e2019RG000660.

Bender, F.A.-M., 2020. Aerosol forcing: still uncertain, still relevant. AGU Adv. 1, e2019AV000128.

Betts, A.K., 1982. Saturation point analysis of moist convective overturning. J. Atmos. Sci. 39, 1484–1505.

Bodas-Salcedo, A., Williams, K.D., Ringer, M.A., Beau, I., Cole, J.N.S., Dufresne, J.-L., Koshiro, T., Stevens, B., Wang, Z., Yokohata, T., 2014. Origins of the solar radiation biases over the Southern Ocean in CFMIP2 models. J. Clim. 27, 41–56.

Bolton, D., 1980. The computation of equivalent potential temperature. Mon. Weather Rev. 108, 1046–1053.

Carleton, A.M., Song, Y., 1997. Synoptic climatology, and intrahemispheric associations, of cold air mesocyclones in the australasian sector. J. Geophys. Res. Atmos. 102, 13873–13887.

Chandra, S., Srivastava, N., Kumar, M., 2019. Vertical structure of atmospheric boundary layer over Ranchi during the summer monsoon season. Meteorog. Atmos. Phys. 131.

Chang, I., Gao, L., Burton, S.P., Chen, H., Diamond, M.S., Ferrare, R.A., Flynn, C.J., Kacenelenbogen, M., LeBlanc, S.E., Meyer, K.G., Pistone, K., 2021. Spatiotemporal heterogeneity of aerosol and cloud properties over the Southeast Atlantic: an observational analysis. Geophys. Res. Lett. 48 (7).

Charlson, R.J., Pilat, M.J., 1969. Climate: the influence of aerosols. J. Appl. Meteorol. Climatol. 8, 1001–1002.

Christian, K., Wang, J., Ge, C., Peterson, D., Hyer, E., Yorks, J., McGill, M., 2019. Radiative Forcing and Stratospheric Warming of Pyrocumulonimbus Smoke Aerosols: First Modeling Results With Multisensor (EPIC, CALIPSO, and CATS) Views from Space. 46(16), pp. 10061–10071.

Divya, U.S., Girija, J., Satyanarayana, S., Zachariah, J.P., 2014. An advanced radiosonde system for aerospace applications. J. Atmos. Ocean. Technol. 31, 2067–2077.

Doherty, S.J., Saide, P.E., Zuidema, P., Shinozuka, Y., Ferrada, G., Gordon, H., Mallet, M., Meyer, K., Painemal, D., Howell, S.G., Freitag, S., 2021. Modeled and observed properties related to the direct aerosol radiative effect of biomass burning aerosol over the Southeast Atlantic. Atmos. Chem. Phys. 22 (1), 1–88.

Draxler, R.R., 1992. Hybrid Single-Particle Lagrangian Integrated Trajectories (HY-SPLIT): version 3.0-user's guide and model description. Air Resources Laboratory Tech. Memo. ERL ARL-195, p. 84.

Field, P.R., Wood, R., 2007. Precipitation and cloud structure in midlatitude cyclones. J. Clim. 20, 233–254.

Fossum, K.N., Ovadnevaite, J., Ceburnis, D., Dall'Osto, M., Marullo, S., Bellacicco, M., Simó, R., Liu, D., Flynn, M., Zuend, A., O'Dowd, C., 2018. Summertime primary and secondary contributions to Southern Ocean cloud condensation nuclei. Sci. Rep. 8, 13844.

Ganguly, D., Jayaraman, A., Gadhavi, H., 2005. In situ ship cruise measurements of mass concentration and size distribution of aerosols over bay of Bengal and their radiative impacts. J. Geophys. Res. Atmos. 110.

Groß, S., Freudenthaler, V., Schepanski, K., Toledano, C., Schäfler, A., Ansmann, A., Weinzierl, B., 2015. Optical properties of long-range transported saharan dust over Barbados as measured by dual-wavelength depolarization raman lidar measurements. Atmos. Chem. Phys. 15, 11067–11080.

Guo, J., Su, T., Chen, D., Wang, J., Li, Z., Lv, Y., Guo, X., Liu, H., Cribb, M., Zhai, P., 2019. Declining summertime local-scale precipitation frequency over China and the United States, 1981–2012: the disparate roles of aerosols. Geophys. Res. Lett. 46, 13281–13289.

Hande, L.B., Siems, S.T., Manton, M.J., 2012. Observed trends in wind speed over the Southern Ocean. Geophys. Res. Lett. 39.

Hansen, A.D.A., Rosen, H., Novakov, T., 1984. The aethalometer — an instrument for the real-time measurement of optical absorption by aerosol particles. Sci. Total Environ. 36, 191–196.

Hansen, A.D.A., 1996. Magee Scientific Aethalometer User's Guide. 56. Magee Scientific Company, Berkeley California, p. 10.

Hersbach, H., Bell, B., Berrisford, P., Hirahara, S., Horányi, A., Muñoz-Sabater, J., Nicolas, J., Peubey, C., Radu, R., Schepers, D., Simmons, A., Soci, C., Abdalla, S., Abellan, X., Balsamo, G., Bechtold, P., Biavati, G., Bidlot, J., Bonavita, M., De Chiara, G., Dahlgren, P., Dee, D., Diamantakis, M., Dragani, R., Flemming, J., Forbes, R., Fuentes, M., Geer, A., Haimberger, L., Healy, S., Hogan, R.J., Hólm, E., Janisková, M., Keeley, S., Laloyaux, P., Lopez, P., Lupu, C., Radnoti, G., de Rosnay, P., Rozum, I., Vamborg, F., Villaume, S., Thépaut, J.-N., 2020. The ERA5 global reanalysis. Q. J. R. Meteorol. Soc. 146, 1999–2049.

Hess, M., Koepke, P., Schult, I., 1998. Optical properties of aerosols and clouds: the software package OPAC. Bull. Am. Meteorol. Soc. 79, 831–844.

Hu, X.M., Hu, J., Gao, L., Cai, C., Jiang, Y., Xue, M., Zhao, T., Crowell, S.M., 2021. Multisensor and multimodel monitoring and investigation of a wintertime air pollution event ahead of a cold front over eastern China. J. Geophys. Res. Atmos. 126 (10).

Hulswar, S., Menon, H.B., Anilkumar, N., 2020. Physical-chemical characteristics of composite aerosols in the Indian Ocean sector of the Southern Ocean and its associated effect on insolation: a climate perspective. Deep-Sea Res. II Top. Stud. Oceanogr. 178, 104801.

Parry, M.L., Canziani, O., Palutikof, J., Van der Linden, P., Hanson, C., 2007. Climate Change 2007-impacts, Adaptation and Vulnerability: Working Group II Contribution to the Fourth Assessment Report of the IPCC. Vol. 4. Cambridge University Press.

Irving, D., Simmonds, I., Keay, K., 2010. Mesoscale cyclone activity over the ice-free Southern Ocean: 1999–2008. J. Clim. 23, 5404–5420.

Kremser, S., Harvey, M., Kuma, P., Hartery, S., Saint-Macary, A., McGregor, J., Schuddeboom, A., von Hobe, M., Lennartz, S.T., Geddes, A., Querel, R., McDonald, A., Peltola, M., Sellegri, K., Silber, I., Law, C.S., Flynn, C.J., Marriner, A., Hill, T.C.J., DeMott, P.J., Hume, C.C., Plank, G., Graham, G., Parsons, S., 2021. Southern Ocean cloud and aerosol data: a compilation of measurements from the 2018 Southern Ocean Ross Sea marine ecosystems and environment voyage. Earth Syst. Sci. Data 13, 3115–3153.

Krishnamurti, T.N., Jha, B., Prospero, J., Jayaraman, A., Ramanathan, V., 1998. Aerosol and pollutant transport and their impact on radiative forcing over the tropical Indian Ocean during the January — February 1996 pre-INDOEX cruise. Tellus Ser. B Chem. Phys. Meteorol. 50, 521–542.

Landwehr, S., Volpi, M., Derkani, M.H., Nelli, F., Alberello, A., Toffoli, A., Gysel-Beer, M., Modini, R.L., Schmale, J., 2020. Sea state and boundary layer stability limit sea spray aerosol lifetime over the southern ocean. Earth Space Sci. Open Arch. 15.

Lang, F., Huang, Y., Siems, S.T., Manton, M.J., 2018. Characteristics of the marine atmospheric boundary layer over the Southern Ocean in response to the synoptic forcing. J. Geophys. Res. Atmos. 123, 7799–7820.

Li, F., Vogelmann, A.M., Ramanathan, V., 2004. Saharan dust aerosol radiative forcing measured from space. J. Clim. 17, 2558–2571.

Lou, M., Guo, J., Wang, L., Xu, H., Chen, D., Miao, Y., Lv, Y., Li, Y., Guo, X., Ma, S., Li, J., 2019. On the relationship between aerosol and boundary layer height in summer in China under different thermodynamic conditions. J. Geophys. Res. Atmos. 6, 887–901.

Lutjeharms, J.R.E., Ansorge, I.J., 2001. The agulhas return current. J. Mar. Syst. 30, 115–138.

Lutjeharms, J.R.E., Gordon, A.L., 1987. Shedding of an agulhas ring observed at sea. Nature 325, 138–140.

Lutjeharms, J.R.E., Van Ballegooyen, R.C., 1988. The retroflection of the agulhas current. J. Phys. Oceanogr. 18, 1570–1583.

Ma, Y., Ye, J., Xin, J., Zhang, W., Vilà-Guerau de Arellano, J., Wang, S., Zhao, D., Dai, L., Ma, Y., Wu, X., Xia, X., Tang, G., Wang, Y., Shen, P., Lei, Y., Martin, S.T., 2020. The stove, dome, and umbrella effects of atmospheric aerosol on the development of the planetary boundary layer in hazy regions. Geophys. Res. Lett. 47, e2020GL087373.

Mace, G.G., Zhang, Q., Vaughan, M., Marchand, R., Stephens, G., Trepte, C., Winker, D., 2009. A description of hydrometeor layer occurrence statistics derived from the first year of merged cloudsat and CALIPSO data. J. Geophys. Res. Atmos. 114.

McCormick, R.A., Ludwig, J.H., 1967. Climate modification by atmospheric aerosols. Science 156, 1358–1359.

McFarquhar, G.M., Bretherton, C.S., Marchand, R., Protat, A., DeMott, P.J., Alexander, S.P., Roberts, G.C., Twohy, C.H., Toohey, D., Siems, S., Huang, Y., Wood, R., Rauber, R.M., Lasher-Trapp, S., Jensen, J., Stith, J.L., Mace, J., Um, J., Järvinen, E., Schnaiter, M., Gettelman, A., Sanchez, K.J., McCluskey, C.S., Russell, L.M., McCoy, I.L., Atlas, R.L., Bardeen, C.G., Moore, K.A., Hill, T.C.J., Humphries, R.S., Keywood, M.D., Ristovski, Z., Cravigan, L., Schofield, R., Fairall, C., Mallet, M.D., Kreidenweis, S.M., Rainwater, B., D'Alessandro, J., Wang, Y., Wu, W., Saliba, G., Levin, E.J.T., Ding, S., Lang, F., Truong, S.C.H., Wolff, C., Haggerty, J., Harvey, M.J., Klekociuk, A.R., McDonald, A., 2021. Observations of clouds, aerosols, precipitation, and surface radiation over the Southern Ocean: an overview of CAPRICORN, MARCUS, MICRE, and SOCRATES. Bull. Am. Meteorol. Soc. 102, E894–E928.

Menon, H.B., Hulswar, S., Anilkumar, N., Chittur, Thelakkat A., Moorthy, K.K., Babu, S., 2015. Spatial heterogeneity in spectral variability of aerosol optical depth and its implications to aerosol radiative forcing in the tropical Indian Ocean and in the Indian Ocean sector of Southern Ocean. Deep-Sea Res. II Top. Stud. Oceanogr. 118, 142–151.

Moore, J.K., Abbott, M.R., Richman, J.G., 1999. Location and dynamics of the Antarctic polar front from satellite sea surface temperature data. J. Geophys. Res. Oceans 104, 3059–3073.

Moorthy, K.K., Satheesh, S.K., Babu, S.S., Saha, A., 2005. Large latitudinal gradients and temporal heterogeneity in aerosol black carbon and its mass mixing ratio over southern and northern oceans observed during a trans-continental cruise experiment. Geophys. Res. Lett. 32.

Morys, M., Mims, F.M., Hagerup, S., Anderson, S.E., Baker, A., Kia, J., Walkup, T., 2001. Design, calibration and performance of MICROTOPS II hand-held ozone monitor and sun photometer. J. Geophys. Res. Atmos. 106, 14573–14582.

Murphy, D., Anderson, J., Quinn, P., McInnes, L., Brechtel, F., Kreidenweis, S., et al., 1998. Influence of sea-salt on aerosol radiative properties in the Southern Ocean marine boundary layer. Nature 392, 62–65.

Nakamura, H., Sampe, T., Tanimoto, Y., Shimpo, A., 2004. Observed associations among storm tracks, jet streams and midlatitude oceanic fronts. Earth's Climate, pp. 329–345.

O'Dowd, C.D., Smith, M.H., Consterdine, I.E., Lowe, J.A., 1997. Marine aerosol, sea-salt, and the marine Sulphur cycle: a short review. Atmos. Environ. 31, 73–80.

Prasad, P., Ghouse, B., Madineni, V.R., 2021. Is the atmospheric boundary layer altitude or the strong thermal inversions that control the vertical extent of aerosols? Sci. Total Environ. 802, 149758.

Quinn, P.K., Coffman, D.J., Johnson, J.E., Upchurch, L.M., Bates, T.S., 2017. Small fraction of marine cloud condensation nuclei made up of sea spray aerosol. Nat. Geosci. 10, 674–679.

Quinn, P.K., Coffman, D.J., Kapustin, V.N., Bates, T.S., Covert, D.S., 1998. Aerosol optical properties in the marine boundary layer during the first aerosol characterization experiment (ACE 1) and the underlying chemical and physical aerosol properties. J. Geophys. Res. Atmos. 103, 16547–16563.

Ramana, M.V., Krishnan, P., Muraleedharan, Nair S., Kunhikrishnan, P.K., 2004. Thermodynamic structure of the atmospheric boundary layer over the Arabian Sea and the Indian Ocean during pre-INDOEX and INDOEX-FFP campaigns. Ann. Geophys. 22, 2679–2691.

Ramanathan, V., Crutzen, P.J., Kiehl, J.T., Rosenfeld, D., 2001. Aerosols, climate, and the hydrological cycle. Science 294, 2119–2124.

Reed, R.J., 1979. Cyclogenesis in polar air streams. Mon. Weather Rev. 107, 38–52.

Ricchiazzi, P., Yang, S., Gautier, C., Sowle, D., 1998. SBDART: a research and teaching software tool for plane-parallel radiative transfer in the Earth's atmosphere. Bull. Am. Meteorol. Soc. 79, 2101–2114.

Sassen, K., 2002. Indirect climate forcing over the western US from Asian dust storms. Goephys. Res. Lett. 29 103-1-103-4.

Schmale, J., Baccarini, A., Thurnherr, I., Henning, S., Efraim, A., Regayre, L., Bolas, C., Hartmann, M., Welti, A., Lehtipalo, K., Aemisegger, F., Tatzelt, C., Landwehr, S., Modini, R.L., Tummon, F., Johnson, J.S., Harris, N., Schnaiter, M., Toffoli, A., Derkani, M., Bukowiecki, N., Stratmann, F., Dommen, J., Baltensperger, U., Wernli, H., Rosenfeld, D., Gysel-Beer, M., Carslaw, K.S., 2019. Overview of the Antarctic circumnavigation expedition: study of preindustrial-like aerosols and their climate effects (ACE-SPACE). Bull. Am. Meteorol. Soc. 100, 2260–2283.

Sepehri, A., Sarrafzadeh, M.H., 2018. Effect of nitrifiers community on fouling mitigation and nitrification efficiency in a membrane bioreactor. Chem. Eng. Process. Process Intensif. 128, 10–18.

Sepehri, A., Sarrafzadeh, M.H., Avateffazeli, M., 2020. Interaction between Chlorella vulgaris and nitrifying-enriched activated sludge in the treatment of wastewater with low C/N ratio. J. Clean. Prod. 247, 119164.

Smith, N.R., Zhaoqian, D., Kerry, K.R., Wright, S., 1984. Water masses and circulation in the region of Prydz Bay, Antarctica. Deep Sea Res. Part A 31, 1121–1147.

Srivastava, R., Asutosh, A., Sabu, P., Anilkumar, N., 2021. Investigation of black carbon characteristics over southern ocean: contribution of fossil fuel and biomass burning. Environ. Pollut. 276, 116645.

Stamnes, K., Tsay, S.C., Wiscombe, W., Laszlo, I., 2000. DISORT, A General-purpose Fortran Program for Discrete-ordinate-method Radiative Transfer in Scattering and Emitting Layered Media: Documentation of Methodology.

Stocker, T., Qinn, D., Platner, G.K., 2013. Climate Change 2013 The Physical Science Basis. 2013. Cambridge University Press.

Stull, R.B., 1988. An Introduction to Boundary Layer Meteorology. Vol. 13. Springer Science & Business Media.

Su, T., Li, Z., Li, C., Li, J., Han, W., Shen, C., Tan, W., Wei, J., Guo, J., 2020. The significant impact of aerosol vertical structure on lower atmosphere stability and its critical role in aerosol–planetary boundary layer (PBL) interactions. Atmos. Chem. Phys. 20, 3713–3724.

Trenberth, K.E., Fasullo, J.T., 2010. Simulation of present-day and twenty-first-century energy budgets of the southern oceans. J. Clim. 23, 440–454.

Truong, S.C.H., Huang, Y., Lang, F., Messmer, M., Simmonds, I., Siems, S.T., Manton, M.J., 2020. A climatology of the marine atmospheric boundary layer over the Southern Ocean from four field campaigns during 2016-2018. J. Geophys. Res. Atmos. 125, e2020JD033214.

Turner, D.B., 2020. Workbook of Atmospheric Dispersion Estimates: An Introduction to Dispersion Modeling. CRC press.

Vinoj, V., Babu, S.S., Satheesh, S.K., Moorthy, K., Kaufman, Y.J., 2004. Radiative forcing by aerosols over the bay of Bengal region derived from shipborne, island-based, and satellite (Moderate-resolution imaging Spectroradiometer) observations. J. Geophys. Res. Atmos. 109.

Winker, D.M., Vaughan, M.A., Omar, A., Hu, Y., Powell, K.A., Liu, Z., Hunt, W.H., Young, S.A., 2009. Overview of the CALIPSO Mission and CALIOP data processing algorithms. J. Atmos. Ocean. Technol. 26, 2310–2323.

Zhang, W., Guo, J., Miao, Y., Liu, H., Song, Y., Fang, Z., He, J., Lou, M., Yan, Y., Li, Y., Zhai, P., 2018. On the summertime planetary boundary layer with different thermodynamic stability in China: a radiosonde perspective. J. Clim. 31, 1451–1465.

Atmospheric Pollution Research 14 (2023) 101797

Contents lists available at ScienceDirect

Atmospheric Pollution Research

journal homepage: www.elsevier.com/locate/apr

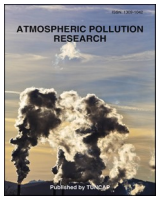

Aerosol and atmospheric dynamics over the tropical Indian ocean: A study from the IInd international Indian Ocean expedition

Atiba A. Shaikh [a,b], S. Neha Salim [a,b], Harilal B. Menon [a,b,*]

[a] Remote Sensing Laboratory, Goa University - 403206, India
[b] School of Earth, Ocean and Atmospheric Sciences, Goa University - 403206, India

ARTICLE INFO

Keywords:
Aerosols
Boundary layer dynamics
Clear-sky direct aerosol radiative forcing (DARF)
Atmospheric heating rate (HR)

ABSTRACT

The study addresses the aerosol distribution, boundary layer dynamics and associated shortwave radiative forcing over the Tropical Indian Ocean. The observations were carried out onboard Ocean Research Vessel *Sagar Nidhi* in December 2015 as a part of the International Indian Ocean Expedition-II (IIOE-II). The dominance of continentally originated aerosols was observed near the coast because of northeasterly winds, while marine aerosols abounded offshore. The uneven distribution of aerosols in the study region was due to varying atmospheric conditions triggered by various convective processes, wherein the convective available potential energy and convective inhibition energy ranged between 0.0274 and 2535.2 J kg^{-1} and 0 and -387.5 J kg^{-1}, respectively. The atmospheric forcing varied in tandem with aerosol loading. It was evident from the high forcing values (17.98 W m^{-2}) and corresponding heating rate of 0.504 K day^{-1} observed near the coast. The average heating rate in the far offshore (stations 6–10) region was 0.063 ± 0.017 K day^{-1}, which amounted to an ~87% decrease from the coastal location.

1. Introduction

Aerosols play a significant role in the atmospheric heat budget through direct and indirect effects. Based on the theory of conservation of energy, the radiation budget represents the net between incoming and outgoing radiation (Charlson et al., 1992; IPCC, 2007). The deficit or surplus energy can decrease or increase atmospheric temperature, eventually affecting the climate (Ramanathan et al., 1992). Various hybrid aerosol structures, such as externally mixed, internally mixed, and coated particles, are present in the atmosphere (Ramanathan et al., 2001). Unlike greenhouse gases, the spatial heterogeneity and the associated aerosol radiative forcing are one of the uncertainties in climate prediction (Hansen et al., 1997). It is observed that about one-third of the aerosol flux is of marine origin (Prospero et al., 1983), which strongly influences the local and regional climate (Prospero, 2002). The aerosols trapped in the lowermost layer of the atmosphere (Wilcox et al., 2016) modulate near-surface energy and moisture flux to the free atmosphere through convective transfer mechanisms (Pyatt et al., 2005; Sun and Zhao, 2020; Chen et al., 2022).

An increased input of absorbing aerosol does have detrimental effects on the environment, e.g., melting of polar ice, depletion of the ozone layer, and changing cloud radiative effects (Wielicki et al., 1995; Garrett and Zhao, 2006; IPCC, 2007). Black carbon aerosol (BC), emitted during the incomplete combustion of fossil fuels and biomass burning (forest fires), has significant control over the local and regional climate, as it absorbs the insolation (Ramanathan and Carmichael, 2008). BC from biomass burning exhibits light absorbance at shorter wavelengths (ultraviolet), whereas BC from fossil fuel absorbs more light at longer wavelengths (infrared) (Sandradewi et al., 2008). IPCC (2014) detailed the increased atmospheric warming due to anthropogenic aerosols emitted during the industrial period. BC impacts the radiative forcing of the atmosphere. Its presence in the marine atmospheric boundary layer (MABL) plays a crucial role in marine ecosystems, even over far ocean regions (Bao et al., 2017). Therefore, aerosol observations from various platforms are necessary to reduce the uncertainties in climate modelling.

The aerosols exhibit significant spatiotemporal heterogeneity over the tropical and subtropical regions of the Indian Ocean due to their proximity to the Asian and African continents (Ramachandran and Jayaraman, 2002; Kumar et al., 2012). The heterogeneity is due to the presence of marine (sea salt and DMS) and anthropogenically originated

Peer review under responsibility of Turkish National Committee for Air Pollution Research and Control.
* Corresponding author. Remote Sensing Laboratory, Goa University, 403206, India.
E-mail address: hbmenon@unigoa.ac.in (H.B. Menon).

https://doi.org/10.1016/j.apr.2023.101797
Received 18 February 2023; Received in revised form 10 May 2023; Accepted 12 May 2023
Available online 15 May 2023
1309-1042/© 2023 Turkish National Committee for Air Pollution Research and Control. Production and hosting by Elsevier B.V. All rights reserved.

aerosols from these continents. Several region-specific campaigns have been carried out over the years to better understand the region's aerosol dynamics. The Indian Ocean Experiment (INDOEX) (Ramanathan et al., 2001; Rasch et al., 2001) investigated the large-scale effects of continental emissions over Indian Ocean and accessed their impact on global climate through an integrated approach of in-situ observations and satellite data. North-south gradient of aerosol loading with lower concentrations south of Inter Tropical Convergence Zone (ITCZ) was observed, with sub-micron size particles being higher over the Arabian Sea (~20–50 μg m^{-3}). Similar gradients were seen for NO_x and CO, which were four-fold more amplified in the north of ITCZ than in the south (Mitra, 2004). BC, which accounted for 10–14% of the total aerosol mass during INDOEX, are potential absorbers of sunlight responsible for decreasing the earth's albedo and a foremost contributor to global warming. Tropospheric Aerosol Radiative Forcing Observational Experiment (TARFOX) (Russell et al., 1999) and Aerosol Characterization Experiment (ACE) 1 and 2 (Covert et al., 1998; Huebert et al., 1998; Quinn et al., 1998; Collins et al., 2000; Durkee et al., 2000; Livingstone et al., 2000; Neusüß et al., 2000; Putaud et al., 2000; Russell and Heintzenberg, 2000; Schmid et al., 2000) were also undertaken to understand the in-situ aerosol over this region. The results obtained during these expeditions are directly applicable to aerosol radiative assessments. Aircraft-based measurements were also adopted to study elevated aerosol layers well above the boundary layer over the Tropical Indian Ocean (TIO).

Integrated Campaign for Aerosols Gases and Radiation Budget (ICARB) (Moorthy et al., 2008; Kumar et al., 2015) carried out extensive studies over the Arabian Sea, the Indian mainland, and the Bay of Bengal (BoB). ICARB provided vital information on aerosol microphysics over the Indian Ocean region, providing a better insight into aerosols' temporal and spatial variability, origin, and long-range transport. The variability in cloud coverage depends on the constantly varying aerosol concentrations acting as cloud condensation nuclei. This leads to spatial and temporal variability in radiative forcing (Hansen et al., 1997). Kumar et al. (2012) did a chemical characterization of aerosols during winter (December 2007) and reported that the Arabian Sea received substantially high aerosol mass loading. The winter campaign of ICARB-2018 conducted till 2 ° S, revealed the heavy continental outflow of anthropogenic aerosols over the marine atmosphere. Total aerosol mass loading varied between 13 and 84 μg m^{-3}, mainly dominated by accumulation mode aerosols (>60%) (Aswini et al., 2020). An intense pollution plume over the southeast coastal Arabian Sea is dominated by anthropogenic aerosols (73%). Further, heavy metals, such as Zn, Cu, Pb, and Mn, were also reported to dominate the region (Gogoi et al., 2019). In TIO, the observations conducted are mostly limited to the north of ITCZ.

2. Study area

The observations were carried out onboard the Ocean Research Vessel (ORV) *Sagar Nidhi* during the IIOE-II. The expedition flagged from Mormugao Port, Goa (15.45 ° N) on the December 4, 2015 and culminated at Port Louis, Mauritius (20.16 ° S) on the December 22, 2015 (Fig. 1). The measurements were conducted between 6th and December 21, 2015, from 67 ° E to 61 ° N, and 13 ° N to15 ° S.

During the study period, ITCZ was situated approximately between 4 ° S and 6 ° S (Fig. 1). Superimposed on the cruise track are surface-level averaged winds (1000 hPa). The wind speeds were between 6 and 14 m s^{-1}, and the atmospheric temperature was ~28 ° C (Table 1).

3. Data and methodology

3.1. Aerosol optical depth (AOD)

MICROTOPS II Sunphotometer (Solar light Co) was used to obtain aerosol optical depth (AOD) at five wavelengths 380 nm, 440 nm, 500 nm, 675 nm, and 870 nm. The instrument comprises of a narrow-band interface and a photodiode suitable for these bands. It had five aligned optical collimators with a field of view of 2.5 °. A quartz window provides access to collimator tubes. The AOD was computed internally from the spectral measurements of direct solar flux using internal calibration coefficients following the principle of Lambert-Beer law (Morys et al., 2001). Observation coordinates obtained from the Global Position System (GPS) were provided to the sunphotometer. The scans were made under clear sky conditions avoiding the ship's exhaust interference.

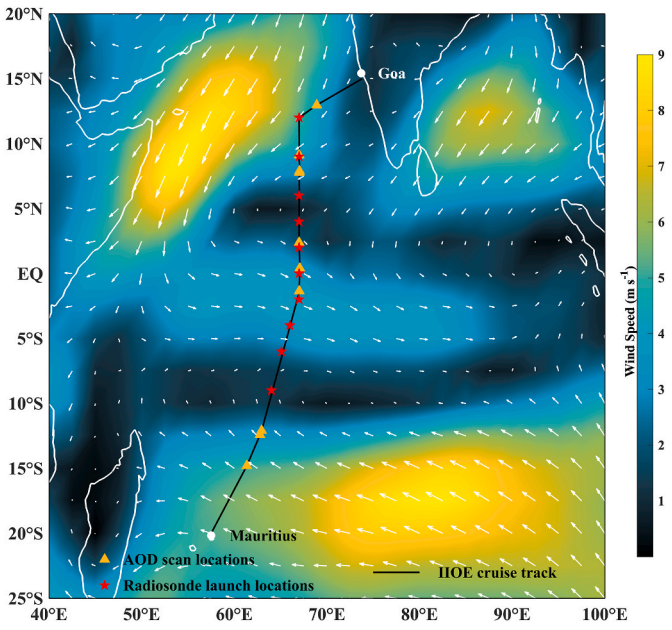

Fig. 1. Study area showing ORV *Sagar Nidhi's* cruise tracks during IIOE-II with synoptic winds at 1000 hPa that are averaged over the study period (6th −21st December 2015).

Table 1
Represents thermodynamic conditions of the atmosphere at different latitudes; it contains convective available potential energy (CAPE), convective inhibition energy (CINE), precipitable water vapour (PWV) and marine atmospheric boundary layer (MABL) height.

Latitude (°S)	Longitude (°E)	CAPE (J kg^{-1})	CINE (J kg^{-1})	PWV (mm)	MABL (km)
12.0	67.0	105.75	−73.89	53.7	0.788
9.0	67.0	3.37	−237.8	52.12	0.793
6.0	67.0	0.76	−248	48.15	0.77
4.0	67.0	1387.9	−19.19	45.12	1.461
2.0	67.0	0.247	−387.5	43.63	1.251
0.0	67.0	306.3	−126.5	49.11	1.033
−2.0	67.0	1057.4	−91.82	51.32	0.955
−4.0	66.0	1946.7	−26.42	62.06	1.776
−6.0	65.1	2535.2	0	56.9	0.62
−9.0	64.0	920.47	0	58.59	1.083
−12.0	62.5	7.27	−155.2	37.12	0.808

3.2. Black carbon mass concentration

Near-surface BC mass concentrations (ng m^{-3}) were estimated using an automated seven-band Aethalometer (M/s Magee Scientific, model AE-42) operating at 370 nm, 470 nm, 520 nm, 590 nm, 660 nm, 880 nm, and 950 nm. BC mass concentration is estimated at 880 nm using the factory-set wavelength-dependent calibration factors and optical transmission techniques (Hansen et al., 1984). The air particles were aspirated through an inlet pipe placed at the height of about 12 m above sea level at the ship's bow, avoiding contamination due to ship exhausts and

fumes. A heated sample line was connected to the inlet, maintaining a constant relative humidity of 60%. The instrument was continuously operated along the cruise track at 5 min intervals with a flow rate of 5 L per minute.

3.3. Vertical profiles of aerosol subtypes

The Cloud-Aerosol Lidar with Orthogonal Polarization (CALIOP) sensor onboard Cloud-Aerosol Lidar and Infrared Pathfinder Satellite Observations (CALIPSO) platform was used to obtain CALIOP level-2 version 4.20 (V4) vertical feature mask and aerosol subtype data products. The CALIOP V4 tropospheric aerosol classification algorithm identifies seven aerosol subtypes based on estimated particulate depolarization ratio (δ_p^{est}), integrated attenuated backscatter, altitude, and surface type (Kim et al., 2018). The CALIOP V4 aerosol subtypes are clean marine, dust, polluted continental/smoke, clean continental, polluted dust, elevated smoke, and dusty marine; the same details are available in Kim et al. (2018).

3.4. Local and synoptic meteorology and active fire count

Understanding the role of local and synoptic meteorology is essential to study aerosol generation and transportation over a geographical scale. The onboard Vaisala AWS was used to measure the local meteorological parameters like pressure, temperature, wind speed, and relative humidity (Table S1). To study the long-range transport of aerosols, seven-day air-mass backward trajectories (AMBT) were computed at 20 and 1500 m altitude, respectively, using the Hybrid Single Particle Lagrangian Integrated Trajectory (HYSPLIT, version 4). NCEP Global Data Assimilation System (GDAS) meteorological data from the data archives of the National Oceanic and Atmospheric Administration- Air Resources Laboratory (NOAA-ARL) was provided to the model (Draxler and Rolph, 2003; Stein et al., 2015). Hourly reanalysis data of u and v components of surface wind were obtained from European Centre for Medium-Range Weather Forecasts (ECMWF) ERA5 to compute the wind vector, which was averaged over the study period (Hellerman and Rosenstein, 1983).

The active fire count data for December 2015 was obtained from Visible Infrared Imaging Radiometer Suite (VIIRS) 375 m thermal anomalies and active fire product (Fig. 5). The VIIRS sensor is installed aboard the Suomi National Polar-orbiting Partnership (Suomi-NPP) satellite. The active fire counts were obtained to locate regions with a high density of actively burning fires to identify the source of biomass burning BC.

3.5. Estimation of biomass burning percentage (BB %)

The spectral absorption of light by the aethalometer is used to compare the percentage of biomass burning to that of fossil fuel. The spectral aerosol absorption coefficient (β_{abs}) is proportional to $\lambda^{-\alpha}$, where λ is the wavelength and α is the absorption Ångström exponent (Srivastava et al., 2021). Based on the values reported earlier, we have considered α_{BB} and α_{FF} as 2.0 and 1.1, respectively (Sandradewi et al., 2008; Fuller et al., 2014). The total absorption at a wavelength ($\beta_{abs}(\lambda)$) is the sum of the absorption due to biomass burning ($\beta_{abs,BB}(\lambda)$) and that due to fossil fuel ($\beta_{abs,FF}(\lambda)$) (Sandradewi et al., 2008), and can be represented as

$$\beta_{abs}(\lambda) = \beta_{abs,BB}(\lambda) + \beta_{abs,FF}(\lambda) \quad (1)$$

The relation between $\beta_{abs,BB}$, $\beta_{abs,FF}$, α_{BB}, and α_{FF} at 470 and 950 nm wavelengths are given by,

$$\frac{\beta_{abs,BB}(470\ \text{nm})}{\beta_{abs,BB}(950\ \text{nm})} = \left(\frac{470}{950}\right)^{-\alpha_{BB}} \quad (2)$$

$$\frac{\beta_{abs,FF}(470\ \text{nm})}{\beta_{abs,FF}(950\ \text{nm})} = \left(\frac{470}{950}\right)^{-\alpha_{FF}} \quad (3)$$

Hence BB% is given by,

$$BB\% = \frac{\beta_{abs,BB}(950\ \text{nm})}{\beta_{abs}(950\ \text{nm})} \times 100 \quad (4)$$

3.6. Estimation of the thermodynamic parameters

3.6.1. Marine atmospheric boundary layer

The MABL height was estimated using the virtual temperature and specific humidity gradient method (Stull, 1988). The individual profiles were screened to identify the height of the capping inversion, which was marked as the top of MABL height.

3.6.2. Convective available potential energy (CAPE)

CAPE indicates the amount of energy available during convection. It is estimated by integrating the local buoyancy of the parcel vertically from the Level of Free Convection (LFC) to the Equilibrium Level (EL).

$$CAPE = \int_{z_f}^{z_n} g\left(\frac{T_{v_{parcel}} - T_{v_{env}}}{T_{v_{env}}}\right) d\,z \quad (5)$$

where, z_f is the altitude of LFC and z_n is the altitude of the EL, $T_{v_{parcel}}$ is the virtual temperature of the parcel, $T_{v_{env}}$ is the virtual temperature of environment, g is the acceleration due to gravity (Moncrieff and Miller, 1976; Doswell and Rasmussen, 1994).

3.6.3. Convective inhibition energy (CINE)

CINE is the amount of energy used to prevent an air parcel from rising above the surface to LFC.

$$CINE = \int_{z_{bottom}}^{z_{top}} g\left(\frac{T_{v_{parcel}} - T_{v_{env}}}{T_{v_{env}}}\right) dz \quad (6)$$

where, z_{bottom} is the altitude of the ground surface and z_{top} is the altitude of the LFC (Colby, 1984).

3.6.4. Precipitable water vapour (PWV)

It is atmosphericwater vapour in a vertical column of a unit cross-sectional area extending between the surface and the upper layer (3 km).

Mathematically, if$x(p)$ is the mixing ratio at the pressure level, p, then the precipitable water vapour, W, contained in a layer bounded by pressures p_1 and $p_2$is given by

$$W = \frac{1}{pg} \int_{p1}^{p2} x dp \quad (7)$$

where,ρ represents the density of water and g is the acceleration due to gravity. In actual rainstorms, particularly thunderstorms, amounts of rain often exceeds the total precipitable water vapour of the overlying atmosphere (Showalter, 1954). PWV results from the converging of large amounts of water vapour surrounding the area.

3.7. Direct aerosol radiative forcing (DARF) and atmospheric heating rate (HR)

Radiative forcing (ΔF) of the atmosphere due to aerosols is defined as the net flux change at the top of the atmosphere (TOA) and Surface (SUR) with and without the effect of aerosols. The clear sky direct aerosol radiative forcing (DARF) was estimated using the model Santa Barbara DISORT (DIScrete Ordinate Radiative Transfer) Atmospheric Radiative Transfer (SBDART) (Ricchiazzi et al., 1998) for shortwave radiation (0.25–4 μm). The input parameters required for running SBDART are solar zenith angle, surface albedo (ocean water), atmospheric profile (tropical), sunphotometer measured spectral AOD, single

scattering albedo (SSA), and asymmetry parameter (ASY). SSA and ASY are obtained using the Optical Properties of Aerosols and Clouds (OPAC) model by Hess et al. (1998). In the present study, for the estimation of SSA and ASY, the number concentrations of total water-soluble components, soot, sea salt (accumulation), sea salt (coarse), and sulphate were given as inputs to the OPAC model, along with the vertical distribution of aerosols and relative humidity as described by Hess et al. (1998). As OPAC allows us to define the aerosol mixture, the aethalometer-measured soot (BC) was kept constant. In contrast, the concentrations of the other aerosol types mentioned above were adjusted until the simulated AOD spectra corroborated (±0.005) with the sunphotometer-measured AOD spectra.

Hence to estimate the clear sky DARF, the values of downwelling irradiance at TOA ($F_{TOA}^{\downarrow}$), upwelling irradiance at TOA ($F_{TOA}^{\uparrow}$), downwelling irradiance at SUR ($F_{SUR}^{\downarrow}$), and upwelling radiance from SUR ($F_{SUR}^{\uparrow}$) in the presence (A) and absence (NA) of aerosols were obtained as outputs of SBDART. The net flux at the TOA and SUR is given by,

$$\left(F_{NA/A}\right)_{TOA/SUR} = F_{TOA/SUR}^{\downarrow} - F_{TOA/SUR}^{\uparrow} \quad (8)$$

$$(\Delta F)_{TOA/SUR} = (F_{NA})_{TOA/SUR} - (F_A)_{TOA/SUR} \quad (9)$$

F_{NA} and F_A are the fluxes estimated respectively under aerosols' presence and absence (control). Hence, the atmospheric forcing (ATM) is,

$$\Delta F_{ATM} = \Delta F_{TOA} - \Delta F_{SFC} \quad (10)$$

Clear sky DARF signifies the amount of energy trapped in the atmosphere due to aerosols for the shortwave spectra, which results in the heating of the atmosphere. The atmospheric heating rate (HR) is given as,

$$\frac{\partial T}{\partial t} = \frac{g}{c_p}\left[\frac{\Delta F_{ATM}}{\triangle P}\right] \times (hr/day) \times 3600\ (sec/hr) \quad (11)$$

where, $\partial T/\partial t$ is the heating rate (K day^{-1}), g is the acceleration due to gravity (m s^{-2}), c_p is the specific heat capacity of air at constant pressure (1006 J kg^{-1} K^{-1}), and ΔP is the pressure difference between the top and bottom layers of the atmosphere. In the current study, ΔP, i.e., the pressure difference between the surface and 3 km has been considered to be 300 hPa, since maximum concentrations of atmospheric aerosols are up to 3 km altitude in the atmosphere (Ramachandran and Kedia, 2010; Kaskaoutis et al., 2013; Singh et al., 2016).

4. Results

4.1. Columnar aerosol optical depth

The spatial variation of the sunphotometer measured AOD_{500} is presented in Fig. 2a. AOD_{500} at 12.97 ° N, near the Indian subcontinent, was maximum (0.630) and decreased towards the southern TIO region. AOD_{500} at 9.12 ° N was 0.119, which increased to 0.180 at 2.39 ° N and decreased at −1.34 ° S (0.116). Due to cloud cover at the time of observations, data could not be generated between 1.4 ° S and 12 ° S. The mean value of AOD_{500}, i.e., 0.134 ± 0.018, was observed between 12 ° S to 15 ° S. The sunphotometer measured AOD spectra (380 nm–870 nm) for station 1 (Fig. 2b, Table S1) followed Junge's power law (Junge, 1955). However, it did not follow the same in the open ocean region (station 2 to station 10). AOD in the open ocean was flat and did not exhibit much spectral variation from 380 nm to 870 nm, a typical feature of the oceanic region. The flat spectra result from lower loading of continentally derived accumulation mode aerosols and an increased contribution of wind-generated coarse mode aerosols (sea salt) (Chaubey et al., 2013). However, a slight dip was observed at 440 nm in the spectra. AOD increased towards the longer wavelength from station 6 to station 10, where AOD_{870} was greater than AOD_{380} as coarse-mode marine aerosols dominate the open ocean region.

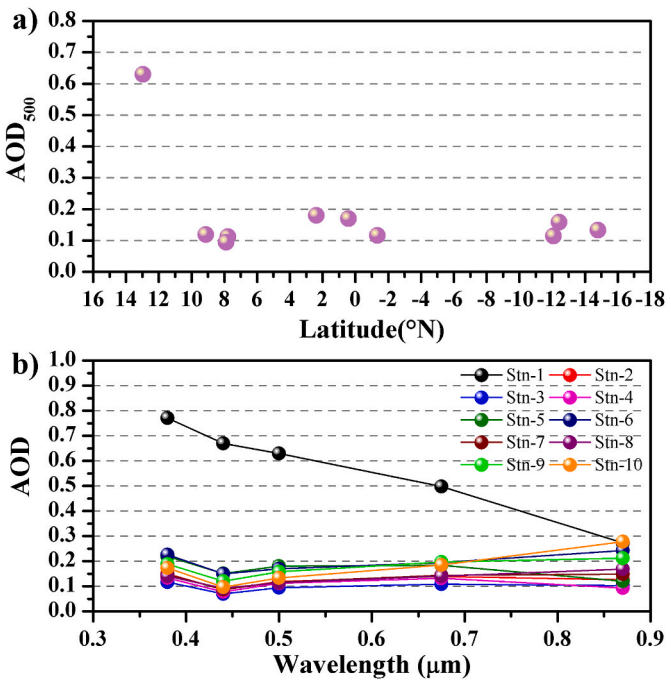

Fig. 2. Depicts the (a) spatial distribution of AOD_{500} and (b) spectral distribution of AOD (380 nm–870 nm) for all 10 stations (Stn).

4.2. BC mass concentration and biomass burning percentage

BC mass concentration was 1382.21 ± 209.10 ng m^{-3} and 1290.83 ± 176.87 ng m^{-3} (Fig. 3a) at 14 ° N and 13 ° N, respectively, near the Indian subcontinent. It further decreased to 990.95 ± 184.79 ng m^{-3} at 11 ° N as we moved towards the open ocean region and had an average of 224.07 ± 58.52 ng m^{-3} in the TIO to the north of ITCZ. BC mass concentration was high between 2 ° N and 0.5 ° N, with an average of 368.68 ± 45.67 ng m^{-3}. BC mass concentration decreased drastically to the south of ITCZ, and an average value of 39.63 ± 14.40 ng m^{-3} was

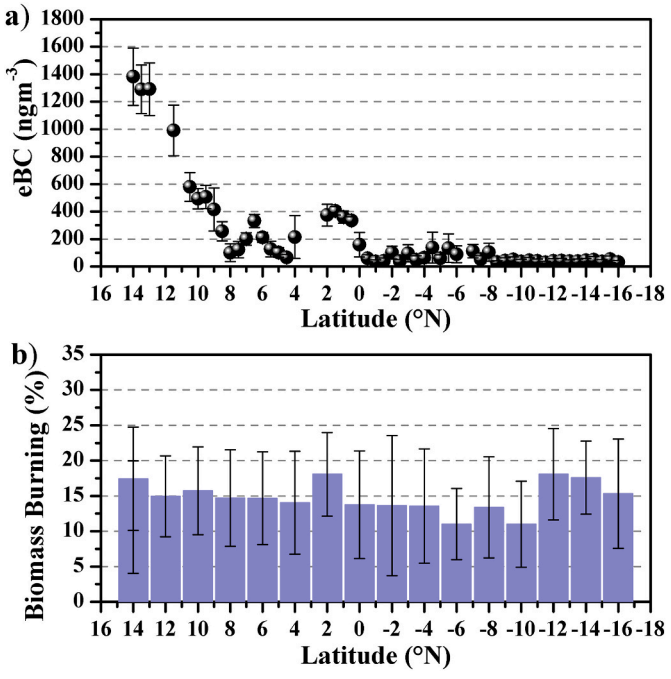

Fig. 3. (a) Latitudinal variability of BC mass concentrations, and (b) mean BB % along with standard deviations.

observed.

The BB% was averaged for every 2° (Fig. 3b); the BB% was 17% near the Indian continent and decreased offshore. At 2° N, with an increase in BC mass concentration, a high BB% (18%) was observed. Higher values of BB% (>15%) were seen between 12 ° S to 16 ° S towards the African continent.

4.3. Vertical distribution of aerosols

The CALIOP vertical feature mask (Fig. S1) and aerosol subtype (Fig. 4) products were shown for selected days to investigate the columnar aerosol loading during IIOE-II. The vertical feature mask profiles identify aerosol layers reaching up to ~10 km from the surface. The composition of the aerosol layers was investigated through the aerosol subtype plots. Dusty marine and polluted continental/smoke aerosols were abundant from the sea surface up to 2.5 km. The naturally predominant marine aerosols mixing with the dust transported near the sea surface lead to the dusty marine subtype. More dust and elevated smoke layers were present throughout the atmospheric column reaching up to 10 km altitude. The mixing of the dust and the elevated smoke gives rise to the polluted dust subtype, which was present at high altitudes (3–8 km). Dust layers were present, from near the sea surface to altitudes of ~10 km in small quantities. Most of the aerosol layers were majorly up to ~3 km. The maximum vertical distribution of different aerosol subtypes was observed around 6 ° S.

4.4. Thermodynamic conditions of the atmosphere

The boundary layer dynamics play an essential role in the transport of aerosols and their vertical distribution (Stull, 1988; Behrendt et al., 2011; Pal et al., 2012, 2013). The higher values of CAPE and low values of CINE depict a largely unstable atmosphere due to the enhanced convective activities resulting in increased updraft motion of the air causing intense mixing (Stull, 1988). Lower CAPE and higher CINE values were observed at 12 ° N, 9 ° N 6 ° N, and the equator indicated a largely stable atmosphere with significantly less convective energy available for updraft motion (Table 1) (Hess, 1979).

At 4 ° N, the value of CAPE increased to 1387.9 J kg^{-1}, and CINE decreased to −19.19 J kg^{-1}, pointing towards an enhanced convective updraft prevailing within the air column. The conditions observed at 2 ° N indicate a nearly stable atmosphere with low CAPE (0.247 J kg^{-1}) and the highest CIN (−387.5 J kg^{-1}). The highly convective conditions with increased moisture content observed at 6 ° S can be attributed to the presence of ITCZ, with a maximum CAPE value of 2535.2 J kg^{-1} and 0 J kg^{-1} CINE values. Below 6 ° S, the convective atmosphere approaches nearly stable conditions with low CAPE values (Hess, 1979).

5. Discussion

5.1. Aerosol distribution over the tropical Indian ocean

High AOD_{500} at 12.96 ° N (Fig. 2a) resulted from the advection of polluted continental aerosols over the Arabian Sea. The aerosols are advected from the subcontinent as a result of northeasterly winds blowing during the winter monsoon season (Moorthy et al., 2001; Gogoi et al., 2019; Aswini et al., 2020). This was further evident from the CALIOP aerosol subtype, which showed the presence of dusty marine and polluted continental/smoke over the region (Fig. 4a). The seven-day backward HYSPLIT trajectories also supplement the argument (Fig. 5). Stable atmospheric conditions with lower CAPE (Table 1) add to the higher aerosols over the region, as it reduces the vertical dispersion of aerosols. Moreover, higher surface winds (9.69 m s^{-1}) generate in-situ aerosols due to entrainment (Table S1) (Moorthy and Satheesh, 2000). High AOD values near the Indian coastal region were also observed by Krishna Moorthy et al. (1997), Krishnamurti et al. (1998), and Satheesh et al. (1999).

High AOD_{500} was observed under stable atmospheric conditions at 2.36 ° N (0.180) and 0.46 ° N (0.169), due to high wind speed (~10 m s^{-1}), and advection of anthropogenic aerosols from the highly polluted Indian subcontinent (Prospero, 1981; Kamra et al., 2003; Aswini et al., 2020) during the winter monsoon season. Many polluted continental/smoke and dusty marine aerosol layers were also seen between 5 ° N and the equator. The maximum vertical distribution of aerosols (10 km) observed near 6 ° S is due to the presence of ITCZ, where the maximum

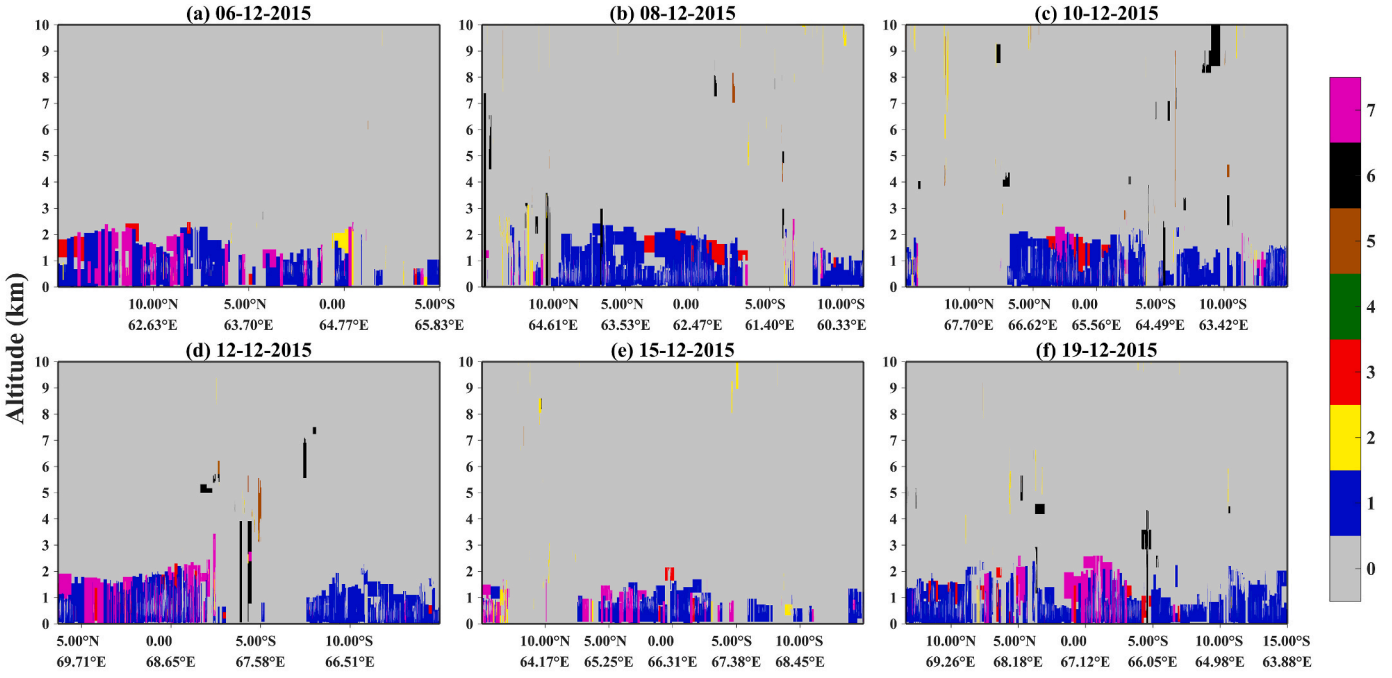

Fig. 4. CALIOP data (a–f) representing vertical distribution of aerosol subtypes on selected days during IIOE-II.

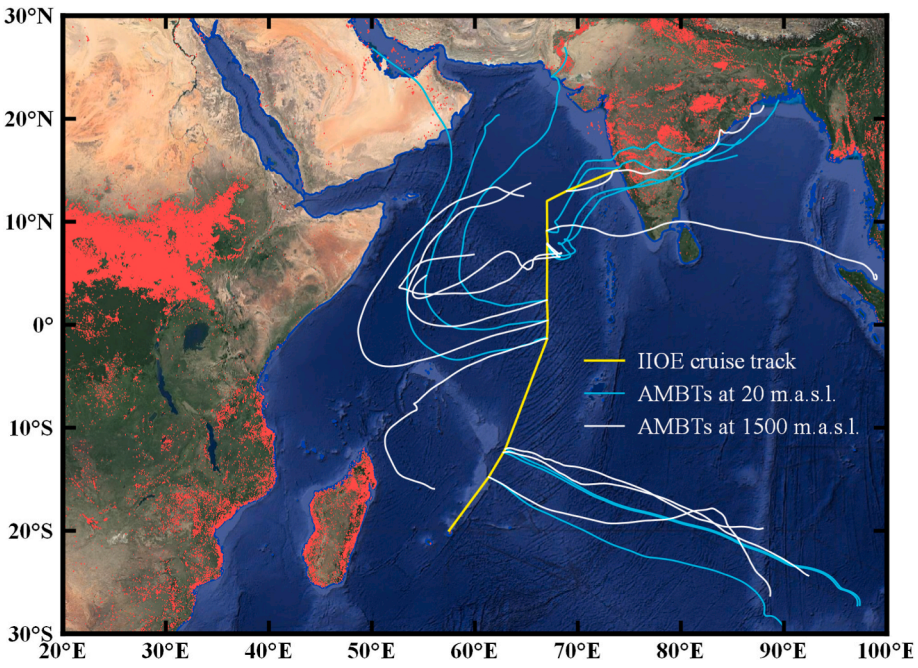

Fig. 5. Seven-day backward wind trajectories at 20 m (blue) and 1500 m (white) from AOD measurement stations along the cruise track, along with the number of open fire events in India and east Africa during December 2015.

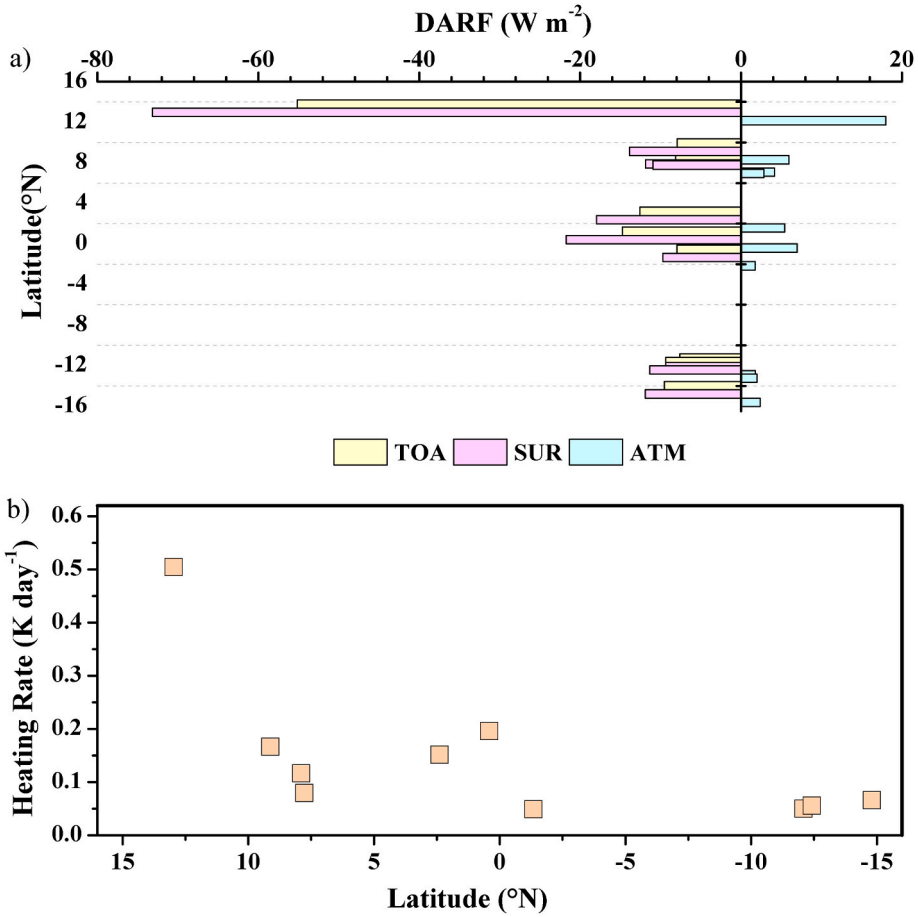

Fig. 6. The spatial distribution of (a) direct aerosol radiative forcing and (b) atmospheric heating rate.

vertical updraft is supported by the highest CAPE (2535.2 J kg^{-1}) and 0 J kg^{-1} CINE. Increased AOD_{500} at 12 ° S is due to in-situ produced aerosols, resulting from high winds (14 m s^{-1}). Aerosol subtype data showed the region being dominated by clean marine aerosols (Fig. 4f). The atmospheric conditions are also stable with low CAPE values, minimizing aerosol dispersion and leading to an increase in their concentrations. Lower values of PWV at 4 ° N (45.12 mm), 2 ° N (43.63 mm), and 12 ° S (37.12 mm) can be the reason for higher AOD_{500}, as a consequence of negligible wet deposition in the area (Moorthy et al., 2001). From station 6 to station 10, AOD_{870} was greater than AOD_{380}

The BC mass concentrations in the open ocean to the north of ITCZ are around six times higher compared to the south of ITCZ. Higher BC mass concentrations observed to the north of ITCZ are due to the northeasterly winds prevailing over the region (Gogoi et al., 2019; Hulswar et al., 2020). The higher concentrations of BC near the coast are due to anthropogenic aerosols advected from the continent (Gogoi et al., 2019). According to Lelieveld et al. (2001), the aerosol loading over the northern Indian Ocean is comparable to the suburban air pollution in Europe and North America. Their study further concluded that fossil fuel combustion and biomass burning lead to the outflow of both organic carbon and BC over the northern Arabian Sea. The highest BB% observed during the expedition was 18%, indicating that the atmosphere is loaded with anthropogenically produced Fossil Fuel BC (~85%). The BB% was 17% near the continent and decreased further as the average lifetime of biomass burning BC is short compared to fossil fuel BC, as the former are larger and are more likely to undergo dry deposition via gravitational settling or wet removal processes (Schwarz et al., 2008; Gogoi et al., 2019). The HYSPLIT trajectories (Fig. 5) and the synoptic wind regime (Fig. 1) confirm the possibility of the advection of BC from the Indian subcontinent. The increase in BC mass concentrations between 4 ° N and 0.5 ° N is also a result of the aerosols advected from the Indian Subcontinent (Fig. 6). Decreased ambient BC mass concentration beyond the equator may also be due to the significant positive CAPE and negligible CINE (Table 1) available for supporting the convective motion of the air, which might have resulted in increased mixing and dispersion of aerosols.

Further, the BC mass concentration (39.63 ± 14.40 ng m^{-3}) to the south of ITCZ was negligible. The density of forest fires is maximum in east Africa during December (Roberts et al., 2009), resulting in the emission of large quantities of biomass burning BC. The higher BB% between 12 ° S to 16 ° S may be because the cruise track was near the African coast, which may have caused the higher sampling of biomass burning BC as a subsequent result of the African forest fires.

5.2. *Clear sky direct aerosol radiative forcing and atmospheric heating rate*

In the coastal region at 12.96 ° N, the radiative forcing at the surface (SUR) (−73.41 W m^{-2}) and top of the atmosphere (TOA) (−55.45 W m^{-2}) were high (Fig. 6a). As a result, the atmospheric forcing due to aerosols, i.e., ATM, was 17.98 W m^{-2}. The high ATM forcing is associated with the high AOD and BC mass concentration over the region. Dust from the Arabian, North African, and Indian region also contributes to the aerosol loading over the Arabian Sea and play an essential role in the radiative forcing (Tegen et al., 1996; Li et al., 1996) along with the anthropogenic aerosols. The ATM forcing drastically decreased southwards as the concentration of aerosols decreased. The ATM forcing was ~75% more at 12.96 ° N compared to the other stations (Fig. 6a). Higher atmospheric forcing at 2.39 ° N (3.24 W m^{-2}) is due to the higher concentration of aerosols and the prevailing atmospheric conditions at this location. Below 12 ° S, despite the AOD being higher, the ATM forcing was lower (Figs. 2a & 6a) as the BC mass concentration was low (35.75 ± 13.04 ng m^{-3}), and the region was dominated by clean marine aerosols, which are scattering in nature. After station 5 (0.42°N), the AOD increased towards the higher wavelength, representing the dominance of coarse mode aerosol (sea salt), which led to high scattering albedo (SSA). The high SSA leads to a low ATM forcing and heating rate, as higher values of SSA represent the presence of more scattering aerosols (Table S1).

The atmospheric heating rate at station 12.96°N was 0.505 K day^{-1} (Fig. 6b) due to anthropogenically derived BC. BC plays a vital role in atmospheric forcing, an absorbing type of aerosol. The dominance of fine-mode aerosols over the Arabian Sea region leads to enhancement in radiative forcing and heating of the atmosphere (Che et al., 2014; Gogoi et al., 2019). The mean heating rate for stations 2 to 5 in the open ocean was 0.1285 ± 0.033 K $day^{-1,}$ where we observed aerosol layers of polluted continental/smoke and dusty marine, whereas, for stations 6 to10 it was 0.063 ± 0.017 K day^{-1} as it was mainly dominated by scattering aerosols.

6. Conclusion

The AOD (0.630) and BC mass concentration (1382.21 ± 209.10 ng m^{-3}) were the highest near the continent and decreased drastically towards the open ocean. A higher AOD near the continent was due to the presence of continentally advected aerosols during the north-east monsoon, also seen from CALIOP aerosol subtype data. Stable atmospheric conditions, supported with lower CAPE (105.75 J kg^{-1}), add to higher aerosol loads over the region as it minimizes their vertical dispersion. Significant positive CAPE (2535.2 J kg^{-1}) and negligible CINE (0 J kg^{-1}) support air's convective motion, resulting in aerosol dispersion even to the free troposphere. In contrast to the atmosphere near the continent loaded with continental advected aerosols, the atmosphere in the far offshore region was dominated by marine aerosol particles. BB% percentage was high near the continent and decreased offshore. CALIOP data showed that the aerosols over the TIO in the lower atmosphere are mainly dominated by polluted continental/smoke, dusty marine, and clean marine. The DARF (17.98 W m^{-2}) and atmospheric heating rate (0.540 K day^{-1}) were the highest at Station 1 and decreased considerably southwards. The heating rate was very low for stations 6 to10 compared to stations 2 to 5, despite the AOD values being around the same range, due to the former region being dominated by scattering aerosols.

Credit author statement

Atiba A. Shaikh: Conceptualization, Formal analysis, Writing-original draft, reviewing, and editing. **S. Neha Salim:** Formal Analysis. **Harilal B. Menon:** Funding acquisition, Resources, Project administration, Supervision, Writing-reviewing, and editing.

Declaration of competing interest

The authors declare that they have no known competing financial interests or personal relationships that could have appeared to influence the work reported in this paper.

Acknowledgements

The study was funded by Indian Space Research Organization (ISRO) under the Geosphere Biosphere programme for projects "Aerosol Radiative Forcing over India (ARFI-IGBP)" and "Network of Observatories for Boundary Layer Experiments (NOBLE-IGBP)", A-38(7) at Goa University. We thank Indian National Centre for Ocean Information Services (INCOIS) for executing the Expedition. The authors express their sincere thanks to Dr. Shrivardhan Hulswar for data curation during IIOE-II and Dr. Avirup Sen for extending help during analysis. The authors thank all the officers, crew members, and scientists onboard ORV *Sagar Nidhi* for the help provided during data collection.

Appendix A. Supplementary data

Supplementary data to this article can be found online at https://doi.org/10.1016/j.apr.2023.101797.

References

Aswini, A.R., Hegde, P., Aryasree, S., Girach, I.A., Nair, P.R., 2020. Continental outflow of anthropogenic aerosols over Arabian Sea and Indian Ocean during wintertime: ICARB-2018 campaign. Sci. Total Environ. 712, 135214 https://doi.org/10.1016/J.SCITOTENV.2019.135214.

Bao, H., Niggemann, J., Luo, L., Dittmar, T., Kao, S.J., 2017. Aerosols as a source of dissolved black carbon to the ocean. Nat. Commun. 81 (8), 1–7. https://doi.org/10.1038/s41467-017-00437-3, 2017.

Behrendt, A., Pal, S., Wulfmeyer, V., Valdebenito, B., Á, M., Lammel, G., 2011. A novel approach for the characterization of transport and optical properties of aerosol particles near sources - Part I: measurement of particle backscatter coefficient maps with a scanning UV lidar. Atmos. Environ. 45, 2795–2802. https://doi.org/10.1016/j.atmosenv.2011.02.061.

Charlson, R.J., Schwartz, S.E., Hales, J.M., Cess, R.D., Coakley, J.A., Hansen, J.E., Hofmann, D.J., 1992. Climate forcing by anthropogenic aerosols. Science 80 255, 423–430. https://doi.org/10.1126/science.255.5043.423.

Chaubey, J.P., Moorthy, K.K., Babu, S.S., Gogoi, M.M., 2013. Spatio-temporal variations in aerosol properties over the oceanic regions between coastal India and Antarctica. J. Atmos. Sol. Terr. Phys. 104, 18–28. https://doi.org/10.1016/J.JASTP.2013.08.004.

Che, H., Xia, X., Zhu, J., Li, Z., Dubovik, O., Holben, B., Goloub, P., Chen, H., Estelles, V., Cuevas-Agulló, E., Blarel, L., Wang, H., Zhao, H., Zhang, X., Wang, Y., Sun, J., Tao, R., Zhang, X., Shi, G., 2014. Column aerosol optical properties and aerosol radiative forcing during a serious haze-fog month over North China Plain in 2013 based on ground-based sunphotometer measurements. Atmos. Chem. Phys. 14, 2125–2138. https://doi.org/10.5194/acp-14-2125-2014.

Chen, A., Zhao, C., Fan, T., 2022. Spatio-temporal distribution of aerosol direct radiative forcing over mid-latitude regions in north hemisphere estimated from satellite observations. Atmos. Res. 266, 105938 https://doi.org/10.1016/j.atmosres.2021.105938.

Colby, F.P., 1984. Convective inhibition as a predictor of convection during AVE-SESAME II. Mon. Weather Rev. 112, 2239–2252. https://doi.org/10.1175/1520-0493(1984)112<2239:CIAAPO>2.0.CO;2.

Collins, D.R., Jonsson, H.H., Seinfeld, J.H., Flagan, R.C., Gassó, S., Hegg, D.A., Russeel, P. B., Schmid, B., Livingston, J.M., Öström, E., Noone, K.J., Russeee, L.M., Putaud, J.P., 2000. In situ aerosol-size distributions and clear-column radiative closure during ACE-2. Tellus Ser. B Chem. Phys. Meteorol. 52, 498–525. https://doi.org/10.3402/tellusb.v52i2.16175.

Covert, D.S., Gras, J.L., Wiedensohler, A., Stratmann, F., 1998. Comparison of directly measured CCN with CCN modeled from the number-size distribution in the marine boundary layer during ACE 1 at Cape Grim, Tasmania. J. Geophys. Res. Atmos. 103, 16597–16608. https://doi.org/10.1029/98JD01093.

Doswell, C.A., Rasmussen, E.N., 1994. The effect of neglecting the virtual temperature correction on CAPE calculations. Weather Forecast. 9, 625–629. https://doi.org/10.1175/1520-0434(1994)009<0625:TEONTV>2.0.CO;2.

Draxler, R., Rolph, G.D., 2003. HYSPLIT (Hybrid Single-Particle Lagrangian Integrated Trajectory) Model Access via NOAA ARL READY Website. NOAA air resources laboratory, Silver spring, MD USA. NOAA. http://www.arl.noaa.gov/ready/hysplit4.html.

Durkee, P.A., Nielsen, K.E., Smith, P.J., Russell, P.B., Schmid, B., Livingston, J.M., Holben, B.N., Tomasi, C., Vitale, V., Collins, D., Flagan, R.C., Seinfeld, J.H., Noone, K.J., Öström, E., Gassó, S., Hegg, D., Russell, L.M., Bates, T.S., Quinn, P.K., 2000. Regional aerosol optical depth characteristics from satellite observations: ACE-1, TARFOX and ACE-2 results. Tellus Ser. B Chem. Phys. Meteorol. 52, 484–497. https://doi.org/10.3402/tellusb.v52i2.16174.

Fuller, G.W., Tremper, A.H., Baker, T.D., Yttri, K.E., Butterfield, D., 2014. Contribution of wood burning to PM10 in London. Atmos. Environ. 87, 87–94. https://doi.org/10.1016/J.ATMOSENV.2013.12.037.

Garrett, T.J., Zhao, C., 2006. Increased Arctic cloud longwave emissivity associated with pollution from mid-latitudes. Nature 440, 787–789. https://doi.org/10.1038/nature04636.

Gogoi, M.M., Tandule, C.R., V, J., Kompalli, S.K., Nair, V.S., Gopal, K.R., Babu, S.S., 2019. Spatial gradient of aerosol mass concentrations and size distributions over southeastern Arabian Sea and equatorial Indian Ocean during ICARB-2018. Atmos. Environ. 213, 727–738. https://doi.org/10.1016/J.ATMOSENV.2019.06.038.

Hansen, A.D.A., Rosen, H., Novakov, T., 1984. The aethalometer - an instrument for the real-time measurement of optical absorption by aerosol particles. Sci. Total Environ. 36, 191–196. https://doi.org/10.1016/0048-9697(84)90265-1.

Hansen, J., Sato, M., Ruedy, R., 1997. Radiative forcing and climate response. J. Geophys. Res. Atmos. 102, 6831–6864. https://doi.org/10.1029/96JD03436.

Hellerman, S., Rosenstein, M., 1983. Normal monthly wind stress over the world ocean with error estimates. J. Phys. Oceanogr. 13, 1093–1104. https://doi.org/10.1175/1520-0485(1983)013<1093:nmwsot>2.0.co;2.

Hess, M., Koepke, P., Schult, I., 1998. Optical properties of aerosols and clouds: the software package OPAC. Bull. Am. Meteorol. Soc. 79, 831–844. https://doi.org/10.1175/1520-0477(1998)079<0831:OPOAAC>2.0.CO;2.

Hess, S.L., 1979. *Introduction To Theoretical meteorology*(No. 551.5 HES).

Huebert, B.J., Howell, S.G., Zhuang, L., Heath, J.A., Litchy, M.R., Wylie, D.J., Kreidler-Moss, J.L., Cöppicus, S., Pfeiffer, J.E., 1998. Filter and impactor measurements of anions and cations during the first aerosol characterization experiment (ACE 1). J. Geophys. Res. Atmos. 103, 16493–16509. https://doi.org/10.1029/98JD00770.

Hulswar, S., Menon, H.B., Anilkumar, N., 2020. Physical-chemical characteristics of composite aerosols in the Indian Ocean sector of the Southern Ocean and its associated effect on insolation: a climate perspective. Deep. Res. Part II Top. Stud. Oceanogr. 178, 104801 https://doi.org/10.1016/j.dsr2.2020.104801.

Junge, C., 1955. The size distribution and aging of natural aerosols as determined from electrical and optical data on the atmosphere. J. Meteorol. 12, 13–25. https://doi.org/10.1175/1520-0469(1955)012<0013:tsdaao>2.0.co;2.

Kamra, A.K., Murugavel, P., Pawar, S.D., 2003. Measured size distributions of aerosols over the Indian Ocean during INDOEX. J. Geophys. Res. Atmos. 108 https://doi.org/10.1029/2002jd002200.

Kaskaoutis, D.G., Sinha, P.R., Vinoj, V., Kosmopoulos, P.G., Tripathi, S.N., Misra, A., Sharma, M., Singh, R.P., 2013. Aerosol properties and radiative forcing over Kanpur during severe aerosol loading conditions. Atmos. Environ. 79, 7–19. https://doi.org/10.1016/J.ATMOSENV.2013.06.020.

Kim, M.H., Omar, A.H., Tackett, J.L., Vaughan, M.A., Winker, D.M., Trepte, C.R., Hu, Y., Liu, Z., Poole, L.R., Pitts, M.C., Kar, J., Magill, B.E., 2018. The CALIPSO version 4 automated aerosol classification and lidar ratio selection algorithm. Atmos. Meas. Tech. 11, 6107–6135. https://doi.org/10.5194/AMT-11-6107-2018.

Krishna Moorthy, K., Satheesh, S.K., Krishna Murthy, B.V., 1997. Investigations of marine aerosols over the tropical Indian Ocean. J. Geophys. Res. Atmos. 102, 18827–18842. https://doi.org/10.1029/97jd01121.

Krishnamurti, T.N., Jha, B., Prospero, J., Jayaraman, A., Ramanathan, V., 1998. Aerosol and pollutant transport and their impact on radiative forcing over the tropical Indian Ocean during the January-February 1996 pre-INDOEX cruise. Tellus Ser. B Chem. Phys. Meteorol. 50, 521–542. https://doi.org/10.3402/tellusb.v50i5.16235.

Kumar, A., Sudheer, A.K., Goswami, V., Bhushan, R., 2012. Influence of continental outflow on aerosol chemical characteristics over the Arabian Sea during winter. Atmos. Environ. 50, 182–191. https://doi.org/10.1016/J.ATMOSENV.2011.12.040.

Kumar, R., Barth, M.C., Nair, V.S., Pfister, G.G., Suresh Babu, S., Satheesh, S.K., Krishna Moorthy, K., Carmichael, G.R., Lu, Z., Streets, D.G., 2015. Sources of black carbon aerosols in south asia and surrounding regions during the integrated campaign for aerosols, gases and radiation budget (ICARB). Atmos. Chem. Phys. 15, 5415–5428. https://doi.org/10.5194/acp-15-5415-2015.

Lelieveld, J., Crutzen, P.J., Ramanathan, V., Andreae, M.O., Brenninkmeijer, C.A.M., Campos, T., Cass, G.R., Dickerson, R.R., Fischer, H., De Gouw, J.A., Hansel, A., Jefferson, A., Kley, D., De Laat, A.T.J., Lal, S., Lawrence, M.G., Lobert, J.M., Mayol-Bracero, O.L., Mitra, A.P., Novakov, T., Oltmans, S.J., Prather, K.A., Reiner, T., Rodhe, H., Scheeren, H.A., Sikka, D., Williams, J., 2001. The Indian Ocean Experiment: widespread air pollution from south and southeast asia. Science 80 291, 1031–1036. https://doi.org/10.1126/science.1057103.

Li, X., Maring, H., Savoie, D., Voss, K., Prospero, J.M., 1996. Dominance of mineral dust in aerosol light-scattering in the North Atlantic trade winds. Nature 380, 416–419. https://doi.org/10.1038/380416a0.

Livingstone, J.M., Kapustin, V.N., Schmid, B., Russel, P.B., Quinn, P.K., Bates, T.S., Durkee, P.A., Smith, P.J., Freudenthaler, V., Wiegner, M., Covert, D.S., Gassó, S., Hegg, D., Collins, D.R., Flagan, R.C., Seinfeld, J.H., Vitale, V., Tomasi, C., 2000. Shipboard sunphotometer measurements of aerosol optical depth spectra and columnar water vapor during ACE-2, and comparison with selected land, ship, aircraft, and satellite measurements. Tellus B Chem. Phys. Meteorol. 52, 594–619. https://doi.org/10.3402/tellusb.v52i2.17122.

Mitra, A.P., 2004. Indian ocean experiment [INDOEX]: an overview. Indian J. Mar. Sci. 33, 30–39.

Moncrieff, M.W., Miller, M.J., 1976. The dynamics and simulation of tropical cumulonimbus and squall lines. Q. J. R. Meteorol. Soc. 102, 373–394. https://doi.org/10.1002/qj.49710243208.

Moorthy, K.K., Saha, A., Prasad, B.S.N., Niranjan, K., Jhurry, D., Pillai, P.S., 2001. Aerosol optical depths over peninsular India and adjoining oceans during the INDOEX campaigns: spatial, temporal, and spectral characteristics. J. Geophys. Res. Atmos. 106, 28539–28554. https://doi.org/10.1029/2001JD900169.

Moorthy, K.K., Satheesh, S.K., 2000. Characteristics of aerosols over a remote island, Minicoy in the Arabian Sea: optical properties and retrieved size characteristics. Q. J. R. Meteorol. Soc. 126, 81–109. https://doi.org/10.1002/qj.49712656205.

Moorthy, K.K., Satheesh, S.K., Babu, S.S., Dutt, C.B.S., 2008. Integrated campaign for aerosols, gases and radiation budget (ICARB): an overview. J. Earth Syst. Sci. https://doi.org/10.1007/s12040-008-0029-7.

Morys, M., Mims, F.M., Hagerup, S., Anderson, S.E., Baker, A., Kia, J., Walkup, T., 2001. Design, calibration, and performance of MICROTOPS II handheld ozone monitor and Sun photometer. J. Geophys. Res. Atmos. 106, 14573–14582. https://doi.org/10.1029/2001JD900103.

Neusüß, C., Weise, D., Birmili, W., Wex, H., Wiedensohler, A., Covert, D.S., 2000. Size-segregated chemical, gravimetric and number distribution-derived mass closure of the aerosol in Sagres, Portugal during ACE-2. Tellus B Chem. Phys. Meteorol. 52, 169–184. https://doi.org/10.3402/tellusb.v52i2.16091.

Pal, S., Haeffelin, M., Batchvarova, E., 2013. Exploring a geophysical process-based attribution technique for the determination of the atmospheric boundary layer depth using aerosol lidar and near-surface meteorological measurements. J. Geophys. Res. Atmos. 118, 9277–9295. https://doi.org/10.1002/jgrd.50710.

Pal, S., Xueref-Remy, I., Ammoura, L., Chazette, P., Gibert, F., Royer, P., Dieudonné, E., Dupont, J.C., Haeffelin, M., Lac, C., Lopez, M., Morille, Y., Ravetta, F., 2012. Spatio-temporal variability of the atmospheric boundary layer depth over the Paris agglomeration: an assessment of the impact of the urban heat island intensity. Atmos. Environ. 63, 261–275. https://doi.org/10.1016/j.atmosenv.2012.09.046.

Prospero, J.M., 1981. Eaolian transport to the world ocean. In: Emiliani (Ed.), The Oceanic Lithosphere, the Sea. John Wiley, New York, pp. 801–874.
Prospero, J.M., 2002. The chemical and physical properties of marine aerosols: an introduction. In: Chemistry of Marine Water and Sediments. Springer, Berlin, Heidelberg, pp. 35–82. https://doi.org/10.1111/j.1749-6632.1967.tb34860.x.
Prospero, J.M., Charlson, R.J., Mohnen, V., Jaenicke, R., Delany, A.C., Moyers, J., Zoller, W., Rahn, K., 1983. The atmospheric aerosol system: an overview. Rev. Geophys. https://doi.org/10.1029/RG021i007p01607.
Putaud, J.P., Van Dingenen, R., Mangoni, M., Virkkula, A., Raes, F., Maring, H., Prospero, J.M., Swietlicki, E., Berg, O.H., Hillamo, R., Mäkelä, T., 2000. Chemical mass closure and assessment of the origin of the submicron aerosol in the marine boundary layer and the free troposphere at Tenerife during ACE-2. Tellus Ser. B Chem. Phys. Meteorol. 52, 141–168. https://doi.org/10.3402/tellusb.v52i2.16090.
Pyatt, H.E., Albrecht, B.A., Fairall, C., Hare, J.E., Bond, N., Minnis, P., Ayers, J.K., 2005. Evolution of marine atmospheric boundary layer structure across the cold tongue-ITCZ complex. J. Clim. 18, 737–753. https://doi.org/10.1175/JCLI-3287.1.
Quinn, P.K., Coffman, D.J., Kapustin, V.N., Bates, T.S., Covert, D.S., 1998. Aerosol optical properties in the marine boundary layer during the First Aerosol Characterization Experiment (ACE 1) and the underlying chemical and physical aerosol properties. J. Geophys. Res. Atmos. 103, 16547–16563. https://doi.org/10.1029/97JD02345.
Ramachandran, S., Jayaraman, A., 2002. Premonsoon aerosol mass loadings and size distributions over the Arabian Sea and the tropical Indian Ocean. AAC J. Geophys. Res. Atmos. 107, 1. https://doi.org/10.1029/2002JD002386, 1.
Ramachandran, S., Kedia, S., 2010. Black carbon aerosols over an urban region: radiative forcing and climate impact. J. Geophys. Res. Atmos. 115, 10202 https://doi.org/10.1029/2009JD013560.
Ramanathan, V., Barkstrom, B.R., Harrison, E.F., 1992. Climate and the earth ` s radiation budget. In: AIP Conference Proceedings. American Institute of Physics, pp. 55–77.
Ramanathan, V., Carmichael, G., 2008. Global and regional climate changes due to black carbon. Nat. Geosci. 1, 221–227. https://doi.org/10.1038/ngeo156.
Ramanathan, V., Crutzen, P.J., Lelieveld, J., Mitra, A.P., Althausen, D., Anderson, J., Andreae, M.O., Cantrell, W., Cass, G.R., Chung, C.E., Clarke, A.D., Coakley, J.A., Collins, W.D., Conant, W.C., Dulac, F., Heintzenberg, J., Heymsfield, A.J., Holben, B., Howell, S., Hudson, J., Jayaraman, A., Kiehl, J.T., Krishnamurti, T.N., Lubin, D., McFarquhar, G., Novakov, T., Ogren, J.A., Podgorny, I.A., Prather, K., Priestley, K., Prospero, J.M., Quinn, P.K., Rajeev, K., Rasch, P., Rupert, S., Sadourny, R., Satheesh, S.K., Shaw, G.E., Sheridan, P., Valero, F.P.J., 2001. Indian Ocean Experiment: an integrated analysis of the climate forcing and effects of the great Indo-Asian haze. J. Geophys. Res. Atmos. 106, 28371–28398. https://doi.org/10.1029/2001JD900133.
Rasch, P.J., Collins, W.D., Eaton, B.E., 2001. Understanding the Indian Ocean Experiment (INDOEX) aerosol distributions with an aerosol assimilation. J. Geophys. Res. Atmos. 106, 7337–7355. https://doi.org/10.1029/2000JD900508.
Ricchiazzi, P., Yang, S., Gautier, C., Sowle, D., 1998. SBDART: a Research and teaching software tool for plane-parallel radiative transfer in the earth's atmosphere. Bull. Am. Meteorol. Soc. 79, 2101–2114. https://doi.org/10.1175/1520-0477(1998)079<2101:SARATS>2.0.CO;2.
Roberts, G., Wooster, M.J., Lagoudakis, E., 2009. Annual and diurnal african biomass burning temporal dynamics. Biogeosciences 6, 849–866. https://doi.org/10.5194/BG-6-849-2009.
Russell, P.B., Heintzenberg, J., 2000. An overview of the ACE-2 clear sky column closure experiment (CLEARCOLUMN). Tellus Ser. B Chem. Phys. Meteorol. 52, 463–483. https://doi.org/10.3402/tellusb.v52i2.16173.
Russell, P.B., Hobbs, P.V., Stowe, L.L., 1999. Aerosol properties and radiative effects in the United States East Coast haze plume: an overview of the tropospheric aerosol radiative forcing observational experiment (TARFOX). J. Geophys. Res. Atmos. 104, 2213–2222. https://doi.org/10.1029/1998JD200028.
Sandradewi, J., Prévôt, A.S.H., Szidat, S., Perron, N., Alfarra, M.R., Lanz, V.A., Weingartner, E., Baltensperger, U.R.S., 2008. Using aerosol light absorption measurements for the quantitative determination of wood burning and traffic emission contribution to particulate matter. Environ. Sci. Technol. 42, 3316–3323. https://doi.org/10.1021/es702253m.
Satheesh, S.K., Ramanathan, V., Li-Jones, X., Lobert, J.M., Podgorny, I.A., Prospero, J.M., Holben, B.N., Loeb, N.G., 1999. A model for the natural and anthropogenic aerosols over the tropical Indian Ocean derived from Indian Ocean Experiment data. J. Geophys. Res. Atmos. 104, 27421–27440. https://doi.org/10.1029/1999JD900478.
Schmid, B., Livingston, J.M., Russell, P.B., Durkee, P.A., Jonsson, H.H., Collins, D.R., Flagan, R.C., Seinfeld, J.H., Gassó, S., Hegg, D.A., Öström, E., Noone, K.J., Welton, E. J., Voss, K.J., Gordon, H.R., Formenti, P., Andreae, M.O., 2000. Clear-sky closure studies of lower tropospheric aerosol and water vapor during ACE-2 using airborne sunphotometer, airborne in-situ, space-borne, and ground-based measurements. Tellus Ser. B Chem. Phys. Meteorol. 52, 568–593. https://doi.org/10.3402/tellusb.v52i2.16659.
Schwarz, J.P., Gao, R.S., Spackman, J.R., Watts, L.A., Thomson, D.S., Fahey, D.W., Ryerson, T.B., Peischl, J., Holloway, J.S., Trainer, M., Frost, G.J., Baynard, T., Lack, D.A., de Gouw, J.A., Warneke, C., Del Negro, L.A., 2008. Measurement of the mixing state, mass, and optical size of individual black carbon particles in urban and biomass burning emissions. Geophys. Res. Lett. 35, 13810 https://doi.org/10.1029/2008GL033968.
Showalter, A.K., 1954. Precipitable water template. Bull. Am. Meteorol. Soc. 35, 129–131.
Singh, A., Srivastava, R., Rastogi, N., Singh, D., 2016. Absorbing and scattering aerosols over the source region of biomass burning emissions: implications in the assessment of optical and radiative properties. Atmos. Environ. 127, 61–68. https://doi.org/10.1016/J.ATMOSENV.2015.12.029.
Srivastava, R., Asutosh, A., Sabu, P., Anilkumar, N., 2021. Investigation of Black Carbon characteristics over southern ocean: contribution of fossil fuel and biomass burning. Environ. Pollut. 276, 116645 https://doi.org/10.1016/J.ENVPOL.2021.116645.
Stein, A.F., Draxler, R.R., Rolph, G.D., Stunder, B.J.B., Cohen, M.D., Ngan, F., 2015. Noaa's hysplit atmospheric transport and dispersion modeling system. Bull. Am. Meteorol. Soc. 96, 2059–2077. https://doi.org/10.1175/BAMS-D-14-00110.1.
Stull, R.B., 1988. An introduction to boundary layer meteorology. In: An Introduction to Boundary Layer Meteorology, first ed. Springer Science & Business Media. https://doi.org/10.1007/978-94-009-3027-8.
Sun, Y., Zhao, C., 2020. Influence of Saharan dust on the large-scale meteorological environment for development of tropical cyclone over North Atlantic Ocean Basin. J. Geophys. Res. Atmos. 125 https://doi.org/10.1029/2020JD033454.
Tegen, I., Lacis, A.A., Fung, I., 1996. The influence on climate forcing of mineral aerosols from disturbed soils. Nature. https://doi.org/10.1038/380419a0.
Wielicki, B.A., Cess, R.D., King, M.D., Randall, D.A., Harrison, E.F., 1995. Mission to Planet Earth: role of clouds and radiation in climate. Bull. Am. Meteorol. Soc. 76, 2125–2154. https://doi.org/10.1175/1520-0477(1995)076<2125:mtpero>2.0.co;2.
Wilcox, E.M., Thomas, R.M., Praveen, P.S., Pistone, K., Bender, F.A.M., Ramanathan, V., 2016. Black carbon solar absorption suppresses turbulence in the atmospheric boundary layer. Proc. Natl. Acad. Sci. U.S.A. 113, 11794–11799. https://doi.org/10.1073/pnas.1525746113.

Bibliography

Abedi, H., Sarkar, S., Johansson, H., 2021. Numerical modelling of neutral atmospheric boundary layer flow through heterogeneous forest canopies in complex terrain (a case study of a Swedish wind farm). Renewable Energy. 180, 806-828. https://doi.org/https://doi.org/10.1016/j.renene.2021.08.036.

Agarwal, P., Kumar Yadav, A., Gulati, A., Raman, S., Rao, S., Singh, M.P., Nigam, S., Reddy, N., 1995. Surface layer turbulence processes in low wind speeds over land. Atmospheric Environment. 29, 2089-2098. https://doi.org/https://doi.org/10.1016/1352-2310(94)00328-I.

Al-Jiboori, M.H., Yumao, X., Yongfu, Q., 2001. Turbulence characteristics over complex terrain in West China. Boundary Layer Meteorology. 101, 109-126. https://doi.org/10.1023/A:1019234724291.

Alappattu, D.P., Kunhikrishnan, P.K., 2010. Observations of the thermodynamic structure of marine atmospheric boundary layer over Bay of Bengal, Northern Indian Ocean and Arabian Sea during premonsoon period. Journal of Atmospheric and Solar Terrestrial Physics. 72, 1318-1326. https://doi.org/https://doi.org/10.1016/j.jastp.2010.07.011.

Albrecht, B., 1989. Aerosols, cloud microphysics, and fractional cloudiness. Science. 245, 1227-1230. https://doi.org/10.1126/science.245.4923.1227.

Albrecht, B.A., Jensen, M.P., Syrett, W.J., 1995. Marine boundary layer structure and fractional cloudiness. Journal of Geophysical Research : Atmospheres. 100, 14209-14222. https://doi.org/https://doi.org/10.1029/95JD00827.

Alexander, S.P., McFarquhar, G.M., Marchand, R., Protat, A., Vignon, É., Mace, G.G., Klekociuk, A.R., 2021. Mixed-phase clouds and precipitation in Southern Ocean cyclones and cloud systems observed poleward of 64°S by ship-based cloud radar and lidar. Journal of Geophysical Research : Atmospheres. 126. https://doi.org/https://doi.org/10.1029/2020JD033626.

Alexander, S.P., Protat, A., 2018. Cloud properties observed from the surface and by satellite at the northern edge of the Southern Ocean. Journal of Geophysical Research : Atmospheres. 123, 443-456. https://doi.org/https://doi.org/10.1002/2017JD026552.

Alexander, S.P., Protat, A., 2019. Vertical profiling of aerosols with a combined Raman-elastic backscatter lidar in the remote Southern Ocean marine boundary layer (43°S – 66°S, 132°E – 150°E). Journal of Geophysical Research : Atmospheres. 124. https://doi.org/10.1029/2019JD030628.

Alroe, J., Cravigan, L.T., Miljevic, B., Johnson, G.R., Selleck, P., Humphries, R.S., Keywood, M.D., Chambers, S.D., Williams, A.G., Ristovski, Z.D., 2020. Marine productivity and synoptic meteorology drive summer-time variability in Southern Ocean aerosols. Atmospheric Chemistry and Physics. 20, 8047-8062. https://doi.org/10.5194/acp-20-8047-2020.

André, J.-C., Goutorbe, J.-P., Perrier, A., 1986. HAPEX—MOBILHY: A Hydrologic Atmospheric Experiment the study of water budget and evaporation flux at the climatic scale. Bulletin of the American Meteorological Society. 67, 138-144. https://doi.org/10.1175/1520-0477-67.2.138.

Andreas, E.L., Hill, R.J., Gosz, J.R., Moore, D.I., Otto, W.D., Sarma, A.D., 1998. Statistics of surface layer turbulence over terrain with metre scale heterogeneity. Boundary Layer Meteorology. 86, 379-408. https://doi.org/10.1023/A:1000609131683.

Angevine, W.M., 2008. Transitional, entraining, cloudy, and coastal boundary layers. Acta Geophysica. 56, 2-20. https://doi.org/http://10.2478/s11600-007-0035-1.

Angevine, W.M., Baltink, H.K., Bosveld, F.C., 2001. Observations of the morning transition of the convective boundary layer. Boundary Layer Meteorology. 101, 209-227. https://doi.org/10.1023/A:1019264716195.

Angevine, W.M., Edwards, J.M., Lothon, M., LeMone, M.A., Osborne, S.R., 2020. Transition periods in the diurnally varying Atmospheric Boundary Layer over land. Boundary Layer Meteorology. 177, 205-223. https://doi.org/10.1007/s10546-020-00515-y.

Anilkumar, N., George, J.V., Chacko, R., Nuncio, N., Sabu, P., 2015. Variability of fronts, fresh water input and chlorophyll in the Indian Ocean sector of the Southern Ocean. New Zealand Journal of Marine and Freshwater Research. 49, 20-40. https://doi.org/https://doi.org/10.1080/00288330.2014.924972.

Anurose, T.J., Subrahamanyam, D.B., Sunilkumar, S.V., 2018. Two years observations on the diurnal evolution of coastal atmospheric boundary layer features over Thiruvananthapuram (8.5∘ N, 76.9∘ E), India. Theoretical and Applied Climatology. 131, 77-90. https://doi.org/10.1007/s00704-016-1955-y.

Ao, C.O., Waliser, D.E., Chan, S.K., Li, J.-L., Tian, B., Xie, F., Mannucci, A.J., 2012. Planetary boundary layer heights from GPS radio occultation refractivity and humidity profiles. Journal of Geophysical Research : Atmospheres. 117. https://doi.org/https://doi.org/10.1029/2012JD017598.

Aravind, A., Srinivas, C.V., Hegde, M.N., Seshadri, H., Mohapatra, D.K., 2022. Sensitivity of surface roughness parameters on the simulation of boundary layer winds over a complex terrain site Kaiga in western India. Meteorology and Atmospheric Physics. 134, 71. https://doi.org/http://10.1007/s00703-022-00912-7.

Arya, 2001. Introduction to micrometeorology. Elsevier.

Arya, P., 1999. Air pollution meteorology and dispersion. Oxford University Press New York.

Arya, S.P., 1988. Marine Atmospheric Boundary Layer, in: Arya, S.P. (Ed.), International Geophysics, Academic Press, pp. 197-222. https://doi.org/https://doi.org/10.1016/S0074-6142(08)60428-3.

Atkins, N.T., Wakimoto, R.M., Weckwerth, T.M., 1995. Observations of the Sea-Breeze Front during CaPE. Part II: Dual-Doppler and Aircraft Analysis. Monthly Weather Review. 123, 944-969. https://doi.org/https://doi.org/10.1175/1520-0493(1995)123<0944:OOTSBF>2.0.CO;2.

Atkinson, B.W., Li, J.-G., Plant, R.S., 2001. Numerical modeling of the propagation environment in the Atmospheric Boundary Layer over the Persian Gulf Journal of Applied Meteorology and Climatology. 40, 586-603. https://doi.org/10.1175/1520-0450(2001)040<0586:Nmotpe>2.0.Co;2.

Aubinet, M., Vesala, T., Papale, D., 2012. Eddy covariance: a practical guide to measurement and data analysis. Springer Science & Business Media.

Augstein, E., Schmidt, H., Ostapoff, F., 1974. The vertical structure of the atmospheric planetary boundary layer in undisturbed trade winds over the Atlantic Ocean. Boundary Layer Meteorology. 6, 129-150. https://doi.org/10.1007/BF00232480.

Avissar, R., Pielke, R.A., 1989. A parameterization of heterogeneous land surfaces for atmospheric numerical models and its impact on regional meteorology. Monthly Weather Review. 117, 2113-2136.

Avissar, R., Schmidt, T., 1998. An evaluation of the scale at which ground-surface heat flux patchiness affects the convective boundary layer using large-eddy simulations. Journal of the Atmospheric Sciences. 55, 2666-2689. https://doi.org/10.1175/1520-0469(1998)055<2666:Aeotsa>2.0.Co;2.

Babić, K., Rotach, M.W., Klaić, Z.B., 2016. Evaluation of local similarity theory in the wintertime nocturnal boundary layer over heterogeneous surface. Agricultural and Forest Meteorology. 228-229, 164-179. https://doi.org/https://doi.org/10.1016/j.agrformet.2016.07.002.

Babu, S.S., Moorthy, K.K., 2002. Aerosol black carbon over a tropical coastal station in India. Geophysical Research Letters. 29, 13-11-13-14. https://doi.org/https://doi.org/10.1029/2002GL015662.

Babu, S.S., Nair, V.S., Moorthy, K.K., 2008. Seasonal changes in aerosol characteristics over Arabian Sea and their consequence on aerosol short-wave radiative forcing: Results from ARMEX field campaign. Journal of Atmospheric and Solar-Terrestrial Physics. 70, 820-834. https://doi.org/https://doi.org/10.1016/j.jastp.2007.10.005.

Banta, R.M., Berri, G., Blumen, W., Carruthers, D.J., Dalu, G., Durran, D.R., Egger, J., Garratt, J., Hanna, S.R., Hunt, J.J.A.P.o.C.T., 1990. Mountain Meteorology. 1-4.

Barlow, J.F., Dunbar, T.M., Nemitz, E.G., Wood, C.R., Gallagher, M.W., Davies, F., O'Connor, E., Harrison, R.M., 2011. Boundary layer dynamics over London, UK, as observed using Doppler lidar during REPARTEE-II. Atmospheric Chemistry and Physics. 11, 2111-2125. https://doi.org/10.5194/acp-11-2111-2011.

Barman, N., Borgohain, A., Kundu, S.S., KiranKumar, N.V.P., 2021. Seasonal variation of mountain-valley wind circulation and surface layer parameters over the mountainous terrain of the northeastern region of India. Theoretical and Applied Climatology. 143, 1501-1512. https://doi.org/10.1007/s00704-020-03491-y.

Barman, N., Borgohain, A., Kundu, S.S., Roy, R., Saha, B., Solanki, R., Kiran Kumar, N.V.P., Raju, P.L.N., 2019. Daytime temporal variation of surface-layer parameters and turbulence kinetic energy budget in topographically complex terrain around Umiam, India. Boundary Layer Meteorology. 172, 149-166. https://doi.org/10.1007/s10546-019-00443-6.

Barthelmie, R.J., Crippa, P., Wang, H., Smith, C.M., Krishnamurthy, R., Choukulkar, A., Calhoun, R., Valyou, D., Marzocca, P., Matthiesen, D., Brown, G., Pryor, S.C., 2014. 3D wind and turbulence characteristics of the atmospheric boundary layer. Bulletin of the American Meteorological Society. 95, 743-756. https://doi.org/10.1175/bams-d-12-00111.1.

Basu, S., Holtslag, A.A.M., Van De Wiel, B.J.H., Moene, A.F., Steeneveld, G.-J., 2008a. An inconvenient “truth” about using sensible heat flux as a surface boundary

condition in models under stably stratified regimes. Acta Geophysica. 56, 88-99. https://doi.org/10.2478/s11600-007-0038-y.

Basu, S., Vinuesa, J.-F., Swift, A., 2008b. Dynamic LES modeling of a diurnal cycle. Journal of Applied Meteorology and Climatology. 47, 1156-1174. https://doi.org/10.1175/2007jamc1677.1.

Beare, R.J., Macvean, M.K., Holtslag, A.A.M., Cuxart, J., Esau, I., Golaz, J.-C., Jimenez, M.A., Khairoutdinov, M., Kosovic, B., Lewellen, D., Lund, T.S., Lundquist, J.K., McCabe, A., Moene, A.F., Noh, Y., Raasch, S., Sullivan, P., 2006. An Intercomparison of Large-Eddy Simulations of the Stable Boundary Layer. Boundary-Layer Meteorology. 118, 247-272. https://doi.org/http://10.1007/s10546-004-2820-6.

Behrangi, A., Song, Y., 2020. A new estimate for oceanic precipitation amount and distribution using complementary precipitation observations from space and comparison with GPCP. Environmental Research Letters. 15, 124042. https://doi.org/10.1088/1748-9326/abc6d1.

Belkin, I.M., Gordon, A.L., 1996. Southern Ocean fronts from the Greenwich meridian to Tasmania. Journal of Geophysical Research : Oceans. 101, 3675-3696. https://doi.org/https://doi.org/10.1029/95JC02750.

Bellouin, N., Quaas, J., Gryspeerdt, E., Kinne, S., Stier, P., Watson-Parris, D., Boucher, O., Carslaw, K.S., Christensen, M., Daniau, A.-L., Dufresne, J.-L., Feingold, G., Fiedler, S., Forster, P., Gettelman, A., Haywood, J.M., Lohmann, U., Malavelle, F., Mauritsen, T., McCoy, D.T., Myhre, G., Mülmenstädt, J., Neubauer, D., Possner, A., Rugenstein, M., Sato, Y., Schulz, M., Schwartz, S.E., Sourdeval, O., Storelvmo, T., Toll, V., Winker, D., Stevens, B., 2020. Bounding global aerosol radiative forcing of climate change. Reviews of Geophysics. 58, e2019RG000660. https://doi.org/https://doi.org/10.1029/2019RG000660.

Bender, F.A.-M., 2020. Aerosol Forcing: still uncertain, still relevant. AGU Advances. 1, e2019AV000128. https://doi.org/https://doi.org/10.1029/2019AV000128.

Betts, A.K., 1992. FIFE atmospheric boundary layer budget methods. Journal of Geophysical Research : Atmospheres. 97, 18523-18531. https://doi.org/https://doi.org/10.1029/91JD03172.

Betts, A.K., 1982. Saturation point analysis of moist convective overturning. Journal of Atmospheric Sciences. 39, 1484-1505.

https://doi.org/https://doi.org/10.1175/1520-0469(1982)039%3C1484:SPAOMC%3E2.0.CO;2.

Betts, A.K., Albrecht, B.A., 1987. Conserved Variable Analysis of the convective boundary layer thermodynamic structure over the tropical oceans. Journal of Atmospheric Sciences. 44, 83-99. https://doi.org/https://doi.org/10.1175/1520-0469(1987)044%3C0083:CVAOTC%3E2.0.CO;2.

Bharali, C., Nair, V.S., Chutia, L., Babu, S.S., 2019. Modeling of the Effects of Wintertime Aerosols on Boundary Layer Properties Over the Indo Gangetic Plain. Journal of Geophysical Research: Atmospheres. 124, 4141-4157. https://doi.org/https://doi.org/10.1029/2018JD029758.

Bhat, G.S., Ameenulla, S., Venkataramana, M., Sengupta, K., 2000. Atmospheric boundary layer characteristics during the BOBMEX-Pilot experiment. Journal of Earth System Science. 109, 229-237. https://doi.org/10.1007/BF02702196.

Bhat, G.S., Thomas, M.A., Raju, J.V.S., Chandrasekhara, C.P., 2003. Surface characteristics observed over the central tropical Indian Ocean during INDOEX-IFP99. Boundary Layer Meteorology. 106, 263-281. https://doi.org/10.1023/A:1021146516729.

Bhumralkar, C.M., 1975. Numerical Experiments on the Computation of Ground Surface Temperature in an Atmospheric General Circulation Model Journal of Applied Meteorology and Climatology. 14, 1246-1258. https://doi.org/https://doi.org/10.1175/1520-0450(1975)014<1246:NEOTCO>2.0.CO;2.

Bischoff, T., Thompson, A.F., 2014. Configuration of a Southern Ocean Storm Track Journal of Physical Oceanography. 44, 3072-3078. https://doi.org/http://10.1175/jpo-d-14-0062.1.

Bodas-Salcedo, A., Williams, K.D., Ringer, M.A., Beau, I., Cole, J.N.S., Dufresne, J.-L., Koshiro, T., Stevens, B., Wang, Z., Yokohata, T., 2014. Origins of the solar radiation biases over the Southern Ocean in CFMIP2 models. Journal of Climate. 27, 41-56. https://doi.org/https://doi.org/10.1175/JCLI-D-13-00169.1.

Boebel, O., Lutjeharms, J., Schmid, C., Zenk, W., Rossby, T., Barron, C., 2003. The Cape Cauldron: a regime of turbulent inter-ocean exchange. Deep Sea Research Part II: Topical Studies in Oceanography. 50, 57-86. https://doi.org/https://doi.org/10.1016/S0967-0645(02)00379-X.

Boers, R., Eloranta, E.W., 1986. Lidar measurements of the atmospheric entrainment zone and the potential temperature jump across the top of the mixed layer. 34, 357-375. https://doi.org/http://10.1007/bf00120988.

Boers, R., Jensen, J.B., Krummel, P.B., 1998. Microphysical and short-wave radiative structure of stratocumulus clouds over the Southern Ocean: Summer results and seasonal differences. Quarterly Journal of the Royal Meteorological Society. 124, 151-168. https://doi.org/https://doi.org/10.1002/qj.49712454507.

Bolton, D., 1980. The computation of equivalent potential temperature. Monthly Weather Review. 108, 1046-1053.

Bony, S., Dufresne, J.-L., 2005. Marine boundary layer clouds at the heart of tropical cloud feedback uncertainties in climate models. Geophysical Research Letters. 32. https://doi.org/https://doi.org/10.1029/2005GL023851.

Bou-Zeid, E., Anderson, W., Katul, G.G., Mahrt, L., 2020. The persistent challenge of surface heterogeneity in boundary-layer meteorology: A review. Boundary Layer Meteorology. 177, 227-245. https://doi.org/10.1007/s10546-020-00551-8.

Bretherton, C., 1997. Convection in stratocumulus-topped atmospheric boundary layers, in: The physics and parameterization of moist atmospheric convection, Springer, pp. 127-142. https://doi.org/http://10.1007/978-94-015-8828-7_5.

Bretherton, C.S., Wyant, M.C., 1997. Moisture Transport, Lower-Tropospheric Stability, and Decoupling of Cloud-Topped Boundary Layers Journal of the Atmospheric Sciences. 54, 148-167. https://doi.org/http://10.1175/1520-0469(1997)054<0148:Mtltsa>2.0.Co;2.

Brost, R.A., Lenschow, D.H., Wyngaard, J.C., 1982a. Marine stratocumulus layers. Part 1: mean conditions Journal of Atmospheric Sciences. 39, 800-817. https://doi.org/10.1175/1520-0469(1982)039<0800:Mslpmc>2.0.Co;2.

Brost, R.A., Wyngaard, J.C., Lenschow, D.H., 1982b. Marine stratocumulus layers. Part 1: mean conditions. Journal of Atmospheric Sciences. 39, 818-836. https://doi.org/10.1175/1520-0469(1982)039<0818:Mslpit>2.0.Co;2.

Brümmer, B., Lange, I., Konow, H., 2012. Atmospheric boundary layer measurements at the 280 m high Hamburg weather mast 1995-2011: mean annual and diurnal cycles. Meteorologische Zeitschrift. 319-335.

Busse, J., Knupp, K., 2012. Observed Characteristics of the Afternoon–Evening Boundary Layer Transition Based on Sodar and Surface Data Journal of Applied Meteorology

and Climatology. 51, 571-582. https://doi.org/https://doi.org/10.1175/2011JAMC2607.1.

Cai, X., Huo, Q., Kang, L., Song, Y., 2014. Equilibrium Atmospheric Boundary-Layer Flow: Computational Fluid Dynamics Simulation with Balanced Forces. Boundary-Layer Meteorology. 152, 349-366. https://doi.org/http://10.1007/s10546-014-9928-0.

Camp, D.W., Turner, R.E., Gilchrist, L.P., 1970. Response tests of cup, vane, and propeller wind sensors. Journal of Geophysical Research (1896-1977). 75, 5265-5270. https://doi.org/https://doi.org/10.1029/JC075i027p05265.

Campbell Scientific, Inc: 1998, CSAT Three Dimensional Sonic Anemometer Instruction Manual, Logan, UT, 14 pp.

Carleton, A.M., Song, Y., 1997. Synoptic climatology, and intrahemispheric associations, of cold air mesocyclones in the Australasian sector. Journal of Geophysical Research : Atmospheres. 102, 13873-13887. https://doi.org/https://doi.org/10.1029/96JD03357.

Carslaw, K.S., Boucher, O., Spracklen, D.V., Mann, G.W., Rae, J.G.L., Woodward, S., Kulmala, M., 2010. A review of natural aerosol interactions and feedbacks within the Earth system. Atmospheric Chemistry and Physics. 10, 1701-1737. https://doi.org/10.5194/acp-10-1701-2010.

Carslaw., K.S., Lee., L.A., Reddington., C.L., Pringle., K.J., Rap., A., Forster., P.M., Mann., G.W., Spracklen., D.V., Woodhouse., M.T., Regayre., L.A., Pierce., J.R., 2013. Large contribution of natural aerosols to uncertainty in indirect forcing. Nature. 503, 67-71. https://doi.org/10.1038/nature12674.

Carter, D.A., Gage, K.S., Ecklund, W.L., Angevine, W.M., Johnston, P.E., Riddle, A.C., Wilson, J., Williams, C.R., 1995. Developments in UHF lower tropospheric wind profiling at NOAA's Aeronomy Laboratory. Radio Science. 30, 977-1001. https://doi.org/https://doi.org/10.1029/95RS00649.

Catto, J.L., Jakob, C., Berry, G., Nicholls, N., 2012. Relating global precipitation to atmospheric fronts. Geophysical Research Letters. 39. https://doi.org/https://doi.org/10.1029/2012GL051736.

Caughey, S.J., 1984. Observed characteristics of the atmospheric boundary layer, in: Atmospheric Turbulence and Air Pollution Modelling, Springer, pp. 107-158.

Chandra, S., Srivastava, N., Kumar, M., 2019a. Vertical structure of atmospheric boundary layer over Ranchi during the summer monsoon season. Meteorology and Atmospheric Physics. 131. https://doi.org/http://10.1007/s00703-018-0600-y.

Chandra, S., Srivastava, N., Kumar, M., 2019b. Vertical structure of atmospheric boundary layer over Ranchi during the summer monsoon season. Meteorology and Atmospheric Physics. 131, 765-773. https://doi.org/10.1007/s00703-018-0600-y.

Chang, S., Huynh, G., Tofsted, D., Turbulence characteristics in Oklahoma City measured from an 83-meters pseudo tower. English Symposium on the Urban Environment. Phoenix, Arizona, January 12 (2009).

Chapman, C.C., Hogg, A.M., Kiss, A.E., Rintoul, S.R., 2015. The Dynamics of Southern Ocean Storm Tracks Journal of Physical Oceanography. 45, 884-903. https://doi.org/10.1175/jpo-d-14-0075.1.

Charlson, R.J., Pilat, M.J., 1969. Climate: The influence of aerosols Journal of Applied Meteorology and Climatology. 8, 1001-1002. https://doi.org/10.1175/1520-0450(1969)008<1001:Ctioa>2.0.Co;2.

Chelton, D.B., Esbensen, S.K., Schlax, M.G., Thum, N., Freilich, M.H., Wentz, F.J., Gentemann, C.L., McPhaden, M.J., Schopf, P.S., 2001. Observations of coupling between surface wind stress and sea surface temperature in the eastern Tropical Pacific. Journal of Climate. 14, 1479-1498. https://doi.org/http://dx.doi.org/10.1175/1520-0442(2001)014%3C1479:OOCBSW%3E2.0.CO;2.

Chepfer, H., Brogniez, H., Noel, V., 2019. Diurnal variations of cloud and relative humidity profiles across the tropics. Scientific Reports. 9, 16045. https://doi.org/10.1038/s41598-019-52437-6.

Christian, K., Wang, J., Ge, C., Peterson, D., Hyer, E., Yorks, J., McGill, M., 2019. Radiative forcing and stratospheric warming of pyrocumulonimbus smoke aerosols: first modelling results with multisensor (EPIC, CALIPSO, and CATS) Views from space. Geophysical Research Letters. 46, 10061-10071. https://doi.org/https://doi.org/10.1029/2019GL082360.

Chubb, T., Huang, Y., Jensen, J., Campos, T., Siems, S., Manton, M., 2016. Observations of high droplet number concentrations in Southern Ocean boundary layer clouds. Atmospheric Chemistry and Physics. 16, 971-987. https://doi.org/https://doi.org/10.5194/acp-16-971-2016.

Chýlek, P., Lesins, G.B., Videen, G., Wong, J.G.D., Pinnick, R.G., Ngo, D., Klett, J.D., 1996. Black carbon and absorption of solar radiation by clouds. Journal of Geophysical Research: Atmospheres. 101, 23365-23371. https://doi.org/https://doi.org/10.1029/96JD01901.

Clarke, A.D., Freitag, S., Simpson, R.M.C., Hudson, J.G., Howell, S.G., Brekhovskikh, V.L., Campos, T., Kapustin, V.N., Zhou, J., 2013. Free troposphere as a major source of CCN for the equatorial pacific boundary layer: long-range transport and teleconnections. Atmos. Chem. Phys. 13, 7511-7529. https://doi.org/http://10.5194/acp-13-7511-2013.

Clarke, A.D., Noone, K.J., 1985. Soot in the Arctic snowpack: a cause for perturbations in radiative transfer. Atmospheric Environment. 19, 2045-2053. https://doi.org/10.1016/0004-6981(85)90113-1.

Clarke, R.H., Dyer, A.J., Brook, R., Reid, D., Troup, A., 1971. The Wangara experiment: Boundary layer data.

Connolley, W.M., 1996. The Antartic temperature inversion. International Journal of Climatology. 16, 1333-1342. https://doi.org/https://doi.org/10.1002/(SICI)1097-0088(199612)16:12<1333::AID-JOC96>3.0.CO;2-6.

Couldrey, M.P., Jullion, L., Naveira Garabato, A.C., Rye, C., Herráiz-Borreguero, L., Brown, P.J., Meredith, M.P., Speer, K.L., 2013. Remotely induced warming of Antarctic Bottom Water in the eastern Weddell gyre. Geophysical Research Letters. 40, 2755-2760. https://doi.org/https://doi.org/10.1002/grl.50526.

Crosman, E.T., Horel, J.D., 2010. Sea and Lake Breezes: A Review of Numerical Studies. Boundary-Layer Meteorology. 137, 1-29. https://doi.org/http://10.1007/s10546-010-9517-9.

Cuxart, J., Holtslag, A.A.M., Beare, R.J., Bazile, E., Beljaars, A., Cheng, A., Conangla, L., Ek, M., Freedman, F., Hamdi, R., Kerstein, A., Kitagawa, H., Lenderink, G., Lewellen, D., Mailhot, J., Mauritsen, T., Perov, V., Schayes, G., Steeneveld, G.J., Svensson, G., Taylor, P., Weng, W., Wunsch, S., Xu, K.M., 2006. Single-Column Model Intercomparison for a Stably Stratified Atmospheric Boundary Layer. Boundary Layer Meteorology. 118, 273-303. https://doi.org/10.1007/s10546-005-3780-1.

Davis, E.V., Rajeev, K., Mishra, M.K., 2020. Effect of clouds on the diurnal evolution of the atmospheric boundary layer height over a tropical coastal station. Boundary Layer Meteorology. 175, 135-152. https://doi.org/10.1007/s10546-019-00497-6.

Davis, E.V., Rajeev, K., Sambhu Namboodiri, K.V., 2022. The convective-atmospheric-boundary-layer height and its dependence upon meteorological variables at a tropical coastal station during onshore and offshore flows. Boundary Layer Meteorology. 183, 143-166. https://doi.org/10.1007/s10546-021-00665-7.

de Boyer Montégut, C., Madec, G., Fischer, A.S., Lazar, A., Iudicone, D., 2004a. Mixed layer depth over the global ocean: An examination of profile data and a profile-based climatology. Journal of Geophysical Research: Oceans. 109. https://doi.org/https://doi.org/10.1029/2004JC002378.

de Boyer Montégut, C., Madec, G., Fischer, A.S., Lazar, A., Iudicone, D., 2004b. Mixed layer depth over the global ocean: An examination of profile data and a profile-based climatology. Journal of Geophysical Research : Atmospheres. 109. https://doi.org/https://doi.org/10.1029/2004JC002378.

de Szoeke, S.P., Skyllingstad, E.D., Zuidema, P., Chandra, A.S., 2017. Cold pools and their influence on the tropical marine boundary layer. Journal of the Atmospheric Sciences. 74, 1149-1168. https://doi.org/10.1175/jas-d-16-0264.1.

De Tomasi, F., Miglietta, M.M., Perrone, M.R., 2011. The Growth of the Planetary Boundary Layer at a Coastal Site: a Case Study. Boundary-Layer Meteorology. 139, 521-541. https://doi.org/10.1007/s10546-011-9592-6.

Deacon, G., 1937. The hydrology of the southern ocean. Cambridge University Press ; Macmillan, London; New York.

Deardorff, J.W., 1980. Stratocumulus-capped mixed layers derived from a three-dimensional model. Boundary Layer Meteorology. 18, 495-527. https://doi.org/10.1007/BF00119502.

Deardorff, J.W., 1974. Three-dimensional numerical study of turbulence in an entraining mixed layer. Boundary Layer Meteorology. 7, 199-226. https://doi.org/10.1007/BF00227913.

Deardorff, J.W., Willis, G.E., 1985. Further results from a laboratory model of the convective planetary boundary layer. Boundary Layer Meteorology. 32, 205-236. https://doi.org/10.1007/BF00121880.

Deardorff, J.W., Willis, G.E., Stockton, B.H., 1980. Laboratory studies of the entrainment zone of a convectively mixed layer. Journal of Fluid Mechanics. 100, 41-64. https://doi.org/10.1017/S0022112080001000.

Deb Burman, P.K., Prabha, T.V., Morrison, R., Karipot, A., 2018. A Case Study of Turbulence in the Nocturnal Boundary Layer During the Indian Summer Monsoon.

Boundary-Layer Meteorology. 169, 115-138. https://doi.org/http://10.1007/s10546-018-0364-4.

Dharmaraj, T., Chinthalu, G.R., Raj, P.E., 2009. Turbulence characteristics in the atmospheric surface layer during summer monsoon of 1997 over a semi-arid location in India. Meteorology and Atmospheric Physics. 104, 113-123. https://doi.org/10.1007/s00703-009-0022-y.

Divya, U.S., Girija, J., Satyanarayana, S., Zachariah, J.P., 2014. An advanced radiosonde system for aerospace applications. Journal of Atmospheric and Oceanic Technology. 31, 2067-2077. https://doi.org/https://doi.org/10.1175/JTECH-D-13-00050.1.

Dong, X., Schwantes, A.C., Xi, B., Wu, P., 2015. Investigation of the marine boundary layer cloud and CCN properties under coupled and decoupled conditions over the Azores. Journal of Geophysical Research: Atmospheres. 120, 6179-6191. https://doi.org/https://doi.org/10.1002/2014JD022939.

Draxler, R.R., Rolph, G.D., HYSPLIT (HYbrid Single-Particle Lagrangian Integrated Trajectory) Model, NOAA Air Resources Laboratory, Silver Spring, MD. Md, Silver Spring (2003).

Driedonks, A.G.M., 1982. Models and observations of the growth of the atmospheric boundary layer. Boundary Layer Meteorology. 23, 283-306. https://doi.org/10.1007/BF00121117.

Dyer, A.J., Garratt, J.R., Francey, R.J., McIlroy, I.C., Bacon, N.E., Hyson, P., Bradley, E.F., Denmead, O.T., Tsvang, L.R., Volkov, Y.A., Koprov, B.M., Elagina, L.G., Sahashi, K., Monji, N., Hanafusa, T., Tsukamoto, O., Frenzen, P., Hicks, B.B., Wesely, M., Miyake, M., Shaw, W., 1982. An international turbulence comparison experiment (ITCE 1976). Boundary Layer Meteorology. 24, 181-209. https://doi.org/10.1007/BF00121667.

Edson, J., Paluszkiewicz, T., Sandgathe, S., Vincent, L., Goodman, L., Curtin, T., Hollister, J., Colton, M., Anderson, S., Andreas, E., 1999. Coupled marine boundary layers and air-sea interaction initiative: Combining process studies, simulations, and numerical models. Office of Naval Reasearch.

Edwards, J.M., Beljaars, A.C.M., Holtslag, A.A.M., Lock, A.P., 2020. Representation of Boundary-Layer Processes in Numerical Weather Prediction and Climate Models. Boundary-Layer Meteorology. 177, 511-539. https://doi.org/10.1007/s10546-020-00530-z.

Efstathiou, G.A., Plant, R.S., Bopape, M.-J.M., 2018. Simulation of an evolving convective boundary layer using a scale-dependent dynamic Smagorinsky model at near-gray-zone resolutions. Journal of Applied Meteorology and Climatology. 57, 2197-2214. https://doi.org/10.1175/jamc-d-17-0318.1.

Falabino, S., Trini Castelli, S., 2017. Estimating wind velocity standard deviation values in the inertial sublayer from observations in the roughness sublayer. Meteorology and Atmospheric Physics. 129, 83-98. https://doi.org/10.1007/s00703-016-0457-x.

Falge, E., Baldocchi, D., Olson, R., Anthoni, P., Aubinet, M., Bernhofer, C., Burba, G., Ceulemans, R., Clement, R., Dolman, H., Granier, A., Gross, P., Grünwald, T., Hollinger, D., Jensen, N.-O., Katul, G., Keronen, P., Kowalski, A., Ta Lai, C., Law, B.E., Meyers, T., Moncrieff, J., Moors, E., William Munger, J., Pilegaard, K., Rannik, Ü., Rebmann, C., Suyker, A., Tenhunen, J., Tu, K., Verma, S., Vesala, T., Wilson, K., Wofsy, S., 2001. Gap filling strategies for long term energy flux data sets. Agricultural and Forest Meteorology. 107, 71-77. https://doi.org/https://doi.org/10.1016/S0168-1923(00)00235-5.

Fan, J., Wang, Y., Rosenfeld, D., Liu, X., 2016. Review of aerosol–cloud interactions: mechanisms, significance, and challenges. Journal of the Atmospheric Sciences. 73, 4221-4252. https://doi.org/10.1175/JAS-D-16-0037.1.

Fedorovich, E., Gibbs, J.A., Shapiro, A., 2017. Numerical Study of Nocturnal Low-Level Jets over Gently Sloping Terrain Journal of the Atmospheric Sciences. 74, 2813-2834. https://doi.org/https://doi.org/10.1175/JAS-D-17-0013.1.

Field, P.R., Wood, R., 2007. Precipitation andcloud structure in midlatitude cyclones. Journal of Climate. 20, 233-254. https://doi.org/10.1175/jcli3998.1.

Finnigan, J., Ayotte, K., Harman, I., Katul, G., Oldroyd, H., Patton, E., Poggi, D., Ross, A., Taylor, P., 2020. Boundary-Layer Flow Over Complex Topography. Boundary-Layer Meteorology. 177, 247-313. https://doi.org/http://10.1007/s10546-020-00564-3.

Fitzjarrald, D.R., Garstang, M., 1981. Vertical Structure of the Tropical Boundary Layer Monthly Weather Review. 109, 1512-1526. https://doi.org/https://doi.org/10.1175/1520-0493(1981)109<1512:VSOTTB>2.0.CO;2.

Foken, T., 2006. 50 Years of the Monin–Obukhov Similarity Theory. Boundary Layer Meteorology. 119, 431-447. https://doi.org/10.1007/s10546-006-9048-6.

Foken, T., Napo, C.J., 2008. Micrometeorology. Springer.

Foken, T., Wichura, B., 1996. Tools for quality assessment of surface-based flux measurements. Agricultural and Forest Meteorology. 78, 83-105. https://doi.org/https://doi.org/10.1016/0168-1923(95)02248-1.

Forbes, R.M., Hogan, R.J., 2006. Observations of the depth of ice particle evaporation beneath frontal cloud to improve NWP modelling. Quarterly Journal of the Royal Meteorological Society. 132, 865-883. https://doi.org/https://doi.org/10.1256/qj.04.187.

Forrer, J., Rotach, M.W., 1997. On the turbulence structure in the stable boundary layer over the Greenland ice sheet. Boundary Layer Meteorology. 85, 111-136. https://doi.org/10.1023/A:1000466827210.

Fortuniak, K., Pawlak, W., Siedlecki, M., 2013. Integral turbulence statistics over a Central European City Centre. Boundary Layer Meteorology. 146, 257-276. https://doi.org/10.1007/s10546-012-9762-1.

Fossum, K.N., Ovadnevaite, J., Ceburnis, D., Dall'Osto, M., Marullo, S., Bellacicco, M., Simó, R., Liu, D., Flynn, M., Zuend, A., O'Dowd, C., 2018. Summertime primary and secondary contributions to southern ocean cloud condensation nuclei. Scientific Reports. 8, 13844. https://doi.org/10.1038/s41598-018-32047-4.

Francey, R.J., Garratt, J.R., 1981. Interpretation of Flux-Profile Observations at ITCE (1976). Journal of Applied Meteorology and Climatology. 20, 603-618. https://doi.org/10.1175/1520-0450(1981)020<0603:IOFPOA>2.0.CO;2.

Franchito, S.H., Brahmananda Rao, V., Oda, T.O., Conforte, J.C., 2007. An observational study of the evolution of the atmospheric boundary-layer over Cabo Frio, Brazil. Ann. Geophys. 25, 1735-1744. https://doi.org/10.5194/angeo-25-1735-2007.

Furtado, K., Field, P., 2017. The role of ice microphysics parametrizations in determining the prevalence of supercooled liquid water in high-resolution simulations of a Southern Ocean midlatitude cyclone. Journal of the Atmospheric Sciences. 74, 2001-2021. https://doi.org/10.1175/jas-d-16-0165.1.

Ganguly, D., Gadhavi, H., Jayaraman, A., Rajesh, T.A., Misra, A., 2005. Single scattering albedo of aerosols over the central India: Implications for the regional aerosol radiative forcing. Geophysical Research Letters. 32. https://doi.org/https://doi.org/10.1029/2005GL023903.

Garratt, J., 1992. Extreme maximum land surface temperatures. Journal of Applied Meteorology and Climatology. 31, 1096-1105. https://doi.org/10.1175/1520-0450(1992)031<1096:EMLST>2.0.CO;2.

Garratt, J., 1990. The internal boundary layer - A review. Boundary Layer Meteorology. 50, 171-203. https://doi.org/http:// 10.1007/BF00120524.

Garratt, J., 1982. Observations in the nocturnal boundary layer. Boundary Layer Meteorology. 22, 21-48.

Garratt, J., 1994. Review: The atmospheric boundary layer. Earth-Science Reviews. 37, 89-134.

Garratt, J., 1993. Sensitivity of climate simulations to land-surface and atmospheric boundary-layer treatments - A review. Journal of Climate. 6, 419-448. https://doi.org/10.1175/1520-0442(1993)006<0419:SOCSTL>2.0.CO;2.

Garratt, J., Hess, G., Physick, W., Bougeault, P., 1996. The atmospheric boundary layer — advances in knowledge and application. Boundary Layer Meteorology. 78, 9-37. https://doi.org/10.1007/BF00122485.

Garratt, J., Physick, W., 1985. The inland boundary layer at low latitudes: II Sea-breeze influences. Boundary Layer Meteorology. 33, 209-231. https://doi.org/10.1007/BF00052056.

Geernaert, G., 2003. Boundary Layers | Surface Layer, in, pp. 305-311. https://doi.org/10.1016/B0-12-227090-8/00092-0.

Gera, B.S., Singal, S.P., Saxena, N., Ramakrishna, Y.S., 1996. Atmospheric boundary layer studies at Jodhpur during MONTBLEX using sodar and tower. Proceedings of the Indian Academy of Sciences - Earth and Planetary Sciences. 105, 261-272. https://doi.org/http://10.1007/BF02841882.

Ghan, S.J., Smith, S.J., Wang, M., Zhang, K., Pringle, K., Carslaw, K., Pierce, J., Bauer, S., Adams, P., 2013. A simple model of global aerosol indirect effects. Journal of Geophysical Research : Atmospheres. 118, 6688-6707. https://doi.org/https://doi.org/10.1002/jgrd.50567.

Goel, M., Srivastava, H.N., 1990. Monsoon Trough Boundary Layer Experiment (MONTBLEX). Bulletin of the American Meteorological Society. 71, 1594-1600. https://doi.org/http://10.1175/1520-0477(1990)071<1594:Mtble>2.0.Co;2.

Govardhan, G., Satheesh, S.K., Moorthy, K.K., Nanjundiah, R., 2019. Simulations of black carbon over the Indian region: improvements and implications of diurnality in emissions. Atmos. Chem. Phys. 19, 8229-8241. https://doi.org/http://10.5194/acp-19-8229-2019.

Grachev, A., Andreas, E., Fairall, C., Guest, P., Persson, O., 2014. Similarity theory based on the Dougherty-Ozmidov length scale. Quarterly Journal of the Royal Meteorological Society. 141. https://doi.org/10.1002/qj.2488.

Grachev, A., Krishnamurthy, R., Fernando, H., Fairall, C., Bardoel, S., Wang, S., 2021. Atmospheric turbulence measurements at a coastal zone with and without fog. Boundary Layer Meteorology. 181. https://doi.org/10.1007/s10546-021-00655-9.

Grachev, A., Leo, L., Di Sabatino, S., Fernando, H., Pardyjak, E., Fairall, C., 2015. Structure of turbulence in katabatic flows below and above the wind-speed maximum. Boundary Layer Meteorology. 159. https://doi.org/10.1007/s10546-015-0034-8.

Grachev, A., Leo, L., Fernando, H., Fairall, C., Creegan, E., Blomquist, B., Christman, A., Hocut, C., 2018a. Air-sea/land interaction in the coastal zone. Boundary Layer Meteorology. 167, 181-210. https://doi.org/10.1007/s10546-017-0326-2.

Grachev, A., Persson, O., Uttal, T., Akish, E., Cox, C., Morris, S., Fairall, C., Stone, R., Lesins, G., Makshtas, A., Repina, I., 2018b. Seasonal and latitudinal variations of surface fluxes at two Arctic terrestrial sites. Climate Dynamics. 51. https://doi.org/10.1007/s00382-017-3983-4.

Grachev, A.A., Andreas, E.L., Fairall, C.W., Guest, P.S., Persson, P.O.G., 2013. The critical Richardson number and limits of applicability of local similarity theory in the stable boundary layer. Boundary Layer Meteorology. 147, 51-82. https://doi.org/10.1007/s10546-012-9771-0.

Grachev, A.A., Andreas, E.L., Fairall, C.W., Guest, P.S., Persson, P.O.G., 2007. SHEBA flux–profile relationships in the stable atmospheric boundary layer. Boundary Layer Meteorology. 124, 315-333. https://doi.org/10.1007/s10546-007-9177-6.

Gras, J., 1995. CN, CCN and particle size in Southern Ocean air at Cape Grim. Atmospheric Research. 35, 233-251.

Grimmond, C.S.B., Oke, T.R., 1999. Aerodynamic properties of urban areas derived from analysis of surface form Journal of Applied Meteorology and Climatology. 38, 1262-1292. https://doi.org/10.1175/1520-0450(1999)038<1262:Apouad>2.0.Co;2.

Groß, S., Freudenthaler, V., Schepanski, K., Toledano, C., Schäfler, A., Ansmann, A., Weinzierl, B., 2015. Optical properties of long-range transported Saharan dust over Barbados as measured by dual-wavelength depolarization Raman lidar measurements. Atmospheric Chemistry and Physics. 15, 11067-11080. https://doi.org/10.5194/acp-15-11067-2015.

Guo, J., Su, T., Chen, D., Wang, J., Li, Z., Lv, Y., Guo, X., Liu, H., Cribb, M., Zhai, P., 2019. Declining summertime local-scale precipitation frequency over China and the United States, 1981–2012: the disparate roles of aerosols. Geophysical Research Letters. 46, 13281-13289. https://doi.org/https://doi.org/10.1029/2019GL085442.

Guo, P., Kuo, Y.-H., Sokolovskiy, S.V., Lenschow, D.H., 2011. Estimating atmospheric boundary layer depth using cosmic radio occultation data. Journal of the Atmospheric Sciences. 68, 1703-1713. https://doi.org/10.1175/2011jas3612.1.

Hadfield, M.G., Cotton, W.R., Pielke, R.A., 1991a. Large-eddy simulations of thermally forced circulations in the convective boundary layer. Part I: A small-scale circulation with zero wind. Boundary-Layer Meteorology. 57, 79-114. https://doi.org/10.1007/BF00119714.

Hadfield, M.G., Cotton, W.R., Pielke, R.A., 1991b. Large-eddy simulations of thermally forced circulations in the convective boundary layer. Part I: A small-scale circulation with zero wind. Boundary Layer Meteorology. 57, 79-114. https://doi.org/10.1007/BF00119714.

Hamilton, L.J., 2006. Structure of the subtropical front in the Tasman sea. Deep Sea Research Part I: Oceanographic Research Papers. 53, 1989-2009. https://doi.org/https://doi.org/10.1016/j.dsr.2006.08.013.

Hande, L.B., Siems, S.T., Manton, M.J., Belusic, D., 2012. Observations of wind shear over the Southern Ocean. Journal of Geophysical Research : Atmospheres. 117. https://doi.org/https://doi.org/10.1029/2012JD017488.

Hande, L.B., Siems, S.T., Manton, M.J., Lenschow, D.H., 2015. An evaluation of COSMIC radio occultation data in the lower atmosphere over the Southern Ocean. Atmospheric Measurement Techniques. 8, 97-107. https://doi.org/10.5194/amt-8-97-2015.

Hansen, A.D.A., Rosen, H., Novakov, T., 1984. The aethalometer — An instrument for the real-time measurement of optical absorption by aerosol particles. Science of the Total Environment. 36, 191-196. https://doi.org/10.1016/0048-9697(84)90265-1.

Hansen, J., Nazarenko, L., 2004. Soot climate forcing via snow and ice albedos. Proceedings of the National Academy of Sciences. 101, 423-428. https://doi.org/10.1073/pnas.2237157100.

Hansen, J., Sato, M., Ruedy, R., 1997. Radiative forcing and climate response. Journal of Geophysical Research: Atmospheres. 102, 6831-6864. https://doi.org/https://doi.org/10.1029/96JD03436.

Hariprasad, K.B.R.R., Srinivas, C.V., Singh, A.B., Vijaya Bhaskara Rao, S., Baskaran, R., Venkatraman, B., 2014. Numerical simulation and intercomparison of boundary layer structure with different PBL schemes in WRF using experimental observations at a tropical site. Atmospheric Research. 145-146, 27-44. https://doi.org/https://doi.org/10.1016/j.atmosres.2014.03.023.

Harriss, R.C., Garstang, M., Wofsy, S.C., Beck, S.M., Bendura, R.J., Coelho, J.R.B., Drewry, J.W., Hoell Jr, J.M., Matson, P.A., McNeal, R.J., Molion, L.C.B., Navarro, R.L., Rabine, V., Snell, R.L., 1990. The Amazon Boundary Layer Experiment: Wet season 1987. Journal of Geophysical Research: Atmospheres. 95, 16721-16736. https://doi.org/https://doi.org/10.1029/JD095iD10p16721.

Harvey, N.J., Hogan, R.J., Dacre, H.F., 2013. A method to diagnose boundary-layer type using Doppler lidar. Quarterly Journal of the Royal Meteorological Society. 139, 1681-1693. https://doi.org/https://doi.org/10.1002/qj.2068.

Haumann, F.A., Moorman, R., Riser, S.C., Smedsrud, L.H., Maksym, T., Wong, A.P.S., Wilson, E.A., Drucker, R., Talley, L.D., Johnson, K.S., Key, R.M., Sarmiento, J.L., 2020. Supercooled Southern Ocean waters. Geophysical Research Letters. 47, e2020GL090242. https://doi.org/https://doi.org/10.1029/2020GL090242.

Haynes, J.M., Jakob, C., Rossow, W.B., Tselioudis, G., Brown, J., 2011. Major characteristics of Southern Ocean cloud regimes and their effects on the energy budget. Journal of Climate. 24, 5061-5080. https://doi.org/https://doi.org/10.1175/2011JCLI4052.1.

Hersbach, H., Bell, B., Berrisford, P., Biavati, G., Dee, D., Horányi, A., Nicolas, J., Peubey, C., Radu, R., Rozum, I., Muñoz-Sabater, J., Schepers, D., Simmons, A., Soci, C., Thépaut, J.-N., Vamborg, F., The ERA5 global atmospheric reanalysis at ECMWF as a comprehensive dataset for climate data homogenization, climate variability, trends and extremes. 21st EGU General Assembly, EGU2019,, Vienna, Austria (2019), p. 10826.

Hersbach, H., Bell, B., Berrisford, P., Hirahara, S., Horányi, A., Muñoz-Sabater, J., Nicolas, J., Peubey, C., Radu, R., Schepers, D., Simmons, A., Soci, C., Abdalla, S., Abellan, X., Balsamo, G., Bechtold, P., Biavati, G., Bidlot, J., Bonavita, M., De Chiara, G., Dahlgren, P., Dee, D., Diamantakis, M., Dragani, R., Flemming, J., Forbes, R., Fuentes, M., Geer, A., Haimberger, L., Healy, S., Hogan, R.J., Hólm, E., Janisková, M., Keeley, S., Laloyaux, P., Lopez, P., Lupu, C., Radnoti, G., de Rosnay, P., Rozum, I., Vamborg, F., Villaume, S., Thépaut, J.-N., 2020. The ERA5 global

reanalysis. Quarterly Journal of the Royal Meteorological Society. 146, 1999-2049. https://doi.org/https://doi.org/10.1002/qj.3803.

Hess, M., Koepke, P., Schreier, F., Trautmann, T., The Aerosol Model OPAC - Contents and New Software. GEISA Workshop: Towards a new vision of spectroscopic databases (2014).

Hess, M., Koepke, P., Schult, I., 1998. Optical Properties of Aerosols and Clouds: The Software Package OPAC. Bulletin of the American Meteorological Society. 79, 831-844. https://doi.org/10.1175/1520-0477(1998)079<0831:Opoaac>2.0.Co;2.

Hofmann, D.J., Rosen, J.M., 1981. On the background stratospheric aerosol layer. Journal of Atmospheric Sciences. 38, 168-181. https://doi.org/10.1175/1520-0469(1981)038<0168:OTBSAL>2.0.CO;2.

Hogan, R.J., Grant, A.L.M., Illingworth, A.J., Pearson, G.N., O'Connor, E.J., 2009. Vertical velocity variance and skewness in clear and cloud-topped boundary layers as revealed by Doppler lidar. Quarterly Journal of the Royal Meteorological Society. 135, 635-643. https://doi.org/https://doi.org/10.1002/qj.413.

Högström, U., 1996. Review of some basic characteristics of the atmospheric surface layer. Boundary Layer Meteorology. 78, 215-246. https://doi.org/10.1007/BF00120937.

Högström, U., Bergström, H., Alexandersson, H., 1982. Turbulence characteristics in a near neutrally stratified urban atmosphere. Boundary Layer Meteorology. 23, 449-472.

Holt, T., Sethuraman, S., 1985. Aircraft and ship observations of the mean structure of the marine boundary layer over the Arabian Sea during MONEX 79. Boundary Layer Meteorology. 33, 259-282. https://doi.org/http://10.1007/BF00052059.

Holte, J., Talley, L.D., Gilson, J., Roemmich, D., 2017. An Argo mixed layer climatology and database. Geophysical Research Letters. 44, 5618-5626. https://doi.org/https://doi.org/10.1002/2017GL073426.

Holtslag, A.A.M., Svensson, G., Baas, P., Basu, S., Beare, B., Beljaars, A.C.M., Bosveld, F.C., Cuxart, J., Lindvall, J., Steeneveld, G.J., Tjernström, M., Van De Wiel, B.J.H., 2013. Stable atmospheric boundary layers and diurnal cycles: challenges for weather and climate models. Bulletin of the American Meteorological Society. 94, 1691-1706. https://doi.org/10.1175/bams-d-11-00187.1.

Honnert, R., Efstathiou, G.A., Beare, R.J., Ito, J., Lock, A., Neggers, R., Plant, R.S., Shin, H.H., Tomassini, L., Zhou, B., 2020. The atmospheric boundary layer and the “gray zone” of turbulence: A critical review. Journal of Geophysical Research :

Atmospheres. 125, e2019JD030317. https://doi.org/https://doi.org/10.1029/2019JD030317.

Hopkins, F.E., Suntharalingam, P., Gehlen, M., Andrews, O., Archer, S.D., Bopp, L., Buitenhuis, E., Dadou, I., Duce, R., Goris, N., Jickells, T., Johnson, M., Keng, F., Law, C.S., Lee, K., Liss, P.S., Lizotte, M., Malin, G., Murrell, J.C., Naik, H., Rees, A.P., Schwinger, J., Williamson, P., 2020. The impacts of ocean acidification on marine trace gases and the implications for atmospheric chemistry and climate. Proceedings of Royal Society A. 476. https://doi.org/https://doi.org/10.1098/rspa.2019.0769.

Hoppel, W.A., Frick, G.M., Fitzgerald, J.W., 2002. Surface source function for sea-salt aerosol and aerosol dry deposition to the ocean surface. Journal of Geophysical Research : Atmospheres. 107, AAC 7-1-AAC 7-17. https://doi.org/https://doi.org/10.1029/2001JD002014.

Hoskins, B.J., Hodges, K.I., 2005. A new perspective on southern hemisphere storm tracks Journal of Climate. 18, 4108-4129. https://doi.org/https://doi.org/10.1175/JCLI3570.1.

Hu, X.-M., Hu, J., Gao, L., Cai, C., Jiang, Y., Xue, M., Zhao, T., Crowell, S.M.R., 2021. Multisensor and Multimodel Monitoring and Investigation of a Wintertime Air Pollution Event Ahead of a Cold Front Over Eastern China. Journal of Geophysical Research : Atmospheres. 126, e2020JD033538. https://doi.org/https://doi.org/10.1029/2020JD033538.

Huang, Y., Franklin, C.N., Siems, S.T., Manton, M.J., Chubb, T., Lock, A., Alexander, S., Klekociuk, A., 2015a. Evaluation of boundary-layer cloud forecasts over the Southern Ocean in a limited-area numerical weather prediction system usingin situ, space-borne and ground-based observations. Quarterly Journal of the Royal Meteorological Society. 141, 2259-2276. https://doi.org/https://doi.org/10.1002/qj.2519.

Huang, Y., Protat, A., Siems, S.T., Manton, M.J., 2015b. A-Train observations of maritime midlatitude storm-track cloud systems: comparing the Southern Ocean against the north Atlantic. Journal of Climate. 28, 1920-1939. https://doi.org/https://doi.org/10.1175/JCLI-D-14-00169.1.

Huang, Y., Siems, S.T., Manton, M.J., Hande, L.B., Haynes, J.M., 2012. The structure of low-altitude clouds over the Southern Ocean as seen by CLOUDSAT. Journal of

Climate. 25, 2535-2546. https://doi.org/https://doi.org/10.1175/JCLI-D-11-00131.1.

Huang, Y., Siems, S.T., Manton, M.J., Thompson, G., 2014. An evaluation of WRF simulations of clouds over the Southern Ocean with A-Train observations. Monthly Weather Review. 142, 647-667. https://doi.org/http://10.1175/mwr-d-13-00128.1.

Hulswar, S., Menon, H.B., Anilkumar, N., 2020. Physical-chemical characteristics of composite aerosols in the Indian Ocean sector of the Southern Ocean and its associated effect on insolation: A climate perspective. Deep Sea Research Part II: Topical Studies in Oceanography. 178, 104801. https://doi.org/https://doi.org/10.1016/j.dsr2.2020.104801.

Humphries, R.S., Keywood, M.D., Gribben, S., McRobert, I.M., Ward, J.P., Selleck, P., Taylor, S., Harnwell, J., Flynn, C., Kulkarni, G.R., Mace, G.G., Protat, A., Alexander, S.P., McFarquhar, G., 2021. Southern Ocean latitudinal gradients of cloud condensation nuclei. Atmospheric Chemistry and Physics. 21, 12757-12782. https://doi.org/http://10.5194/acp-21-12757-2021.

Hyder, P., Edwards, J.M., Allan, R.P., Hewitt, H.T., Bracegirdle, T.J., Gregory, J.M., Wood, R.A., Meijers, A.J.S., Mulcahy, J., Field, P., Furtado, K., Bodas-Salcedo, A., Williams, K.D., Copsey, D., Josey, S.A., Liu, C., Roberts, C.D., Sanchez, C., Ridley, J., Thorpe, L., Hardiman, S.C., Mayer, M., Berry, D.I., Belcher, S.E., 2018. Critical Southern Ocean climate model biases traced to atmospheric model cloud errors. Nature Communications. 9, 3625. https://doi.org/10.1038/s41467-018-05634-2.

IPCC, 2014. Climate Change 2013 – The Physical Science Basis: Working Group I Contribution to the Fifth Assessment Report of the Intergovernmental Panel on Climate Change. Cambridge University Press, Cambridge https://doi.org/http://10.1017/CBO9781107415324.

IPCC, 2013. Climate Change 2013: The Physical Science Basis. . T. F. Stocker et al., Eds., Cambridge University Press, 1535 pp.

Irving, D., Simmonds, I., Keay, K., 2010. Mesoscale cyclone activity over the ice-free Southern Ocean: 1999–2008. Journal of Climate. 23, 5404-5420. https://doi.org/https://doi.org/10.1175/2010JCLI3628.1.

Jaenicke, R., 1980. Natural aerosols. Annals of the New York Academy of Sciences. 338, 317-329.

Jain, A.R., Panwar, V., Mandal, T.K., Rao, V.R., Goel, A., Gautam, R., Das, S.S., Dhaka, S.K., 2010. Mesoscale convection system and occurrence of extreme low tropopause temperatures: observations over Asian summer monsoon region. Ann. Geophys. 28, 927-940. https://doi.org/http://10.5194/angeo-28-927-2010.

Jeeva Prakash, J.W., Ramachandran, R., Nair, K.N., Sen Gupta, K., Kunhikrishnan, P.K., 1992. On the structure of sea-breeze fronts observed near the coastline of Thumba, India. Boundary-Layer Meteorology. 59, 111-124. https://doi.org/http://10.1007/BF00120689.

Jensen, D.D., Nadeau, D.F., Hoch, S.W., Pardyjak, E.R., 2016. Observations of near-surface heat-flux and temperature profiles through the early evening transition over contrasting surfaces. Boundary Layer Meteorology. 159, 567-587. https://doi.org/10.1007/s10546-015-0067-z.

Jensen, J.B., Lee, S., Krummel, P.B., Katzfey, J., Gogoasa, D., 2000. Precipitation in marine cumulus and stratocumulus.: Part I: Thermodynamic and dynamic observations of closed cell circulations and cumulus bands. Atmospheric Research. 54, 117-155. https://doi.org/https://doi.org/10.1016/S0169-8095(00)00040-5.

Johnson, R.H., Ciesielski, P.E., 2017. Multiscale variability of the atmospheric boundary layer during DYNAMO. Journal of the Atmospheric Sciences. 74, 4003-4021. https://doi.org/10.1175/jas-d-17-0182.1.

Jones, C.R., Bretherton, C.S., Leon, D., 2011. Coupled vs. decoupled boundary layers in VOCALS-REx. Atmospheric Chemistry and Physics. 11, 7143-7153. https://doi.org/10.5194/acp-11-7143-2011.

Jullien, N., Vignon, É., Sprenger, M., Aemisegger, F., Berne, A., 2020. Synoptic conditions and atmospheric moisture pathways associated with virga and precipitation over coastal Adélie Land in Antarctica. The Cryosphere. 14, 1685-1702. https://doi.org/https://doi.org/10.3929/ethz-b-000418970.

Kailas, S., Goel, M., 1996. Planning MONTBLEX — An overview. Proceedings of the Indian Academy of Sciences - Earth and Planetary Sciences. 105, 209-225. https://doi.org/http://10.1007/BF02841880.

Kaimal, J.C., 1973. Turbulenece spectra, length scales and structure parameters in the stable surface layer. Boundary Layer Meteorology. 4, 289-309. https://doi.org/10.1007/BF02265239.

Kaimal, J.C., Finnigan, J.J., 1994. Atmospheric boundary layer flows: their structure and measurement. Oxford university press.

Kaimal, J.C., Gaynor, J.E., 1991. Another look at sonic thermometry. Boundary Layer Meteorology. 56, 401-410. https://doi.org/10.1007/BF00119215.

Kaimal, J.C., Wyngaard, J.C., 1990. The Kansas and Minnesota experiments. Boundary Layer Meteorology. 50, 31-47. https://doi.org/10.1007/BF00120517.

Kaimal, J.C., Wyngaard, J.C., Haugen, D.A., Coté, O.R., Izumi, Y., Caughey, S.J., Readings, C.J., 1976. Turbulence structure in the convective boundary layer. Journal of Atmospheric Sciences. 33, 2152-2169. https://doi.org/10.1175/1520-0469(1976)033<2152:Tsitcb>2.0.Co;2.

Kaimal, J.C., Wyngaard, J.C., Izumi, Y., Coté, O.R., 1972. Spectral characteristics of surface-layer turbulence. Quarterly Journal of the Royal Meteorological Society. 98, 563-589. https://doi.org/https://doi.org/10.1002/qj.49709841707.

Kala, J., Lyons, T.J., Abbs, D.J., Nair, U.S., 2010a. Numerical Simulations of the Impacts of Land-Cover Change on a Southern Sea Breeze in South-West Western Australia. Boundary-Layer Meteorology. 135, 485-503. https://doi.org/http://10.1007/s10546-010-9486-z.

Kala, J., Lyons, T.J., Abbs, D.J., Nair, U.S., 2010b. Numerical simulations of the impacts of land-cover change on a southern sea breeze in south-west western Australia. Boundary Layer Meteorology. 135, 485-503. https://doi.org/10.1007/s10546-010-9486-z.

Kala, J., Lyons, T.J., Nair, U.S., 2011. Numerical Simulations of the Impacts of Land-Cover Change on Cold Fronts in South-West Western Australia. Boundary-Layer Meteorology. 138, 121-138. https://doi.org/http://10.1007/s10546-010-9547-3.

Kannemadugu, H.b.s., 2019. Seasonal Characteristics of Atmospheric Boundary Layer and its Associated Dynamics over Central India. Asia-Pacific Journal of Atmospheric Sciences. https://doi.org/10.1007/s13143-019-00138-5.

Kaser, L., Patton, E.G., Pfister, G.G., Weinheimer, A.J., Montzka, D.D., Flocke, F., Thompson, A.M., Stauffer, R.M., Halliday, H.S., 2017. The effect of entrainment through atmospheric boundary layer growth on observed and modeled surface ozone in the Colorado Front Range. Journal of Geophysical Research: Atmospheres. 122, 6075-6093. https://doi.org/https://doi.org/10.1002/2016JD026245.

Kawai, H., Yabu, S., Hagihara, Y., Koshiro, T., Okamoto, H., 2015. Characteristics of the cloud top heights of marine boundary layer clouds and the frequency of marine fog

over mid-latitudes. Journal of the Meteorological Society of Japan. Ser. II. 93, 613-628. https://doi.org/http://dx.doi.org/10.2151/jmsj.2015-045.

KiranKumar, N.V.P., Jagadeesh, K., Niranjan, K., Rajeev, K., 2019. Seasonal variations of sea breeze and its effect on the spectral behaviour of surface layer winds in the coastal zone near Visakhapatnam, India. Journal of Atmospheric and Solar-Terrestrial Physics. 186, 1-7. https://doi.org/https://doi.org/10.1016/j.jastp.2019.01.013.

Klein, S.A., Hartmann, D.L., 1993. The seasonal cycle of low stratiform clouds. Journal of Climate. 6, 1587-1606. https://doi.org/https://doi.org/10.1175/1520-0442(1993)006%3C1587:TSCOLS%3E2.0.CO;2.

Klipp, C., Mahrt, L., 2003. Conditional analysis of an internal boundary layer. Boundary Layer Meteorology. 108, 1-17. https://doi.org/10.1023/A:1023034932094.

Klipp, C.L., Mahrt, L., 2004. Flux–gradient relationship, self-correlation and intermittency in the stable boundary layer. Quarterly Journal of the Royal Meteorological Society. 130, 2087-2103. https://doi.org/https://doi.org/10.1256/qj.03.161.

Kohler, M., Mauree, D., Nadège, B., Clappier, A., 2012. Paper 60: Development of a canopy model for a multiscale urban climate system. ICUC8.

Kremser, S., Harvey, M., Kuma, P., Hartery, S., Saint-Macary, A., McGregor, J., Schuddeboom, A., von Hobe, M., Lennartz, S.T., Geddes, A., Querel, R., McDonald, A., Peltola, M., Sellegri, K., Silber, I., Law, C.S., Flynn, C.J., Marriner, A., Hill, T.C.J., DeMott, P.J., Hume, C.C., Plank, G., Graham, G., Parsons, S., 2021. Southern Ocean cloud and aerosol data: a compilation of measurements from the 2018 Southern Ocean Ross Sea marine ecosystems and environment voyage. Earth System Science Data. 13, 3115-3153. https://doi.org/10.5194/essd-13-3115-2021.

Krishnamurti, T.N., Jha, B., Prospero, J., Jayaraman, A., Ramanathan, V., 1998. Aerosol and pollutant transport and their impact on radiative forcing over the tropical Indian Ocean during the January — February 1996 pre-INDOEX cruise. Tellus B: Chemical and Physical Meteorology. 50, 521-542. https://doi.org/10.3402/tellusb.v50i5.16235.

Krishnan, P., Kunhikrishnan, P.K., 2002. Some characteristics of atmospheric surface layer over a tropical inland region during southwest monsoon period. Atmospheric Research. 62, 111-124. https://doi.org/https://doi.org/10.1016/S0169-8095(02)00004-2.

Kuma, P., McDonald, A.J., Morgenstern, O., Alexander, S.P., Cassano, J.J., Garrett, S., Halla, J., Hartery, S., Harvey, M.J., Parsons, S., Plank, G., Varma, V., Williams, J., 2020. Evaluation of Southern Ocean cloud in the HadGEM3 general circulation model and MERRA-2 reanalysis using ship-based observations. Atmospheric Chemistry and Physics. 20, 6607-6630. https://doi.org/https://doi.org/10.5194/acp-20-6607-2020.

Kumar, K.K., Jain, A.R., 2006. L band wind profiler observations of convective boundary layer over Gadanki, India (13.5°N, 79.2°E). Radio Science. 41, 1-12. https://doi.org/10.1029/2005RS003259.

Kumar, V., Svensson, G., Holtslag, A.A.M., Meneveau, C., Parlange, M.B., 2010. Impact ofsurface flux formulations and geostrophic forcing on large-eddy simulations of diurnal atmospheric boundary layer flow. Journal of Applied Meteorology and Climatology. 49, 1496-1516. https://doi.org/10.1175/2010jamc2145.1.

Kunhikrishnan, P., Gupta, K., Ramachandran, R., JevevaPrakash, W., Narayanan Nair, K., Study on thermal internal boundary layer structure over Thumba, India. Annales geophysicae (1988) (1993), pp. 52-60.

Kuwagata, T., Kondo, J., Sumioka, M., 1994. Thermal effect of the sea breeze on the structure of the boundary layer and the heat budget over land. Boundary-Layer Meteorology. 67, 119-144. https://doi.org/https://doi.org/10.1007/BF00705510.

Landwehr, S., Volpi, M., Derkani, M.H., Nelli, F., Alberello, A., Toffoli, A., Gysel-Beer, M., Modini, R.L., Schmale, J., 2020. Sea state and boundary layer stability limit sea spray aerosol lifetime over the Southern Ocean. Geophysical Research Letters.

Lang, F., Huang, Y., Protat, A., Truong, S.C.H., Siems, S.T., Manton, M.J., 2021. Shallow convection and precipitation over the Southern Ocean: A case study during the CAPRICORN 2016 field campaign. Journal of Geophysical Research : Atmospheres. 126. https://doi.org/https://doi.org/10.1029/2020JD034088.

Lang, F., Huang, Y., Siems, S.T., Manton, M.J., 2018. Characteristics of the marine atmospheric boundary layer over the Southern Ocean in response to the synoptic forcing. Journal of Geophysical Research : Atmospheres. 123, 7799-7820. https://doi.org/https://doi.org/10.1029/2018JD028700.

Lang, F., Huang, Y., Siems, S.T., Manton, M.J., 2020. Evidence of a diurnal cycle in precipitation over the Southern Ocean as observed at Macquarie island. Atmosphere. 11, 181.

Lange, B., Larsen, S., Højstrup, J., Barthelmie, R., 2004. The influence of thermal effects on the wind speed profile of the coastal marine boundary layer. Boundary Layer Meteorology. 112, 587-617. https://doi.org/10.1023/B:BOUN.0000030652.20894.83.

Lee, J.-Y., Marotzke, J., Bala, G., Cao, L., Corti, S., Dunne, J.P., Engelbrecht, F., Fischer, E., Fyfe, J.C., Jones, C., 2021. Future global climate: scenario-based projections and near-term information, in: IPCC. https://doi.org/https://doi.org/10.1017/9781009157896.006.

Lee, T.R., Pal, S., 2017. On the Potential of 25 Years (1991–2015) of Rawinsonde Measurements for Elucidating Climatological and Spatiotemporal Patterns of Afternoon Boundary Layer Depths over the Contiguous US. Advances in Meteorology. 2017, 6841239. https://doi.org/http://10.1155/2017/6841239.

Leelőssy, Á., Molnár, F., Izsák, F., Havasi, Á., Lagzi, I., Mészáros, R., 2014. Dispersion modeling of air pollutants in the atmosphere: A review. Open Geosciences. 6, 257-278. https://doi.org/doi:10.2478/s13533-012-0188-6.

LeMone, M.A., Angevine, W.M., Bretherton, C.S., Chen, F., Dudhia, J., Fedorovich, E., Katsaros, K.B., Lenschow, D.H., Mahrt, L., Patton, E.G., Sun, J., Tjernström, M., Weil, J., 2019. 100 Years of Progress in Boundary Layer Meteorology Meteorological Monographs. 59, 9.1-9.85. https://doi.org/https://doi.org/10.1175/AMSMONOGRAPHS-D-18-0013.1.

LeMone, M.A., Angevine, W.M., Dudhia, J., 2021. The role of radiation in heating the clear-air convective boundary layer: Revisiting CASES-97. Boundary Layer Meteorology. 178, 341-361. https://doi.org/10.1007/s10546-020-00577-y.

Lenschow, D.H., 1973. Two examples of planetary boundary layer modification over the great lakes. Journal of Atmospheric Sciences. 30, 568-581. https://doi.org/10.1175/1520-0469(1973)030<0568:Teopbl>2.0.Co;2.

Li, Q., Zhang, H., Cai, X., Song, Y., Zhu, T., 2021. The impacts of the atmospheric boundary layer on regional haze in North China. Climate and Atmospheric Science. 4, 9. https://doi.org/10.1038/s41612-021-00165-y.

Li, X., Yang, X., Zheng, W., Zhang, J.A., Pietrafesa, L.J., Pichel, W.G., 2015. Synergistic Use of Satellite Observations and Numerical Weather Model to Study Atmospheric Occluded Fronts. IEEE Transactions on Geoscience and Remote Sensing. 53, 5269-5279. https://doi.org/10.1109/TGRS.2015.2420312.

Li, Z., Guo, J., Ding, A., Liao, H., Liu, J., Sun, Y., Wang, T., Xue, H., Zhang, H., Zhu, B., 2017. Aerosol and boundary-layer interactions and impact on air quality. National Science Review. 4, 810-833. https://doi.org/10.1093/nsr/nwx117.

Li, Z., Lee, K.-H., Wang, Y., Xin, J., Hao, W.-M., 2010. First observation-based estimates of cloud-free aerosol radiative forcing across China. Journal of Geophysical Research : Atmospheres. 115. https://doi.org/https://doi.org/10.1029/2009JD013306.

Licker, R., 2022. Global climate change. https://doi.org/10.1036/1097-8542.757541.

Listowski, C., Delanoë, J., Kirchgaessner, A., Lachlan-Cope, T., King, J., 2019. Antarctic clouds, supercooled liquid water and mixed phase, investigated with DARDAR: geographical and seasonal variations. Atmospheric Chemistry and Physics. 19, 6771-6808. https://doi.org/10.5194/acp-19-6771-2019.

Liu, B., Ma, X., Ma, Y., Li, H., Jin, S., Fan, R., Gong, W., 2022. The relationship between atmospheric boundary layer and temperature inversion layer and their aerosol capture capabilities. Atmospheric Research. 271, 106121. https://doi.org/https://doi.org/10.1016/j.atmosres.2022.106121.

Liu, D., Hu, K., Zhao, D., Ding, S., Wu, Y., Zhou, C., Yu, C., Tian, P., Liu, Q., Bi, K., Wu, Y., Hu, B., Ji, D., Kong, S., Ouyang, B., He, H., Huang, M., Ding, D., 2020. Efficient vertical transport of black carbon in the planetary boundary layer. Journal of Geophysical Research : Atmospheres. 47. https://doi.org/https://doi.org/10.1029/2020GL088858.

Liu, S., Liang, X.-Z., 2010. Observed diurnal cycle climatology of planetary boundary layer height. Journal of Climate. 23, 5790-5809. https://doi.org/10.1175/2010jcli3552.1.

Lock, A.P., 2004. The sensitivity of a GCM's marine stratocumulus to cloud-top entrainment. Quarterly Journal of the Royal Meteorological Society. 130, 3323-3338. https://doi.org/https://doi.org/10.1256/qj.03.114.

Long, M.C., Stephens, B.B., McKain, K., Sweeney, C., Keeling, R.F., Kort, E.A., Morgan, E.J., Bent, J.D., Chandra, N., Chevallier, F., Commane, R., Daube, B.C., Krummel, P.B., Loh, Z., Luijkx, I.T., Munro, D., Patra, P., Peters, W., Ramonet, M., Rödenbeck, C., Stavert, A., Tans, P., Wofsy, S.C., 2021. Strong Southern Ocean carbon uptake evident in airborne observations. Science. 374, 1275-1280. https://doi.org/10.1126/science.abi4355.

Lothon, M., Lenschow, D.H., Mayor, S.D., 2009. Doppler Lidar Measurements of Vertical Velocity Spectra in the Convective Planetary Boundary Layer. Boundary-Layer Meteorology. 132, 205-226. https://doi.org/10.1007/s10546-009-9398-y.

Lothon, M., Lohou, F., Pino, D., Couvreux, F., Pardyjak, E.R., Reuder, J., Vilà-Guerau de Arellano, J., Durand, P., Hartogensis, O., Legain, D., Augustin, P., Gioli, B., Lenschow, D.H., Faloona, I., Yagüe, C., Alexander, D.C., Angevine, W.M., Bargain, E., Barrié, J., Bazile, E., Bezombes, Y., Blay-Carreras, E., van de Boer, A., Boichard, J.L., Bourdon, A., Butet, A., Campistron, B., de Coster, O., Cuxart, J., Dabas, A., Darbieu, C., Deboudt, K., Delbarre, H., Derrien, S., Flament, P., Fourmentin, M., Garai, A., Gibert, F., Graf, A., Groebner, J., Guichard, F., Jiménez, M.A., Jonassen, M., van den Kroonenberg, A., Magliulo, V., Martin, S., Martinez, D., Mastrorillo, L., Moene, A.F., Molinos, F., Moulin, E., Pietersen, H.P., Piguet, B., Pique, E., Román-Cascón, C., Rufin-Soler, C., Saïd, F., Sastre-Marugán, M., Seity, Y., Steeneveld, G.J., Toscano, P., Traullé, O., Tzanos, D., Wacker, S., Wildmann, N., Zaldei, A., 2014. The BLLAST field experiment: Boundary-Layer Late Afternoon and Sunset Turbulence. Atmos. Chem. Phys. 14, 10931-10960. https://doi.org/http://10.5194/acp-14-10931-2014.

Lou, M., Guo, J., Wang, L., Xu, H., Chen, D., Miao, Y., Lv, Y., Li, Y., Guo, X., Ma, S., Li, J., 2019. On the relationship between aerosol and boundary layer height in summer in China under different thermodynamic conditions. Earth and Space Science. 6, 887-901. https://doi.org/https://doi.org/10.1029/2019EA000620.

Luhar, A.K., Sawford, B.L., Hacker, J.M., Rayner, K.N., 1998a. The Kwinana Coastal Fumigation Study: II – Growth of the Thermal Internal Boundary Layer. Boundary-Layer Meteorology. 89, 385-405. https://doi.org/http://10.1023/A:1001746303967.

Luhar, A.K., Sawford, B.L., Hacker, J.M., Rayner, K.N., 1998b. The Kwinana coastal fumigation study: II – Growth of the thermal internal boundary layer. Boundary Layer Meteorology. 89, 385-405. https://doi.org/10.1023/A:1001746303967.

Lui, Y., Jia, R., Dai, T., Xie, Y., Shi, G., 2015. A review of aerosol optical properties and radiative effects. Journal of Meteorological Research. 28, 1003-1028. https://doi.org/10.1007/s13351-014-4045-z.

Luo, T., Yuan, R., Wang, Z., 2014. Lidar-based remote sensing of atmospheric boundary layer height over land and ocean. Atmospheric Chemistry and Physics. 7, 173-182. https://doi.org/10.5194/amt-7-173-2014.

Lutjeharms, J.R.E., Ansorge, I.J., 2001. The Agulhas Return Current. Journal of Marine Systems. 30, 115-138. https://doi.org/https://doi.org/10.1016/S0924-7963(01)00041-0.

Lutjeharms, J.R.E., Gordon, A.L., 1987. Shedding of an Agulhas ring observed at sea. Nature. 325, 138-140. https://doi.org/http://10.1038/325138a0.

Lutjeharms, J.R.E., Valentine, H.R., 1988. Eddies at the subtropical convergence south of Africa Journal of Physical Oceanography. 18, 761-774. https://doi.org/https://doi.org/10.1175/1520-0485(1988)018%3C0761:EATSCS%3E2.0.CO;2.

Lutjeharms, J.R.E., Valentine, H.R., 1984. Southern ocean thermal fronts south of Africa. Deep Sea Research Part A. Oceanographic Research Papers. 31, 1461-1475. https://doi.org/https://doi.org/10.1016/0198-0149(84)90082-7.

Lutjeharms, J.R.E., Van Ballegooyen, R.C., 1988. The Retroflection of the Agulhas Current. Journal of Physical Oceanography. 18, 1570-1583. https://doi.org/https://doi.org/10.1175/1520-0485(1988)018%3C1570:TROTAC%3E2.0.CO;2.

Lyons, W.A., Cole, H.S., 1973. Fumigation and Plume Trapping on the Shores of Lake Michigan During Stable Onshore Flow Journal of Applied Meteorology and Climatology. 12, 494-510. https://doi.org/https://doi.org/10.1175/1520-0450(1973)012<0494:FAPTOT>2.0.CO;2.

Lyons, W.A., Pielke, R.A., Tremback, C.J., Walko, R.L., Moon, D.A., Keen, C.S., 1995. Modeling impacts of mesoscale vertical motions upon coastal zone air pollution dispersion. Atmospheric Environment. 29, 283-301. https://doi.org/https://doi.org/10.1016/1352-2310(94)00217-9.

Ma, Y., Ye, J., Xin, J., Zhang, W., Vilà-Guerau de Arellano, J., Wang, S., Zhao, D., Dai, L., Ma, Y., Wu, X., Xia, X., Tang, G., Wang, Y., Shen, P., Lei, Y., Martin, S.T., 2020. The stove, dome, and umbrella effects of atmospheric aerosol on the development of the planetary boundary layer in hazy regions. Geophysical Research Letters. 47. https://doi.org/https://doi.org/10.1029/2020GL087373.

Mace, G., G., Benson, S., Hu, Y., 2020. On thefrequency of occurrence of the ice phase in supercooled Southern Ocean low clouds derived from CALIPSO and CLOUDSAT. Geophysical Research Letters. 47. https://doi.org/https://doi.org/10.1029/2020GL087554.

Mace, G., G., Protat, A., 2018a. Clouds over the Southern Ocean as observed from the R/V investigator during CAPRICORN. Part I: Cloud occurrence and phase partitioning. Journal of Applied Meteorology and Climatology. 57. https://doi.org/https://doi.org/10.1175/JAMC-D-17-0194.1.

Mace, G., G., Protat, A., 2018b. Clouds over the Southern Ocean as Observed from the R/V Investigator during CAPRICORN. Part I: Cloud Occurrence and Phase Partitioning. Journal of Applied Meteorology and Climatology. 57, 1783-1803.

Mace, G., G., Protat, A., Benson, S., 2021. Mixed-Phase clouds over the Southern Ocean as observed from satellite and surface based lidar and radar. Journal of Geophysical Research : Atmospheres. 126. https://doi.org/https://doi.org/10.1029/2021JD034569.

Mace, G., G., Zhang, Q., Vaughan, M., Marchand, R., Stephens, S., Trepte, C., Winker, D., 2009. A description of hydrometeor layer occurrence statistics derived from the first year of merged Cloudsat and CALIPSO data. Journal of Geophysical Research : Atmospheres. 114. https://doi.org/https://doi.org/10.1029/2007JD009755.

Mahrt, L., 1998a. Nocturnal boundary-layer regimes. Boundary Layer Meteorology. 88, 255-278.

Mahrt, L., 1998b. Stratified atmospheric boundary layers and breakdown of models. Theoretical and Computational Fluid Dynamics. 11, 263-279. https://doi.org/10.1007/s001620050093.

Mahrt, L., 2010. Variability and maintenance of turbulence in the very stable boundary layer. Boundary Layer Meteorology. 135, 1-18. https://doi.org/10.1007/s10546-009-9463-6.

Mahrt, L., Thomas, C.K., Grachev, A.A., Persson, P.O.G., 2018a. Near-surface vertical flux divergence in the stable boundary layer. Boundary Layer Meteorology. 169, 373-393. https://doi.org/10.1007/s10546-018-0379-x.

Mahrt, L., Thomas, C.K., Grachev, A.A., Persson, P.O.G., 2018b. Near-Surface Vertical Flux Divergence in the Stable Boundary Layer. Boundary-Layer Meteorology. 169, 373-393. https://doi.org/http://10.1007/s10546-018-0379-x.

Manghnani, V., Raman, S., Niyogi, D.S., Parameswara, V., Morrison, J.M., Ramana, S.V., Raju, J.V.S.S., 2000. Marine Boundary-Layer Variability Over The Indian Ocean During Indoex (1998). Boundary-Layer Meteorology. 97, 411-430. https://doi.org/http://10.1023/A:1002730405170.

Manninen, A.J., Marke, T., Tuononen, M., O'Connor, E.J., 2018. Atmospheric boundary layer classification with doppler lidar. Journal of Geophysical Research : Atmospheres. 123, 8172-8189. https://doi.org/https://doi.org/10.1029/2017JD028169.

Markowski, P., Lis, N., Turner, D., Lee, T., Buban, M., 2019. Observations of near-surface vertical wind profiles and vertical momentum fluxes from vortex-se 2017: comparisons to Monin–Obukhov Similarity Theory. Monthly Weather Review. 147. https://doi.org/10.1175/MWR-D-19-0091.1.

Martin, G.M., Johnson, D.W., Rogers, D.P., Jonas, P.R., Minnis, P., Hegg, D.A., 1995. Observations of the Interaction between Cumulus Clouds and Warm Stratocumulus Clouds in the Marine Boundary Layer during ASTEX Journal of Atmospheric Sciences. 52, 2902-2922. https://doi.org/10.1175/1520-0469(1995)052<2902:Ootibc>2.0.Co;2.

Mauder, M., Foken, T., Cuxart, J., 2020. Surface-energy-balance closure over land: A review. Boundary Layer Meteorology. 177, 395-426. https://doi.org/10.1007/s10546-020-00529-6.

Mayewski, P.A., Meredith, M.P., Summerhayes, C.P., Turner, J., Worby, A., Barrett, P.J., Casassa, G., Bertler, N.A.N., Bracegirdle, T., Naveira Garabato, A.C., Bromwich, D., Campbell, H., Hamilton, G.S., Lyons, W.B., Maasch, K.A., Aoki, S., Xiao, C., van Ommen, T., 2009. State of the Antarctic and Southern Ocean climate system. Reviews of Geophysics. 47.

McCormick, R.A., Ludwig, J.H., 1967. Climate modification by atmospheric aerosols. Climate Change. 156, 1358-1359. https://doi.org/doi:10.1126/science.156.3780.1358.

McCoy, D.T., Hartmann, D.L., Zelinka, M.D., Ceppi, P., Grosvenor, D.P., 2015. Mixed-phase cloud physics and Southern Ocean cloud feedback in climate models. Journal of Geophysical Research : Atmospheres. 120, 9539-9554. https://doi.org/https://doi.org/10.1002/2015JD023603.

McFarquhar, G.M., Bretherton, C.S., Marchand, R., Protat, A., DeMott, P.J., Alexander, S.P., Roberts, G.C., Twohy, C.H., Toohey, D., Siems, S., Huang, Y., Wood, R., Rauber, R.M., Lasher-Trapp, S., Jensen, J., Stith, J.L., Mace, J., Um, J., Järvinen, E., Schnaiter, M., Gettelman, A., Sanchez, K.J., McCluskey, C.S., Russell, L.M., McCoy, I.L., Atlas, R.L., Bardeen, C.G., Moore, K.A., Hill, T.C.J., Humphries, R.S., Keywood, M.D., Ristovski, Z., Cravigan, L., Schofield, R., Fairall, C., Mallet,

M.D., Kreidenweis, S.M., Rainwater, B., D'Alessandro, J., Wang, Y., Wu, W., Saliba, G., Levin, E.J.T., Ding, S., Lang, F., Truong, S.C.H., Wolff, C., Haggerty, J., Harvey, M.J., Klekociuk, A.R., McDonald, A., 2021. Observations of clouds, aerosols, precipitation, and surface radiation over the Southern Ocean: An overview of CAPRICORN, MARCUS, MICRE, and SOCRATES. Bulletin of the American Meteorological Society. 102, 894-928. https://doi.org/https://doi.org/10.1175/BAMS-D-20-0132.1.

McGibbon, J., Bretherton, C.S., 2017. Skill of ship-following large-eddy simulations in reproducing MAGIC observations across the northeast Pacific stratocumulus to cumulus transition region. Journal of Advances in Modeling Earth Systems. 9, 810-831. https://doi.org/https://doi.org/10.1002/2017MS000924.

McGrath-Spangler, E.L., Denning, A.S., 2013. Global seasonal variations of midday planetary boundary layer depth from CALIPSO space-borne LIDAR. Journal of Geophysical Research: Atmospheres. 118, 1226-1233. https://doi.org/https://doi.org/10.1002/jgrd.50198.

Meijers, A.J.S., Klocker, A., Bindoff, N.L., Williams, G.D., Marsland, S.J., 2010. The circulation and water masses of the Antarctic shelf and continental slope between 30∘E and 80∘E. Deep Sea Research Part II: Topical Studies in Oceanography. 57, 723-737. https://doi.org/https://doi.org/10.1016/j.dsr2.2009.04.019.

Melecio-Vázquez, D., Ramamurthy, P., Arend, M., González-Cruz, J.E., 2018. Thermal structure of a coastal – Urban boundary layer. Boundary Layer Meteorology. 169, 151-161. https://doi.org/10.1007/s10546-018-0361-7.

Melfi, S.H., Spinhirne, J.D., Chou, S.-H., Palm, S.P., 1985. Lidar observations of vertically organized convection in the planetary boundary layer over the ocean. Journal of Applied Meteorology and Climatology. 24, 806-821. https://doi.org/10.1175/1520-0450(1985)024<0806:Loovoc>2.0.Co;2.

Menon, H.B., Hulswar, S., Anilkumar, N., Chittur Thelakkat, A., Moorthy, K.K., Babu, S., 2015. Spatial heterogeneity in spectral variability of aerosol optical depth and its implications to aerosol radiative forcing in the tropical Indian Ocean and in the Indian Ocean Sector of Southern Ocean. Deep Sea Research Part II: Topical Studies in Oceanography. 118, 142-151. https://doi.org/https://doi.org/10.1016/j.dsr2.2015.03.012.

Menon, H.B., Sangekar, N., Lotliker, A., Krishna Moorthy, K., Vethamony, P., 2011. Aerosol optical thickness and spatial variability along coastal and offshore waters

of the eastern Arabian Sea. ICES Journal of Marine Science. 68, 745-750. https://doi.org/http://10.1093/icesjms/fsq191.

Menon, H.B., Shirodkar, S., Kedia, S., S, R., Babu, S., Moorthy, K.K., 2014. Temporal variation of aerosol optical depth and associated shortwave radiative forcing over a coastal site along the west coast of India. Science of The Total Environment. 468-469, 83-92. https://doi.org/https://doi.org/10.1016/j.scitotenv.2013.08.013.

Messager, C., Speich, S., Key, E., 2012. Marine atmospheric boundary layer over some Southern Ocean fronts during the IPY BGH 2008 cruise. Ocean Science. 8, 1001-1023. https://doi.org/https://doi.org/10.5194/os-8-1001-2012.

Miao, J.-F., Wyser, K., Deliang, C., Ritchie, H., 2009. Impacts of boundary layer turbulence and land surface process parameterizations on simulated sea breeze characteristics. Annales Geophysicae. 27. https://doi.org/10.5194/angeo-27-2303-2009.

Miao, Y., Liu, S., 2019. Linkages between aerosol pollution and planetary boundary layer structure in China. Science of The Total Environment. 650, 288-296. https://doi.org/https://doi.org/10.1016/j.scitotenv.2018.09.032.

Michibata, T., 2020. Aerosol–cloud interactions in the climate system, in: Akimoto, H., Tanimoto, H. (Eds.), Handbook of Air Quality and Climate Change, Springer Singapore, Singapore, pp. 1-42. https://doi.org/10.1007/978-981-15-2527-8_35-1.

Miller, M.A., Albrecht, B.A., 1995. Surface-Based Observations of Mesoscale Cumulus–Stratocumulus Interaction during ASTEX Journal of Atmospheric Sciences. 52, 2809-2826. https://doi.org/10.1175/1520-0469(1995)052<2809:Sboomc>2.0.Co;2.

Miller, R.L., Perlwitz, J., Tegen, I., 2004. Feedback upon dust emission by dust radiative forcing through the planetary boundary layer. Journal of Geophysical Research : Atmospheres. 109. https://doi.org/https://doi.org/10.1029/2004JD004912.

Miller, S., Keim, B., 2003. Synoptic-scale controls on the sea breeze of the central new England coast. Weather and Forecasting. 18, 236-248. https://doi.org/10.1175/1520-0434(2003)018<0236:Scotsb>2.0.Co;2.

Miller, S., Keim, B., Talbot, R., Mao, H., 2003. Sea breeze: structure, forecasting, and impacts. Reviews of Geophysics. 41. https://doi.org/https://doi.org/10.1029/2003RG000124.

Mitra, A.K., Gupta, M.D., Paliwal, R.K., Singh, S.V., 2003. Observed daily large-scale rainfall patterns during BOBMEX-1999. Journal of Earth System Science. 112, 223-232. https://doi.org/http://10.1007/BF02701988.

Moeng, C.-H., 1984. A large-eddy-simulation model for the study of planetary boundary-layer turbulence. Journal of Atmospheric Sciences. 41, 2052-2062. https://doi.org/10.1175/1520-0469(1984)041<2052:Alesmf>2.0.Co;2.

Moeng, C.-H., Wyngaard, J.C., 1989. Evaluation ofturbulent transport and dissipation closures in second-order modeling. Journal of Atmospheric Sciences. 46, 2311-2330. https://doi.org/10.1175/1520-0469(1989)046<2311:EOTTAD>2.0.CO;2.

Moeng, C.-H., Wyngaard, J.C., 1984. Statistics of conservative scalars in the convective boundary layer. Journal of Atmospheric Sciences. 41, 3161-3169. https://doi.org/10.1175/1520-0469(1984)041<3161:Socsit>2.0.Co;2.

Mohanty, U.C., Mohan Kumar, N., 1990. A study on energy fluxes in the surface boundary layer of the Indian seas during different epochs of the Asian summer monsoon. Atmospheric Environment. Part A. General Topics. 24, 823-828. https://doi.org/https://doi.org/10.1016/0960-1686(90)90283-S.

Monin, A., Yaglom, A., 1975. Statistical fluid mechanics: mechanics of turbulence, 2 MIT Press. Cambridge MA.

Monin, A., Yaglom, A.M., 1971. Statistical fluid mechanics, vols. 1 and 2. MIT Press, Cambridge, MA. 1975, 11.

Monin, A.S., Obukhov, A.M., 1954. Basic laws of turbulent mixing in the surface layer of the atmosphere. J Contrib. Geophys. Inst. Acad. Sci. USSR. 151, e187.

Monti, P., Fernando, H.J.S., Princevac, M., Chan, W.C., Kowalewski, T.A., Pardyjak, E.R., 2002. Observations of Flow and Turbulence in the Nocturnal Boundary Layer over a Slope %J Journal of the Atmospheric Sciences. 59, 2513-2534. https://doi.org/https://doi.org/10.1175/1520-0469(2002)059<2513:OOFATI>2.0.CO;2.

Moore, J.K., Abbott, M.R., Richman, J.G., 1999a. Location and dynamics of the Antarctic Polar Front from satellite sea surface temperature data. Geophysical Research Letters. 104, 3059-3073. https://doi.org/https://doi.org/10.1029/1998JC900032.

Moore, J.K., Abbott, M.R., Richman, J.G., 1999b. Location and dynamics of the Antarctic Polar Front from satellite sea surface temperature data. Journal of Geophysical Research: Oceans. 104, 3059-3073. https://doi.org/https://doi.org/10.1029/1998JC900032.

Moorthy, K.K., Babu, S.S., Satheesh, S.K., 2003. Aerosol spectral optical depths over the Bay of Bengal: Role of transport. Geophysical Research Letters. 30. https://doi.org/https://doi.org/10.1029/2002GL016520.

Moorthy, K.K., Murthy, B.V.K., Nair, P.R., 1993. Sea-Breeze Front Effects on Boundary-layer Aerosols at a Tropical Coastal Station. Journal of Applied Meteorology and Climatology. 32, 1196-1205. https://doi.org/https://doi.org/10.1175/1520-0450(1993)032<1196:SBFEOB>2.0.CO;2.

Moorthy, K.K., Satheesh, S.K., Babu, S.S., Dutt, C.B.S., 2008. Integrated Campaign for Aerosols, gases and Radiation Budget (ICARB): An overview. Journal of Earth System Science. 117, 243-262. https://doi.org/http://10.1007/s12040-008-0029-7.

Moorthy, K.K., Satheesh, S.K., Babu, S.S., Saha, A., 2005a. Large latitudinal gradients and temporal heterogeneity in aerosol black carbon and its mass mixing ratio over southern and northern oceans observed during a trans-continental cruise experiment. Geophysical Research Letters. 32. https://doi.org/https://doi.org/10.1029/2005GL023267.

Moorthy, K.K., Sunilkumar, S.V., Pillai, P.S., Parameswaran, K., Nair, P.R., Ahmed, Y.N., Ramgopal, K., Narasimhulu, K., Reddy, R.R., Vinoj, V., Satheesh, S.K., Niranjan, K., Rao, B.M., Brahmanandam, P.S., Saha, A., Badarinath, K.V.S., Kiranchand, T.R., Latha, K.M., 2005b. Wintertime spatial characteristics of boundary layer aerosols over peninsular India. Journal of Geophysical Research: Atmospheres. 110. https://doi.org/https://doi.org/10.1029/2004JD005520.

Moraes, O., Acevedo, O., Degrazia, G., Anfossi, D., da Silva, R., Anabor, V., 2005. Surface layer turbulence parameters over a complex terrain. Atmospheric Environment. 39, 3103-3112.

Morrow, R., Birol, F., Griffin, D., Sudre, J., 2004. Divergent pathways of cyclonic and anti-cyclonic ocean eddies. Geophysical Research Letters. 31. https://doi.org/https://doi.org/10.1029/2004GL020974.

Morwal, S.B., Seetaramayya, P., 2003. Thermodynamic structure of the marine atmosphere over the region 80–87°E along 13°N during August (phase II) BOBMEX-99. Journal of Earth System Science. 112, 295-312. https://doi.org/10.1007/BF02701994.

Morys, M., Mims III, F.M., Hagerup, S., Anderson, S.E., Baker, A., Kia, J., Walkup, T., 2001. Design, calibration, and performance of MICROTOPS II handheld ozone monitor and Sunphotometer. Journal of Geophysical Research : Atmospheres. 106, 14573-14582. https://doi.org/https://doi.org/10.1029/2001JD900103.

Muhlbauer, A., McCoy, I.L., Wood, R., 2014. Climatology of stratocumulus cloud morphologies: microphysical properties and radiative effects. Atmospheric

Chemistry and Physics. 14, 6695-6716. https://doi.org/https://doi.org/10.5194/acp-14-6695-2014.

Muppa, S.K., Anandan, V.K., Kesarkar, K.A., Rao, S.V.B., Reddy, P.N., 2012. Study on deep inland penetration of sea breeze over complex terrain in the tropics. Atmospheric Research. 104-105, 209-216. https://doi.org/https://doi.org/10.1016/j.atmosres.2011.10.007.

Muppa, S.K., Behrendt, A., Späth, F., Wulfmeyer, V., Metzendorf, S., Riede, A., 2016. Turbulent Humidity Fluctuations in the Convective Boundary Layer: Case Studies Using Water Vapour Differential Absorption Lidar Measurements. Boundary-Layer Meteorology. 158, 43-66. https://doi.org/http://10.1007/s10546-015-0078-9.

Murphy, D., Anderson, J., Quinn, P., McInnes, L., Brechtel, F., Kreidenweis, S., Middlebrook, A., Pósfai, M., Thomson, D., Buseck, P., 1998. Influence of sea-salt on aerosol radiative properties in the Southern Ocean marine boundary layer. Nature. 392, 62-65.

Murthy, B.S., Latha, R., Sukumaran, C., Shivaji, A., Sivaramakrishnan, S., 2009. On the influence of spatial heterogeneity on an internal boundary layer at a short fetch. Journal of Earth System Science. 118, 61-70. https://doi.org/http://10.1007/s12040-009-0006-9.

Murthy, B.S., Sivaramakrishnan, S., 2005. Surface fluxes over Goa during Indian monsoon. MAUSAM. 56, 251-256. https://doi.org/http://10.54302/mausam.v56i1.900.

Murty, V.S.N., Sarma, Y.V.B., Rao, D.P., 1996. Variability of the oceanic boundary layer characteristics in the northern Bay of Bengal during MONTBLEX-90. Proceedings of the Indian Academy of Sciences - Earth and Planetary Sciences. 105, 41-61. https://doi.org/http://10.1007/BF02880758.

Nagi Reddy, S.K., Nadimpally, K., Gopal, K., Balakrishnaiah, G., Reddy, K., 2021. Characteristics of atmospheric surface layer during winter season over Anantapur (14.62° N, 77.65° E), a semi-arid location in peninsular India. Journal of Atmospheric and Solar Terrestrial Physics. 216, 105554. https://doi.org/10.1016/j.jastp.2021.105554.

Nair, S.K., Madhusoodanan, M.S., Mehajan, R.K., 2018. The role of Boundary Layer Height (BLH) variations on pollution dispersion over a coastal station in the Southwest Peninsular India. Journal of Atmospheric and Solar-Terrestrial Physics. 179, 273-280. https://doi.org/https://doi.org/10.1016/j.jastp.2018.07.011.

Nair, V.S., Moorthy, K.K., Alappattu, D.P., Kunhikrishnan, P.K., George, S., Nair, P.R., Babu, S.S., Abish, B., Satheesh, S.K., Tripathi, S.N., Niranjan, K., Madhavan, B.L., Srikant, V., Dutt, C.B.S., Badarinath, K.V.S., Reddy, R.R., 2007. Wintertime aerosol characteristics over the Indo-Gangetic Plain (IGP): Impacts of local boundary layer processes and long-range transport. Journal of Geophysical Research: Atmospheres. 112. https://doi.org/https://doi.org/10.1029/2006JD008099.

Nakamura, H., Sampe, T., Tanimoto, Y., Shimpo, A., 2004. Observed associations among storm tracks, jet streams and midlatitude oceanic fronts, in: Earth's Climate, pp. 329-345. https://doi.org/https://doi.org/10.1029/147GM18.

Namboodiri, K.V.S., Puthillam Krishnan, D., Karunakaran Nileshwar, R., Mammen, K., Kiran kumar, N., 2014. Coastal boundary layer characteristics of wind, turbulence, and surface roughness parameter over the Thumba equatorial rocket launching station, India. Journal of Climatology. 2014, 504178. https://doi.org/http://10.1155/2014/504178.

Narasimha, R., Prasad, S.N., 1994. Leading edge shape for flat plate boundary layer studies. Experiments in Fluids. 17, 358-360. https://doi.org/http://10.1007/BF01874418.

Naud, C.M., Booth, J.F., Del Genio, A.D., 2014. Evaluation of ERA-Interim and MERRA cloudiness in the Southern Ocean. Journal of Climate. 27, 2109-2124. https://doi.org/https://doi.org/10.1175/JCLI-D-13-00432.1.

Naud, C.M., Booth, J.F., Del Genio, A.D., 2016. The relationship between boundary layer stability and cloud cover in the post-cold-frontal region. Journal of Climate. 29, 8129-8149. https://doi.org/https://doi.org/10.1175/JCLI-D-15-0700.1.

Neumann, J., Mahrer, Y., 1971. A Theoretical Study of the Land and Sea Breeze Circulation Journal of Atmospheric Sciences. 28, 532-542. https://doi.org/https://doi.org/10.1175/1520-0469(1971)028<0532:ATSOTL>2.0.CO;2.

Nicholls, S., 1984. The dynamics of stratocumulus: Aircraft observations and comparisons with a mixed layer model. Quarterly Journal of the Royal Meteorological Society. 110, 783-820. https://doi.org/https://doi.org/10.1002/qj.49711046603.

Nieuwstadt, F.T.M., 1984. The turbulent structure of the stable, nocturnal boundary layer. Journal of Atmospheric Sciences. 41, 2202-2216. https://doi.org/10.1175/1520-0469(1984)041<2202:Ttsots>2.0.Co;2.

Nieuwstadt, F.T.M., Duynkerke, P.G., 1996. Turbulence in the atmospheric boundary layer. Atmospheric Research. 40, 111-142. https://doi.org/https://doi.org/10.1016/0169-8095(95)00034-8.

Noone, K.J., Clarke, A.D., 1988. Soot scavenging measurements in Arctic snowfall. Atmospheric Environment (1967). 22, 2773-2778. https://doi.org/https://doi.org/10.1016/0004-6981(88)90444-1.

O'Dowd, C.D., Smith, M.H., Consterdine, I.E., Lowe, J.A., 1997. Marine aerosol, sea-salt, and the marine sulphur cycle: A short review. Atmospheric Environment. 31, 73-80. https://doi.org/https://doi.org/10.1016/S1352-2310(96)00106-9.

O, K.-T., Wood, R., Tseng, H.-H., 2018. Deeper, Precipitating PBLs Associated With Optically Thin Veil Clouds in the Sc-Cu Transition. Geophysical Research Letters. 45, 5177-5184. https://doi.org/https://doi.org/10.1029/2018GL077084.

Orsi, A.H., Johnson, G.C., Bullister, J.L., 1999. Circulation, mixing, and production of Antarctic Bottom Water. Progress in Oceanography. 43, 55-109. https://doi.org/https://doi.org/10.1016/S0079-6611(99)00004-X.

Orsi, A.H., Whitworth, T., Nowlin, W.D., 1995. On the meridional extent and fronts of the Antarctic Circumpolar Current. Deep Sea Research Part I: Oceanographic Research Papers. 42, 641-673. https://doi.org/https://doi.org/10.1016/0967-0637(95)00021-W.

Pahlow, M., Parlange, M.B., Porté-Agel, F., 2001. On Monin–Obukhov Similarity in the stable atmospheric boundary layer. Boundary Layer Meteorology. 99, 225-248. https://doi.org/10.1023/A:1018909000098.

Pal, S., Haeffelin, M., 2015. Forcing mechanisms governing diurnal, seasonal, and interannual variability in the boundary layer depths: Five years of continuous lidar observations over a suburban site near Paris. Journal of Geophysical Research: Atmospheres. 120, 11,936-911,956. https://doi.org/https://doi.org/10.1002/2015JD023268.

Pal, S., Lee, T.R., 2019. Contrasting air mass advection explains significant differences in boundary layer depth seasonal cycles under onshore versus offshore flows. Geophysical Research Letters. 46, 2846-2853. https://doi.org/https://doi.org/10.1029/2018GL081699.

Pal, S., Lee, T.R., Clark, Nicholas E., 2020. The 2019 Mississippi and Missouri river flooding and its impact on atmospheric boundary layer dynamics. Journal of

Geophysical Research : Atmospheres. 47, e2019GL086933. https://doi.org/https://doi.org/10.1029/2019GL086933.

Panofsky, H., Dutton, J., 1984. Atmospheric turbulence, models and methods for engineering applications. John Wiley & Sons, New York.

Pant, P., Hegde, P., Dumka, U.C., Sagar, R., Satheesh, S.K., Moorthy, K.K., Saha, A., Srivastava, M.K., 2006. Aerosol characteristics at a high-altitude location in central Himalayas: Optical properties and radiative forcing. Journal of Geophysical Research: Atmospheres. 111. https://doi.org/https://doi.org/10.1029/2005JD006768.

Parameswaran, K., 2001. Influence of micrometeorological features on coastal boundary layer aerosol characteristics at the tropical station, Trivandrum. Journal of Earth System Science. 110, 247-265. https://doi.org/http://10.1007/BF02702240.

Parameswaran, K., Rajeev, K., Sen Gupta, K., 1997. An observational study of night time aerosol concentrations in the lower atmosphere at a tropical coastal station. Journal of Atmospheric and Solar-Terrestrial Physics. 59, 1727-1737. https://doi.org/https://doi.org/10.1016/S1364-6826(97)00013-8.

Parasnis, S.S., Morwal, S.B., 1991. The Convective Boundary Layer over the Deccan Plateau, India during the summer monsoon. Boundary-Layer Meteorology. 54, 59-68. https://doi.org/http://10.1007/BF00119412.

Parish, T.R., Cassano, J.J., 2003a. Diagnosis of the katabatic wind influence on the wintertime Antarctic surface wind field from numerical simulations. Monthly Weather Review. 131, 1128-1139. https://doi.org/https://doi.org/10.1175/1520-0493(2003)131%3C1128:DOTKWI%3E2.0.CO;2.

Parish, T.R., Cassano, J.J., 2003b. The role of katabatic winds on the Antarctic surface wind regime. Monthly Weather Review. 131, 317-333. https://doi.org/https://doi.org/10.1175/1520-0493(2003)131%3C0317:TROKWO%3E2.0.CO;2

Parry, M.L., Canziani, O., Palutikof, J., Van der Linden, P., Hanson, C., 2007. Climate change 2007-impacts, adaptation and vulnerability: Working group II contribution to the fourth assessment report of the IPCC. Cambridge University Press.

Paulson, C.A., 1970. The mathematical representation of wind speed and temperature profiles in the unstable atmospheric surface layer. Journal of Applied Meteorology and Climatology. 9, 857-861. https://doi.org/10.1175/1520-0450(1970)009<0857:Tmrows>2.0.Co;2.

Phillips, H.E., Rintoul, S.R., 2000. Eddy variability and energetics from direct current measurements in the Antarctic circumpolar current south of Australia. Journal of Physical Oceanography. 30, 3050-3076. https://doi.org/https://doi.org/10.1175/1520-0485(2000)030%3C3050:EVAEFD%3E2.0.CO;2.

Pielke, R., Segal, M., 1986. Mesoscale circulations forced by differential terrain heating, in: Mesoscale Meteorology and Forecasting, Springer, pp. 516-548.

Pierrehumbert, R., Swanson, K., 1995. Baroclinic instability. Annual review of fluid mechanics. 27, 419-467.

Pillai, K.M.C., Sai, K.S., Swamy, N.S., Nataraja, H.R., Tiwari, S.B., Rao, B.N., 2004. Heat transfer in a viscoelastic boundary layer flow through a porous medium. Computational Mechanics. 34, 27-37. https://doi.org/http://10.1007/s00466-004-0550-8.

Plant, R.S., Keith, G.J., 2007. Occurrence of Kelvin-Helmholtz billows in sea-breeze circulations. Boundary Layer Meteorology. 122, 1-15. https://doi.org/10.1007/s10546-006-9089-x.

Porson, A., Steyn, D.G., Schayes, G., 2007a. Sea-breeze scaling from numerical model simulations, Part I: Pure sea breezes. Boundary-Layer Meteorology. 122, 17-29. https://doi.org/http://10.1007/s10546-006-9090-4.

Porson, A., Steyn, D.G., Schayes, G., 2007b. Sea-breeze scaling from numerical model simulations, Part I: Pure sea breezes. Boundary Layer Meteorology. 122, 17-29. https://doi.org/10.1007/s10546-006-9090-4.

Porson, A., Steyn, D.G., Schayes, G., 2007c. Sea-breeze scaling from numerical model simulations, part II: Interaction between the sea breeze and slope flows. Boundary-Layer Meteorology. 122, 31-41. https://doi.org/http://10.1007/s10546-006-9092-2.

Pörtner, H.O., Roberts, D.C., Adams, H., Adler, C., Aldunce, P., Ali, E., Begum, R.A., Betts, R., Kerr, R.B., Biesbroek, R., 2022. Climate change 2022: Impacts, adaptation and vulnerability. IPCC.

Prabha, T.V., Venkatesan, R., Mursch-Radlgruber, E., Rengarajan, G., Jayanthi, N., 2002. Thermal internal boundary layer characteristics at a tropical coastal site as observed by a mini-SODAR under varying synoptic conditions. Journal of Earth System Science. 111, 63-77. https://doi.org/http://10.1007/BF02702223.

Pradeep Kumar, P., Broekhuizen, K., Abbatt, J.P.D., 2003. Organic acids as cloud condensation nuclei: Laboratory studies of highly soluble and insoluble species. Atmos. Chem. Phys. 3, 509-520. https://doi.org/http://10.5194/acp-3-509-2003.

Prakash, J.W., Ramachandran, R., Nair, K.N., Sen Gupta, K., Kunhikrishnan, P.K., 1992. On the structure of sea-breeze fronts observed near the coastline of Thumba, India. Boundary Layer Meteorology. 59, 111-124. https://doi.org/10.1007/BF00120689.

Prasad, K.B.R.R.H., Srinivas, C.V., Singh, A.B., Naidu, C.V., Baskaran, R., Venkatraman, B., 2019. Turbulence characteristics of surface boundary layer over the Kalpakkam tropical coastal station, India. Meteorology and Atmospheric Physics. 131, 827-843. https://doi.org/http://10.1007/s00703-018-0605-6.

Prasad, P., Ghouse, B., Madineni, V.R., 2021. Is the atmospheric boundary layer altitude or the strong thermal inversions that control the vertical extent of aerosols? Science of The Total Environment. 802. https://doi.org/10.1016/j.scitotenv.2021.149758.

Proestakis, E., Amiridis, V., Marinou, E., Georgoulias, A.K., Solomos, S., Kazadzis, S., Chimot, J., Che, H., Alexandri, G., Binietoglou, I., Daskalopoulou, V., Kourtidis, K.A., de Leeuw, G., van der A, R.J., 2018. Nine-year spatial and temporal evolution of desert dust aerosols over South and East Asia as revealed by CALIOP. Atmospheric Chemistry and Physics. 18, 1337-1362. https://doi.org/10.5194/acp-18-1337-2018.

Pruppacher, H.R., Klett, J.D., 1978. Microstructure of atmospheric clouds and precipitation, in: Microphysics of Clouds and Precipitation, Springer, pp. 9-55.

Quan, J., Dou, Y., Zhao, X., Liu, Q., Sun, Z., Pan, Y., Jia, X., Cheng, Z., Ma, P., Su, J., Xin, J., Liu, Y., 2020. Regional atmospheric pollutant transport mechanisms over the North China Plain driven by topography and planetary boundary layer processes. Atmospheric Environment. 221, 117098. https://doi.org/https://doi.org/10.1016/j.atmosenv.2019.117098.

Quan, L., Hu, F., 2009. Relationship between turbulent flux and variance in the urban canopy. Meteorology and Atmospheric Physics. 104, 29-36. https://doi.org/10.1007/s00703-008-0012-5.

Quinn, P.K., Bates, T.S., Coffman, D.J., Miller, T.L., Johnson, J.E., Covert, D.S., Putaud, J.P., Neusüß, C., Novakov, T., 2000. A comparison of aerosol chemical and optical properties from the 1st and 2nd aerosol characterization experiments. Tellus B: Chemical and Physical Meteorology. 52, 239-257. https://doi.org/10.3402/tellusb.v52i2.16103.

Quinn, P.K., Coffman, D.J., Johnson, J.E., Upchurch, L.M., Bates, T.S., 2017. Small fraction of marine cloud condensation nuclei made up of sea spray aerosol. Nature Geoscience. 10, 674-679. https://doi.org/10.1038/ngeo3003.

Quinn, P.K., Coffman, D.J., Kapustin, V.N., Bates, T.S., Covert, D.S., 1998. Aerosol optical properties in the marine boundary layer during the First Aerosol Characterization Experiment (ACE 1) and the underlying chemical and physical aerosol properties. Journal of Geophysical Research : Atmospheres. 103, 16547-16563. https://doi.org/https://doi.org/10.1029/97JD02345.

Rai, D., Pattnaik, S., 2019. Evaluation of WRF planetary boundary layer parameterization schemes for simulation of monsoon depressions over India. Meteorology and Atmospheric Physics. 131, 1529-1548. https://doi.org/http://10.1007/s00703-019-0656-3.

Rajeev, K., Manoj Kumar, M., Sunilkumar, S.V., Sijikumar, S., Dual polarization micropulse lidar observations of the diurnal evolution of atmospheric boundary layer over a tropical coastal station. Proc.SPIE (2016), p. 98790V.

Ramachandran, R., Prakash, J.W.J., Gupta, K.S., Nair, K.N., Kunhikrishnan, P.K., 1994a. Variability of surface roughness and turbulence intensities at a coastal site in India. Boundary Layer Meteorology. 70, 385-400. https://doi.org/10.1007/BF00713777.

Ramachandran, R., Prakash, J.W.J., Gupta, K.S., Nair, K.N., Kunhikrishnan, P.K., 1994b. Variability of surface roughness and turbulence intensities at a coastal site in India. Boundary-Layer Meteorology. 70, 385-400. https://doi.org/http://10.1007/BF00713777.

Ramana, M., Krishnan, P., Kunhikrishnan, P.K., 2004a. Surface boundary layer characteristics over a tropical inland station : Seasonal features. Boundary Layer Meteorology. 111, 153-157. https://doi.org/10.1023/B:BOUN.0000010999.25921.1a.

Ramana, M., Krishnan, P., Muraleedharan, S., Kunhikrishnan, P.K., 2004b. Thermodynamic structure of the Atmospheric Boundary Layer over the Arabian Sea and the Indian Ocean during pre-INDOEX and INDOEX-FFP campaigns. Annales Geophysicae. 22, 2679-2691. https://doi.org/10.5194/angeo-22-2679-2004.

Ramana, M.V., Gupta, K.S., Ramachandran, R., Ravindran, S., Ameenulla, S., Raju, J.V.S., 1999. Latitude variation of boundary layer height over Indian Ocean during pre- and First Field Phase (FFP-98) of INDOEX. Current Science. 76, 898-902.

Ramana, M.V., Krishnan, P., Muraleedharan Nair, S., Kunhikrishnan, P.K., 2004. Thermodynamic structure of the Atmospheric Boundary Layer over the Arabian Sea and the Indian Ocean during pre-INDOEX and INDOEX-FFP campaigns. Ann. Geophys. 22, 2679-2691. https://doi.org/http://10.5194/angeo-22-2679-2004.

Ramanathan, V., Crutzen, P.J., Kiehl, J.T., Rosenfeld, D., 2001. Aerosols, Climate, and the Hydrological Cycle. Science. 294, 2119-2124. https://doi.org/doi:10.1126/science.1064034.

Ramaswamy, V., Collins, W., Haywood, J., Lean, J., Mahowald, N., Myhre, G., Naik, V., Shine, K.P., Soden, B., Stenchikov, G., Storelvmo, T., 2019. Radiative forcing of climate: the historical evolution of the radiative forcing concept, the forcing agents and their quantification, and applications. Meteorological Monographs. 59. https://doi.org/10.1175/AMSMONOGRAPHS-D-19-0001.1.

Ramdas, L., Atmanathan, S., 1932. The vertical distribution of air temperature near the ground at night. Journal of Beit. Geophys. 37, 116-117.

Ramis, C., Romero, R., A first numerical simulation of the development and structure of the sea breeze on the island of Mallorca. Annales Geophysicae (1995), p. 981.

Rao, K., Narasimha, R., Prabhu, A., 1996. Estimation of drag coefficient at low wind speeds over the monsoon trough land region during MONTBLEX-90. Geophysical Research Letters. 23, 2617-2620. https://doi.org/https://doi.org/10.1029/96GL02368.

Rao, P.A., Fuelberg, H.E., 2000. An investigation of convection behind the Cape Canaveral sea-breeze front. Monthly Weather Review. 128, 3437-3458. https://doi.org/10.1175/1520-0493(2000)128<3437:Aiocbt>2.0.Co;2.

Rao, P.S., 2005. Arabian Sea monsoon experiment: An overview. MAUSAM. 56, 1-6. https://doi.org/http://10.54302/mausam.v56i1.849.

Ratnam, M.V., Basha, S.G., 2010. A robust method to determine global distribution of atmospheric boundary layer top from COSMIC GPS RO measurements. Atmospheric Science Letters. 11, 216-222. https://doi.org/https://doi.org/10.1002/asl.277.

Raupach, M.R., Finnigan, J.J., 1997. The influence of topography on meteorogical variables and surface-atmosphere interactions. Journal of Hydrology. 190, 182-213. https://doi.org/https://doi.org/10.1016/S0022-1694(96)03127-7.

Reddy, N.N., Rao, Kusuma G., 2016. Roughness lengths at four stations within the micrometeorological network over the Indian monsoon region. Boundary Layer Meteorology. 158, 151-164. https://doi.org/10.1007/s10546-015-0080-2.

Reddy, T.V.R., Mehta, S.K., Ananthavel, A., Ali, S., Annamalai, V., Rao, D.N., 2021. Seasonal characteristics of sea breeze and thermal internal boundary layer over Indian east coast region. Meteorology and Atmospheric Physics. 133, 217-232. https://doi.org/10.1007/s00703-020-00746-1.

Reed, R.J., 1979. Cyclogenesis in Polar Air Streams. Monthly Weather Review. 107, 38-52. https://doi.org/10.1175/1520-0493(1979)107<0038:Cipas>2.0.Co;2.

Reichstein, M., Falge, E., Baldocchi, D., Papale, D., Aubinet, M., Berbigier, P., Bernhofer, C., Buchmann, N., Gilmanov, T., Granier, A., Grünwald, T., Havránková, K., Ilvesniemi, H., Janous, D., Knohl, A., Laurila, T., Lohila, A., Loustau, D., Matteucci, G., Meyers, T., Miglietta, F., Ourcival, J.-M., Pumpanen, J., Rambal, S., Rotenberg, E., Sanz, M., Tenhunen, J., Seufert, G., Vaccari, F., Vesala, T., Yakir, D., Valentini, R., 2005. On the separation of net ecosystem exchange into assimilation and ecosystem respiration: Review and improved algorithm. Global Change Biology. 11, 1424-1439. https://doi.org/https://doi.org/10.1111/j.1365-2486.2005.001002.x.

Renju, R., Raju, C.S., Mishra, M.K., Mathew, N., Rajeev, K., Moorthy, K.K., 2017. Atmospheric Boundary Layer Characterization Using Multiyear Ground-Based Microwave Radiometric Observations Over a Tropical Coastal Station. IEEE Transactions on Geoscience and Remote Sensing. 55, 6877-6882. https://doi.org/http://10.1109/TGRS.2017.2735626.

Ricchiazzi, P., Yang, S., Gautier, C., Sowle, D., 1998. SBDART: A research and teaching software tool for plane-parallel radiative transfer in the earth's atmosphere. Bulletin of the American Meteorological Society. 79, 2101-2114. https://doi.org/10.1175/1520-0477(1998)079<2101:Sarats>2.0.Co;2.

Rintoul, S.R., 2018. The global influence of localized dynamics in the Southern Ocean. Nature. 558, 209-218. https://doi.org/10.1038/s41586-018-0182-3.

Rittmeister, F., Ansmann, A., Engelmann, R., Skupin, A., Baars, H., Kanitz, T., Kinne, S., 2017. Profiling of Saharan dust from the Caribbean to western Africa – Part 1: Layering structures and optical properties from shipborne polarization/Raman lidar observations. Atmospheric Chemistry and Physics. 17, 12963-12983. https://doi.org/10.5194/acp-17-12963-2017.

Roh, W., Satoh, M., Hashino, T., Okamoto, H., Seiki, T., 2020. Evaluations of the thermodynamic phases of clouds in a cloud-system-resolving model using CALIPSO and a satellite simulator over the Southern Ocean. Journal of the Atmospheric Sciences. 77, 3781-3801. https://doi.org/10.1175/jas-d-19-0273.1.

Roth, M., 2000. Review of atmospheric turbulence over cities. Quarterly Journal of the Royal Meteorological Society. 126, 941-990. https://doi.org/https://doi.org/10.1002/qj.49712656409.

Roth, M., 1993. Turbulent transfer relationships over an urban surface. II: Integral statistics. Quarterly Journal of the Royal Meteorological Society. 119, 1105-1120. https://doi.org/https://doi.org/10.1002/qj.49711951312.

Rouault, M., Lutjeharms, J.R.E., 2000. Air-sea exchange over an Agulhas eddy at the subtropical convergence. Global Atmosphere and Ocean System. 7, 125-150.

Russell, L.M., Lenschow, D.H., Laursen, K.K., Krummel, P.B., Siems, S.T., Bandy, A.R., Thornton, D.C., Bates, T.S., 1998. Bidirectional mixing in an ACE 1 marine boundary layer overlain by a second turbulent layer. Journal of Geophysical Research : Atmospheres. 103, 16411-16432. https://doi.org/https://doi.org/10.1029/97JD03437.

Sallée, J.B., 2018. Southern Ocean Warming. Oceanography. 31, 52-62. https://doi.org/https://www.jstor.org/stable/26542651.

Sallée, J.B., Speer, K., Morrow, R., 2008. Response of the Antarctic Circumpolar Current to atmospheric variability. Journal of Climate. 21, 3020-3039. https://doi.org/https://doi.org/10.1175/2007JCLI1702.1.

Sallée., J.B., Shuckburgh, E., Bruneau, N., Meijers, A.J.S., Bracegirdle, T.J., Wang, Z., Roy, T., 2013. Assessment of Southern Ocean water mass circulation and characteristics in CMIP5 models: Historical bias and forcing response. Journal of Geophysical Research : Oceans. 118, 1830-1844. https://doi.org/https://doi.org/10.1002/jgrc.20135.

Sandeep, A., Rao, T.N., Ramkiran, C.N., Rao, S.V.B., 2014a. Differences in Atmospheric Boundary-Layer Characteristics Between Wet and Dry Episodes of the Indian Summer Monsoon. Boundary-Layer Meteorology. 153, 217-236. https://doi.org/10.1007/s10546-014-9945-z.

Sandeep, A., Rao, T.N., Ramkiran, C.N., Rao, S.V.B., 2014b. Differences in atmospheric boundary-layer characteristics between wet and dry episodes of the Indian summer

monsoon. Boundary Layer Meteorology. 153, 217-236. https://doi.org/10.1007/s10546-014-9945-z.

Sanjay, J., 2008. Assessment of Atmospheric Boundary-Layer Processes Represented in the Numerical Model MM5 for a Clear Sky Day Using LASPEX Observations. Boundary-Layer Meteorology. 129, 159-177. https://doi.org/http://10.1007/s10546-008-9298-6.

Sassen, K., 2002. Indirect climate forcing over the western US from Asian dust storms. Geophysical Research Letters. 29, 103-101-103-104. https://doi.org/https://doi.org/10.1029/2001GL014051.

Satheesh, S.K., Krishna Moorthy, K., Kaufman, Y.J., Takemura, T., 2006a. Aerosol optical depth, physical properties and radiative forcing over the Arabian Sea. Meteorology and Atmospheric Physics. 91, 45-62. https://doi.org/http://10.1007/s00703-004-0097-4.

Satheesh, S.K., Moorthy, K.K., Babu, S.S., Vinoj, V., Dutt, C.B.S., 2008. Climate implications of large warming by elevated aerosol over India. Geophysical Research Letters. 35. https://doi.org/https://doi.org/10.1029/2008GL034944.

Satheesh, S.K., Vinoj, V., Moorthy, K.K., 2006b. Vertical distribution of aerosols over an urban continental site in India inferred using a micro pulse lidar. Geophysical Research Letters. 33. https://doi.org/https://doi.org/10.1029/2006GL027729.

Sathyanadh, A., Prabhakaran, T., Patil, C., Karipot, A., 2017. Planetary boundary layer height over the Indian subcontinent: Variability and controls with respect to monsoon. Atmospheric Research. 195, 44-61. https://doi.org/https://doi.org/10.1016/j.atmosres.2017.05.010.

Satyanarayana, A.N.V., Lykossov, V.N., Mohanty, U.C., 2000. A Study On Atmospheric Boundary-Layer Characteristics At Anand, India Using Lsp Experimental Data Sets. Boundary-Layer Meteorology. 96, 393-419. https://doi.org/http://10.1023/A:1002699522932.

Satyanarayana, A.N.V., Lykossov, V.N., Mohanty, U.C., Machul'skaya, E.E., 2003. Parameterization of Land Surface Processes to Study Boundary Layer Characteristics over a Semiarid Region in Northwest India Journal of Applied Meteorology and Climatology. 42, 528-540. https://doi.org/https://doi.org/10.1175/1520-0450(2003)042<0528:POLSPT>2.0.CO;2.

Savijärvi, H., 2006. Radiative and turbulent heating rates in the clear-air boundary layer. Quarterly Journal of the Royal Meteorological Society. 132, 147-161. https://doi.org/https://doi.org/10.1256/qj.05.61.

Savijärvi, H., Matthews, S., 2004. Flow over Small Heat Islands: A Numerical Sensitivity Study. Journal of the Atmospheric Sciences. 61, 859-868. https://doi.org/10.1175/1520-0469(2004)061<0859:Foshia>2.0.Co;2.

Schmale, J., Baccarini, A., Thurnherr, I., Henning, S., Efraim, A., Regayre, L., Bolas, C., Hartmann, M., Welti, A., Lehtipalo, K., Aemisegger, F., Tatzelt, C., Landwehr, S., Modini, R.L., Tummon, F., Johnson, J.S., Harris, N., Schnaiter, M., Toffoli, A., Derkani, M., Bukowiecki, N., Stratmann, F., Dommen, J., Baltensperger, U., Wernli, H., Rosenfeld, D., Gysel-Beer, M., Carslaw, K.S., 2019. Overview of the Antarctic Circumnavigation Expedition: Study of preindustrial-like aerosols and their climate effects (ACE-SPACE). Bulletin of the American Meteorological Society. 100, 2260-2283. https://doi.org/https://doi.org/10.1175/BAMS-D-18-0187.1.

Schuddeboom, A., Varma, V., McDonald, A.J., Morgenstern, O., Harvey, M., Parsons, S., Field, P., Furtado, K., 2019. Cluster-based evaluation of model compensating errors: A case study of cloud radiative effect in the Southern Ocean. Geophysical Research Letters. 46, 3446-3453. https://doi.org/https://doi.org/10.1029/2018GL081686.

Seetha, C.J., Mehta, S.K., Kakkanattu, S.P., Purushotham, P., Betsy, K.B., Musaid, P.P., 2023. Characteristics of the atmospheric boundary layer during transient conditions of the Indian summer monsoon. Theoretical and Applied Climatology. https://doi.org/http://10.1007/s00704-023-04578-y.

Segal Rozenhaimer, M., Barton, N., Redemann, J., Schmidt, S., LeBlanc, S., Anderson, B., Winstead, E., Corr, C.A., Moore, R., Thornhill, K.L., Cullather, R.I., 2018a. Bias and Sensitivity of Boundary Layer Clouds and Surface Radiative Fluxes in MERRA-2 and Airborne Observations Over the Beaufort Sea During the ARISE Campaign. Journal of Geophysical Research: Atmospheres. 123, 6565-6580. https://doi.org/https://doi.org/10.1029/2018JD028349.

Segal Rozenhaimer, M., Barton, N., Redemann, J., Schmidt, S., LeBlanc, S., Anderson, B., Winstead, E., Corr, C.A., Moore, R., Thornhill, K.L., Cullather, R.I., 2018b. Bias and Sensitivity of Boundary Layer Clouds and Surface Radiative Fluxes in MERRA-2 and Airborne Observations Over the Beaufort Sea During the ARISE

Campaign. Journal of Geophysical Research: Atmospheres. 123, 6565-6580. https://doi.org/https://doi.org/10.1029/2018JD028349.

Seidel, D.J., Ao, C.O., Li, K., 2010. Estimating climatological planetary boundary layer heights from radiosonde observations: Comparison of methods and uncertainty analysis. Journal of Geophysical Research : Atmospheres. 115. https://doi.org/https://doi.org/10.1029/2009JD013680.

Seinfeld, J., Pandis, S., Atmospheric Chemistry and Physics, 430 pp., 1117 pp., 1153 pp. John Wiley & Sons, Inc., New York, USA (1998).

Sellers, P., Hall, F., Asrar, G., Strebel, D., Murphy, R., 1988. The first ISLSCP field experiment (FIFE). Bulletin of the American Meteorological Society. 69, 22-27.

Sen Gupta, A., Santoso, A., Taschetto, A.S., Ummenhofer, C.C., Trevena, J., England, M.H., 2009. Projected changes to the Southern Hemisphere ocean and sea ice in the IPCC AR4 climate models. Journal of Climate. 22, 3047-3078. https://doi.org/https://doi.org/10.1175/2008JCLI2827.1.

Shao, Y., 1992. Turbulent dispersion in coastal atmospheric boundary layers: An application of a Lagrangian model. Boundary-Layer Meteorology. 59, 363-385. https://doi.org/10.1007/BF02215459.

Shao, Y., Hacker, J.M., Schwerdtfeger, P., 1991. The structure of turbulence in a coastal atmospheric boundary layer. Quarterly Journal of the Royal Meteorological Society. 117, 1299-1324. https://doi.org/https://doi.org/10.1002/qj.49711750209.

Sikka, D.R., Narasimha, R., 1995. Genesis of the monsoon trough boundary layer experiment (MONTBLEX). Proceedings of the Indian Academy of Sciences - Earth and Planetary Sciences. 104, 157-187. https://doi.org/http://10.1007/BF02839270.

Simmonds, I., Lim, E.-P., 2009. Biases in the calculation of Southern Hemisphere mean baroclinic eddy growth rate. Geophysical Research Letters. 36. https://doi.org/https://doi.org/10.1029/2008GL036320.

Simmonds., I., 2003. Modes of atmospheric variability over the Southern Ocean. Journal of Geophysical Research : Atmospheres. 108, SOV 5-1-SOV 5-30. https://doi.org/https://doi.org/10.1029/2000JC000542.

Simpson, R.L., Strickland, J.H., Barr, P.W., 1977. Features of a separating turbulent boundary layer in the vicinity of separation. Journal of Fluid Mechanics. 79, 553-594. https://doi.org/10.1017/S0022112077000329.

Sinclair, V., Belcher, S.E., Gray, S., 2010. Synoptic controls on boundary layer characteristics. Boundary Layer Meteorology. 134. https://doi.org/10.1007/s10546-009-9455-6.

Singh, A., Srivastava, R., Rastogi, N., Singh, D., 2016. Absorbing and scattering aerosols over the source region of biomass burning emissions: Implications in the assessment of optical and radiative properties. Atmospheric Environment. 127, 61-68. https://doi.org/https://doi.org/10.1016/j.atmosenv.2015.12.029.

Singh, S., Nath, S., Kohli, R., Singh, R., 2005. Aerosols over Delhi during pre-monsoon months: Characteristics and effects on surface radiation forcing. Geophysical Research Letters. 32. https://doi.org/https://doi.org/10.1029/2005GL023062.

Singha, A., Sadr, R., 2012. Characteristics of surface layer turbulence in coastal area of Qatar. Environmental Fluid Mechanics. 12, 515-531. https://doi.org/10.1007/s10652-012-9242-7.

Siva Kumar, N., KiranKumar, N.V.P., Rama Gopal, K., Balakrishnaiah, G., Rajaobul Reddy, K., 2021. Characteristics of atmospheric surface layer during winter season over Anantapur (14.62° N, 77.65° E), a semi-arid location in peninsular India. Journal of Atmospheric and Solar Terrestrial Physics. 216, 105554. https://doi.org/https://doi.org/10.1016/j.jastp.2021.105554.

Siva Kumar Reddy, N., KiranKumar, N.V.P., Rama Gopal, K., Balakrishnaiah, G., Rajaobul Reddy, K., 2021. Characteristics of atmospheric surface layer during winter season over Anantapur (14.62° N, 77.65° E), a semi-arid location in peninsular India. Journal of Atmospheric and Solar Terrestrial Physics. 216, 105554. https://doi.org/https://doi.org/10.1016/j.jastp.2021.105554.

Sivaramakrishnan, S., Saxena, S., Vernekar, K.G., 1992. Characteristics of turbulent fluxes of sensible heat and momentum in the surface boundary layer during the Indian summer monsoon. Boundary Layer Meteorology. 60, 95-108. https://doi.org/10.1007/BF00122063.

Slinn, S., Slinn, W., 1981. Modeling of atmospheric particulate deposition to natural waters. Atmospheric Pollutants in Natural Waters. p 23-53.

Small, R.J., deSzoeke, S.P., Xie, S.P., O'Neill, L., Seo, H., Song, Q., Cornillon, P., Spall, M., Minobe, S., 2008. Air–sea interaction over ocean fronts and eddies. Dynamics of Atmospheres and Oceans. 45, 274-319. https://doi.org/https://doi.org/10.1016/j.dynatmoce.2008.01.001.

Small, R.J., Tomas, R.A., Bryan, F.O., 2014. Storm track response to ocean fronts in a global high-resolution climate model. Climate Dynamics. 43, 805-828. https://doi.org/10.1007/s00382-013-1980-9.

Smedman, A.-S., 1988. Observations of a multi-level turbulence structure in a very stable atmospheric boundary layer. Boundary Layer Meteorology. 44, 231-253. https://doi.org/10.1007/BF00116064.

Smith, N.R., Zhaoqian, D., Kerry, K.R., Wright, S., 1984. Water masses and circulation in the region of Prydz Bay, Antarctica. Deep Sea Research Part A. Oceanographic Research Papers. 31, 1121-1147. https://doi.org/https://doi.org/10.1016/0198-0149(84)90016-5.

Smith, T.M., Reynolds, R.W., 2004a. Improved Extended Reconstruction of SST (1854–1997) Journal of Climate. 17, 2466-2477. https://doi.org/https://doi.org/10.1175/1520-0442(2004)017<2466:IEROS>2.0.CO;2.

Smith, T.M., Reynolds, R.W., 2004b. Improved extended reconstruction of SST (1854–1997). Journal of Climate. 17, 2466-2477. https://doi.org/10.1175/1520-0442(2004)017<2466:Ieros>2.0.Co;2.

Sokolov, S., Rintoul, S.R., 2002. Structure of Southern Ocean fronts at 140°E. Journal of Marine Systems. 37, 151-184. https://doi.org/https://doi.org/10.1016/S0924-7963(02)00200-2.

Solanki, R., Guo, J., Li, J., Singh, N., Guo, X., Han, Y., Lv, Y., Zhang, J., Liu, B., 2021. Atmospheric boundary layer height variation over mountainous and urban sites in Beijing as derived from radar wind-profiler measurements. Boundary Layer Meteorology. 181, 125-144. https://doi.org/10.1007/s10546-021-00639-9.

Solanki, R., Macatangay, R., Sakulsupich, V., Sonkaew, T., Mahapatra, P.S., 2019a. Mixing layer height retrievals from MiniMPL measurements in the Chiang Mai valley: Implications for particulate matter pollution. Frontiers in Earth Science. 7. https://doi.org/10.3389/feart.2019.00308.

Solanki, R., Singh, N., Kiran Kumar, N.V.P., Rajeev, K., Dhaka, S.K., 2016a. Time variability of surface-layer characteristics over a mountain ridge in the central Himalayas during the spring season. Boundary Layer Meteorology. 158, 453-471. https://doi.org/10.1007/s10546-015-0098-5.

Solanki, R., Singh, N., Kiran Kumar, N.V.P., Rajeev, K., Dhaka, S.K., 2016b. Time variability of surface layer characteristics over a mountain ridge in the central

Himalayas during the spring season. Boundary Layer Meteorology. 158, 453-471. https://doi.org/10.1007/s10546-015-0098-5.

Solanki, R., Singh, N., Kiran Kumar, N.V.P., Rajeev, K., Imasu, R., Dhaka, S.K., 2019b. Impact of mountainous topography on surface-layer parameters during weak mean-flow conditions. Boundary Layer Meteorology. 172, 133-148. https://doi.org/10.1007/s10546-019-00438-3.

Sorbjan, Z., 1989a. Local similarity functions derived from second-moment budgets in the convective boundary layer. Boundary Layer Meteorology. 46, 1-11. https://doi.org/10.1007/BF00118443.

Sorbjan, Z., 1989b. Structure of the atmospheric boundary layer.

Srinivas, C.V., Venkatesan, R., Bagavath Singh, A., 2007. Sensitivity of mesoscale simulations of land–sea breeze to boundary layer turbulence parameterization. Atmospheric Environment. 41, 2534-2548. https://doi.org/https://doi.org/10.1016/j.atmosenv.2006.11.027.

Srivastava, R., Asutosh, A., Sabu, P., Anilkumar, N., 2021. Investigation of black carbon characteristics over Southern Ocean: contribution of fossil fuel and biomass burning. Environmental Pollution. 276, 116645. https://doi.org/https://doi.org/10.1016/j.envpol.2021.116645.

Srivastava, R., Ramachandran, S., Rajesh, T.A., Kedia, S., 2011. Aerosol radiative forcing deduced from observations and models over an urban location and sensitivity to single scattering albedo. Atmospheric Environment. 45, 6163-6171. https://doi.org/https://doi.org/10.1016/j.atmosenv.2011.08.015.

Srivastava, R., Ramesh, R., Prakash, S., Anilkumar, N., Sudhakar, M., 2007. Oxygen isotope and salinity variations in the Indian sector of the Southern Ocean. Geophysical Research Letters. 34. https://doi.org/https://doi.org/10.1029/2007GL031790.

Stammer, D., 1998. On eddy characteristics, eddy transports, and mean flow properties. Journal of Physical Oceanography. 28, 727-739. https://doi.org/https://doi.org/10.1175/1520-0485(1998)028%3C0727:OECETA%3E2.0.CO;2.

Stamnes, K., Tsay, S.-C., Wiscombe, W., Laszlo, I., 2000. DISORT, a general-purpose Fortran program for discrete-ordinate-method radiative transfer in scattering and emitting layered media: documentation of methodology.

Stevens, B., 2000. Cloud transitions and decoupling in shear-free stratocumulus-topped boundary layers. Geophysical Research Letters. 27, 2557-2560. https://doi.org/https://doi.org/10.1029/1999GL011257.

Stevens, B., Duan, J., McWilliams, J.C., Münnich, M., Neelin, J.D., 2002. Entrainment, rayleigh friction, and boundary layer winds over the tropical Pacific. Journal of Climate. 15, 30-44. https://doi.org/10.1175/1520-0442(2002)015<0030:Erfabl>2.0.Co;2.

Steyn, D.G., 2003. Scaling the Vertical Structure of Sea Breezes Revisited. Boundary-Layer Meteorology. 107, 177-188. https://doi.org/http://10.1023/A:1021568117280.

Stull, R., 1988. An introduction to boundary layer meteorology. Kluwer Academic Publishers, Dordrecht, Netherlands.

Stull, R., Eloranta, E., 1984. Boundary Layer Experiment—1983. Bulletin of the American Meteorological Society. 65, 450-456. https://doi.org/10.1175/1520-0477(1984)065<0450:BLE>2.0.CO;2.

Su, T., Li, Z., Li, C., Li, J., Han, W., Shen, C., Tan, W., Wei, J., Guo, J., 2020. The significant impact of aerosol vertical structure on lower atmosphere stability and its critical role in aerosol–planetary boundary layer (PBL) interactions. Atmospheric Chemistry and Physics. 20, 3713-3724. https://doi.org/10.5194/acp-20-3713-2020.

Subrahamanyam, D., Radhika , R., 2003a. Structural characteristics of marine atmospheric boundary layer (MABL) and its associated dynamics over the central Arabian sea during INDOEX, IFP-99 campaign. Current Science. 1334-1340. https://doi.org/http://www.jstor.org/stable/24108137.

Subrahamanyam, D., Radhika , R., 2003b. Structural characteristics of marine atmospheric boundary layer (MABL) and its associated dynamics over the central Arabian sea during INDOEX, ifp-99 campaign. Current Science. 85, 1334-1340.

Subrahamanyam, D., Ramachandran, R., Gupta, K., Mandal, T., 2003. Variability of mixed-layer heights over the Indian ocean and central Arabian sea during INDOEX, IFP-99. Boundary Layer Meteorology. 107, 683-695. https://doi.org/http://10.1023/A:1022811512160.

Subrahamanyam, D.B., Ramachandran, R., Gupta, K.S., Mandal, T.K., 2003. Variability of Mixed-Layer Heights over the Indian Ocean and Central Arabian Sea during INDOEX, IFP-99. Boundary-Layer Meteorology. 107, 683-695. https://doi.org/10.1023/A:1022811512160.

Sudeepkumar, B.L., Babu, C.A., Varikoden, H., 2020. Atmospheric boundary layer height and surface parameters: Trends and relationships over the west coast of India. Atmospheric Research. 245, 105050. https://doi.org/https://doi.org/10.1016/j.atmosres.2020.105050.

Svensson, G., Holtslag, A.A.M., Kumar, V., Mauritsen, T., Steeneveld, G.J., Angevine, W.M., Bazile, E., Beljaars, A., de Bruijn, E.I.F., Cheng, A., Conangla, L., Cuxart, J., Ek, M., Falk, M.J., Freedman, F., Kitagawa, H., Larson, V.E., Lock, A., Mailhot, J., Masson, V., Park, S., Pleim, J., Söderberg, S., Weng, W., Zampieri, M., 2011. Evaluation of the Diurnal Cycle in the Atmospheric Boundary Layer Over Land as Represented by a Variety of Single-Column Models: The Second GABLS Experiment. Boundary-Layer Meteorology. 140, 177-206. https://doi.org/10.1007/s10546-011-9611-7.

Swart, N.C., Gille, S.T., Fyfe, J.C., Gillett, N.P., 2018. Recent Southern Ocean warming and freshening driven by greenhouse gas emissions and ozone depletion. Nature Geoscience. 11, 836-841. https://doi.org/https://doi.org/10.1038/s41561-018-0226-1.

Takashi, K., Fumitaka, S., Yuki, H., Optical properties of Kosa aerosols estimated from multispectral polarization. Proc.SPIE (2003), pp. 413-418.

Talbot, C., Augustin, P., Leroy, C., Willart, V., Delbarre, H., Khomenko, G., 2007. Impact of a sea breeze on the boundary-layer dynamics and the atmospheric stratification in a coastal area of the North Sea. Boundary Layer Meteorology. 125, 133-154. https://doi.org/10.1007/s10546-007-9185-6.

Talley, L.D., Pickard, G.L., Emery, W.J., Swift, J.H., 2011. Southern Ocean, in: Talley, L.D., Pickard, G.L., Emery, W.J., Swift, J.H. (Eds.), Descriptive Physical Oceanography (Sixth Edition), Academic Press, Boston, pp. 437-471. https://doi.org/https://doi.org/10.1016/B978-0-7506-4552-2.10013-7.

Tang, G., Zhu, X., Xin, J., Hu, B., Song, T., Sun, Y., Zhang, J., Wang, L., Cheng, M., Chao, N., Kong, L., Li, X., Wang, Y., 2017. Modelling study of boundary-layer ozone over northern China - Part I: Ozone budget in summer. Atmospheric Research. 187, 128-137. https://doi.org/https://doi.org/10.1016/j.atmosres.2016.10.017.

Thomas, M.A., Devasthale, A., Kahnert, M., 2022. Marine aerosol properties over the Southern Ocean in relation to the wintertime meteorological conditions. Atmospheric Chemistry and Physics. 22, 119-137. https://doi.org/10.5194/acp-22-119-2022.

Thompson, A.F., Richards, K.J., 2011. Low frequency variability of Southern Ocean jets. Journal of Geophysical Research : Oceans. 116. https://doi.org/https://doi.org/10.1029/2010JC006749.

Timbal, B., Drosdowsky, W., 2013. The relationship between the decline of Southeastern Australian rainfall and the strengthening of the subtropical ridge. International Journal of Climatology. 33, 1021-1034. https://doi.org/https://doi.org/10.1002/joc.3492.

Trenberth, K.E., 2011. Changes in precipitation with climate change. Climate Research. 47, 123-138. https://doi.org/http://dx.doi.org/10.3354/cr00953.

Trenberth, K.E., Fasullo, J.T., 2010. Simulation of present-day and twenty-first-century energy budgets of the Southern Oceans. Journal of Climate. 23, 440-454.

Trenberth, K.E., Fasullo, J.T., Kiehl, J., 2009. Earth's global energy budget. Bulletin of the American Meteorological Society. 90, 311-324. https://doi.org/10.1175/2008bams2634.1.

Trini Castelli, S., Falabino, S., 2013. Analysis of the parameterization for the wind-velocity fluctuation standard deviations in the surface layer in low-wind conditions. Meteorology and Atmospheric Physics. 119, 91-107. https://doi.org/10.1007/s00703-012-0219-3.

Trini Castelli, S., Falabino, S., Mortarini, L., Ferrero, E., Richiardone, R., Anfossi, D., 2014. Experimental investigation of surface-layer parameters in low wind-speed conditions in a suburban area. Quarterly Journal of the Royal Meteorological Society. 140, 2023-2036. https://doi.org/https://doi.org/10.1002/qj.2271.

Truong, S.C.H., Huang, Y., Lang, F., Messmer, M., Simmonds, I., Siems, S.T., Manton, M.J., 2020a. A climatology of the marine atmospheric boundary layer over the Southern Ocean from four field campaigns during 2016–2018. Journal of Geophysical Research : Atmospheres. 125. https://doi.org/https://doi.org/10.1029/2020JD033214.

Truong, S.C.H., Huang, Y., Lang, F., Messmer, M., Simmonds, I., Siems, S.T., Manton, M.J., 2020b. A climatology of the marine atmospheric boundary layer over the Southern Ocean from four field campaigns during 2016–2018. Journal of Geophysical Research : Atmospheres. 125, e2020JD033214. https://doi.org/https://doi.org/10.1029/2020JD033214.

Tsvang, L.R., Zubkovskii, S.L., Kader, B.A., Kallistratova, M.A., Foken, T., Gerstmann, V., Przadka, A., Pretel, Y., Zeleny, Y., Keder, J., 1985. International turbulence

comparison experiment (ITCE-81). Boundary Layer Meteorology. 31, 325-348. https://doi.org/10.1007/BF00120834.

Tucker, S.C., Banta, R.M., Langford, A.O., Senff, C.J., Brewer, W.A., Williams, E.J., Lerner, B.M., Osthoff, H.D., Hardesty, R.M., 2010. Relationships of coastal nocturnal boundary layer winds and turbulence to Houston ozone concentrations during TexAQS 2006. Journal of Geophysical Research : Atmospheres. 115. https://doi.org/https://doi.org/10.1029/2009JD013169.

Turner, D.B., 2020. Workbook of atmospheric dispersion estimates: an introduction to dispersion modeling. CRC press.

Ulrickson, B.L., 1992. Effects of surface property variations on simulated daytime airflow over coastal Southern California. Monthly Weather Review. 120, 2264-2279. https://doi.org/10.1175/1520-0493(1992)120<2264:Eospvo>2.0.Co;2.

Večenaj, Ž., De Wekker, S.F.J., 2015. Determination of non-stationarity in the surface layer during the T-REX experiment. Quarterly Journal of the Royal Meteorological Society. 141, 1560-1571. https://doi.org/https://doi.org/10.1002/qj.2458.

Venkata Ramana, M., Krishnan, P., Kunhikrishnan, P.K., 2004. Surface boundary layer characteristics over a tropical inland station: Seasonal features. Boundary Layer Meteorology. 111, 153-157. https://doi.org/10.1023/B:BOUN.0000010999.25921.1a.

Venkatram, A., 1977. A model of internal boundary-layer development. Boundary-Layer Meteorology. 11, 419-437. https://doi.org/http://10.1007/BF02185869.

Vernekar, K.G., Sinha, S., Sadani, L.K., Sivaramakrishnan, S., Parasnis, S.S., Mohan, B., Dharmaraj, S., Patil, M.N., Pillai, J.S., Murthy, B.S., Debaje, S.B., Bagavathsingh, A., 2003. An Overview of the Land Surface Processes Experiment (Laspex) over a Semi-Arid Region of India. Boundary-Layer Meteorology. 106, 561-572. https://doi.org/http://10.1023/A:1021283503661.

Vickers, D., Mahrt, L., 1997. Fetch limited drag coefficients. Boundary Layer Meteorology. 85, 53-79. https://doi.org/10.1023/A:1000472623187.

Vignon, É., Alexander, S.P., DeMott, P.J., Sotiropoulou, G., Gerber, F., Hill, T.C.J., Marchand, R., Nenes, A., Berne, A., 2021. Challenging and improving the simulation of mid-level mixed-phase clouds over the high-latitude Southern Ocean. Journal of Geophysical Research : Atmospheres. 126. https://doi.org/https://doi.org/10.1029/2020JD033490.

Vignon, É., Besic, N., Jullien, N., Gehring, J., Berne, A., 2019a. Microphysics of snowfall over coastal east Antarctica simulated by polar WRF and observed by radar. Journal of Geophysical Research : Atmospheres. 124, 11452-11476. https://doi.org/https://doi.org/10.1029/2019JD031028.

Vignon, É., Traullé, O., Berne, A., 2019b. On the fine vertical structure of the low troposphere over the coastal margins of East Antarctica. Atmospheric Chemistry and Physics. 19, 4659-4683. https://doi.org/10.5194/acp-19-4659-2019.

Vinoj, V., Babu, S.S., Satheesh, S.K., Moorthy, K., Kaufman, Y.J., 2004. Radiative forcing by aerosols over the Bay of Bengal region derived from shipborne, island-based, and satellite (Moderate-Resolution Imaging Spectroradiometer) observations. Journal of Geophysical Research : Atmospheres. 109. https://doi.org/https://doi.org/10.1029/2003JD004329.

Von Engeln, A., Teixeira, J., Wickert, J., Buehler, S.A., 2005. Using CHAMP radio occultation data to determine the top altitude of the planetary boundary layer. Journal of Geophysical Research : Atmospheres. 32. https://doi.org/https://doi.org/10.1029/2004GL022168.

Wall, C.J., Hartmann, D.L., Ma, P.-L., 2017. Instantaneous Linkages between Clouds and Large-Scale Meteorology over the Southern Ocean in Observations and a Climate Model. Journal of Climate. 30, 9455-9474. https://doi.org/10.1175/jcli-d-17-0156.1.

Wang, H., You, Y., Kulie, M., 2018. Global virga precipitation distribution derived from three spaceborne radars and its contribution to the false radiometer precipitation detection. Geophysical Research Letters. 45, 4446-4455. https://doi.org/https://doi.org/10.1029/2018GL077891.

Wang, X., Wang, K., 2016. Homogenized variability of radiosonde-derived atmospheric boundary layer height over the global land surface from 1973 to 2014. . Journal of Climate. 29, 6893-6908. https://doi.org/10.1175/jcli-d-15-0766.1.

Wang, Z., Siems, S.T., Belusic, D., Manton, M.J., Huang, Y., 2015. A Climatology of the Precipitation over the Southern Ocean as Observed at Macquarie Island. Journal of Applied Meteorology and Climatology. 54, 2321-2337.

Warren, S.G., Clarke, A.D., 1990. Soot in the atmosphere and snow surface of Antarctica. Journal of Geophysical Research : Atmospheres. 95, 1811-1816. https://doi.org/https://doi.org/10.1029/JD095iD02p01811.

Webb, P., 2021. Introduction to oceanography. Roger Williams University.

Weber, S., Kordowski, K., 2010. Comparison of atmospheric turbulence characteristics and turbulent fluxes from two urban sites in Essen, Germany. Theoretical and Applied Climatology. 102, 61-74. https://doi.org/10.1007/s00704-009-0240-8.

Wei, J., Tang, G., Zhu, X., Wang, L., Liu, Z., Cheng, M., Münkel, C., Li, X., Wang, Y., 2018. Thermal internal boundary layer and its effects on air pollutants during summer in a coastal city in North China. Journal of Environmental Sciences. 70, 37-44. https://doi.org/https://doi.org/10.1016/j.jes.2017.11.006.

Wichink Kruit, R.J., Holtslag, A.A.M., Tijm, A.B.C., 2004. Scaling of the sea-breeze strength with observations in the Netherlands. Boundary Layer Meteorology. 112, 369-380. https://doi.org/10.1023/B:BOUN.0000027904.18874.75.

Wilczak, J., Dabberdt, W., Kropfli, R., 1991. Observations and numerical model simulations of the atmospheric boundary layer in the Santa Barbara coastal region. Journal of Applied Meteorology and Climatology. 652-673.

Wilczak, J., Gossard, E., Neff, W., Eberhard, W., 1996. Ground-based remote sensing of the atmospheric boundary layer: 25 years of progress. Boundary Layer Meteorology. 321-349.

Wilczak, J.M., Gossard, E.E., Neff, W.D., Eberhard, W.L., 1996. Ground-based remote sensing of the atmospheric boundary layer: 25 years of progress. Boundary-Layer Meteorology. 78, 321-349. https://doi.org/http://10.1007/BF00120940.

Wilczak, J.M., Oncley, S.P., Stage, S.A., 2001. Sonic anemometer tilt correction algorithms. Boundary Layer Meteorology. 99, 127-150. https://doi.org/10.1023/A:1018966204465.

Willis, G.E., Deardorff, J.W., 1974. A laboratory model of the unstable planetary boundary layer. Journal of Atmospheric Sciences. 31, 1297-1307. https://doi.org/10.1175/1520-0469(1974)031<1297:Almotu>2.0.Co;2.

Wilson, J.D., 2008. Monin-Obukhov functions for standard deviations of velocity. Boundary Layer Meteorology. 129, 353-369. https://doi.org/10.1007/s10546-008-9319-5.

Winker, D.M., Vaughan, M.A., Omar, A., Hu, Y., Powell, K.A., Liu, Z., Hunt, W.H., Young, S.A., 2009. Overview of the CALIPSO Mission and CALIOP data processing algorithms. Journal of Atmospheric and Oceanic Technology. 26, 2310-2323. https://doi.org/10.1175/2009jtecha1281.1.

Winning, T.E., Chen, Y.-L., Xie, F., 2017. Estimation of the marine boundary layer height over the central North Pacific using GPS radio occultation. Atmospheric Research. 183, 362-370. https://doi.org/https://doi.org/10.1016/j.atmosres.2016.08.005.

Winston Prakash, J.J., Ramchandran, R., Nair, K.N., Gupta, K.S., Kunhikrishnan, P.K., 1993a. On the spectral behaviour of atmospheric boundary-layer parameters at Thumba, India. 119, 187-197. https://doi.org/https://doi.org/10.1002/qj.49711950908.

Winston Prakash, J.J., Ramchandran, R., Nair, K.N., Gupta, K.S., Kunhikrishnan, P.K., 1993b. On the spectral behaviour of atmospheric boundary-layer parameters at Thumba, India. Quarterly Journal of the Royal Meteorological Society. 119, 187-197. https://doi.org/https://doi.org/10.1002/qj.49711950908.

Wood, C.R., Lacser, A., Barlow, J.F., Padhra, A., Belcher, S.E., Nemitz, E., Helfter, C., Famulari, D., Grimmond, C.S.B., 2010. Turbulent flow at 190 m height above London during 2006–2008: a climatology and the applicability of similarity theory. Boundary Layer Meteorology. 137, 77-96. https://doi.org/10.1007/s10546-010-9516-x.

Wood, R., Bretherton, C.S., 2004. Boundary Layer Depth, Entrainment, and Decoupling in the Cloud-Capped Subtropical and Tropical Marine Boundary Layer. Journal of Climate. 17, 3576-3588. https://doi.org/10.1175/1520-0442(2004)017<3576:Bldead>2.0.Co;2.

Wood, R., Bretherton, C.S., 2006. On the relationship between stratiform low cloud cover and lower-tropospheric stability. Journal of Climate. 19, 6425-6432. https://doi.org/https://doi.org/10.1175/JCLI3988.1.

Wyngaard, J.C., 1990. Scalar fluxes in the planetary boundary layer - Theory, modeling, and measurement. Boundary Layer Meteorology. 50, 49-75. https://doi.org/10.1007/BF00120518.

Wyngaard, J.C., 2010. Turbulence in the Atmosphere. Cambridge University Press.

Wyngaard, J.C., Coté, O.R., 1972. Cospectral similarity in the atmospheric surface layer. Quarterly Journal of the Royal Meteorological Society. 98, 590-603. https://doi.org/https://doi.org/10.1002/qj.49709841708.

Wyngaard, J.C., Coté, O.R., Izumi, Y., 1971. Local free convection, similarity, and the budgets of shear stress and heat flux. Journal of Atmospheric Sciences. 28, 1171-1182. https://doi.org/10.1175/1520-0469(1971)028<1171:Lfcsat>2.0.Co;2.

Xu, Y., Zhou, C., Li, Z., Zhang, W., 1997. Turbulent structure and local similarity in the tower layer over the Nanjing area. Boundary Layer Meteorology. 82, 1-21.

Yang, T., Wang, H., Li, H., Guo, X., Wang, D., Chen, X., Wang, F., Xin, J., Sun, Y., Wang, Z., 2022. Quantitative attribution of wintertime haze in coastal east China to local emission and regional intrusion under a stagnant internal boundary layer. Atmospheric Environment. 276, 119006. https://doi.org/https://doi.org/10.1016/j.atmosenv.2022.119006.

Yashvant, D.A.S., Uma Charan, M., 2021. Simulation of boundary layer characteristics using 1-D PBL model over Goa during ARMEX-I. Contributions to Geophysics and Geodesy. 37.

Yersel, M., Goble, R., 1986. Roughness effects on urban turbulence parameters. Boundary Layer Meteorology. 37, 271-284. https://doi.org/10.1007/BF00122989.

Yue, P., Zhang, Q., Wang, R., Li, Y., Wang, S., 2015. Turbulence intensity and turbulent kinetic energy parameters over a heterogeneous terrain of Loess Plateau. Advances in Atmospheric Sciences. 32, 1291-1302. https://doi.org/10.1007/s00376-015-4258-9.

Yum, S.S., Hudson, J.G., 2005. Adiabatic predictions and observations of cloud droplet spectral broadness. Atmospheric Research. 73, 203-223. https://doi.org/https://doi.org/10.1016/j.atmosres.2004.10.006.

Yusup, Y.B., Daud, W.R.W., Zaharim, A., Talib, M.Z.M., 2008. Structure of the atmospheric surface layer over an industrialized equatorial area. Atmospheric Research. 90, 70-77. https://doi.org/https://doi.org/10.1016/j.atmosres.2008.04.003.

Zeman, O., Jensen, N.O., 1987. Modification of turbulence characteristics in flow over hills. Quarterly Journal of the Royal Meteorological Society. 113, 55-80. https://doi.org/https://doi.org/10.1002/qj.49711347505.

Zeng, X., Brunke, M.A., Zhou, M., Fairall, C., Bond, N.A., Lenschow, D.H., 2004. Marine atmospheric boundary layer height over the eastern pacific: Data analysis and model evaluation. Journal of Climate. 17, 4159-4170. https://doi.org/https://doi.org/10.1175/JCLI3190.1.

Zhang, H., Chen, J., Park, S.-U., 2001. Turbulence structure in unstable conditions over various surfaces. Boundary Layer Meteorology. 100, 243-261. https://doi.org/10.1023/A:1019223316895.

Zhang, J.A., Katsaros, K.B., Black, P.G., Lehner, S., French, J.R., Drennan, W.M., 2008. Effects of Roll Vortices on Turbulent Fluxes in the Hurricane Boundary Layer. Boundary-Layer Meteorology. 128, 173-189. https://doi.org/http://10.1007/s10546-008-9281-2.

Zhang, L., Dawes, W.R., Walker, G.R., 2001. Response of mean annual evapotranspiration to vegetation changes at catchment scale. Water Resources Research. 37, 701-708. https://doi.org/https://doi.org/10.1029/2000WR900325.

Zhang, L., Vet, R., 2006. A review of current knowledge concerning size-dependent aerosol removal. China Particuology. 04, 272-282. https://doi.org/10.1142/S1672251506000546.

Zhang, M., Marandino, C.A., Yan, J., Lin, Q., Park, K., Xu, G., 2021. DMS sea-to-air fluxes and their influence on sulfate aerosols over the Southern Ocean, south-east Indian Ocean and north-west Pacific Ocean. Environmental Chemistry Letters. 18, 193-201. https://doi.org/https://doi.org/10.1071/EN21003.

Zhang, W., Guo, J., Miao, Y., Liu, H., Song, Y., Fang, Z., He, J., Lou, M., Yan, Y., Li, Y., Zhai, P., 2018. On the summertime planetary boundary layer with different thermodynamic stability in China: A radiosonde perspective. Journal of Climate. 31, 1451-1465. https://doi.org/10.1175/jcli-d-17-0231.1.

Zheng, Y., Li, Z., 2019a. Episodes of warm-air advection causing cloud-surface decoupling during the MARCUS. Journal of Geophysical Research : Atmospheres. 124, 12227-12243. https://doi.org/https://doi.org/10.1029/2019JD030835.

Zheng, Y., Li, Z., 2019b. Episodes of Warm-Air Advection Causing Cloud-Surface Decoupling During the MARCUS. Journal of Geophysical Research: Atmospheres. 124, 12227-12243. https://doi.org/https://doi.org/10.1029/2019JD030835.

Zheng, Y., Rosenfeld, D., Li, Z., 2018a. Estimating the Decoupling Degree of Subtropical Marine Stratocumulus Decks From Satellite. Journal of Geophysical Research: Atmospheres. 45, 12,560-512,568. https://doi.org/https://doi.org/10.1029/2018GL078382.

Zheng, Y., Rosenfeld, D., Li, Z., 2018b. The Relationships Between Cloud Top Radiative Cooling Rates, Surface Latent Heat Fluxes, and Cloud-Base Heights in Marine Stratocumulus. Journal of Geophysical Research: Atmospheres. 123, 11,678-611,690. https://doi.org/https://doi.org/10.1029/2018JD028579.